PHYSICAL MODELING TECHNIQUES FOR MISSILE AND OTHER PROTECTIVE STRUCTURES

Papers Submitted for Presentation During the
American Society of Civil Engineers
National Spring Convention
Las Vegas, April 1982

Sponsored By the ASCE Engineering Mechanics Division
Committee on Experimental Analysis and Instrumentation

Edited By: T. Krauthammer and C. D. Sutton

REPRODUCTION QUALITY NOTICE

This document is the best quality available. The copy furnished to DTIC contained pages that may have the following quality problems:

- Pages smaller or larger than normal.
- Pages with background color or light colored printing.
- Pages with small type or poor printing; and or
- Pages with continuous tone material or color photographs.

Due to various output media available these conditions may or may not cause poor legibility in the microfiche or hardcopy output you receive.

☐ If this block is checked, the copy furnished to DTIC contained pages with color printing, that when reproduced in Black and White, may change detail of the original copy.

Contents:-

Collected Papers
on
Physical Modeling Techniques for Missile and Other Protective Structures

Incl "Determination of Soil Properties Through Ground Motion Analysis", by John Frye and Norman Lipner, Defense and Space Systems Group, TRW, Inc., Redondo Beach, CA. -- 40 pages (includes abstract).

"Survey of Experimental Work on the Dynamic Behavior of Concrete Structures in the USSR", by Leonid Millstein and Gajanan M. Sabnis, Sheladia Associates, Inc., Riverdale, MD. -- 35 pages.

10/14/82

Preface

On April 27, 1982, at the 1982 American Society of Civil Engineers National Spring Convention held in Las Vegas, Nevada, the ASCE Engineering Mechanics Division Committee on Experimental Analysis and Instrumentation sponsored a session entitled "Physical Modeling Techniques for Missile and Other Protective Structures". The oral presentations made in this session were summary versions of the papers comprising this volume. The papers presented herein are concerned with experimental research programs related to the development of protective structures for missiles. Further, most are reports of work carried out, under Department of Defense auspices, in support of development of M-X missile protective shelter concepts.

During the early stages in planning the convention session it became readily apparent that there was considerable interest in the session among those who had performed research and developmental work for the M-X project. Since it would have been impossible to accomodate all qualified papers within the limits of the session, the sponsoring Committee decided that publication of a volume of all these papers was indicated. This volume is the product of that decision.

The majority of the papers were necessarily subject to review by appropriate military security authorities prior to release for publication. The sponsoring Committee is indebted to Lt. Col. Niel Buttimer and Lt. Carol Schalkman of BMO/PA, Norton Air Force Base, California for their cooperation in expediting this task.

Oftentimes the information on experimental techniques and physical modeling generated as a result of specialized military contract work is lost to the general engineering audience because of the lack of a suitable forum for reporting the work. It is the hope of the sponsoring Committee that this collection of papers will be of interest not only to those directly concerned with the M-X project, but also to those who are seeking knowledge regarding unique and different applications of physical modeling and experimental analysis.

Session Co-Chairmen:

Theordor Krauthammer
C. D. Sutton

Committee on Experimental Analysis and Instrumentation
Engineering Mechanics Division
American Society of Civil Engineers

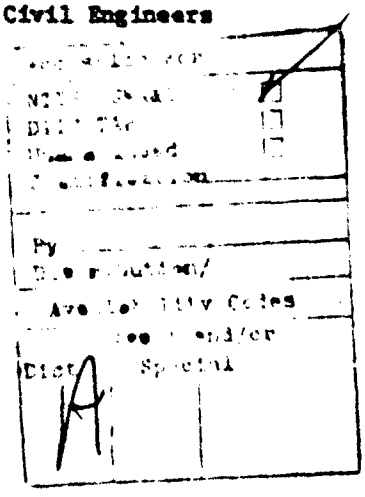

DEPARTMENT OF THE AIR FORCE
HEADQUARTERS BALLISTIC MISSILE OFFICE (AFSC)
NORTON AIR FORCE BASE, CALIFORNIA 92409

REPLY TO ATTN OF: PA

29 Jun 83

SUBJECT: Review of Material for Public Release

TO: Mr. James Shafer
Defense Technical Information Center
DDAC
Cameron Station
Alexandria, VA 22314

The following technical papers have been reviewed by our office and are approved for public release. This headquarters has no objection to their public release and authorizes publication.

1. (BMO 81-296) "Protective Vertical Shelters" by Ian Narain, A.M. ASCE, Jerry Stepheno, A.M. ASCE, and Gary Landon, A.M. ASCE.

2. (BMO 82-020) "Dynamic Cylinder Test Program" by Jerry Stephens, A.M. ASCE.

3. (AFCMD/82-018) "Blast and Shock Field Test Management" by Michael Noble.

4. (AFCMD/82-014) "A Comparison of Nuclear Simulation Techniques on Generic MX Structures" by John Betz.

5. (AFCMD/82-013) "Finite Element Dynamic Analysis of the DCT-2 Models" by Barry Bingham.

6. (AFCMD/82-017) "MX Basing Development Derived From H. E. Testing" by Donald Cole.

7. (BMO 82-017) "Testing of Reduced-Scale Concrete MX-Shelters-Experimental Program" by J. I. Daniel and D. M. Schultz.

8. (BMO 82-017) "Testing of Reduced-Scale Concrete MX-Shelters-Specimen Construction" by A. T. Ciolko.

9. (BMO 82-017) "Testing of Reduced-Scale Concrete MX-Shelters-Instrumentation and Load Control" by N. W. Hanson and J. T. Julien.

10. (BMO 82-003) "Laboratory Investigation of Expansion, Venting, and Shock Attenuation in the MX Trench" by J. K. Gran, J. R. Bruce, and J. D. Colton.

11. (BMO 82-003) "Small-Scale Tests of MX Vertical Shelter Structures" by J. K. Gran, J. R. Bruce, and J. D. Colton.

12. (BMO 82-001) "Determination of Soil Properties Through Ground Motion Analysis" by John Frye and Norman Lipner.

13. (BMO 82-062) "Instrumentation for Protective Structures Testing" by Joe Quintana.

14. (BMO 82-105) "1/5 Size VHS Series Blast and Shock Simulations" by Michael Koble.

15. (BMO 82-126) "The Use of Physical Models in Development of the MX Protective Shelter" by Eugene Sevin.

*16. REJECTED: (BMO 82-029) "Survey of Experimental Work on the Dynamic Behavior of Concrete Structures in the USSR" by Leonid Millstein and Gajanen Sabnis.

CAROL A. SCHALKHAM, 1Lt, USAF
Public Affairs Officer

Cy To: Dr. T. Krauthammer
Associate Professor
Department of Civil and
Mineral Engineering
University of Minnesota

27 APR 1982

THE USE OF PHYSICAL MODELS IN DEVELOPMENT OF THE M-X PROTECTIVE SHELTER

By Eugene Sevin[1]

1. INTRODUCTION

At the heart of the controversy over the M-X weapons system development has been the plan for basing the missile; that is, how a force of some 200 M-X missiles can be made to survive a massive attack of several thousand nuclear weapons. Until recently, the preferred basing was the so-called Multiple Protective Structure (MPS) concept where the actual locations of the missiles were concealed among a large number of hardened structures under the assumption that an enemy could not "afford" to attack all possible locations.

In view of the presumed accuracy of enemy warheads, no one shelter is intended to survive a direct nuclear attack. However, to enforce the "price," multiple shelter kills from the same attacking weapon must be avoided. Thus, the requirement for nuclear hardening (i.e., to avoid collateral damage from an attack on a neighboring shelter) has been a primary consideration in shelter configuration, land requirements (i.e., shelter spacing) and, hence, system cost.

While the level of hardening selected for the several MPS variants generally has been well within the state-of-the-art of protective facility design, the magnitude of the construction program ($3 billion for shelter-related costs in FY 1978 dollars; $11 billion for the entire military construction program--about twice as much in "then year" dollars) is nearly without precedent. Thus, cost considerations have motivated the search for innovative structural concepts and construction methods, and have driven design margins to the minimum. It has been in the latter regard that physical modeling has played an extremely influential role in the M-X shelter design process.

The majority of the papers in this session deal with one or another aspect of these activities undertaken in support of M-X protective shelter development over the past six years. This paper considers the scope of physical modeling employed in the design of the three primary protective shelter concepts for the M-X missile: the Shallow Buried Trench, the Vertical Shelter (Silo), and the Horizontal Shelter. However, emphasis is on the trench-related models because they are more innovative and relatively less well known.

2. OVERVIEW

In 1976, the Air Force entered into a two-year concept validation program to select a final (sic!) basing mode for the M-X missile. The

---

[1]Assistant to the Deputy Director (Science and Technology) for Experimental Research, Defense Nuclear Agency, Washington, DC 20305

two main candidates at that time were the (1) Horizontal Shelter--an earth-mounded, garage-type structure for a single missile and its transporter/erector/launcher (TEL) interconnected by an extensive open road network, and (2) the Shallow Buried Trench--a single 35 km long section of underground tube allowing random movement of a missile/TEL "train." The entire 200 M-X missile force would require either 4600 horizontal shelters or 200 lengths of buried trench to meet minimal survival goals under the postulated threat.

As the horizontal shelter and buried trench designs became better defined, and their estimated costs increased, interest was renewed in other basing alternatives. A comprehensive basing review was undertaken in mid-1978 and, as a result, both concepts were abandoned in favor of a vertical shelter system. As seems to be the fate of M-X, however, the silo was replaced only one year later by a more austere version of the horizontal shelter, as a consequence of mounting concerns over arms control implications--a principal reason for rejecting silos in the first place. Thus, by 1980, M-X basing virtually had come full-circle.

The nuclear hardness requirement for both the horizontal shelter and buried trench concepts was selected to be in the 400 to 600 psi overpressure range on the basis of system cost optimization studies. (N.B. 600 psi peak surface pressure occurs at a distance of about 565 m from a one megaton (1 MT) surface burst). Optimum hardness for the vertical shelter was determined to be between 1000 and 1500 psi.

Each shelter concept was to be hardened in a balanced manner against all nuclear weapons effects (e.g., nuclear and thermal radiation, electromagnetic pulse, dynamic pressures, and crater ejecta), and physical models were employed extensively to develop design approaches and to gather hardness data in all of the disciplines involved. This paper, however, will be concerned entirely with the use of physical models relating to blast and shock resistant design.

The scope of the modeling effort undertaken for the three basic shelter configurations is summarized in the Test Objective Matrix tables (Tables 1-3). These activities were conducted over a six-year period and involved major laboratory and field investigations employing mechanical test devices, high explosive (HE) simulations of nuclear airblast and ground shock, and underground nuclear tests.

Small-scale (1/100 to 1/40) non-responding models were used to determine airblast loads on the horizontal shelter. Intermediate scale (1/21 to 1/5) responding models of generic structural elements provided information on critical response features for all concepts, assisted in the screening of alternative shelter design approaches, and lent insight into fidelity requirements for blast and shock load simulators. Larger scale (1/2 to 3/4) models of complete structural

systems, notably for the buried trench and horizontal shelter concepts, helped resolve significant design issues relating to structure-medium interaction, structural subsystem interactions, and the motion environment specifications for internal shelter equipment. Relatively lesser effort was devoted to the vertical shelter because of the existing data base for silo structures.

3. THE SHALLOW BURIED TRENCH

In the shallow buried trench concept, location of the missile was concealed by its intermittent movement within a buried tube. The original baseline design, uniformly hardened against 600 psi peak surface loads (Fig. 1), was a fiber-reinforced concrete cylinder, 4 m internal diameter, 40 cm thick with 1.5 m soil overburden. The missile canister could be erected at any location by being forced up through the roof of the tube and soil overburden; the top was jointed to facilitate this action. (N.B. Two alternative full-sized breakout mechanisms were demonstrated successfully during trench development.) In view of its large cost, a hybrid trench concept subsequently was developed with hardened sections every several thousand feet (from which the missile could be erected more conveniently) connected by unhardened tube sections of conventional design.

To protect the missile against the possibility of airblast entering through damaged "upstream" portions of the trench, massive plugs were provided at either end of the missile/TEL train. The uniformly hardened tube had internal ribs that acted as stiffeners and aided in locking the blast plugs to the tube walls. Eliminating the ribs in the hybrid design was another significant cost saving.

A variety of physical models were used to gain insight into the loading and response of the tube structure and blast plugs in an effort to demonstrate the feasibility of the concept and to develop a data base for minimum cost design. The scope of this ambitious experimental program is summarized in the Test Objective Matrix, Table 1. The purpose of most of the structural model testing was to determine response modes and post-yield capacity of the fiber-reinforced concrete tube for a representative range of cylinder and backfill stiffness and breakout joint details. The principal static response tests /1-3/ and dynamic response tests /4, 5/ are reported in this session.

The blast plug was a major design consideration. It was postulated that airblast loads could be introduced into the tube upstream of the blast plugs by (1) airblast leakage through tube sections damaged by surface pressures in excess of 600 psi, (2) internally generated airblast due to piston-like implosion of the tube (caused by external airblast and ground shock loading) or, for small miss distances, (3) breeching of the tube by the attacking weapon or the resulting crater.

Inasmuch as the latter case could not be ruled out from projections of weapon delivery accuracy, the concern that the trench might become a gigantic nuclear shock tube destroying everything within, came to be the dominant feasibility issue for the trench concept. Theoretical studies indicated that pressure leakage within the tube would not produce as severe in-tube environments as the other mechanisms. Two possible implosion modes were considered, one dominated by the close-in ground shock and the other, a progressive collapse of the tube roof, caused by the surface airblast. The latter so-called "toothpaste tube" response was investigated early-on in a high explosive field experiment in which a 1/8 scale section of tube was exposed to peak surface overpressures decaying from 5000 psi to 1500 psi along its length /6/. The test results demonstrated that progressive collapse of the tube could occur, but would not give rise to a propagating air shock, despite measured local pressure peaks of nearly a kilobar. This served to corroborate theoretical analyses and led to dismissing this mechanism as a means of generating significant in-tube pressures.

Preliminary calculations suggested that the ground shock-induced implosion mechanism depended sensitively on the nature of the coupling and tube collapse mechanism, and could cause a much more severe in-tube environment. This mode of response was studied experimentally in a series of high explosive tests on a 1/16 scale section of buried tube /7/. The experimental setup is shown in Fig. 2. A rectangular slab of TNT was positioned on the ground surface directly above the tube and sized to induce a 90 kbar shock at the tube wall (based on source region predictions). Primary instrumentation consisted of high-speed photography to record the tube collapse process, air and impact pressures within the rapid closure region directly under the charge, shock time of arrival (TOA), pressures along the tube and conditions within the free-field.

Two instrumentation check-out tests were conducted using commercially available 6 in diameter concrete pipe. Fig. 3 shows the collapse process at a cross-section within the rapid closure region as constructed from high-speed photographic records obtained in one of these tests. A comparison with pre-test predictions also is shown. While the general shape and timing of the upper tube surface is reproduced well, formation of the two-lobe pattern was not anticipated. It was estimated that the pressure within the lobes did not exceed about 1 kbar, and was the first indication that this collapse mechanism might not prove effective in generating a strong shock in the tube.

Data recovery from the main experiment was disappointing. The Fastax camera broke before reaching full speed, and only the first phase of tube collapse within the rapid closure region was recorded. Even then, surface blow off material obscured much of the early time record. Nevertheless, observations were consistent with those of the

preliminary tests. The lobe pattern formed, trapping air at the sides of the tube and preventing the uniform build-up of large pressures as the tube completely collapsed. Pressures along the tube, as measured and inferred from TOA data, are shown in Fig. 4, indicating the absence of a strong propagating air shock outside of the rapid closure region. The results of these experiments led to the development of a "leaky-piston" response model for the ground shock-dominated collapse mechanism, according to which the preliminary estimates of the in-tube environment were reduced significantly.

The breeching mechanism refers to the direct coupling of a portion of the bomb's energy to the tube and occurs whenever the radius of vaporization (about 10 m for a 1 MT burst) intersects a portion of the tube. A worst case scenario clearly is when the bomb lands directly overhead, penetrates the overburden, and detonates inside the tube. In this event, initially all of the bomb's energy is coupled directly to the tube.

A more probable occurrence is when the bomb detonates on the surface directly overhead. It is estimated that only about 1 percent of the energy couples to the tube in this case, the balance going into the fireball (95%) and other regions of the ground. Unfortunately, reducing a 1 MT on-line surface burst to the equivalent of a 10 KT in-tube burst did not appear to resolve the feasibility of designing a survivable blast plug.

Detailed two-dimensional radiation coupled hydrodynamic calculations indicated that (for a 1 MT surface burst) only about 30 percent of energy initially coupled remains in the (volume bounded by the expanding) tube after the first 100 msec /8/. The effective source region for the in-tube airblast consists of hot vaporized soil and tube wall material mixed with air extending out to about 6 m in either direction from the point of the explosion. At these early times, the shock pressures in the tube remain relatively constant as the mitigating effects of various flow loss mechanisms are counteracted by the collapsing action of the tube under the outrunning surface air blast. The interior shock was expected to overtake the surface airblast after about 7 msec (and 180 m from the source), whereupon expansion of the tube volume and venting of tube gases to the atmosphere became significant loss mechanisms.

The gas behind the shock front at this time is in a very high enthalpy state (pressures of 5-15 kbar and temperatures of 1-10 electron volts), far in excess of the level required to vaporize the tube walls. While entrainment of ablated wall material serves to slow and cool the flow, the quantitative effect depends strongly on the formation of a turbulent boundary layer behind the shock and the consequent flow mixing process. At pressures below about 10 kbar, the shock attenuating effect of wall friction was thought to be important also.

An intensive effort was undertaken to model these loss mechanisms and to quantify their influence on shock attenuation. The "then" state-of-the-art predictions of peak shock pressures within the tube, highlighting the effect of losses, is shown in Fig. 5. It seemed clear that, if the "no loss" case prevailed, pressures in excess of 40,000 psi at the plugs would render the trench concept infeasible (accepting the premise of an on-line surface burst attack). At the other extreme, the combined effect of all loss mechanisms suggested that this near worst case attack scenario was no more severe than an off-line attack at the 600 psi hardness level, and well within the capability of plug design.

In view of the these extremes, and the uncertainties associated with the theoretical basis for the predictions, a major experimental program was undertaken in early 1977 (see Table 1). The high enthalpy flows required to study the role of ablation (of crucial importance as seen in Fig. 5) could be obtained only from a nuclear source. Accordingly, an underground nuclear test (HYBLA GOLD) was conducted to obtain ablation data on concrete pipes, 15 cm to 90 cm diameter; data on wall friction, tube expansion, and the influence of ribs also were obtained. Description and results of this fascinating test must be obtained elsewhere /9/. Suffice it to say that a wealth of data was obtained which, in conjunction with follow-on laboratory experimentation and considerable theoretical work, led to an acceptably complete understanding of the role of ablation in shock attenuation, the upshot of which is mentioned later.

The major modeling uncertainty associated with venting had to do with early-time expansion and cracking of the overburden, and formation of flow paths to the surface. Sufficiently rapid venting immediately upstream of the blast plug (where reflected pressures increase some seven-fold) would limit the impulse delivered to the plug and suggest an energy absorbing plug design. Because of the need to maintain a free surface, venting experiments were restricted to lower pressure regimes.

Shock tube experiments employing fiber-reinforced concrete models at 1/26-size (6 in inside diameter) were performed to study tube expansion and venting and plug/tube interactions /10, 11/. The models had simulated breakout joints and were buried to scaled depth in representative soils. In-tube pressures of between 400 psi and 3600 psi were generated with an explosively driven shock tube by reflecting the shock from a rigid wall at the end of the test section. A Lucite window was used for the reflecting wall so that the tube and soil response could be photographed from the end by a high-speed movie camera; the soil surface was photographed from the side as well. Pressures were measured within the test section on the reflecting wall and, for the plug tests, behind the plug assembly.

The experimental setup for the expansion and venting tests is shown in Fig. 6. A representative suite of data for one of the tests (700 psi reflected pressure) is presented in Fig. 7. The high-speed movies show that cracks form in the tube almost immediately after shock arrival. The tube then expands symmetrically until a rarefaction wave returns from the free soil surface, whereupon the roof moves off at a greater speed than the lower portion. Typically, venting to the atmosphere begins at a roof crack near the crown when the roof has moved about to the level of the original soil surface.

Once venting starts, the trench "unzips" along its length at roughly the speed of the reflected shock. Over the range of parameters investigated, the roof motion depended on the pressure levels and densities of the soil and tube material, but not on their strengths. Soil strength did affect expansion of the lower tube sections. Roof cracking and vent initiation were influenced by the strength and geometry of the tube; at higher pressures, venting occurred sooner and at correspondingly lesser roof displacement. Venting, even at late times, occurs only directly above the crown.

Candidate M-X blast plug designs combined the concepts of an upstream "leaky plug" which allows some blow-by and a downstream "solid plug" to completely seal off the trench and provide a safe section for the missile/TEL. Three plug/tube interaction tests were performed using smooth and ribbed tube sections; short and long solid plug models and a simplified leaky plug model were used. The experimental setup was the same as in the venting tests, except for a longer shock tube. Additional measurements included pressures behind the plug and reaction forces on the plugs.

The leaky plug model is shown in Fig. 8 and was intended to represent the first of a two-stage leaky/solid plug design. Representative data for a nominal 600 psi incident loading (3600 psi plug face loading) are shown in Fig. 9. A post-test photo is shown in Fig. 10. The results indicated that longitudinal cracking of the tube can defeat the plug function. In both the short solid and leaky plug tests, longitudinal cracks propagated beyond the plug face, allowing the surrounding tube to expand and providing a substantial flow path for the high pressure upstream gas to blow by the plug. However, the longer solid plug performed more successfully, suggesting the feasibility of the two-stage concept. Indeed, by the conclusion of the trench development program, the Air Force had demonstrated two successful full-size blast plugs at the 600 psi design level.

The cooperative effort between theory and experiment led to substantial revision in the computer-based prediction methods and the development of "second generation" codes. These were utilized in an extensive series of parametric analyses dealing with airblast propagation uncertainties /8/. Ablation was determined to be the

dominating attenuation effect for near-miss surface bursts (within about 10 m for 1 MT), resulting in pressures at the plug less than those on the surface. Expansion and venting, on the other hand, was found to contribute very little to shock attenuation, contrary to earlier expectations. For off-line attacks where tube collapse is driven by the fireball, surface airblast and ground shock, ablation effects were insignificant and the trench concept appeared entirely feasible.

4. SUMMARY

The design of candidate M-X protective shelters made extensive use of engineering data developed from tests on physical models. This paper has described the effort associated with structural hardening of the three principal M-X shelter concepts: Horizontal Shelter, Vertical Shelter, and Shallow Buried Trench. Primary emphasis was on the trench concept in which a highly coordinated program of theory and experiment provided the data base for (1) characterization of the airblast loading within the trench structure (i.e., shallow buried tube), (2) feasibility determination of blast plug concepts, and (3) developing a minimum cost design for the hardened shallow buried tube.

The experimental activities supporting this effort included laboratory and field shock tube testing, high explosive field testing, and an underground nuclear test. Most innovative, from a structural engineering perspective, was the modeling of (1) coupled airblast and ground shock loading and damage-level response of shallow buried fiber-reinforced concrete tubes, (2) expansion and venting of the tube under internal airblast loading, and (3) coupled flow-structural response of the plug/tube system.

APPENDIX I. - REFERENCES

1. Ciolko, A.T., "Testing of Reduced-Scale Concrete M-X Shelters - Specimen Construction," Collected Papers, Session 22-EM, ASCE National Convention, April, 1982

2. Schultz, D.M. and Daniel, J.I., "Testing of Reduced-Scale Concrete M-X Shelters - Experimental Programs," Collected Papers, Session 22-EM, ASCE National Convention, April, 1982

3. Hanson, N.W. and Julien, J.T., "Testing of Reduced-Scale Concrete M-X Shelters - Instrumentation and Load Control," Collected Papers, Session 22-EM, ASCE National Convention, April, 1982

4. Cole, D.M., "The Role of Large Scale High Explosive Testing in Determining Technology Requirements and Design Methodology for M-X Protective Structures Concepts," Collected Papers, Session 22-EM, ASCE National Convention, April, 1982

5. Stephens, J., "Dynamic Cylinder Test Program," Collected Papers, Session 22-EM, ASCE National Convention, April, 1982

6. Wampler, H.W., "In-Trench Airblast Simulation Development," Air Force Weapons Laboratory, Technical Note DE-TN-76-023, November 1976

7. Baker, J.C., et al, "HE Simulation of Ground Shock-Induced M-X Trench Collapse," Defense Nuclear Agency, Report DNA-5182F, 18 October 1980

8. Barthel, J.R. and Wu, H.E., "Blast and Shock Propagation in M-X Buried Trenches," Defense Nuclear Agency, Report DNA-5424F, July, 1980

9. Stockton, J.R., "Summary Report HYBLA GOLD Event," Defense Nuclear Agency, Report DNA-5107F, 1 November 1979

10. Bruce, J.R., et al, "Use of Experiments at Small Scale to Support Validation of the M-X Trench Concept," Collected Papers, Session 22-EM, ASCE National Convention, April, 1982

11. Bruce, J.R. and Gran, J.K., "Laboratory Investigation of Expansion and Venting and Plug Response in the M-X Trench, Defense Nuclear Agency, Report DNA-5235F, 1 February 1979

APPENDIX II. - TABLES AND FIGURES

TABLES

FIGURES

TABLE 1. SHALLOW BURIED TRENCH TEST OBJECTIVE MATRIX

		Concept								Validation							
Test Article		Spur	Ring	Tube						Tube/Plug					Plug	Tube Sys.	
Scale		1/26	1/2	1/9	1/26	1/9	1/6	1/4	Full	1/13	1/6	1/26	1/13	1/4	1/4	1/2	3/4
Objective \ Test Env.		D	S	S	D	D	D	D	—	S	S	D	D	D	D	D	D
Environment	Airblast –External –Internal Ground Shock	●			●			●				●		●		●	●
Test Methods	Instrumentation							●								●	●
	Simulation																
	–External							●								●	●
	–Internal							●						●		●	●
	–Scaling													●		●	●
Hardness Design Data	Analytical Model Dev. & Eval.		●											●	●	●	●
	Design Concept Screening		●	●		●	●	●		●	●		●			●	●
	Structure/Media Interaction			●		●	●	●						●		●	●
	Structure Element Interaction									●	●		●	●	●	●	●
	Fragility/Ductility Determination		●			●	●	●		●	●		●				
	Scaling					●		●		●	●		●	●		●	●
	Constructability								●								
	Breakout															●	
	Static/Dynamic Correlation			●		●				●			●				

S-Static D-Dynamic

TABLE 2. HORIZONTAL SHELTER TEST OBJECTIVE MATRIX

Test Article	Concept Validation				Full Scale Engineering Development															
Scale	Closure		Shelter		Cylinder		Closure		B.O. Joints		Sal Ports		Back Fill		Shelter					
Objective / Test E.W.	1/6		1/6	1/2	1/6		1/6		1/6		1/6		1/6		1/186	1/21	1/5			
	S	D	D	D	S	D	S	D	S	D	S	D	S	D	D	D	D			
Environment: Airblast –Single Burst –HOB			●																	
Environment: Groundshock																				
Environment: Rhaltiberst			●																	
Test Methods: Instrumentation															●	●	●			
Test Methods: Simulation –Scaling			●																	
Test Methods: –Fidelity			●	●											●		●			
Hardness Design Data: Analytical Model Dev. & Eval.	●	●	●		●	●	●	●	●							●	●			
Hardness Design Data: Design Concept Screening																				
Hardness Design Data: Structure/Media Interaction			●		●	●											●			
Hardness Design Data: Structure Element Interaction			●	●	●	●	●	●	●								●			
Hardness Design Data: Fragility/Ductility Determination	●	●	●	●	●	●	●	●	●								●			
Hardness Design Data: Scaling			●																	

Tested in Conjunction with Static & Dynamic Cylinder Tests

S-Static D-Dynamic

TABLE 3. VERTICAL SHELTER TEST OBJECTIVE MATRIX

		Concept				Validation			
Test Article		Closure		Cylinder		Shelter			
Scale		1/6		1/6		1/30	1/6	1/3	Full
Objective \ Test Env.		—	D	S	D	D	D	D	—
Environment	Airblast -Single Burst -HOB Groundshock Multiburst	Tested in Conjunction with Shelter Tests and in Hard Rock Site Program						●	
Test Methods	Instrumentation Simulation -Scaling -Fidelity				●		●	● ●	
Hardness Design Data	Analytical Model Dev. & Eval. Design Concept Screening Structure/Media Interaction Structure Element Interaction Fragility/Ductility Determination Scaling Constructability			● ●	● ● ● ● ●	● ● ●	● ● ● ● ●	● ● ● ● ●	●

S-Static D-Dynamic

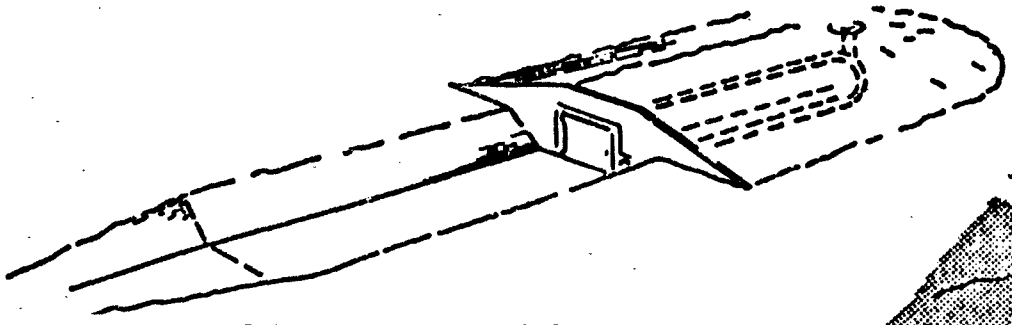

Shelter Facility

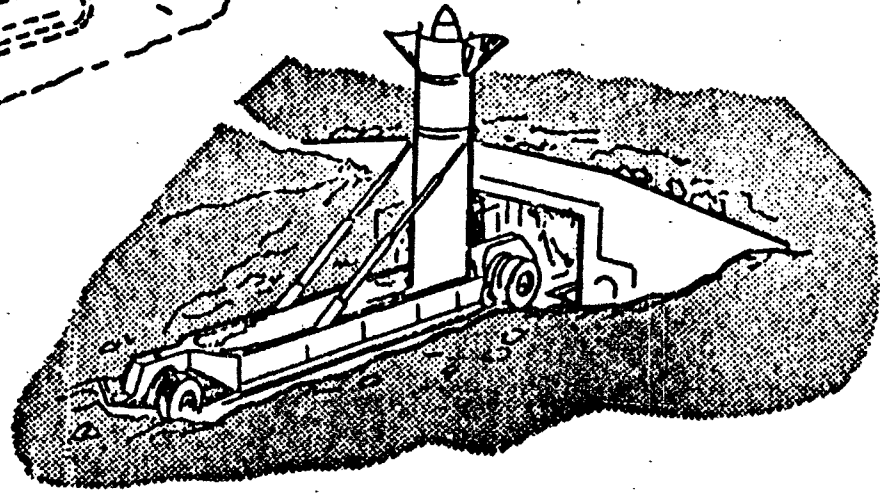

Missile Launch Vehicle

Fig. 1. MX horizontal protective shelter concept

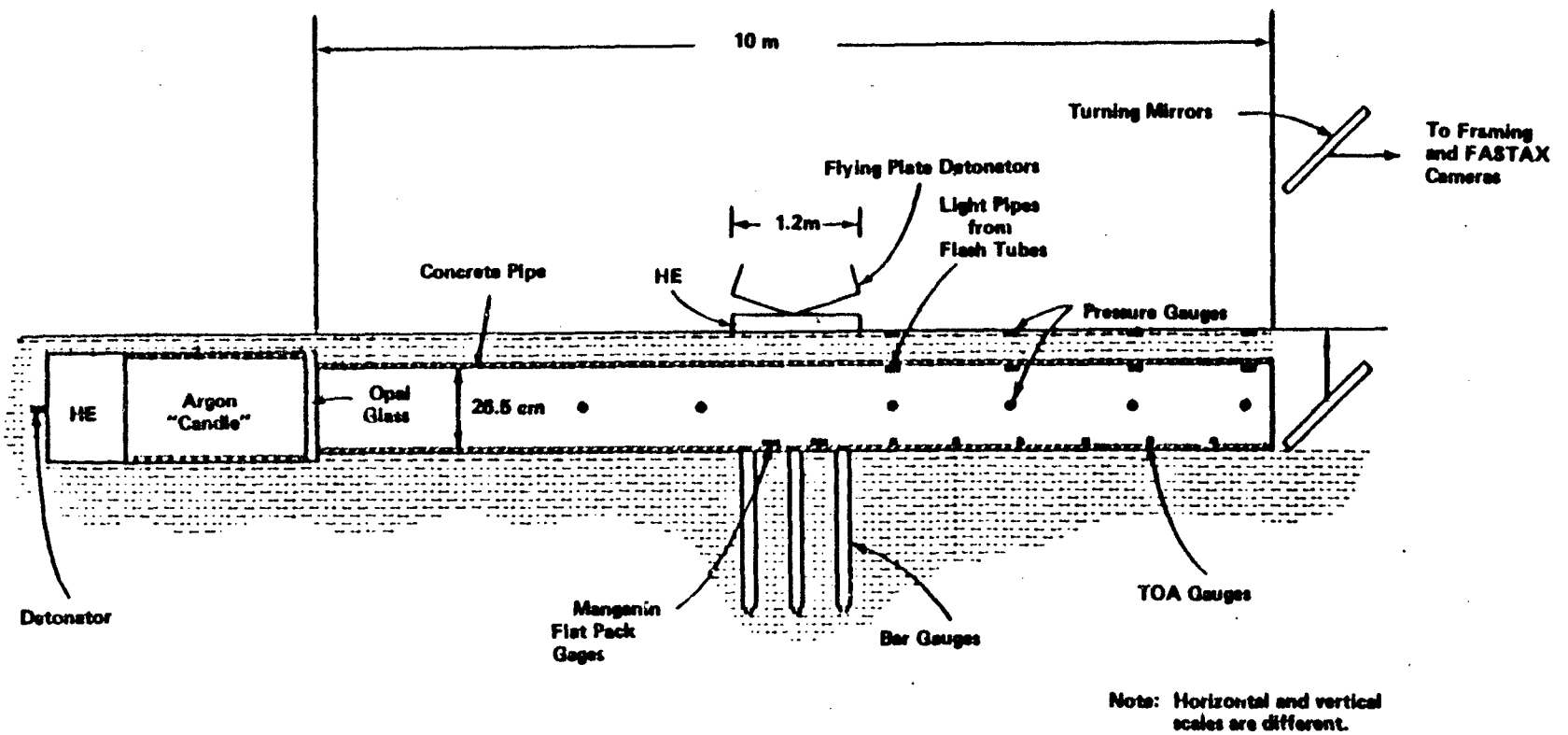

Fig. 2. Experimental set-up for ground shock-induced collapse

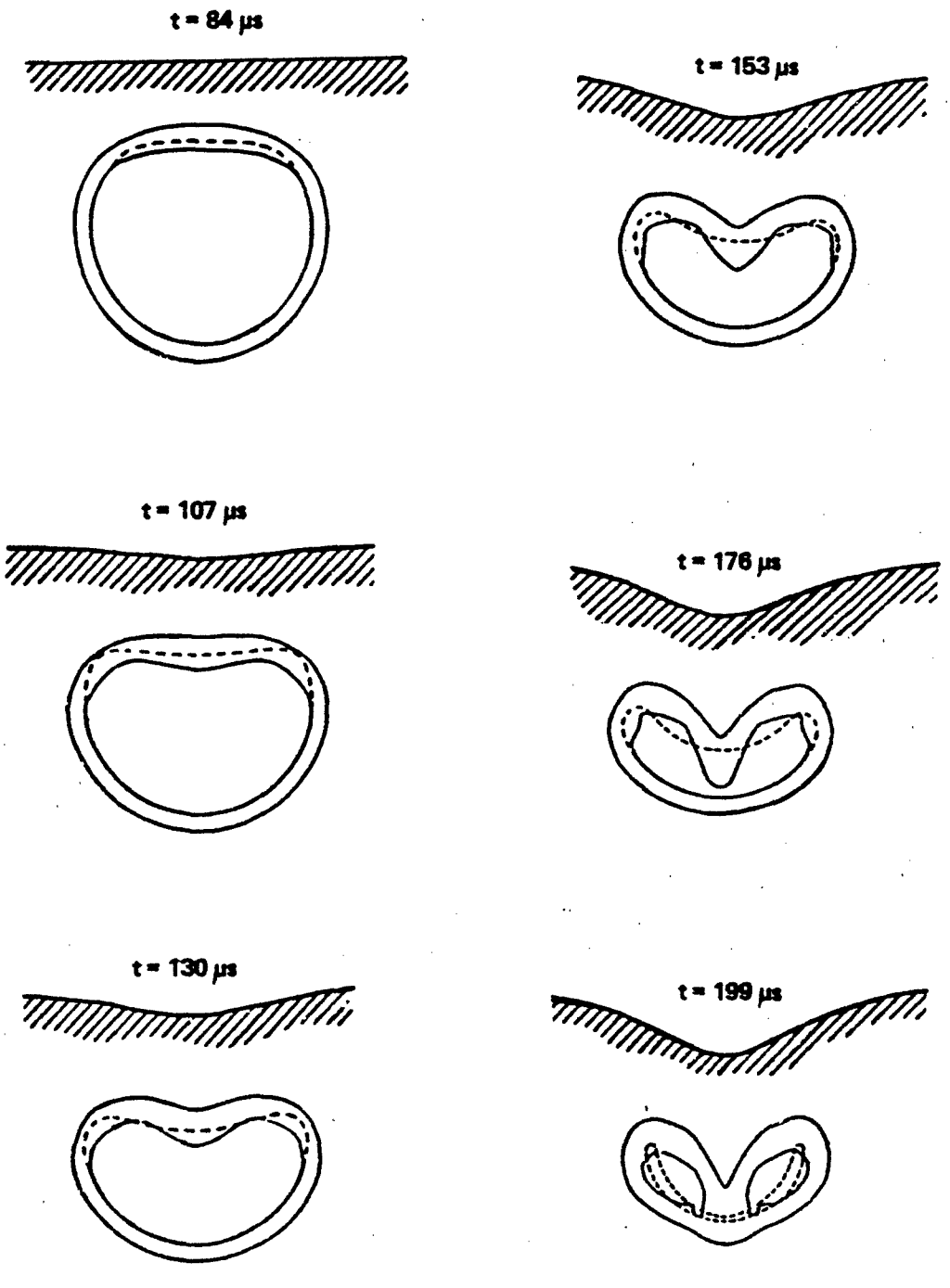

Fig. 3. Tube crush-up: Comparison of measurements and predictions

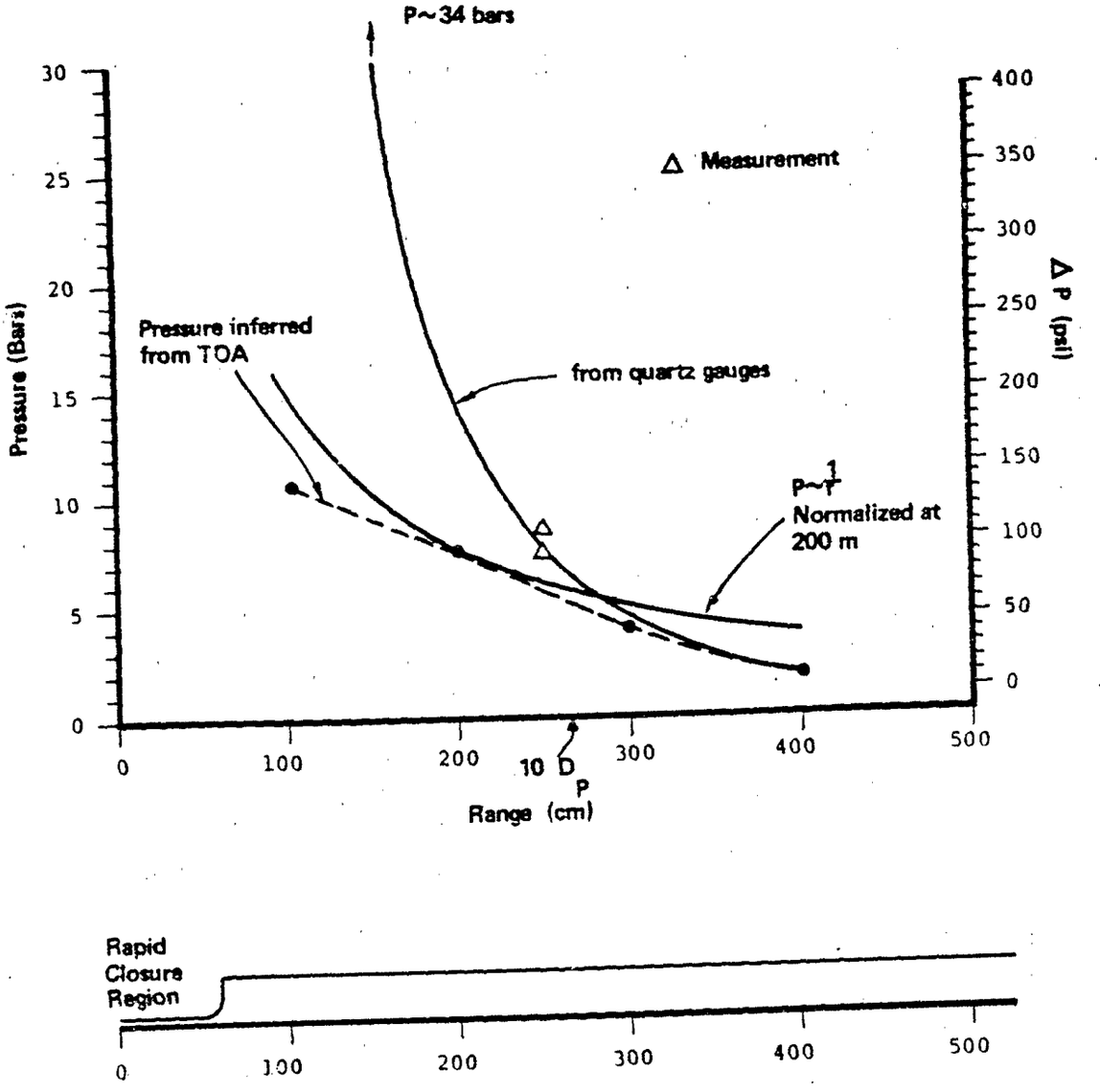

Fig. 4. Airblast pressures generated by tube crush-up

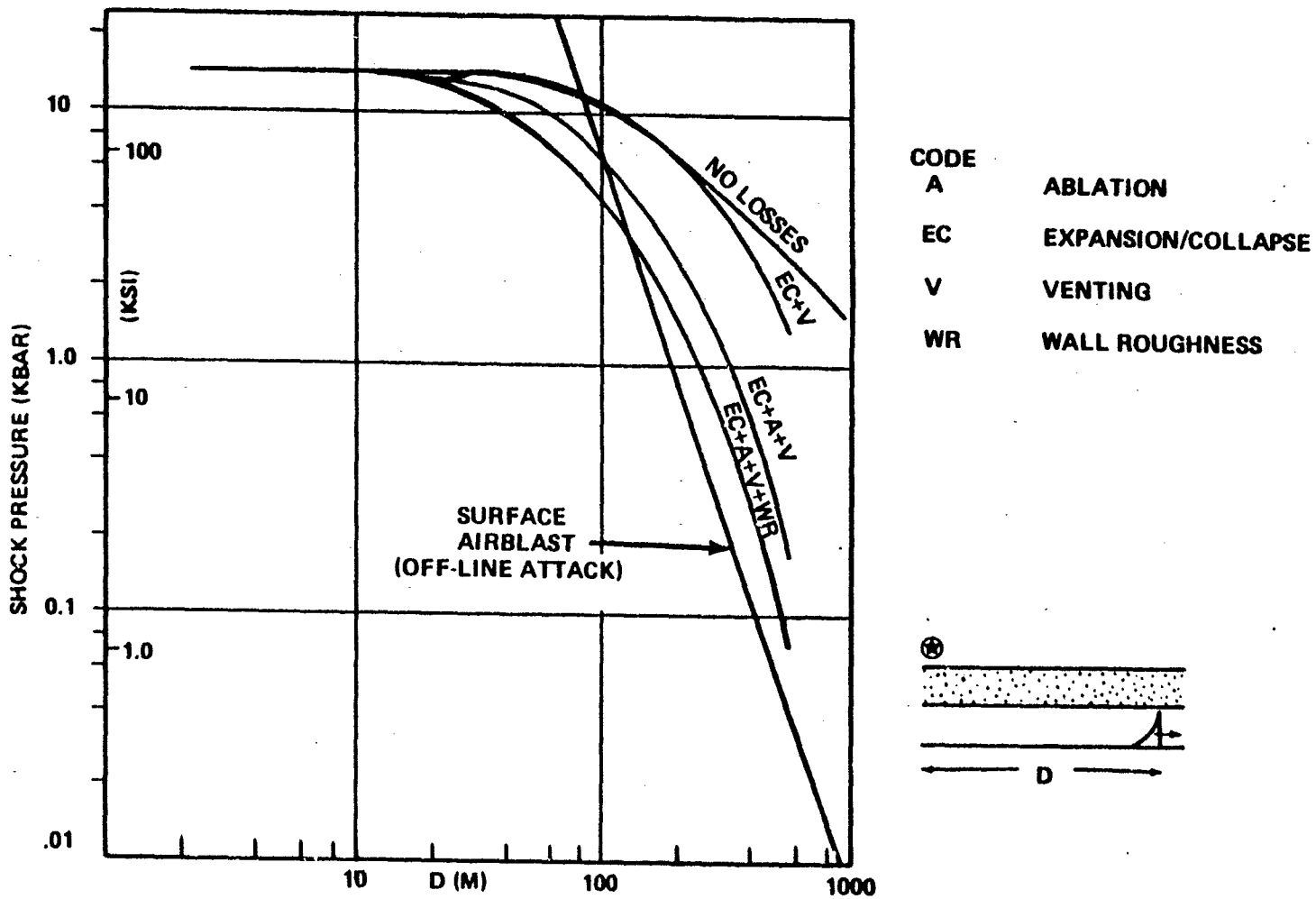

Fig. 5. Estimated in-tube airblast from a 1 MT on-line surface burst

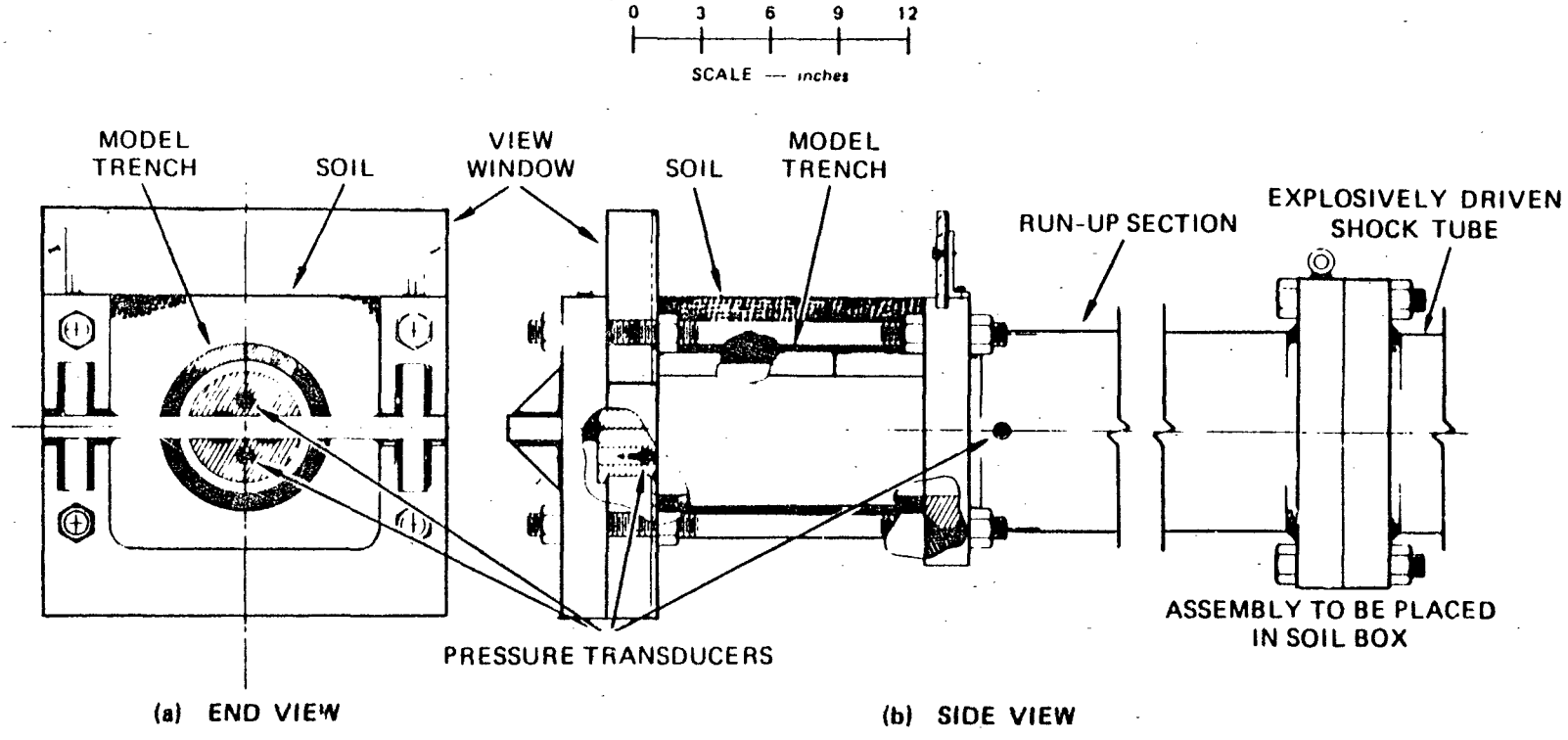

Fig. 6. Experimental set-up for tube expansion and venting

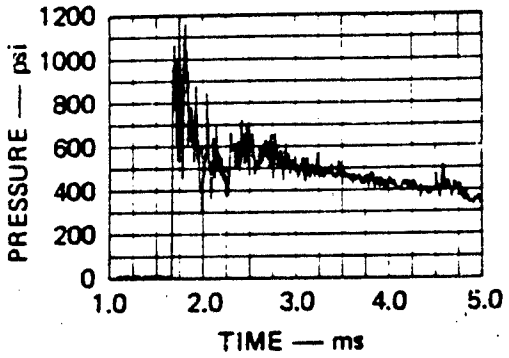

AT REFLECTING WALL

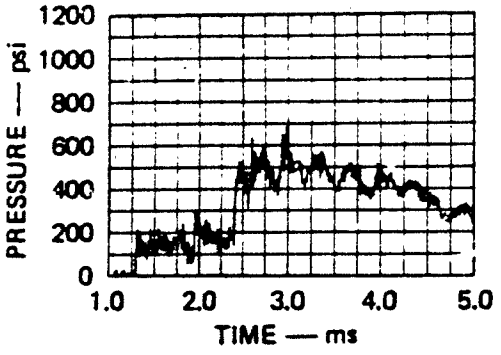

15.5 in. FROM
REFLECTING WALL

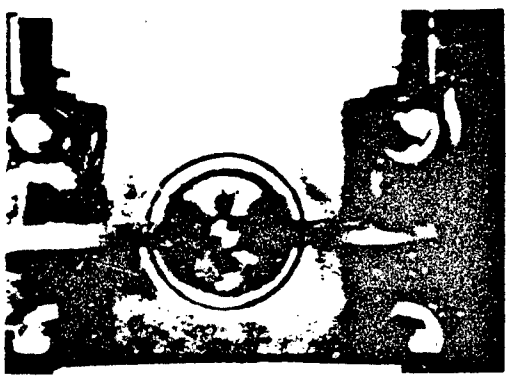

t = 0 ms

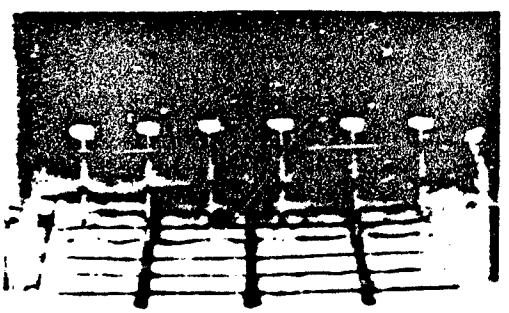

t = 0 ms

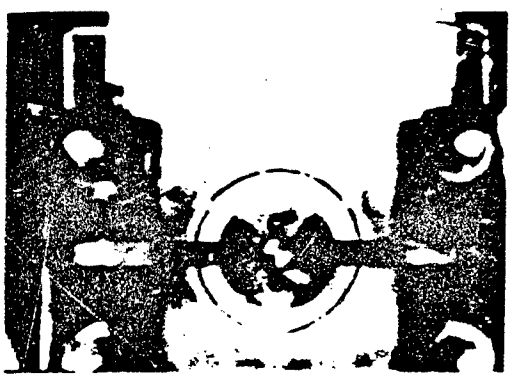

t = 2.20 ms

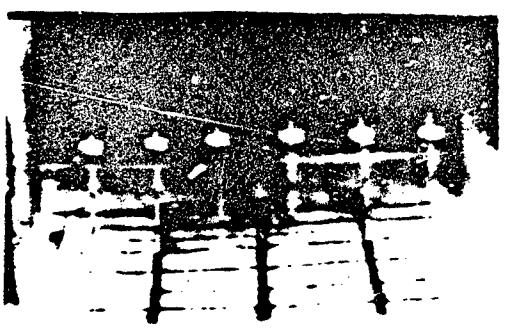

t = 2.67 ms

Fig. 7. Selected results from tube expansion and venting tests

t = 3.71 ms

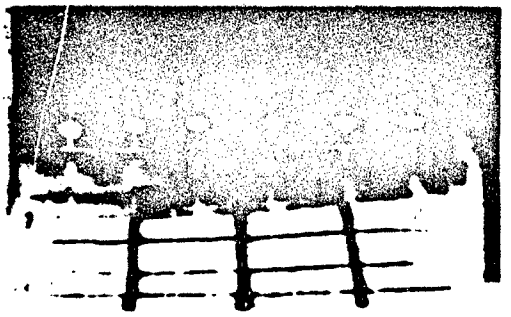

t = 3.43 ms

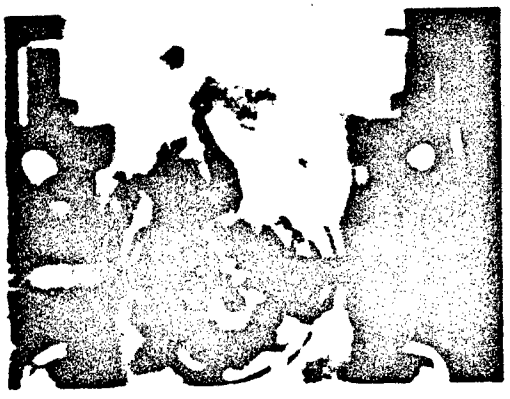

t = 4.21 ms

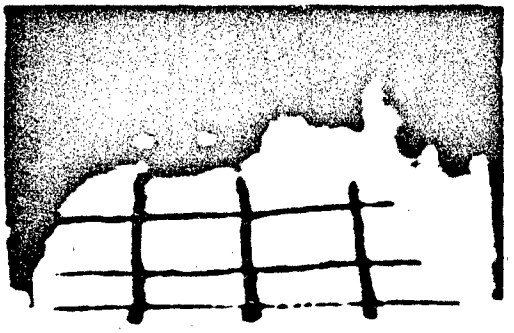

t = 4.47 ms

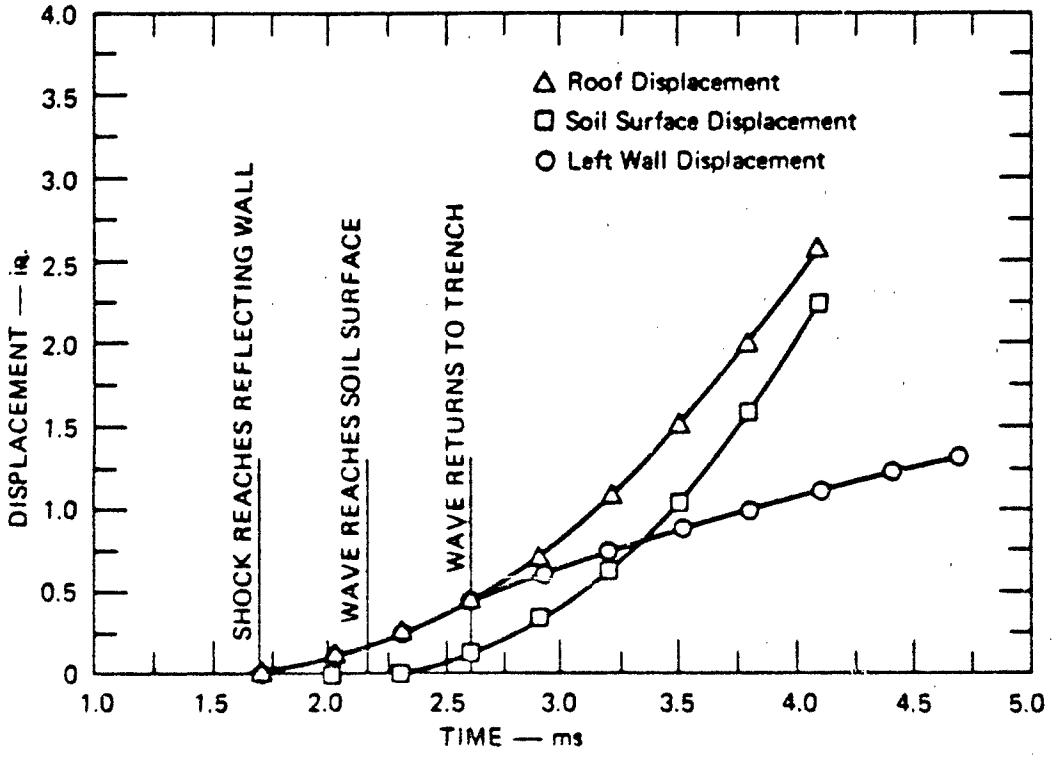

SYMMETRIC TRENCH EXPANSION PHASE (Test 17)

Fig. 7. (continued)

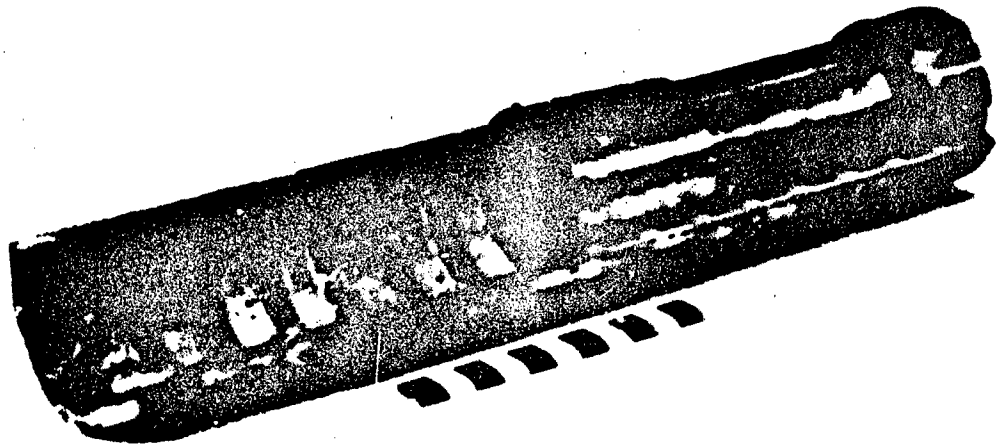

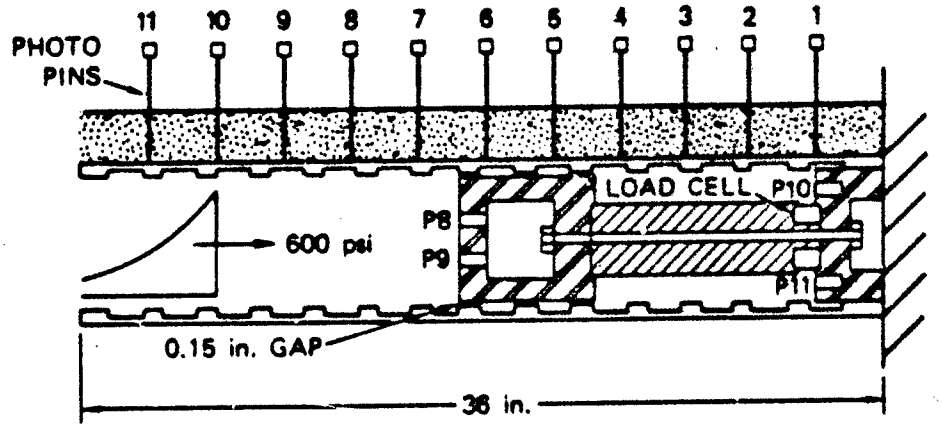

Fig. 8. Leaky plug model for plug/tube interaction tests

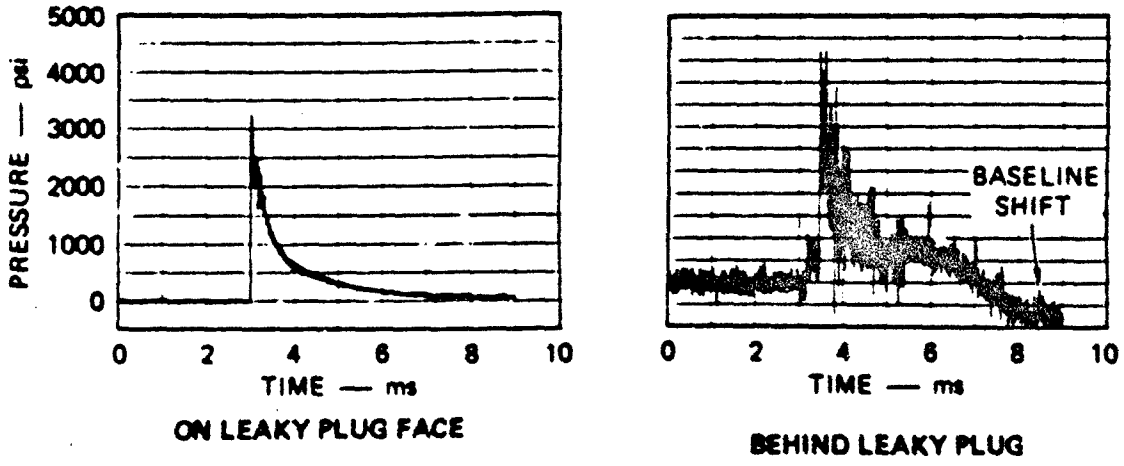

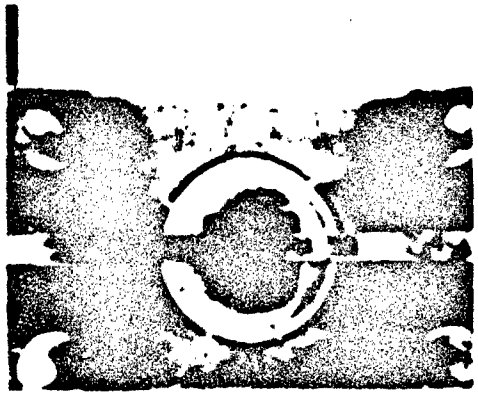

t = 4.88 ms

t = 4.71 ms

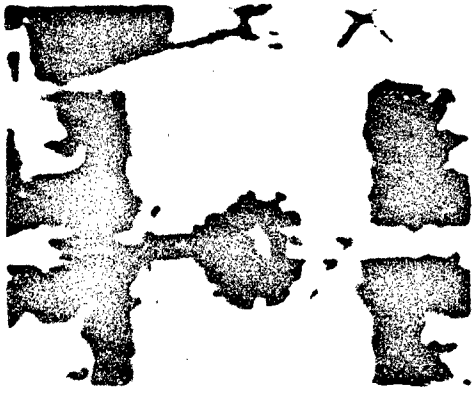

t = 8.73 ms

t = 8.66

Fig. 3. Selected results from leaky plug/tube interaction test

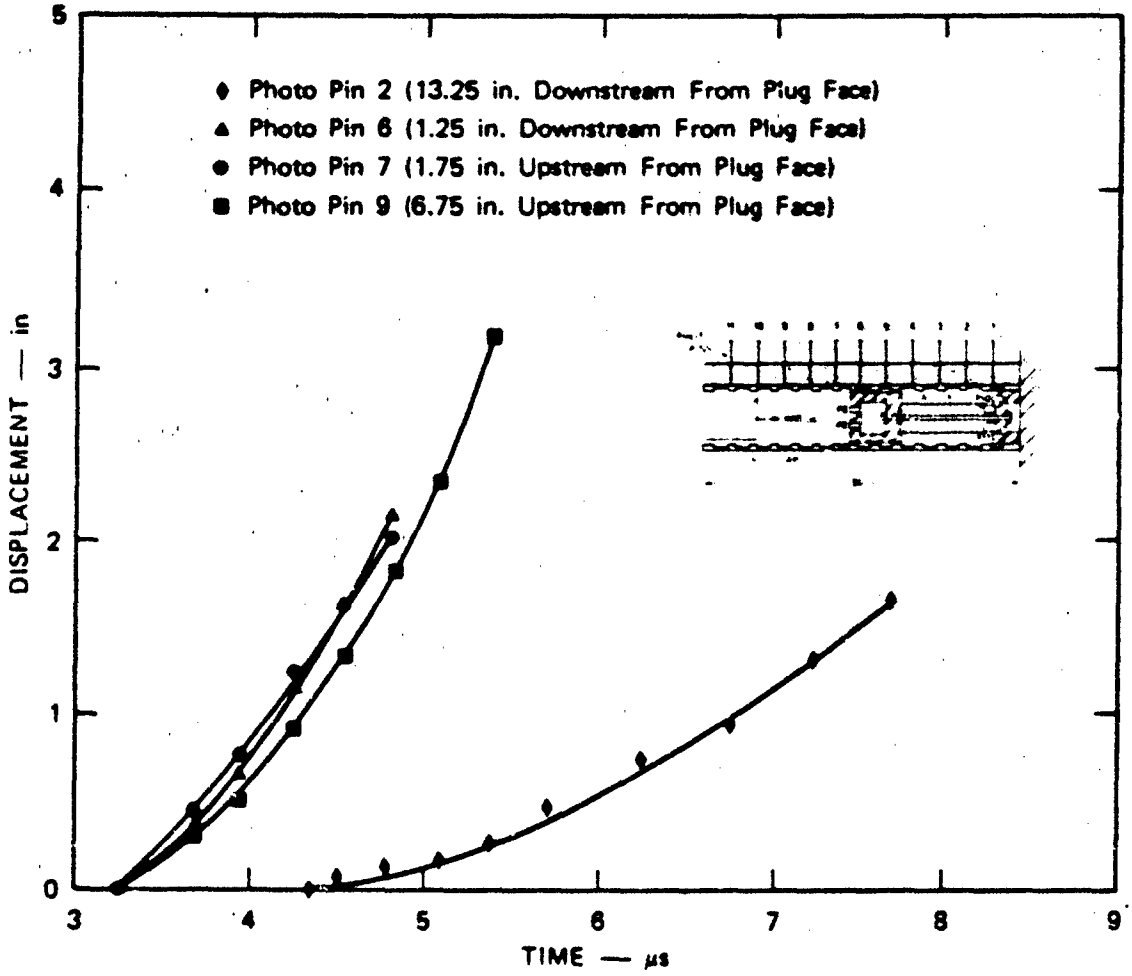

Fig. 9. (continued)

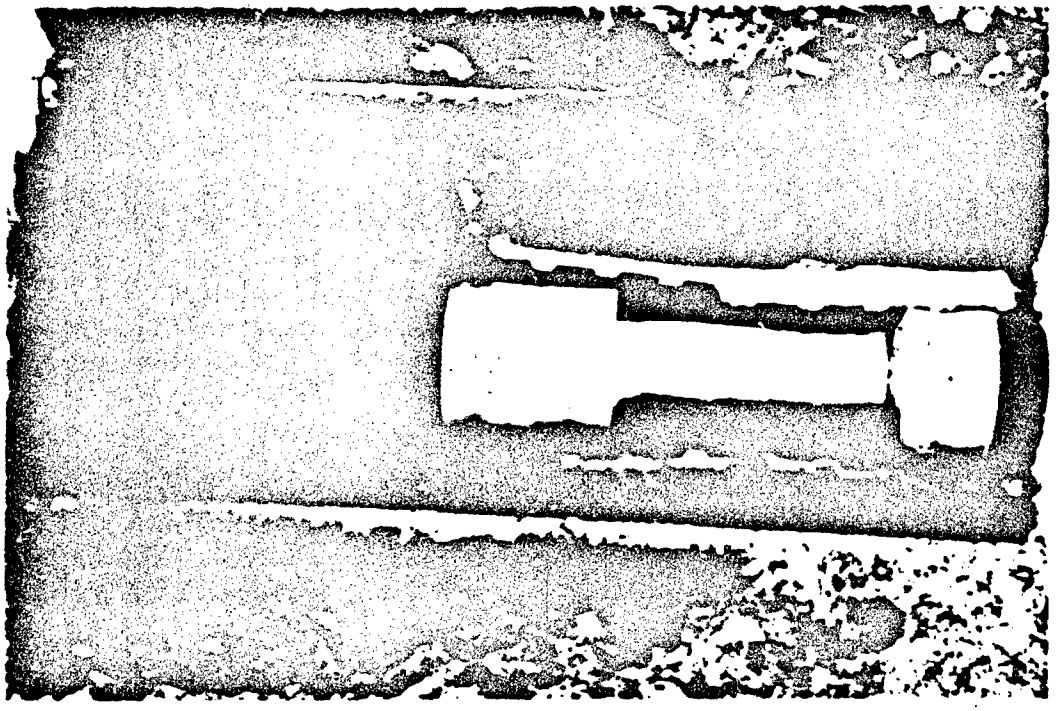

Fig. 10. Post-test condition of leaky plug/tube (after soil removal)

TESTING OF REDUCED-SCALE CONCRETE MX-SHELTERS

SPECIMEN CONSTRUCTION

KEY WORDS: Breakout joint; Construction; liner thickness; Missle; Models; Plain concrete; Reinforced concrete; Reinforcement; SAL panel; Shelter; Structural engineering; Stud spacing; Tolerances; Variables; Wall thickness

ABSTRACT: An experimental program involving construction and testing of reduced-scale concrete Horizontal MX-Shelters was conducted. This paper describes the construction of 43 reduced-scale cement models of the Shelters. Twenty-two different prototypes were constructed. All specimens had a 2-ft (0.61 m) inside diameter with plain or reinforced concrete walls 1.8 (46 mm) or 2.4-in. (61 mm) thick. Specimen test length was 4 ft (1.22 m) with 1 ft (0.30 m) at each end for load transfer.

Variables in specimen construction included wall thickness, amount of reinforcing, breakout joint details, liner thickness, spacing of studs, and Z-insert gap of the SAL inspection panel. Sensitivity of test results to variations in specimen dimensions required unusually rigid tolerances. In spite of manufacturing complexities, specimens were manufactured at a rate of three per week.

TESTING OF REDUCED-SCALE CONCRETE MX-SHELTERS

SPECIMEN CONSTRUCTION

by

Adrian T. Ciolko*

INTRODUCTION

An experimental program involving construction and testing of reduced-scale concrete Horizontal MX-Shelters was conducted by Construction Technology Laboratories, a Division of the Portland Cement Association. The program included 43 specimens tested under static loading conditions. Each specimen represented a "candidate design" being considered for prototype construction.

One deployment concept involved MX missiles stored in underground horizontal shelters. One purpose of the shelter was to protect the missiles from nearby nuclear weapon attack such that the missiles could be successfully launched after an attack. In the testing program, loads modeling combinations of forces that might occur from an attack were applied to the specimens. Loads consisted of axial thrust and non-uniform radial surface pressure. Data obtained from this test program were used to analyze shelter behavior under "known" loading conditions.

* Evaluation Engineer, Structural Evaluation Section, Construction Technology Laboratories, a Division of Portland Cement Association, Skokie, Illinois.

This is the second of three individual papers describing the test program. Other papers describe the Experimental Program[1] and Instrumentation and Load Control.[2]

OBJECTIVE

The objective of the Specimen Construction program was to fabricate 43 reduced-scale concrete models of MX-Horizontal shelters for testing in the Experimental Program.[1] Following sections of this paper describe the test specimens, materials, and construction.

TEST SPECIMENS

All specimens had a 2-ft (0.61 m) inside diameter with either plain or reinforced concrete walls 1.8 (46 mm) or 2.4-in. (61 mm) thick. As shown in Fig. 1, specimen test length was 4 ft (1.22 m) with an additional 1 ft (0.30 m) at each end for load transfer. Overall specimen length was 6 ft (1.83 m). At specimen mid-length, there was a 90° wide removable segment 1-ft (0.31 m) long representing the MX-Shelter Strategic Arms Limitation (SAL) panel. This panel was fitted into the specimen with "Z"-shaped joints. Weakened plane joints, when required, were simulated at $\pm$ 45° from the crown in the remaining specimen length.

Design Configurations

Twenty-two different prototypes were constructed. Each design was modeled at approximately 1/7-th scale. There were seven "basic" wall design configurations. They were designated

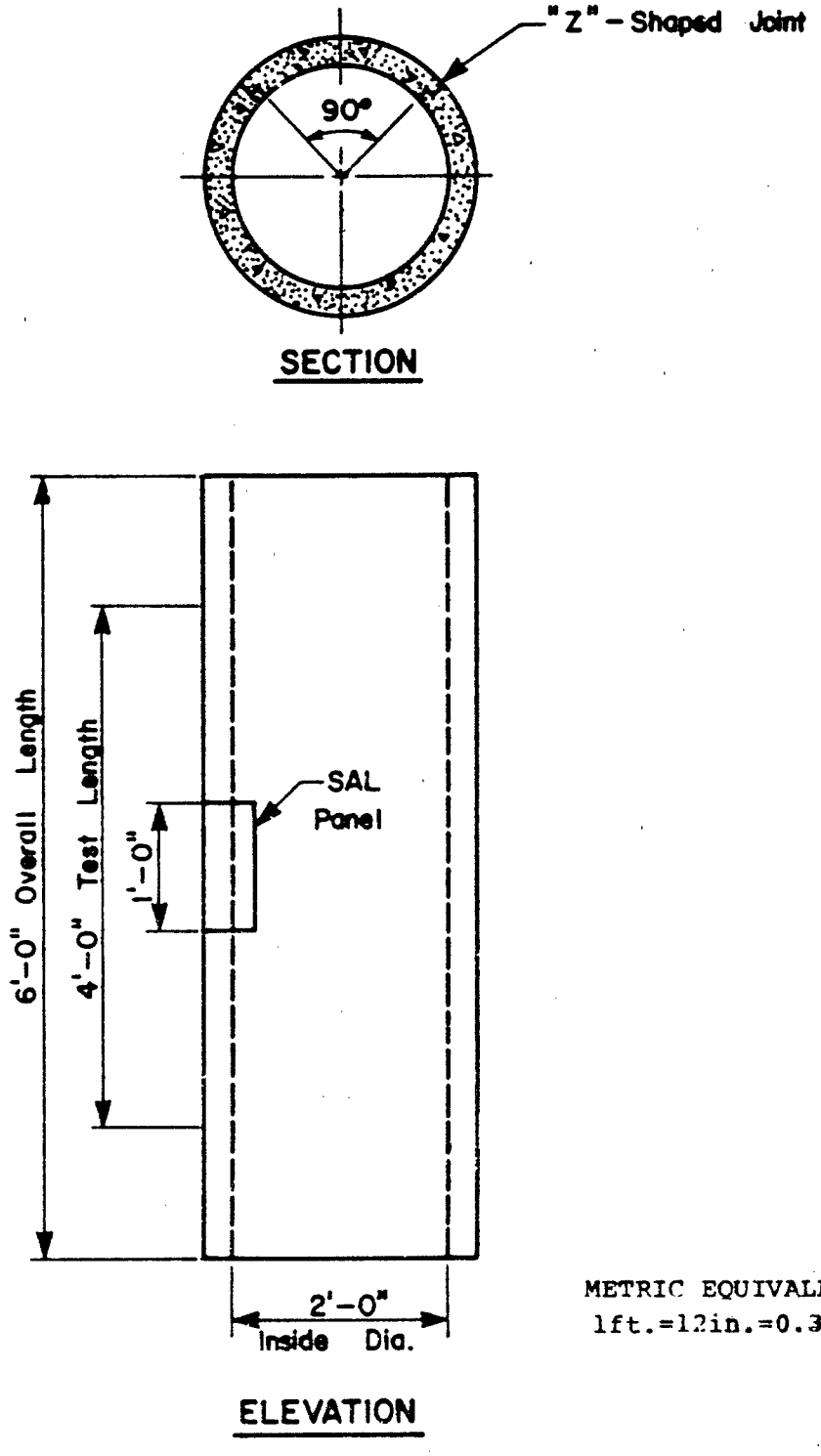

Fig. 1 Horizontal MX Shelter Model

as follows:

A1 - plain concrete, no SAL panel

A2 - double layer reinforcement, no SAL panel

A3 - plain concrete, with SAL panel

B1 - double layer reinforcement, with SAL panel

B2 - single layer reinforcement, with SAL panel

C1 - steel liner with stud anchors, plain concrete, with SAL panel

C2 - steel liner with stud anchors, single layer reinforcement, with SAL panel

Additional variables within the basic design configurations included wall thickness, amount of reinforcing, breakout joint details, thickness of liner, spacing of studs, and gap between inner and outer Z-insert. Variable matrix and quantities are given in Table 1.

Acceptance Criteria and Tolerances

Because of the sensitivity of test results to variations in specimen dimensions, unusually rigid tolerances were required. A construction specification was written[3] which included procedures for fabrication of specimens as well as materials specifications and tolerances.

Acceptance of shelters was based on tolerances intended to prevent unintentional eccentricity of loading during tests. In addition, physical dimensions and properties had to accurately model the full-size shelter. Tolerances of $\pm$0.10 in. (2.5 mm) were required for specimen wall thickness and outside diameter. Specimen length was required to be 6 ft. (1.83 m) $\pm$ 0.125 in.

TABLE 1 - MX-HORIZONTAL SHELTERS SPECIMEN DESCRIPTION

Construction Phase	Specimen Identification Number	Reinforcing	Liner, Studs	SAL Gap (in.)	Breakout Joint	Thickness (in.)	Total Quantity
I	A1	None	None	No SAL	Yes	1.8	2
	A2	2 layer, 1/2% ewef	None	No SAL	Yes	1.8	3
	A3	None	None	0.025	Yes	1.8	3
	B1	2 layer, 1/2% ewef	None	0.025	Yes	1.8	6
	B2	1 layer, 1% ew	None	0.025	Yes	1.8	3
	C1	None	16 Ga, 3-1/2 in. oc	0.025	Yes	1.8	6
	C2	1 layer, 1/3% ew	16 Ga, 3-1/2 in. oc	0.025	Yes	1.8	3
II	B1.2	2 layer, 1/4% ewef	None	0.025	No	1.8	2
	B1.3	2 layer, 1% ewef	None	0.025	No	1.8	2
	C1.2	None	20 Ga, 4 in. oc	0.025	No	1.8	2
	C1.3	None	16 Ga, 4 in. oc	0.025	No	1.8	2
	C1.4	None	16 Ga, 3 in. oc	0.025	No	1.8	2
III	C2.2	1 layer, 1/3% ew	20 Ga, 3 in. oc	0.025	No	1.8	1
	C2.3	1 layer, 1/3% ew	20 Ga, 3 in. oc	0.025	No	2.4	4
	C2.4	1 layer, 1/3% ew	20 Ga, 3 in. oc	0.05	No	2.4	1
	C2.5	1 layer, 1/3% ew	20 Ga, 3 in. oc	0.10	No	2.4	1

Notes:

ew = each way
ewef = each way, each face
Ga = gage
oc = on center

Metric Equivalent:

1 in. = 25.4 mm

(3.2 mm). Similar requirements were placed on steel reinforcement. Steel cages were tied at tolerances of ± 0.05 in. (1.3 mm) on the clear distance to formed surfaces, and ± 0.125 in. (3.2 mm) on the spacing between bars.

MATERIALS

To meet stringent construction specifications, innovative materials were developed for modeling concrete shelters. The following sections describe concrete and steel reinforcement for the specimens.

Concrete

A micro-concrete was developed to satisfy modeling requirements as well as demands for casting and consolidation. All cement was purchased from one manufacturing burn. Type III cement was used. Maximum aggregate size was 3/8 in. (9.5 mm). A short program of placement tests was performed to evaluate consolidation techniques for the micro-concrete. Specimen mock-ups including reinforcing and simulated SAL panels were used as shown in Fig. 2.

A 28-day compressive strength of concrete of 6000 psi (41 MPa) was required for the 4-ft (1.22 m) middle portion of the specimens. The proportion of ingredients for the mix were 1.0 part Portland Cement to 4.75 parts aggregate to 0.50 parts water. In addition, an 8000 psi (55 MPa) 28-day compressive strength micro-concrete was designed for the 1-ft (0.30 m) long load transfer portions at the specimen ends.

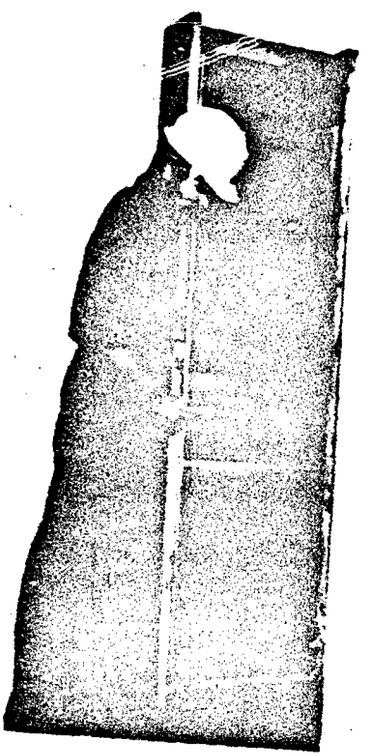

Fig. 2 Specimen Mock-up During Placement Test

Reinforcing

To satisfy modeling requirements, reinforcing steel was scaled down. Size D3 cold worked deformed steel wire, annealed to produce properties of Grade 60 reinforcement, was used as reinforcing bars. No. 2 Grade 60 plain steel reinforcing bars were used for dowels in weakened plane joints. Cold drawn steel wire, size No. W1, was used for fabricating stirrups.

For specimens requiring liner plates, various thicknesses of Grade 45 cold rolled sheet steel were used. This material was also used to fabricate the Z-inserts for SAL panels. Partially threaded 1-5/8-in. (41 mm) long studs with nuts were used as shear connectors for liner plates. They were welded to liner plates using drawn arc capacitor discharge stud welders. Figure 3 shows a liner plate with attached studs.

FORMWORK AND EQUIPMENT

Because of strict acceptance criteria on shelter models, steel forms for casting were manufactured with tolerances less than $\pm$ 0.01 in. (0.3 mm). Forms consisted of a base ring, an inner form, and an outer form. The precisely machined base ring held inner and outer forms in place. The inner form was rolled and machined from 0.50-in. (12 mm) thick steel plate. It contained a 4-in. (101 mm) wide removable gate along its entire length. Removal of the gate permitted collapsing the inner form. The entire inner form could then be removed from the interior of the specimen after hardening of the concrete.

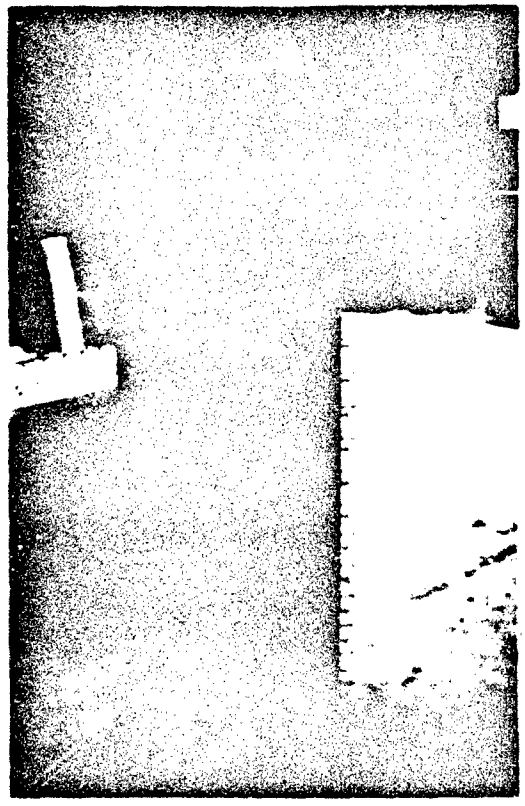

Fig. 3 Liner Plate with Studs

The outer form consisted of 180° wide halves. They were connected using heavy pins and bolts. Joints in all forms were sealed to prevent leakage of mortar using O-ring gaskets. Figs. 4 and 5 show the shelter form.

A separate form was manufactured for casting SAL panels. It was a horizontal form which matched the tolerances of shelter forms. It permitted casting of three SAL panels simultaneously. The Z-inserts were bolted to the outside of the form. The form was filled with concrete and carefully finished so that the completed SAL panels would fit inside the shelter form. Figure 6 shows the form with two Z-inserts in place before casting.

Other equipment required for casting included two external form vibrators attached opposite each other to the outer form. Vibrators were selected based on placement tests of mock-up specimens and discussion with manufacturers. Vibration was transmitted to the entire length of the form through channel sections welded to the outer form wall. Vibrators were rated for 1650-lb (7.3 kN) centrifugal force at approximately 3600 vibrations per minute.

CONSTRUCTION

Complete construction of a shelter model consisted of many important tasks to meet strict specifications. Although casting of the concrete took only about 45 minutes, numerous hours were spent preparing each specimen.

Fig. 4 Inner Form and Rear Outer Form Attached to Base Ring

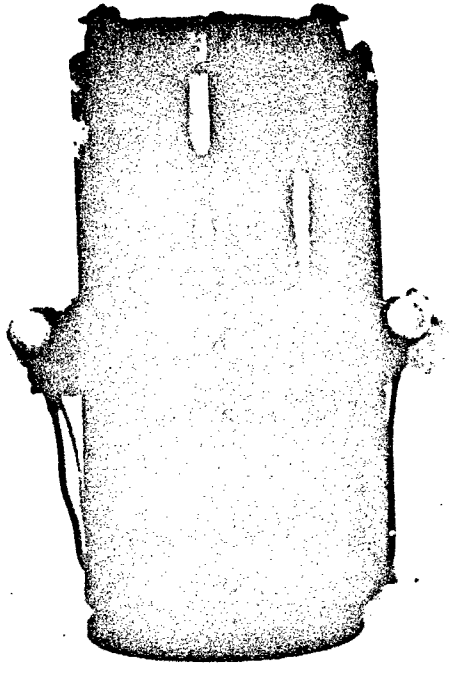

Fig. 5 Completely Assembled Form Vibrators Attached

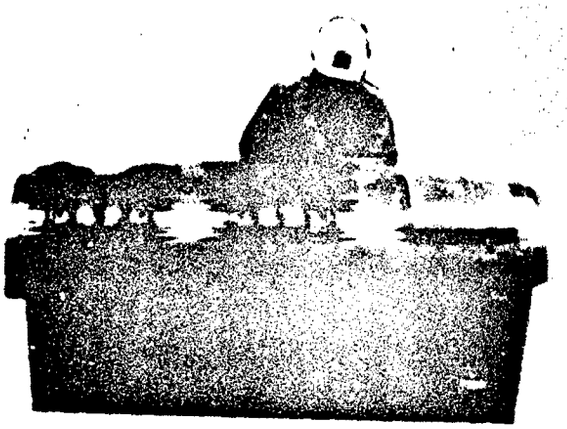

Fig. 6 SAL Panel Form

Fabrication and Placing of Reinforcement

The most difficult type of reinforcement to fabricate prior to casting was the double layer reinforcing cage. A portion of the steel cage was tied as shown in Fig. 7. It was then positioned over the inner shelter form. Tying of steel continued as shown in Fig. 8. After the longitudinal and circumferential steel was in place, stirrups were attached. Strain gages and inserts for attaching displacement transducers to the specimen were also positioned at this time. Figure 9 shows strain gages attached to the reinforcement. Figure 10 shows a complete cage with precast SAL panel in place.

For specimens requiring liner plates, steel fabrication procedures were similar. A liner plate was positioned over the inner form, and studs, if required, were welded to it. If required, a steel cage was then assembled and instrumentation was attached.

After fabrication of reinforcing steel and placing of instrumentation, the outer shelter form was attached to the base ring and preparations were begun for concrete casting.

Concrete Production

Concrete for shelter models was batched and mixed in the Batch Plant of Construction Technology Laboratories. Prior to batching, weights of aggregate and water were adjusted for moisture conditions of the aggregate. Mixing of concrete took place in a 6-cu ft (0.17 m^3) drum-type mixer. Two concrete mixes were

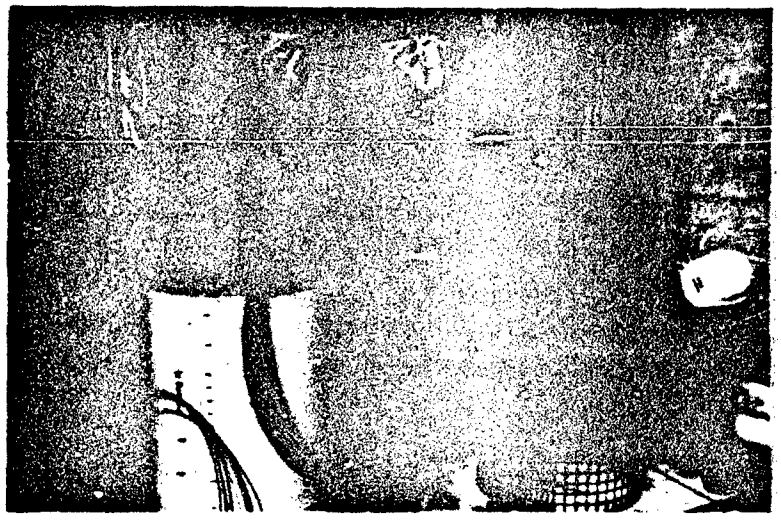

Fig. 7 Tying Bottom Portion of Steel Cage

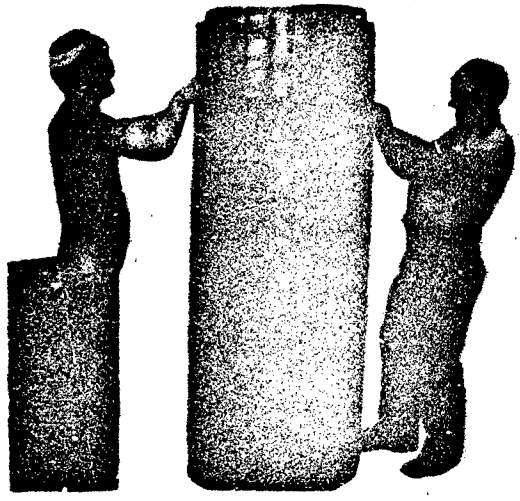

Fig. 8 Tying Top Portion of Steel Cage

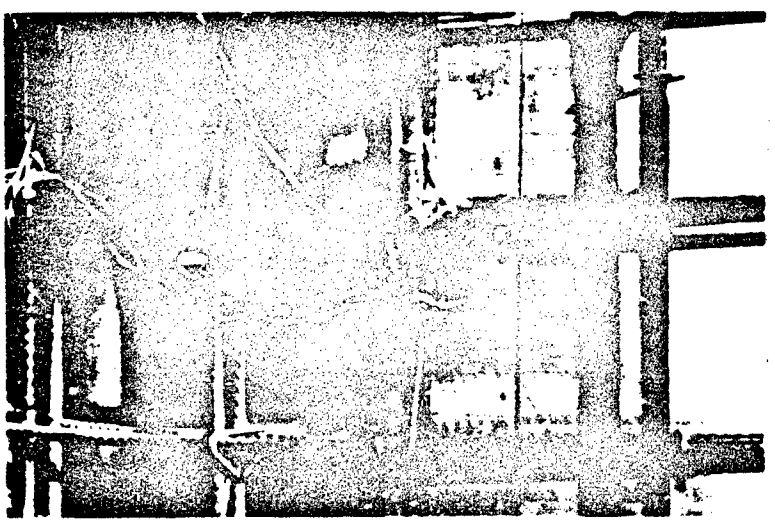

Fig. 9 Closeup of Reinforcement with Strain Gages

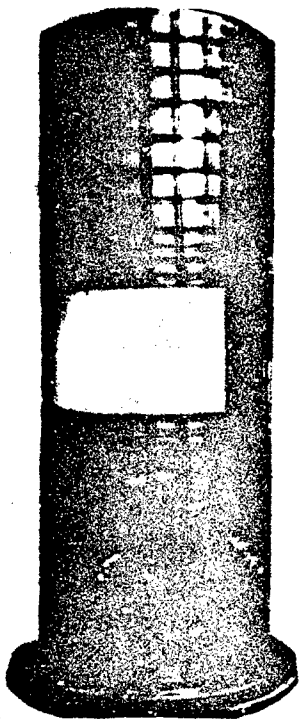

Fig. 10 Complete Reinforcing Steel Cage

used for each specimen. Higher strength concrete was used in the first and last foot of each specimen.

Concrete Placement, Handling and Curing

Before starting concrete placement, forms were checked for roundness and embedded items were checked to verify location. Specimens were cast by depositing concrete between the inner and outer forms. The first and last foot of the specimen was cast using the high-strength mix. The remainder of the specimen was cast using the 6000 psi (41 MPa) compressive strength micro-concrete. Figure 11 shows casting of a specimen. External form vibrators operated continuously during placement.

Forms were removed within 24 hrs after casting. Specimens were cured in large plastic bags until needed for testing. Figure 12 shows a specimen awaiting testing. Immediately after forms were removed, preparations were begun for casting the next specimen.

Quality Control

Concrete materials were tested during manufacture of the shelters. During mixing, slump was determined using applicable procedures outlined in the Construction Specification.[3] Also, six-6x12-in. (152x305 mm) cylinders were cast to represent concrete in each shelter. Two cylinders were tested for compressive strength at 7 and 28 days, and two were tested for modulus of elasticity and compressive strength at an age representing testing of the shelter. Quality control charts were

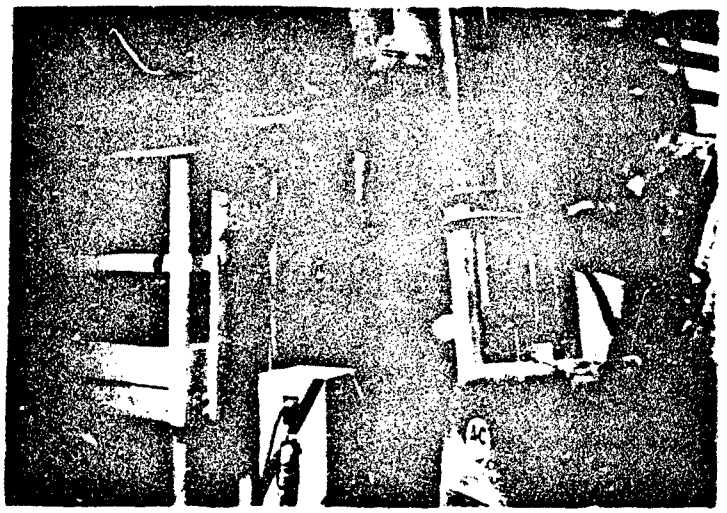

Fig. 11 Specimen Casting

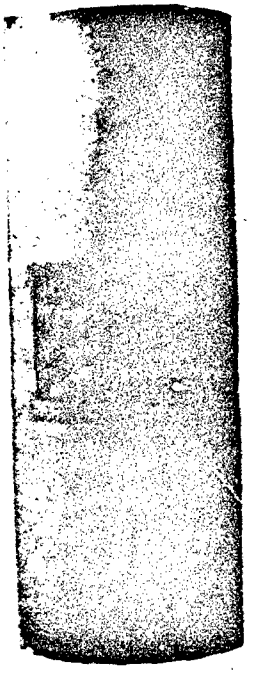

Fig. 12 Specimen Prior to Testing

established to monitor performance of the micro-concrete mix with respect to specifications.

RESULTS

Although the nature of the manufacturing process was complex and delicate, specimens were constructed at a rate of three per week, with no rejections based on either material properties or workmanship.

ACKNOWLEDGMENTS

This investigation was sponsored by Karagozian & Case, Structural Engineers, Los Angeles, California, under contract to Ballistic Missle Office, Norton Air Force Base, MNNXH, San Bernardino, Ca. Ralph Leistikow was Principal in Charge for the sponsor. Work was conducted in the Structural Development Department, Dr. H. G. Russell, Director, as part of the contract research activities of the Construction Technology Laboratories, a Division of the Portland Cement Association. Mr. D. M. Schultz, Assistant Manager, Structural Development Department, was Principal Investigator.

REFERENCES

1. Daniel, J.I. and Schultz, D.M., "Testing of Reduced-Scale Concrete MX-Shelters - Experimental Program," Paper submitted to ASCE Committee on Experimental Analysis and Instrumentation, January 1982.

2. Hanson, N.W. and Julien, J.T., "Testing of Reduced-Scale Concrete MX-Shelters - Instrumentation and Load Control," Paper submitted to ASCE Committee on Experimental Analysis and Instrumentation, January 1982.

3. Ciolko, A.T. and Schultz, D.M., "Specification for Construction of MX-Horizontal Shelters with Inspection Panels," Report submitted to Karagozian and Case, Structural Engineers, April 1980.

PCA R/D Ser. No. 1694

TESTING OF REDUCED-SCALE CONCRETE MX-SHELTERS

EXPERIMENTAL PROGRAM

KEY WORDS: Concrete, Deformations; Loads (axial); Missile; Models; Nuclear Attack; Pressure (surface); Reinforced concrete; Shelter; Strains; Structural engineering; Tests

ABSTRACT: An experimental program involving construction and testing or reduced-scale concrete horizontal MX-Missile Shelters was conducted. The program consisted of 43 shelter specimens tested under static loading conditions. Applied loads modeled forces that might occur on the shelters from a nearby nuclear weapon attack. Loads consisted of various combinations of non-uniform radial surface pressure and axial thrust. Loads, deformations, and reinforcement strains were measured. Strength and ductility of specimens were determined. Test results were used to analyze shelter behavior under "known" loading conditions and to assist in selection of feasible shelter candidates for design.

TESTING OF REDUCED-SCALE CONCRETE MX-SHELTERS

EXPERIMENTAL PROGRAM

by

J. I. Daniel and D. M. Schultz,* M.ASCE

INTRODUCTION

An experimental program involving construction and testing of reduced-scale concrete horizontal MX-Shelters was conducted by Construction Technology Laboratories, a Division of the Portland Cement Association. The program included 43 specimens tested under static loading conditions. Each specimen represented a "candidate design" being considered for prototype construction.

One deployment concept involved MX missiles stored in underground horizontal shelters. One purpose of the shelter was to protect the missile from a nearby nuclear weapon attack such that the missile could be successfully launched after an attack. In the testing program, loads modeling various combinations of forces that might occur from an attack were applied to the specimens. Loads consisted of axial thrust and non-uniform radial surface pressure. Data obtained from the test program were used to analyze shelter behavior under "known" loading conditions.

* Respectively, Associate Structural Engineer and Assistant Manager, Structural Development Department, Construction Technology Laboratories, a Division of the Portland Cement Association, Skokie, Illinois.

This is the first of three papers describing the test program. Other papers describe Specimen Construction [1] and Instrumentation and Load Control.[2]

OBJECTIVES AND SCOPE

The primary objective of the experimental program was to determine strength and ductility of plain and reinforced concrete specimens.

The objective of this investigation was accomplished within the following scope:

1. Loading techniques were developed to model design forces on reduced-scale shelters.
2. Test fixtures were designed and constructed for the simultaneous application of axial compression and non-uniform radial surface pressure on the specimens.
3. Forty-three static load tests were performed.

Final results included a set of data plots for each specimen. These data together with specific test notes, crack mapping, and pictures of tested specimens assisted in the selection of feasible candidates for shelter design.

TEST SPECIMENS

All specimens had a 2-ft (0.61 m) inside diameter with either plain or reinforced concrete walls 1.8 (46 mm) or 2.4-in. (61 mm) thick. As shown in Fig. 1, specimen test length was 4 ft (1.22 m) with an additional 1 ft (0.30 m) at each end for load transfer. Overall specimen length was 6 ft (1.83 m). At

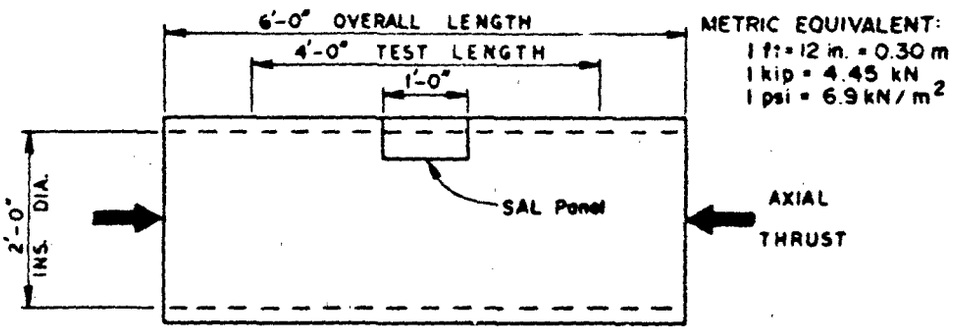

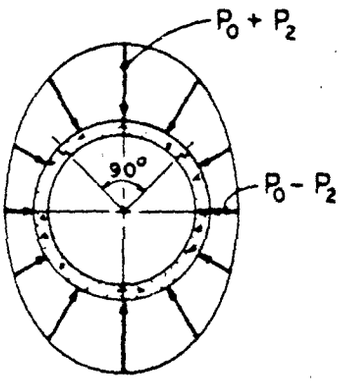

RADIAL PRESSURE COMPONENT

$P_{TOTAL} = P_0 + P_2 \cos 2\theta \leq 1200$ psi

P_0 = UNIFORM PRESSURE

$P_2 = 0.05 P_0$ TO $0.20 P_0 \leq 150$ psi

AXIAL THRUST COMPONENT

T = AXIAL THRUST $\leq$ 1500 kips

$= P_0 \times$ (TOTAL END AREA)

$P_0 = 0$, $1.0 P_0$, $2.0 P_0$

Fig. 1 Schematic of Test Specimen and Prototype Loading

specimen mid-length, there was a 90° wide segment 1-ft (0.30 m) long that represented the MX-Shelter Strategic Arms Limitation (SAL) panel. This panel was fitted into the specimen with "Z" shaped joints.

Early concepts for shelter design required breakout joints (weakened plane joints) located at ± 45° from the specimen crown on both sides of the SAL panel. Breakout joints were required in Phase 1 specimens only.

There were seven "basic" wall design configurations comprising a total of 16 wall designs. Basic design configurations were classified as follows:

A1 - plain concrete, no SAL panel

A2 - double layer reinforcement, no SAL panel

A3 - plain concrete, with SAL panel

B1 - double layer reinforcement, with SAL panel

B2 - single layer reinforcement, with SAL panel

C1 - steel liner with stud anchors, plain concrete, with SAL panel

C1 - steel liner with stud anchors, single layer reinforcement, with SAL panel

Additional variables within the basic design configurations included wall thickness, amount of reinforcement, breakout joint details, thickness of liner, spacing of studs, and gap between inner and outer Z-insert. Variable matrix and quantities included in the program are given in Table 1.

TABLE 1 - MX-HORIZONTAL SHELTERS SPECIMEN DESCRIPTION

Construction Phase	Specimen Identification Number	Reinforcing	Liner, Studs	SAL Gap (in.)	Breakout Joint	Thickness (in.)	Total Quantity
I	A1	None	None	No SAL	Yes	1.8	2
	A2	2 layer, 1/2% ewef	None	No SAL	Yes	1.8	3
	A3	None	None	0.025	Yes	1.8	3
	B1	2 layer, 1/2% ewef	None	0.025	Yes	1.8	6
	B2	1 layer, 1% ew	None	0.025	Yes	1.8	3
	C1	None	16 Ga, 3-1/2 in. oc	0.025	Yes	1.8	6
	C2	1 layer, 1/3% ew	16 Ga, 3-1/2 in. oc	0.025	Yes	1.8	3
II	B1.2	2 layer, 1/4% ewef	None	0.025	No	1.8	2
	B1.3	2 layer, 1% ewef	None	0.025	No	1.8	2
	C1.2	None	20 Ga, 4 in. oc	0.025	No	1.8	2
	C1.3	None	16 Ga, 4 in. oc	0.025	No	1.8	2
	C1.4	None	16 Ga, 3 in. oc	0.025	No	1.8	2
III	C2.2	1 layer, 1/3% ew	20 Ga, 3 in. oc	0.025	No	1.8	1
	C2.3	1 layer, 1/3% ew	20 Ga, 3 in. oc	0.025	No	2.4	4
	C2.4	1 layer, 1/3% ew	20 Ga, 3 in. oc	0.05	No	2.4	1
	C2.5	1 layer, 1/3% ew	20 Ga, 3 in. oc	0.10	No	2.4	1

Notes:

ew = each way
ewef = each way, each face
Ga = gage
oc = on center

Metric Equivalent:

1 in. = 25.4 mm

TEST LOAD REQUIREMENTS

Specimens were subjected to static loads consisting of axial thrust and non-uniform radial surface pressures that represented pressures defined in Fig. 1. Applied radial pressure modeled a distribution around the specimen circumference equal to $P_o + P_2 \cos 2\theta$, where P_o was a uniform pressure and P_2 ranged from $0.05\ P_o$ to $0.20\ P_o$. Axial thrust pressure, P_a, was applied as a multiple of the uniform radial pressure; i.e., $0.0\ P_o$, $1.0\ P_o$, $2.0\ P_o$, and uniaxial load only. In general, axial thrust was applied with an initial eccentricity of zero on the specimen end.

Sixteen different combinations of P_a/P_o were used in the testing program. A description of each loading condition is given in Table 2.

All specimens were to be tested to failure or to the limits of the test equipment.

DESCRIPTION OF TESTING APPARATUS

The test apparatus was designed to apply any one of the following loadings:

1. Axial load only
2. Axial load with radial surface pressure
3. Radial surface pressure only

Radial Surface Pressure Loading

Radial pressure was applied to the specimen by pressure bladders housed between the specimen and a steel pressure

TABLE 2 - LOADING CONFIGURATIONS

Type	Description	P_a/P_o	P_2/P_o
A	Uniform Radial Only	0	0
B	Nonuniform Radial Only	0	0.05
C	Nonuniform Radial Only	0	0.10
D	Axial and Nonuniform Radial	1.0	0.05
E	Axial and Nonuniform Radial	1.0	0.10
F	Axial Only	-	-
G	Axial and Nonuniform Radial	2.0	0.05
H	Axial and Nonuniform Radial	2.0	0.10
I	Axial and Nonuniform Radial	1.0	0.15
J	Axial and Nonuniform Radial	2.0	0.15
K	Nonuniform Radial Only	0	0.15
L	Nonuniform Radial Only	0	0.20
M	Nonuniform Radial Only	0	$P_2 - P_o = 25$ psi
N	Nonuniform Radial Only	0	$P_2 - P_o = 50$ psi
P	Axial and Nonuniform Radial	1.0	0.20
Q	Axial and Nonuniform Radial	2.0	0.20

Metric Equivalent:

1 psi = 6.9 kPa

vessel. The pressure vessel is shown schematically in Figs. 2 and 3.

Bending in the pressure vessel due to non-uniform radial pressure was resisted by steel ribs around the circumference of the 1-1/2-in. (38 mm) thick steel vessel wall.

The pressure vessel could resist the combined effects of P_o and P_2 equal to 1050 psi (7.2 MPa) and 150 psi (1.0 MPa), respectively. In addition, it could accommodate $\pm$ 4 in. (102 mm) of diameter change under non-uniform radial pressure. Vessel weight of 15,000 lb (6800 kg) was supported on its own legs and not by the specimen prior to or during the test.

The radial pressure component indicated in Fig. 1 was modeled using three distinct pressures applied by eight specially made neoprene bladders housed between the specimen and steel vessel. Pressure bladders labeled A in Fig. 2 applied the largest pressure. Pressure bladders labeled B applied the smallest pressure. Pressure bladders labeled C applied the middle pressure. Segments A and B were 60° wide and Segments C were 30° wide. Bladders were partially separated by steel partitions to limit force transfer between adjacent bladders.

To develop the model pressure loading, a computer program was written to determine the effects of several pressure configurations around the circumference of the specimen. The model that was finally selected closely approximated the moments, shears, and thrusts, induced from the prototype loading

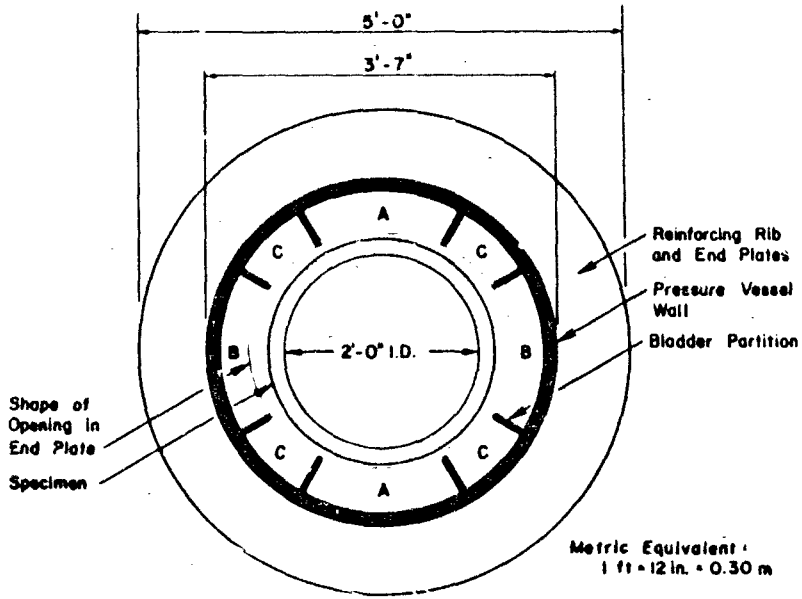

Fig. 2 Cross-Section of Pressure Vessel (Plan)

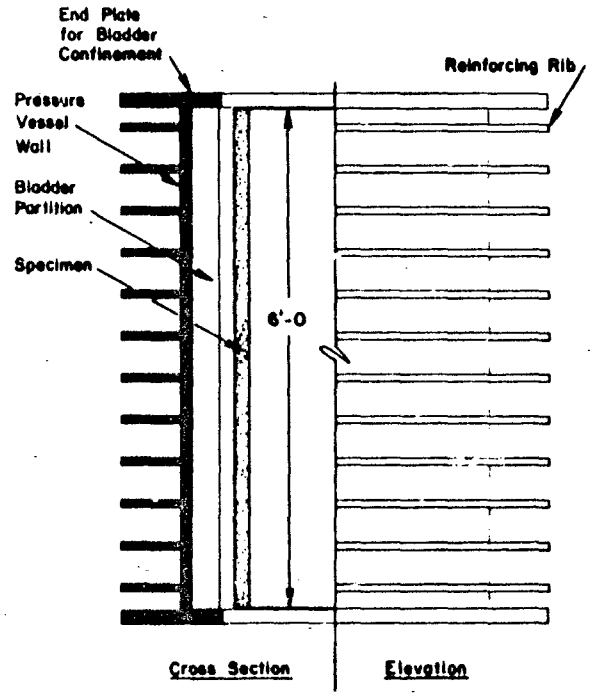

Fig. 3 Cross-Section and Elevation of Pressure Vessel

distribution shown in Fig. 1. Plots of moment, shear, and thrust occurring on the specimen due to both the prototype component and modeled pressure component are shown in Fig. 4. As indicated, model load application provided nearly identical moments, shears, and thrusts at all locations where maximum and minimum values occurred. This included shear at the 45° line in the specimen.

Uniaxial Compressive Loading

Arrangement of the testing apparatus for uniaxial compressive loading is shown in Figs. 5 and 6. Also indicated in these figures is the position of the radial pressure vessel. Test specimens were positioned with their longitudinal axis in a vertical direction.

The axial test fixture was constructed of prestressed concrete to minimize stored energy. Reduction of stored energy in the system during testing facilitated recording of inelastic specimen behavior. The reaction frame was capable of resisting 1500 kips (6670 kN) of axial force. Axial load was applied by a 3500-kip (15,570 kN) hydraulic ram acquired on loan from National Aeronautics and Space Administration.

As shown in Fig. 6, bearing plates transferred axial load from ram to specimen and from specimen to laboratory floor. Bearing plates were constructed of reinforced concrete and steel plates. The shape of each bearing plate conformed to the opening in the end plate of the pressure vessel. There was a 1/16-in. (1.6 mm) gap between the bearing plate sides and the

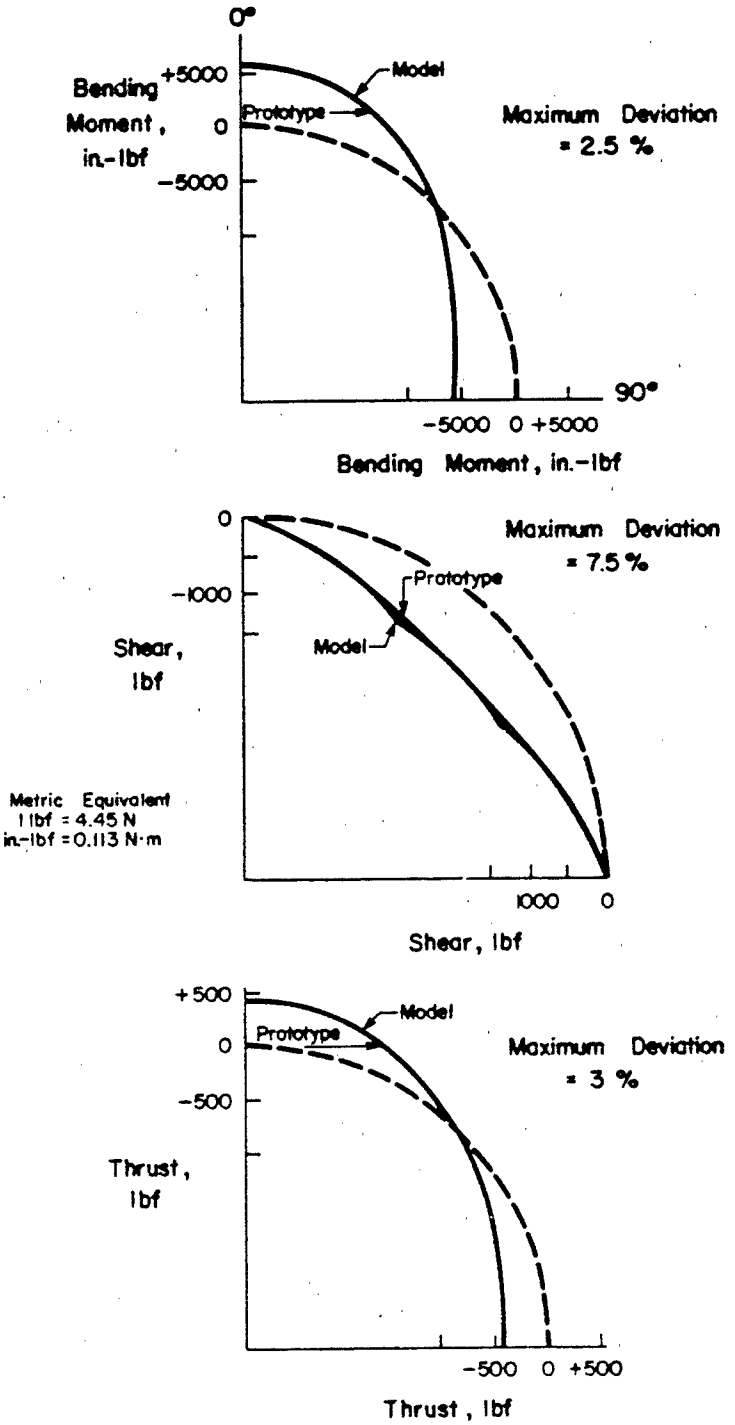

Fig. 4 Plots of Bending Moment, Shear, and Thrust for Prototype and Model Load Application

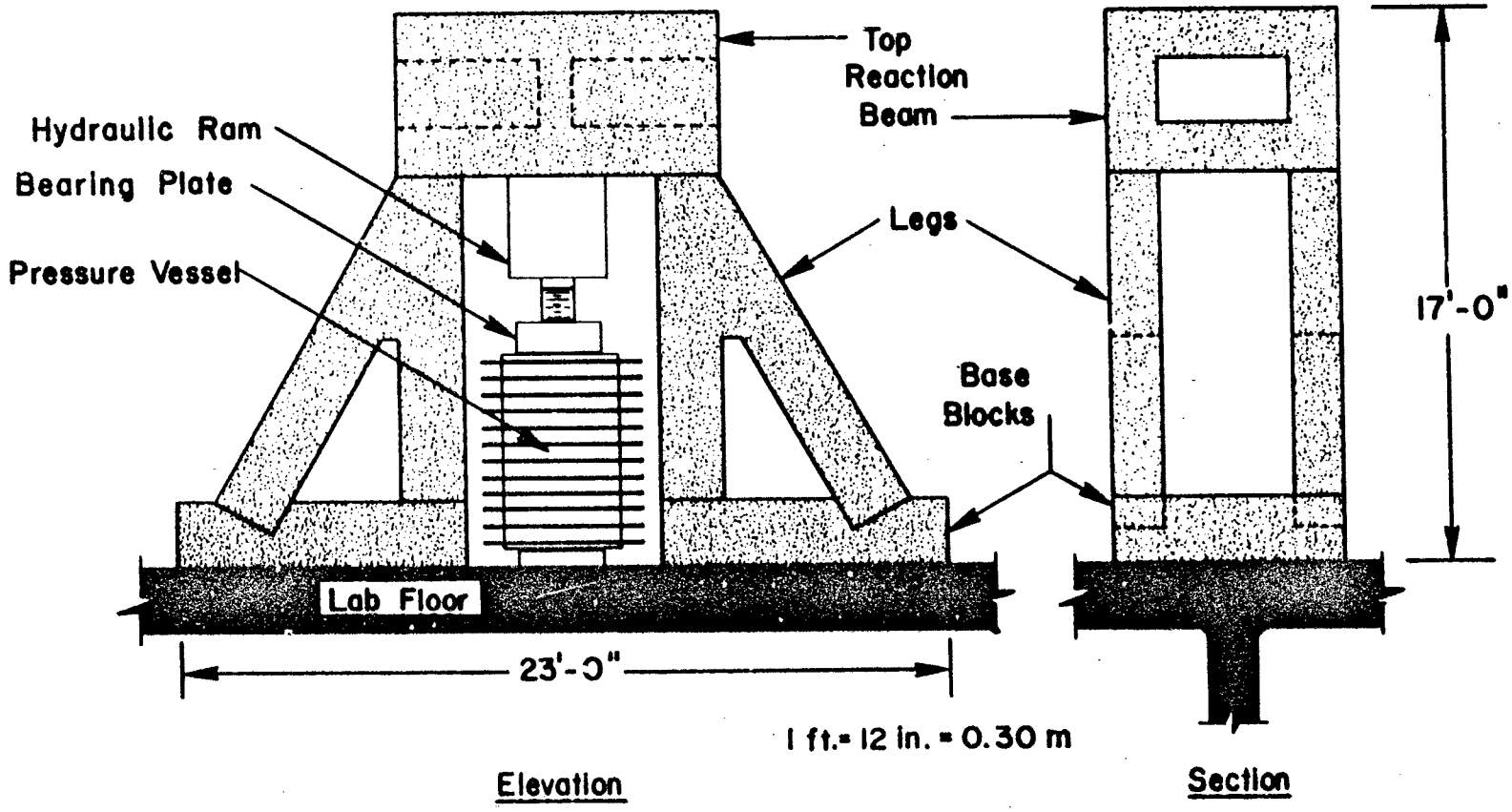

Fig. 5 Axial Reaction Frame

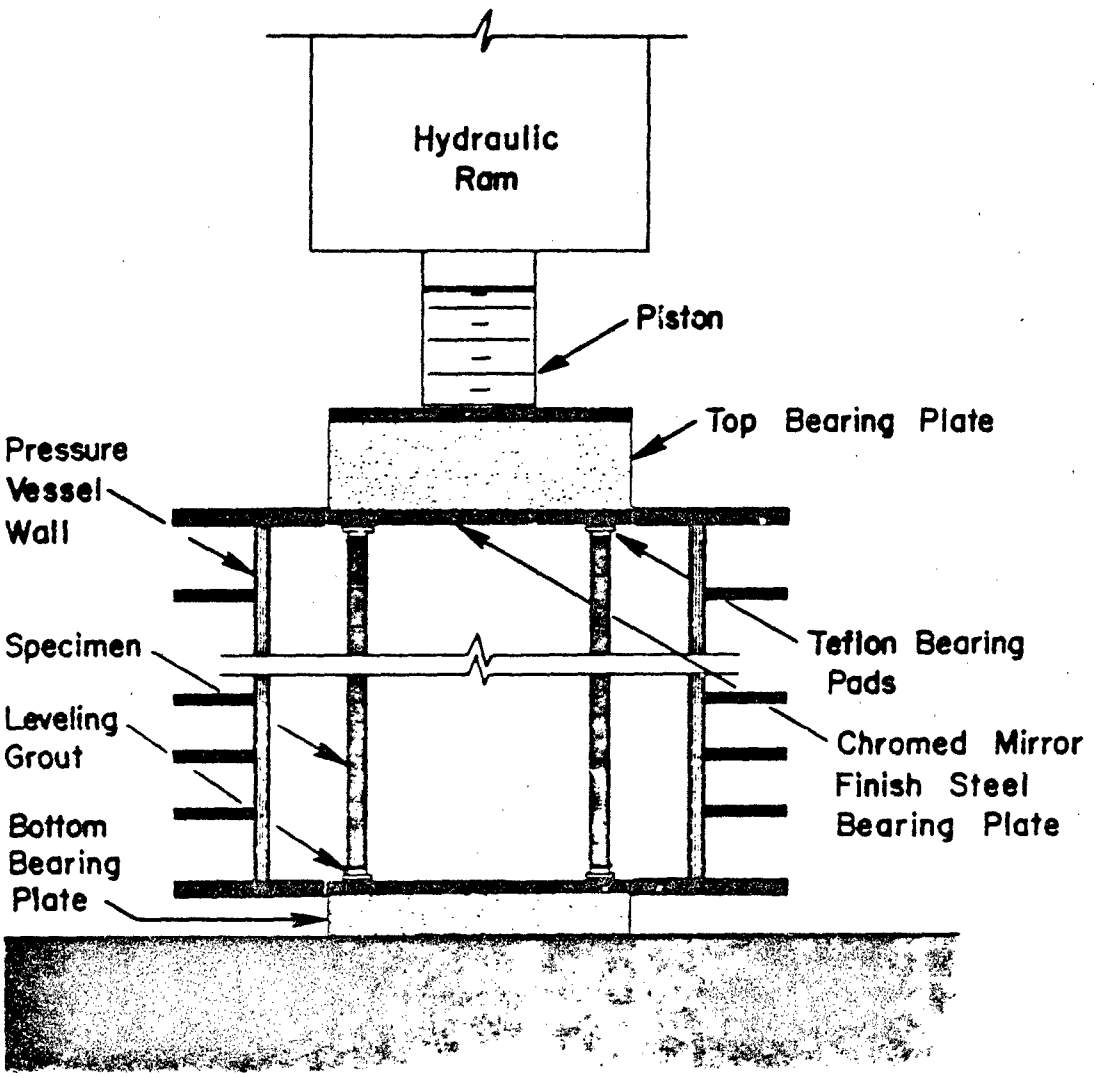

Fig. 6 Cross-Section of Axial and Radial Load Application System

end plates sides of the pressure vessel. This "fit" assured continuous alignment of the pressure vessel during each test. The combination of bearing plate and end plate also assured complete and continuous confinement for the enclosed pressure bladders described earlier.

The steel bearing plates were level and flat with a mirror-finish chrome plating. Teflon bearing pads, shown in Fig. 6, were placed on the grout capped ends of each specimen. The combination of Teflon on chrome gave a coefficient of friction of about 0.04. Low friction allowed the specimen to deform radially under combined axial and radial load while inducing minimum bending stresses into the specimen wall. Capping specimen ends with grout facilitated leveling of specimen ends, thus ensuring initial uniform axial load application.

A photograph of the test setup is shown in Fig. 7.

Calibration

Calibration of radial pressure and axial load was performed using a specially built calibration rig shown in Fig. 8. This calibration rig was a solid reinforced concrete cylinder, identical in size to a test specimen. Inside the calibration rig were six 100-kip (445 kN) load cells housed behind a 48.0 x 7.2-in. (1220 x 180 mm) piston.

The calibration rig was inserted into the pressure vessel and the upper bearing plate was lowered to contact its top. The bladders were then pressurized while loads applied into the piston and into the top bearing plate were being recorded.

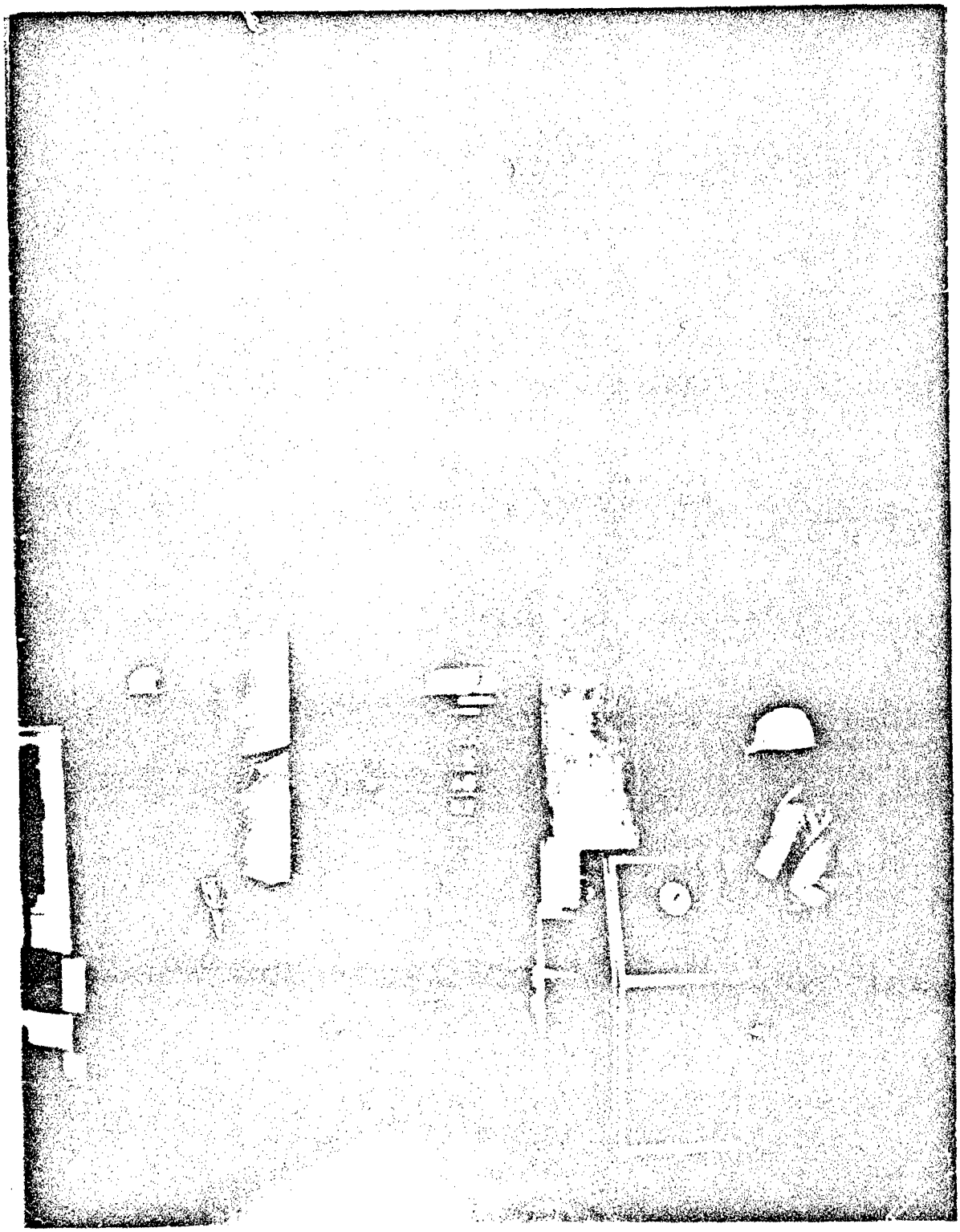

Fig. 7 Photograph of Test Setup

Fig. 8 Calibration Rig

Calibration factors used to correct applied load or pressure were determined using the recorded calibration loads and known contact areas. These factors were directly programmed into the computer to automatically correct subsequent test data.

TEST PROCEDURE

Preparation and testing of one specimen took approximately four hours.

Specimen Preparation

Prior to testing, each specimen was checked against construction specifications.[1] Steps in specimen preparation were as follows:

1. Exterior instrumentation[2] was connected to the inside wall of the specimen.
2. Specimen bottom was leveled with a quick setting grout using a specially built leveling platform. This procedure was similar to capping a 6 x 12-in. (152 x 305 mm) concrete cylinder.
3. Instrumentation was plugged into the data acquisition system and checked for proper functioning prior to inserting specimen into the pressure vessel.
4. All visible cracks in a specimen prior to testing were recorded.
5. Specimen was inserted into the pressure vessel.
6. Specimen/vessel combination was rolled on rails into the axial test fixture.

7. Instrumentation was plugged in and cables were taken out through an opening in the top bearing plate. Teflon pads were placed under the specimen.
8. Pressure vessel was lowered into the proper position.
9. Quick setting grout was placed on the specimen top. The level top bearing plate was lowered to contact and squeeze enough grout out to ensure a level specimen top. Grout was allowed to dry.
10. Top bearing plate was raised to permit placement of the top Teflon bearing pads. Top bearing plate was lowered again.
11. Pressure bladders were filled with oil. All air was bled from the bladders.
12. Test was ready to begin.

Test Conduct

Each test was fully computerized. The responsibility of the testing engineers was to monitor test progress, make any necessary manual adjustments, and take test notes. Technicians were posted around the test fixture only to note the occurrence of anything out of the ordinary.

Prior to the start of each test, the proper loading functions were programmed into the computer controlled loading system. A detailed description of the load control system is given in Ref. 2. During the test, an entire set of data was collected by the data acquisition system approximately every 10 seconds. In this time, the computer was programmed to accept and store

raw data. In addition, there was ample time to reduce and display necessary data for observation of test progress. This "Test Control" information was continuously displayed on a video screen (CRT) and updated every 10 seconds. A spontaneous user request provided a hardcopy of the data. Control information consisted of the following items:

1. Axial Load
2. Three Radial Pressures
3. Axial Shortening
4. Radial Deformation
5. All Strain Gage Data

In addition to control data displayed on the CRT, continuous plots were recorded on X-Y plotters. Detailed description of the data acquisition system, instrumentation, and data handling are given in Ref. 2.

A test was terminated under any of the following conditions:

1. Design axial load or radial pressure limits were reached
2. Specimen failed catastrophically
3. Axial load or radial pressures dropped to 50% of peak values
4. Allowable specimen deformation, i.e., 4-in. (102 mm) was exceeded

Post-Test Examination

Observed failure mode of each specimen was recorded. Photographs were taken and pre- and post-test crack patterns were plotted.

TEST RESULTS

Approximately 24 hours after each test, the client was provided with the following test results:

1. Test notes
2. Reduced data recorded on magnetic tape
3. Data plots
4. Map of crack patterns

Photographs were provided to the client on a weekly basis. Tested specimens are shown in Fig. 9. Examples of data plots are presented in Ref. 2.

SUMMARY

The fast-paced test program was successfully completed within 11 months, from November 1979 to October 1980. In this time the following was accomplished:

1. Design and construction of test fixtures
2. Calibration of test fixtures
3. Design and setup of load control and instrumentation systems[2]
4. Design and fabrication of specimen forms for casting[1]
5. Casting and instrumenting 43 test specimens[1]
6. Testing 43 specimens

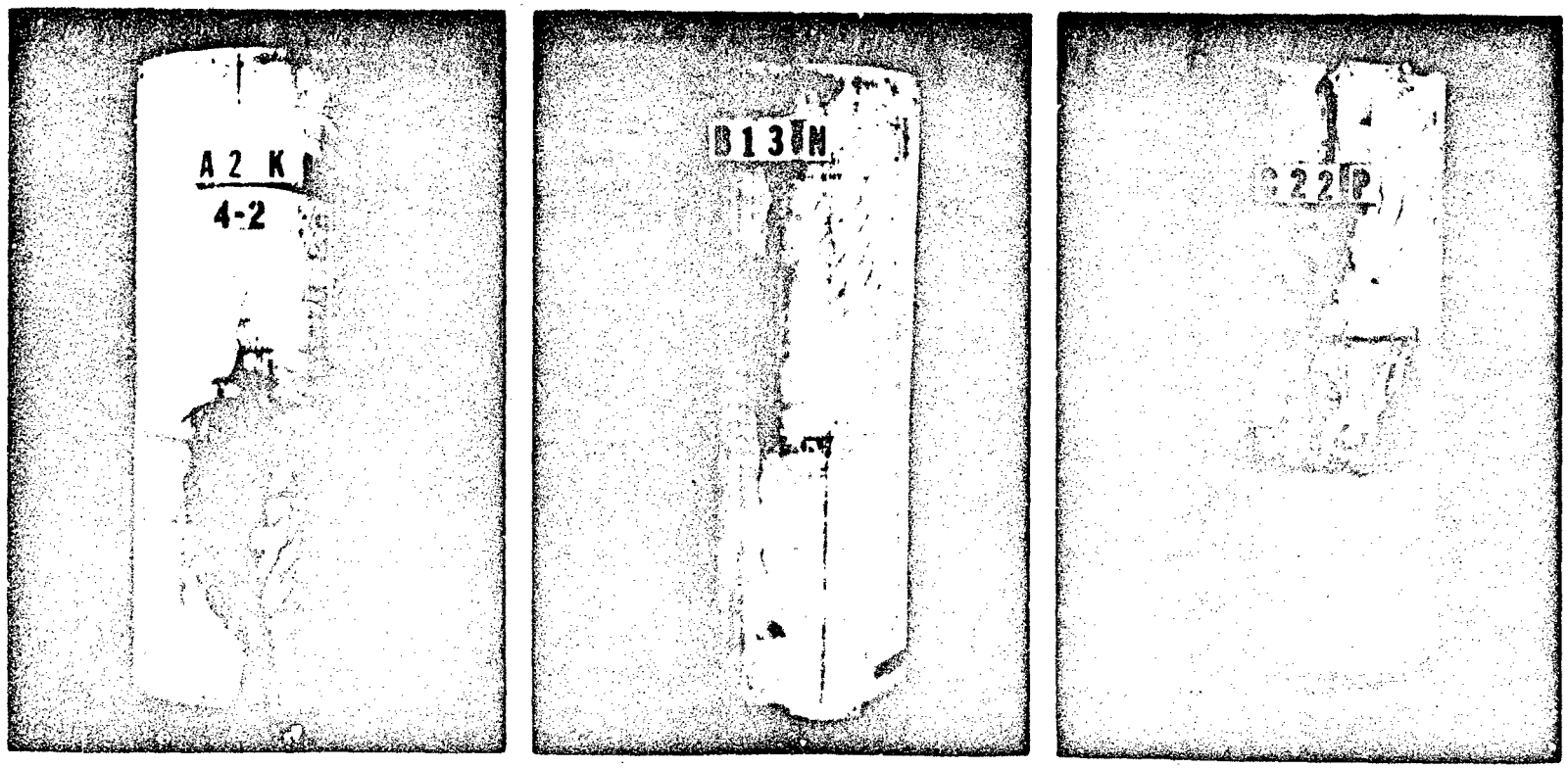

Fig. 9 Specimens After Testing

Test results were used to analyze shelter behavior under "known" loading conditions and to assist in the selection of feasible candidates for shelter design.

ACKNOWLEDGMENTS

This investigation was sponsored by Karagozian & Case, Structural Engineers, Los Angeles, California, under contract to Ballistic Missile Office, Norton Air Force Base, MNNXH, San Bernardino, California. Ralph Leistikow was Principal in charge for the sponsor. Work was conducted in the Structural Development Department, Dr. H. G. Russell, Director, as part of the contract research activities of the Construction Technology Laboratories, a Division of the Portland Cement Association.

REFERENCES

1. Ciolko, A.T., "Testing of Reduced-Scale Concrete MX-Shelters - Specimen Construction," Paper submitted to ASCE Committee on Experimental Analysis and Instrumentation, January 1982.

2. Hanson, N.W. and Julien, J.T., "Testing of Reduced-Scale Concrete MX-Shelters - Instrumentation and Load Control," Paper submitted to ASCE Committee on Experimental Analysis and Instrumentation, January 1982.

19 JAN 1982

TESTING OF REDUCED-SCALE CONCRETE MX-SHELTERS

INSTRUMENTATION AND LOAD CONTROL

KEY WORDS: Data systems; Deformations; Loads; Measuring instruments; Models; Pipes (tubes); Reinforced concrete; Shelters; Strains; Testing

ABSTRACT: Equipment and methods are described for application of axial load and non-uniform radial pressure to concrete specimens in constant strain rate tests. Forty-three specimens modeled candidate designs for horizontal MX-shelters. Loading combinations represented forces from nearby nuclear weapon attack. Servo-controlled hydraulic loading equipment and instrumentation were combined to apply specified loads and monitor both test performance and specimen behavior.

TESTING OF REDUCED-SCALE CONCRETE MX-SHELTERS

INSTRUMENTATION AND LOAD CONTROL

by

N. W. Hanson, M. ASCE, and J. T. Julien*

An experimental program involving construction and testing of reduced-scale concrete Horizontal MX-Shelters was conducted by Construction Technology Laboratories, a Division of the Portland Cement Association. The program included 43 specimens tested under static loading conditions. Each specimen represented a "candidate design" being considered for prototype construction.

One deployment concept involved MX-missiles stored in underground horizontal shelters. One purpose of the shelter was to protect the missile from a nearby nuclear weapon attack such that the missile could be successfully launched after an attack. In the testing program, loads modeling combinations of forces that might occur from an attack were applied to the specimens. Loads consisted of axial thrust and non-uniform radial surface pressure. Data obtained from this test program were used to analyze shelter behavior under "known" loading conditions.

*Respectively, Principal Structural Engineer, Structural Development Department, and Associate Construction Engineer, Construction Methods Section, Construction Technology Laboratories, a Division of the Portland Cement Association, Skokie, Illinois.

This is the last of three papers describing the program. Other papers describe Experimental Program[1] and Specimen Construction.[2]

OBJECTIVES

Testing of the shelter model shown in Fig. 1 included application of selected combinations of axial thrust and radial pressures. Displacement control and data handling during testing are discussed in this paper. Objectives of instrumentation, test control, and data handling were:

1. Install sensors as necessary to provide data for control and for documentation of structural behavior.
2. Maintain a selected relationship between all loads while generating a monotonic increase in a measured displacement at a selected rate.
3. Measure and store data at 10 second intervals of time and display suitable reduced data at each interval for status check by test engineer.
4. Produce reduced data in the form of tables, charts, and digital tape for delivery to client within 24 hours of each test.
5. Provide semi-automatic instrumentation checkout and calibration procedures to allow two tests per day.

INSTRUMENTATION

Measurements of strain, load, displacement, and time were recorded at intervals during the test for later analysis of results. Some measurements were also displayed on X-Y recorders

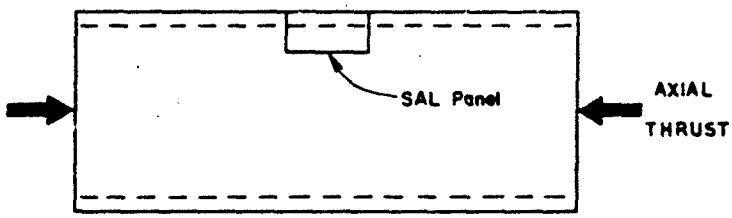

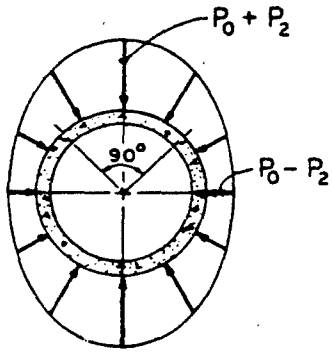

RADIAL PRESSURE COMPONENT

$P_{TOTAL} = P_0 + P_2 \cos 2\theta$

P_0 = UNIFORM PRESSURE

$P_2 = 0.05P_0$ TO $0.20P_0$

AXIAL THRUST COMPONENT

T = AXIAL THRUST

$= P_0 \times$ (TOTAL END AREA)

$P_0 = 0$, $1.0P_0$, $2.0P_0$

Fig. 1 Schematic of Test Specimen and Loading

for visual observation and verification of the test. Certain measurements were also used by the servo-controlled load system for test control. Table 1 lists types and locations of instrumentation. For reference purposes, specimens were positioned with their longitudinal axis vertical and with the SAL panel facing North.

A digital data acquisition system sampled all data items at about 10 second intervals during each test. Each sample was recorded at a rate of about 10 items per second. An average test had over 100 samples of data.

Longitudinal Strains

Axial change in length was sensed by linear potentiometers attached to the inner surface of the specimen. Measurements were made over a gage length of 50 in. (1.25 m). Potentiometers were spaced at quarter points around the inner circumference with one potentiometer centered on the SAL panel. Waters Model SLF-2 position transducers with 2-in. (50 mm) stroke were used for longitudinal strain measurements. Strain was calculated as axial length change divided by gage length.

Radial Displacements

Linear potentiometers were attached to the inner surface of each specimen to sense changes in diameter. Locations are given in Table 1. Two measurements on orthogonal diameters were made at each of two cross-sections. One cross-section was at mid-height with one diameter measurement centered on the SAL panel.

TABLE 1 - INSTRUMENTATION

Item	Description
Longitudinal Strains	
Potentiometer	Axial #1 - west side
Potentiometer	Axial #2 - east side
Potentiometer	Axial #3 - south side (opposite SAL)
Potentiometer	Axial #4 - at SAL Panel (north side)
Radial Displacement	
Potentiometer	Axial #1 - mid-height - north-south (SAL panel)
Potentiometer	Axial #2 - mid-height - east-west
Potentiometer	Axial #3 - above mid-height - north-south
Potentiometer	Axial #4 - above mid-height - east-west
Radial Forces and Axial Load	
Pressure Cell	Radial load #1 - north-south (highest pressure)
Pressure Cell	Radial load #2 - 4 places (intermediate pressure)
Pressure Cell	Radial load #3 - east-west (lowest pressure)
Pressure Cell	Axial ram
Specimen Strains	
6 Strain gages	On circumferential reinf. at mid-height
2 Strain gages	On radial reinforcement at mid-height
2 Strain gages	On longitudinal reinforcement at mid-height
6 Strain gages	On circumferential reinforcement above mid-height
2 Strain gages	On radial reinforcement above mid-height
2 Strain gages	On longitudinal reinf. above mid-height

The second measurement was 12 in. (300 mm) above mid-height. Waters Model SLF-6 position transducers with 6-in. (150 mm) stroke were used for radial displacement measurements.

Radial Forces

Radial surface pressures were applied by means of inflated pressure bladders pressing against zones on the specimen. Each zone was duplicated at symmetrical locations. Hydraulic pressure in each of the three zones was measured by a strain gaged pressure cell.

Axial Load

Force applied to axially compress the specimen was determined from a strain gaged pressure measuring cell. This cell sensed hydraulic pressure in the large axial load ram.

Specimen Strains

Strain gages were bonded on special small diameter steel rods or reinforcing steel embedded in the concrete of each test specimen. Strains were monitored at the 20 locations listed in Table 1.

Time

A digital clock in the data acquisition system provided a time reference for each data sampling.

Instrumentation Plan

Connections between sensors and instruments are shown in Fig. 2. Sensors, cables, and strain gage leads inside the specimen were connected to a junction box. Figure 3 shows the

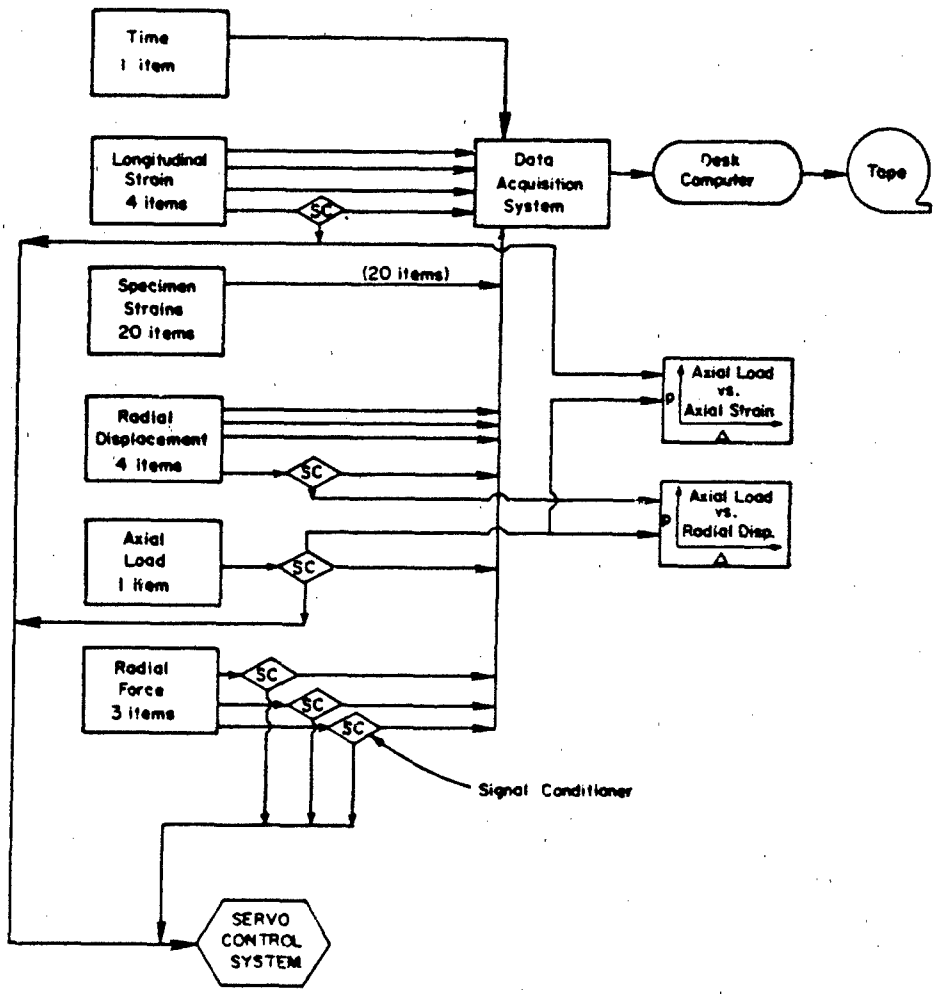

Fig. 2 Schematic of Data Acquisition System

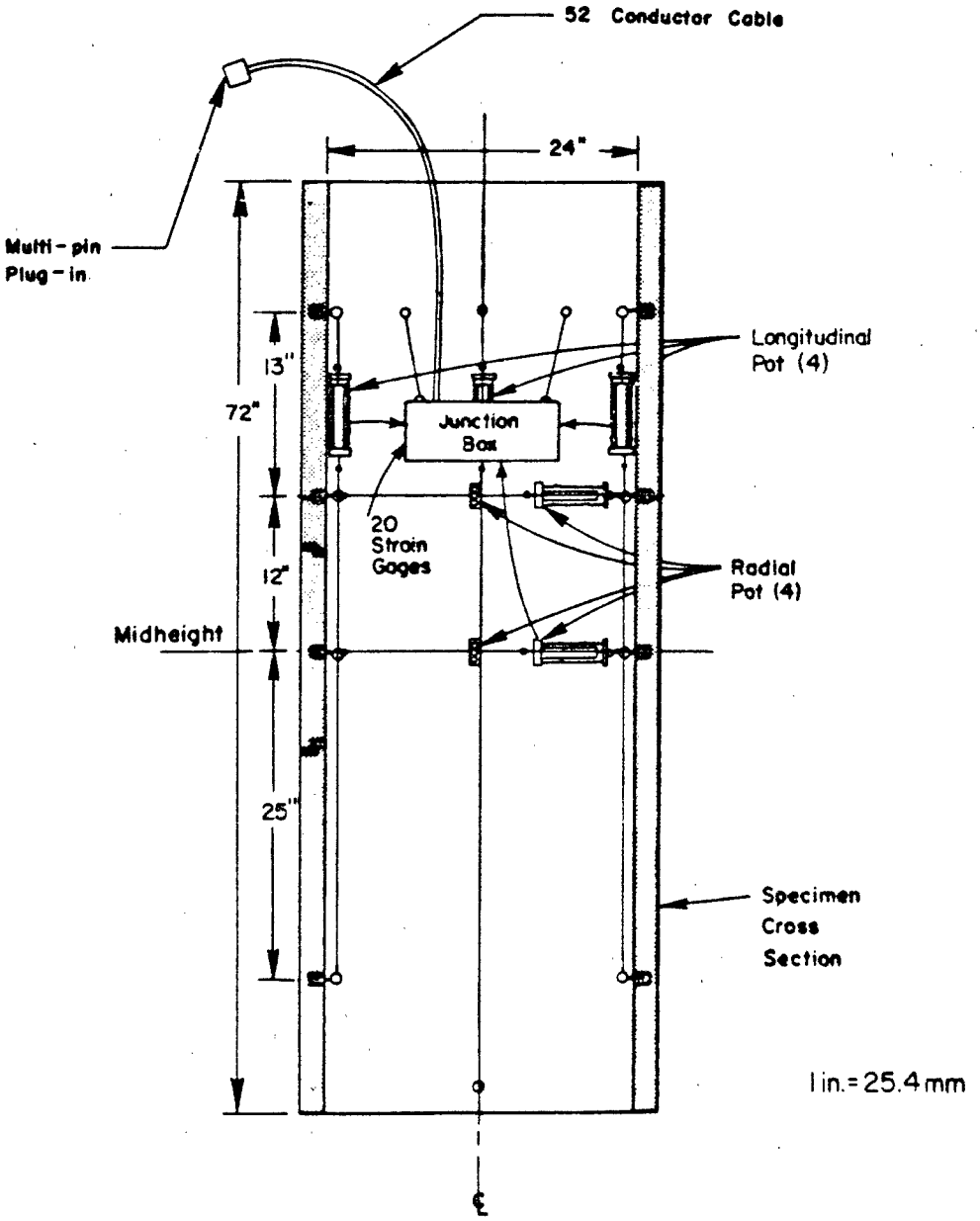

Fig. 3 Partial Instrumentation Layout

junction box with a short cable and multipin connector for attachment to the data acquisition system. All analog data were converted to digital data by a Hewlett-Packard Model 3052 Automatic Data Acquisition System. Digital information on each channel was stored on cartridge tape on a Hewlett-Packard Model 9845B desk computer.

LOAD CONTROL

The standard test involved application of combined uniaxial compression and radial surface pressure. In this configuration, radial load was applied as necessary to maintain a near constant rate of diameter deformation. Axial and radial loads were applied in proportions that developed the necessary P_a/P_o and P_2/P_o ratios. P_a, P_o, and P_2 are defined in Fig. 1. Closed loop electrohydraulic equipment by MTS Systems Corp. provided servo-control of loads.

The standard test at a constant rate of diameter deformation was conducted in about 30 minutes.

A schematic representation of load control is shown in Fig. 4. A radial displacement signal was manually compared to a predetermined ramp function to generate a control signal. This control signal was then used as program input to four MTS Model 406.11 Servo Controllers.

The combination of four individual closed loop servo-controlled loads within an overall closed loop incorporating manual rather than servo-control functioned well for these very slow tests. Using Servo-control in the outer loop tended to

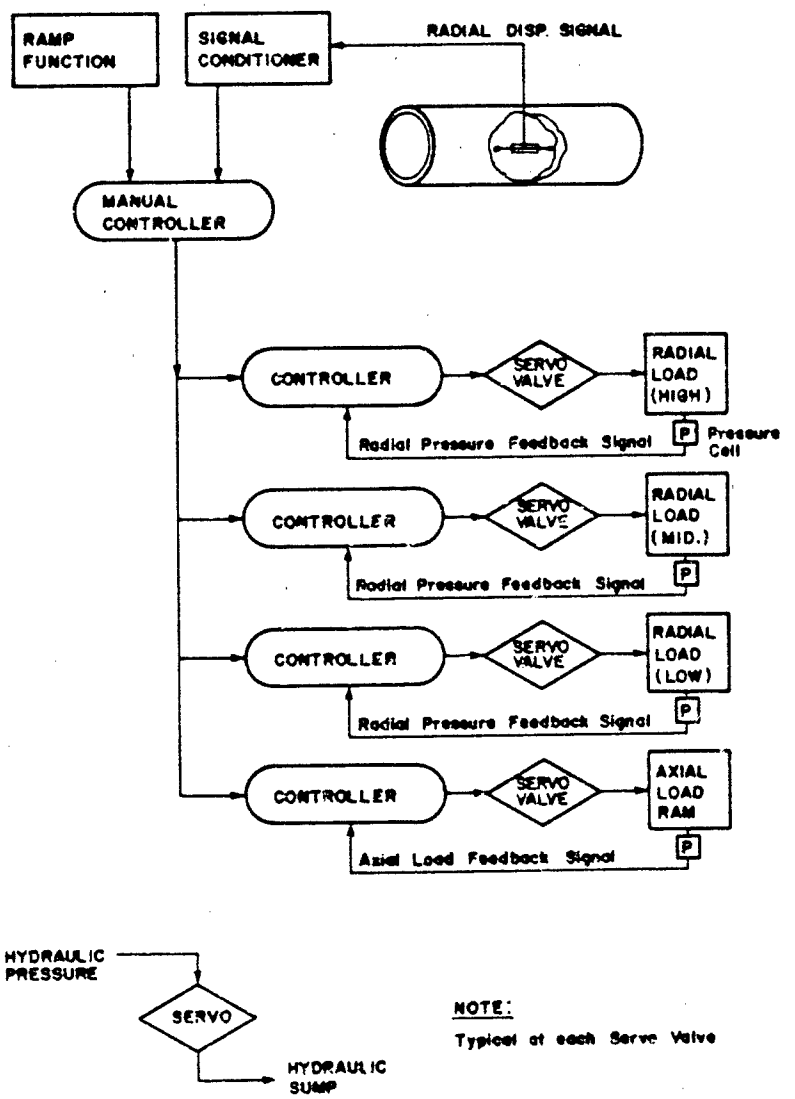

Fig. 4 Schematic of Load Control System for Standard Test

produce very low cycle oscillations (one cycle in 2 minutes) in the control circuit. Manual control was incorporated as a practical solution since the project schedule did not allow time for the experimentation needed to otherwise solve the problem.

The feedback signal for each controller came from a pressure cell, BLH type DHF, at each radial loading assembly and at the axial ram. Each controller compared the feedback signal to the program input signal to generate a control signal that operated a servo valve in the loading system. An MTS Model 252.22 Servo Valve controlled hydraulic pressure applied to high, middle, and low pressure loading assemblies, and to the axial ram. These valves, which had flow rates of 2.5 gallons (9.5 L) per minute, were matched to required flow rates to minimize load pulsations.

A predefined relationship was maintained between radial pressures in the three zones and axial load. Adjustment of each controller set the proportionality factor between radial pressures and axial load.

The preceding description applied to the standard test which included both axial and radial load. When only radial load was applied, program input on the axial load controller was set to zero. For tests of axial load only, program input on the three radial load controllers was set to zero. Axial load tests were based on constant rate of axial strain rather than diameter deformation.

DATA HANDLING

As a test progressed, data items were sequentially connected by the scanner to a digital voltmeter that measured voltage and

sent voltage data to the computer. The 32 data items plus time were measured in an elapsed time of about 3 seconds at intervals of 10 seconds. The computer stored each 10-second data as a record in a random access file on magnetic tape. Data were then reduced to engineering units and ratios for presentation on the screen of the HP9845B computer. Since the test specimen was completely hidden from view during a test, the test engineer had to judge conduct of the test from the constantly updated data display. An example of a screen display of data is shown in Fig. 5.

Data Reduction

After each test, data files on tape were read into the computer for reduction to engineering units and plots. Tables of data were printed and relationships between variables were plotted. An example of a table and a plot are shown in Figs. 6 and 7 respectively. The data files on a raw data tape for a test included descriptive information concerning the test, zero readings on all items, calibration factors, and data records for each time interval. A reduced data tape was made for the client. That tape included descriptive information and data records prepared in engineering units. A package of tables, plots, and tape, such as shown in Fig. 8, was sent to the client within 24 hours of each test.

An additional improvement in the reduced data was made for the final report. In tests that included non-uniform radial load, there were data points in which the load ratio P_2/P_o deviated from the specified ratio. Final reduced data included only those points with the ratio of P_2/P_o within $\pm 10\%$ of the specified ratio.

```
FINISHED WITH LINE  92                AT  14  42  48


AXIAL LOAD=  298                 PP/P0=+1.001          LOAD STAGE#    92

RADIAL PRESS HIGH=   541     ,P2/P0=+0.090               TIME  14   42   48
RADIAL PRESS MID=    497
RADIAL PRESS LOW=    454     ,P2/P0=+0.096                  AXIAL  STRAIN
                                                             North (SAL)
STR GAGES     Midheight          Upper                       -0.000851
Outer Circum+0.970693 North -0.001606
Inner        -0.000109       +0.000680          West +0.000529    +0.000490 East
Outer        +0.000517 West  +0.000404
Inner        -0.000126       -0.001864                   -0.000458
Outer        -0.000713 45 Deg-0.001315                    South
Inner        +0.000110       -0.000496

Near Radial +0.000389 45 Deg+0.000269          RADIAL DISPLACEMENT (in)
Far          +0.000871       +0.000296
                                                          Midheight      Upper
Outer Longit+0.001233 North +0.000053      North-South     -0.687        -0.586
Inner        +0.000491       -0.000039     East-West       +0.502        +0.495
```

Fig. 5 Data Display on HP 9845B Computer Screen.

LOAD STAGE	AXIAL STRAIN WEST (IN/IN)	AXIAL STRAIN EAST (IN/IN)	AXIAL STRAIN SOUTH (IN/IN)	AXIAL STRAIN NORTH (IN/IN)	PAD. DIFF. SAL N-S (INCHES)
1	-0.00001	-0.00000	-0.00000	-0.00001	-0.000
2	-0.00001	-0.00001	-0.00001	-0.00003	-0.001
3	-0.00002	-0.00002	-0.00001	-0.00005	-0.002
4	-0.00004	-0.00003	-0.00003	-0.00010	-0.003
5	-0.00006	-0.00005	-0.00006	-0.00015	-0.004
6	-0.00009	-0.00009	-0.00009	-0.00020	-0.005
7	-0.00014	-0.00013	-0.00014	-0.00027	-0.006
8	-0.00019	-0.00017	-0.00018	-0.00034	-0.007
9	-0.00023	-0.00021	-0.00022	-0.00039	-0.008
10	-0.00027	-0.00024	-0.00025	-0.00043	-0.009
11	-0.00030	-0.00027	-0.00028	-0.00047	-0.010
12	-0.00034	-0.00029	-0.00031	-0.00050	-0.010
13	-0.00036	-0.00032	-0.00034	-0.00054	-0.011
14	-0.00039	-0.00034	-0.00037	-0.00057	-0.011
15	-0.00042	-0.00037	-0.00041	-0.00060	-0.012
16	-0.00045	-0.00039	-0.00043	-0.00063	-0.013
17	-0.00047	-0.00042	-0.00046	-0.00066	-0.013
18	-0.00050	-0.00044	-0.00049	-0.00069	-0.014
19	-0.00053	-0.00046	-0.00052	-0.00072	-0.015
20	-0.00056	-0.00049	-0.00055	-0.00075	-0.016
21	-0.00059	-0.00051	-0.00058	-0.00079	-0.016
22	-0.00061	-0.00055	-0.00061	-0.00082	-0.017
23	-0.00064	-0.00057	-0.00065	-0.00085	-0.018
24	-0.00067	-0.00060	-0.00068	-0.00088	-0.019
25	-0.00070	-0.00062	-0.00071	-0.00091	-0.019
26	-0.00073	-0.00065	-0.00074	-0.00094	-0.021
27	-0.00076	-0.00067	-0.00078	-0.00098	-0.021
28	-0.00078	-0.00070	-0.00081	-0.00101	-0.022
29	-0.00081	-0.00072	-0.00083	-0.00104	-0.023
30	-0.00084	-0.00075	-0.00086	-0.00107	-0.023
31	-0.00087	-0.00077	-0.00090	-0.00110	-0.025
32	-0.00090	-0.00081	-0.00092	-0.00113	-0.027
33	-0.00092	-0.00084	-0.00097	-0.00116	-0.028
34	-0.00095	-0.00086	-0.00099	-0.00119	-0.029
35	-0.00098	-0.00089	-0.00103	-0.00122	-0.030
36	-0.00100	-0.00091	-0.00106	-0.00125	-0.031
37	-0.00103	-0.00094	-0.00110	-0.00129	-0.032
38	-0.00106	-0.00097	-0.00113	-0.00131	-0.033
39	-0.00109	-0.00100	-0.00117	-0.00135	-0.034
40	-0.00111	-0.00102	-0.00120	-0.00137	-0.035
41	-0.00114	-0.00105	-0.00123	-0.00140	-0.035
42	-0.00117	-0.00108	-0.00126	-0.00142	-0.036
43	-0.00119	-0.00111	-0.00129	-0.00144	-0.037
44	-0.00122	-0.00114	-0.00132	-0.00148	-0.037
45	-0.00125	-0.00116	-0.00136	-0.00151	-0.038
46	-0.00128	-0.00119	-0.00139	-0.00154	-0.039
47	-0.00130	-0.00121	-0.00143	-0.00156	-0.039
48	-0.00133	-0.00124	-0.00147	-0.00160	-0.041
49	-0.00136	-0.00127	-0.00150	-0.00162	-0.041
50	-0.00139	-0.00129	-0.00153	-0.00165	-0.042
51	-0.00141	-0.00133	-0.00156	-0.00167	-0.042
52	-0.00144	-0.00135	-0.00159	-0.00170	-0.043
53	-0.00147	-0.00137	-0.00163	-0.00173	-0.044
54	-0.00150	-0.00140	-0.00166	-0.00176	-0.044
55	-0.00153	-0.00143	-0.00169	-0.00177	-0.045
56	-0.00155	-0.00145	-0.00173	-0.00180	-0.046
57	-0.00158	-0.00148	-0.00176	-0.00183	-0.046
58	-0.00160	-0.00151	-0.00180	-0.00186	-0.047

Fig. 6 Data Table.

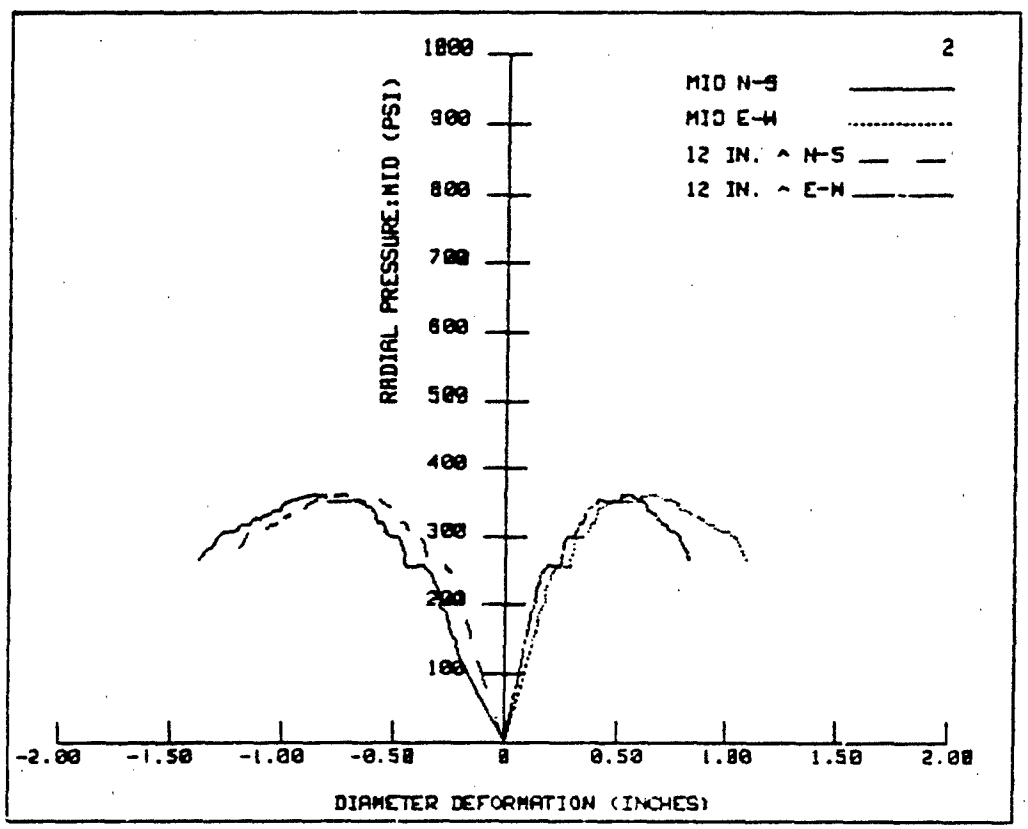

RADIAL PRESSURE (MID) VS DIAMETER DEFORMATION

Metric Equivalent: 1 psi = 6.9 kPa
1 in. = 25.4 mm

Fig. 7 Data Plot.

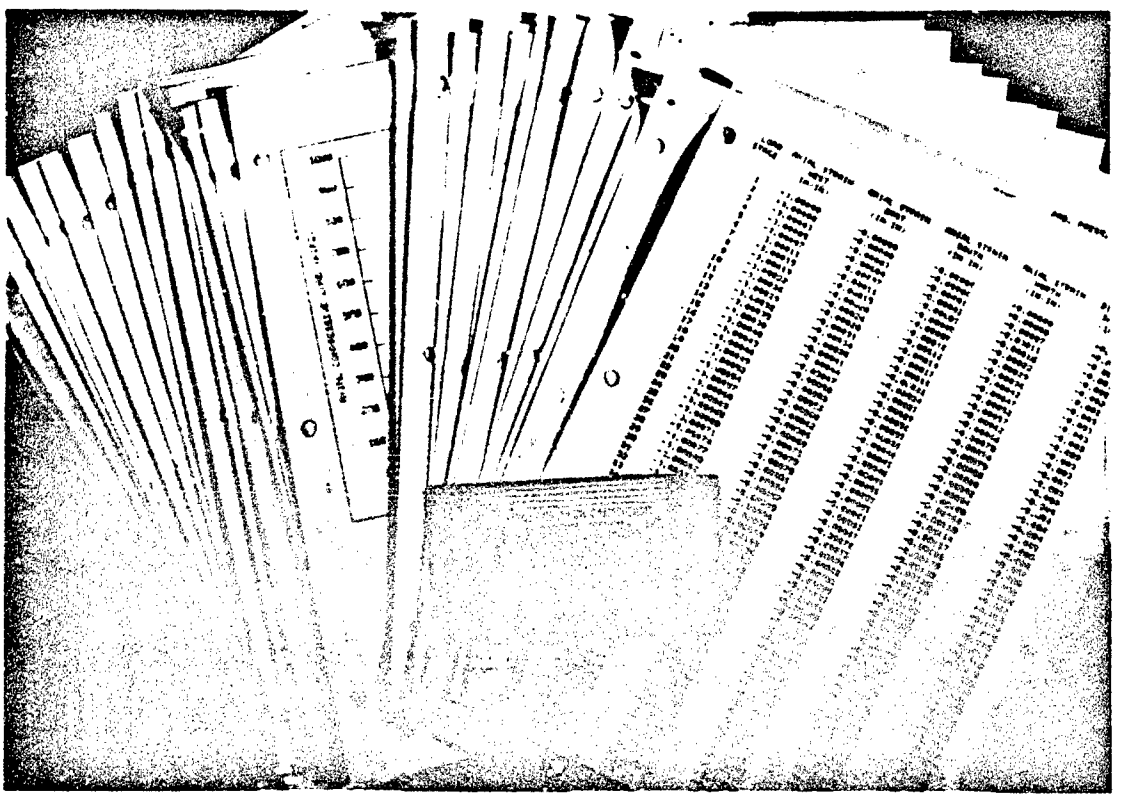

Fig. 8 Data Package.

Each test started from zero load and pressure so it was difficult to develop data within the specified ratio limits early in the test. Valid data points were joined by straight lines on graphs showing relationships.

CALIBRATIONS

The computer and data acquisition system were utilized during check-out of instrumentation before a specimen was placed in the test rig. At that time, the junction box was connected and a recording of data was made to check that all strain gages were connected. Open or short curcuits not previously assigned to gage failure were corrected. Repeated recordings of data were used to check stability of each gage. Drifting gages, not previously noted to have low resistance to ground, indicated poor connections that could be corrected. Similar checks of potentiometers revealed continuity, initial stroke settings, and stability. Two complete sets of potentiometers and junction boxes were used to allow specimen instrumentation and checkout to be completed prior to test time.

After a specimen was installed in the test rig, the junction box shown in Fig. 3 was again connected to the system. Screen display on the computer was used to prompt successive steps in calibration and adjustment needed to prepare for a test.

Power supply voltage to the junction box was read and compared with a specified value automatically. If adjustment was needed, prompts on the screen helped the technican make the adjustment. A similar bridge voltage check and adjustment was made on a standard voltage in the M.T.S. control equipment.

Pressure cells at the axial load hydraulic ram and in the hydraulic connection to the three zones of radial pressure were calibrated by shunt resistors inserted manually from the console. On prompt from the computer, the four calibrations were made and bridge voltage adjusted.

The initial output of each displacement potentiometer was set to zero by adjustment on the console. Prompts from the computer guided the zero adjustment sequence. Total preparation for test using these prompts from the computer was completed in about 10 minutes.

SUMMARY

Instrumentation and load control were used to meet the objectives for testing reduced scale concrete MX-Horizontal Shelters. Details of instrumentation, load control, data handling, and calibrations are presented.

ACKNOWLEDGMENTS

This investigation was sponsored by Karagozian & Case, Structural Engineers, Los Angeles, California under contract to Ballistic Missile Office, Norton Air Force Base, MNNXH, San Bernardino, CA. Ralph Leistikow was Principal in Charge for the sponsor. Work was conducted in the Structural Development Department, Dr. H. G. Russell, Director, as part of the contract research activities of the Construction Technology Laboratories, a Division of the Portland Cement Association. Mr. D. M. Schultz, Assistant Manager, Structural Development Department, was Principal Investigator.

REFERENCES

1. Daniel, J. I., and Schultz, D. M., "Testing of Reduced-Scale Concrete MX-Shelters - Experimental Program," Paper submitted to ASCE Committee on Experimental Analysis and Instrumentation, January 1982.

2. Ciolko, A. T., "Testing of Reduced-Scale Concrete MX-Shelters - Specimen Construction," Paper submitted to ASCE Committee on Experimental Analysis and Instrumentation, January 1982.

PCA R/D Ser. No. 1695

BLAST AND SHOCK FIELD TEST MANAGEMENT

By Michael L. Noble[1]

INTRODUCTION

The Blast and Shock field test management structure has been shaped by a blend of the program manager philosophy and the technical functional area structures. This integrative management approach in Blast and Shock field testing is given the title of matrix management. This paper will discuss and outline the field test matrix management structure as it pertains to the Air Force's Blast and Shock testing. The Air Force Weapons Laboratory, Civil Engineering Research Division (AFWL/NTE) has been the responsible agent for Blast and Shock testing of the Nuclear Hardness and Survivability (NH&S) of protective structures and systems within the Air Force Systems Command. This organization's management structure will be presented. The discussion will focus primarily on the alignment of the field test's organizational structure and the technical integration roles and procedures.

DEFENSE SYSTEM POLICY

It is important to bring out the Air Force's macro program management policy. The Major Systems Acquisition regulations have a dominant role in structuring the primary test program objectives and milestones through which the Blast and Shock test management responds as a participating agency. These regulations state the policy for managing all Air Force acquisition programs which are funded through the Research, Development, Test and Evaluation appropriations. Responsibility for the management of acquisition programs is

[1]Chief, Effects Simulation Section, Weapons Effects Branch, Civil Engineering Research Division, Air Force Weapons Laboratory, Kirtland Air Force Base, Albuquerque, New Mexico

delegated to the implementing command. Each acquisition program will be managed by a single person known as the Program Manager (PM). The Program Manager role for the Air Force's test management is thus directed by regulation and provides the macro management cornerstone for any major defense system program.

The Program Manager is responsible for all management decisions within the approved acquisition program. The PM's decisions are directives on all participating commands. The program's tasks are contained in the Program Management Plan (PMP). This plan is the management outline through which the participating agencies lend their support to meet the program's objectives, constraints, and thresholds.

The system acquisition process is a sequence of specified phases and decision points directed towards the achievement of the DOD established program objectives in the acquisition of the defense system. The process is initiated with the approval of a mission need statement and extends through the successful completion of development on to system deployment.

The current system R&D process decision points identified with the separate phases of program activity are structured as follows:

Milestone 0 - Program Initiation

The Secretary of Defense requests, or a DOD Component Head perceives, a mission need to exist and determines that a new capability is to be acquired to meet the need. The DOD Component Head submits a statement of the mission need to the Secretary of Defense for approval to proceed, to identify, and to explore alternative solutions to the mission need. The considerations to support the determination of the mission need are documented in the Mission Need Statement (MENS).

The Secretary of Defense will approve the mission need and direct, one or more, of the DOD Components to systematically and progressively explore and develop alternative system concepts to satisfy the approved need.

Milestone I - Demonstration and Validation

When the DOD Component completes the competitive exploration of alternative system concepts to the point where the selected alternatives warrant system demonstration, the DOD Component Head requests approval to proceed with the demonstration and validation effort. The recommendations shall be documented in a Decision Coordination Paper (DCP) and reviewed by the Defense System Acquisition Review Council (DSARC) and the (Service) System Acquisition Review Council ((S)SARC) prior to the Secretary of Defense decision.

The Secretary of Defense action will reaffirm the mission need and approve, one or more, selected alternatives for competitive demonstration and validation.

Milestone II - Full-Scale Engineering Development

When the demonstration and validation activity has been completed, the Component Head is prepared to recommend the preferred systems for full-scale engineering development. The recommendations are documented in an updated DCP and reviewed by the DSARC and (S)SARC prior to the Secretary of Defense decision.

The Secretary of Defense will reaffirm the mission need, and approve the selection of a system for full-scale engineering development, including procurement of longlead production items and limited production for operational test and evaluation.

Milestone III - Production and Deployment

When the Component Head is prepared to recommend production of the system, the recommendations are documented in an updated DCP and reviewed by the DSARC and (S)SARC prior to the Secretary of Defense decision.

The Secretary of Defense will reaffirm the mission need, confirm the system ready for production, approve the system for production, and authorize the Component to deploy the system to the using activity.

MACRO-MANAGEMENT SUMMARY

Test and evaluation of any defense system shall commence as early as possible. Testing directly supports the system's estimates of military utility, operational effectiveness, operational suitability, and design modifications to meet mission requirements. These utility determinants shall be made prior to large-scale production commitments. The most realistic test environment possible and an acceptable model of the future operational system will be used in the testing. A specific test or test series, keyed to an appropriate decision point, will normally be conducted within each phase.[1]

The preceeding background reviews the present foundations of DOD management structuring: a PM policy and the decision point milestones. The typical system Research and Development (R&D) cycle, showing the phases and DSARC milestones, is shown in chart A. Thus, field testing has its macro operational management outline.

As of this writing, the DSARC process for system's R&D is being streamlined. It will cut the number of formal DSARC milestones from the present four to two. In brief, first it will meld the MENS point with the DSARC I milestone. Secondly, DSARC II was made the key decision point. The "go-ahead" decisions for both full-scale engineering development and production will be at DSARC II. This management direction clearly will increase momentum in the system acquisition R&D process. Regulations are pending on the new "tailored" DSARC system.

A point of discussion must be emphasized. The Air Force Systems Command (AFSC) conducts independently long-lead-time technology base programs,

[1]DOD Directive 5000.1, "Acquisition of Major Defense Systems," January 18, 1977.

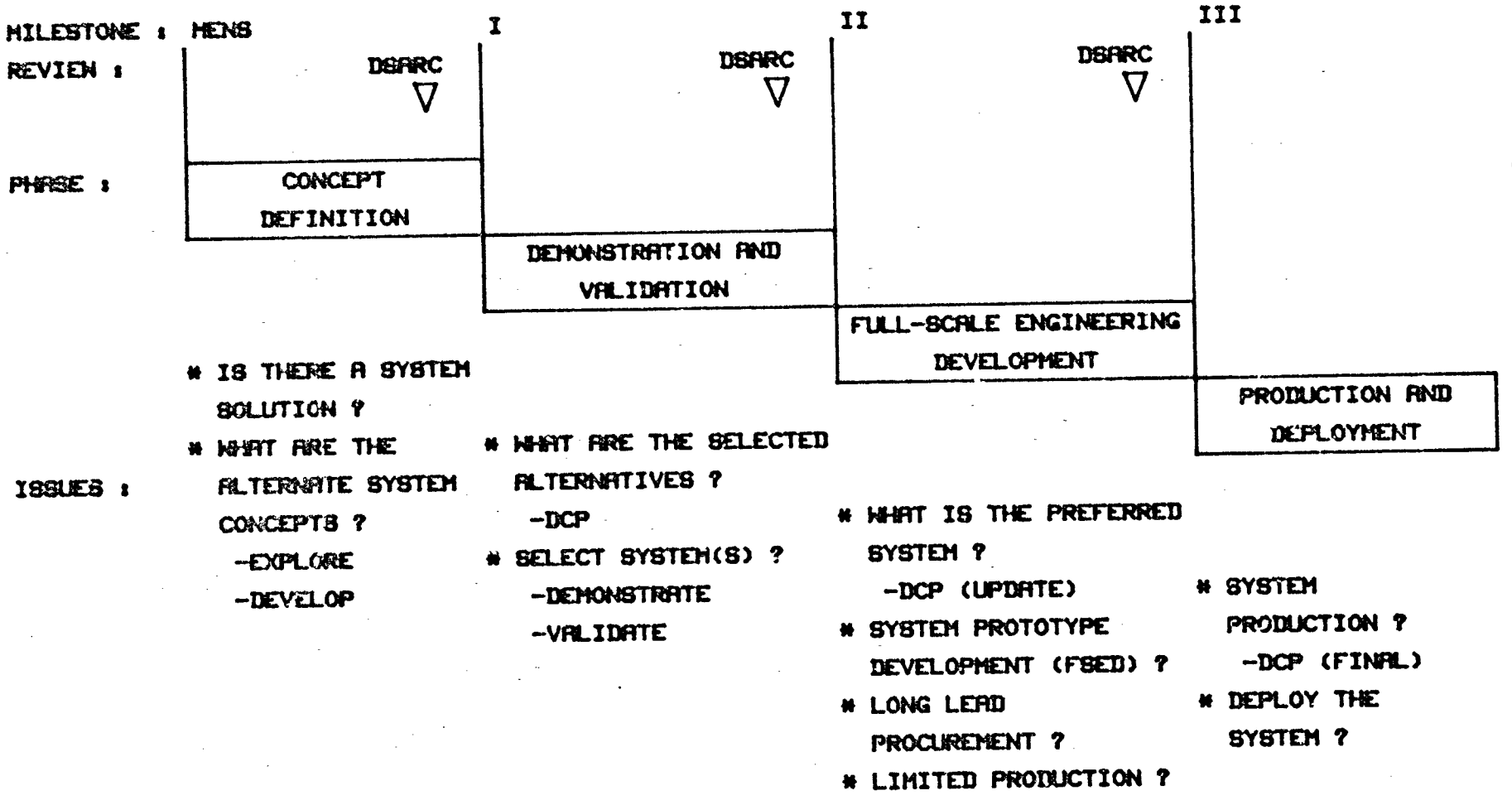

CHART A. SYSTEM RESEARCH AND DEVELOPMENT (R & D) CYCLE

deemed research and exploratory development, to support future acquisitions. In general, these programs are unconstrained from the system acquisition process due to the long-term needs time element. However, in developing research programs, the program management orthodox is parallel.

FIELD TEST MANAGEMENT OVERVIEW

The AFWL/NTE handles its Blast and Shock test management for either basic research or system related developmental/validation testing using the same approach. The only difference is in a programmatic sense, i.e., definition by DOD of a specific system. The use of a system directed test will be followed throughout this discussion.

Blast and Shock field testing is a direct statement towards achievement of a fundamental defense system mission need requirement. It exercises the system's NH&S capabilities. This assessment task is performed at early stages of system development and repeated as necessary throughout the design optimization process.

The maintenance of this ability to meet the system's field testing criteria is a mission responsibility of AFWL/NTE. The successful management of system field testing depends upon a strong and viable Blast and Shock technology base and field test support management organization. The ability to fluidly adjust the technical staff to meet the field test requirement is fundamental to the organization's mission responsiveness. Management must pattern itself to cross established functional area lines to obtain the necessary personnel to efficiently execute the technical tasks. The AFWL/NTE uses a matrix management approach to provide the program support service. The basic organizational form is depicted in chart B, entitled Matrix Organization.

It should be emphasized that a matrix management system has the strong potential to grow in an inter-organizational sense. This expansion process necessarily develops from the research concept to a system demonstration/validation testing phases. The SPO involvement becomes pronounced when

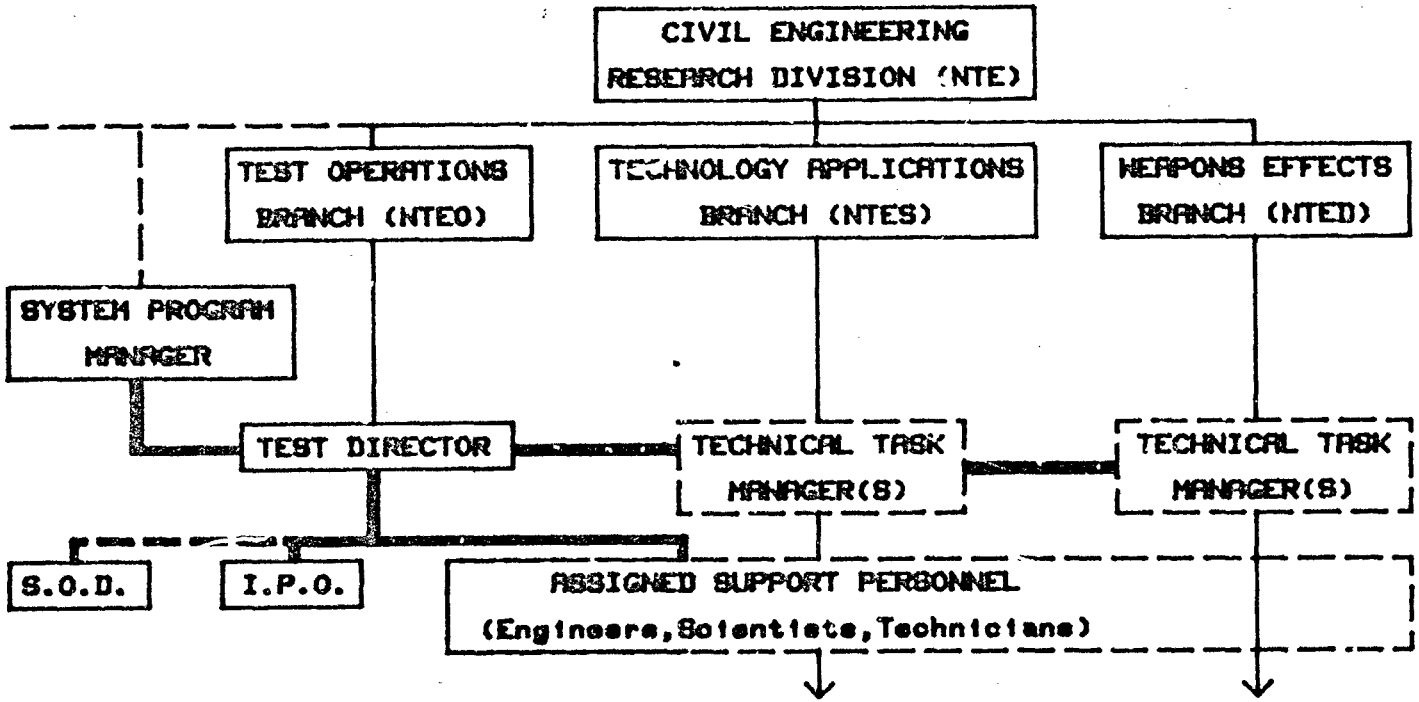

LEGEND

IPO	Instrumentation Project Officer
SOD	Site Operations Director
	Dotted line = Intra / Inter Organization Manning Selected
	Broad line = Matrix Flow

CHART B. MATRIX ORGANIZATION

alternative solutions are narrowed; a specific system is selected for proof-testing and prototype development. Also, with this programmatic shift brings the mandatory addition of a system program manager. However, lets proceed with the basic development of the Blast and Shock field test management structure.

Two basic management elements, whereby the nature of ones dependence on and adherence to, provide the structural framework for productive field test mangement. Those conditional elements are personnel and planning. Test planning is the primary requisite to insure that all technical tasks intermesh whereby progress is made to meet the objective, a successful field test execution. Test personnel provide the control to implement the test plan.

TEST PERSONNEL

The manpower involvement level for all field test management operations is directly dependent upon each test's magnitude. It is recognized that not all test programs are of the same scope; therefore, some of the positions described may be embodied in one individual.

In order to expedite flow of information, task accomplishment, and decision making, each test program has personnel designated by the technical area's leadership (Branch Chief) with the concurrence of the Division head. Major task requirements are coordinated through the technical task manager(s). Performance period scheduling and manpower commitments are coordinated through the responsible section chief, the administrative supervisor. Finally, the coordination of day-to-day activities involving technical support tasks flows horizontally between the individual test personnel. This lateral interaction is the central thrust of the matrix management organization. Once the line authority is cognizant of the individual(s) task, the direction and control of duties for each test will reside with the Test Director. The broad line segment in chart B shows the generalized AFWL/NTE organization established to implement the test.

The basic task and responsibilities of the primary test management personnel are the following:

Program Manager (PM)

Responsible for the coordination, scheduling, and overall program management of the blast and shock activity. Maintains the primary interface with the SPO and participating agencies line management. Defines program and test objectives. Ultimately responsible for the appropriate theoretical and experimental programs, budgets, and schedules which support the system's research and development.

Test Director (TD)

Responsible for all the facets of test direction, from planning through execution. Determines the priority, adequacy and the integrated design plan of experiments for the field test. Directs the test-related technical work and coordinates the Program Manager's test requirements. The essence of his task is patterned after the Air Force's PM philosophy. However, the scope is adjusted to be centered on a specific test event.

The TD's functional tasks include monitoring procurement actions and directing test scheduling. The scheduling effort is a critical role. The use of Critical Path Methods (CPM) is a managment tool which is highly recommended. He manages the test's budget, coordinates administrative requirements (test plan, construction drawings, and reports), and support functions (photo, fabrication, and meteorology).

The TD is the technical interface with both the test site personnel and the technical support personnel. All the test technical support requirements and experiments are approved by or requested through the Test Director. Participating agencies coordinate their activities through the Test Director and are responsible to the Site Operations Director during the

fielding of their experiments. All major changes must be approved by the Test Director, while minor field modifications approval coordination rests with the Site Operations Director. The intent is to have the Test Director responsible for all pertinent interfaces with the field operations and technical support units for the test. The Test Director is the integrator. He translates and conveys the test's technical tasks from the technical staff to the field operational personnel who are under the direction of the Site Operations Director (SOD).

Site Operations Director (SOD)

Responsible for all On-Site Test Operations. Reports directly to the Test Director. The SOD must be cognizant of the intent and purpose of all field experiments. A deviation of construction practices set down in the test plan and/or construction drawings may nullify either the experiment or compromise the test. The interdependence between the TD and SOD cannot be understated.

The Site Operations Director's functional tasks include both the management of field test support activities and assistance towards the execution of the test event. Responsible for on-site construction inspection, quality control, and test event firing. Specific delegated activities encompass the field operations integration; such as, facility operations, contract services, equipment and supplies, personnel administration, communications, security, and vehicles. Maintains the as-built working drawings and applies the field procedures for construction and other operational test support.

Instrumentation Project Officer (IPO)

Responsible for all instrumentation support required in the fielding of the test. This task encompasses the engineering of B&S measurement

techniques from gage to recorder. The IPO must integrate the measurement and recording equipment using a systems engineering approach. He must be cognizant of field emplacement techniques and be able to apply selected gage types to provide the experimenter's data. The management of van operations and recording practices is a field operational facet delegated from the Test Director.

The IPO's functional tasks include responsibility to procure, select, and provide order information for wire, cable, and transducers. He ensures that the field test's measurement requirements are coordinated and translated to gages in place and that data is properly calibrated, conditioned, and recorded. He publishes planned channel assignments and as-built measurement lists. He interfaces with data processing personnel to produce the data report.

Documentation is an essential responsibility, for it provides the link between the test design and product. The experimenter relies on accurate reporting of gage placement, as well as a complete record of the environment (waveforms).

Technical Task Manager(s)

Field testing requires select technology support. The translation of NH&S assessment support within technical functional areas is a method of providing a continuing expertise in select engineering and scientific disciplines. The technical support framework is held independent of the test requirements, thereby it can develop and progress with the state-of-the-art.

Within the organization's functional areas (Branches) are personnel whose task is to maintain each technical discipline. The TD coordinates with those technical task managers to develop and outline the test plan. Technical task managers also recommend individual support personnel for assignment on

the respective test. The task manager is responsible to insure the appropriate methodology is applied to the test effort. Some technical tasks which are maintained at AFWL/NTE are: siting (geology and geophysics); airblast phenomenology; ground shock phenomenology; cratering; debris and dust definition; instrumentation development and technology; effects simulation development and technology; structural loads and response technology; and systems assessment methods.

TEST OPERATIONAL PLANNING

Management Principles

Management planning's foundation is in controlling the fundamental measurands of task, schedule, and funding. Field test management necessarily must incorporate these "triple constraints" in its operational planning to effectively control the test program. Blast and Shock field testing is restrictive in its NH&S program character. Field testing is frequently constrained by both a fixed date decision point and a fiscal year funds ceiling. Thus, the test integrator's latitude diminishes to only one independently manageable parameter. This is the Work Breakdown Statement (WBS), with its derivative elements (task versus manpower) to apply towards test execution. Thus, a detailed development within this outline is required.

Test personnel must be bound in a unified commitment towards obtaining the specific goals and requirements set by the system's program manager. Engineers and scientists are regimented by their respective professions. Their technical outlooks, emphases, and methodologies are quite different. The TD's task and purpose is to blend their technical expertise to meet the test objectives. A means to that end is the test plan.

Test Planning Overview

A system oriented field test, by its very nature, is a short-term program occurrence. It has specific PM directed objectives to meet the

respective R&D phase's DSARC milestone. This situation requires a process by which the technical issues and procedures can be focused. The test plan produces the mechanism for quickly achieving technical tasks integration. A comprehensive test plan can bridge the specific test objectives and non-standard test requirements with standardized field operational practices. As with technical issues, the test plan binds the participating agencies. Organizational commitment is an important factor in a successfully managed test program. Without functional line management's approval and backing, the Test Director is essentially void of any authority to implement the test.

Test Plan

The test plan is a written outline formatting management means: test definitions, task assignments, and the technical/operational methodologies. It links the test objectives with the commitment of technical resources through a formalized document. Appendix I provides an example of the typical Blast and Shock (B&S) test plan's scope. The principle test plan control linkage, as stated previously, is the Work Breakdown Statement (WBS). A detailed WBS example for a multi-participant field test is developed in Appendix II. Critical in test development and planning is clarity of tasking. The WBS details the elemental tasks and sets, in parallel, the responsibilities. It is important to establish in the WBS structure both hardware and nonhardware deliverables. This action keys the participants into a responsive mode through the WBS checklist activity. Other plan annexes support the development of task and resource management by detailing the functional support areas. Principal annexes which carry a continual integrative responsibility (update) are: Schedule, Instrumentation Plan, and Construction Package. These annexes are implementative in nature and a great deal of participant interaction is concentrated in these areas. The questions of

"how" and "when" correlate directly with the proper utilization of the WBS, the allocaton of time and manpower. The test plan's overall purpose is to ensure the test objectives are met. Failure of one technical task to be completed on time or at the proper level of effort could quite possibly jeopardize the test execution, thereby seriously impacting the system's R&D milestone.

Test Program Controls

Control systems are invaluable tools to the TD. They provide WBS tasks forecasting of critical paths. Analysis techniques vary, but the program mangement thrusts remain constant. These techniques provide methods to highlight any task deviation and indicate a relative measure of the task magnitude. The techniques may range from a simple milestone-bar chart (detailing short-term deliverables) to a complex CPM network (shoting the task interdependence and time scales). The author recommends a CPM for it will relate two important parameters: the task's schedule period and the task's interface logic. The use of program controls respective to support task personnel has minor utility. However, the TD is the true benefactor of this analysis. Its utility further increases with the test's technical complexity and multi-participant involvement. The Test Director must be able to control the course of all test activities. Program control techniques provide an activity road map for the Test Director to apply his management skills.

Reprogramming

A test program can only be responsive to the system's R&D needs if there are avenues for reprogramming actions. These actions normally occur at the macro-level upon R&D phase transitions; however, unscheduled program directives do occur with some frequency. System program modifications are inevitable.

The TD should set his own pattern of micro-level decision points. Develop a conscious attitude of periodically holding test program integration

checkpoints. Particularly, at the initial stages of test planning, it is essential to convey this tone. Vital test program technical issues are to be communicated. The TD must relate the test objectives in the proper context to all participants, develop the WBS commitments, and set the proper management interfaces between functional line management and the test matrix management. Constructive management practices communicate and convey, as well as integrate and direct. Why expect to have a participant commit to any test implementation if he was not a party to the test plan development.

The test plan is the embodiment of the system's current test requirements and specifications. The test momentum can only progress, if and only if, there is full cognizance.

The initial test plan must necessarily have an administrative revision procedure. When the test objectives change upon a major system level concept redirection, a more extensive feedback practice may be necessary, i.e., a comprehensive technical review.

Reviews

Technical reviews are an extension of reprogramming actions. Management reviews have a high frequency of occurrence; however, they differ greatly in purpose and style. The utility, as previously stated, lies in communication.

At AFWL/NTE, the principal reviews in which the TD institutes test program controls are: the initial test plan briefing, the construction package review, the field test management meetings (weekly) and the pre/post test data analysis briefings. The preceeding reviews are built into the test management outline.

During the course of the test program a broad spectrum of task specific technical interchange meetings take place. The majority of these

meetings are set at the technical task level and may generate into formalized task working groups. B&S field testing technical interchange areas which historically maintain a formalized state are: instrumentation, simulation, and pressure/crater related effects.

SUMMARY

The Air Force has developed a system management policy under which a program manager directs the macro-level R&D program flow. This philosophy of a single-point integrator is applied to AFWL/NTE's Blast and Shock field test program management.

The Test Director performs this role as integrator. He uses a matrix management approach in fulfilling the system's field test support requirements.

Matrix management is the organizational framework which enables AFWL/NTE to respond with the progressive nature of a system's R&D cycle. The matrix's horizontal decision and task flow can adjust to specific system test requirements and select technical expertise. The test support can progress without interfering with the fabric of technical functional area roles. The matrix management approach's essence is in the segregation of a short-term system field test program relative to the long-term research technology base development.

The field test operational planning and principal personnel are the basic management control elements. A dominant management practice of all the test personnel outlined is a knowledge of communication. The field test staff must communicate and convey technical tasks, as well as perform their integration and direction management responsibilities.

The management tools for a test program provide the mechanism for the test integration and direction. The key working document is the test plan. It brings into focus the system test objectives with the comprehensive annexes, detailed to specific test requirements and operational practices.

APPENDIX I - TEST PLAN (EXAMPLE)

SECTION I - INTRODUCTION

1. Objective. Discussion to provide foundation information to individuals or groups involved in planning, implementing, executing, and supporting the test operation.

2. Test Overview. Discussion giving the program baseline; i.e., mission needs, criteria, etc. for the Blast and Shock simulation of the nuclear environment on a system.

SECTION II - PROGRAM MANAGEMENT

1. Sponsors and Agreements.

a. Statement of program scope and directives for the test is being sponsored by the System Program Office (SPO). Select excerpts from the program plan specific to the testing support.

b. Memorandum of Agreement.

2. Test Direction and Technical Supervision. Test direction and technical supervision is the responsibility of

Discussion on the authority necessary to perform the fielding of this experiment being delegated to the Test Director and functional relationships with the line authority.

3. Organization and Responsibilities. (See Annex)

SECTION III - DESCRIPTION OF TEST

1. Requirements and Justification: SPO directed requirements, AFR 80-38, etc. (Specify applicable portions, and use direct quotes.)

2. Type of Test and General Descriptions (Succinct general statements)

a. The overall objectives of this test are:

(1) To develop

(2) To demonstrate

(3) To validate

b. General background on field testing techniques, if required.

3. Technical Discussion: Approximately 250 words - details of #2

4. Operations Approach: (overview)

a. Work Breakdown Statement (WBS) (see Annex)

b. Schedule (see Annex).

c. Construction Package (see Annex)

OUTLINE

Annex	Description	Responsible Annex Executor	Annex Writer	Revision
A	Location and Site Description (with Site Support Layout)			
B	Geology and Geophysics (Site)			
C	Schedule			
D	Test Organization (Chart)			
E	Safety Plan			
F	Test Event Operations Plan			
	-Explosives Transit and Storage			
	-Dry Run Procedures			
	-Test Arming & Firing Checklist			
	-Critical Measurements List			
	-Hold Conditions & Procedures			
	-Misfire Procedures			
	-Pre/Post Event Procedures			
G	Security Plan (Site)			
H	Security Classification (Documents, Data, Briefings)			
I	Environmental Impact Assessment			
J	Environmental Effects Monitoring			

Appendix I

Annex	Description	Responsible Annex Executor	Annex Writer	Revision
K	Communications Plan			
L	Meteorological Support Plan			
M	Photo Plan			
N	Construction Package (Drawings and Procedures)			
O	Instrumentation Plan			
P	Data Reduction & Analysis			
Q	Technical Reports (Requirements & Schedules/Philosophy/Briefings)			
R	Theoretical Support			
S	Travel & Billeting Procedures			
T	Vehicle and Equipment Control Procedures			
U	Community Relations			
V	Funding			
W	Equipment/Data Listings (GFE/GFD, CFE/CFD)			

Note: 1. The Test Director is the coordinator for assembling the Test Plan.

2. Executor(s) listed above may change for a given test dependent on when, where and how it is performed.

APPENDIX II - BLAST AND SHOCK TEST REQUIREMENTS AND RESPONSIBILITIES

Legend: A - Primary Agency
B - Secondary Agency
C - Tertiary Agency

WORK BREAKDOWN STATEMENT (EXAMPLE)

WORK UNIT	PERFORMER	APPROVING AUTHORITY	COMMENTS
1. General Requirements (criteria)	B	B	
a. Geology	B	B	
b. Simulation	B	B	
c. Structure	B	B	
2. Preliminary Design (Measurement List & Plans)	A	A	
a. Ground Shock	A		
b. Simulation	A		
c. Structure	A		
d. Development	A		
3. Site Investigation	A/B	A/B	
4. General Inst. Req. (Test Plan)	A		
5. Preliminary Analysis	A		
6. Testbed Design	A	A	
a. Instrumentation Layout	A		
b. Gage Ranging	A		
c. Trench Plan	A		
7. Instrumentation Systems Plan and Procedures	A	A	
8. Final Structure Design Drafting	A	A	
9. Final Simulator Design Drafting	A	A	
10. Final Test Plan w/Drawings and Procedures	A	A	
11. Test Plan Reviews	A	A	
12. Precast Structure Fab	A	A	
13. Simulator Materials	A	A	

	WORK UNIT	PERFORMER	APPROVING AUTHORITY	COMMENTS
14.	Testbed Inst. Materials (%GFE)			
	a. Structural - Cast Gages (100%)	A		
	b. Structural - Other (100%)	A		
	c. Simulator - (100%)	A		
	d. Free-Field (100%)	A		
	e. Developmental (100%)	A		
	f. Camera Protection, Camera Control, Suspended Mounts and Light Boards	C		
	g. Cameras, Film and Batteries	A	A	Aerial Photo is GFD
15.	Field Inst. Mat. (% GFE)		A	
	a. Cable (100%)	A		
	b. Recording Eqpmnt (100% GFE)	A		Including recording materials and spares
	c. Bunkers (100%)	A		
	d. Pre-Amplifiers (100%)	A		
16.	Instrumentation Calibration	A	A	
17.	Test Logistics (Site)	B	A,B	
	a. General	B		
	b. Instrumentation Installation Material Crimps, Wire, etc.	B,C		
	c. Precast Structure Shipment	B		
18.	Testbed Construction	B	A,B	
	a. Construction and Installation Support Work Package	C		
	b. Construction and Test Integration Management	C		
	c. Preparation (Survey, Siting, Digging)	B		
	d. General Tasks (Welding, Carpentry etc)	B		
	e. As-Built Drawings	C		
	f. Inspections	A,B,C		
	g. Simulator	B		
	h. Structural (Install)	B		
	i. Gage (Install)	A,C		
	j. Photo (Fab & Install)	A,C		
	k. Cables (Install)	C		Lay all cables and connect I-Van. A splices all gages.

Appendix II

	WORK UNIT	PERFORMER	APPROVING AUTHORITY	COMMENTS
19.	Pretest Predictions (Analysis)	A	A	To participate as part of transition (over the shoulder training)
20.	Pretest Reports	A	A	To participate as part of transition (over the shoulder training)
21.	Test Instrumentation Recording			
	a. Environmental Monitoring	A		
	b. Van Preparation (Dry Runs)	A		
	c. Pre-Amplifier (Checkout)	A		
	d. Photo	A,C		
	e. Test Event Data Acquisiton	A		
	f. Photo Control System Support	C		
22.	Test System (Dry Run)	A	A	
23.	Test Readiness Review	A,B,C	A,B	
24.	Test Execution	A		
25.	Post-Test Analysis			
	a. Post-Test Inspection	A,B,C	A,B	
	b. Data Processing (100% GFE)	A		
	c. Data Analysis	A		
	d. Quick-Look Report (30 days)	A		
	e. Corrected Data Analysis	A		
	f. Data Report	A		
	g. Final Report	A		
26.	Post-Test Cleanup	B		

BLAST AND SHOCK FIELD TEST MANAGEMENT

KEY WORDS: Military Engineering; Organizations; Planning; Tests; Program Manager; Matrix Management; Test Director; Test Integrator; Blast and Shock Testing

ABSTRACT: Matrix management functions as the principal field test management technique. The key is integrating the functional technology areas and a field test support organization. The Blast and Shock Field Test Management structure for ballistic missile acquisitions system's test integrator role has changed responsibility among several different organizations and site operating locations. However, management's logic plan for accomplishing a multi-participant field test has basically remained constant. The program's flow for the performance of a field test is directed from the system's program manager through major decision points, with select developmental milestones. Blast and Shock field test provides a direct statement, through the exercising of the system's Nuclear Hardness and Survivability (NH&S) capability, in meeting select decision point needs. A test integrator (test director) is the responsible agent in the management of any Blast and Shock field test program. The central thrust of the discussion is to present the Air Force Weapons Laboratory, Civil Engineering Division's (AFWL/NTE) integrative (matrix) structure with its test planning and operating elements.

Blast and Shock Field Test Management, by Michael L. Noble. The matrix management technique is presented as a principal field test management structure. The test integrator (test director) is the responsible agent in coupling the functional technology areas and a field test support organization. Planning and operating elements are presented.

A COMPARISON OF NUCLEAR SIMULATION TECHNIQUES ON GENERIC MX STRUCTURES

By John F. Betz[1]

INTRODUCTION.

Land based MX missiles represent an important system in the offensive triad of the United States military strategy. Deployment of this new weapon system in a shallow-buried horizontal configuration created the need for a missile shelter design which could ensure survivability. Structural designs had to be accomplished starting with simplified techniques and proceeding with testing and advanced computer analysis. Once a generic MX protective structure had been developed to a stage nearing completion, large scale testing of the structure under anticipated attack scenarios began.

Two main nonnuclear simulation techniques which are used to reproduce nuclear airblast pressure loading were considered for use at large scale (1/5 scale up to full scale). These are the Dynamic Airblast Simulator (DABS) and the High Explosive Simulation Technique (HEST). The DABS is a high quality simulator which reproduces both static and dynamic airblast pressure loadings. The DABS configuration for the 1/5 scale test on the generic protective structure is shown in Figure 1. The simulator is essentially a semicircular cylinder with an explosive driver on one end and a free surface on the other end, with the test structure located at the desired range in between. The results from the DABS pressure loading in that 1/5 scale test were used to design the HEST layout for the follow-on test. Shown in Figure 2, the HEST was designed with eight different zones to duplicate the DABS loading on and around the generic structure.

Although each test revealed much about the structural response and survivability of the protective structure, the reason both tests were performed was to see if the HEST could perform as well as the DABS in simulating nuclear blast pressure loading. Cost was a driving force

[1]Research Engineer, Structural Response Section, Technology and Applications Branch, Civil Engineering Research Division, Air Force Weapons Laboratory, Kirtland Air Force Base, Albuquerque, New Mexico.

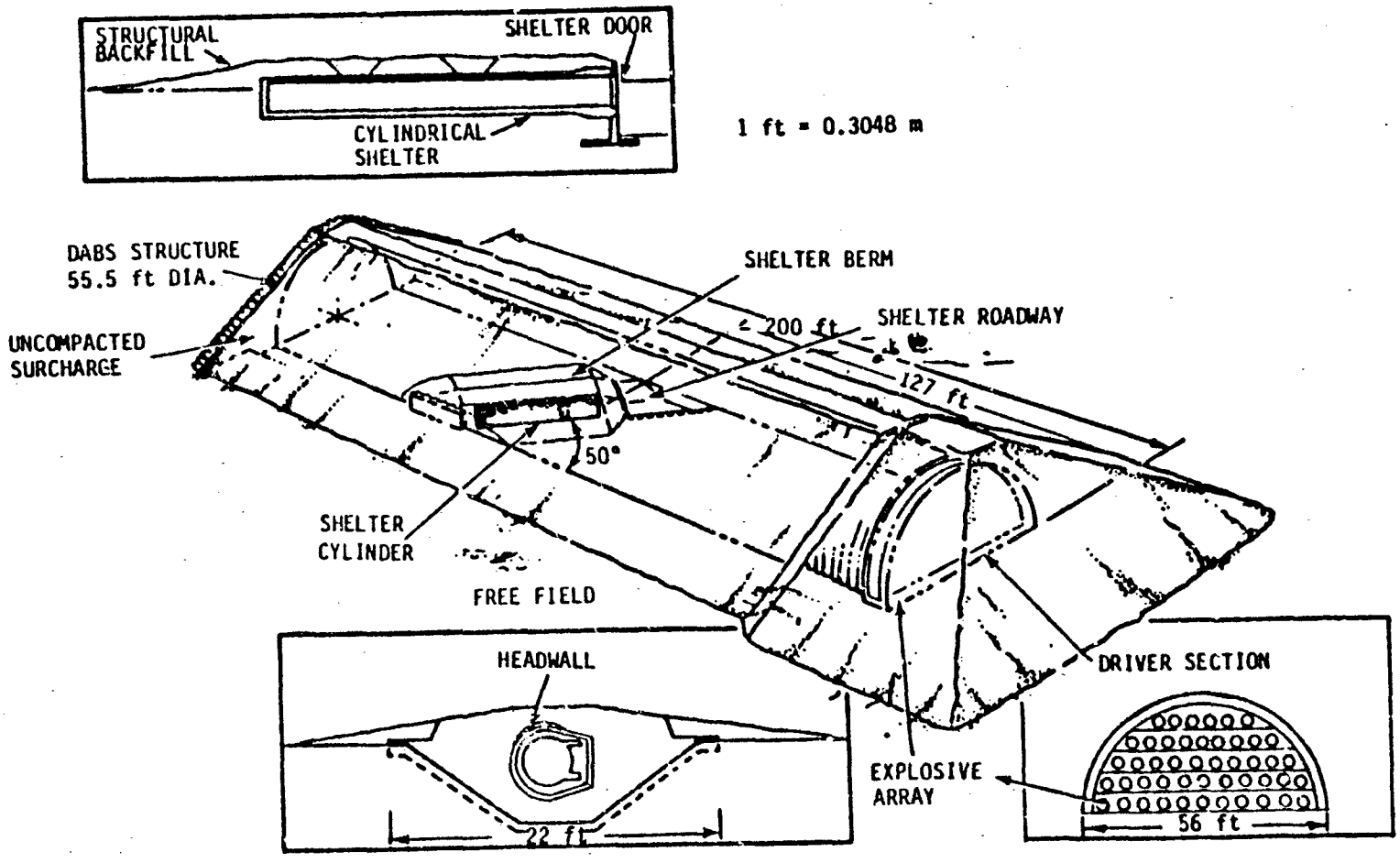

Figure 1. DABS layout for 1/5 scale D-1 test.

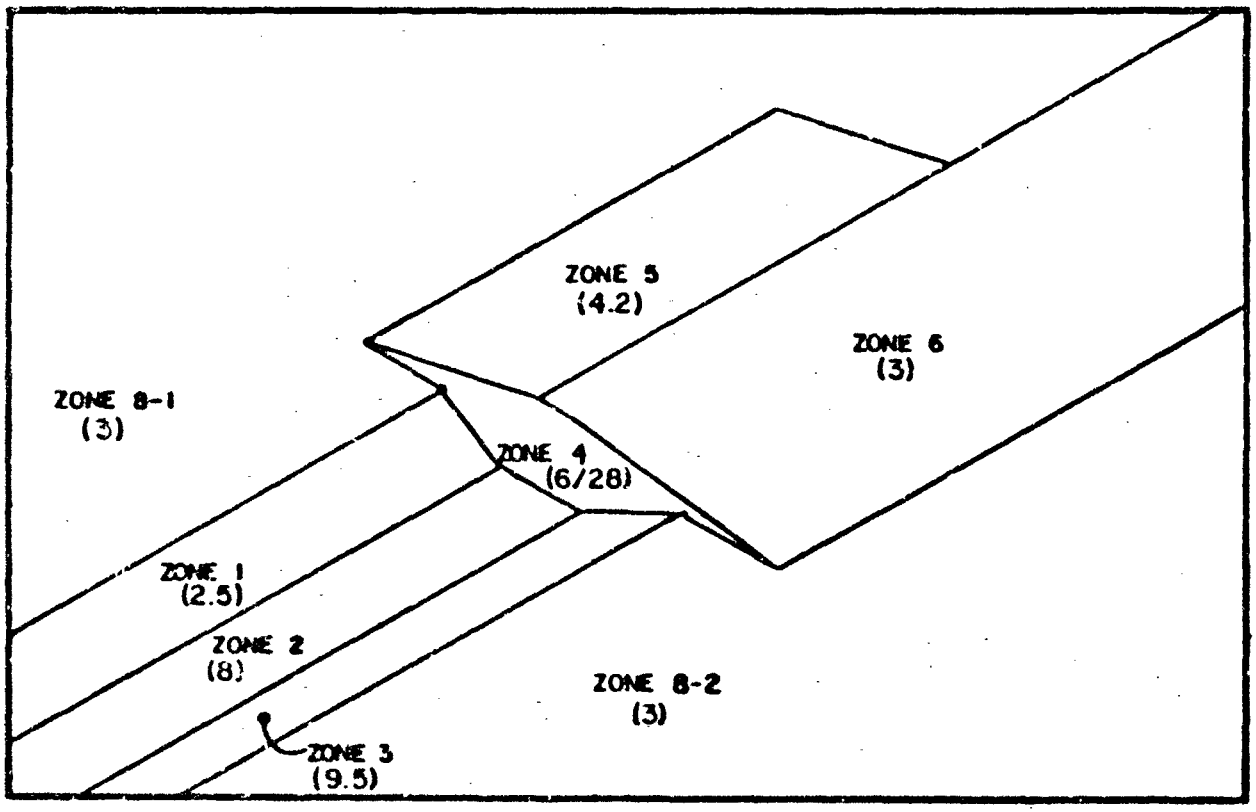

( ) PRESSURE IN MPa
1 MPa = 145 psi

Figure 2. HEST configuration for 1/5 scale test (SH-1) based on DABS pressures.

behind this evaluation, because for tests 1/5 scale and larger, DABS simulation is at least twice as expensive as HEST simulation. Therefore, using the generic model response as a yardstick, the HEST simulation was measured against the DABS standard.

SURFACE PRESSURES.

Overall, the SH-1 (HEST test) and D-1 (DABS test) airblast pressure loading were very similar in magnitude, waveform and timing. Peak pressure loading of the front of the structure and the surrounding headwall was 20 to 50 percent higher than D-1 for SH-1. Impulse loading is also around 20 percent higher than D-1 along the face of the structure.

Airblast pressure loading on the berm and berm sides atop the structure had higher peak magnitudes and impulse loadings in SH-1 than D-1. As was the case for the headwall loading, the peak pressures and the impulse were 20 to 50 percent higher for SH-1 than for D-1.

An examination of the near field soil stresses and velocities indicated the same trend shown in the airblast pressure data. While the near field soil gages had more variation than the blast pressure readings, the data for SH-1 tended to be 25 to 100 percent greater in peak magnitude than for D-1. The timing and shape of the soil near field waveforms, like the airblast pressure waveforms, were very closely matched between the two simulations.

With the airblast pressure data and soil near field data indicating that the two tests had very similar simulations, structural response parameters from D-1 and SH-1 should match quite well with SH-1 data magnitudes generally greater than D-1 magnitudes.

STRUCTURAL RESPONSE.

In evaluating the similarity between the structural loads and response between SH-1 and D-1, data from three main sources were used. First of all, normal stress at the soil-structure interface provided a comparison of the normal stress on the structure through the soil. Then, velocity and integrated acceleration data showed how well structural motions matched between the tests. Finally, strain data indicated the modes of response and their relative severity in both D-1 and SH-1.

Before examining the specific structural data, however, some general understanding of the comparison would help clarify the data which will be presented. Neither the D-1 nor the SH-1 test exhibited any signs of severe plastic behavior. There was minor hairline tensile cracking in each test due to ovaling and due to other deformations under loads. Generally, structural response indicates initial response due to direct airblast loading only, then the response is affected more and more by normal stress and shear stress loading of the structure. Vertical longitudinal bending of the structure occurred in both tests, as did two distinct cycles of positive ovaling response (crown and invert move closer). Although the responses of both tests matched well overall, the position of maximum response was not always the same. For example, the location of the maximum vertical longitudinal bending moment was farther aft in SH-1 than D-1 due to the greater magnitude of SH-1 airblast pressure loading of the headwall, which caused the effective support of the front of the structure to extend farther aft. Overall, D-1 and SH-1 waveforms and timing matched very nicely, but the magnitudes of the response in SH-1 were 50 to 100 percent greater on the average.

SMI CHARACTERIZATION.

Structure-Media Interaction (SMI) loading on the structure provides the second major loading transmitter to the structure (direct airblast loading is the other one). While direct airblast loading causes the most immediate response of the structure, airblast-induced ground shock generates structural response in concert with the remaining direct airblast loading of the structure after the primary compressive wave effects. This is seen in both tests in the longitudinal response of the structure, which consists of two distinct peaks: the first due to direct airblast loading, and the second due to reflected airblast loading and soil drag-back shear stress occurring in the frontal region of the structure. Separating the two peaks (seen in both longitudinal velocity and strain data) is a relief caused by the normal stress induced by airblast loading of the berm atop the structure propagating along the structure and "gripping" the structure.

As seen in Figure 3, the normal stress at the crown, springlines, and invert at the region just behind the headwall agrees overall

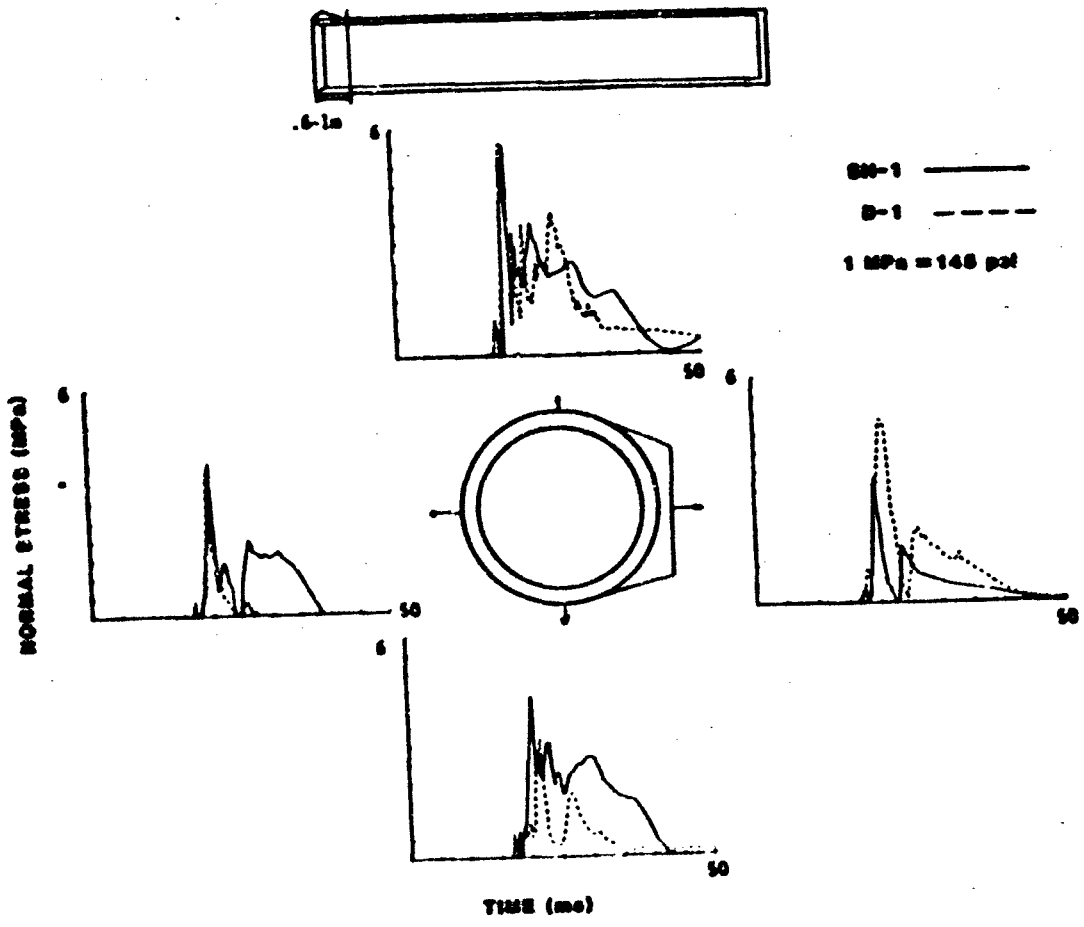

Figure 3. Forward normal stress.

in timing and waveform with the normal stress tracings from corresponding locations in D-1. The magnitudes are slightly higher for SH-1, as seen at the upstream springline and invert. However, the waveform does not seem similar at the invert, and the D-1 normal stress magnitudes are higher at the downstream springline. First of all, when the structure is placed at the test site, it rests in a 120° cradle of sand. Good contact between the invert gage and the surrounding media is not controllable in those conditions. Therefore, those gage readings are not always the best, and that variation seen at the invert is not beyond reasonable agreement for two tests. Second of all, the reading at the downstream springline, while showing a greater D-1 normal stress, shows very good agreement in the waveforms. Once again, the variation in the waveforms could be due to placement problems with the soil against the gage for SH-1. Regardless of that, the variation is not beyond that which can be seen in a single test alone.

Figure 4, which illustrates the normal stresses at the rear of the structure, shows the D-1 normal stresses to be higher across the section. The overall agreements are good for magnitudes and waveforms, except at the upstream springline, where the SH-1 normal stress data must have a problem with the scale but the waveforms are quite similar in peak timing and shape. SH-1 berm loading was not as high at the aft end of the structure as in the more forward regions, so that could be a partial explanation for the lower magnitude of SH-1 normal stresses.

Higher frontal loading in SH-1 causes higher longitudinal soil velocities which are reflected in part in both the longitudinal shear stress and the longitudinal structural velocity. SH-1 had greater drag-back shear stress magnitudes and a greater portion of the length which this drag-back shear acted upon than D-1. This, in turn, is reflected in the second longitudinal velocity peak and the secondary compressive strain pulse, although the separation of effects between initial airblast loading and later shear stress and reflected airblast loading grows less distinct toward the end wall.

SMI effects, then, are similar in comparison with the airblast pressure and the near field parameters already investigated. SH-1 mimics D-1 very closely in SMI behavior, but generally the magnitudes in SH-1 are greater due to the greater loading in the simulation.

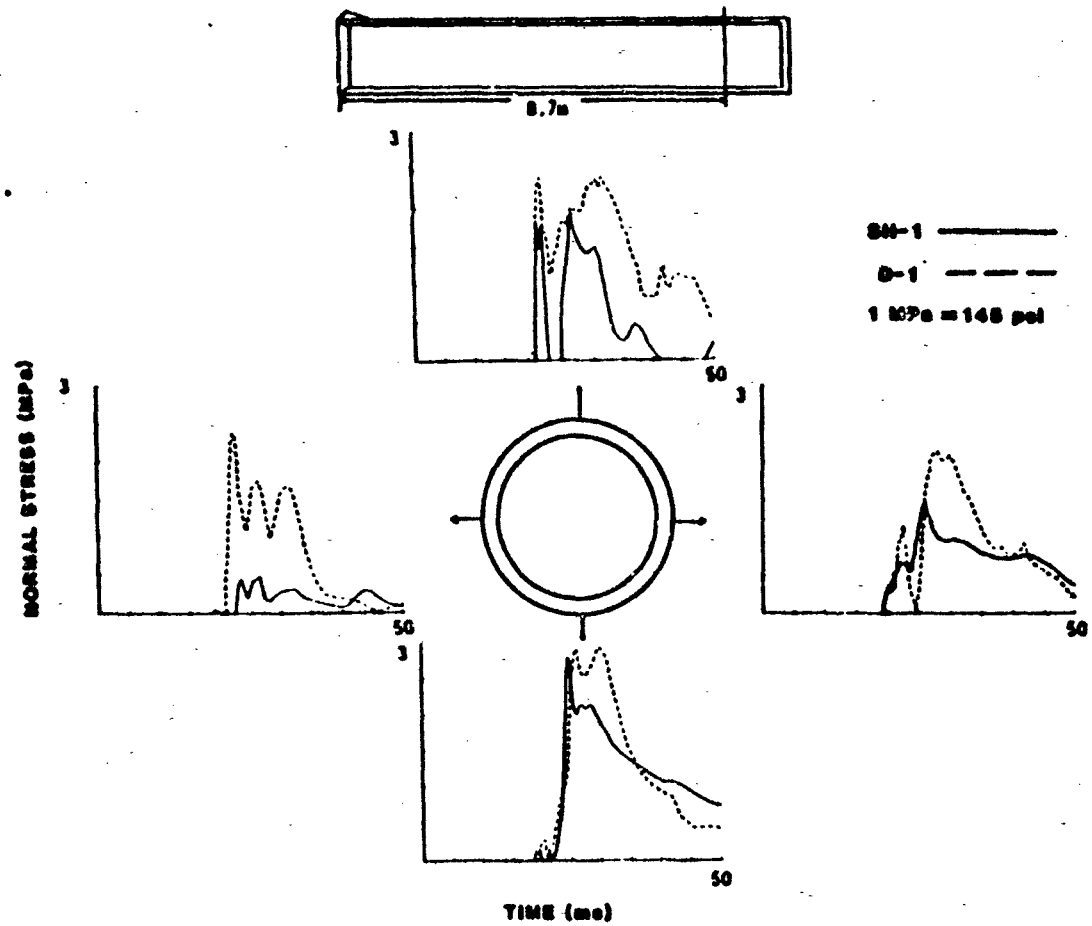

Figure 4. Aft normal stress.

VELOCITY CHARACTERIZATION.

Structural velocities are useful in examining the movement response of the structure under the loading caused by the attack scenario. The overall waveforms are usually easy to explain, especially in light of the loading conditions already explored.

Structural longitudinal velocities are presented in Figure 5. As already explained, they consist mainly of a double peak positive waveform with a relief seen in-between. The initial velocity peak is due to the direct airblast loading on the face of the structure. Normal stress application caused by vertical airblast-induced ground shock accounts for the slowing in-between peaks, while the second longitudinal velocity peak is due to both secondary airblast peaks loading the structure face directly and positive "drag-back" shear stress acting in the frontal third of the structure. As shown in Figure 5, the structural longitudinal velocities are greater in SH-1 than in D-1 due to the slightly higher airblast loading. Near coincidence of the peaks in the aft of the structure accounts for the higher velocity magnitudes.

The vertical structural velocity profile is given in Figure 6. This waveform is characterized by an initial high peak due to incident normal stress from vertical airblast-induced ground shock, with a usually minor second peak as the ground shock envelops the cross-section and a rigid-body vertical displacement occurs. Once again, the waveforms agree between D-1 and SH-1, with greater magnitudes seen in SH-1 due to the greater airblast loads on the berm. The forward velocity readings for this profile are more rounded because of the type of gage used to record the data.

The lateral structural velocities are shown in Figure 7. The best agreement is seen at the rear of the structure when comparing D-1 and SH-1. The expected velocity waveform for lateral velocities is shown consistently in D-1 data, where the crown of the structure displaces downstream, followed by the invert when the vertically-propagating ground shock arrives there. SH-1 showed consistently negligible lateral movement in the forward half of the structure. This could be due in part to the higher downstream stresses caused by greater airblast loading acting to restrain lateral motion.

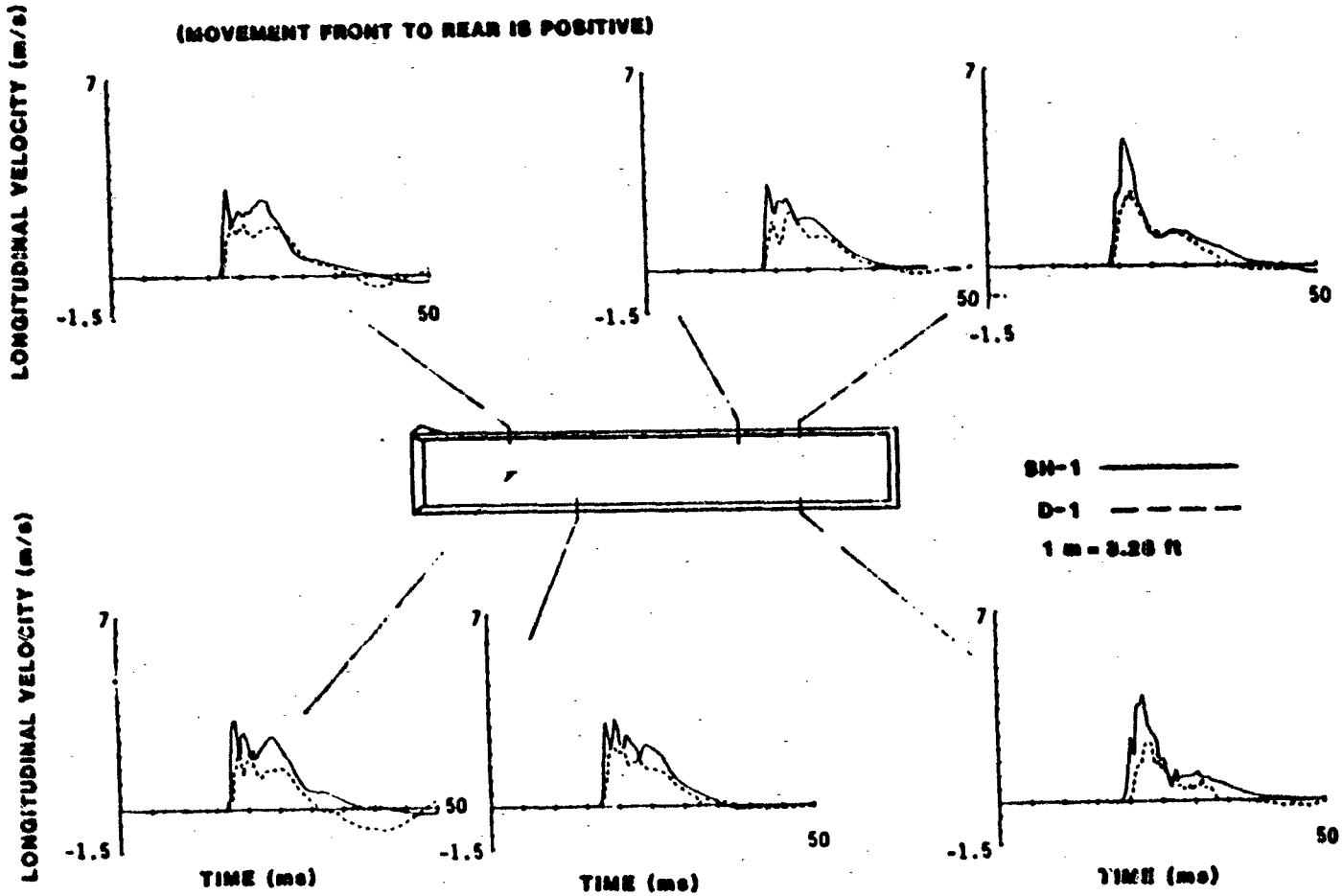

Figure 5. Structural longitudinal velocities.

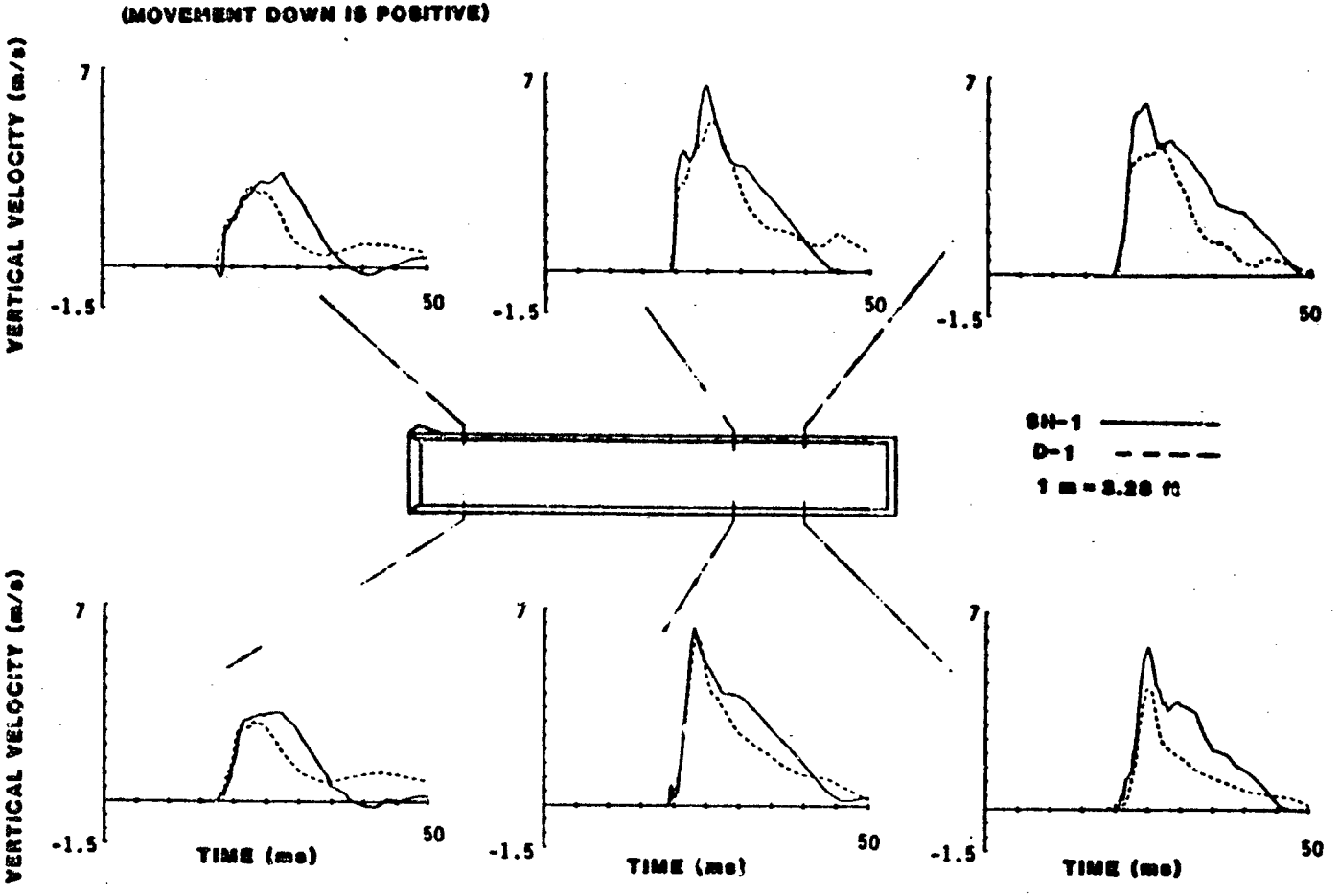

Figure 6. Structural vertical velocities.

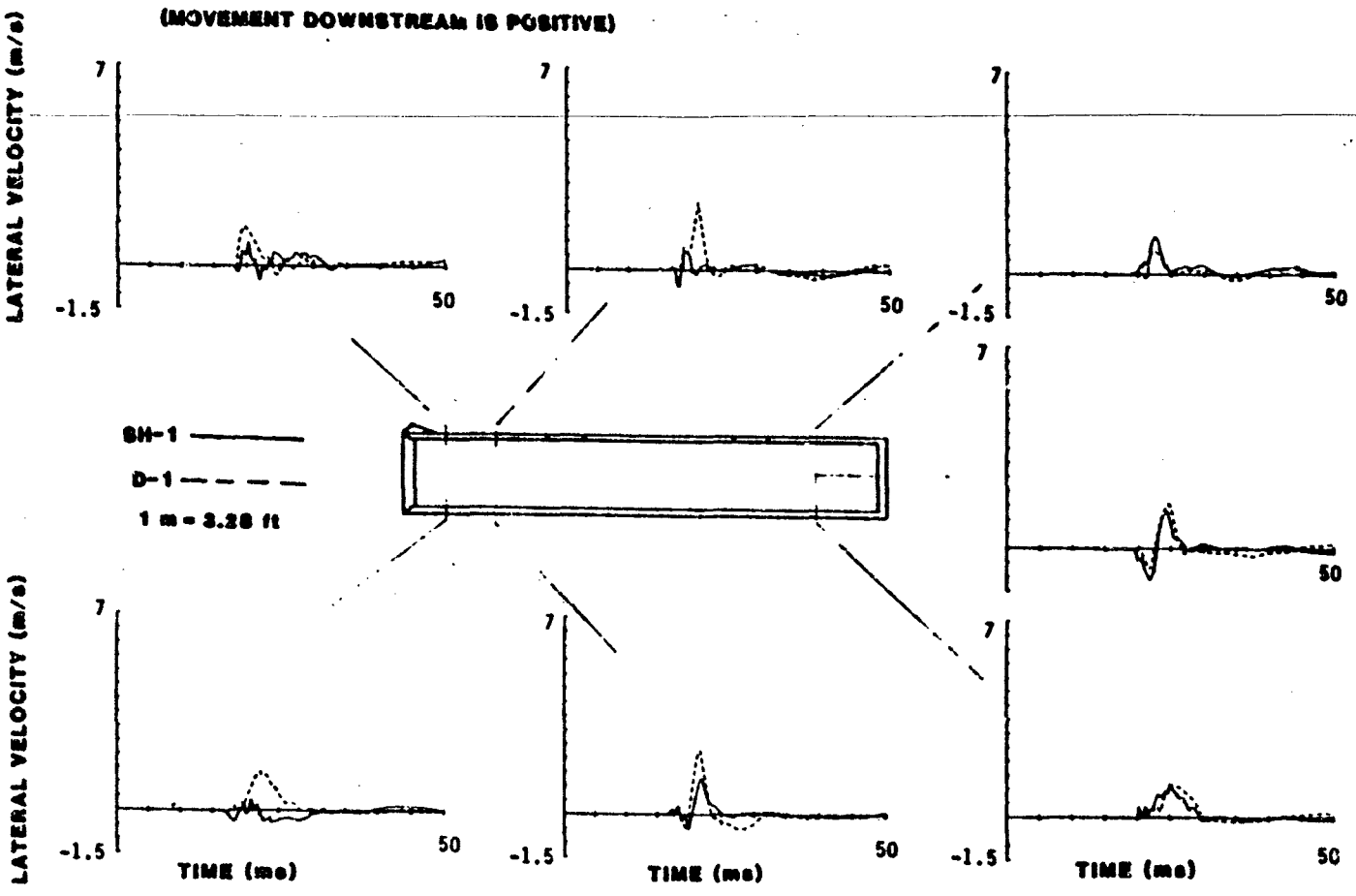

Figure 7. Structural lateral velocities.

Taking an overview of the velocity profiles shows that the vertical structural velocities were of greatest magnitude, followed closely by the longitudinal structural velocities. Both the vertical and longitudinal velocities agreed with the D-1 waveforms but had higher magnitudes. The SH-1 lateral structural velocities were consistently lower than D-1 except in the aft third of the structure, where the waveforms and magnitudes matched well for the two tests. Agreement of the velocity data between the two tests is surprisingly close, given the difference in blast simulators and the higher SH-1 loading. Indications are that similar structural responses occurred in both tests, since no noteworthy variations were seen in the velocity comparisons for the two tests. An investigation of the strain data will be the final measure of the capability of a HEST simulator to reproduce a DABS blast loading of a test structure.

STRAIN CHARACTERIZATION.

Structural strain data from the D-1 and SH-1 tests gave the best indications of structural response, especially in light of the loading conditions and the velocity response of each test. A great number of strain gages were placed in the structure at specific regions so that response could be defined in a more detailed manner. Representative cases will be used for this comparison between SH-1 and D-1 strain data. Cases will be examined in cross-sections from the front to the rear of the structure.

Strain near the supported edge of the closure base pan is presented in Figure 8. Tensile strain is expected in the data from the vertically-oriented gage, and both D-1 and SH-1 reflect this condition as the closure dishes inward under the airblast load. The waveforms reflect the higher SH-1 loading, but the timing of the three peaks in both tests coincide regardless of the airblast loading differences. This is because the peaks reflect the closure frequency of 500 Hz, which should agree in both tests with the same closure design.

Longitudinal strains at a section 2 meters from the front of the structure are seen in Figure 9. Inner and outer strains for both tests are shown at the crown and upstream springline, while only outer longitudinal strains are shown at the invert and downstream springline.

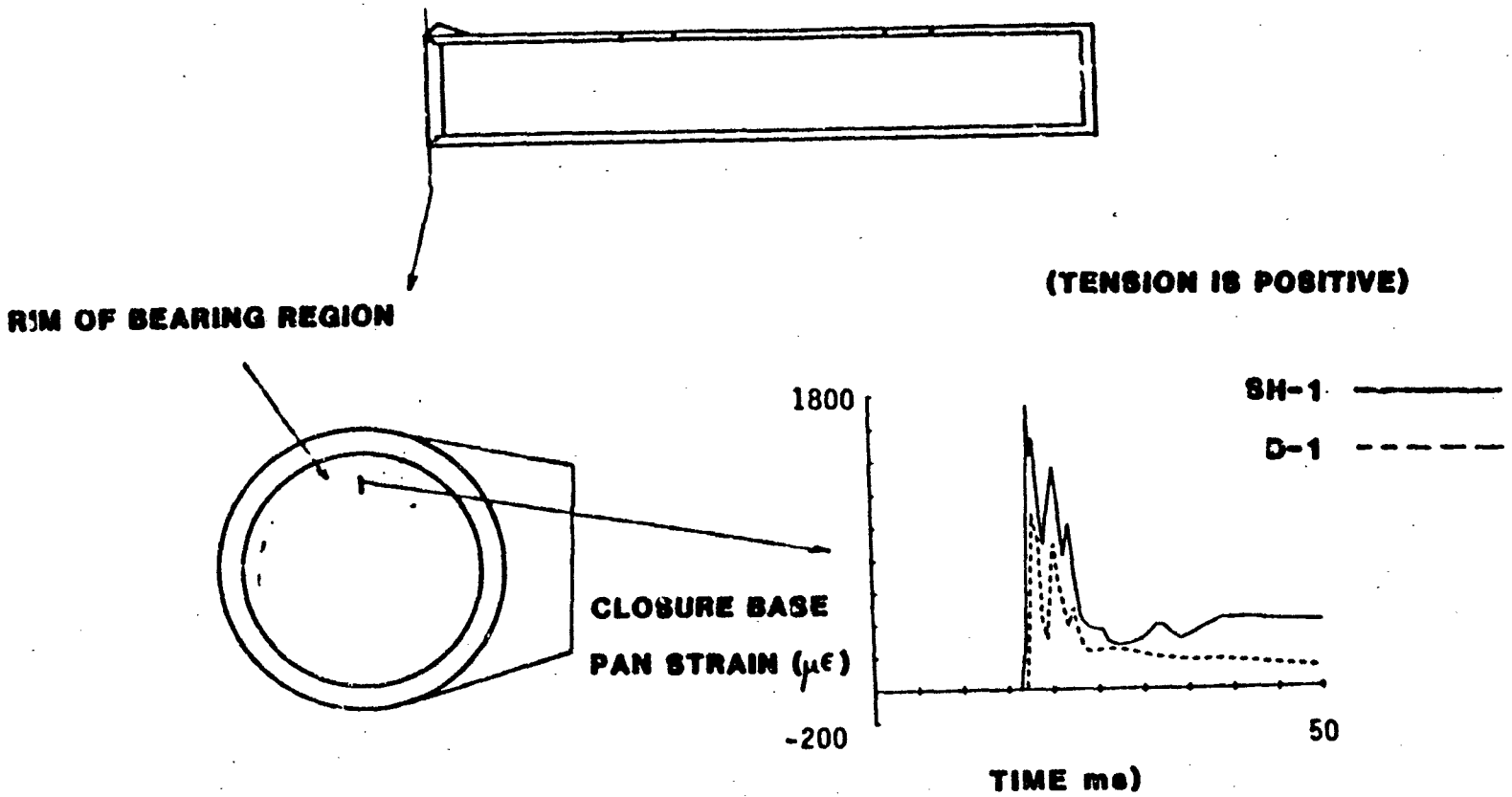

Figure 8. Closure base pan strain.

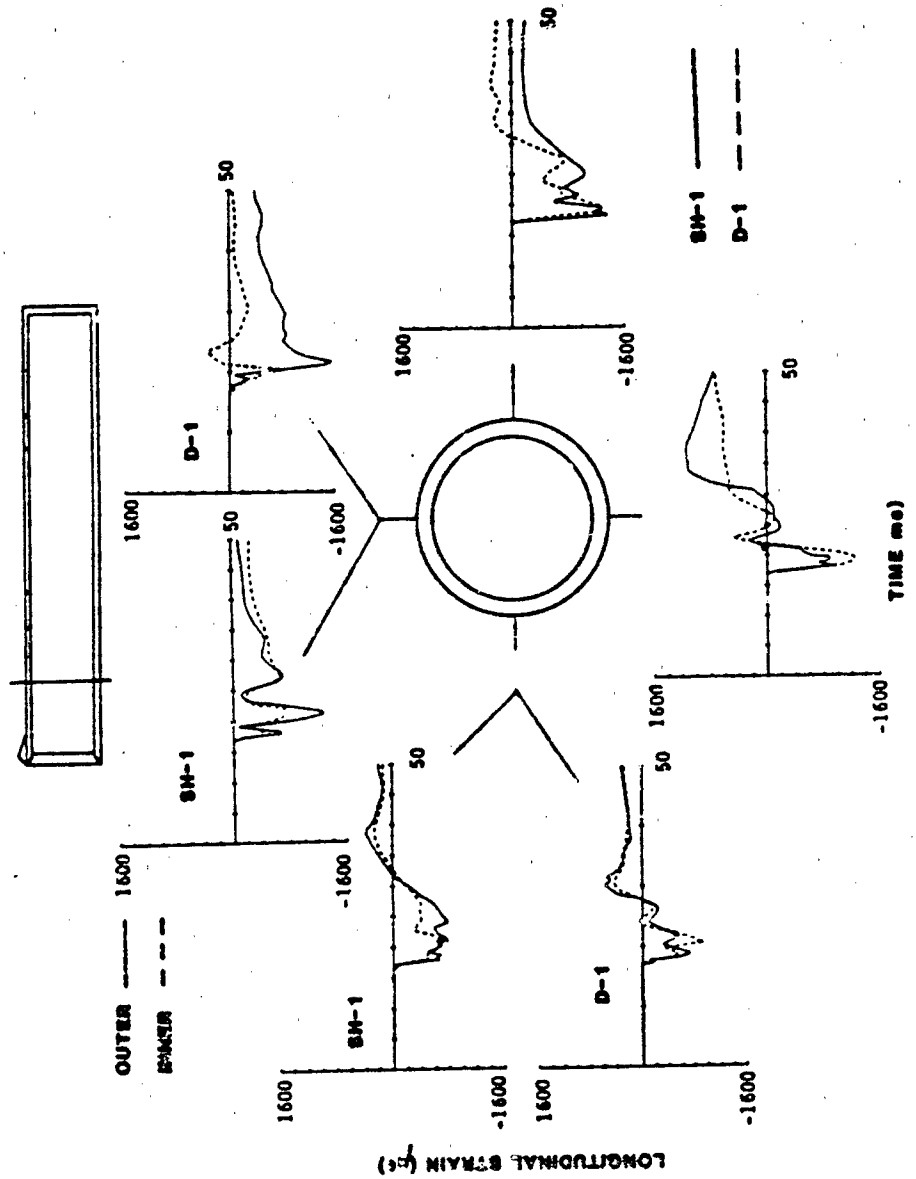

Figure 9. Longitudinal strain at 2 meters.

The overall agreement is very good between waveforms and magnitudes. Several differences are apparent due to the loading condition variation between the DABS and the HEST. The D-1 frontal airblast loading was greater at the bottom of the headwall than the top of the headwall and greater on the downstream side than the upstream side of the closure. The result was a bending moment seen in the strain data during the initial airblast loading compressive peak. The strain data displayed greater compression at the invert than the crown and greater compression at the downstream springline (due to the hinge area and the greater airblast pressure loading) than at the upstream springline. While this same bending moment occurs in the horizontal direction in SH-1 (influenced most by the presence of the hinge), the vertical moment is not seen in SH-1 due to the constant load distribution vertically on the face of the structure. These longitudinal strain comparisons also illustrate the common longitudinal modes of response: an initial compressive peak due to direct airblast loading, followed by relief and a vertical longitudinal bending which causes compression in the crown as the normal stress from airblast loading of the berm arrives and generates large shear stresses. These shear stresses act to slow the structural motions, and the normal stresses also induce the vertical longitudinal bending of the structure. The severity of the normal stress on the crown can also cause localized wall bending, which is seen clearly in the D-1 data but more moderately in the SH-1 data at this location. The final longitudinal response mode is seen at around 26 to 28 milliseconds as the drag-back shear stress in the forward region of the structure interacts with the resisting shear stress and the end wall support further aft to cause a smooth transient compressive strain pulse as the structure vertically bends.

Mid-structure longitudinal strains, shown in Figure 10, follow the trends seen in the more forward location. All the waveforms agree in shape and timing, but SH-1 shows more extreme strains due to the higher loading (except at the crown). The difference in strain at the crown between 20 and 25 ms is due to the vertical longitudinal bending in SH-1, which occurs farther back from the headworks than in D-1 and results in more compressive strains in the crown as the bending takes

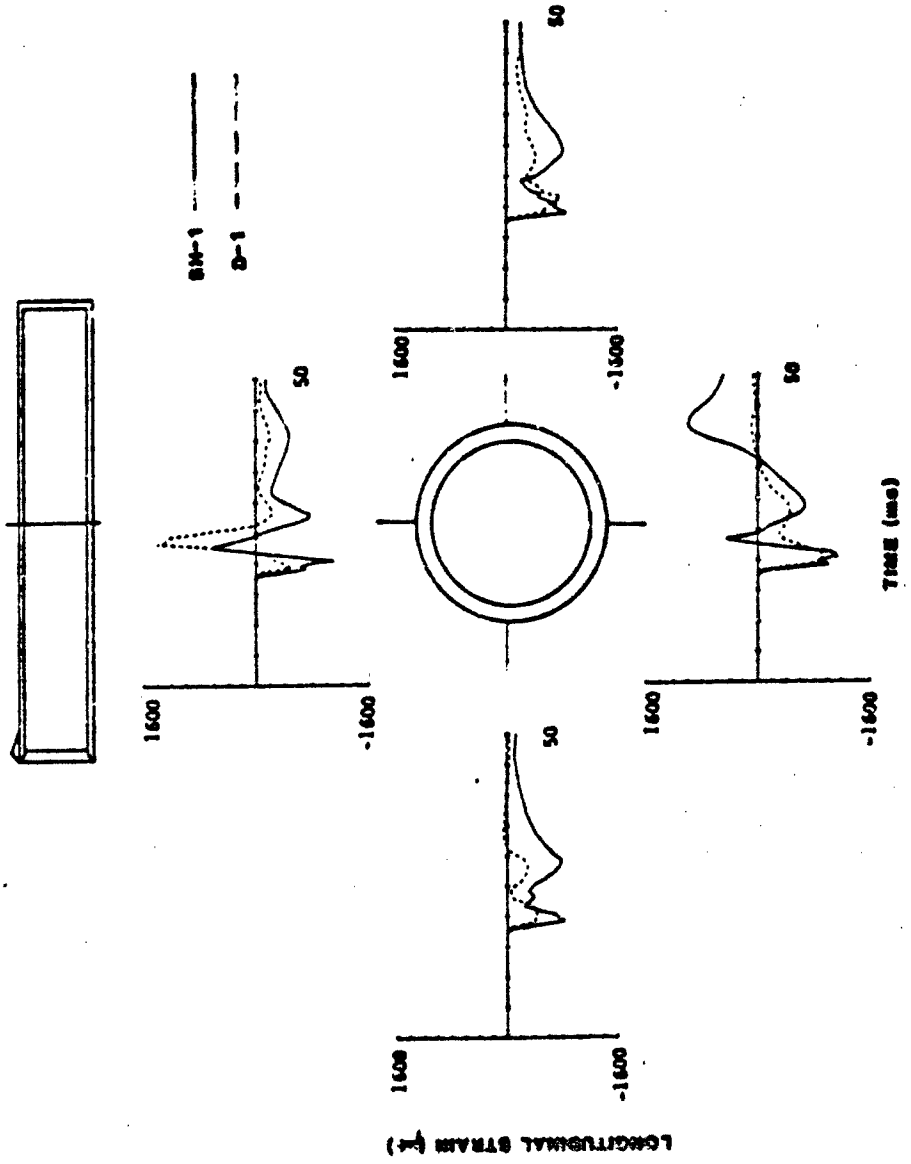

Figure 10. Mid-structure longitudinal strains.

place. This effect due to vertical longitudinal bending is seen in the invert strain data as well, where the tensile strains caused by the bending show up in SH-1 but are not as severe in D-1 data. The pronounced relief seen in both tests between 20 and 25 milliseconds is due to the fact that the normal stress and resultant shear stresses are acting to restrain the longitudinal motion of the forward portion of the structure while the aft portion of the structure is reaching peak longitudinal motions due to direct airblast loading. However, the major point of this comparison is that both tests continue to direct the identical response modes from the structure with slight changes due to the difference in loading in the two simulations.

Figure 11 compares the circumferential strains for D-1 and SH-1 test structures from data taken at the inner face and outer longitudinal rebar at each location in the cross-section. As mentioned earlier, the structural ovaling response consists of two positive ovaling phases (crown and invert move closer) with a relief in between. The relief between positive ovaling response peaks is more pronounced in D-1, when negative ovaling occurred at times between the positive ovaling responses. The initial ovaling phase was caused by the application of normal stress at the crown due to airblast pressure loading of the berm over the structure, while the relief was caused by the flow of the normal stress around to the springlines as it propagated vertically. Finally, the second positive phase occurred as the normal stress engulfed the structure and the vertical motion of the structure downward was halted due to the compaction of the cradle material beneath the invert. The second positive ovaling phase seems more severe due to the higher strain magnitudes, but the reduced concrete cross-section due to cracking of the concrete in the initial positive ovaling phase accounts for that exaggeration. Figure 11 illustrates all of these points, and once again the SH-1 response is generally greater due to the higher loading in the simulation. The springlines provide the closest match, while higher ovaling modes seem to be present at the crown in SH-1 and at the invert in D-1.

Shown in Figure 12, lateral strains on the inner and outer surfaces of the endwall are compared for D-1 and SH-1 at the center and the rim. Timing and shape of the waveforms agree very well in all cases, with SH-1 experiencing the higher strains, as expected. At the center,

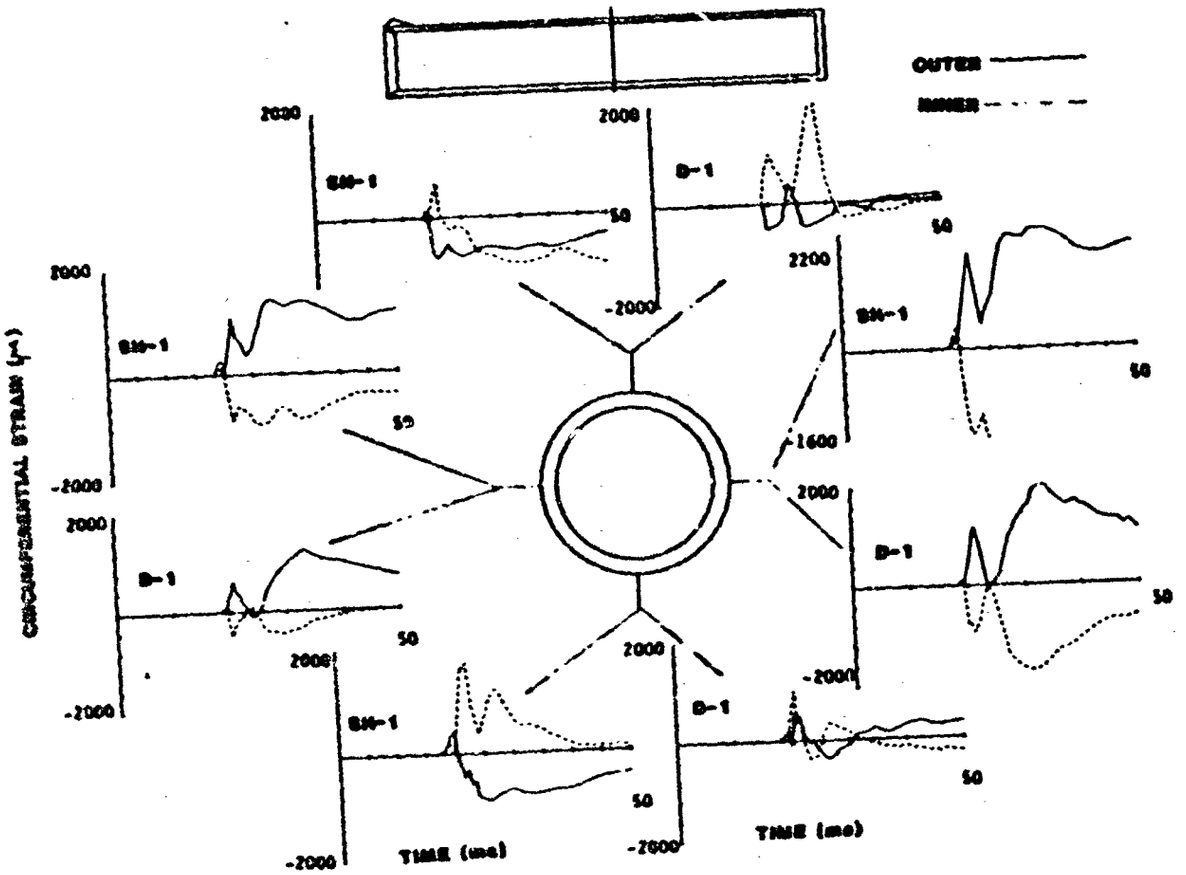

Figure 11. Mid-structure circumferential strains.

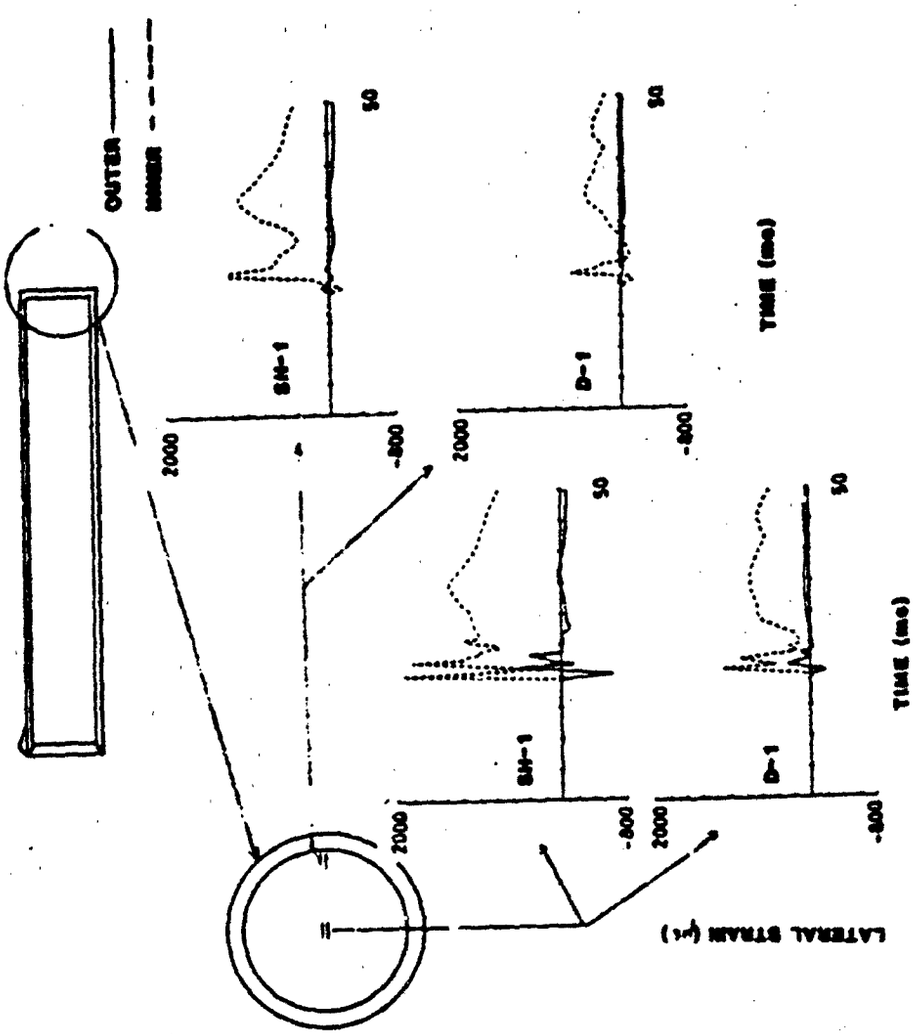

Figure 12. End wall lateral strains.

the endwall dishing into the structure causes initial outer surface compression and inner surface tension. As the load increases, the endwall goes into overall section tension with the bending moment still evident in the data. The initial peak is due to structural displacement under direct airblast loading. The second peak is caused by the propagation of the vertical airblast-induced ground shock down through the berm, and the final long peak is due to the same cause as the second longitudinal strain and longitudinal velocity peaks seen throughout the SH-1 structure-secondary airblast peak loads on the face of the structure and drag-back shear stress acting in the frontal region of the structure. The same effects are seen at the rim, except that the outer strain gage is relieved of load due to edge effects near the outer corner of the structures, and thus that gage gives a very minor strain reading. The inner strains at the rim go into initial compression as the endwall dishes in, but then the load increases to cause overall section tension seen in the gage. The second peak, due to vertical airblast-induced ground shock, is not as isolated an event at the rim, and that peak is seen as a bump on the decreasing side of the initial peak. Given the complexity of the response of the endwall, the two tests agree very well in timing and shape, with the only discrepancy being the greater magnitudes in SH-1 strains due to the loading differences with D-1.

Strain data analysis, based on understanding of the loading condition differences and motion data, makes a very strong case for the ability of a HEST simulator to mimic the loading of a DABS when simulating a given blast environment.

CONCLUSION.

Comparisons between the D-1 test data and the SH-1 test data reveal that similar structural response modes were observed in both tests. The only differences stem from the difference in the airblast loading simulation in SH-1 compared to a D-1 standard, and that is a discrepancy which can be corrected with a refined HEST design and proper calibration of the HEST design. Using structural response as a yardstick, therefore, the less costly HEST simulator is as viable a choice in testing generic structure designs under anticipated airblast conditions as the more expensive DABS simulator.

SUMMARY

A Comparison of Nuclear Simulation Techniques on Generic MX Structures, by John F. Betz. Two separate 1/5 scale tests were run on a generic MX protective structure using different simulators to create a standard blast environment. Based on analysis of the structural data, the less expensive HEST simulator was as good a simulator as the more expensive DABS simulator.

A COMPARISON OF NUCLEAR SIMULATION TECHNIQUES ON GENERIC MX STRUCTURES

KEY WORDS: Explosions, Nuclear Explosions, Missiles, Shelters

ABSTRACT: A HEST (High Explosive Simulation Technique) is as good a simulator of an airblast environment as a DABS (Dynamic Airblast Simulator). A study performed on the results of two identical 1/5 scale protective structures when tested under matching environments produced by each of the simulators revealed data which supports the viability of the HEST simulator, which is less costly and was thought to be of less fidelity than a DABS simulation. Structural response data, which is used as a yardstick to compare simulators, shows identical response modes are produced by the two simulators as arranged in the matching tests.

ASCE SPRING CONVENTION

26-30 APRIL 1982

SESSION 22FM

PHYSICAL MODELING TECHNIQUES FOR MISSILE AND OTHER PROTECTIVE STRUCTURES

ABSTRACT

INSTRUMENTATION FOR PROTECTIVE STRUCTURES TESTING

Joe V. Quintana

Selected stress and motion parameters associated with test input stimulus, free-field response, and specimen structure responses are identified as measurands in simulation testing of Air Force (AF) protective structures. For each measurand the corresponding sensor and sensing technique used by the AF is illustrated and briefly described. Observed performance is noted and other factors reveal implementation guidelines.

INSTRUMENTATION FOR PROTECTIVE STRUCTURES TESTING

JOE V. QUINTANA[1]

INTRODUCTION

Critical to the success of efforts to develop survivable protective structures is the data acquired in experimental field tests. Real-time measurements characterizing the test input stimulus, free field responses and structure responses are indispensable for accurate empirical assessments of structure survivability and verification of physical models.

This paper is an overview of instrumentation used in simulation testing by the Air Force Civil Engineering Research Division of the Air Force Weapons Laboratory (AFWL/NTE). The techniques presented have evolved over several years and have been used in a number of programs for nuclear blast simulator development and subsequent survivability testing. In this paper selected stress and motion parameters in the areas of stimulation, free field response, and structure response are identified as specific measurands of interest. A description of the corresponding sensor (transducer and its mounting hardware) and the sensing technique is presented with pertinent considerations and observed performance parameters. Emphasis is on the sensing end of the measurement channel although a brief description of system topics such as signal conditioning electronics and cabling schemes is included. The techniques described generally represent current approaches at the Civil Engineering Research Division. However, they do not reflect ongoing instrumentation development efforts toward utilizing the latest in transducer materials technology, electro-optics, semiconductor devices, fiber optics, and others to enhance fieldability, accuracy and survivability of the instrumentation.

It is hoped that the descriptions will enable readers to assess the techniques in view of their own current practices or interests and enter a technical dialogue with the author toward optimizing the instrumentation for specific applications. Only with such information exchanges can the experimental community realize mutual benefit in fielding instrumentation to obtain the necessarily high quality of field test measurement data required.

TEST INPUT STIMULUS

Blast Pressure

Considering that large masses of high explosives are used to create the tailored blast environments for simulation testing it follows that a most

---

[1] Air Force Weapons Laboratory
Civil Engineering Research Division
Kirtland Air Force Base, New Mexico
A.C. 505-944-0156; Autovon 244-0156

significant parameter to characterize test input stimulus is the blast pressure time history. The hostility of the total test environment and the stringent characteristics of the measurand require a highly specialized transducer. The unit developed to AFWL/NTE specifications specifically for use in simulator applications is designated the HKS-11-375-10K. The resistance-based transducer incorporates a silicon integrated sensor (IS) disk with diffused semiconductor strain gages in an essentially monolithic construction to provide outstanding shock hardness. The silicon IS enables extremely high resonant frequency, and thermal barrier provisions minimize flash thermal responses in the use environment. Evaluation testing and successful applications of the HKS-11-375-10K since 1975 have demonstrated shock acceleration hardness to greater than 5C Kg (indicated), natural resonant frequency greater than 700KHz, on-axis acceleration sensitivity less than 0.4 μv/g , and less than 0.2 mv response from flash thermal stimulus applied per NBS Bulletin 905 to the sensing face of the transducer. The basic unit is available in various performance ranges from 3.4 MPa (500 psi) to 137.9 MPa (20,000 psi) from Kulite Semiconductor Products, Inc., originators of the IS silicon disk element for pressure transducers. Figure 1 is a representation of the unit.

For events using the HEST simulator the specific measurand is the blast overpressure loading the ground surface directly under the explosives array. To measure blast overpressure sensors are installed flush in the testbed surface. Normally sensors are located throughout the total area to observe propagation of the blast wave front. To provide stable sensing platforms concrete masses on the order of $0.2m^3$ are poured at the sensing locations. Steel mounting hardware and provisions for cable protection are embedded in the pour. After concrete cure, the cable and the plug-in sensor module (with transducer) are installed to complete the stable flush-mount installation. Figure 2 shows the AFWL/NTE blast pressure sensor hardware. Figure 3 shows a typical HEST blast pressure sensing installation. HEST cavity pressures to 35 MPa (5 K psi) have been measured using the concrete high mass scheme.

Time of Arrival

A parameter used to cross-correlate blast pressure data, monitor HE detonation rate, and characterize detonation wave front symmetry is the time of arrival (TOA). The specific measurand is the time lapse between the explosives initiation at T-zero and the time the detonation front arrives at uniquely predetermined precisely established positions throughout the explosives array. Up to 300 sensors (depending on size of the simulator explosives area) may be fielded to acquire the TOA data with a TOA digitizing system designated as TOADS II. TOADS II is the second generation of a system developed to AFWL/NTE requirements specifically for simulator applications. Typically, a TOA sensor consists of a relatively inexpensive 1 cm dia X 5 mm thick ferroceramic (PZT-5) disc secured directly to the explosive element at the established location. Each sensor is assigned a unique identifying number, and each is cabled directly to the TOADS forward system (FS) electronics unit usually within 50 meters of the HE array. The TOADS, totally independent of the instrumentation system, functions as an electronic stop-watch with all channels starting to count simultaneously at T-zero and stopping when a pulse is generated by the piezoelectric disc on arrival of the detonation wave front. All elapsed time data is stored on receipt during the event. After the test the FS is retrieved and the data is dumped, digitized,

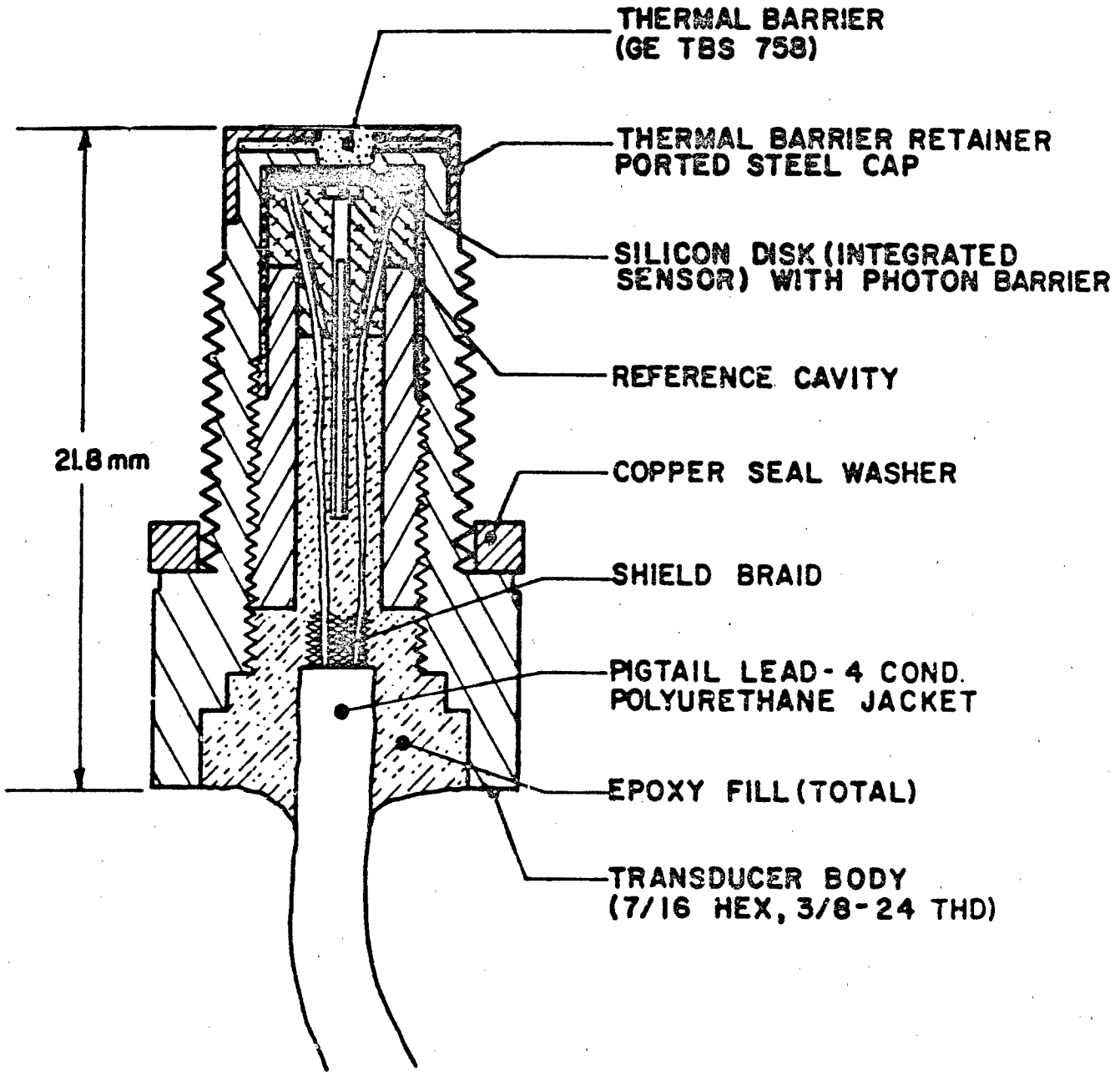

FIGURE 1. HKS-11-375-10K BLAST PRESSURE TRANSDUCER

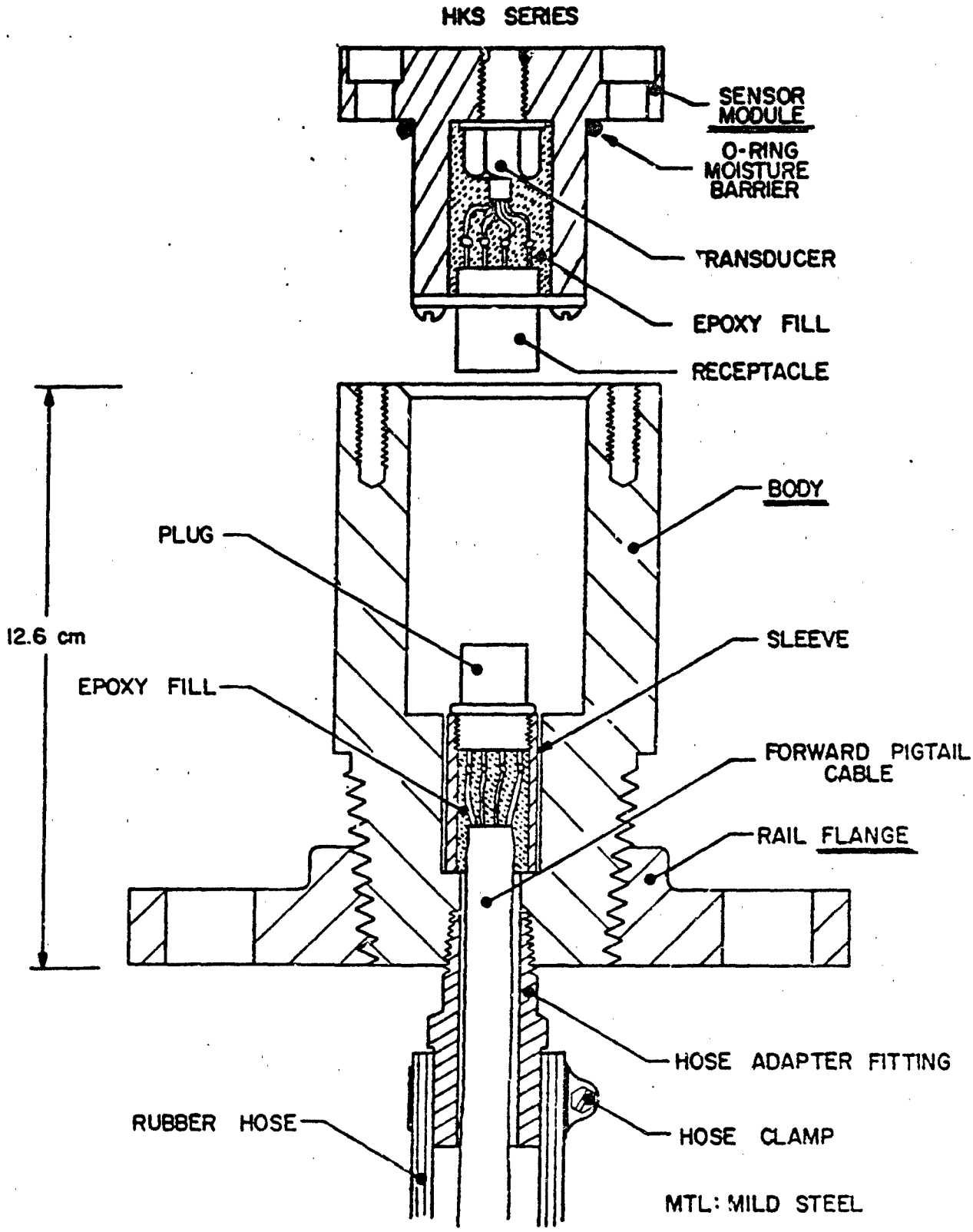

FIGURE 2. AFWL BP SENSOR HARDWARE

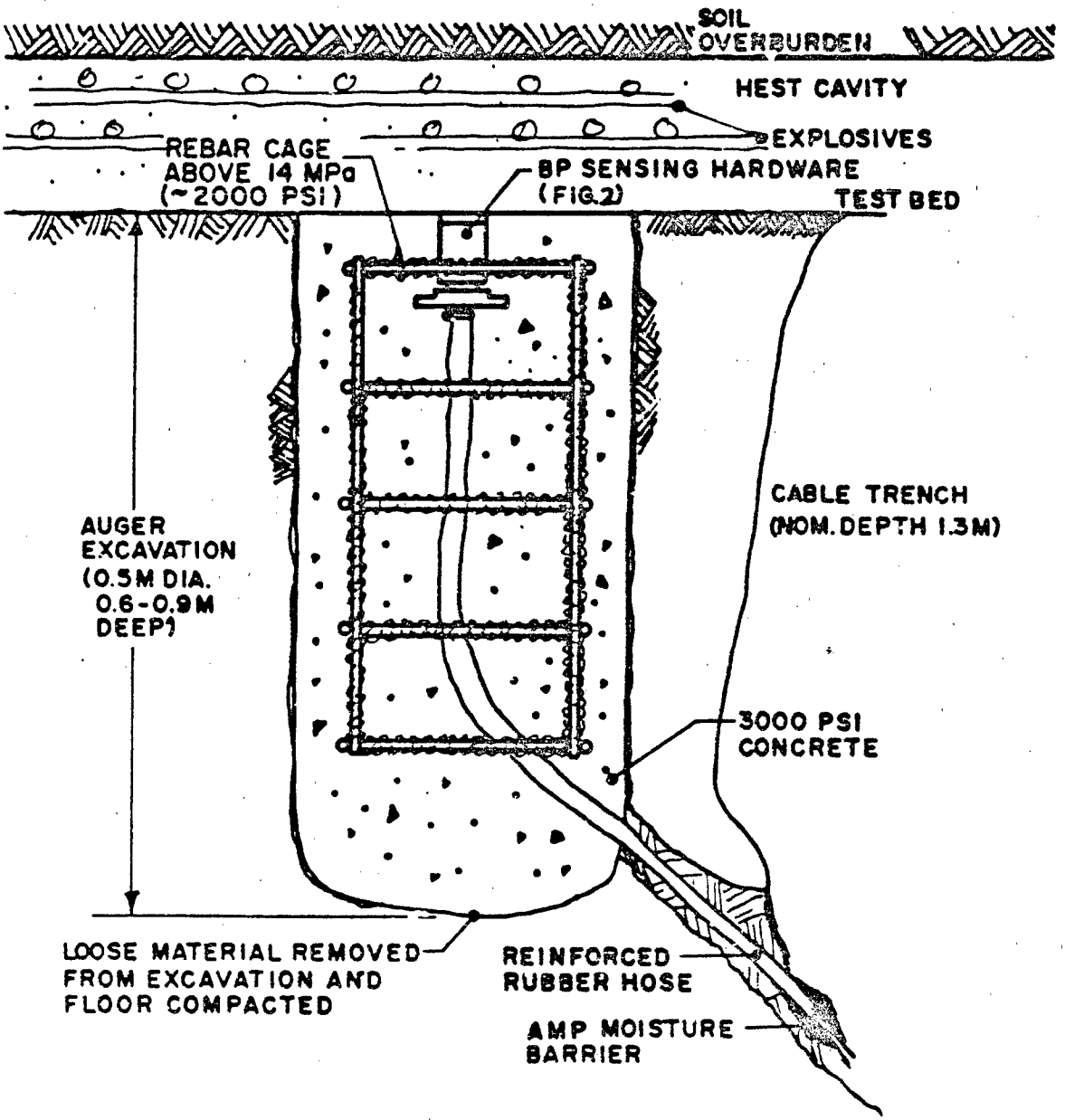

FIGURE 3. HEST CAVITY BP SENSING INSTALLATION.

and printed on paper tape by a central control (CC) unit in the control van. Each channel is uniquely listed with its corresponding elapsed time in microseconds. Data accuracy, a function of the internal clock, is on the order of $\pm$0.2 μs. Resolution is $\pm$0.4 μs, and data yield is consistently above 95%. Figure 4 shows a typical TOA sensing installation.

Total Pressure

For applications in shock-tube-like simulators, such as the Dynamic Airblast Simulator (DABS), a prime parameter toward characterizing input stimulus is total pressure. Again, considering the masses of TNT used to drive the simulator and the resulting hostility of the test environment, highly specialized instrumentation is required. Considering that total pressure must be sensed with the transducer oriented head-on into the oncoming flow, and considering presence of blast driven debris particles, the primary concern is protecting the transducer with minimum perturbation of the measurand. The design of the HKS-11-375 sensing face is such that only particles impacting a 2 mm diameter area at the center can cause transducer failure. Thus, protecting the central area is all that is necessary for survivability against blast driven particles. The method used was to design a cap which could be threaded down over the transducer face. The flat surface of the cap was then machined to provide the necessary central area protection and apertures for enabling blast flow to the transducer face for total pressure sensing minus debris effects. Thus an effective "debris shield." Figure 5 shows the debris shield configuration designated the Mod VI "church-window" as used in conjunction with the HKS-11-375 transducer. The design features the maximum aperture area to offer minimum restriction to blast flow thus minimizing effect on rise-time and peak amplitude. The aperture configuration also precludes definition of a cavity which could support acoustic oscillations. The principle of deep beams theoretically enables the thin webs to support the critical protective area against hypervelocity impact of 1 mm^3 mild steel particles. Originally designed for use up to 69 MPa (10,000 psi) measurements to 100 MPa (14,500 psi) have been performed by using hardened (heat-treated) debris shields and thermal barrier retainers on the face of the transducer. Numerous successful head-on sensing applications in a variety of blast environments has demonstrated adequacy of the technique. Signal analyses of acquired data verifies the antiresonance of the "cavity". However, during the shock tube evaluations in developing the shield it was found that at levels of reflected pressure in the range to 20.7 MPa (3000 psi) a perturbation of early time data profile was noted such that validity of the first ~50 μsec by comparison with an unshielded reference measurement was questionable. Thus selective application of the technique is required as for all measurement applications.

Incident Overpressure

In applications where structures are tested with blast wave stimuli generated by "point-source" explosives simulating nuclear surface burst weapons, the principal parameter (and the measurand) is incident overpressure (IOP). IOP measurements are made with the sensor surface flush in the free field and oriented side on to the direction of blast wave front propagation.

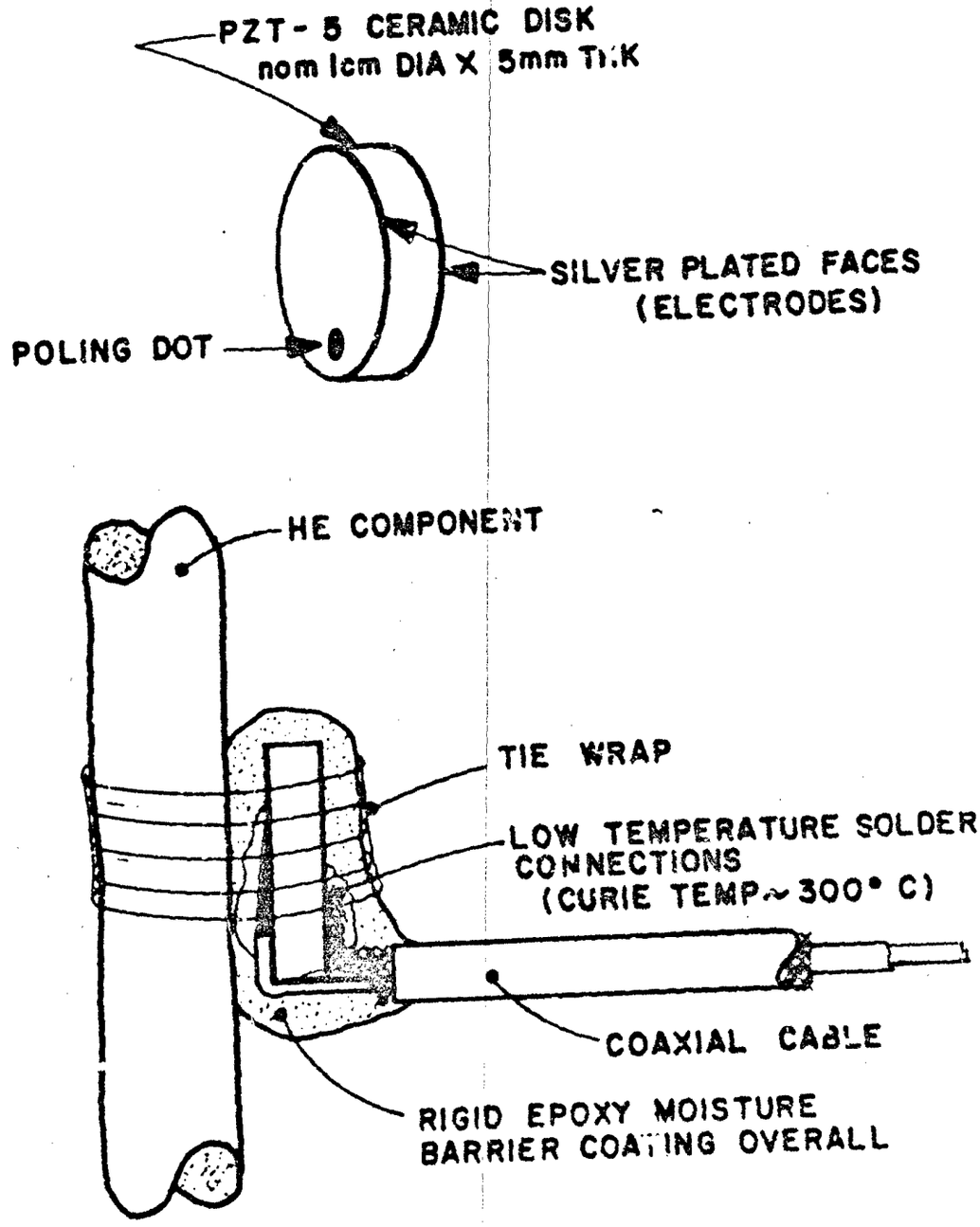

FIGURE 4. PIEZOLECTRIC TOA SENSOR

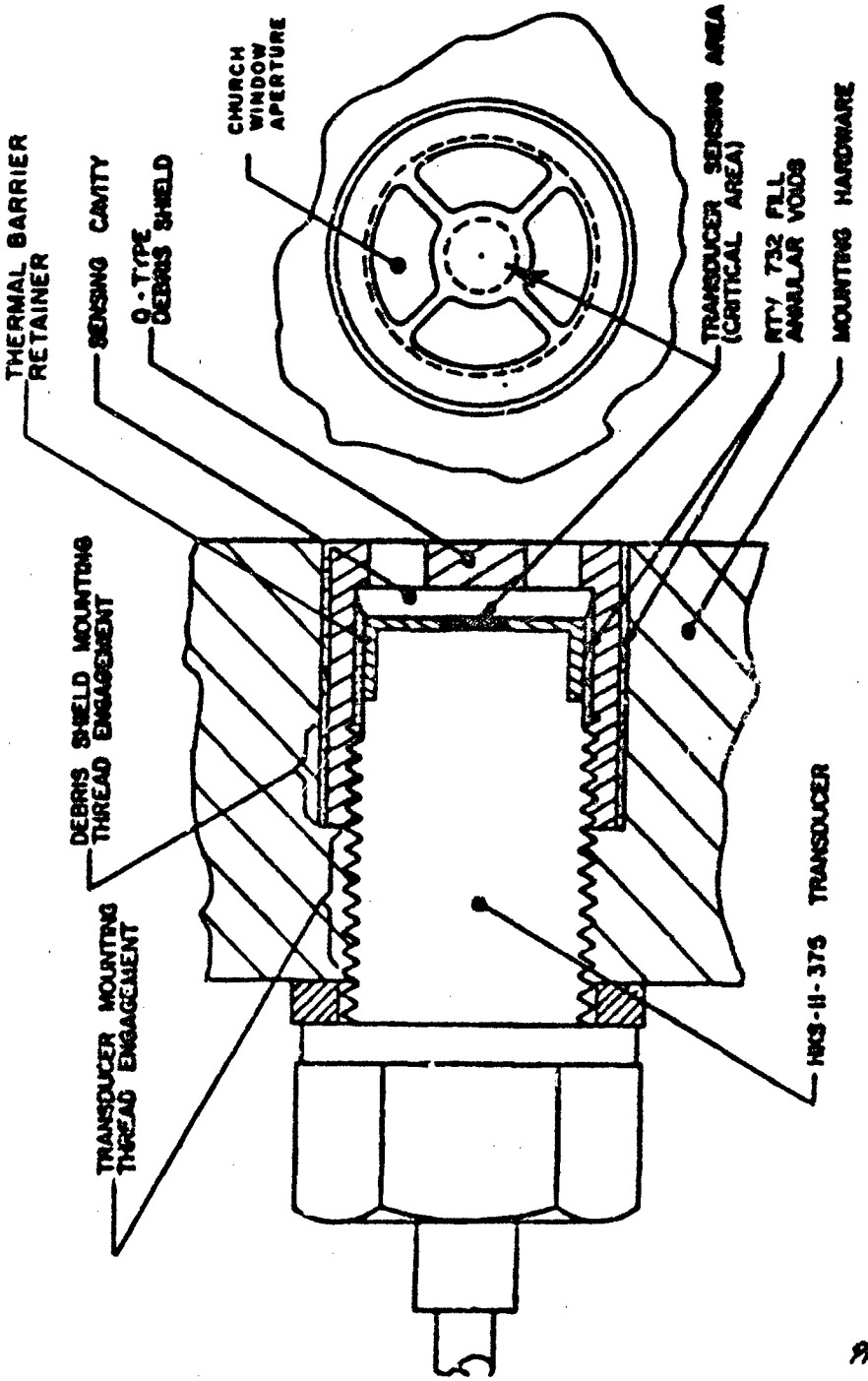

FIGURE 5 DEBRIS SHIELD SCHEME FOR HEAD-ON SENSING

FIGURE 5. DEBRIS SHIELD SCHEME FOR HEAD-ON SENSING.

In this orientation the sensor experiences a relatively mild shock acceleration environment compared to that in the HEST. Consequently, it was established that the concrete high mass sensing technique would also work in IOP sensing applications. Thus the IOP sensing technique has been the poured-in-place concrete mass with embedded hardware as described earlier for the HEST. However, because of the wide range of IOP magnitudes possible in a given test event (typically from 35 MPa "close-in" to the HE stack to .035 MPa at "far-field" locations) transducers other than the HKS-11-375 series are required. For gage pressure measurements down to .03 MPa the Kulite XTS-1-190 series transducer has been used in suitably modified plug-in sensor modules.

For IOP and HEST measurement applications where constraints preclude use of the concrete mass, an alternate sensing technique has been devised. Designated the "pipe mount", the technique consists of standard rigid pipe and pipe fittings in an in-line assembly with the regular plug-in module mounting hardware at the sensing end. Figure 6 is a typical assembly. Subject to properties of the free field geology the assembly, with a "driving head" in place of the sensor body, is impact driven vertically into the free field at the sensing location. At proper depth the driving head is removed and a regular sensor body is threaded into the upper coupling. A hand excavation is made to enable routing the cable downward and out into the cable trench. With the cable in place and covered over the plug-in sensor module is installed, a minor backfill and surface compaction effort is performed, and the low mass blast pressure sensor is ready. The pipe mount has been fielded in a number of HEST and non-HEST applications in a wide range of environment severities and has demonstrated highly satisfactory performance. Pre and post test optical surveys of sensor location and orientation together with analyses of acquired data have indicated as good, if not better performance than the high-mass concrete in terms of maintaining an established sensor location and orientation. The consideration is that if the sensor is the same post-test as it was pre-test, there is reason to believe that the sensor did not displace with respect to the free field and did not become disoriented from perpendicular with respect to the propagating overpressure wave: two critical factors in acquiring valid pressure measurement data.

FREE FIELD RESPONSE

Particle Acceleration

Of critical importance in characterizing free field response to test input stimuli is particle acceleration. Fortunately there are many makes of accelerometers which will very accurately sense the magnitude of acceleration which it has experienced. The difficulty here is to couple the transducer to the free field such that it will experience the average accelerations that a typical soil particle experiences as a result of a specific stimulus. Historically, the accepted method has been to enclose the accelerometer in a package whose selected physical properties closely approximate those of the specific free field and comply with the free field motion response. A variety of metal canisters (usually aluminum) has been devised and used by experimenters in many free field measurement applications. However, due to

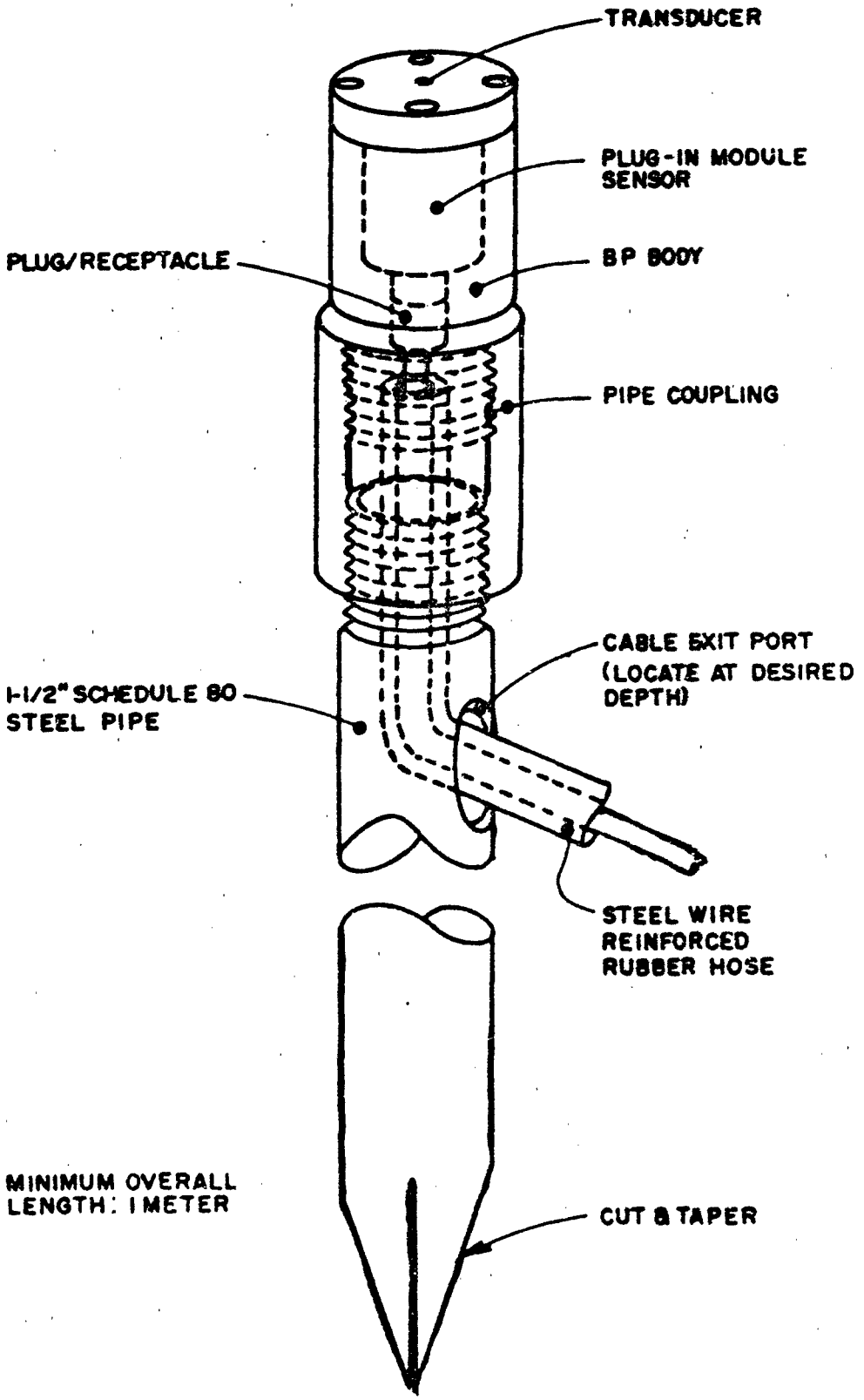

FIGURE 6. AFWL BP PIPE MOUNT

the propensity to ring when shock excited and a number of problems inherent in fabricating, waterproofing, and fielding metal can packages, the AFWL developed the castable canister sensing technique. Main feature of the technique is that the package containing the accelerometers is of cast epoxy. With epoxy of suitable properties and with re-useable molds, cost effective mass production methods are easily implemented. Normally, a sensor package is made in two pours. The first forms the base and the pillar for mounting the accelerometers on 3 mutually perpendicular surfaces. Accelerometers are then bonded to the surfaces with cyanoacrylate resin to sense along the axes as desired. Wiring transition from the very small transducer wire to the larger forward landline cable is effected without tedious splicing activity by using miniature terminal strips also bonded to the pillar. The second pour completes the cylindrical geometry and effects total encapsulation. After overnight cure, the resulting miniature package is a moisture impervious, 3-d sensing, essentially monolithic cylinder with relatively high natural frequency for sensing free field accelerations. Figure 7 shows the AFWL/NTE epoxy micro-canister. For placing the sensor in the free field an NX-size 7.6 cm (3in) diameter vertical hole is drilled at the desired location. An indexed and graduated placement rod is connected to a fastener cast into the upper face, and the sensor assembly is lowered to the desired depth. Vertical orientation and azimuth are carefully established and maintained while soil-matching expansive grout is injected to effect coupling of the sensor to the free field. After a suitable cure time the placement rod is unfastened from the sensor and a final injection of grout completes the coupling for the sensing installation.

Soil Pressure

To observe load stresses in the free field as well as in backfill regions around emplaced structures, measurements are made of a principal axis stress or "soil pressure". The transducer used is the "SE" gage developed to specifications of the U.S. Army Corps of Engineers, Waterways Experiment Station. The transducer is wafer-like with sensitive diaphragms forming the central area of each surface. A flat ring encircles and is soft coupled to the central area to isolate it from transverse stresses. The ring also functions to provide the proper diameter such that the central area registers true stress and is not affected by arching in the soil media. Figure 8 shows the transducer. Most critical in sensing soil pressure is the placement of the transducer such that intimate coupling with the media and accurate sensing orientation are established and maintained. In backfill areas and in near-surface free field applications careful hand placement in sieved soil beds with strict attention to reconstituting the soil around the transducer has yielded correlatable data to 14 MPa. Various placement schemes for vertical and horizontal sensing at depths greater than 1 m in the free field have been only partially successful due primarily to the inability to establish and verify intimate coupling to the unknown in-situ media conditions at the deep (6 m) sensing location. Vertical boreholes to partial depth have somewhat alleviated the placement problem for sensing the horizontal component. However, more development is needed for deep placement of the sensor.

EPOXY MICROCANISTER

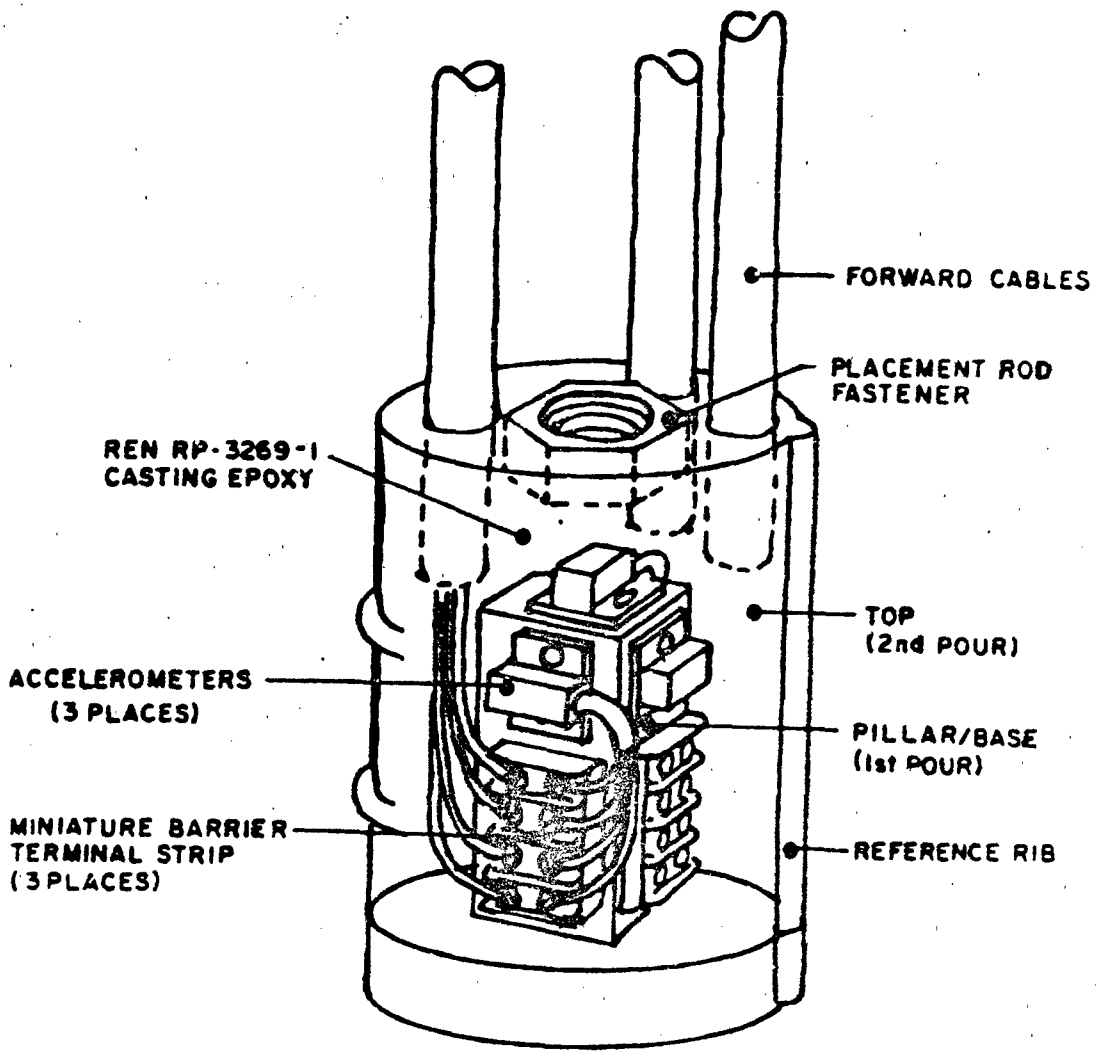

FIGURE 7. FREE FIELD ACCELERATION SENSOR

WES SE GAGE

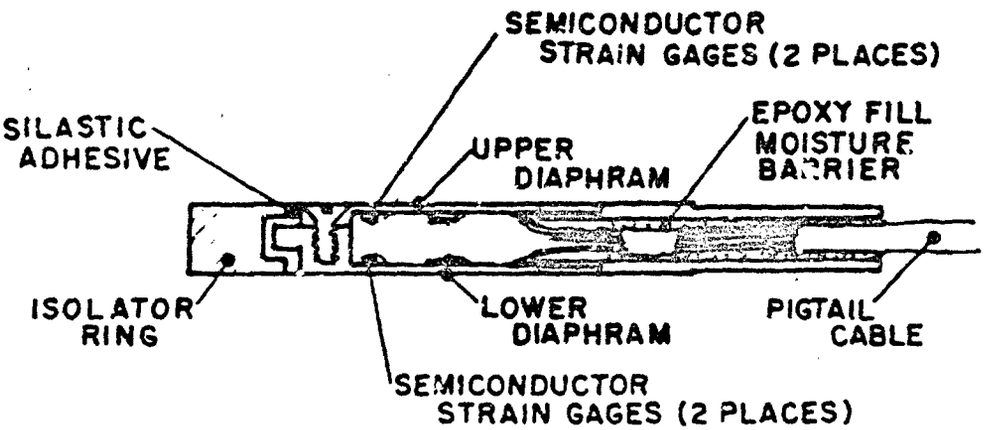

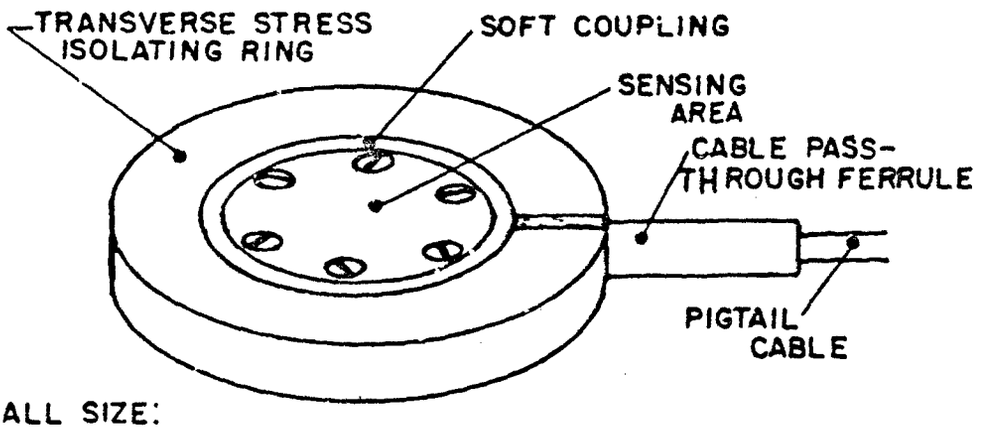

OVERALL SIZE:
51mm DIA. x 7mm THK.

FIGURE 8. SOIL PRESSURE TRANSDUCER

STRUCTURE PARAMETERS

With a specific test input stimulus characterized by blast pressure data and propagation through the free field revealed by particle motion and stress data, the bottom line is to determine specimen integrity as characterized by structure data. Comprehensive and accurate determinations require knowledge of real time blast and ground shock induced loads as well as the resulting response parameters. Thus a variety of types of measurements is normally fielded such that data is acquired on specific measurands and cross-correlations may be enabled with other related parameters.

Blast Induced Load

Basically 3 modes of airblast loading occur in simulation testing. Depending on simulator configuration these are (1) downward direct as in HEST (2) total loading horizontally as in DABS (3) incident loading as from "point-source" HE. Although the transducer used for all blast load measurements is the HKS-11-375, each sensing environment is unique. Thus each measurement channel must be designed only after careful consideration of all information pertinent to the environment and each sensing location.

(1) Direct Loading

The sensing technique used for measuring airblast loading of the exposed surface in HEST environments is similar to free field blast pressure measurements i.e. a high mass concrete mount with embedded gage mounting hardware. However, in this case the high mass concrete is the structure itself. The most competent, stable location in the structure surface is selected and gage mount hardware is placed prior to concrete pour. Normally, care is taken to isolate all transducer mounting hardware from rebar or other structural steel components in the structure. Thus, shock stresses are not directly coupled into the transducer, and a possible source of shock-induced noise is eliminated. Rigid plastic or metal tubing leads from the mount to the interior of the structure. Thus the cable is locally protected against cable noise induced by shock stress and gross motion. Ultimately the cable exits the structure via a cable penetration provision through the structure wall at depth into the free field. For measuring blast loading the sensor is flush with the structure surface which in turn is flush with the testbed. Thus, blast load measurements on structures in HEST simulators register the same measurand as the free field blast pressure measurements, and the data is directly correlatable.

(2) Total Loading

Sensors to measure loading in DABS-like simulators experience a somewhat different environment. Total reflected pressure magnitudes tend to be higher with generally higher attendant shock environment. The thermal environment is driven by hypervelocity compression in addition to HE detonation and burn.

Large quantities of debris, especially soil particles and explosives residue, are driven down the simulator and impact specimen surfaces. The sensing technique for full duration measurements of blast load on surfaces is to employ the church window debris shield as for DABS free-stream total pressure measurements. Again, the blast load sensor hardware is cast into the structure such that the sensor is surface flush. The regular plug-in sensing module face is simply counterbored and the debris shield is threaded on to the transducer. With the debris shield in place full duration data yield for measurements of blast loading in debris-laden environments has consistently been above 95% of the channels fielded. Measurements to 68.9 MPa (10,000 psi) have been made using the technique.

(3) Incident Loading

Load measurements in field tests driven by point sources such as HE stacks are generally of the incident overpressure type sensed side-on. The sensing environment associated with this measurement is by far the least severe of all. The regular blast pressure sensing hardware is cast in at the desired sensing location such that the plug-in module is surface flush. The HKS-11-375 transducer is installed and the sensor is complete. For measurements less than 1.7 MPa (250 psi) the plug-in module is modified to accommodate the Kulite XTS-1-190 series transducer. Measurements to 0.03 MPa (5 psi) are enabled such as those in the far field.

GROUND SHOCK LOADING

Overall loading on the specimen structure cannot be characterized without knowledge of the load stresses transmitted to the structure through the geologic media. Although a wide variety of interface stress and motion measurements has been fielded to measure interface parameters toward characterizing structure-media interactions, measurements of normal and shear stress at the interface are required to provide the necessary structure loading data.

Interface Stress

Characterization of load stresses in AFWL simulation testing has been from information of normal stress and biaxial shear stresses. Currently two sensors are employed to measure normal stress, and one is used to sense shear and normal stresses at the interface. The two configurations of normal stress sensors are the WAM gage and the NS gage. Both employ similar steel cases cast into the structure at the sensing location and strain-gaged aluminum elements installed from the outside to effect a surface-flush normal stress sensor. Figure 9 shows typical installations. With total moisture impervious strain gage installations both sensors have yielded comparable data for a given environment. The NS gage geometry is better suited to use in transverse shock acceleration environments above 2 Kg. The lower mass, stiffer element produces less noise response from transverse shock accelerations and transverse load stresses acting on the sensing face. For sensing shear stresses and normal stress with one transducer the TRIAX gage is used. As for

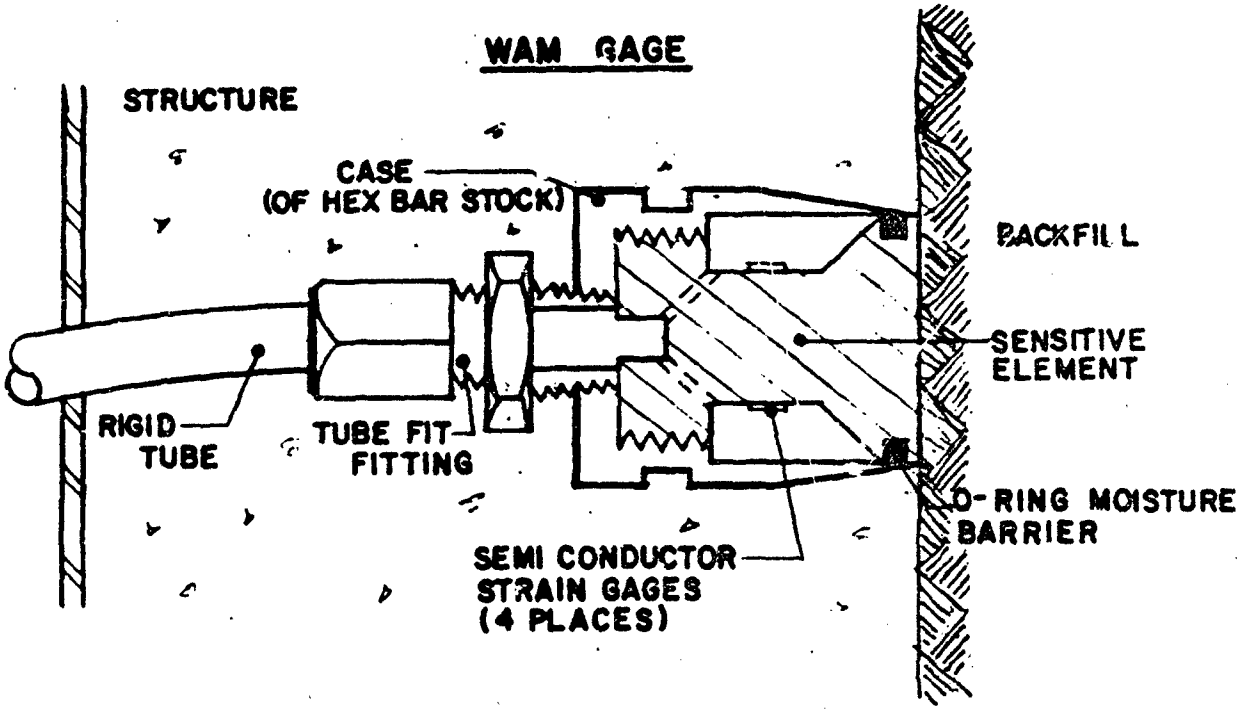

OVERALL SIZE: 44mm DIA. x 50mm LGTH.

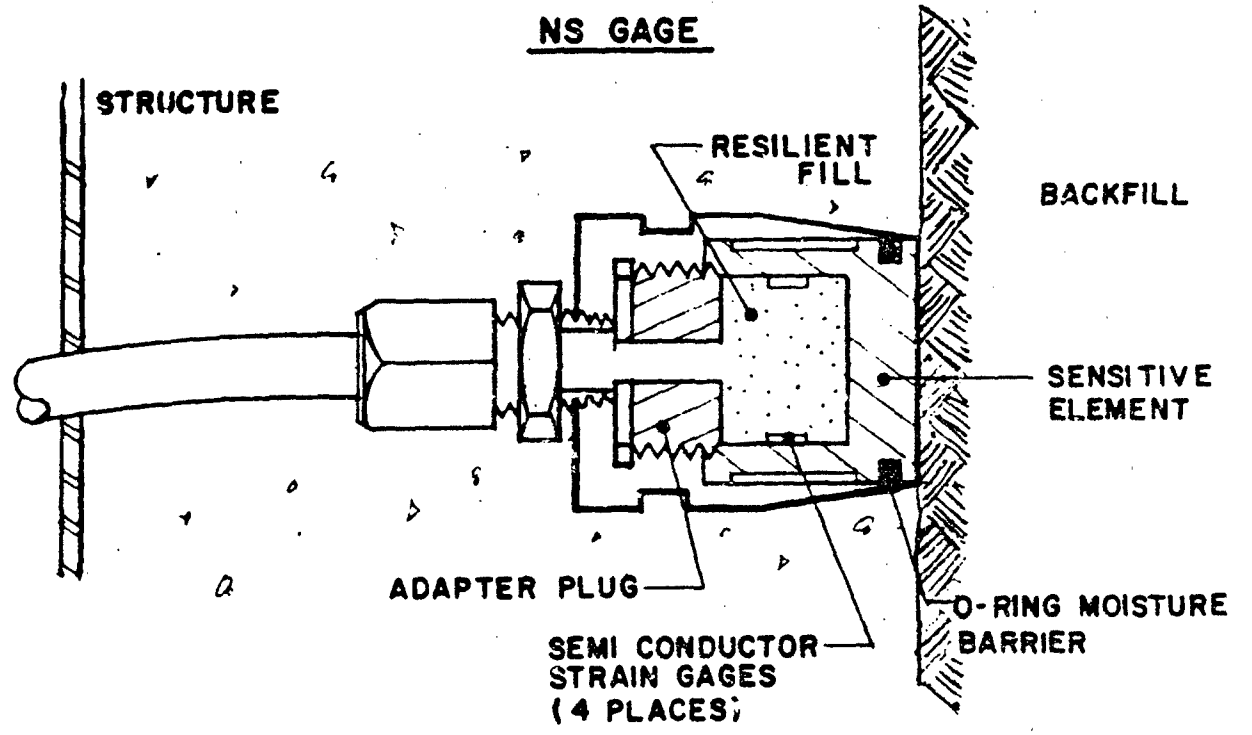

AR
JVS

FIGURE 9. NORMAL STRESS SENSORS

the normal stress gages, a steel case is first cast into the structure and the sensitive element installed after concrete cure. However, the triax case is carefully oriented such that the sensitive element will be properly indexed and sensing axes will be correct. The triax element is installed from the inside. The geometry of the element with its strain gaged cantilever beams is such that, in addition to sensitivities in three axes, there is an acceleration compensation effect in the transverse axes. Sensing end of the case is tapered to the sensing face diameter for minimum surface texture perturbation. Additionally, the face of the element is filled with a concrete/epoxy mix to duplicate the actual concrete texture for required shear coupling with the soil media. Figure 10 shows a typical triax gage installation.

Rebar Strain

A prime parameter to assess structure response to loading stresses is strain in the steel reinforcing components, rebar strain. A successful technique for sensing rebar strain is the use of four separate foil strain gages all at the strain sensing location. Two are applied diametrically on the bar to sense tension-compression and the other two are on separate metal tabs as dummies. The tabs are mounted near the sensing location such as to be mechanically isolated from, but thermally coupled to, the rebar. Thus the tab-mounted gages are fully temperature compensating dummy gages in keeping with good strain gage instrumentation practice for high accuracy data. Strain gages are bonded with cyanoacrylate adhesive to enable a 15 minute cure time installation free of all adversities associated with 2 part-mix, long-time or heat accelerated cure epoxy adhesives. The complete installation is waterproofed and overlayed with a tough, two-part shrinkfit jacket against damage during concrete pour and vibrating. The inner layer of the jacket is a resilient waterproofing material which also serves to isolate the strain installation from back-side stresses. Leads connected to each strain gage are routed from the sensing installation to the structure interior. Figure 11 illustrates the technique. Maximum length for the completed installation can be around 38 mm. The strain gage bridge connections can conveniently be made, and all electrical parameters for defining sensitivity can be monitored essentially at the bridge with the circuit in the actual use configuration. The sensing technique with bridge excitation voltages to 30 vdc has demonstrated 50 με resolution direct (i.e. unamplified) data and yields in the range above 90% of channels installed. (One test event used the strain sensors after a 7 month period during which the emplaced silo structure was from 1/3 to 2/3 full of water!)

Structure Acceleration

Gross structural acceleration responses are among the less troublesome measurements performed in survivability testing. Sensing techniques require embedding prepared metal mounting plates in the surface to enable attachment of the motion transducers. Pre-drilling, tapping, and welding Nelson studs facilitates proper orientation and ensures intimate coupling to the concrete mass. Figure 12 shows a typical sensor. Care is taken to isolate the mounting plates from rebar and other structural steel members to preclude

NMERI TRIAX GAGE

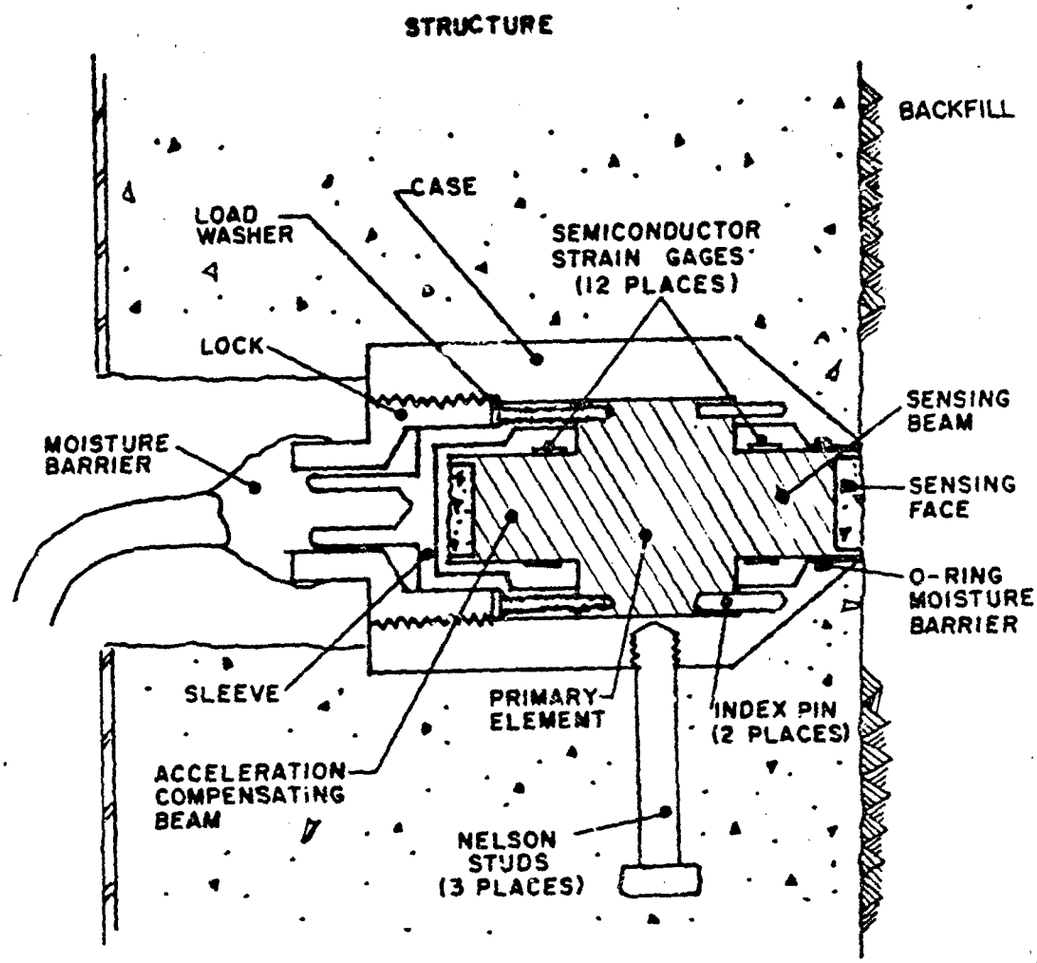

OVERALL SIZE:
~64mm DIA x ~89mm LONG

JVR

FIGURE 10. NORMAL AND SHEAR STRESS SENSOR

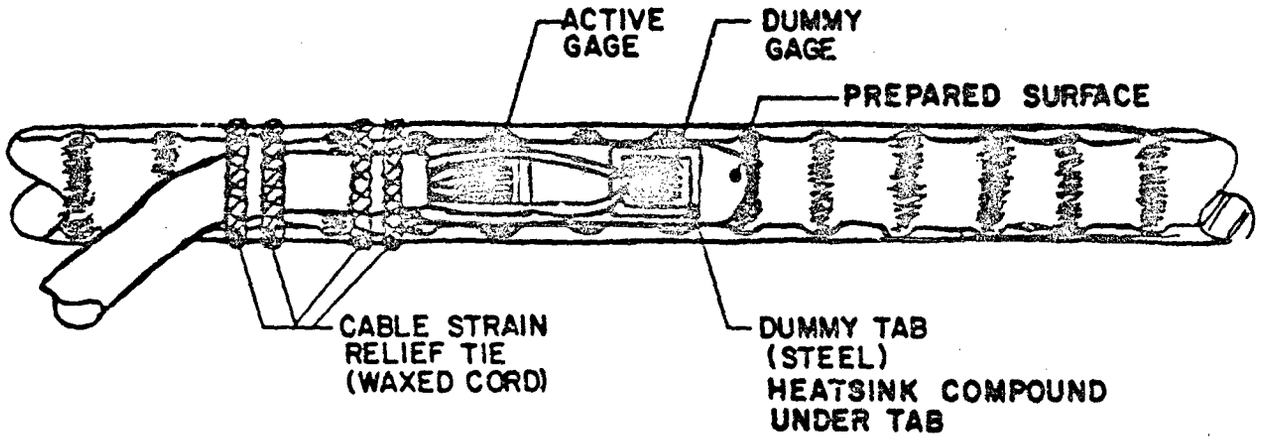

MOISTURE BARRIER AND MECHANICAL BARRIER NOT SHOWN

VIEW OF INSTALLATION (HALF)

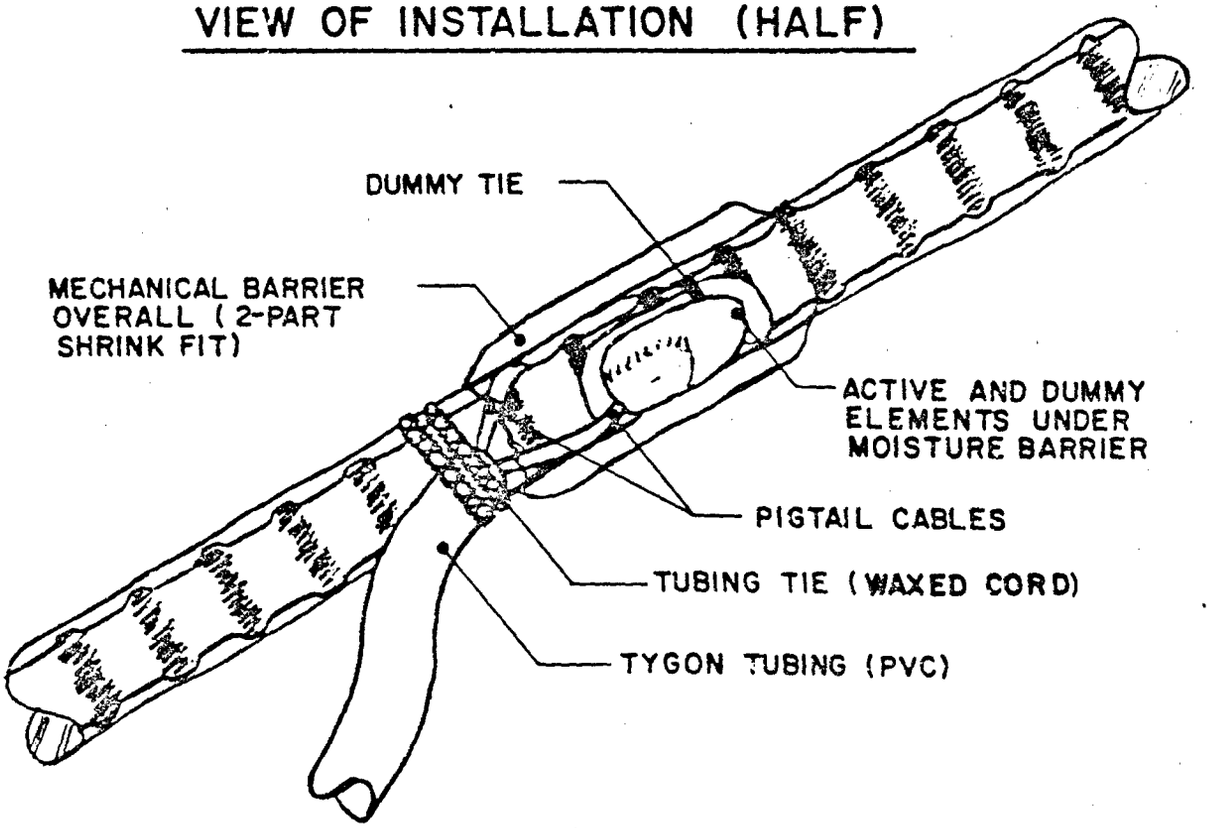

VIEW OF COMPLETED INSTALLATION (TYP)

FIGURE 11. REBAR STRAIN SENSOR

BIAXIAL ACCELERATION

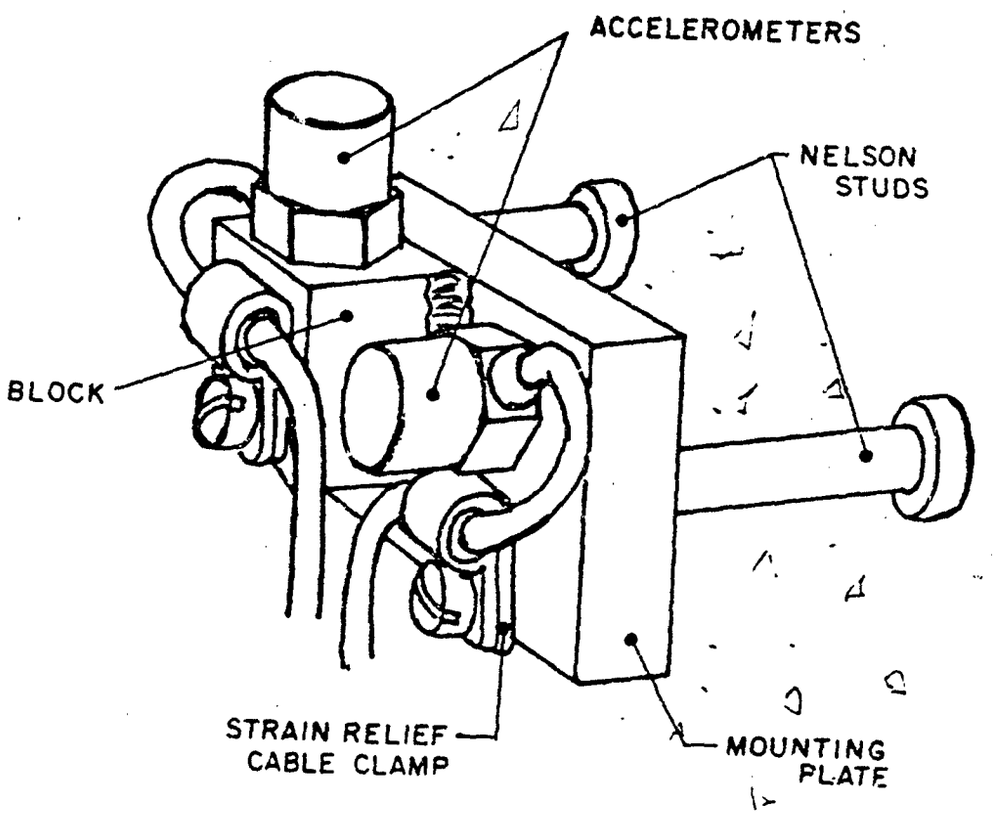

JVA

FIGURE 12. STRUCTURE ACCELERATION SENSOR

possible noise inducing shock stresses. Design considerations for the plates include sizing to the minimum for the highest possible natural resonant frequency (at least 10 X the highest expected motion frequency) while accommodating the transducer. Where the requirement is for biaxial sensing at a particular location a block is welded or otherwise securely fastened to the plate to mount the orthogonal motion transducer. Generally, transducers can be any of a number of available accelerometers with small critically fluid damped units preferred for gross motion measurements. Such a unit is the Endevco 2262C-2000. Of extreme importance in such installations is the proper strain relief and retention means for cabling. If not properly implemented initial shock motions may easily cause cable failure at worst or cable slap and flexure induced noise at best. Pre-planned cable routing and anchors embedded in the structure surface for cable clamps enable adequate retention. Also, for successful installations total moisture imperviousness must be achieved at all cable splice connections. A combination of AMP sealing/dielectric compound overwrapped with Scotch 88 electrical tape has proven highly successful in structures as well as in all other field test locations.

Relative Displacement

A most difficult response measurement is the relative displacement between one point on a structure interior surface with respect to another during the violent transient test environment. Such measurements are required for characterizing deformations of structures under transient loading. Complicating the task is that generally the static distance (span) between points can be up to 2 m. The requirement to sense motion ranges to $\pm$13 cm with required resolution of 2 mm is not uncommon. Other troublesome aspects include shock-driven debris and blow-by combustion products (which preclude use of radiative sensing techniques) and the fact that the points on the structure move randomly with respect to each other while under up to 3 Kg shock loading. A sensing technique most suited to withstand the shock accelerations, remain intact during random shock motions of sensing points, and yield effective displacement data is to use a "pull-wire potentiometer" (PWP). The unit consists of a constant-tension clock spring motor whose shaft is common with a low-inertia pulley and the shaft of a rotary potentiometer. The PWP is fastened to a mounting plate embedded in the structure surface at the sensing point having the least severe initial shock environment. A pre-cut span length of low mass high strength 1 mm diameter braided steel cable (wire) is connected to an anchor at the other sensing point. The similar type cable wound on the pulley in the unit is now pulled out against spring tension and coupled to the span cable. The sensing points changing effective separation vary the length of cable which rotates the potentiometer shaft producing as proportional voltage. Figure 13 is a diagram of the PWP unit. Early (1973) applications of the technique used a commercially available unit from Celesco Transducer Products, Inc. in California. The ruggedized PT-101RX model was obtained and modified for special application. The units yielded smooth data profiles of displacements at indicated velocities to about 10m/s. Critical to using the technique is the proper tension in the spring motor and adequate shock hardness of the potentiometer. Tension of the spring motor produces corresponding tension in the pull-wire

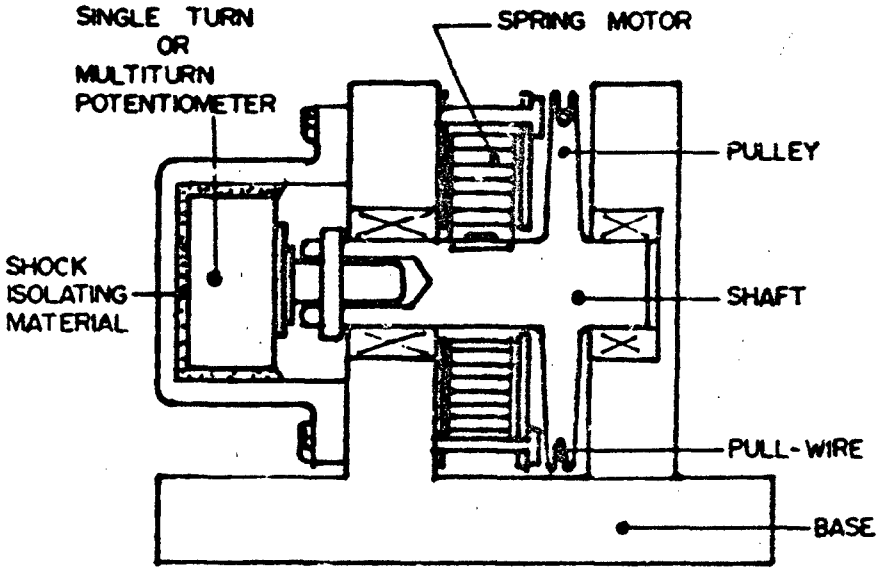

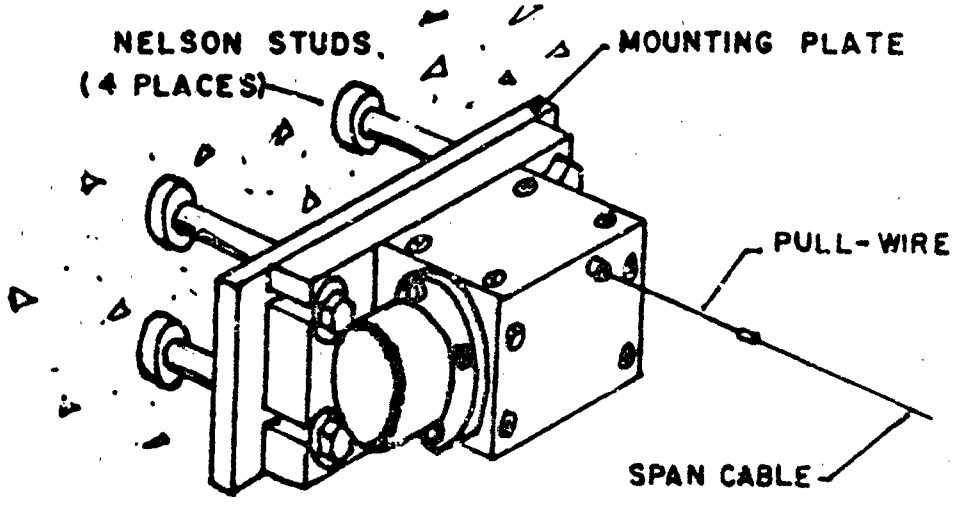

FIGURE 13: RELATIVE DISPLACEMENT SENSOR

which enables fast retraction with decreasing span and increases the fundamental vibrating frequency of the cable span. Shock hardness of the potentiometer establishes survivability with a minimum of shock-induced noise. Obviously careful consideration of these two parameters as well as the others is mandatory for the acquisition of accurate full duration relative displacement data.

SYSTEM TOPICS

Cabling

Extremely important is the requirement that the analog signal from the seusor be transmitted without alteration via landline cable to the electronics. Cabling considerations are separated into two general areas based on environment (a) the forward cable (typically 70 m) from sensor to the close-in ISC 230 signal conditioners (b) the trunkline cable (typically 600 m) from conditioners to the instrumentation vans in a remote location. The forward cable experiences ambient direct burial conditions and the blast induced stress and motion environment of the testbed. Thus, cable design must require a mechanical construction that will minimize stress induced piezoelectrical noise effects and flexure-induced triboelectric noise. Electrical design is to ensure minimum impedance at frequencies of interest. Cables must be properly placed in well-designed trench arrays to minimize broadside stress impingement and to accommodate differential motion of the free field. Slabs of 5 cm thick expanded polyethylene beadboard placed over the cables in the trench prior to backfill and compaction may be of benefit in testbeds especially where high stress (35 MPa, 5000 psi) will be applied. Expanded beadboard is also used in various designs at structure cable penetrations to the free field to mitigate the shear and tensile failure conditions occurring at initial motion. Trunkline cable, normally unburied, must withstand the ambient meteorologic and solar radiation environment and present the minimum possible electrical impedance at the frequencies of interest.

Signal Conditioning

Since all transducers normally fielded are resistance based and connected as Wheatstone bridge circuits, signal conditioning is simple and straight forward. Electronics providing transducer excitation and signal amplification is located in shelters as near as practical to the testbed. Design of the special AFWL/NTE ISC 230 conditioner includes electro-optic as well as electromagnetic techniques to provide signal isolation. Thus, flexibility in system grounding and shielding is enabled to effect highly favorable signal-to-noise ratios with dynamic performances of 60 db typical. Long term zero signal and gain stability over the temperature range -10°C to +50°C, a 26 KHz frequency response and remote shunt calibration capability are other features included to ensure fieldability and performance. Conditioned analog signals are recorded on magnetic tape in the single channel-per-track (CPT) FM mode or with FM subcarrier multiplex (multiple channels per track) in the direct mode. Data bandwidths can range to 80 KHz with CPT recording and up to

32 KHz with multiplex configurations. Thus, a wide range of data frequencies can be recorded; everything from the very rapid transient of a blast pressure to the relatively slow rigid body response of the specimen structure.

On completion of current upgrade activities sponsored by the USAF Ballistic Missile Office, the AFWL/NTE will operate and maintain six fully equipped instrumentation vans with a combined data channel capability of approximately 1600 channels. With two additional vans for timing, control, and communications, a major capability will exist for data acquisition in simulation development and field testing of protective structures in MX as well as other critical Air Force programs.

CONCLUSION

The foregoing overview has attempted to give some insight to instrumentation techniques successfully applied by the Air Force Civil Engineering Research Division in simulation field testing of protective structures. Although such descriptions tend to give a "no-problem" impression of simplicity, nothing is farther from fact! The author cannot overemphasize the importance of considering every known or suspected factor surrounding each measurement requirement as a uniquely definitive parameter extremely able to allow Murphy to prevail. Thus, the author hopes that if the descriptions stimulate any interest, pro or con, a telephone call will open the topic to the kind of indepth technical discussions which will hopefully defeat Murphy in all his guises and result in better techniques toward acquiring the highest quality field test data.

JOE V. QUINTANA
Air Force Weapons Laboratory
Civil Engineering Research Division
Kirtland AFB, NM 89717
(505) 844-0156 Autovon 244-0156

FINITE ELEMENT DYNAMIC ANALYSIS OF DCT-2 MODEL E

by

B. L. Bingham, 1st Lt, USAF
DTC Project Officer
Air Force Weapons Laboratory
Structural Dynamics Section

ABSTRACT

This report discusses quasi three-dimensional finite element dynamic analysis performed for a buried reinforced concrete cylindrical shell explosive test conducted by AFWL at Kirtland AFB, NM. The test (conducted on 27 Feb 81) included two horizontal ICBM shelter models with rectangular roof cut-outs, inner steel liners, longitudinal interior rails, and two different thickness to inner radius ratios (0.18 and 0.28). Both models were subjected to a combined axial and transverse simulated nuclear environment. The finite element analysis examines the axial response to include the initial compressive wave, structure-media interaction loads, longitudinal vertical bending, axial strains and motion, and effects of certain structural details such as rectangular roof cutouts and varying thickness to internal radius ratio. The reinforced concrete material model is piecewise linear, perfectly plastic with smeared steel.

Key Words: Dynamic Structural Response, Horizontal Buried Cylinders, Finite Element Analysis, Axial Response, Longitudinal Bending, Structural Modeling.

FINITE ELEMENT DYNAMIC ANALYSIS OF DCT-2 MODEL E

by Barry L. Bingham[1]

INTRODUCTION

Background

Shallow buried, scaled horizontal cylindrical shelters for Inter-Continental Ballistic Missiles (ICBMs) were subjected to a simulated nuclear airblast environment. This test, the second Dynamic Cylinder Test (DCT-2) subjected these generic horizontal shelter models to a combined axial and transverse airblast environment. This shelter concept consists of a closure/headworks region which opens into a roadway and is directly subjected to airblast loading. The rest of the cylinder is covered by soil berm. The closure/headworks region is elevated above the front roadway such that the soil directly underneath the shelter is loaded. Each of the models in DCT-2 contained two rectangular roof cut-outs (called Strategic Arms Limitation Talks, SALT, ports). These ports are designed for removal for missile verification. The models also have inner steel liners, longitudinal support beams near the springline to support a missile mass simulator, and two different thickness to inner radius ratios (T/IR = 0.18 and 0.28). Posttest data analysis of DCT-2 concluded that a low frequency longitudinal vertical bending moment dominated structural response with moment concentration occurring at the first SALT port.

Analysis Objectives

The objective of the SAMSON (Ref. 1) two dimensional (quasi three-dimensional) finite element dynamic analysis of a 1/4.22 scale generic horizontal shelter is to examine and define axial response in a combined axial and transverse loading environment. Specific items of interest in axial response include the initial longitudinal compressive wave down the length of the model, the reflected relief wave off the backwall, axial strains and motion, structure-media interaction (SMI) loads,

---

[1]Structural Dynamics Research Engineer, 1st Lt, USAF, at the Air Force Weapons Laboratory, Civil Engineer Research Division, Structural Response Section, Kirtland AFB, New Mexico.

longitudinal vertical bending, and effects of certain structural details such as SALT ports.

Scope

A SAMSON two dimensional (2-D) finite element computer code calculation was performed to simulate the response of DCT-2 structure E (T/IR = 0.18). The 2-D model was subjected to axial and transverse waveforms determined to be best fits to DCT-2 environmental data. This model is very simple to use and inexpensive to run, while being extensive and reliable in information gained. It is capable of simulating longitudinal structural motion, longitudinal structural strains, longitudinal near field soil motion, SMI shear stresses, SMI normal stresses, vertical soil motion and stresses, and structural ovaling. Each of the structural parameters vary from crown to invert. This report mainly focuses on comparison of the calculation results to test data. An AFWL technical report yet to be published (under the same name as this report) discusses theoretical development of this modeling procedure in greater detail.

DESCRIPTION OF ANALYTICAL MODELING PROCEDURES

Finite Element Grid

The basic model configuration in the DCT-2 testbed is shown in Figure 1. The entire two dimensional SAMSON finite element grid (Figure 2) is a representation of the elevation view shown in Figure 1. The finite element grid can be separated into two main element groups; (1) the structural elements and (2) the soil elements.

There are 95 bilinear displacement quadrilateral structural elements and 120 structural nodes (Figure 2). The largest element dimension is 0.758 meter (29.8 in) and the smallest is 0.246 meter (9.7 in). A single element represents each of the two SALT port lids located at third points down the length of the structure. The SALT port joint gaps are represented by the element material properties. The tube section of the structure is represented by five layers of plane stress elements (Figure 3).

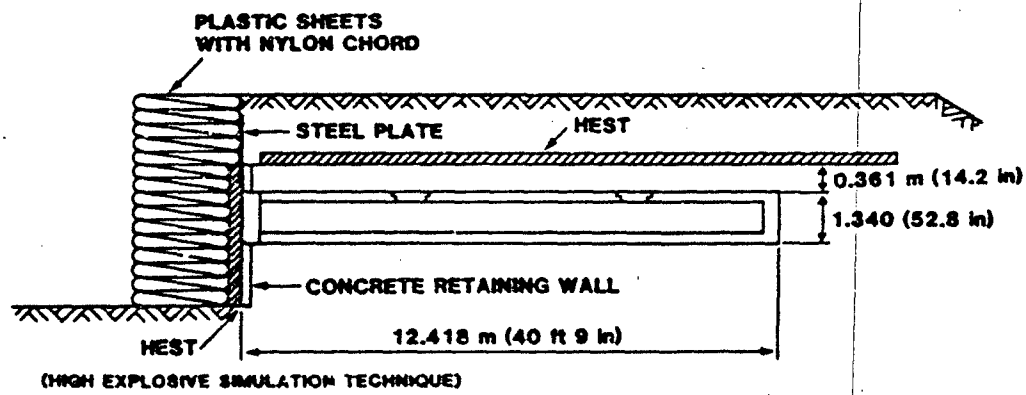

Figure 1. DCT-2 elevation view.

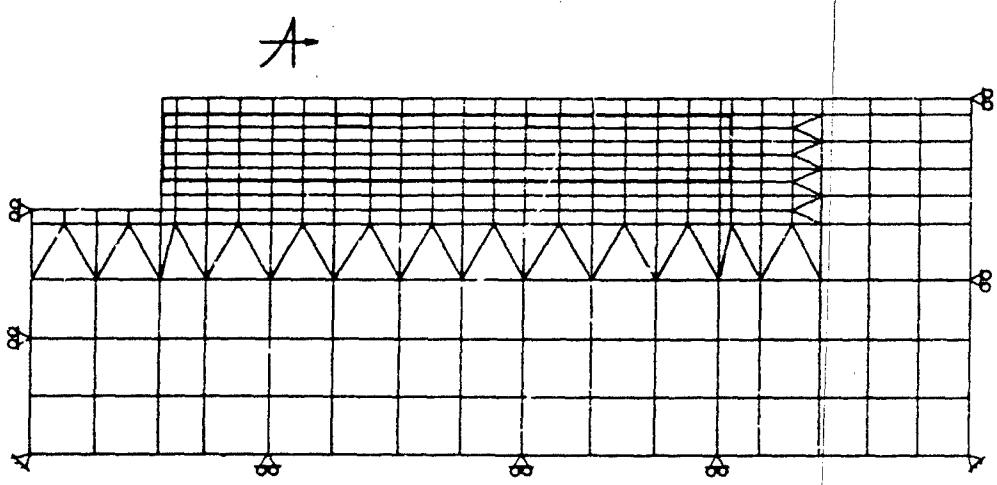

Figure 2. DCT-2 grid.

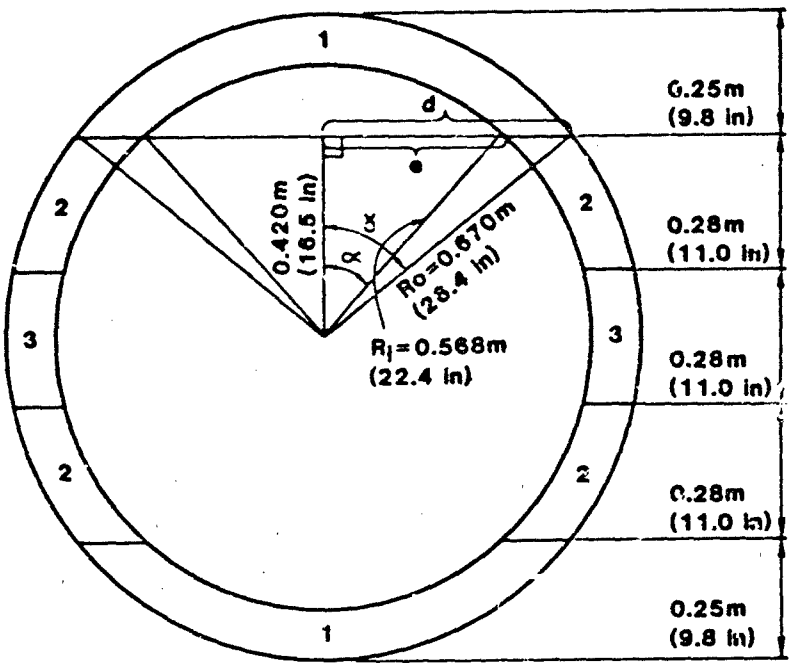

Figure 3. SAMSON 1 grid break-up DCT-2 Model E.

The structure sits in a soil island grid (Figure 2) which is simply supported along the bottom and outermost sides. There are 311 bilinear displacement quadrilateral soil elements and 320 soil nodes (Figure 2). The grid is 20.4 meters (66 ft 11.2 in) wide and 7.3 meters (23 ft 11.4 in) high. The largest element dimension is 1.394 meters (54.9 in) and the smallest is 0.246 meter (9.7 in). The soil elements make up a continuous grid with the structural elements overlaying soil elements. This type of grid allows for full development of ground shock from airblast loading, while load is also being applied to the structure. There are seven sliding/separating boundaries (SSB) between the soil and structure elements. One SSB defines the interface at the backwall. The remaining six SSB's are all horizontal with respect to the grid in Figure 2 and extend down the entire length of the structure. The top and bottom SSB's are at the crown and invert, respectively, with the other four SSB's corresponding to the structural layers in between. The three SSB's above the structure springline are such that downward moving soil cannot pass through any of the SSB's, but the soil is free to move

upward. The three SSB's below the structure springline are such that downward motion of the structure is restricted by the soil. The elements on either side of the SSB can slide relative to each other, separate, and impact after separation. The SSB's transmit normal and shear forces at the nodes across the interface.

Structural Modeling

The structure consists of five layers of tube elements, two SALT port elements, five loader lid elements, and five backwall elements. All of the structural elements are anisotropic with different material models in the horizontal (X) and vertical (Z) directions. The horizontal or longitudinal material model for the tube elements is shown in Figure 4. The axial reinforced concrete (R/C) behavior is represented by an elastic-plastic material model. The SALT port joint gap is represented by a 1.0 με shift in the stress-strain curve and a zero tensile cutoff (Figure 5).

The vertical elastic modulus for the structure tube elements has to be modified to allow for ovaling of the cylinder. The equation for the vertical ovaling modulus, E_v, is derived in an Air Force Weapons Laboratory (AFWL) technical report yet to be published (under the same name as this report) from concepts presented in Timoshenko's "Theory of Plates and Shells" (Ref. 2, pp 5 and 502).

$$E_v = \frac{L}{A} \frac{EI}{0.149\, a^3 (1-\nu^2)} \tag{1}$$

where

L = Total depth of the structure elements (1.340 meters)

A = Weighted average (with respect to the element vertical depths) of the element vertical areas for a 1.0 meters long section (0.295 m^2)

E = Young's Modulus for concrete (3.45×10^4 MPa)

I = Area moment of inertia of a cracked wall cross section 1.0 meters long (2.66×10^{-5} m^4)

a = Average cylinder radius (0.619 meter)

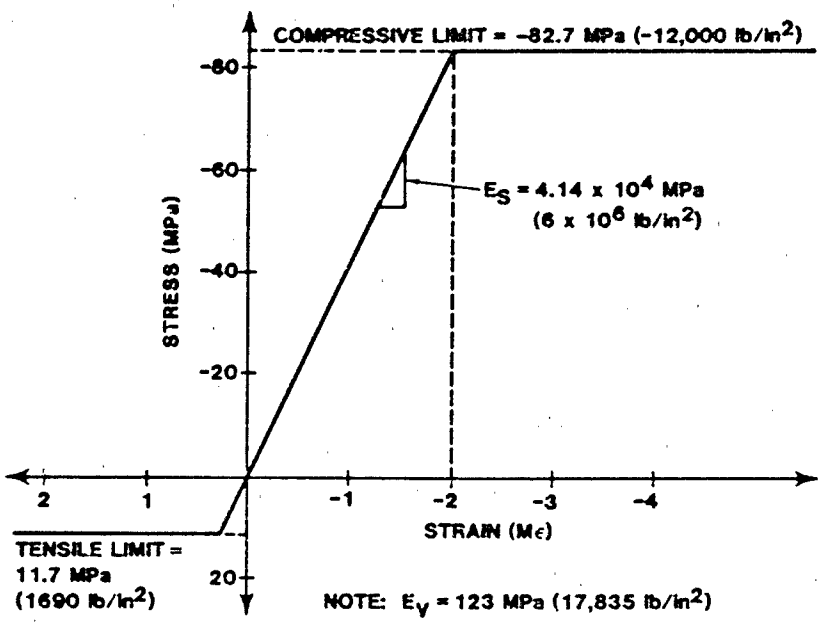

Figure 4. DCT-2 R/C material model.

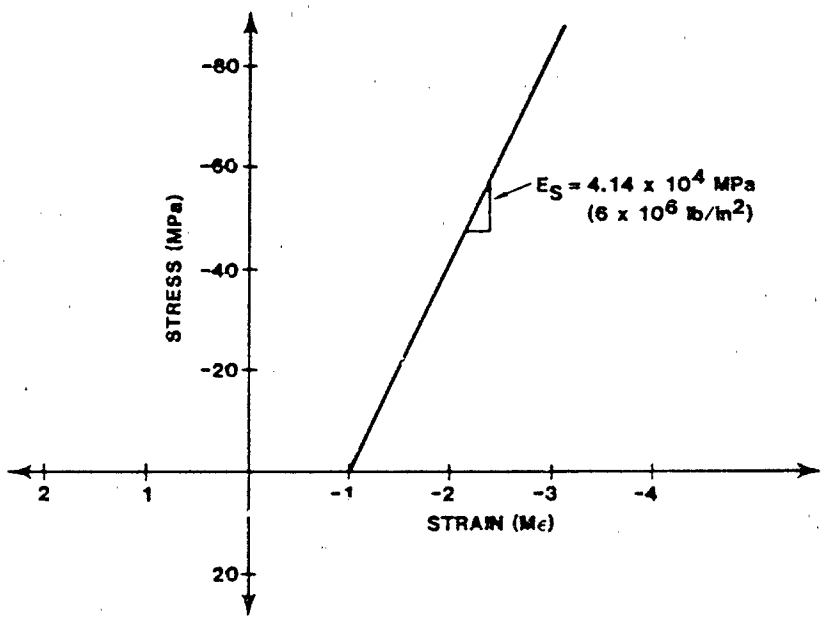

Figure 5. DCT-2 SALT port lid material model.

ν = Poisson's ratio for concrete (0.2)

E_v = Ovaling modulus (123.0 MPa)

This vertical ovaling modulus resulted in the relative displacement between the crown and invert nodes (at mid structure) shown in Figure 6. The peak relative displacement is 26.5 mm (1.04 in) which is characteristic of DCT-2 test data.

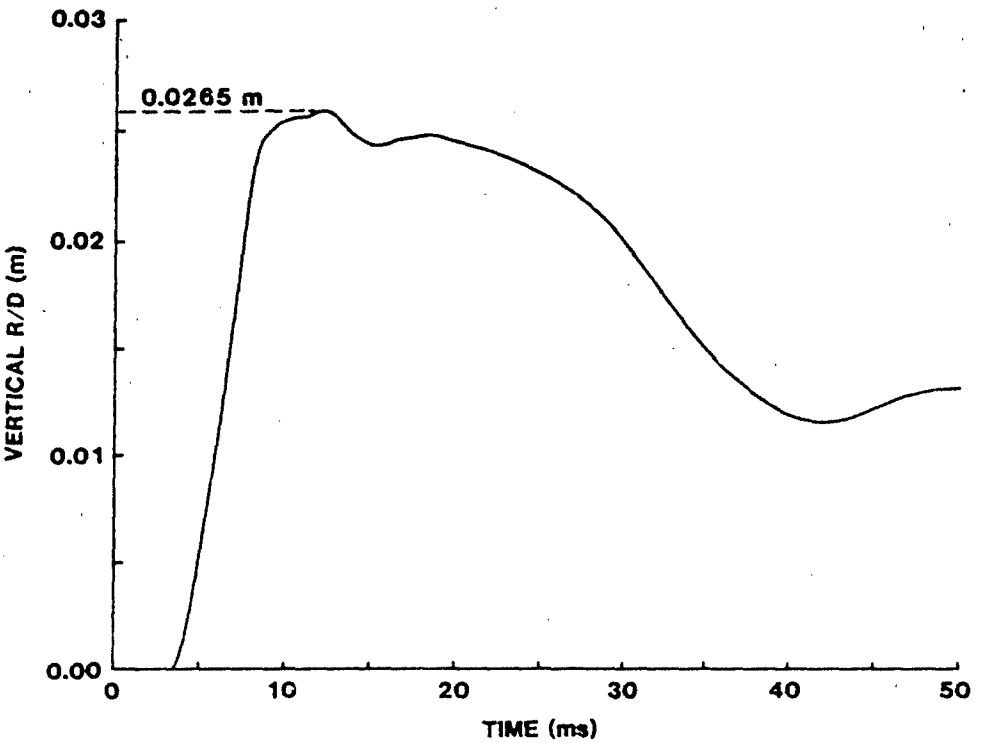

Figure 6. Relative displacement between crown and invert nodes at mid-structure.

Airblast Representation

Figure 7 shows the assessed axial and transverse loading environments for DCT-2. The pressure waveforms were input into SAMSON as pressure-time pairs (also shown in Figure 7). The transverse pressure waveform traveled over the top of the finite element grid (Figure 2) from left to right with a velocity of 2936 m/s (9630 ft/s). The axial pressure waveform was applied to the full layer of soil elements and the

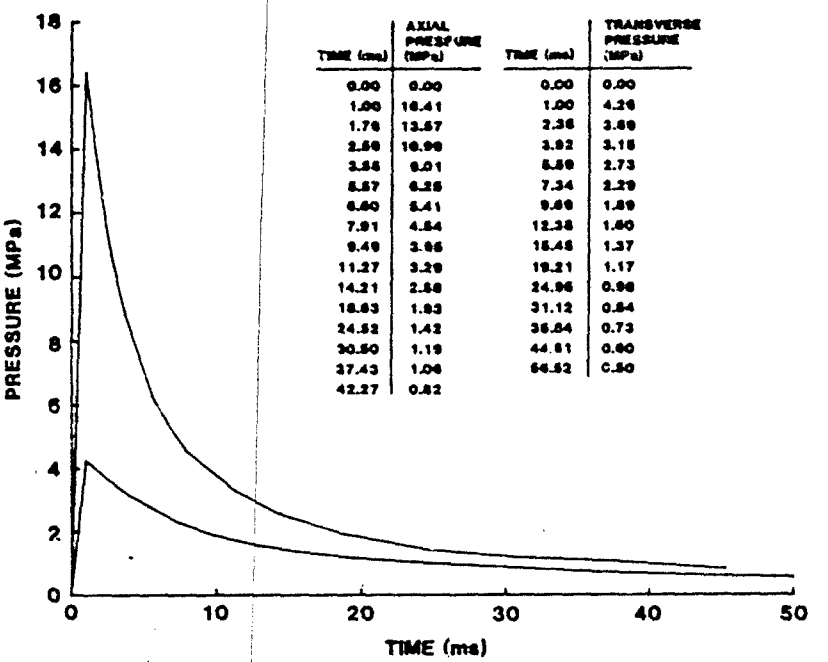

TIME (ms)	AXIAL PRESSURE (MPa)	TIME (ms)	TRANSVERSE PRESSURE (MPa)
0.00	0.00	0.00	0.00
1.00	16.41	1.00	4.26
1.76	13.57	2.36	3.69
2.50	10.99	3.92	3.15
3.35	9.01	5.59	2.73
5.57	6.25	7.34	2.29
6.60	5.41	9.69	1.89
7.91	4.54	12.38	1.60
9.49	3.86	15.48	1.37
11.27	3.29	19.21	1.17
14.21	2.58	24.96	0.98
18.63	1.83	31.12	0.84
24.52	1.42	38.84	0.73
30.50	1.19	44.81	0.60
37.43	1.06	66.52	0.50
42.27	0.82		

Figure 7. DCT-2 axial and transverse loading environments.

overlayed structural elements. The axial pressure waveform traveled over the front face of the soil and structure elements from top to bottom with a velocity of 6400 m/s (21000 ft/s).

COMPARISON OF ANALYSIS TO TEST DATA

Structure Response

DCT-2 test data relevant to the SAMSON calculation is in two categories; (1) longitudinal motion and (2) longitudinal strains.

Longitudinal Motion.

Longitudinal motion data from DCT-2 model E is rather limited. Gage placement only measured longitudinal motion in the structure at the springline and at seven locations along the length, X = 2.108 meters, 4.159 meters, 6.209 meters, 7.799 meters, 8.259 meters, 9.284 meters, and 12.172 meters. Figure 8 compares the nearest SAMSON calculation plot (solid lines) to each of the measured data plots (dash dot lines).

In general the comparison is excellent. The first peak is matched very well in timing and magnitude. Between X = 2.109 meters (6.9 ft) and X = 7.799 meters (25.6 ft) (Figure 8 (a) - (d)) SAMSON tends to overestimate the magnitude of the second peak. There are three main possibilities for this discrepancy; (1) the calculation did not allow enough SMI shear damping, or (2) the structural damping coefficient (0.04) was too low, or (3) the gage measurements are in error after early time response (after 6.0 ms). As of this writing the above possibilities have not been thoroughly investigated. At X = 8.259 meters (27.1 ft) and beyond (Figure 8 (e) - (g)) the second peak is matched very well in timing and magnitude.

Longitudinal Strains.

Figure 9 shows plots of DCT-2 E axial strains at seven locations along the length of the structure; X = 2.109 meters, 3.699 meters, 4.159 meters, 5.184 meters, 6.209 meters, 8.259 meters, and 10.309 meters, respectively. Figure 10 shows the corresponding SAMSON strains. Comparing Figures 9 and 10 reveal many similarities. At approximately X = 2.1 meters (Figure 9 (a) and 10 (a)) the axial strain at the crown has an initial peak strain followed by a larger second peak strain at 6.0 ms. This second peak strain is most likely due to initiation of vertical bending. The invert strain in Figure 9 (a) seems to be contrary to indicated response with the measurement showing compression rather than tension after 10.0 ms. At approximately X = 3.5 meters (Figure 9 (b) and 10 (b)) and X = 4.1 meters (Figure 9 (c) and 10 (c)) notice that the SAMSON calculation overestimates the initial peak strain at the crown. Therefore, the assumption of 1.0 ms for the SALT port joint gap is most likely too low. In general after 5.0 ms in both the DCT-2 E and SAMSON data the highest compressive strains occur at the crown and the highest tensile strains occur at the invert. Other than this general view, timing coordination between the two sets of data is difficult. At approximately 5.0 meters on back timing of the peak bending moment seems to be in fair agreement between the two sets of data. Again, the invert measurement in Figure 9 (d) seems to be contrary to indicated response after 10.0 ms. The best agreement occurs at X = 6.209 meters (Figure 9 (e) and 10 (e)) for timing and impulse of the initial peak compressive

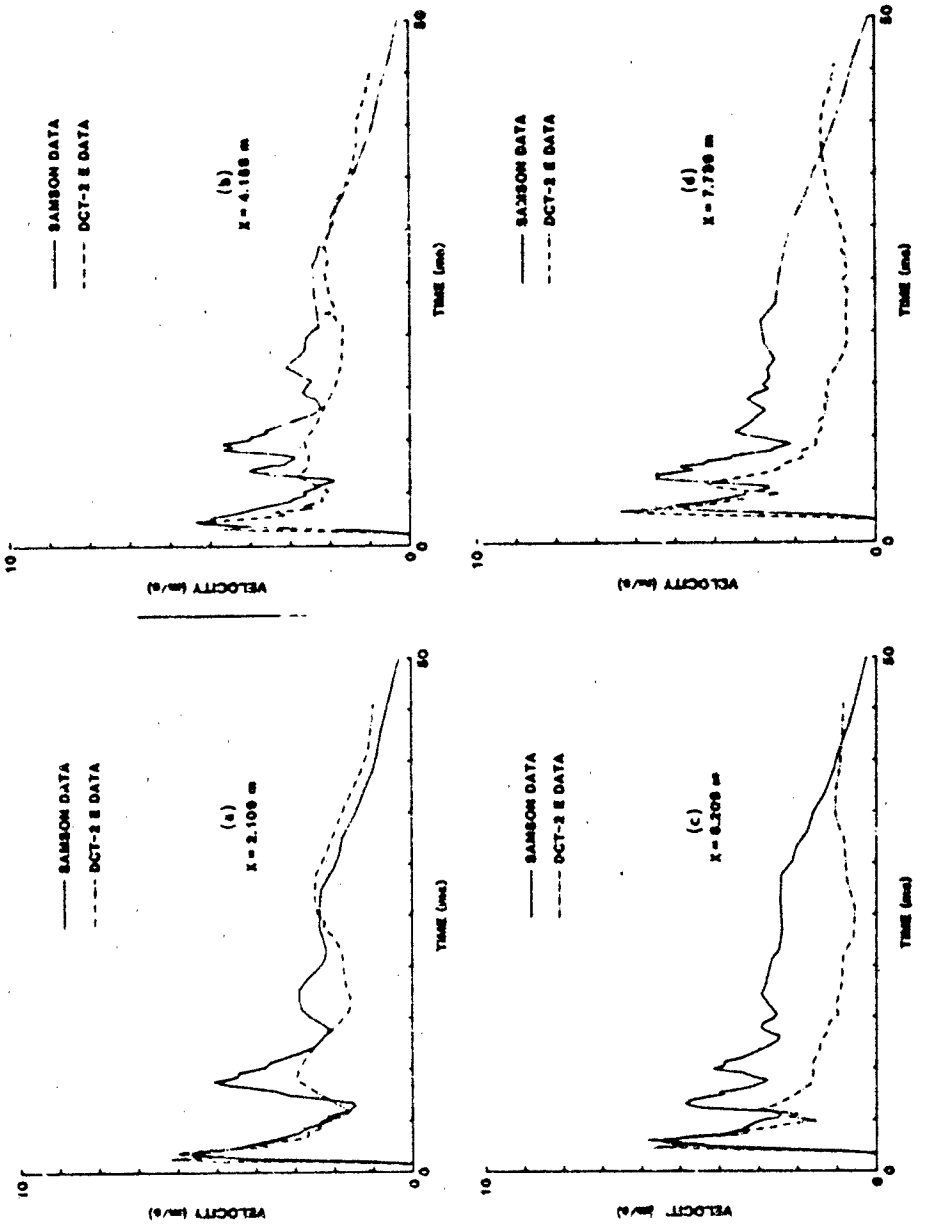

Figure 8. Comparison of longitudinal motion.

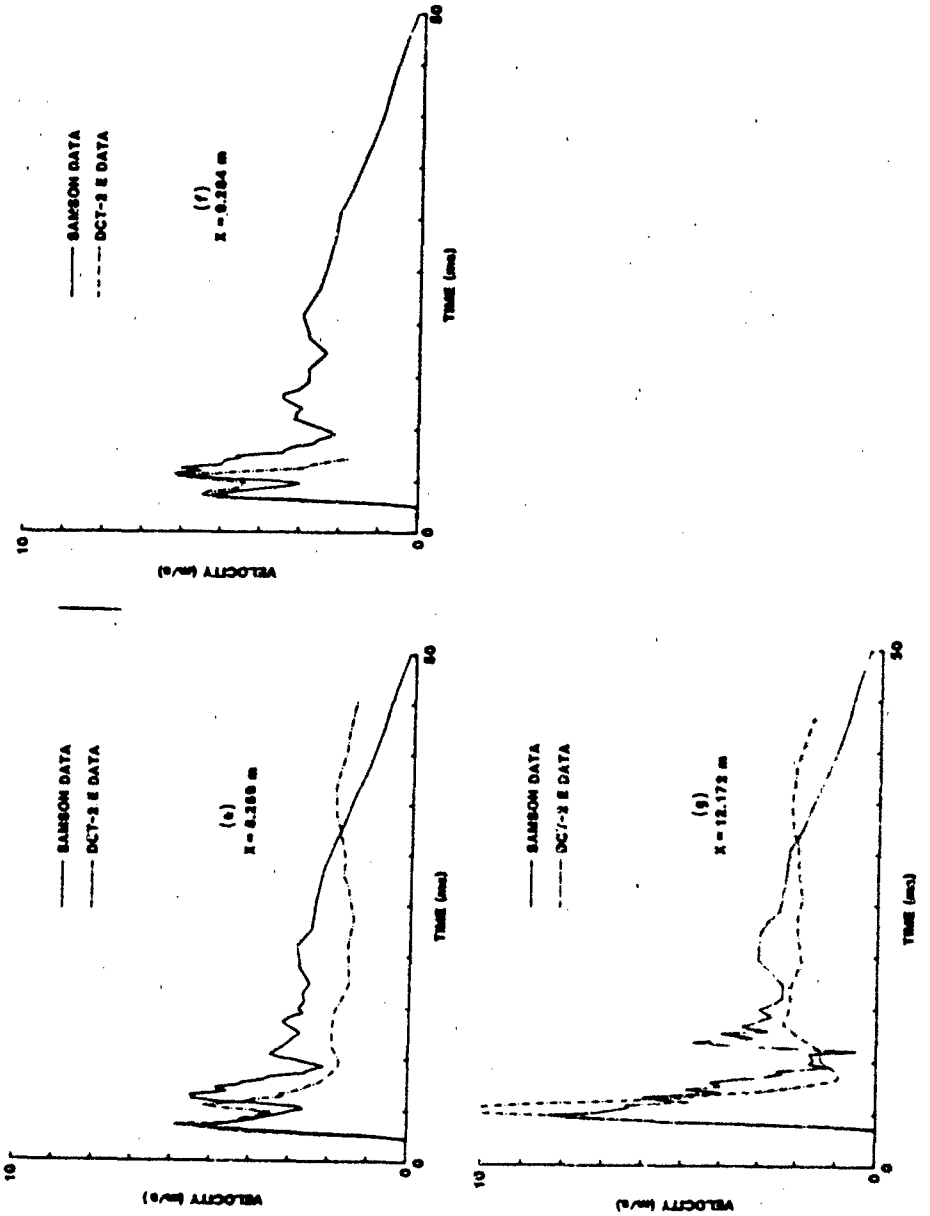

Figure 8. Comparison of longitudinal motion (continued).

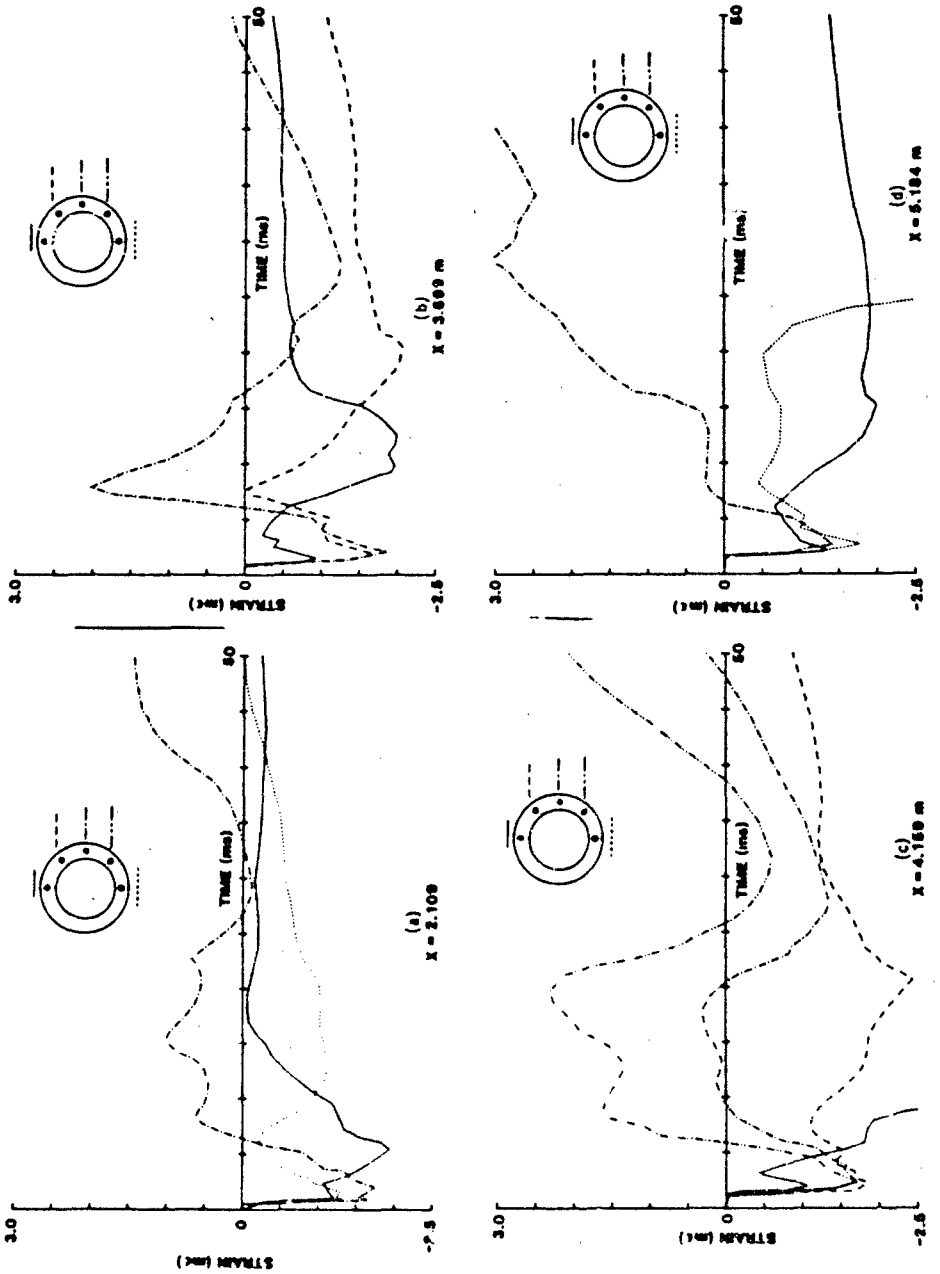

Figure 9. DCT-2 E axial strains.

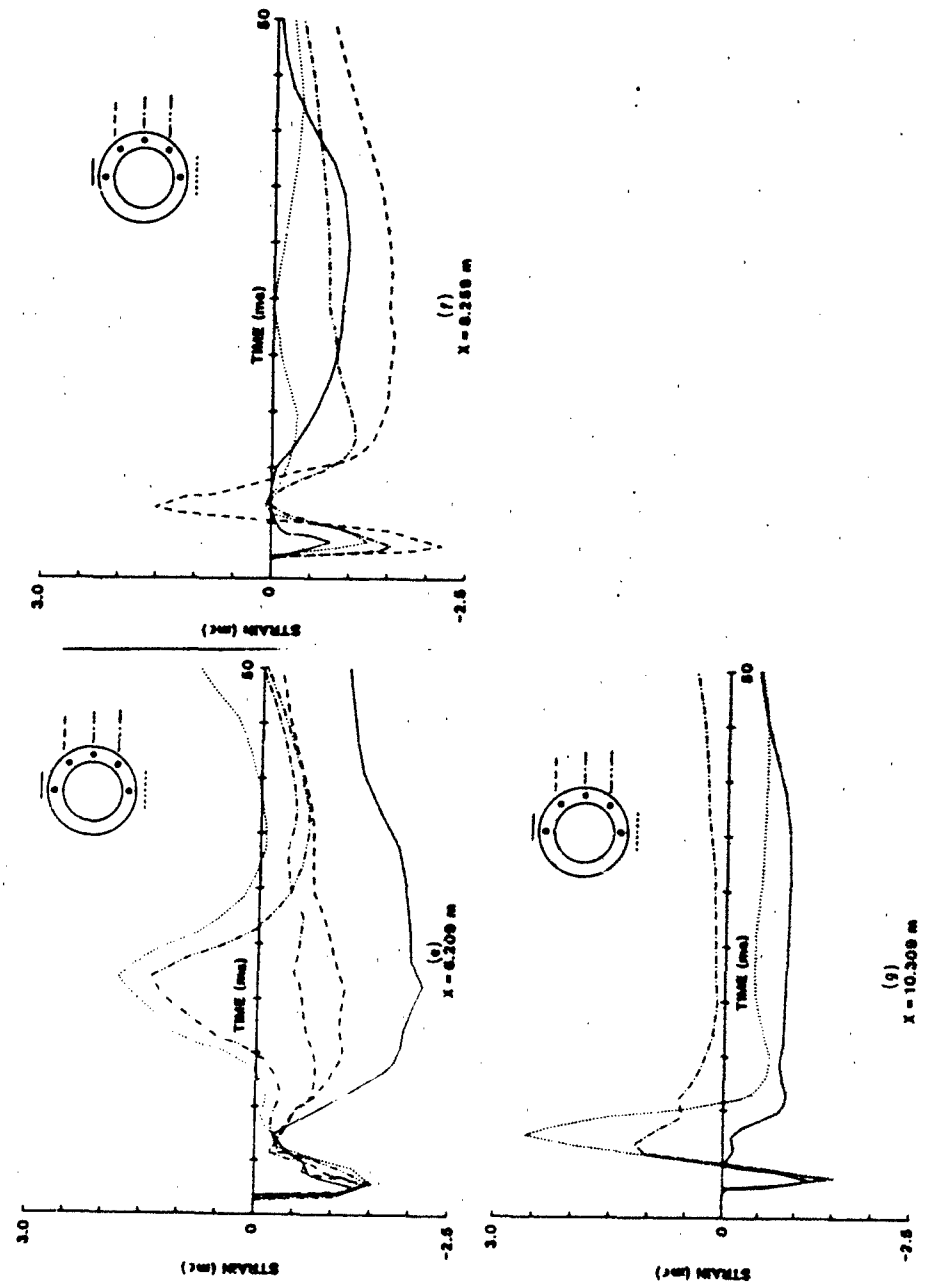

Figure 9. DCT-2 E axial strains (continued).

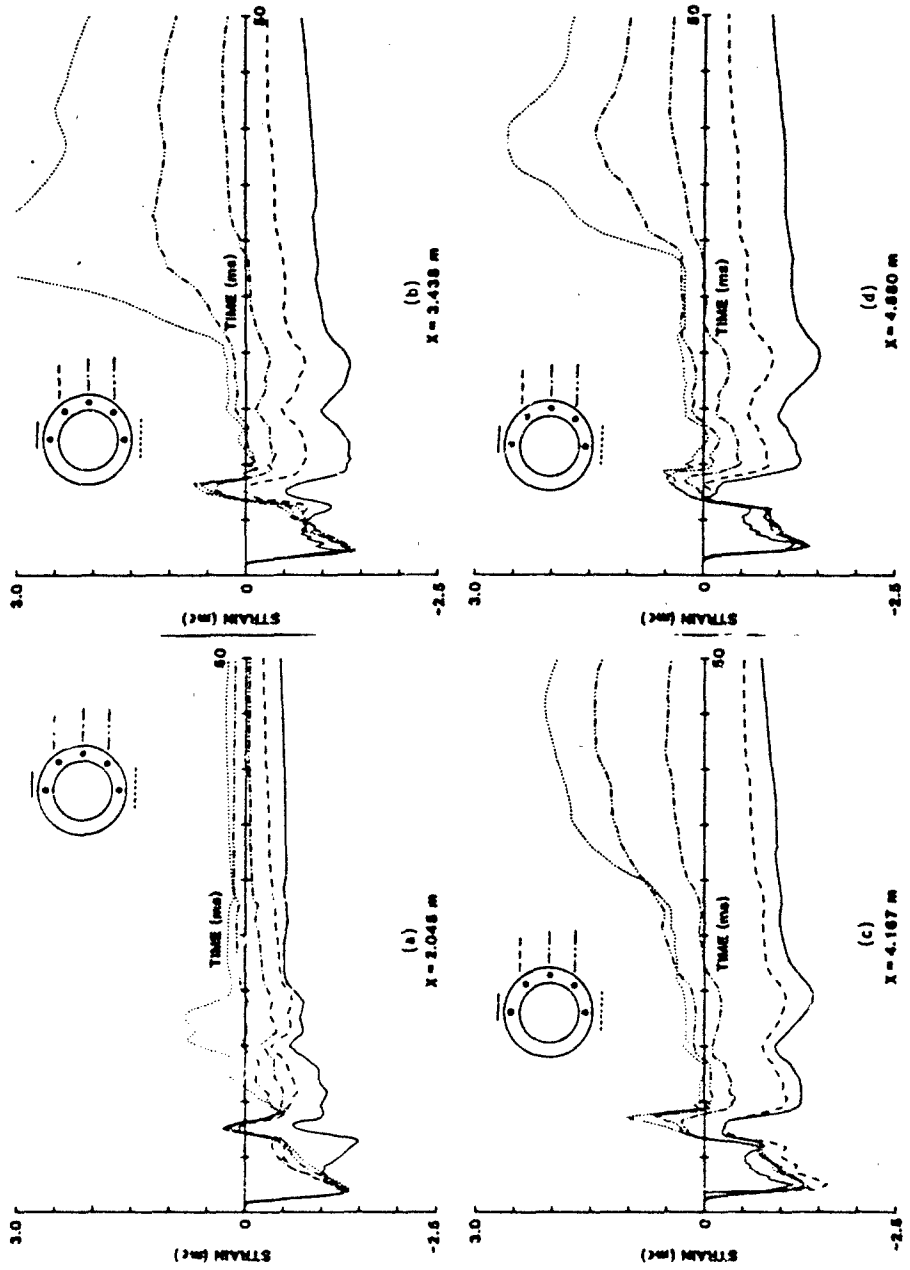

Figure 10. SAMSON structural axial strains.

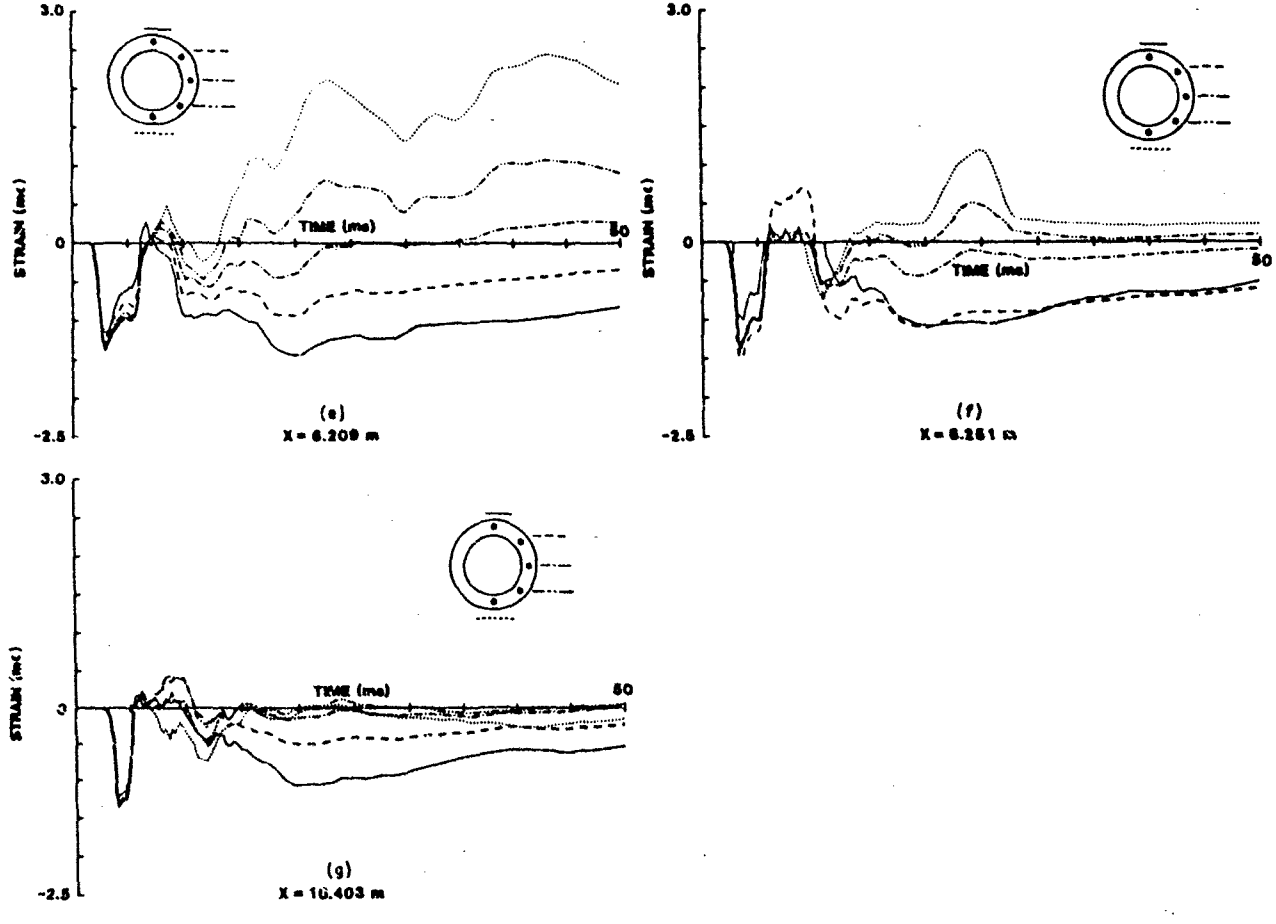

Figure 10. SAMSON structural axial strains (continued).

strain and for timing and magnitude of the bending moment. At X = 8.25 meters Figure 9 (f) and 10 (f) both sets of data indicate a detour of the axial stress path from around the SALT port lid and concentrated between the bottom of the lid and springline. Tensile strain from the relief wave off of the backwall-soil interface also concentrates at this point. Also, the bending moment has substantially reduced in both sets of data (although more so in the test data). At X = 10.3 meters (Figure 9 (g) and 10 (g)) the initial peak strain impulse is low and the bending moment has essentially disappeared in both sets of data. The SAMSON calculation underestimates the peak tensile strains due to the reflected relief wave, possibly, because the assumed R/C material (Figure 4) overestimates tensile capability.

Soil Response

DCT-2 test data relevant to the SAMSON calculation are in two categories; (1) longitudinal motion and (2) vertical motion.

Longitudinal Motion.

Soil deformation under a simulated nuclear environment can be very large. But under relatively short distances, attenuation of peak soil motion and stresses can also be very large. Therefore, unless a node point in a finite element grid is at the same relative location as a gage measurement in the testbed, the two resultant plots may be very different, and rightly so. The DCT-2 measured data is shown in Figure 11 compared to SAMSON data from nodes located on either side. The DCT-2 gage measurements were 0.7 meter (27.6 in) away from the structure, whereas the SAMSON soil nodes are immediately adjacent to and directly influenced by the structure. Due to the structure influence, the SAMSON data will have high early time velocity (when the structure initially punches through, dragging the soil back) and low late time peak velocity (when the structure retards the progression of the ground shock). Even the DCT-2 test data shows a hint of early time structural influence at X = 4.159 meters and 6.209 meters (Figure 11 (b) and (c)).

Vertical Motion.

Figure 12 (a), (b), and (c) shows plots of free field soil vertical velocities at three different depths, Z = 0.250 meter, 1.031 meters, and

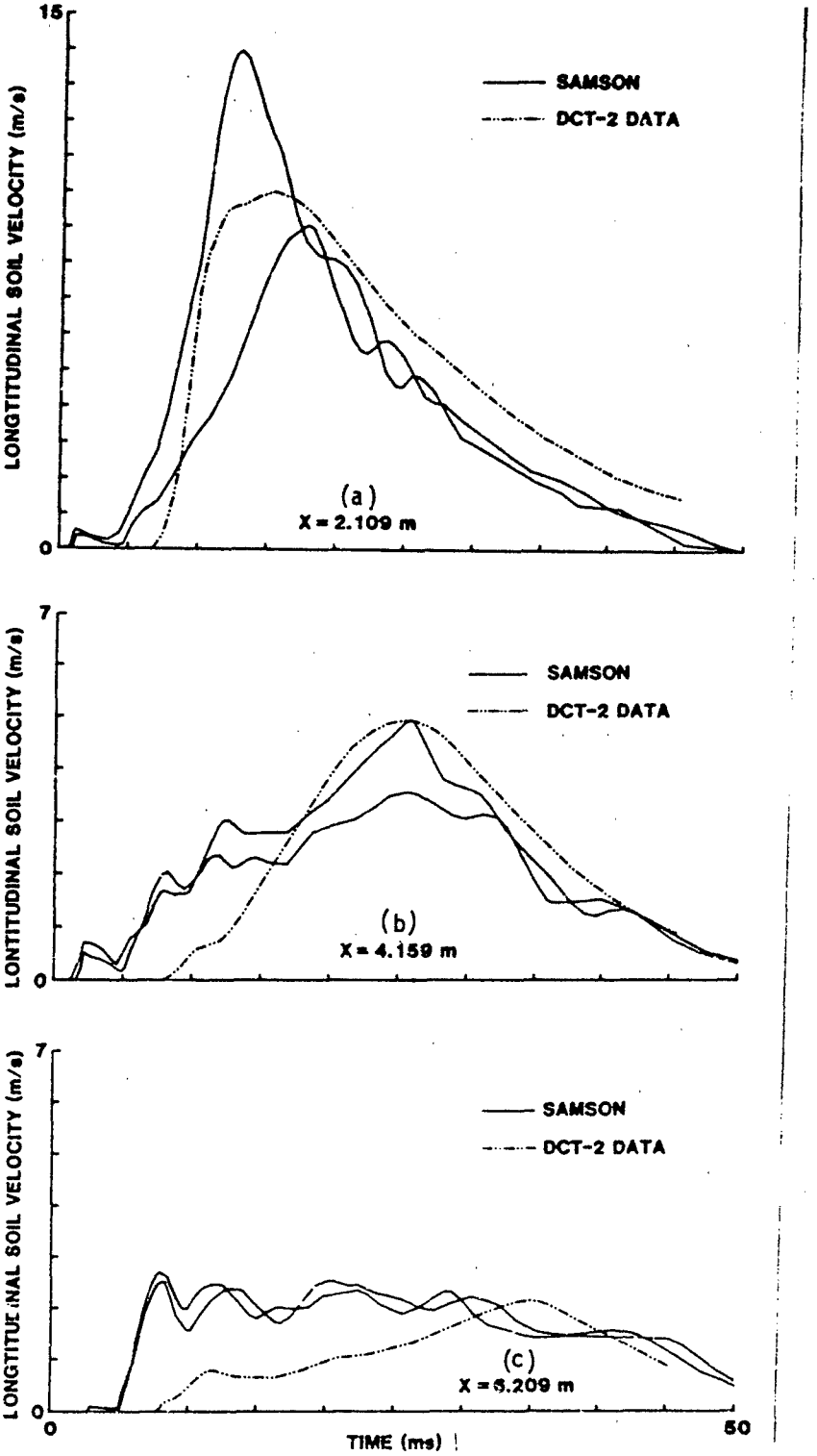

Figure 11. Longitudinal soil motions.

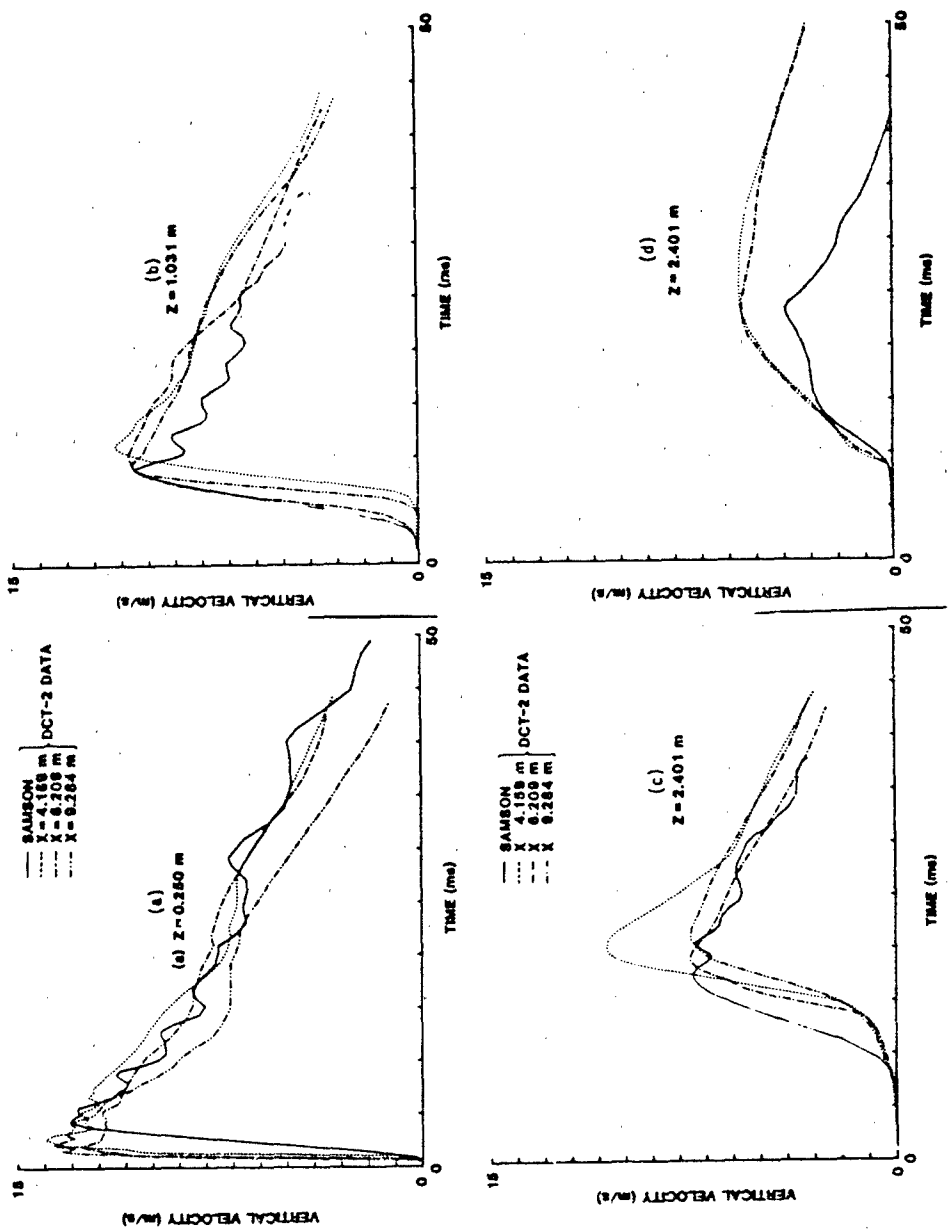

Figure 12. Comparison of vertical soil motions.

2.401 meters, respectively, for both the SAMSON calculation and DCT-2 test data. Figure 12 (d) shows plots of near field soil vertical velocities directly beneath the structure at a depth of Z = 2.401 meters. The SAMSON data agrees very well with the free field test data. One DCT-2 free field test data measurement did not agree well with the others (the dotted line in Figure 12 (c)). There are a couple of possibilities for this odd measurement; (1) the gage measurement was incorrect or (2) the location of X = 4.159 meters and Z = 2.401 meters may be feeling the combined effects of the horizontal and vertical HEST cavities. Timing of the vertical and horizontal ground shock does not support the second possibility.

The peak vertical velocity of the near field test data at Z = 2.401 meters (Figure 12 (d)) is 5.5 m/s, which is lower than the peak vertical velocity in the free field at the same depth (7.5 m/s, Figure 12 (c)). This is due to the shadowing effect of the structure on the vertical ground shock. The SAMSON calculation overestimates this shadowing effect and results in an even lower peak vertical velocity (4.0 m/s, Figure 12 (d)). The soil underneath the structure in the testbed is influenced by vertical soil flow around the structure. The SAMSON finite element grid has no way of accounting for this phenomenon.

SMI Normal Stress

Figure 13 shows plots of SMI normal stresses at the crown and invert at four locations down the length of the structure, X = 0.152 meter, 0.652 meter, 6.209 meters, and 11.820 meters, respectively. At each location there is a plot of the crown normal stress (dash dot line), the invert normal stress (dotted line), and the sum of the two curves (solid line). Positive stress is a downward load on the structure. At X = 0.152 meter (Figure 13 (a)) there is an overwhelming pressure load from underneath the structure trying to force the front portion of the structure up out of the soil. This high pressure region is caused by the airblast pressure loading on the front wall and is a result of the soil confinement. The soil over the crown is loaded in the same manner, but there is a nearby free air surface and the pressure in the soil is only able to develop to the transverse load airblast pressure. At X = 0.652 meter (Figure 13 (b)) the high pressure region

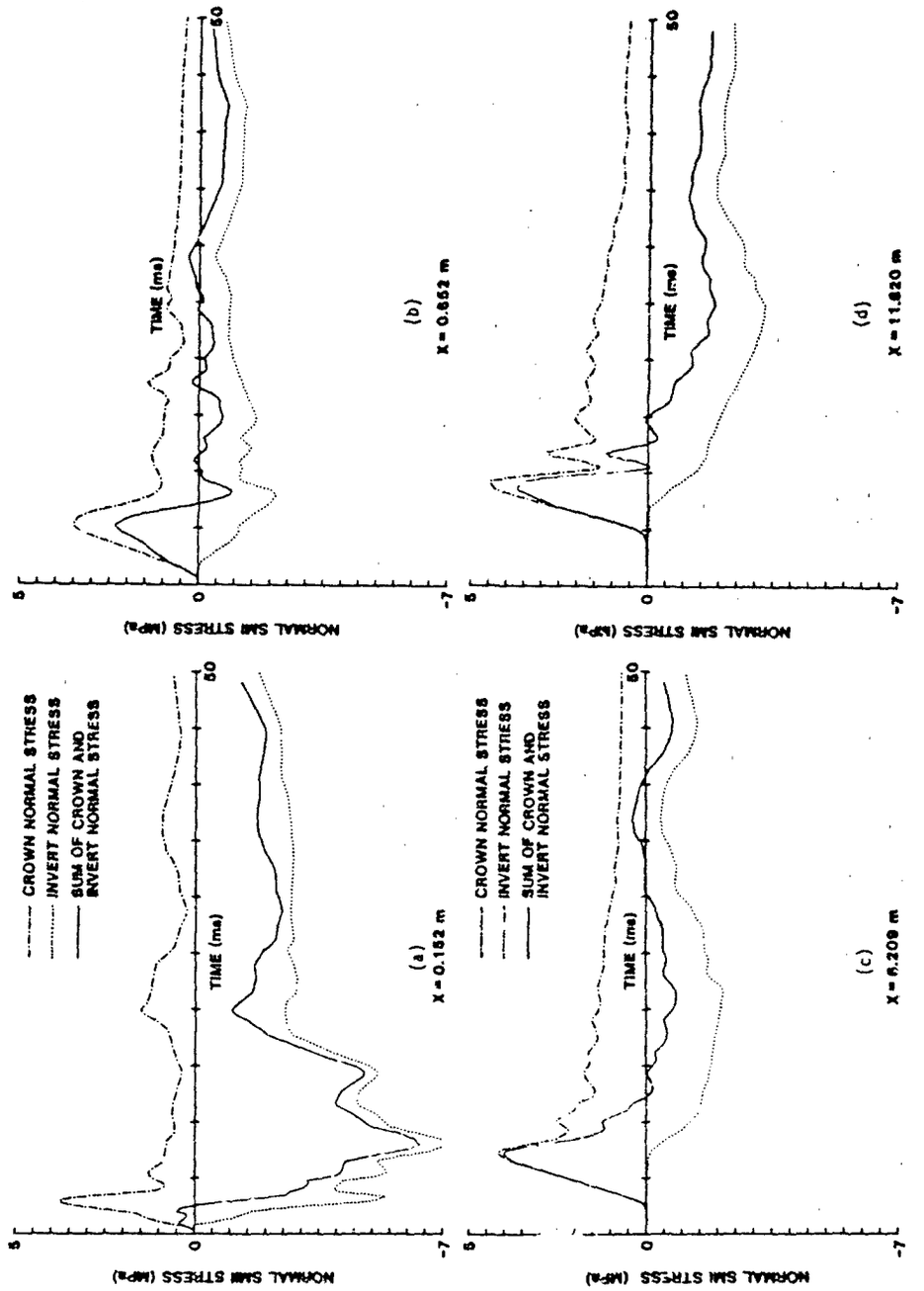

Figure 13. SMI normal stresses.

has disappeared. Here the pressure load is primarily downward. This is a moment couple which initiates moment wave traveling down the structure from front to rear. Figure 13 (c) shows a typical loading distribution for the center of the structure with the pressure load predominantly downward. But at the back (Figure 13 (d)) the pressure load shifts at late time (greater than 15.0 ms) to a predominant upward load again. This is the reaction pressure at the structure invert due to the vertical bending moment.

Figure 14 shows a comparison of crown SMI normal stresses for the SAMSON calculation (solid line) and test data (broken lines). At early time (prior to 5.0 ms) the SAMSON calculation does not match the spiked stresses in the test data. This is most likely due to the fact that the finite element grid is coarse and unable to transmit such high frequency response. The early time pressure spikes may be matched better with a fine grid. This coarse grid analysis assumes that such early time spiking is insignificant to overall structural response. After 5.0 ms the agreement between the two sets of data is excellent.

Figure 15 shows a comparison of invert SMI normal stresses for both sets of data. Here the agreement is also excellent. Both plots show a slow rise time to a peak stress of 2.4 MPa and then a slow decay (although the decay is more pronounced in the SAMSON data). The excellent match in the two sets of data shows that the ovaling model was very successful in filtering the load from the crown to the invert.

CONCLUSION

A quasi three-dimensional finite element modeling procedure of a horizontal buried shelter has been developed. This procedure is simple to use and inexpensive to run. It models structural response to include the initial longitudinal compressive wave, longitudinal vertical bending, and ovaling. It is extensive and reliable in information gained. The results of this analysis model closely the dynamic response of the structural field test data. This procedure can also be applied to vertical shelter response, particularly if one is concerned about bending of the longitudinal axis of the tube.

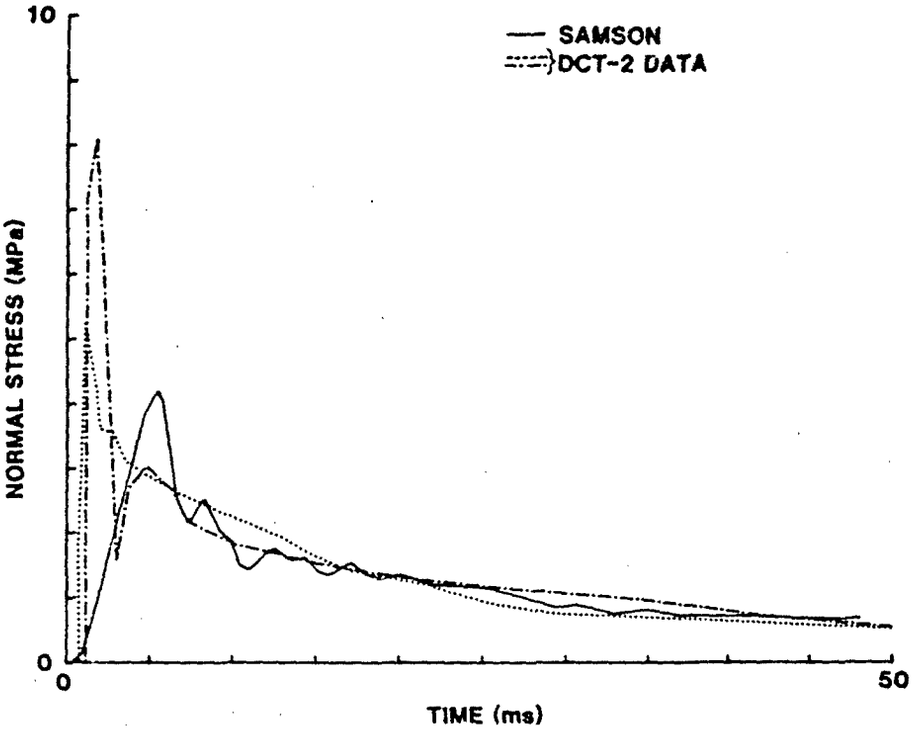

Figure 14. Crown normal SMI.

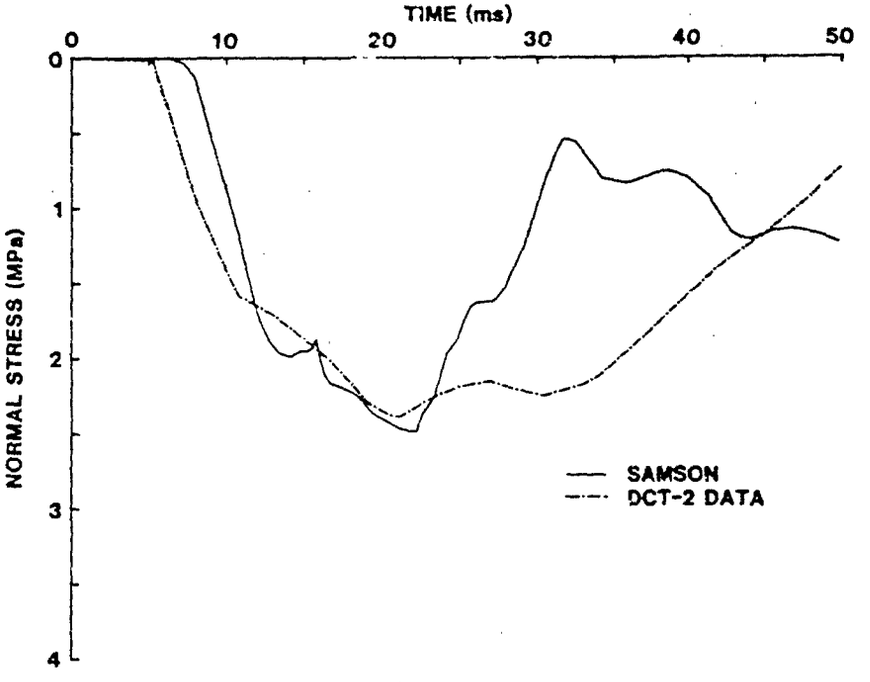

Figure 15. Invert normal SMI.

REFERENCES

1. Bartel, H. D., and Cole, D. M., "User Manual for SAMSON and Family," AFWL DE-TN-74-009, Air Force Weapons Laboratory, Kirtland AFB, New Mexico, 1974.

2. Timoshenko, S., and Woinowsky-Krieger, S., "Theory of Plates and Shells," Second Edition, McGraw-Hill Book Co., New York, 1959.

SUMMARY

FINITE ELEMENT DYNAMIC ANALYSIS OF THE DCT-2 MODELS, by Barry L. Bingham. This report discusses a quasi three dimensional finite element analysis of a horizontal buried missile shelter. The analysis examines axial response to include longitudinal bending.

MX BASING DEVELOPMENT DERIVED FROM H.E. TESTING

Donald M. Cole

ABSTRACT

The large size testing associated with the buried trench, horizontal and vertical shelter basing concepts is evaluated for its role in the development of structural design concepts. The major impact of the testing was in general to revise baseline concepts and to develop confident design and analysis procedures.

KEY WORDS: MX, BASING TECHNOLOGY, STRUCTURAL RESPONSE BLAST AND SHOCK TESTING, REINFORCED CONCRETE, SOIL-STRUCTURE INTERACTION

MX BASING DESIGN DEVELOPMENT DERIVED FROM H.E. TESTING[a]

By Donald M. Cole[1], M. ASCE

INTRODUCTION

From the early 1970's to the present the Air Force assisted by the Defense Nuclear Agency has conducted an intense study of the suitability of protective basing concepts for the MX missile (and required support equipment) for conditions of nuclear attack. This paper will concentrate on large size, high explosive field testing, which was only one aspect of the overall Nuclear Hardness and Survivability Program that supported the development of an MX Weapon System. After a brief presentation of background information, the large size field testing associated with the first-three of four basing concepts will be analyzed to determine if fundamental assumptions for structural loading and response were confirmed or altered. These fundamental assumptions become critical when they define the design requirements for the protective structural concept. The first basing concept will be treated in detail and the remaining concepts summarized.

---

[a]Presented at the April 1981, ASCE National Convention held at Las Vegas, Nevada.

[1]Research Structural Engineer, Civil Engineering Research Division, Air Force Weapons Laboratory, Kirtland Air Force Base, New Mexico.

In many cases, the large scale testing and associated analysis influenced requirements for supplemental research. Where appropriate, the interaction of the large size testing and the supplemental research will be discussed.

BACKGROUND

Until October 1981, the Air Force concentrated MX basing studies on concepts relying on dispersion and deception in addition to hardening to provide survivability for the weapons system under conditions of nuclear attack. This strategy included considerations of current and projected Soviet capabilities, long range United States goals for Strategic Arms Limitations and the United States defense policy of maintaining a survivable "Triad" structure of nuclear strategic forces. For greater detail on the complex issues affecting this strategy, references 2, 27, 28 and 29 are recommended as a starting point.

The chronology of basing concepts and associated large size testing is given in figure 1. Initially the continuously hardened buried trench concept was selected from the many concepts considered by the Air Force for intensive analytical and experimental study. Recognizing that the trench concept contained substantial technical risk, a system of discrete horizontally aligned shelters connected by a surface road network was chosen as a back-up basing mode. Large size field testing on structural elements of both basing concepts began in April 1977 and continued to October 1978. The change to a vertical shelter concept in 1978 resulted largely from considerations of survivability, economy and from public interface issues associated with land

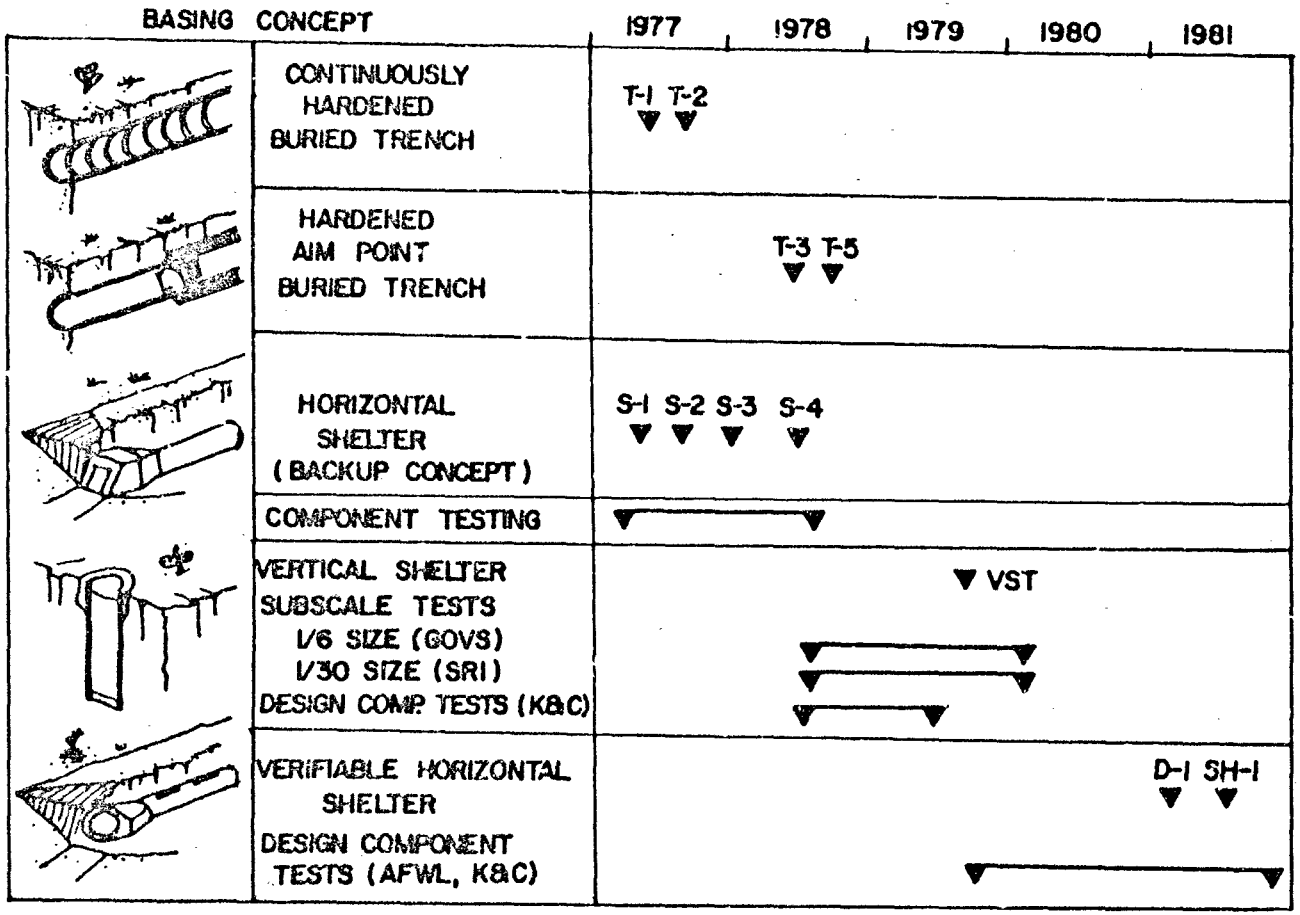

FIGURE 1. BASING CONCEPT & TEST CHRONOLOGY

withdrawal. The change to a verifiable horizontal shelter concept in late 1979 reflected increased emphasis on SAL negotiations.

While this paper will focus on the technical issues associated with design and analysis of the protective structures, it is important to remember the dominant influence that international politics, public policy and opinion and economic considerations may have on the design of any major emergency project.

BURIED TRENCH BASING CONCEPTS

As initially conceived, the buried trench was actually a set of shallow concrete tunnels each approximately twenty miles long and each containing a single mobile missile protected by a blast plug both fore and aft (figure 2). This train of vehicles would change location frequently so that the entire tunnel length would have to be targeted with weapons to assure destruction of the missile. The number of tunnels and tunnel length were determined based on estimates of the number of warheads available to an attacker. The tunnels were planned to run roughly parallel to each other along the valleys selected for basing, and were not interconnected. The lateral spacing between tunnels (S_t) was selected based on nuclear weapons effects considerations so that no single weapon could significantly damage more than one tunnel. Following an attack, a surviving launcher would erect the missile cannister by breaking out through the roof of the tunnel and pushing through the soil overburden; and would then launch the missile.

Since thousands of miles of tunnel construction would be required, use of highly automated construction techniques had to be anticipated in the design of

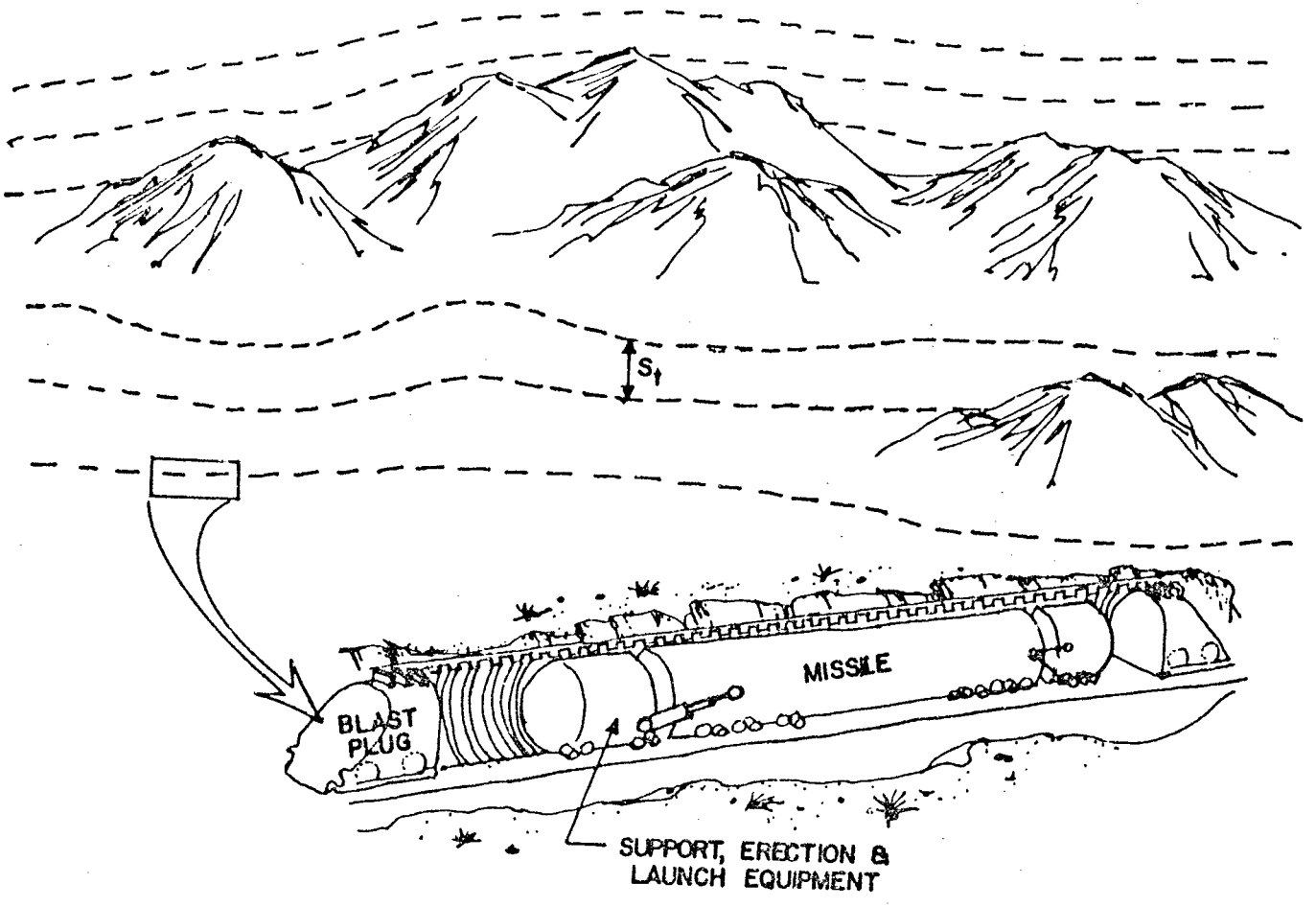

FIGURE 2. BURIED TRENCH BASING CONCEPT

the tunnel structure. This requirement coupled with direction to minimize construction costs, led to a baseline structural concept with constant wall thickness and rib dimensions and using fiber rather than conventional reinforcing for rapid automated construction. This initial baseline configuration is shown in figure 3.

At the beginning of the validation study on the buried trench concept, a number of issues were identified as significant to the adequacy of the concept. These are listed in Table 1. The large size testing discussed in this paper primarily addresses structural loading and response issues. The impact of this testing and associated experimental and analytical efforts was principally to force changes in the conceptual design.

The first two large size test (T-1, T-2, figure 1) were designed to provide very fundamental information on loading and response assumptions used in the concept definition process. Designs for the test articles were derived from the baseline configuration of figure 3. Since model mechanical blast plugs were not yet developed, simple concrete masses were used to examine the fundamental behavior of trench-plug interaction.

Under envisioned attack conditions, breaching of the shallow tunnel structure was thought to be a likely event. This would occur if the crater formed by the attacking weapon intersected the trench structure. When this occurred, radioactive plasma would enter the trench and generate a shock running though the tunnel structure. The amount of energy that would be injected or coupled into the trench was unknown and analytical estimates varied substantially. Similarly, quantitative estimates of the attenuation of this flow could not be confidently estimated without substantial experimental data. The Defense Nuclear Agency (DNA) undertook the task of providing an analytical and experimental program to define the coupling and attenuation

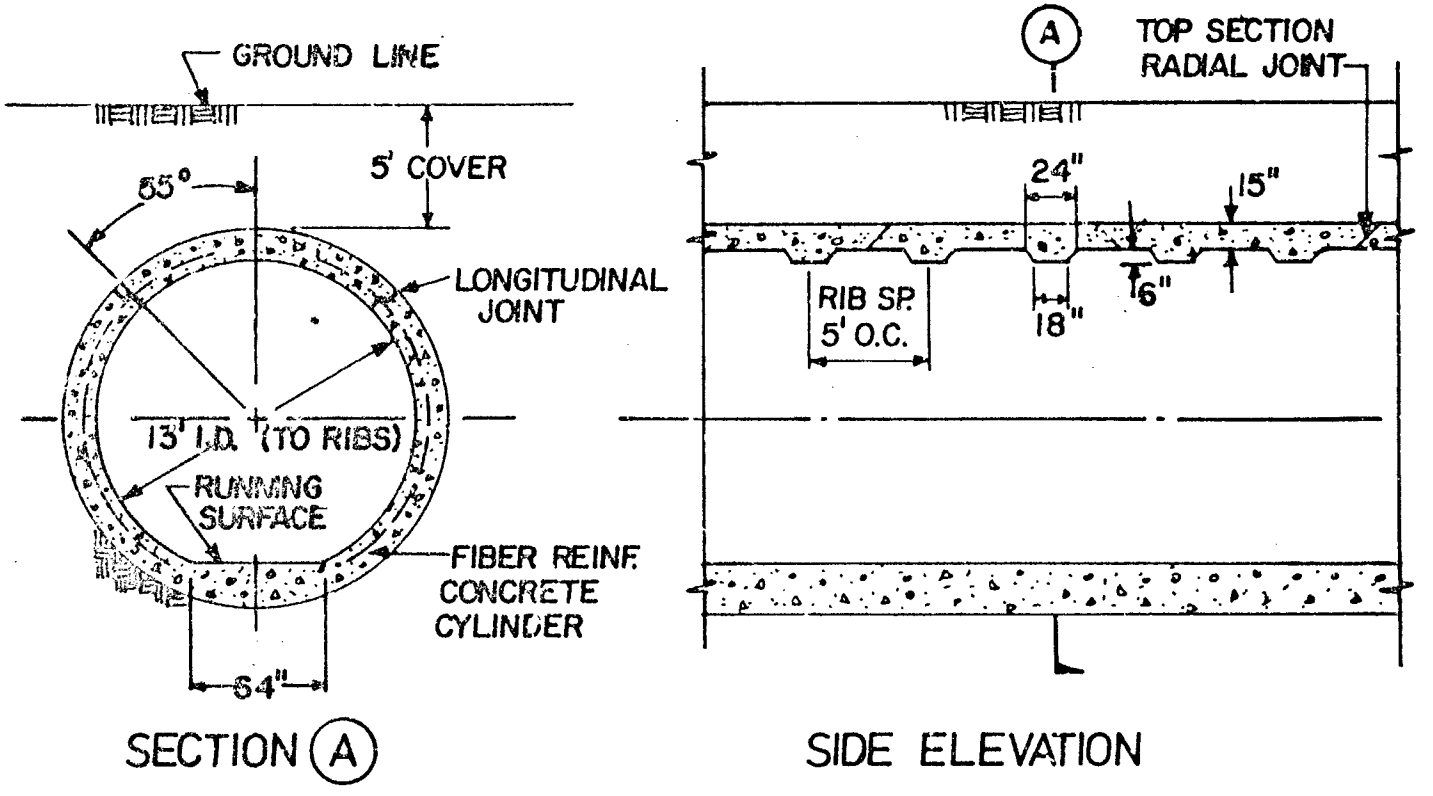

FIGURE 3. BASELINE TRENCH CONFIGURATION

TABLE 1

BURIED TRENCH BASING CONCEPT ISSUES

NUCLEAR ENVIRONMENT ISSUES

- DIRECT ENERGY COUPLING (PLASMA PENETRATION INTO TRENCH)
- SHOCK AND FLOW ATTENUATION WITHIN TRENCH
- CRATER PROJECTILES & DEBRIS

STRUCTURAL LOADING & RESPONSE ISSUES

- EXTERNAL LOADING & RESPONSE
  - ▲ NORMAL & SHEAR SURFACE LOADING (STRUCTURE-MEDIA INTERACTION)
  - ▲ TRANSVERSE LOAD CAPACITY
  - ▲ DAMAGE/DEFORMATION PREDICTIVE CAPABILITY
- INTERNAL LOADING & RESPONSE
  - ▲ TRENCH-PLUG INTERACTION (PLUG INDUCED LOADS, STRUCTURE AXIAL CAPACITY, RIB SHEAR CAPACITY)
  - ▲ EXPANSION UNDER INTERNAL PRESSURE
  - ▲ BREAKOUT RESPONSE

OTHER ISSUES

- DETECTION (EMISSION CONTROL, DECOY REQUIREMENTS)
- LAND WITHDRAWAL
  - ▲ AREA VS POINT SECURITY POLICY (PUBLIC ACCESS)
  - ▲ PUBLIC VS PRIVATE LAND
  - ▲ ENVIRONMENTAL IMPACT
- SALT NEGOTIATIONS
  - ▲ FUTURE THREAT
  - ▲ VERIFICATION REQUIREMENTS
- COST - SURVIVABILITY TRADEOFFS

processes. In the absence of a well defined shock environment within the trench, the first large field test (T-1) was designed to develop structural loading and response data for a known internal shock environment. In addition, analytical techniques for predicting loading and response were evaluated and revised for use as results from the DNA internal environment definition program became available.

The half-sized T-1 test is described in figure 4. The test model closely resembles the baseline shown in figure 3 with some notable exceptions. First, the model was precast in 6 meter long sections and joined on the test site with a form of bell and spigot joint. This procedure was chosen over the automated cast in place construction envisioned in the baseline to reduce modeling costs and to improve quality control for construction and placement of instrumentation. Unfortunately, the presence of this joint did influence both loading and response and was redesigned for later testing. Other exceptions included elimination of the running surface and alteration of the details of the upper 110^{o} of the cylinder (a series of interlocking panels to facilitate breakout of the missile after attack). The design of an economical structure which would resist external nuclear environments and provide for easy breakout of the missile post attack was not entirely a straightforward problem and other approaches would be proposed and tested during concept development.

The major contribution of T-1 was to provide data on the response of the trench structure near the plug. At the face of the plug, the shock flow is abruptly halted resulting in very large reflected pressures. These large pressures, in turn, rapidly accelerate the expansion of the tunnel. Understanding this expansion response was important for two reasons. First,

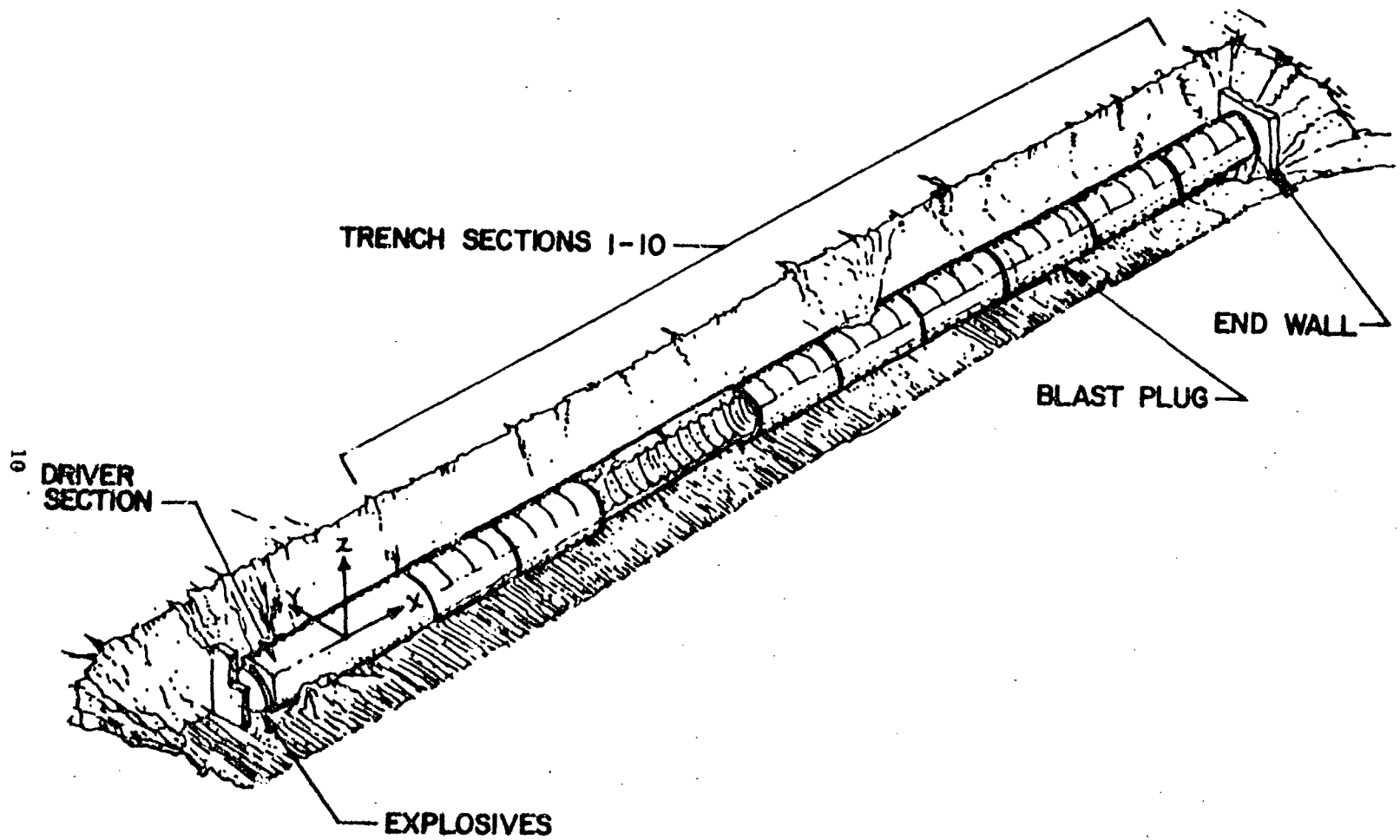

FIGURE 4a. HIGH EXPLOSIVE TEST T-1

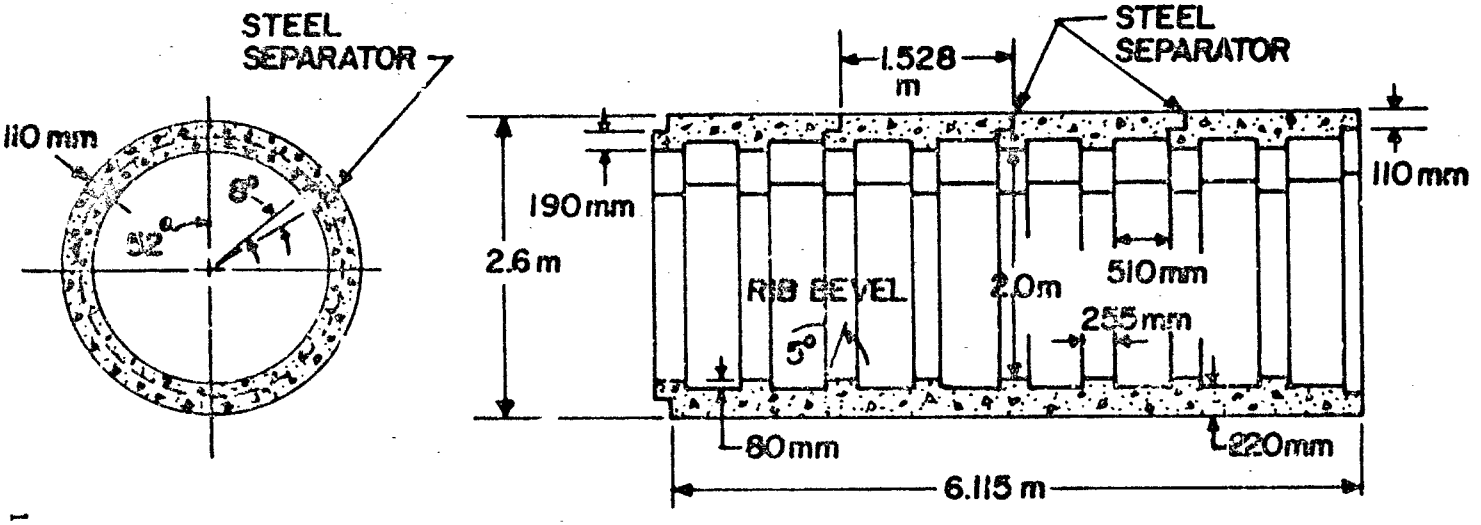

- ℓ = 2% FIBER
- f'_c = 6000 psi (41 MPa)
- Z TYPE LONGITUDINAL & TRANSVERSE ROOF JOINTS
- BELL/SPIGOT JOINT BETWEEN TRENCH SECTIONS

FIGURE 4b. TYPICAL TRENCH MODEL SECTION

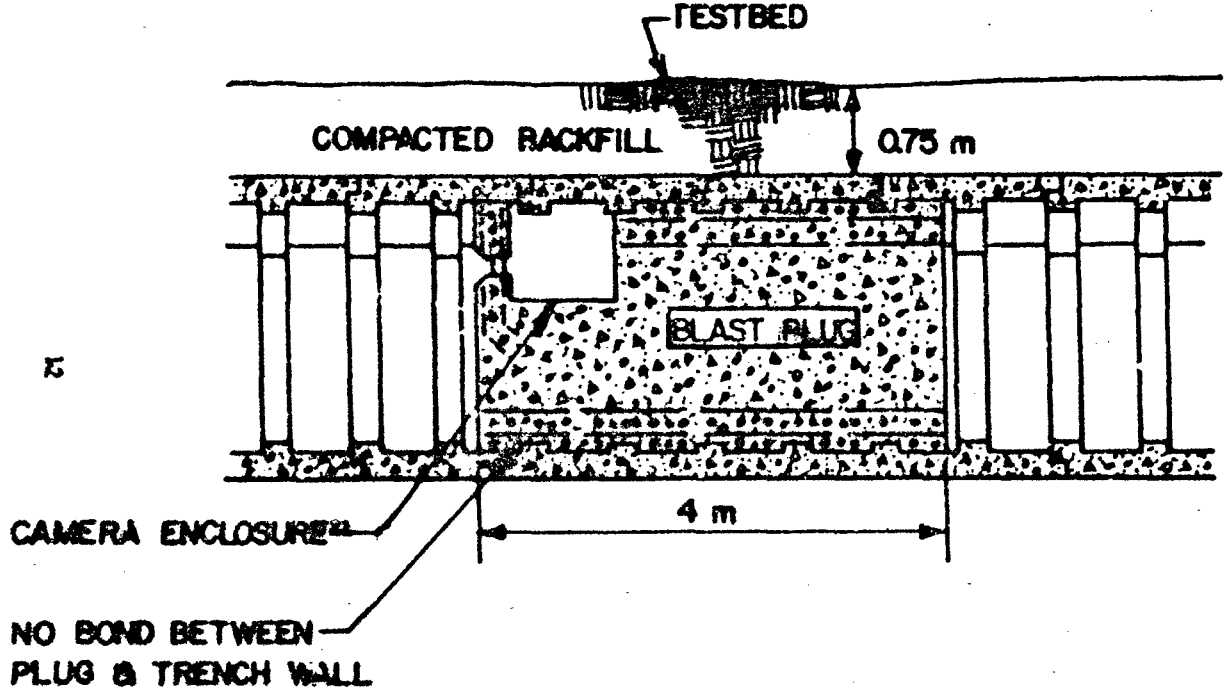

FIGURE 4c. T-1 GENERIC BLAST PLUG

the duration of the high reflected pressure was significantly influenced by both the rate of expansion and the subsequent time required to expand to the point where the gas trapped in the trench could vent to the outside. This process determined the form of the pressure time history on the face of the plug and the resulting axial loading transferred by the plug to the wall of the trench structure behind the plug (figure 5). The second important consideration was the behavior of the trench wall at the rib engagement location of the plug. Circumferential shear failure in the wall would limit the expansion of the wall around the plug and prevent disengagement of the plug. Otherwise, the shock could penetrate around the plug and destroy the missile, and the plug itself would be propelled toward the missile launcher.

Test data confirmed the general predictive capability for shock loading on the plug and expansion of the trench given an incident shock environment. In addition, failure of the trench wall behind the plug did occur as predicted due to loads coupled into the wall from the plug. However, the transverse bell and spigot joint behind the plug appeared on post-test examination to have played a role in the wall failure and this joint was not modeled explicitly in the pretest one-dimensional finite element analysis. Small scale static model tests (reference 10) conducted just prior to T-1 demonstrated wall failure in the absence of transverse joints at loading well below the peak dynamic loads of T-1. Based on the static data and subsequent analysis of the T-1 configuration (references 20 & 13), failure behind the plug is attributed to the magnitude of the plug loading, the eccentricity of the load application (at the ribs), and the presence of the longitudinal joints separating the 110° arc roof panels from the remaining trench

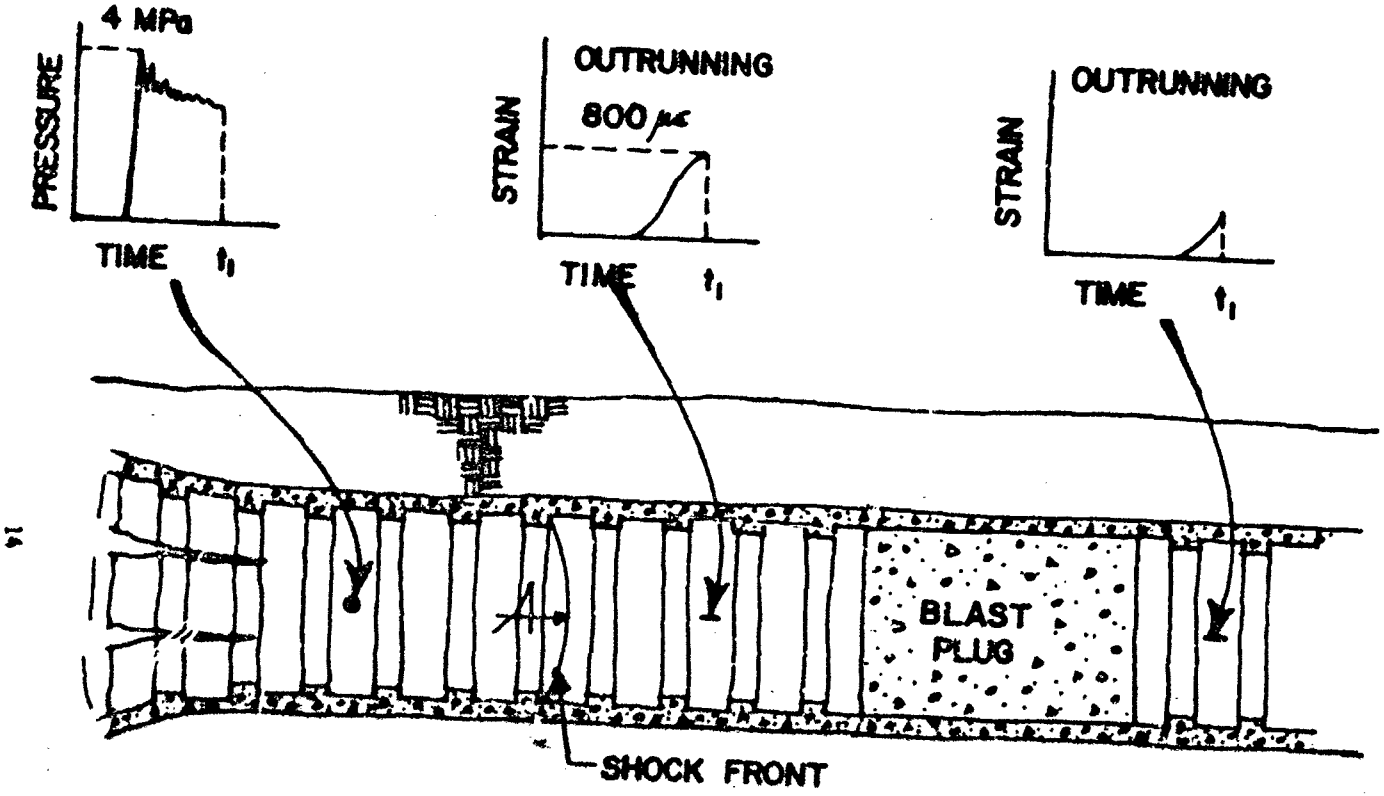

EXPECTED BEHAVIOR PRIOR TO PLUG LOADING
($t = t_1$)

FIGURE 5. GENERALIZED RESPONSE TO INTERNAL LOADING

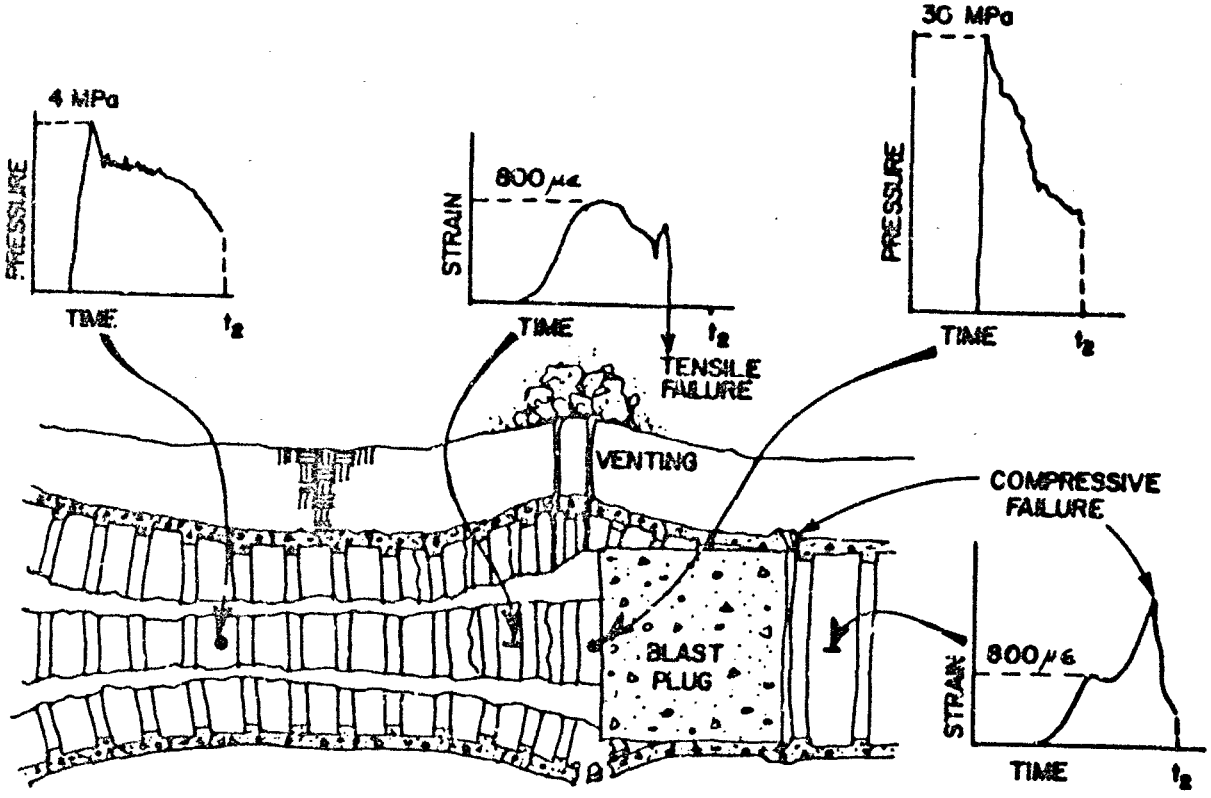

EXPECTED BEHAVIOR AFTER PLUG IS LOADED
($t = t_2$)

FIGURE 5. GENERALIZED RESPONSE TO INTERNAL LOADING (CONT.)

structure below. While the transverse bell and spigot joint appeared to influence the behavior at failure, it is not believed to be a primary cause of failure.

The response behavior at the front of the plug also differed from prediction. Expansion of the wall adjacent to the plug was expected based on two-dimensional analysis of a cross-section of the trench at the face of the plug (reference 20). This expansion did occur from the face of the plug back to the first engaged rib. At this point the trench wall failed circumferentially limiting the zone of expansion. The failure was attributed to a combination of shear due to expansion and tension from the plug loading. An additional factor may have been the extremely close fit of the plug with the trench structure. The plug was cast directly against the trench wall separated only by a coat of paint to prevent bonding. This consideration influenced a redesign of the cast in place plugs for T-2.

The second major contribution of T-1 was to provide data on the interaction of the trench ribs with the internal airblast. This interaction couples loading into the trench wall which outruns the airblast and arrives at the blast plug prior to arrival of the airblast. In addition, the secondary shock formed by the collision of the airshock with the ribs is strong enough to perturb the main shock flow in the trench. The primary effect is to convert kinetic energy in the flow to enhance the static overpressure and subsequently to accelerate expansion of the trench. This effect is ultimately important to the designer because of its reduction of the loading measured at the plug. The rib loading coupled into the wall is significant if it reduces the effective capacity of the wall to resist plug loads.

T-1 pretest analysis indicated that longitudinal compressive strains of approximately 800 $\mu\varepsilon$ due to rib loading would arrive at the plug prior to the

airblast, reducing the remaining capecity for plug loading to approximately two-thirds of the unloaded wall capacity (figure 5). Although blast pressure data recorded in T-1 confirmed pretest analysis of the rib shock interaction process, the longitudinal data showed substantially lower outrunning strains. Maximum outrunning compressive strains of 150 $\mu\epsilon$ were recorded in the trench walls and no clearly observable outrunning was evident in the roof panels. Again, the transverse joints were suspected of influencing test results. Subsequent analysis would show that the shock propagation was slowed by the joints and later testing would provide higher measured values of outrunning strain. However for T-1, outrunning strain was not a significant factor in response.

The T-1 test established the fundamental aspects of loading and response behavior for a known internal environment. It also raised questions about the capability of the baseline design to react plug loading. This data was particularly important as it came at a time when system planners had just altered the baseline design to reduce projected system costs.

Late in 1976, the program office for MX development (The Space and Missile Systems Organization or SAMSO, now the Ballistic Missile Office or BMO) convened a "Blue-ribbon Panel" chaired by Dr. Newmark of the University of Illinois to review the baseline concept design. This panel considered only transverse response from external loads, and, based on the information presented them, the panel concluded that the design was excessively conservative. Early in 1977, SAMSO initiated a 90 day study to define a less conservative base line. The Air Force Weapons Laboratory (AFWL) participated in the study and based on experimental and analytical studies recommended

against reducing the baseline capacity (reference 3). Despite this recommendation, an alternate baseline was adopted in May 1977, which was identical to the original baseline except that the wall thickness was reduced by one-third to ten inches (254 mm), the amount of fiber reinforcing was reduced by three-quarters to one-half percent, and the nominal concrete strength was increased from 6000 psi (41 MPa) to 8500 psi (59 MPa). Refer to figure 3 for the original baseline design. The decision to change the baseline came at a time when the test model construction for T-1 was already complete. To change the wall thickness for T-2 would have required the fabrication of new forms and would have substantially delayed the test. As a result, T-1 was conducted as planned and only three changes were made to T-2. The concrete strength was increased and the steel fiber percentage was reduced to match the new baseline values. Also, the roof panels were eliminated so that the structure could be cast as a continuous cylinder. This last change reflected a revised estimate of breakout requirements and capabilities.

Although the data from T-1 was not expected to be available in time to alter the design of T-2, recommendations based on T-1 results were included in a redesign of the blast plugs for T-2. The number of ribs engaged was reduced to two to conform with current mechanical plug design concepts and the design of the rib engagement was altered to prevent the cast in place plug construction from influencing expansion and wall failure at the rib engagement.

The half-sized T-2 test is described in figure 6. As with T-1, the major emphasis of the test was to obtain fundamental loading and response data. However, T-2 included the simulation of the external airblast environment which would accompany the internal environment during an attack. This external environment, unlike the internal environment could be relatively well

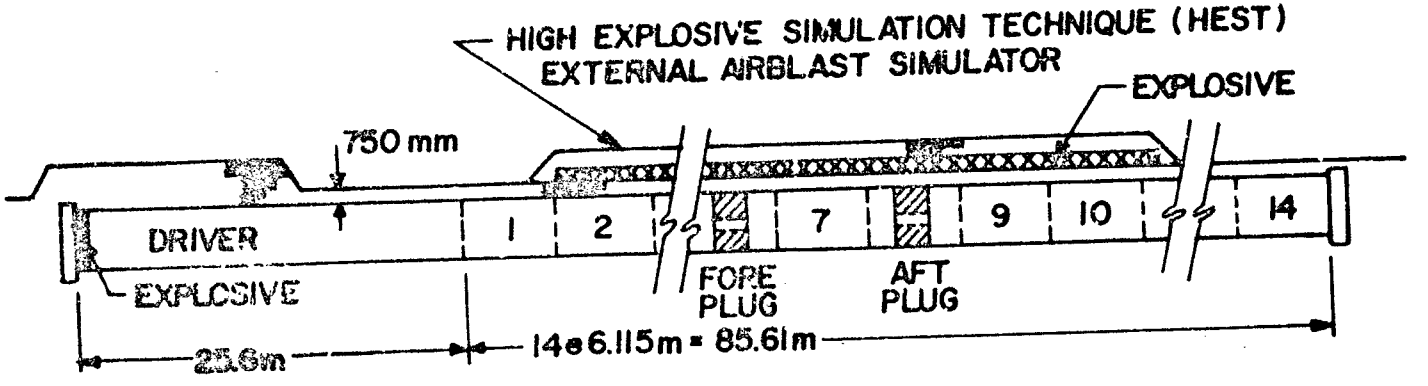

TEST SCHEMATIC

TRENCH SECTION DESIGN

- SAME GEOMETRY AS T-1
- ℓ_f = 1/2 % FIBER
- f'_c = 8500 psi (59 MPa)
- NO LONGITUDINAL JOINTS
- NO TRANSVERSE ROOF JOINTS

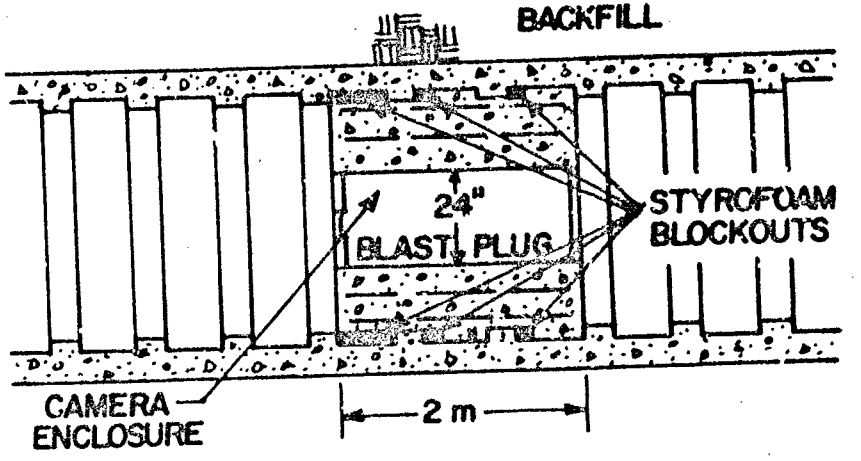

FORE PLUG DETAIL

FIGURE 6. T-2 TEST CONFIGURATION

characterized for a given attack scenario. The major effects of this external environment were to offer restraint to the trench expansion ahead of the blast plug region and to provide external loading resulting in displacement and deformation of the trench structure behind the blast plug. Another, important effect of the external loading was to reduce the longitudinal motion of the trench (due to internal rib and plug loading) by increasing the longitudinal shear resistance at the soil-structure interface.

In addition to examining the importance of external loading, the study of trench-plug interaction in T-2 was continued. While contractors for SAMSO were developing mechanical blast plug designs to attenuate the loading applied through the ribs to the trench wall, the T-2 test examined basic rib shear behavior and the concept of a simple two plug system to attenuate internal loads. In this dual plug concept, the first plug would couple the full internal loading into the trench structure forcing rib shear and/or wall failure in the region between the two plugs. The bulk of the energy associated with the internal shock would be dissipated first through inelastic damage to the ribs and trench wall adjacent to the first plug and between the plugs and finally through venting from the damaged trench. The second plug would see much reduced loading and could safely protect the missile and launcher.

Pretest analysis for T-2 (reference 22) examined the longitudinal response of the trench. This analysis gave the first estimate of the importance of shear resistance at the soil-structure interface to longitudinal response. Three calculations were performed to predict the longitudinal response of the trench wall behind the plug due to loading from the internal airshock. The

first was a simple single degree of freedom calculation as shown in figure 7a. The mass used was the mass of the fore plug and the stiffness was based on the trench wall between plugs. The force time history was simplified from the predicted loading on the plug but matched peak force and total impulse at 20 ms. The resulting peak force in the spring was 190 MN (43 million lbs). The second calculation was a one dimensional multiple degree of freedom analysis described in figure 7b. This analysis represented each of the fourteen 6 meter trench sections with four masses and springs. Mass and stiffness values were increased at each plug location so that the plugs were modeled integrally with the trench sections. The numerical values were derived in a manner consistent with the single degree of freedom analysis. The soil at the downstream end of the trench model was also represented by a series of masses and springs. Two forms of loading were applied. Each of the 21 masses upstream of the fore plug was loaded with a force (F_{Ri} for the ith mass) which represented the drag force of the internal shock on the ribs. The magnitude and time of arrival (TOA) of these forces were adjusted for each mass, but the waveform used was constant as shown in figure 7b. This loading was derived from the analysis of an axisymmetric hydrodynamic calculation of flow in the ribbed trench. The second type of loading was the direct plug loading applied at Mass 22 which was also analytically derived. The multiple degree of freedom analysis differed from the single degree of freedom analysis primarily by accounting for the internal loading and response of the trench upstream of the fore plug and by accounting for the deformation of the trench from the rear plug downstream. The effect of modeling the upstream region was to generate an outrunning force of 22 MN (5 million lbs, 22% of the static

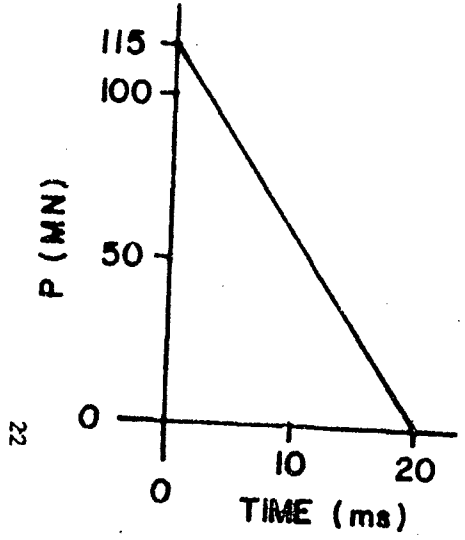

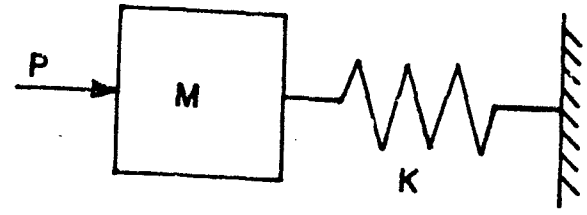

M = 22500 kg (FORE PLUG MASS)

K = 4.87 GN/m (STIFFNESS OF TRENCH BETWEEN PLUGS)

FIGURE 7a. SINGLE DEGREE OF FREEDOM ANALYSIS

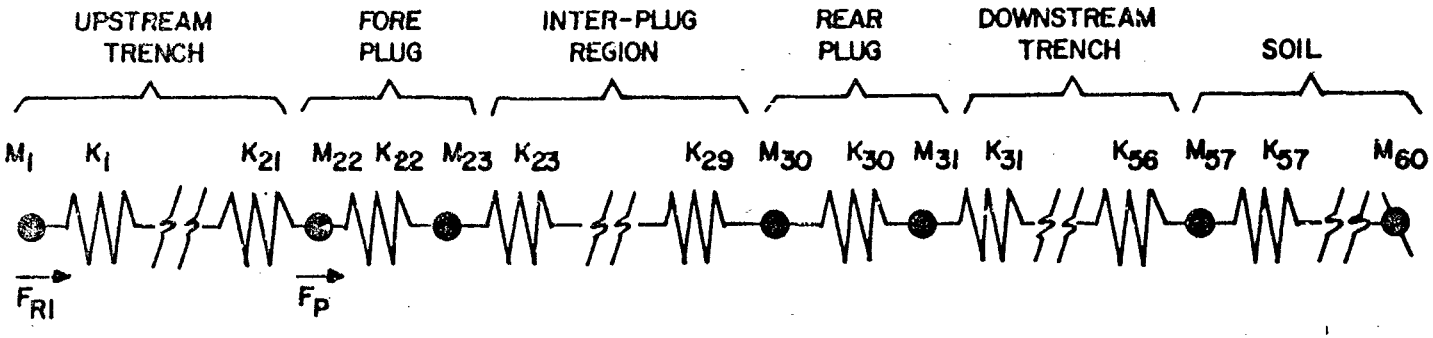

$M_{22} = M_{23} = M_{30} = M_{31}$ = 12,750 kg
OTHERWISE M_1 THROUGH M_{56} = 6 330 kg
SOIL: M_{57} THROUGH M_{66} = 14,000 kg

$K_{22} = K_{30}$ = 95.3 GN/m
OTHERWISE K_1 THROUGH K_{56} = 38.5 GN/m
SOIL: K_{57} THROUGH K_{65} = 1.4 MN/m

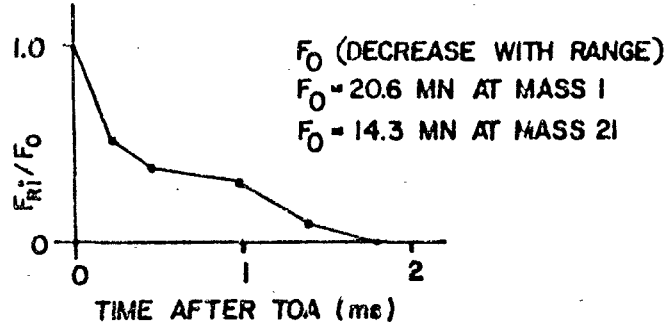

RIB LOADING WAVE FORM

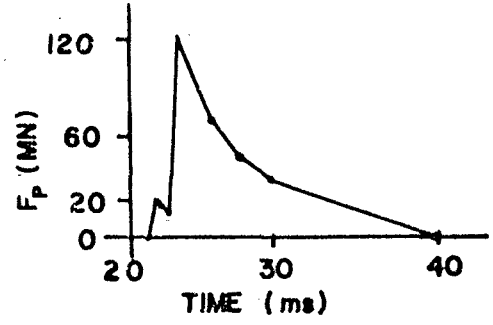

PLUG LOADING

FIGURE 7b. MULTIPLE DEGREE OF FREEDOM ANALYSIS

wall capacity) in the upstream wall of the trench prior to arrival of the plug loading. The more dramatic effect of including the downstream portion of the trench was to reduce the peak force due to plug loading in the region between the plugs to 40 MN (9 million lbs). This 80 percent reduction of the force estimate provided by the single degree of freedom analysis resulted by allowing deformation and displacement of the rear plug and the trench downstream. While the results of these two calculations may be taken as bounds on the axial response of the trench wall between the two plugs, the expected behavior ranges from essentially elastic to failure (based on a calculated static axial wall capacity of 98 MN or 22 million lbs). While the rigid downstream boundary condition in the single degree of freedom analysis clearly leads to unrealistically high wall force estimates, the multiple degree of freedom analysis provides low estimates by ignoring the longitudinal shear force which develops at the soil structure interface and which resists the downstream motion of the trench. To gain an improved estimate of the influence of this force, an axisymmetric finite element calculation was performed. The geometry of the calculation is shown in figure 7c. The calculation included the entire test model surrounded by an annulus of soil in the axisymmetric representation. Rib loading and the internal normal pressure were applied sequentially upstream of the fore plug to model the loading of the internal airblast running toward the plug. An appropriately timed pressure time history was applied to the plug. The external airblast loading was also applied sequentially to the surface of the soil. To match the test design condition the arrival of the external shock was approximately five milliseconds behind the arrival of the internal shock. The interface between the soil and structure was represented with a sliding, debonding interface

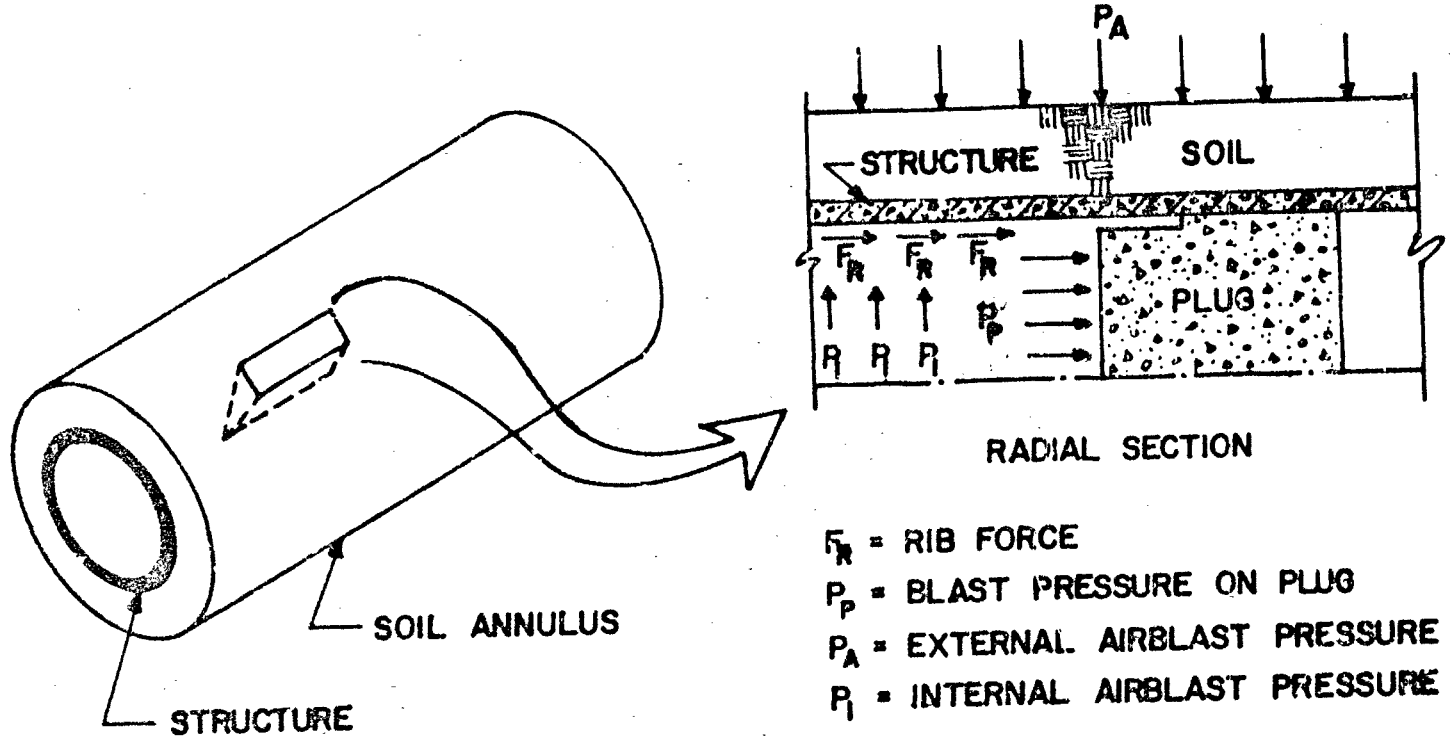

FIGURE 7c. AXISYMMETRIC FINITE ELEMENT ANALYSIS

with a Coulomb friction model. The SAMSON structure-media interaction code used in the analysis is described in reference 1.

Using internal loading and material properties consistent with the previous two calculations, the finite element calculation predicted an outrunning wall force of 5.8 MN (1.3 million lbs) compared with 22 MN (5 million lbs) in the multiple degree of freedom analysis. The peak wall force immediately behind the plug was predicted to be 95-115 MN (21.4-26 million lbs) compared to 40 MN (9 million lbs) in the multiple degree of freedom analysis and 190 MN (43 million lbs) in the single degree of freedom analysis. Since the soil stress due to the external airblast environment attenuates rapidly with depth in the dry sandy soil, the effect of external shear was overemphasized in the calculation. Ahead of the plug, this shear force acts to attenuate rib induced loading while close behind the plug it tends to increase the wall stresses due to plug loading. This error was not considered to be too significant because the five millisecond delay in external loading in general caused the effects of the external force to appear only after the peak longitudinal strain had occurred. Post test analysis revealed that the actual internal environment was different from the values used in the predictions. The peak pressure was slightly high, but within ten percent of the value used in the predictions. However, the impulse delivered to the plug during the first twenty milliseconds of loading was thirty percent low and the delay between internal and external shock fronts was only 2.6 ms. Forces in the trench wall were calculated from experimental strain data using standard test day material property data and the approximation of elastic behavior. The out-running force derived by this method (reference 14) was 30 MN (6.7 million lbs) while the plug induced force was 76 MN (17 million lbs). Comparing the

experimental results with the pretest calculations was not entirely straightforward. The reduced impulse was shown to have significantly reduced the plug induced loading in the wall. The source of the higher than expected outrunning strain could not be directly traced, but it appeared to have been affected by shock loading coupled directly into the wall by the explosive driver and not modeled in the analysis.

However, the most significant result of the comparison of the experimental data with the calculations was the confirmation of the external shear loading as a major contributor to the longitudinal response. The measured wall response to plug loading was almost twice the value predicted in the multiple degree of freedom analysis despite the reduced experimental plug loading. The results were far more closely represented by the finite element analysis including longitudinal shear effects.

The results of the axisymmetric analysis were also used to predict that rib shear would occur at the fore plug. The ribs were not modeled explicitly in the calculation. Rather, rib shear was inferred by comparing the calculated force transmitted by the plug to the wall with a calculated static rib shear capacity. The calculation also indicated expansion of the trench wall along the side of the fore plug up to the first engaged rib where shear and flexural failure of the wall would occur.

A two-dimensional plane strain analysis of a transverse cross section of the test model under external loading was performed using the SAMSON code. The geometry of the calculation is shown in figure 8. Based on the results of this calculation collapse of the region between the plugs and behind the

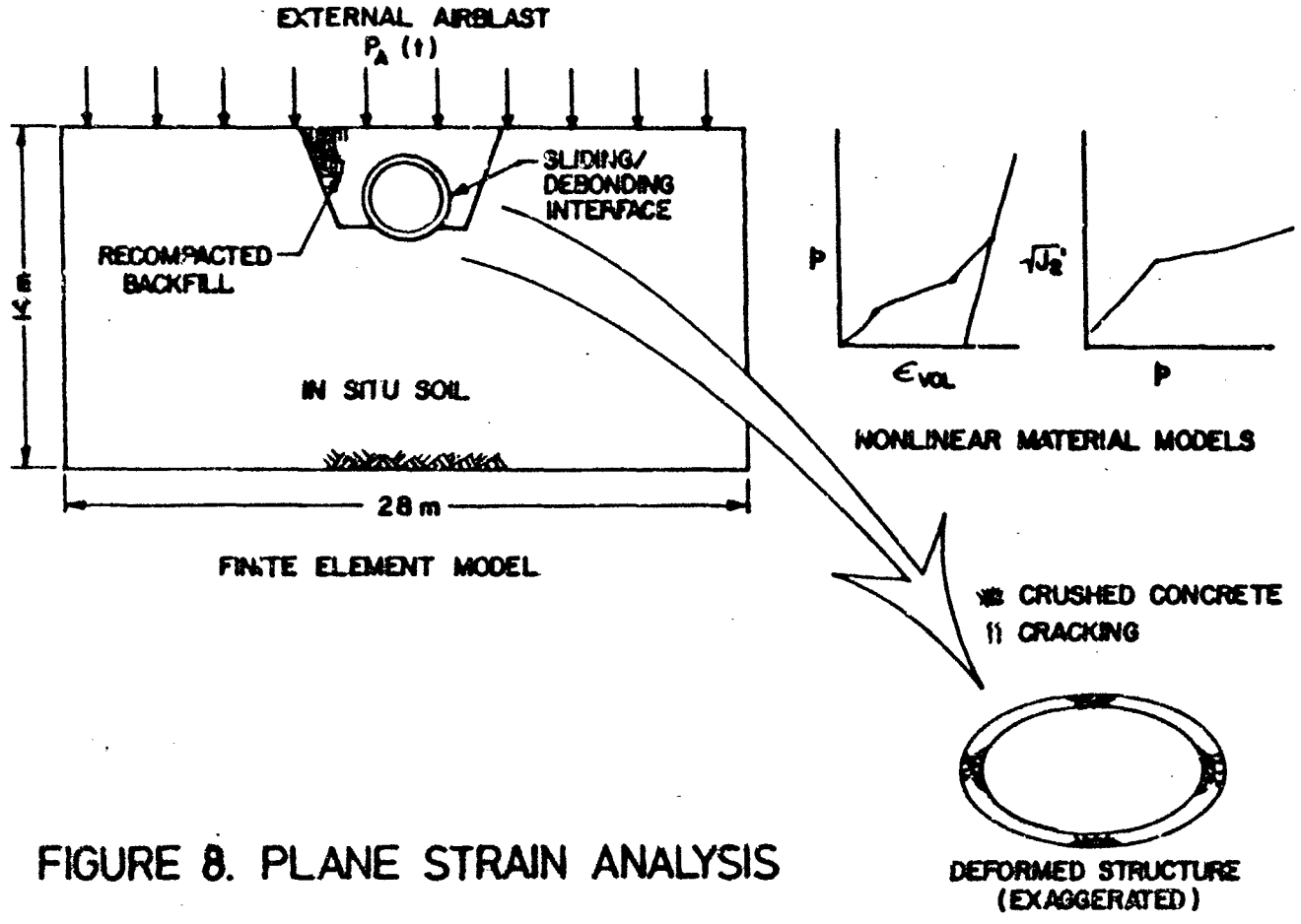

FIGURE 8. PLANE STRAIN ANALYSIS

second plug due to external loading was not expected. However, local wall failure (concrete crushing, substantial cracking) at the crown, springline and invert associated with transverse bending of the cross section in the primary bending mode was predicted.

The actual T-2 test results in general confirmed the predicted results (references 22 and 14) with some exceptions. The wall adjacent to the blast plug did expand and the plug sheared both engaged trench ribs and the next rib back, before coming to rest on the second rib past its original position. The concrete rib engagements on the plug itself were severely damaged. Blast pressure measured in the region between the plugs showed that low level (25 psi or 180 kPa) pressure did get past the first plug. The external airblast loading did cause local wall failure at the crown, invert and springline in the region between the plugs and behind the second plug as predicted. However, the wall damage in the region between the plugs was sufficient to cause collapse. In addition, external load damage to the region behind the second plug was extensive and this region appeared near collapse (figure 9).

After the T-2 test, a substantial change in the baseline design occurred. Instead of providing a uniform design for the entire twenty mile trench structure, the new hybrid concept provided a series of hardened parking segments connected by a soft tunnel structure. The capacity of the hardened regions would be substantially increased when compared with the concepts tested to date.

The analysis of experimental data from T-1 and T-2 made significant contributions to the decision to alter the baseline. The first contribution was to clarify internal loading behavior. The two tests provided a basic

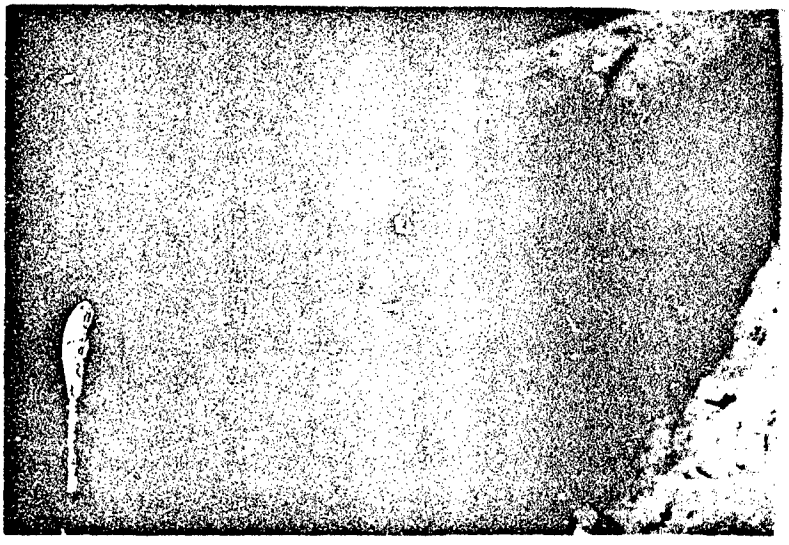

EXTERNAL DAMAGE
AT REAR PLUG

COMPRESSIVE FAILURE
AT SPRINGLINE
(BEHIND REAR PLUG)

FIGURE 9. POST TEST DAMAGE NEAR REAR PLUG

description of the loading coupled into the trench near a blast plug for simplified plugs and a known incident internal airshock. Comparisons of calculations with experimental data confirmed the ability of analytical methods to provide reasonable estimates of loading, accounting for local effects of rib attenuation and wall expansion. However, the far more difficult job of predicting the incident internal environment which provides the initial conditions for the loading calculations was not yet complete. For a more complete description of the problems associated with calculating initial coupling and the effects of upstream attenuation see reference 26. Regardless, using the predictive techniques evaluated in T-1 and T-2 and the best estimate incident environment, it was clear that significant outrunning strain could be expected from airblast loading of the ribs and substantial load attenuation would be required from the mechanical blast plugs to prevent rib shear or wall failure in the trench.

The second contribution was to provide basic data on the behavior of the trench in the region of the plug. In T-1, wall expansion was stopped at the first engaged rib through a combined shear and tension failure of the wall. Since the cast in place construction of the T-1 plug was thought to have influenced the wall failure, the design of the T-2 plugs was revised. In T-2 substantial wall expansion alongside the plug did occur, but not enough to completely disengage ribs or to allow substantial pressure penetration behind the fore plug. Three one-thirteenth size dynamic tests conducted by AFWL's Civil Engineering Research Facility also indicated that wall expansion would limit rib engagement (reference 11) and that a reduction of fiber percentage from two to one-half percent significantly lowered the energy dissipated in

rib shear. The models tested had wall dimensions scaled from T-1 and T-2 designs and used nominal 8500 psi (59 MPa) concrete. In all tests, substantial rib shear, wall damage and pressure penetration beyond the plug due to wall expansion were experienced. In addition, a quarter-size test of a mechanical blast plug concept developed the Martin Marietta Corporation was conducted by the AFWL as a precursor to the T-5 event (reference 4). The trench response in this test produced a catastrophic failure of the trench-plug system. The wall design was essentially scaled from T-2 with one-half percent fiber reinforcing and a design concrete strength of 8500 psi (59 MPa). The rib dimensions and spacing were altered to match the Martin Marietta plug design. Failure in the test was initiated when the outrunning compressive shock in the trench wall accelerated the trench wall downstream with respect to the plug. At the arrival of the internal airshock at the first engaged rib, the outward and downstream motion of the trench wall provided a gap for pressure penetration to the region between the two engaged ribs. Subsequent expansion of the trench wall adjacent to the plug occurred so quickly that the first rib was never engaged and the effective capacity of the second rib was reduced. The plug translated approximately 1.26 m, shearing two downstream ribs, before coming to rest. As a result of the larger and smaller size testing and associated analysis, the behavior of continuously hardened baseline concepts in the region of a blast plug was determined to be unacceptable. The smaller size testing in particular had demonstrated problems with expansion under internal loading. In addition, the results of T-1 and T-2 had raised concerns with the mechanical plug designers for the capability of fiber reinforced concrete ribs and wall sections to react the

anticipated plug forces. With the shift to the hybrid "Hardened Aim Point Concept," baseline designs would have substantially increased capacity, not only to resist expansion, but to accommodate plug forces as well.

The third major contribution was the demonstration in T-2 of the damage that might be expected from external loading in the lightly fiber reinforced trench. This confirmed the severe damage behavior observed with one-sixth size models added to the S-1 and S-2 tests. In the S-2 test, side-by-side comparisons of original and alternate baseline structures indicated that while both models had substantial damage, the thinner wall alternate baseline suffered the most severe damage (reference 21). The amount of deformation of the cross-section was substantially larger than predicted in the pretest finite element analysis. This discrepancy highlights the difficulty of predicting behavior when material failure occurs but prior to collapse. Extensive improvements to constitutive models and numerical techniques are required to model this behavior accurately. Providing the capacity to resist external loading for the region where the missile launcher would be parked would continue to remain a concern. Solutions would have to accommodate missile breakout and launch requirements. A suitable design concept had not been demonstrated at the time the preferred basing mode was changed to the vertical shelter.

The main objective of both the T-3 and T-5 tests was to demonstrate the performance of the mechanical blast plug designs developed by the Boeing Company and Martin Marietta Corporation. The test configurations are shown in figures 10 and 11. For the concrete trench structure, the most significant aspects of behavior were the response of the hardened sections to plug induced loading and the response of test sections behind the plugs to external loading.

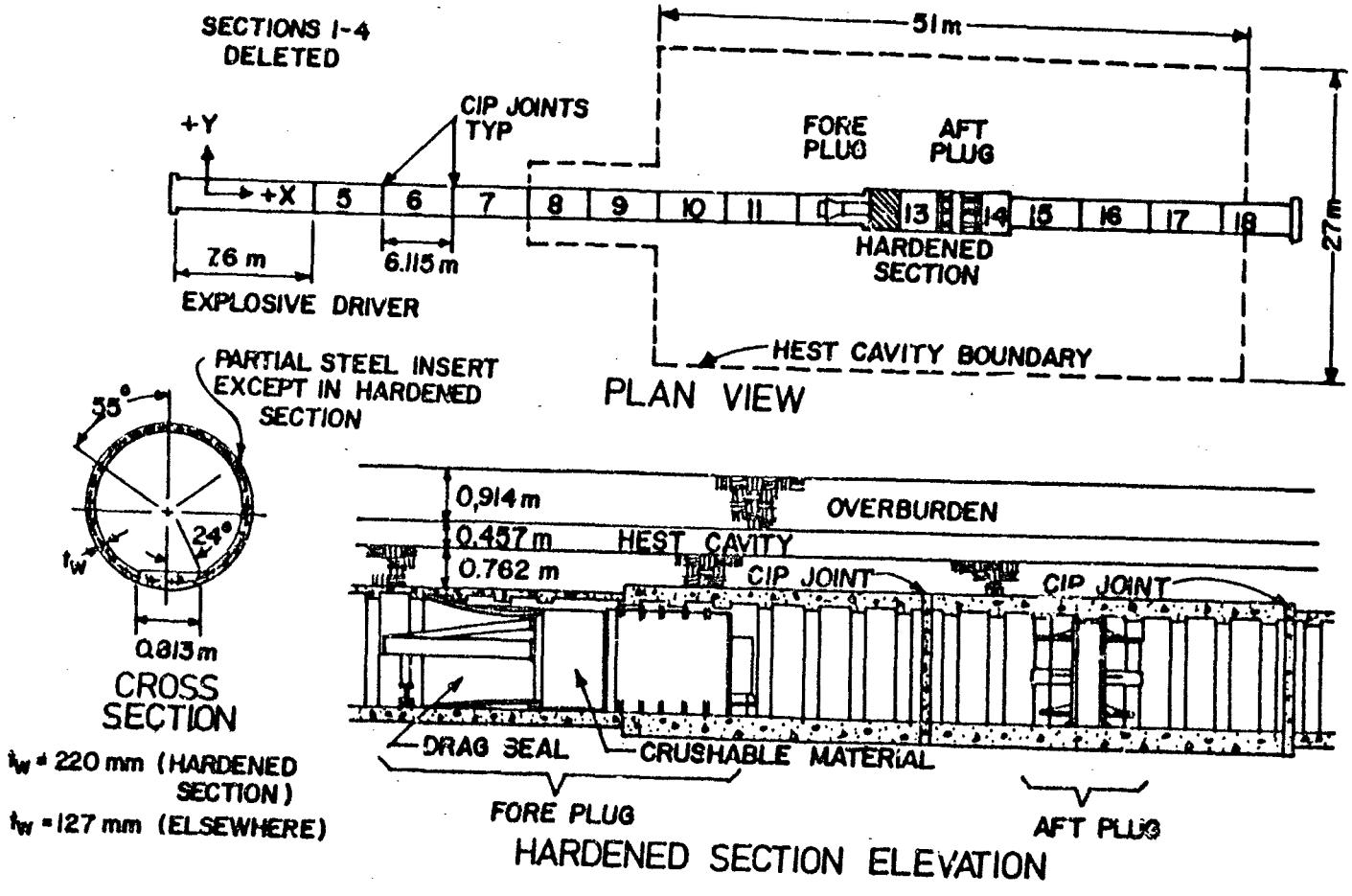

FIGURE 10. T-3 TEST CONFIGURATION

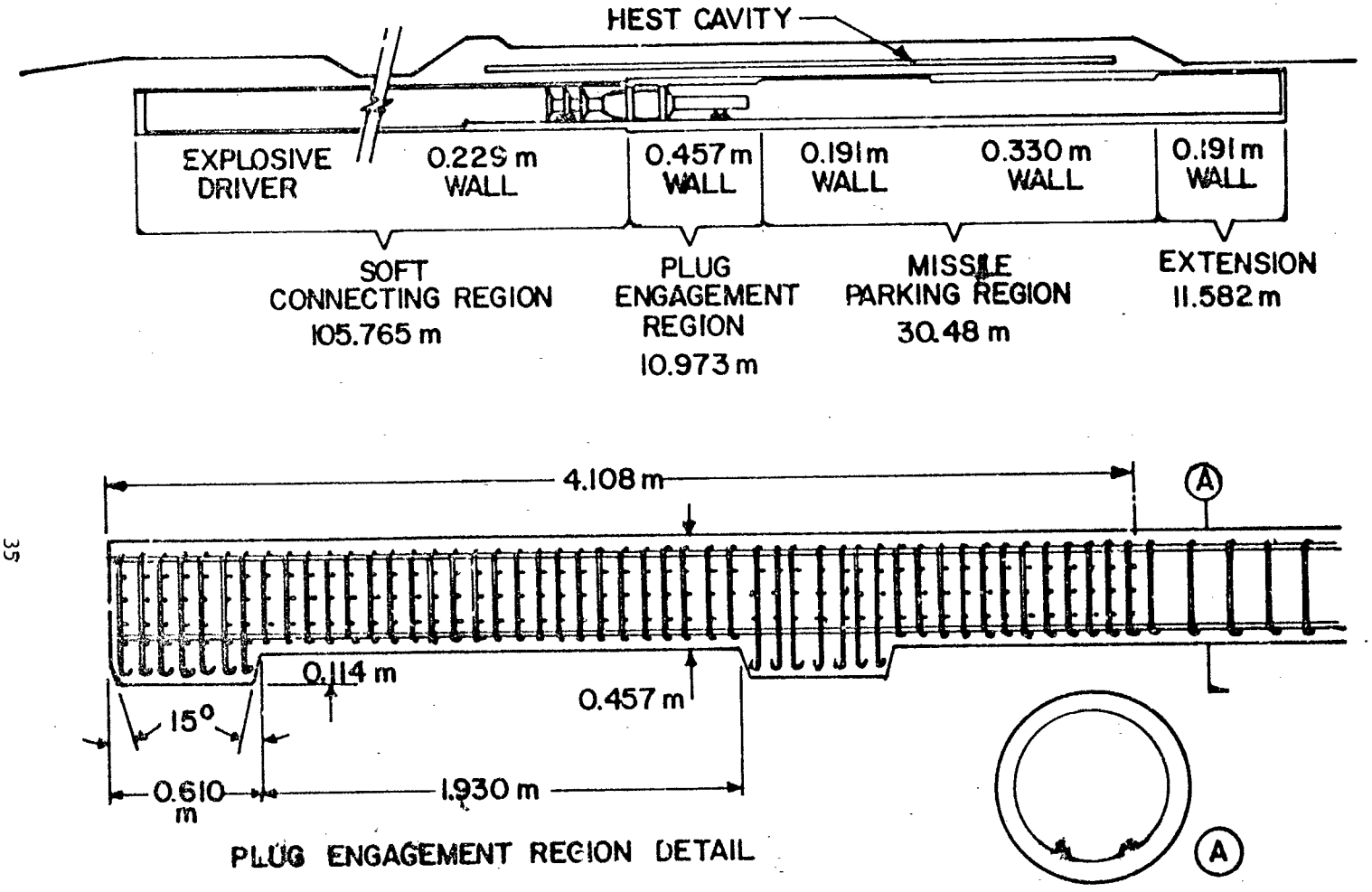

FIGURE 11. T-5 TEST CONFIGURATION

For the half-sized T-3 test, model trench sections were already under construction when the decision to change to a hybrid baseline was made. The test structure originally would have modeled the alternate baseline configuration (full size wall thickness = 10 inches or 254 mm, f_c' = 8500 psi or 59 MPa, one-half percent fiber reinforcing). The test was modified by using the already constructed alternate baseline models to represent the soft connecting tunnel and by constructing two hardened sections to model the plug engagement location (Sections 13 and 14, figure 9). The region where the missile would park was not modeled, but alternate baseline sections were placed behind the hardened section to react the longitudinal stress created by the internal loading. The hardened section contained two percent conventional reinforcing in both the longitudinal and circumferential directions. The test day concrete strength averaged approximately 70 MPa (10,000 psi) in soft connection regions and 67 MPa (9700 psi) in the hardened region. The connection between soft and hardened regions was designed to limit shear to reduce wall expansion at the plug engagement location. The design of the hardened region was straightforward in all aspects except for predicting the shear capacity of the ribs.

The method proposed by the AFWL was empirically derived and fundamentally based on a study performed in 1973 for SAMSO (reference 19). Specimens were loaded quasi-statically to failure. Concrete strength, shear reinforcing and normal confining stress (σ_n) across the shear plane were varied during testing. Experimental data is shown in figure 12 along with the recommended analytical expression for maximum shear stress (τ_{max}). This expression is a summation of three terms representing the contribution of the concrete, the

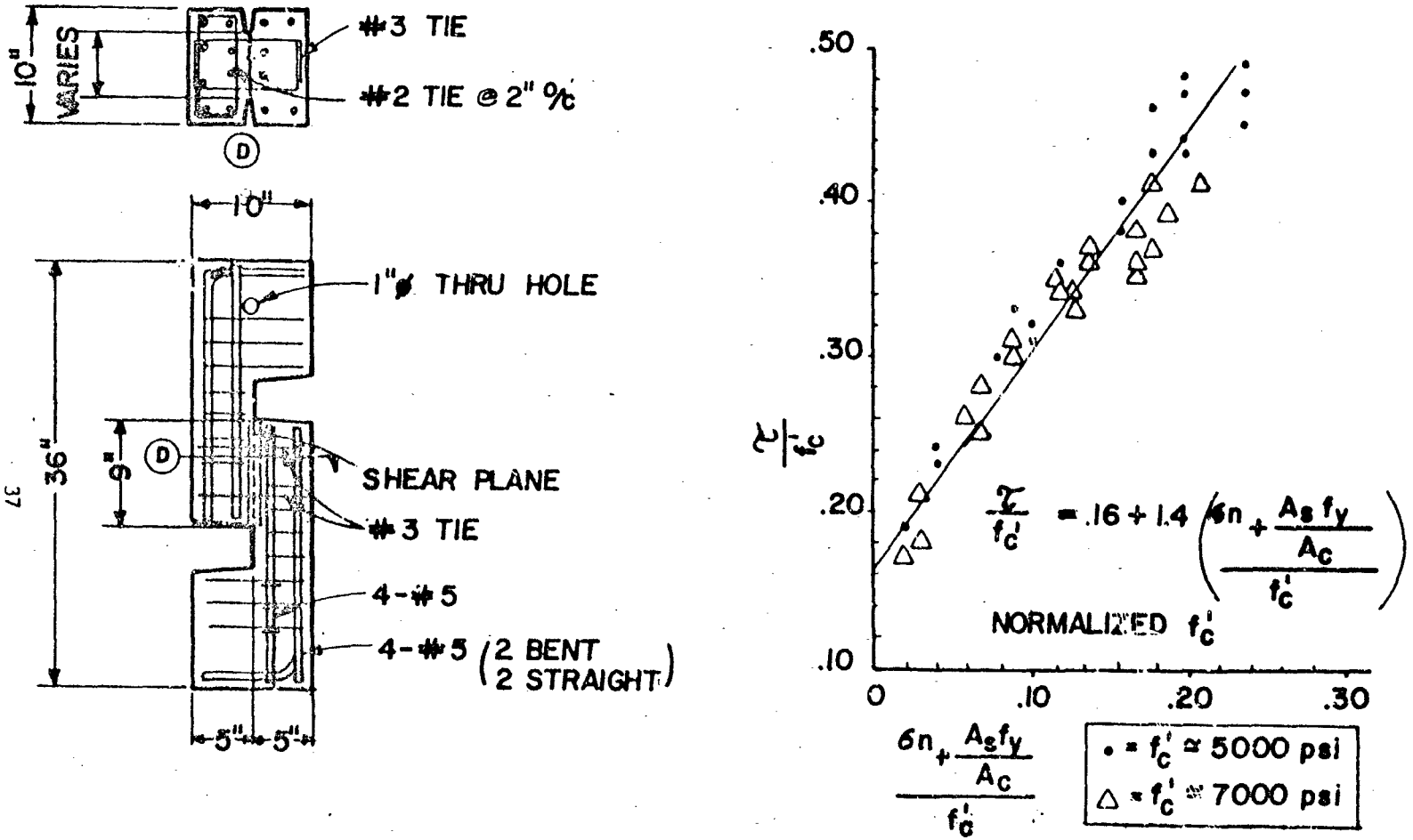

FIGURE 12. KARAGOZIAN & CASE SHEAR STUDY RESULTS (REFERENCE 19)

confining stress and the steel shear reinforcing. The third term is identical to the American Concrete Institute shear friction formulation (ACI 318-77, reference 18). At the AFWL, the first term was revised based on the static rib shear data in reference 10. The recommended expression is:

$$\tau_{max} = .1\ f'_c + 1.4\ (\sigma_n + A_s f_y / A_c)$$

where A_s = cross-sectional area of shear reinforcement across the shear plane

A_c = cross-sectional area of concrete along the shear plane

σ_n = externally applied confining stress normal to the shear plane

f'_c = unconfined compressive strength of concrete

f_y = yield stress of shear reinforcement

The above expression was developed after the T-3 design was finalized, and predicted that the design would have a margin of safety exceeding sixty percent. During the test, although the fore plug attenuation and sealing mechanisms did not perform as expected, the trench section did not fail under expansion nor was rib shear a problem. Because the fore plug was not totally effective, the region between the plugs experienced a pressure pulse with a peak of .85 MPa (125 psi) and relatively long duration of 240 ms. This was successfully resisted by the aft plug, demonstrating the value of a dual plug concept.

The T-3 test provided the first experimental data for large size models of the continuously hardened alternate baseline design for conditions of external loading. Based on numerical analysis (reference 23) and the

experimental data from T-2 and smaller sized component tests (reference 7), collapse of the thin wall region behind the hardened blast plugs was not certain, but appeared likely. The difficulty in predicting damage states when substantial cracking and crushing occurs has been discussed. To improve the performance of this region, the backfill stiffness was increased by compacting the backfill to a minimum dry density of 2000 kg/m^3 (125 lbs/ft^3, 95% of maximum density as determined by ASTM D-1557, Modified Proctor Compaction Test). This value compares with 1760 kg/m^3 (110 lbs/ft^3) for the backfill used in T-2 and also for the insitu soil. However, failure planes between compacted lifts of backfill reduced the effective stiffness observed in the test. As a result the effective constrained modulus for the T-3 backfill was approximately the same as for the insitu soil and approximately twice that of the T-2 backfill. Both theory and previous experimental data established that the stiffer soil would reduce the effective loading and the resulting damage associated with the external loading. The actual test provided interesting results. Substantial local crushing and cracking did occur, and plastic hinges were formed at the crown and invert as well as at the longitudinal separato. joint (55^o either side of the crown) and at 30^o below each springline. Surprisingly, the structures did not collapse immediately. Movies taken during the test show the structures moving to peak response (20 ms) and recovering. When the light fails at 200 ms the structures were still standing. However, the structures had extensive damage and were only marginally stable with six complete hinges formed around the circular section. At about eight seconds after test detonation a very low level groundshock was caused by fall back of the loose soil overburden which had

confined the explosives for the external loading simulator and this was sufficient to collapse the structures (reference 15).

The T-5 test was similar to T-3 not only in objectives, but also in results. Although the Martin Marietta Corporation designed blast plug was substantially different in approach and design when compared to the two plug Boeing concept, it also experienced difficulty with sealing and attenuating the internal loading environment. In addition, although T-5 included test sections, behind the blast plug, specifically designed as model parking regions for the missile, the inappropriate design of a longitudinal breakout joint led to the failure of this region under external loading.

As with T-3, the region of plug engagement was specifically designed to accommodate the Martin Marietta plug design. T-5 was a three-quarter size test and the wall thickness in the plug engagement region was 457 mm (18 inches) and contained 1.5 percent reinforcing longitudinally and 6.75 percent circumferentially. The plug engagement region performed satisfactorily despite the higher than anticipated loading transferred to the rib when the shock absorbing mechanical engagement arms on the plug bottomed out (references 16 and 24). The first engaged rib was observed to have crushed longitudinally 80 to 100 mm at the forward face, however no evidence of significant rib shear was seen. The second engaged rib did show shear damage between rails at the invert where the inner hoop reinforcement is not continuous, and minor cracking and spalling of concrete was seen at other locations. The plug did remain engaged and cracking due to expansion was very minor. Despite the larger than anticipated plug response and some pressure penetration, performance of the plug and trench combination appeared to be within the required limits.

The behavior of sections behind the plug in response to external loading was not nearly as successful. The test region behind the plug actually incorporated two separate designs for hardened parking locations for the missile launcher. Requirements to minimize cost and to provide a design which would allow the launcher to break out through the roof of the trench after an attack, lead to lightly reinforced section designs with marginal capacity to resist external loading. The thinner wall section (190 mm or 7.5 inches) had one percent conventional reinforcement circumferentially while the thicker wall section (330 mm or 13 inches) had 0.7 percent. To allow breakout, the circumferential rebar design for both sections contained short (80 mm or 3 inch) splices at 55° either side of the crown facilitating tensile failure of the wall at that location under the erection loading. Similar designs showed satisfactory performance in smaller size testing (reference 7); however, in T-5 this detail proved inadequate to resist the flexure occurring at that location resulting from initial external loading of the crown. The splice on the outer rebar separated in tension forming a longitudinal crack on the outer surface. The wall capacity in shear was then insufficient and the entire roof between splices punched through as a rigid piece. Later testing and analysis of joint sections would provide more suitable joint designs, however the trench concept would be abandoned as a basing concept before candidate designs could be evaluated.

HORIZONTAL SHELTER CONCEPT

This basing concept is essentially comprised of a series of horizontal

bermed shelters connected by a surface road network. A single vehicle per missile served to shuttle the missile between shelters as well as to erect and launch the missile (figure 13). This concept avoided the difficulties of defining in-trench environments and dealing with breakout requirements. It was carried through the concept validation phase of system development as a back-up to the trench concept in the event that the technical issues associated with the trench could not be resolved.

In general, the development of a design was a straightforward process. The two major structural uncertainties addressed during large size testing were definition of the reflected and drag loading on the structure and the evaluation of analytical methods for loading and response to support design and assessment of the structure.

The four large size tests are shown in figure 14. The tests will not be individually discussed in detail; rather, the overall results will be summarized. In addition, reference 9 describes the analysis and component testing which also supported development of this basing mode. The first three tests (S-1, S-2, S-3, figure 14) used a Dynamic Airblast Simulator (DABS) to determine reflected and drag loading waveforms for 0^{o} (head-on), 90^{o} (side-on) and 30^{o} orientations of the shelter with respect to the direction of propagation of the shockfront. The DABS is essentially a large shock tube of corrigated arch construction with a soil cover to reduce early time expansion of the simulator. This technique reproduces the shock flow and subsequently, reflection and drag effects on loading waveforms. One-sixth size instrumented shelter models were used to determine the applied loading and the fundamental response modes. This data was used to evaluate numerical

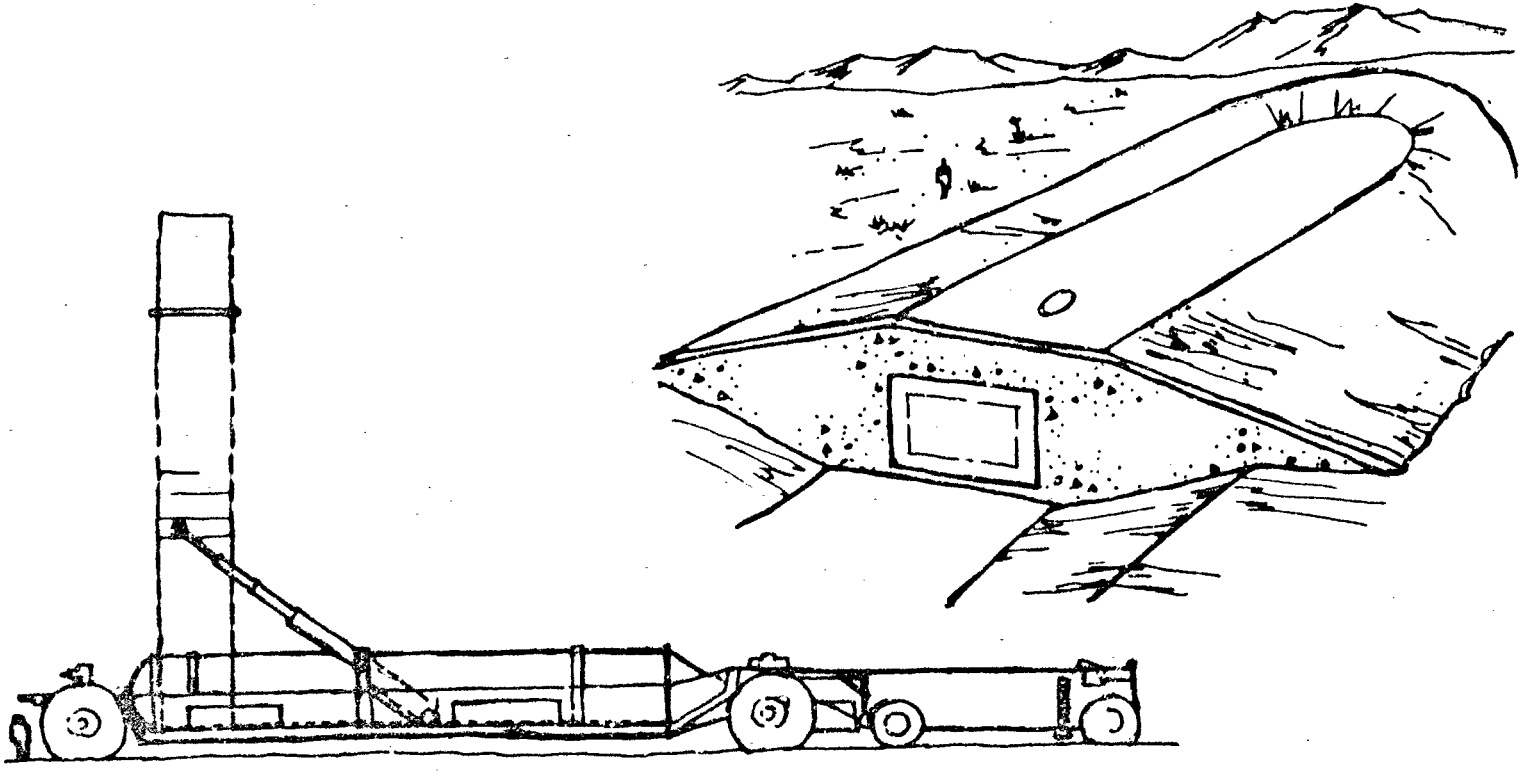

FIGURE 13. HORIZONTAL SHELTER CONCEPT

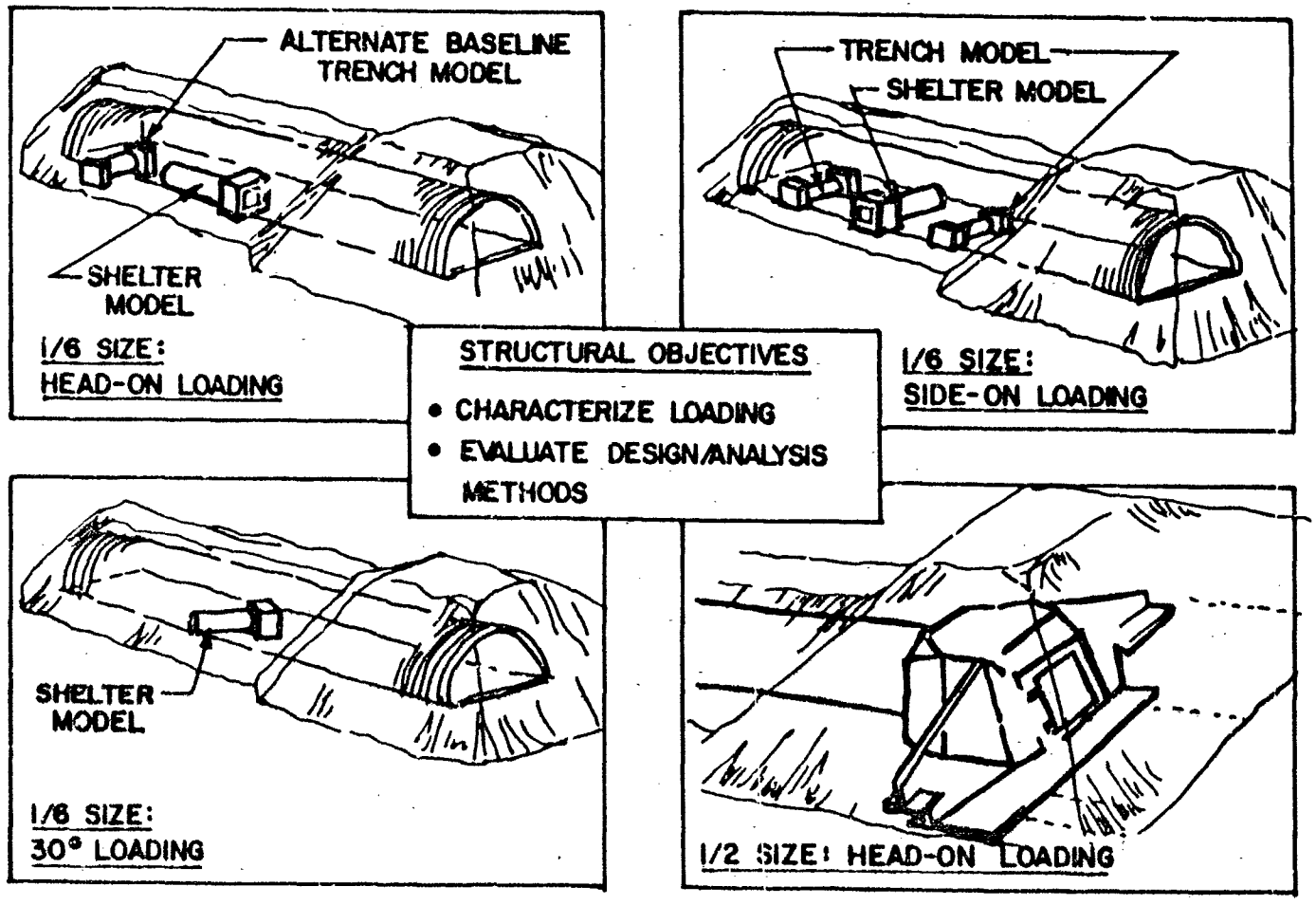

FIGURE 14. LARGE SIZE HORIZONTAL SHELTER TESTS

analysis procedures for airblast loading and for structural response. The final test (S-4) was at one-half size and contained an operational closure and bearing frame designed by the Boeing Company (reference 12). This test loaded only the forward portion of the shelter using a High Explosive Simulation Technique (HEST) to reproduce the loading wave forms defined by the earlier DABS testing and subsequent analysis. The HEST technique uses a thin cavity of explosives to reproduce a specified pressure time history. For S-4, the HEST was designed to reproduce the high pressure (30 MPa, 4400 psi) loading corresponding to reflection and drag effects of a head-on attack. The test model responded as expected with only limited compression damage where the large headworks transitioned into the smaller tube section. The closure opened easily after the test.

As a result of the first tests the headworks design was streamlined to reduce both the magnitude of loading and the surface area exposed to loading. The S-4 test demonstrated a feasible design for worst case attack conditions. The one region where design revision may have been required was the transition from the large load accumulating headworks to the much smaller tube section. Inelastic response seemed unavoidable unless the tube crossectional capacity was substantially increased. A recommended alternative was a ductile, energy absorbing connection at the front of the tube section.

VERTICAL SHELTER CONCEPT

A number of factors influenced the Air Force decision to adopt a vertically oriented shelter for MX basing. In general, the buried trench

basing mode was abandoned for both technical and political reasons. Technical concerns included not only the design issues discussed above but also uncertainty associated with the nuclear environment coupled into the trench as well as uncertainty associated with the detectability of the missile during normal operations and under a low level attack. Political concerns included cost and issues associated with public access to the basing region. The decision to adopt discrete shelters included consideration of the enhanced structural loading generated by the drag sensitive configuration of the shelter. For the dry deep alluvial valleys considered for basing, a surface flush vertical shelter design would reduce the effective peak blast loading by as much as a factor of eight and, as a result, the hardness and cost required to survive a given threat. However, one advantage of the horizontal concept was the ability to rapidly move the missile (termed a "Dash" capability), since the integral transport and launch vehicle was garaged in the shelters. For the vertical concept, the transport vehicle has to pick up the missile at one shelter and unload it at another. As the entire weapons system design evolved, the requirement for a dash capability was reevaluated and dropped. With this change in requirements the vertical shelter became the preferred basing mode.

Because the majority of the supporting equipment was designed to be incorporated into the canister containing the missile, the shelter geometry was quite simplified compared to launch facilities for the existing MINUTEMAN or TITAN missiles. An artist's concept is shown in figure 15. The major uncertainty in the design process is the longitudinal shear loading due to relative motion the soil structure interface. The only large size test of this

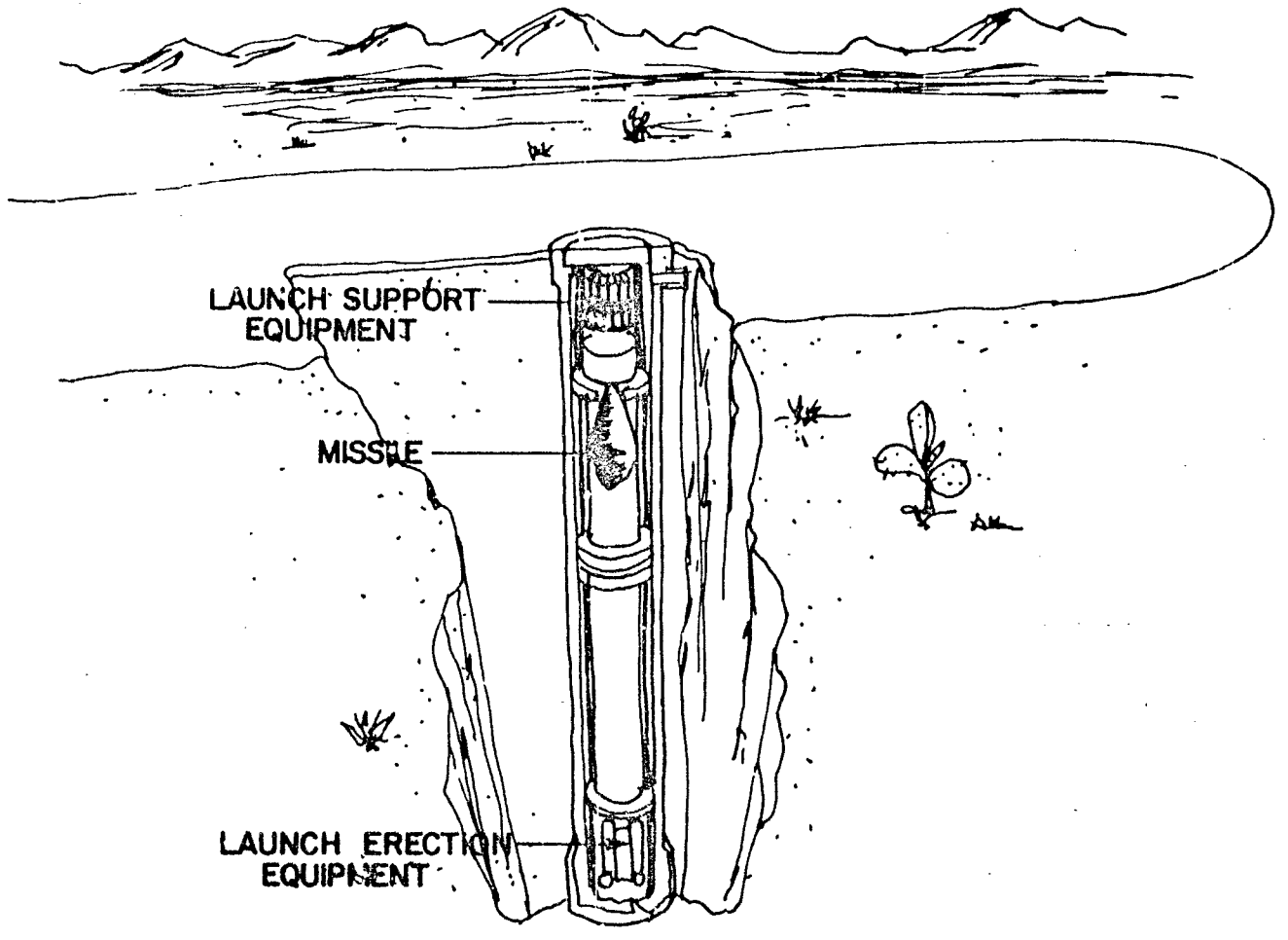

FIGURE 15. VERTICAL SHELTER CONCEPT

basing concept addressed the definition of this shear loading and the influence that it had on the structural response.

The one-third size vertical shelter test is illustrated in figure 16. Three similar models were tested, two designed to respond without significant damage and one designed to have major longitudinal compression damage in the tube wall (reference 25). The reinforcing for all models was one percent longitudinal and two percent circumferentially, at the headworks, transitioning to two-thirds percent circumferentially in the tube section. The A and B models were conventionally reinforced as was the headworks of the C model. The tube section (lower 11 m of the model) was constructed of plain concrete with reinforcing supplied by an unbonded inner steel liner. All models were cast in place against native soil.

The test was extremely successful and provided the first experimentally measured shear loading data for large cast in place structures. The structures behaved as predicted with negligible damage in B and C structures and with substantial crushing of the upper wall of the A structure reducing the overall length by 0.3 m.

The experimental measurements of normal and shear stress at the soil-structure interface were extremely difficult to obtain and there is considerable scatter in the data. The experimental transducer used is described in reference 17. Nevertheless, the basic loading behavior could be established as well as the variation in loading caused by the post-yield response of the A model. As a result of the analysis of this data and the data from associated smaller scale testing (references 8 and 5), the analytical expression for shear loading developed in the prediction report

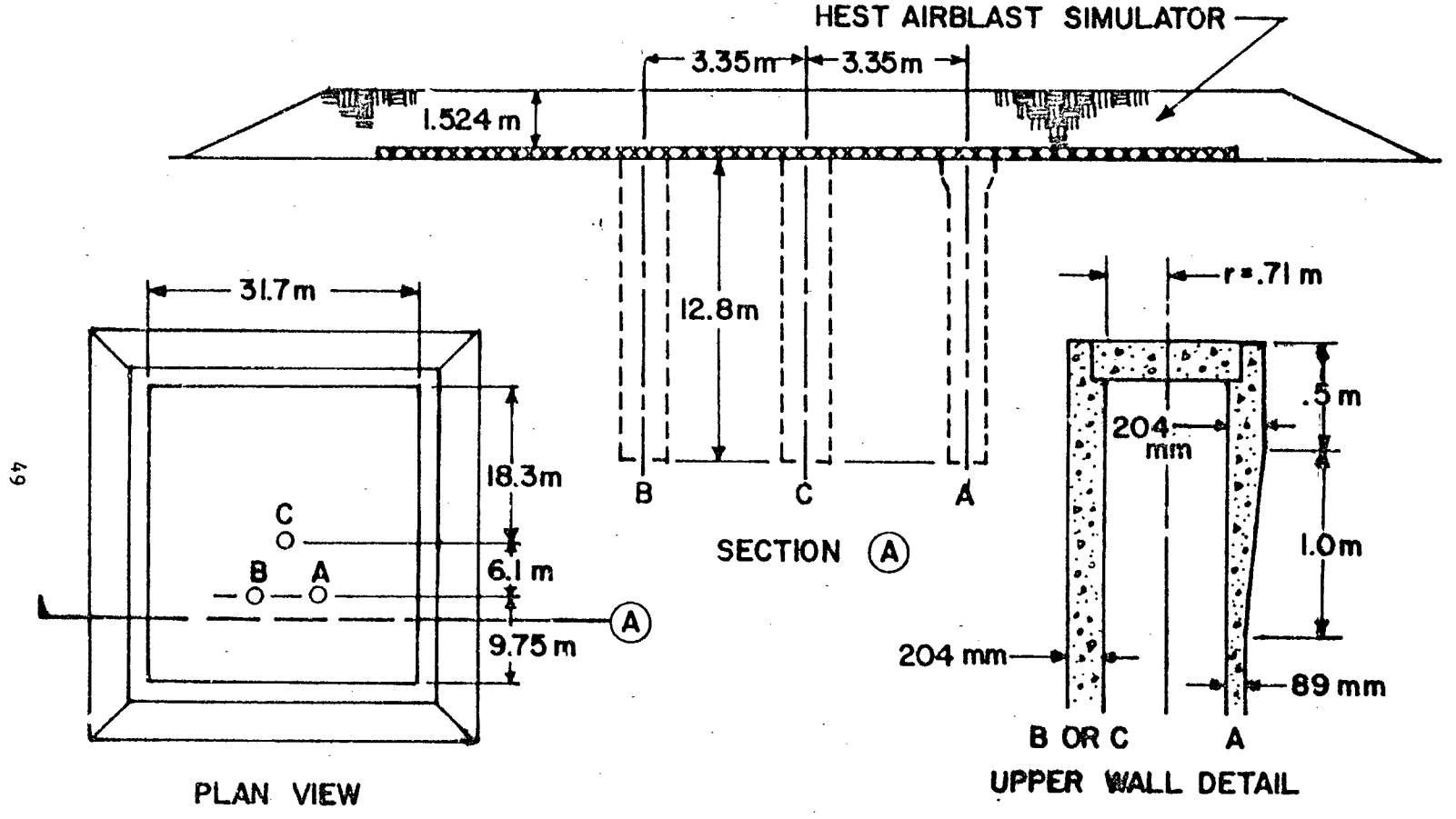

FIGURE 16. VERTICAL SHELTER TEST CONFIGURATION

(reference 25) was confirmed as adequate. The recommended formulation is:

$$\tau(t) = \rho C_s V(t); \qquad \tau(t) \leq \tau_{max}(t)$$

where: ρ = soil density

C_s = soil shear wave velocity

$V(t)$ = relative velocity at the soil-structure interface parallel to the interface

$= V_{STR}(t) - V_{SOIL}(t)$

The shear stress calculated by this formulation is limited by the shear capacity of the soil and of the interface (τ_{max}). The formulation of this failure surface is illustrated in figure 17 and represents an adaptation of an analytical and laboratory experimental study reported in reference 6. Analysis using this formulation represented the basic character of the loading observed experimentally although significant variations were observed. In general, the loading was well enough characterized to provide confident design and analysis procedures.

Considering only hardness against nuclear weapons effects, the vertical shelter clearly provided the best basing solution of the three concepts considered. However, as discussed previously a number of issues in addition to weapon effects survivability must be evaluated in the selection of a preferred basing mode. In late 1979, considerable attention was focused on Strategic Arms Limitations and verification of the number of strategic weapons was a major consideration. The Presidential decision was to adopt a Verifiable Horizontal Shelter Concept as the weapon system moved into its Full Scale Engineering Development phase.

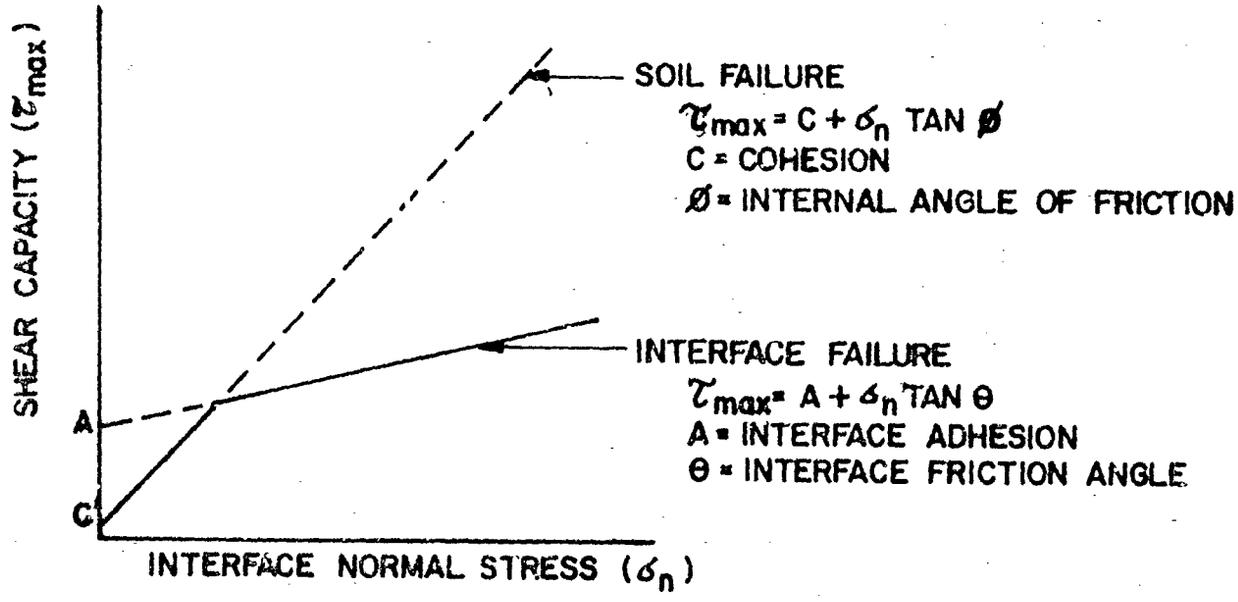

FIGURE 17. INTERFACE FAILURE SURFACE

SUMMARY

The large size testing of structural models associated with MX basing concepts played a major role in defining the expected loading and response modes. This data, in turn led to concept design revisions and was used to develop, refine and evaluate numerical analysis and assessment procedures. The large size testing was most valuable when it formed an integrated part of a combined program including structural component testing and numerical analysis. Both component test data and numerical calculations were essential for interpreting the complex behavior observed in the large size tests. In addition, the evaluation of analysis procedures provided the capability to more confidently adapt designs for siting or attack conditions not represented in the testing.

The major role of this combined testing and analysis program was to alter and refine preliminary design concepts. However, nuclear hardness and survivability considerations are only one of many factors that must be considered in selecting or changing basing concepts. The development of a modern weapons system such as MX involves committment of significant national resources and influences our national and international policy. Technical considerations as well as political, must be viewed with this perspective.

APPENDIX I - REFERENCES

1. Belytschko, T., and Chiapetta, R. L., A Computer Code for Dynamic Stress Analysis of Media-Structure Problems with Nonlinearities (SAMSON), AFWL-TR-72-104, Air Force Weapons Laboratory, Kirtland AFB, NM, Feb 1973.

2. Bennett, B.W., "How to Assess the Survivability of U.S. ICBM's," R-2577-FF-R-2578-FF, Rand Corporation, Santa Monica, CA, Jun 1980.

3. Bradshaw, J.C., "MX Trench Validation 90-day Study," Nuclear Technology Digest, AFWL-TR-78-110, Air Force Weapons Laboratory, Kirtland AFB, NM, Aug 1978.

4. Gagnon, L., Reason, J., and Click, F., Plug in Trench Simulation (PITS-1), AFWL-TR-78-145, Air Force Weapons Laboratory, Kirtland AFB, NM, May 1979.

5. Gran, J and Bruce, J., Small Scale Tests of MX Vertical Shelter Structures, SRI project 8176, SRI International, Menlo Park, CA, Apr 1980.

6. Huck, P., et al, Dynamic Response of Soil/Concrete Interfaces at High Pressure, AFWL-TR-73-264, Air Force Weapons Laboratory, Kirtland AFB, NM, Apr 1974.

7. Landon, G., et al, Dynamic Side-on Trench (DSOT) Tests, AFWL-TR-79-201, Air Force Weapons Laboratory, Kirtland AFB, NM, Nov 1979.

8. Landon, G., et al, Giant Reusable Airblast Simulator (GRABS) on Vertical Shelters (GOVS), AFWL-TR-80-157, Air Force Weapons Laboratory, Kirtland AFB, NM, May 1981.

9. Ma, C., et al, C-6 Wrap-up Study on Missile X Shelter Concept, AFWL-TR-79-23, Air Force Weapons Laboratory, Kirtland AFB, NM, Dec 1979.

10. Marquis, J.P., Static Trench/Plug Interaction Tests, AFWL-TR-79-8, Air Force Weapons Laboratory, Kirtland AFB, NM, Sep 1979.

11. Marquis, J.P., Dynamic Trench/Plug Interaction Tests, AFWL-TR-79-119, Air Force Weapons Laboratory, Kirtland AFB, NM, May 1980.

12. McNickle, P., et al, HAVE HOST Shelter Pretest Prediction and Quick-Look Report S-4, AFWL-TR-79-114, Vol IV, Air Force Weapons Laboratory, Kirtland AFB, NM, Feb 1981.

13. Morrison, D., et al, Analysis of HAVE HOST Event T-1, AFWL-TR-78-30, Air Force Weapons Laboratory, Kirtland AFB, NM, Jun 1979.

14. Morrison, D., et al, Analysis of HAVE HOST Event T-2, AFWL-TR-78-112, Air Force Weapons Laboratory, Kirtland AFB, NM, JUN 1979.

15. Morrison, D., et al, Analysis of HAVE HOST Event T-3, AFWL-TR-79-153, Air Force Weapons Laboratory, Kirtland AFB, NM, Sep 1980.

16. Morrison, D., and Bevacqua, M., Analysis of HAVE HOST Event T-5, AFWL-TR-80-84, Air Force Weapons Laboratory, Kirtland AFB, NM, Dec 1980.

17. Pickett, S., Development and Evaluation of a Triaxial Interface Stress Transducer, AFWL-TR-77-90, Air Force Weapons Laboratory, Kirtland AFB, NM, Aug 1977.

18. , Building Code Requirements for Reinforced Concrete (ACI 318-77), American Concrete Institute, Detroit Mich, Dec 1977.

19. , CONSTRUCTION JOINT TEST PROGRAM (FINAL REPORT), Karagozian and Case Structural Engineers, Los Angeles, CA, Jan 1973.

20. , HAVE HOST Trench Pretest Prediction and Quick-Look Report, Vol I, Event T-1, AFWL-TR-79-60, Vol I, Air Force Weapons Laboratory, Kirtland AFB, NM, Nov 1979.

21. , HAVE HOST Shelter Pretest Prediction and Quick-Look Report, Vol II, S-2 Event, AFWL-TR-79-114, Vol II, Air Force Weapons Laboratory, Kirtland AFB, NM, Mar 1980.

22. , HAVE HOST Trench Pretest Prediction and Quick-Look Report, Vol II, Event T-2, AFWL-TR-79-60, Air Force Weapons Laboratory, Kirtland AFB, NM, Jun 1980.

23. , HAVE HOST Trench Pretest Prediction and Quick-Look Report, Vol III, Event T-3, AFWL-TR-79-60, Vol III, Air Force Weapons Laboratory, Kirtland AFB, NM, Aug 1980.

24. , HAVE HOST Trench Pretest Prediction and Quick-Look Report, Vol IV, Event T-5, AFWL-TR-79-60, Vol IV, Air Force Weapons Laboratory, Kirtland AFB, NM, Mar 81.

25. , HAVE HOST Phase III, Vertical Shelter Test (VST) Pretest Prediction and Quick-Look Report, AFWL-TR-81-56, Air Force Weapons Laboratory, Kirtland AFB, NM, Aug 1981.

26. , A Review of MX Trench Testing Requirements, Headquarters, Defense Nuclear Agency, Washington, DC, Nov 1977.

27. , SALT II Agreement, Vienna, Jun 18, 1979, Department of State Publication 8984, General Foreign Policy Series 316, U.S. Government Printing Office, Washington, DC, 20402, (Stock Number 044-000-01749-1).

28. , SALT II and American Security, Revised Edition, Jun 1979, U.S. Government Printing Office, Washington, DC, 20402, (Stock Number 044-000-01744-0).

29. , "Special Report: Modernizing Strategic Forces," Aviation Week and Space Technology, Vol 112, No. 24, Jun 16, 1980, pp 56-290.

1/5 SIZE VHS SERIES BLAST AND SHOCK SIMULATIONS

By Michael L. Noble[1]

INTRODUCTION

A high explosive test series was conducted in 1981 to evaluate the respective performance of simulation techniques for Blast and Shock environments. Two tests were conducted on a 1/5 size Verifiable Horizontal Shelter (VHS) in the Multiple Protective Shelter (MPS) configuration. The purpose of the 1/5 size tests was to compare the effectiveness of a Shaped High Explosive Simulation Technique (HEST) to the Dynamic Airblast (DABS) technique for Blast and Shock effects simulation through the response of the test structure before proceeding to the first full size test on an MX prototype horizontal shelter. The nuclear airblast simulation environment was produced in the D-1 test through the DABS technique in which, the dynamic blast interacted with the target's geometry. The resultant pressure loads were reproduced by a multipressure-zoned HEST in the SH-1 test. A HEST characteristically produces a waveform without the physics that occur due to diffracted and reflected shocks. The simulation objective of the 1/5 VHS test series was to demonstrate the capability of a High Explosive Simulation Technique (HEST) simulator to adequately duplicate the test structure's input loads. This paper will highlight the simulation aspects of the 1/5 VHS test series. The discussion will focus primarily on the comparisons of the two simulator's loading waveforms.

[1]Chief, Effects Simulation Section, Weapons Effects Branch, Civil Engineering Research Division, Air Force Weapons Laboratory, Kirtland Air Force Base, Albuquerque, New Mexico

BACKGROUND

Defense requirements for the simulation of nuclear weapons effects were recognized when the Limited Nuclear Test Ban Treaty was signed in the fall of 1963. Specifically, the Nuclear Hardness and Survivability (NH&S) criteria and assessment tasks were initiated in designing and testing military structures to withstand severe nuclear environments. Development of Blast and Shock simulation techniques for testing defense structures ensued. The Air Force Weapons Laboratory (AFWL) has maintained an ongoing research and development program to meet the NH&S needs of present and future defense systems. In the absence of nuclear blast effects data to determine a system's response, simulation tests using conventional explosives are performed. Two of the most successful for simulating nuclear airblast effects are the Dynamic Airblast Simulator (DABS) and the High Explosive Simulation Technique (HEST).

DABS

The DABS is basically a large expendable shock tube. The explosive driver chamber contains an explosive charge array placed against the rear wall of either steel plate or concrete. The driver's chamber is lined with a steel plate to minimize the amount of debris thrown into the shock-induced flow by the explosion. Upon explosive driver initiation the hot gases flow down the tube forming a shock wave in the air of the tunnel. The tunnel section confines the shock wave. The wave propagates down the tube to the target section where the test structural model is subjected to the specified waveform. A tube runout section is normally required past the target to prevent the post shock rarefactions from limiting the simulation time of the air shock's positive phase. A DABS can be constructed in several cross-sectional configurations, preferably, either a full circle or hemicylinder tube.[1]

HEST

The typical HEST consists of explosives arranged within a planar cavity of air or foam which is confined by soil overburden. The target section (structure) is placed in the ground, either surface flush at the bottom face of the cavity or buried in the test bed. The explosive array can be initiated either simultaneously or sequentially. Initiation in the vertical direction will produce a near-instantaneous spike while horizontal initiation will produce a sweeping wave. Either can be tuned to achieve the appropriate loading signature required on the test structure. Also, the distribution of explosives within the cavity can be varied for the specified pressure profile loading effect. The overburden covering the explosion cavity serves as a tamping agent to contain the high-pressure gases created by the explosives and to tailor the simulation time of the experiment. A HEST can be constructed in any size or pattern necessary to obtain the desired simulation.[1]

Originally conceived, the HEST was not thought to be useful for test articles sensitive to dynamic pressure loads associated with the flow behind a nuclear shock front. However, the 1/5 VHS test series work has shown not only the feasibility but the application of using the blast overpressure from a specially designed HEST to approximate the dynamic and reflected shock loading on above ground structures. If the structural loads are known for a particular dynamic airblast environment, either from calculations or from previous experiments, a HEST can be designed to reproduce those loads. The nuclear airblast simulator used in the SH-1 test was a recently developed variation of the High Explosive Simulation Technique (HEST) which has been used in the past. The variation, called "Shaped-HEST," presumes knowledge of the airblast waveform which is to be applied in several regions on and about the target structure.

HEST simulators possess a distinct cost advantage over other nuclear airblast simulation techniques such as, free-air conventional explosives or the Dynamic Airblast Simulator (DABS). HEST is at least an order of magnitude cheaper than these other methods, but one must be willing to accept the dominant nonsimulation effects. A HEST is designed to generate nuclear shock-front overpressures without the dynamic winds normally associated with shock propagation. Therefore, it is not possible to use the HEST in examining the shock flow phenomenology of shock interactions with structures. Once again, if through previous tests or calculations, the dynamic airblast loading can be specified, then the HEST may be used to simulate this loading just as though it was an incident overpressure. The airblast waveforms, which were applied in designing the multizone SH-1 test, were established using data from the D-1 test's loads and earlier DABS developmental tests

TEST SERIES CRITERIA

The Blast and Shock environment was formulated to be consistent with the NH&S validation objectives for a one-on-two surface burst attack on a shelter spacing of 1585 m (5200 ft). The airblast loading objective at the structure closure (door) was 3 MPa from a 24 KT surface burst, equivalent to a 3 MT yield at full scale. The test structure was located at a 50 degree aspect angle to the airblast which is consistent with an attack scenario for the MPS basing geometry. D-1 pretest analysis projected that the region of the first Stragegic Arms Limitation Talks (SALT) verification port had the highest susceptibility for deformation. As a result, both simulators and testbed designs focused on providing the longest simulation at that point. Simulation time for the events corresponded to the projected time span required to achieve peak ovaling response at the first SALT port location. This criteria set the simulation time at 16 ms. The first ground shock

relief effects originate at each simulator's boundaries. The first SALT port, located near the center of the testbeds, is the last to receive these relief effects. The SH-1 simulator size was chosen on the basis of shear wave propagation velocities, a dominant factor in non-simulation relief wave interactions.[2]

TEST SERIES OBJECTIVES

The test series was planned to yield data required to meet the following composite objectives: (1) Determine location, distribution, magnitude and duration of loads on a generic MX horizontal shelter design; (2) Evaluate localized effects on loading and response due to the incorporated baseline structural details. The details incorporated in the test article are: two SALT verification ports, a closure transition area with a hinge mass region, and the cylinder with a single rebar cage and steel liner; (3) Evaluate analytical techniques for hardness design procedures; (4) Evaluate a Shaped-HEST as a technically viable alternate simulator to the DABS technique. The fourth objective is the thrust of this paper.[2]

TEST CONSTRUCTION

D-1 Simulator Facility

The D-1 DABS facility, shown in Figure 1, is the largest of its type to date. The facility was constructed using commercially available double-corrugated metal arch sections to achieve a span of 17.4 m, a rise of 7.72 m and a length of 60 m. The driver end of the facility was closed off by a cast-in-place reinforced concrete wall 0.6 m thick. To prevent the explosives from cratering and injecting debris into the flow, a steel plate covered a concrete floorpad extending over the entire width of the facility and to a downstream range of 6.1 m. Additionally, a 0.3 m thick layer of concrete was cast over the steel arch to a range of 6.0 m.

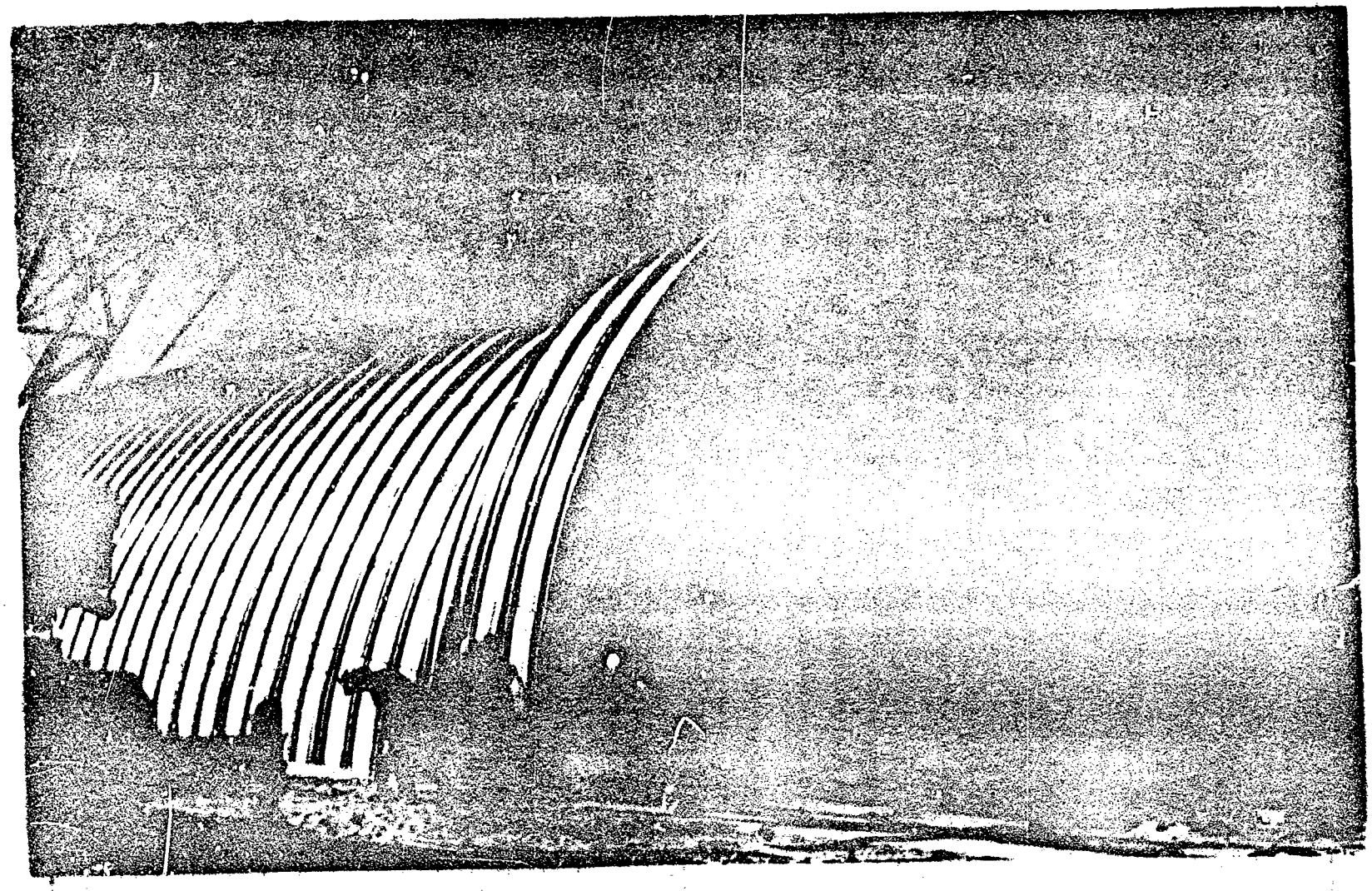

Figure 1. D-1 DABS Facility

The D-1 explosive charge consisted of Iretol 30T27-C blocks, a castable TNT-sensitized AN (ammonium-nitrate) slurry explosive. The blocks were uniformly distributed over the endwall of the DABS facility (Figure 2). Each block weighed approximately 20 kg and was initiated by a Pentolite booster and by a length of detonating cord. The charge array was initiated simultaneously by a three-dimensional array of 54-grain detonating cord which branched out from two initiation points in front of the explosives to achieve a near simultaneous detonation of each charge. Redundancy in the detonating cord array was provided to insure reliability of initiation. Unconsolidated soil overburden was placed over the arch and outside the concrete endwall. This overburden was designed to provide confinement during the 16 ms simulation time, but also to allow the entire facility to blow out and away from the testbed after completion of the simulation (t_s>100 ms). To facilitate this process of facility expansion and overburden dispersal, the base of the arch was attached to a concrete footing to provide lateral restraint and to provide a hinge for rotation. Additionally, a minimum of 1 m overburden depth was placed over the crown with increasing depths progressing down the side to provide maximum velocity near the top and to cause rotation of the arch and overburden around the hinge at the base. Typical behavior of the simulator facility is for most of the overburden and arch materials to be thrown clear of the testbed. The arch and overburden did not disperse as well as desired, but this had no effect on the overall simulator performance.[3]

SH-1 Simulator Facility

The SH-1 simulator was constructed with polystyrene beaded foam, cord type explosives and soil overburden. The testbed's planar dimensions were 26.5 m by 25.6 m. The foam for the SH-1 test had a density of .016 gms/cm^3 (1.0 lbs/ft^3)

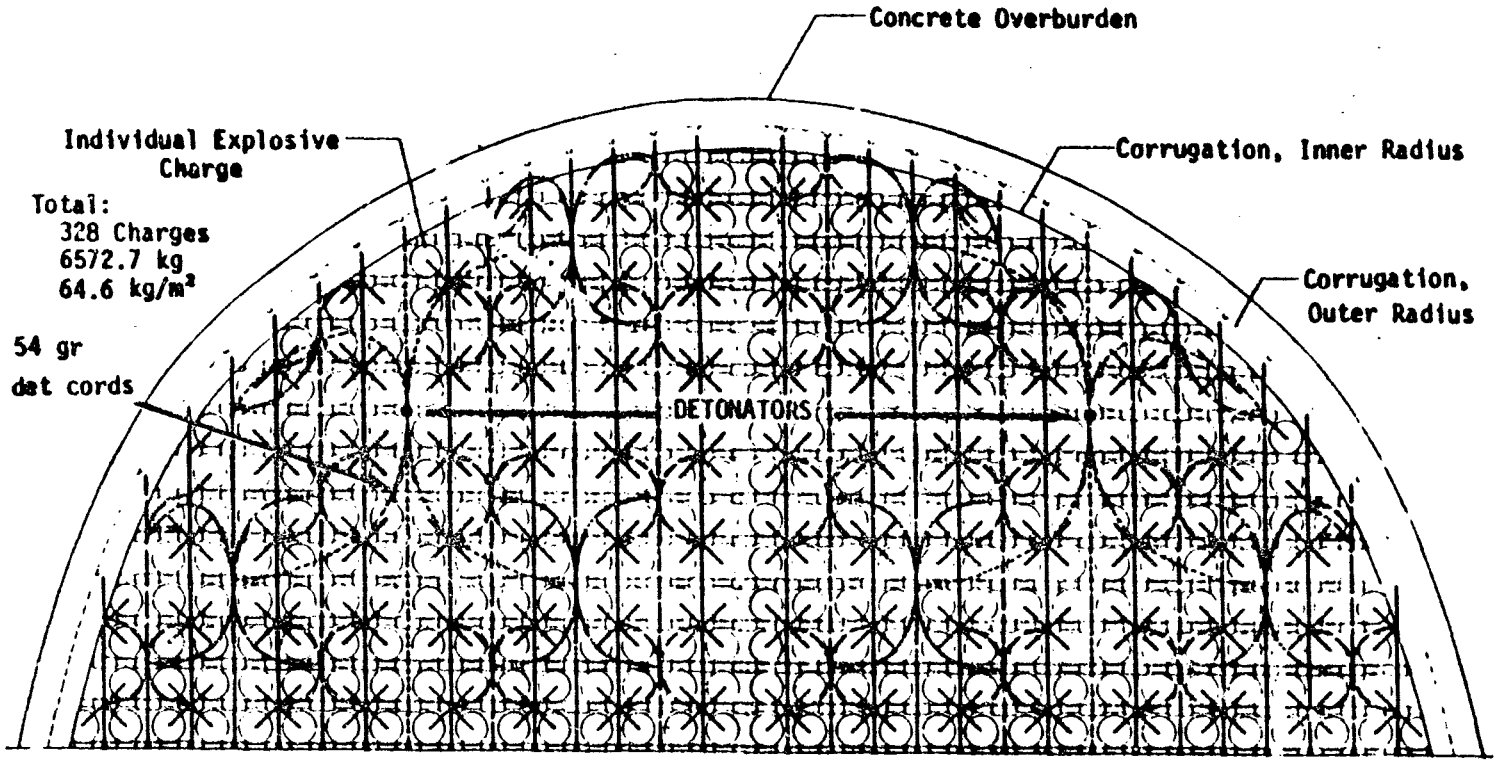

Figure 2. D-1 DABS explosive charge with detonating cord initiation system.

while the 1.3 m native soil overburden had a nominal dry density of 1.76 gms/cm^3 (110 lbs/ft^3). The test used a 100% foam structure to form each HEST cavity zone. This construction structure provides for both the maintenance of the proper explosive charge dimensions and for supporting the overburden. Figure 3 shows a testbed detail of the SH-1 simulator during construction. The explosive charge was constructed using 400-grain PETN detonating cord. Zones 1, 2, 3 and 4 were preassembled and placed on the testbed. Zones 8-1, 8-2, 5 and 6 were fabricated in place as shown in Figure 3. The major zones' primary timing system was through edge timing with the tie-zone concept for interior zones. The tie zones interconnect splices, used to ensure timing continuity across zones 8-1, 8-2, 5 and 6, were preassembled and placed on the testbed prior to assembly of the major zones. The tie-zones' foam panels were grooved to accept both the primary detonating cord and the redundant firing system.[4]

The SH-1 simulator consisted of eight separate representative HEST zones (Figure 4), each with a specific peak overpressure and airblast waveform. Each zone has the same environment in terms of peak pressure and decay over its entire area, with the exception of zone 4. Zones 8-1 and 8-2, both identical in design, were intended to simulate the free field airblast from a 24 KT nuclear explosion at the 3 MPa overpressure range through the use of the Brode nuclear equation. Zone 4, located along the headwall and closure of the test structure, contained the low pressure and high pressure cavity designed to produce the flow-resultant double peak waveform. All the nearfield zones were designed to produce a specified overpressure and waveform defined in D-1 loads data. Each sloped region on the D-1 testbed had a different pressure time history resulting from the dynamic component of the flow.[4]

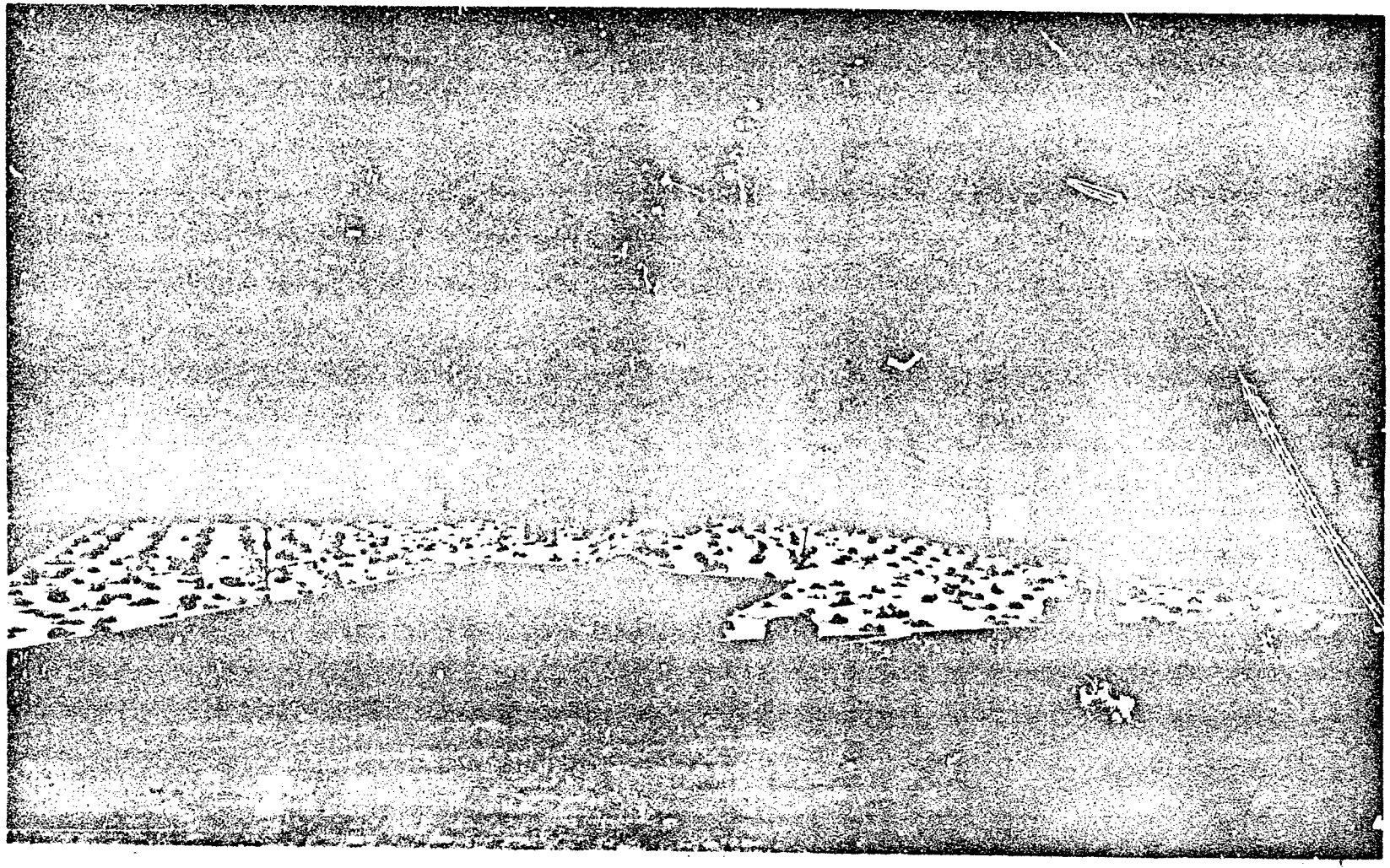

Figure 3. SH-1 Testbed.

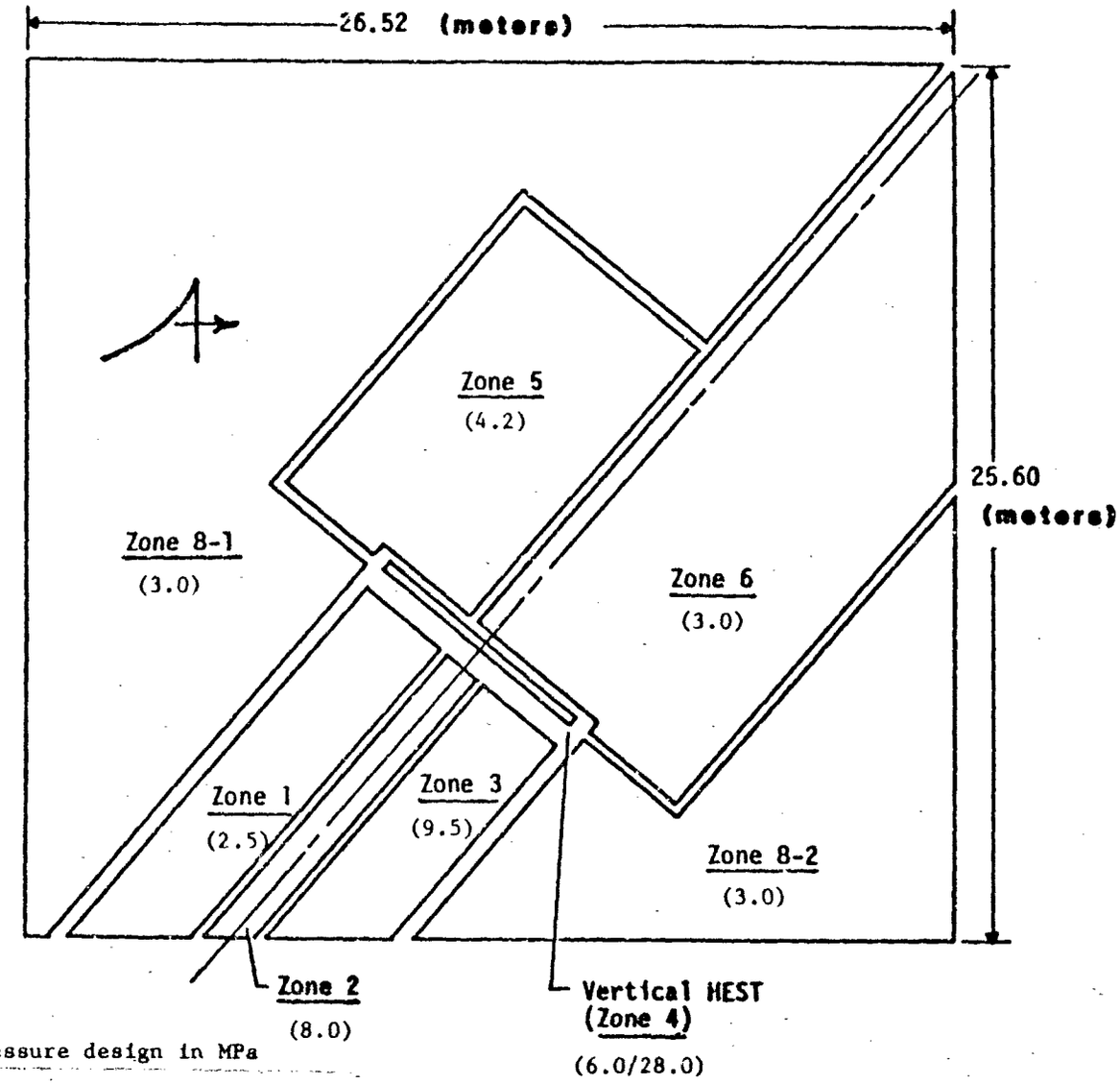

( )Overpressure design in MPa

Figure 4. SH-1 testbed plan view.

SIMULATOR INSTRUMENTATION

The instrumentation fielded to assess the airblast simulation consisted of piezoelectric crystals, blast pressure gages, and photopoles. The crystals measured time of arrival (TOA) of the blast wave at various simulator locations for determining the velocity and planarity. Blast pressure gages were installed both direct and side-on to the blast wave to measure the overpressure waveforms at various locations across each testbed. Locations of near field and structural gages were essentially the same for both tests. A comparison of diagnostic (pressure) gage locations between D-1 and SH-1 is shown in Figure 5. The photopoles in SH-1 served to provide impulse histories for each zone. The velocities of these poles when combined with the density and thickness of the overburden are indicative of the impulse in each HEST zone and provide a means of assessing the HEST cavity performance.

AIRBLAST EFFECTS

The D-1 test provided the baseline data for the test series airblast effects associated with the shelter's configuration. The MPS configuration geometry had significant affects upon the nominal 3 MPa targeted overpressure environment. Primary differential loading factors were the 50 degree aspect angle, the shelter's berm exposure, the driveway cut and the headwall profile.

Headwall Shock Dynamics

The shock front reached the entry point into the driveway ramp prior to reaching the structure's closure. The blast began to move down the ramp, across the driveway and up the opposite side. Upon impact with the ramp on the opposite side, a reflected shock was generated and moved along that side ramp towards the structure.

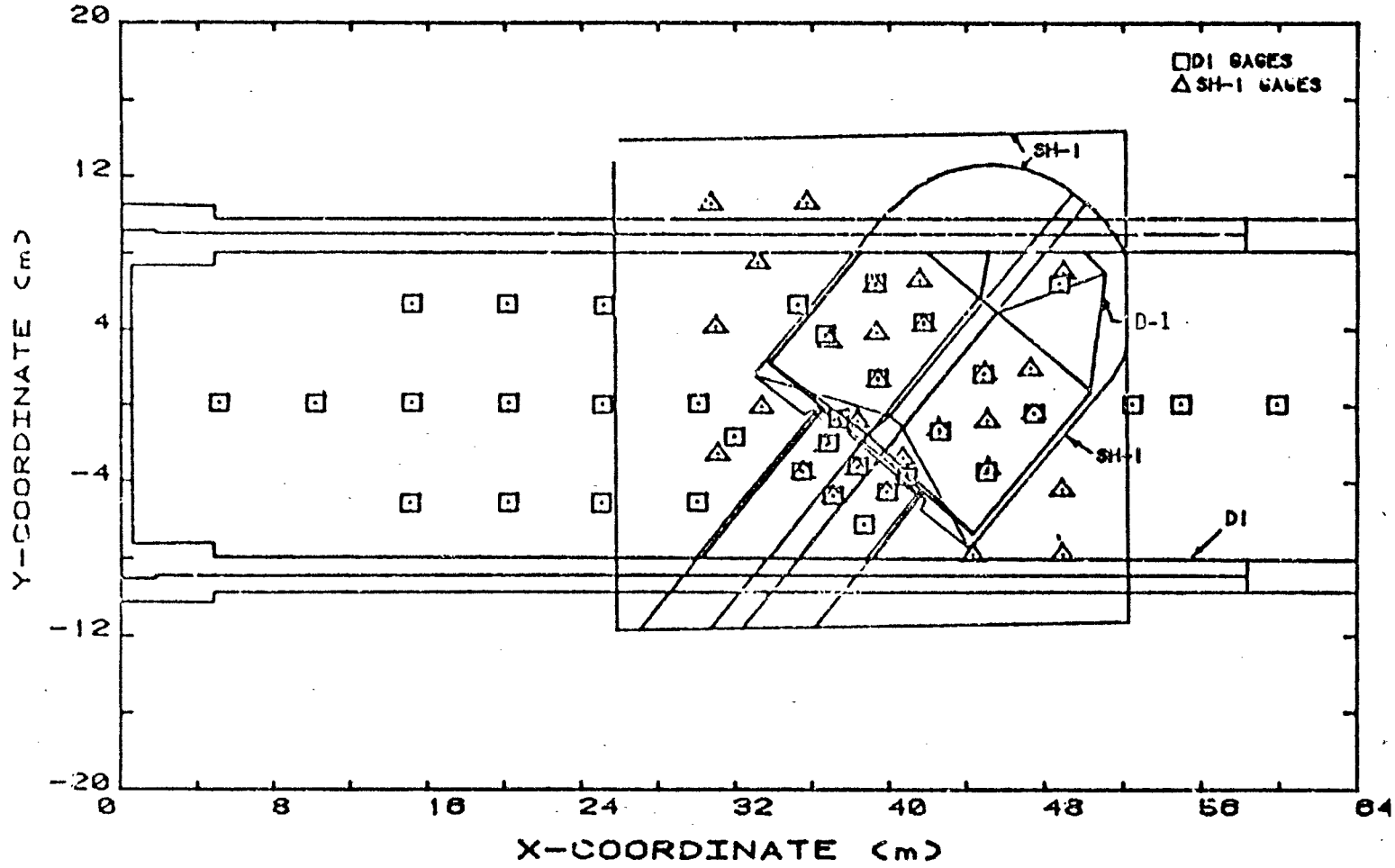

Figure 5. SH-1 and D-1 plan view gage comparison.

Meanwhile, the main shock front encountered the front face of the headwall and began moving across it. These two shock systems collided near the face of the structure near the y = -2 m structure coordinate (Figure 6). This shock collision spawned a large reflected shock which accounts for the 27 MPa peak pressure observed at the y = -2 m range and the other high pressures in that headwall region.[3] This strong reflected shock is similar to what would be expected from a nuclear airblast loading at the 50 degree aspect angle for a 3 MPa overpressure. In general, the airblast pressures on the headwall and closure were higher on the downstream side (right) compared to those upstream.

Berm Area Dynamics

Overpressure waveforms measured as the blast wave passed over the shelter model are shown in Figure 7. Pressures along the upstream side of the berm are approximately 20 percent higher than along the downstream side. The airblast arrived at the first airblast gage on the upstream berm at 16 ms and then swept over the berm traveling at 1900 m/s. The airblast moved from this gage to the last near-field gage in about 5 ms. Figure 7 shows the locations and waveforms of several airblast measurements on the berms and the driveway of the structure. At axial distances of several meters behind the headwall, the vertical overpressure on the upstream berm (left) was higher than the downstream. The peak overpressures on the headwall and door varied (from left to right) from about 6 MPa to 11 MPa. Except for the region within approximately a meter of the headwall, peak overpressures on the upstream berm were about 4 MPa $\pm$ 0.4 MPa while peak overpressures on the downstream (right) berm were about 3.1 to 3.5 MPa.[3]

COMPARATIVE ANALYSIS

Scope

Replication of the preceeding D-1 headwall and berm areas airblast loading effects were the goals in the SH-1 HEST test. A principal feature of the SH-1

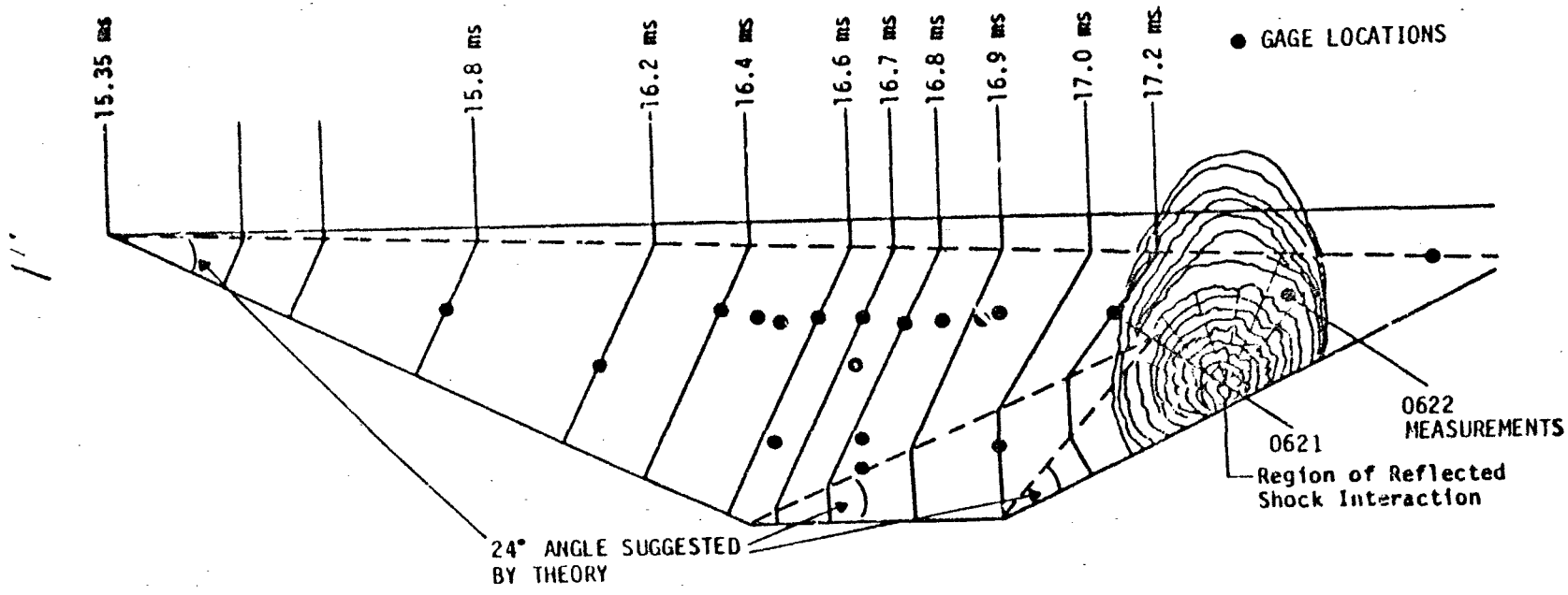

Figure 6. Sweeping shock wave and focus point on D-1 headwall.

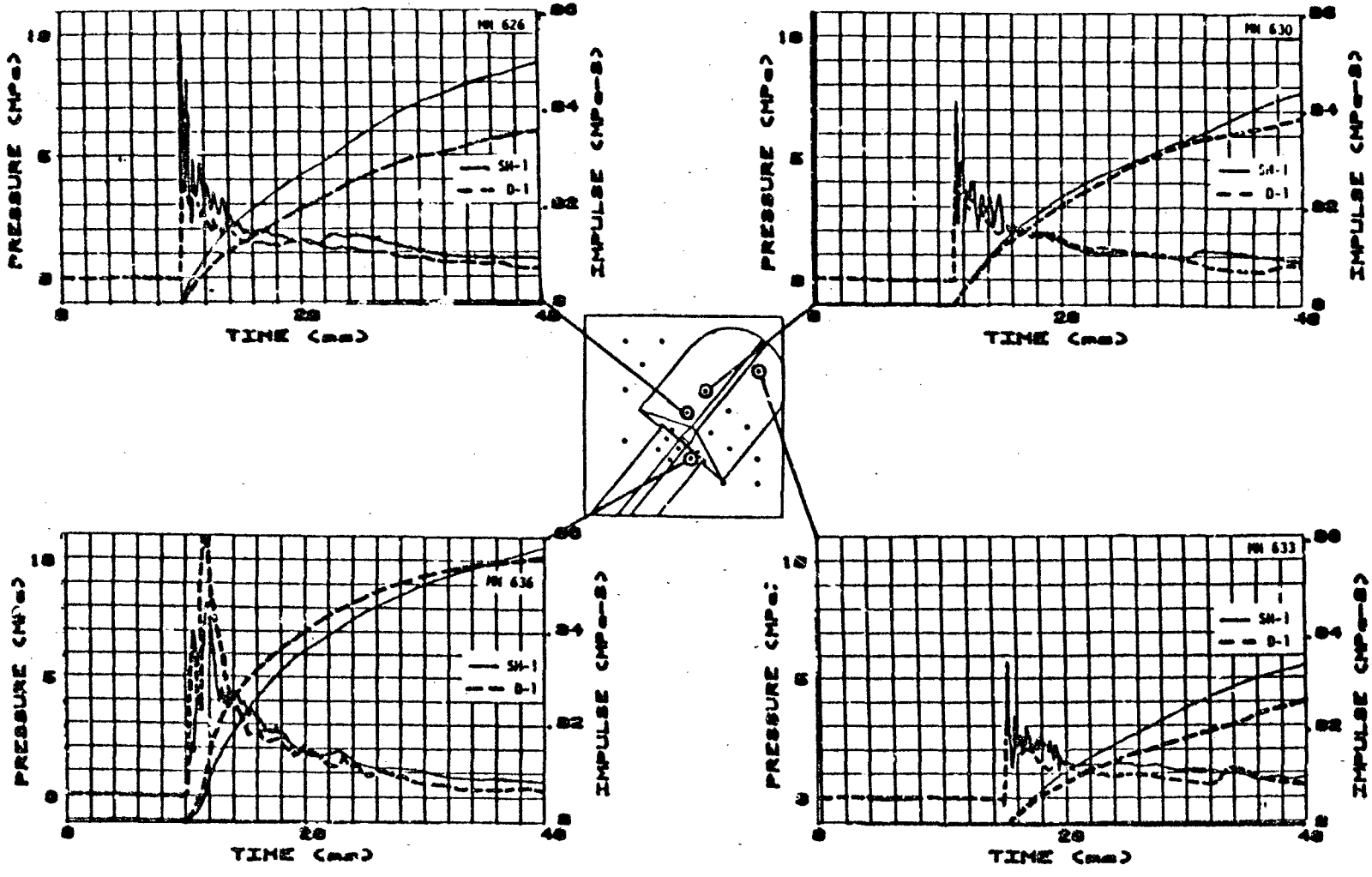

Figure 7. SH-1 to D-i pressure and impulse comparison.

simulator design was the requirement to produce the double peak waveform across the headwall and closure face. This was accomplished by using a HEST (zone 4) designed to produce a low pressure region and a high pressure region, both within the same cavity. The detonation of the explosives in the low pressure region produced a working gas through which secondary shocks could propagate. Upon detonation of the high pressure region a secondary shock propagated back through the low pressure region creating the second peak and the desired waveform.

A redundant zone-interconnecting and timing system was used to ensure the proper propagation rate of the shock front across each region and from one region to the other. The SH-1 simulator timing was a critical simulation feature. In order to be completely successful, all zones must fire at the proper time and sweep at the required rate. The detonating front in each zone was designed to travel at the free-field nuclear velocity 1684 m/s (5525 ft/s) and at a direction of 50 degrees to the longitudinal axis of the structure. The blast wave's propagation timing the various zones in SH-1 was done externally and does not result from flow, except as stated in the secondary wave of zone 4. The near-field zones were designed to produce the peak effective pressures resulting from the blast flow dynamics with the berm. The pressures were normalized in the areas shown in Figure 4.

Headwall and Closure

The times of arrival of the blast wave propagating across the headwall and face of the structural model are shown in Figure 8 along with the arrival times for the second pulse which travels back across the face and headwall. The primary blast wave traveled across the headwall at approximately 2486 m/s, which was slightly faster than the 2424 m/s predicted value. The second pulse caused by the high pressure region in zone 4 traveled back across the headwall at approximately 630 m/s. The SH-1 value was slower than the 850 m/s rate observed in the D-1

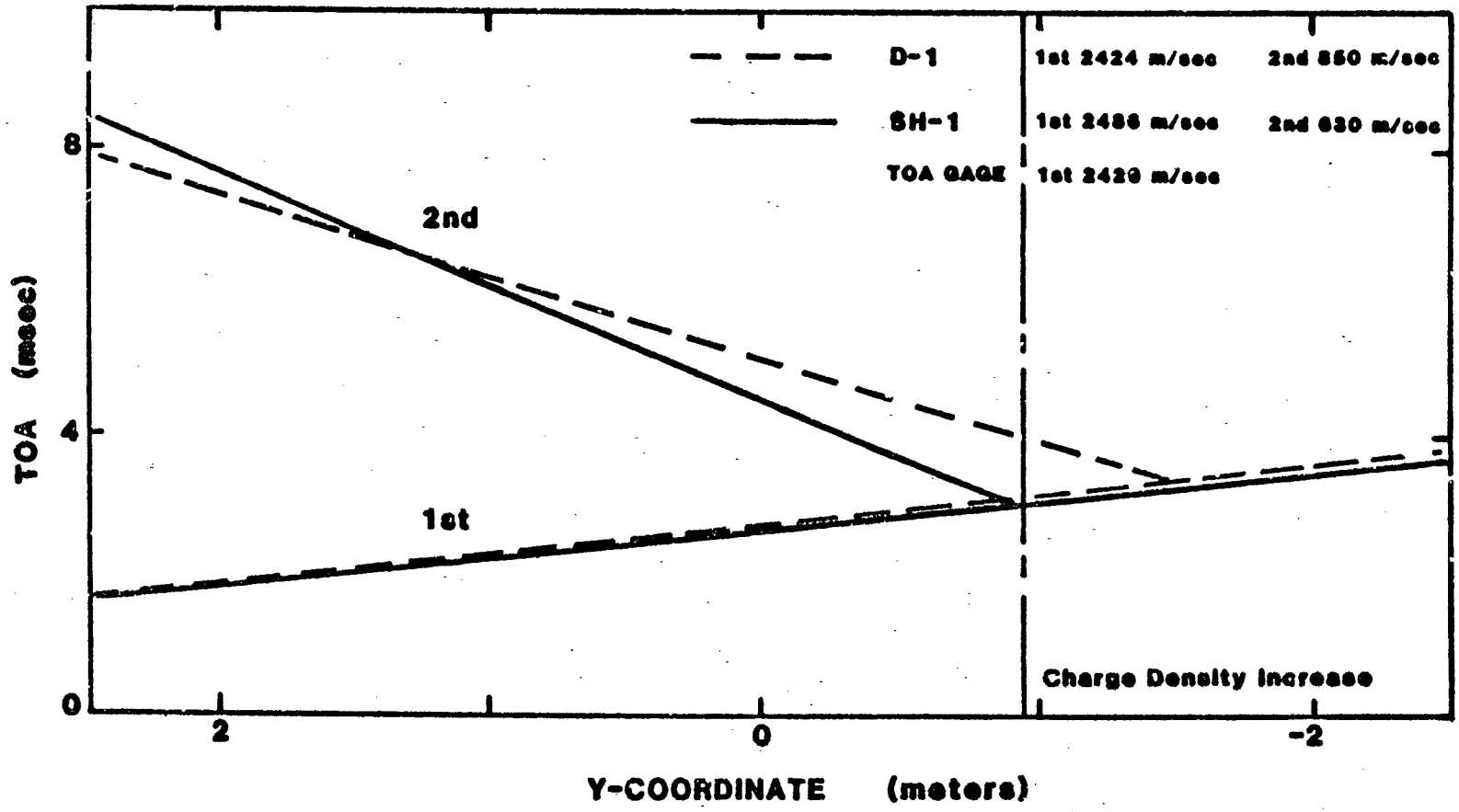

Figure 8. Wave Propagation on headwall.

test. The second shock in SH-1 propagated through a gas composed of detonation products and vaporized foam rather than air, which accounts for its rate being slower than that observed in D-1. The blast overpressure waveforms measured at selected locations across the headwall and closure are shown in Figures 9, 10 and 11. The single peak waveform over the downstream high pressure region and the double peak waveform over the upstream low pressure region are clearly observable. Waveforms measured at comparable locations in the D-1 test are overdrawn on the SH-1 waveforms. Values for peak simulation pressure (PP_S) and for the second peak were plotted as a function of the y-coordinate across the headwall and face of the structure in Figure 12. Smooth curves were visually fitted through the data and corresponding data for D-1 were also included. PP_S in the low pressure region of zone 4 (upstream headwall) was approximately 9.5 MPa for SH-1 as compared to 6.5 MPa for D-1. In the high pressure region of zone 4 (downstream headwall) the PP_S was approximately 34 MPa in SH-1 as compared to 27 MPa for D-1.[5]

Free-Field and Berm (Testbed)

The blast overpressure waveforms at selected locations across the SH-1 testbed are shown in Figure 13 with comparisons of the associated Brode waveforms. Although the front end spikes and oscillations typical of a HEST are present, the waveforms produced agree well. The free-field overpressure is estimated to be 3.5 MPa and yield to be 24 KT, slightly higher than the 3 MPa, 24 KT design goal.[5]

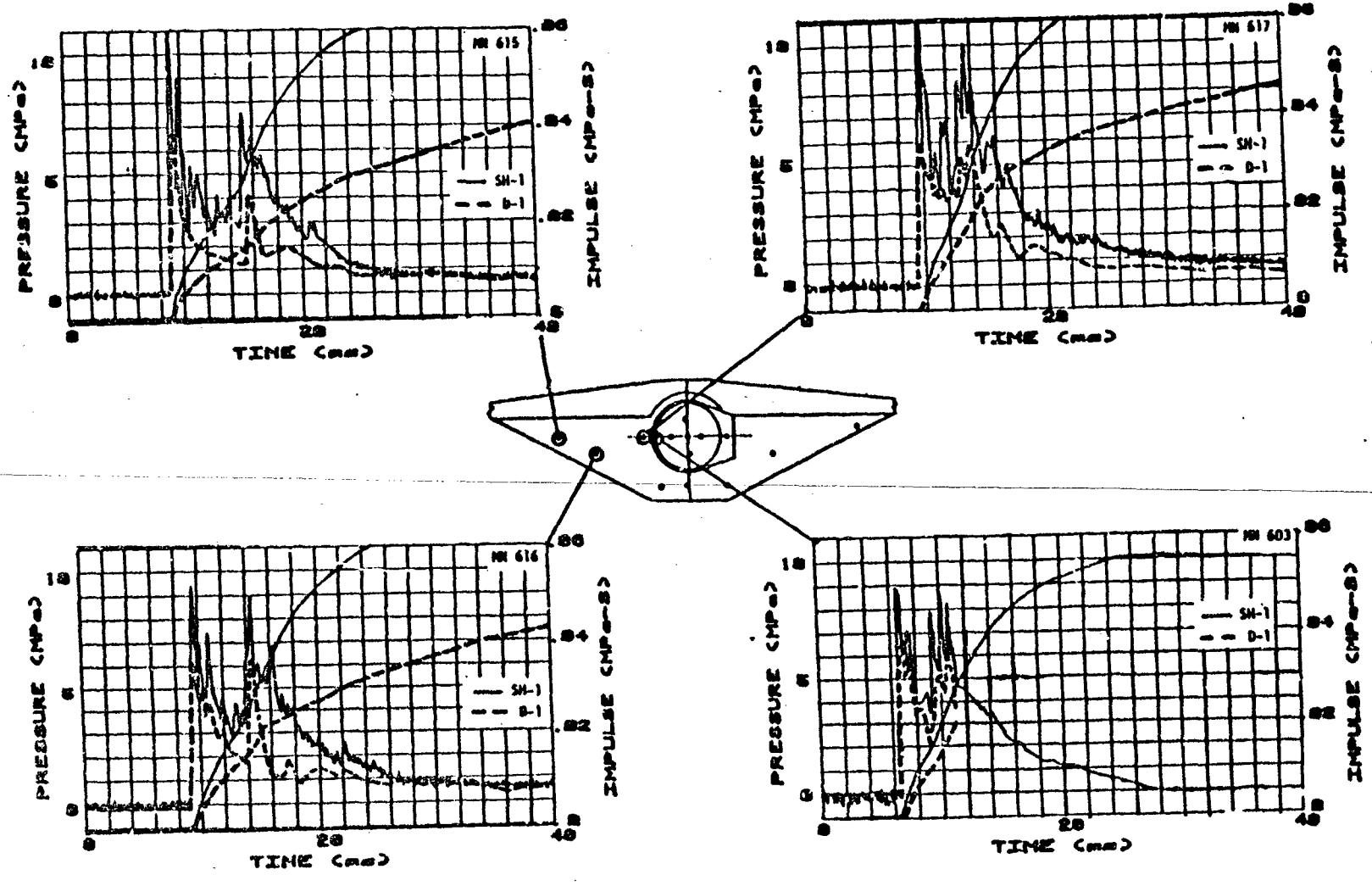

Figure 9. SH-1 to D-1 pressure and impulse comparison.

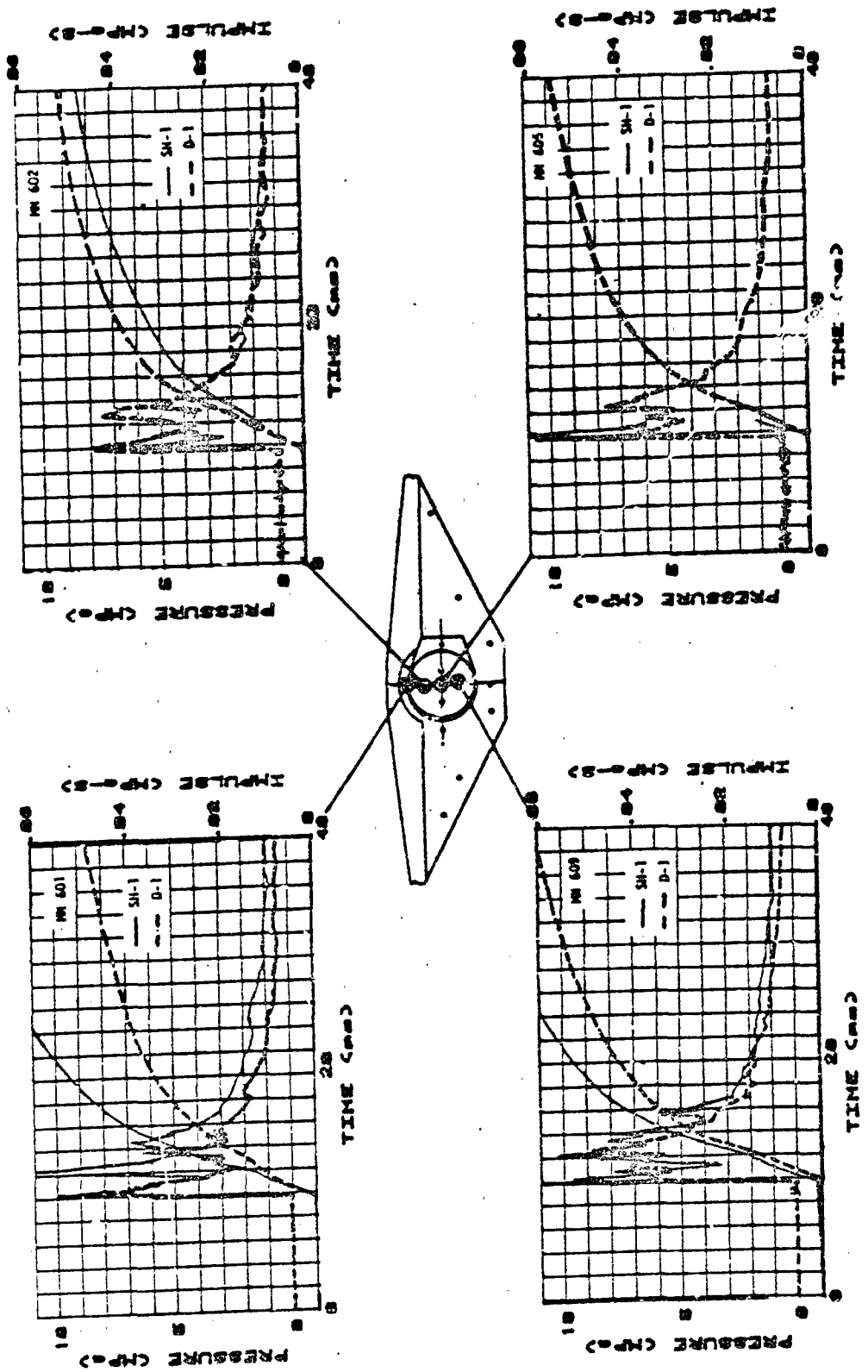

Figure 10. SH-1 to D-1 pressure and impulse comparison.

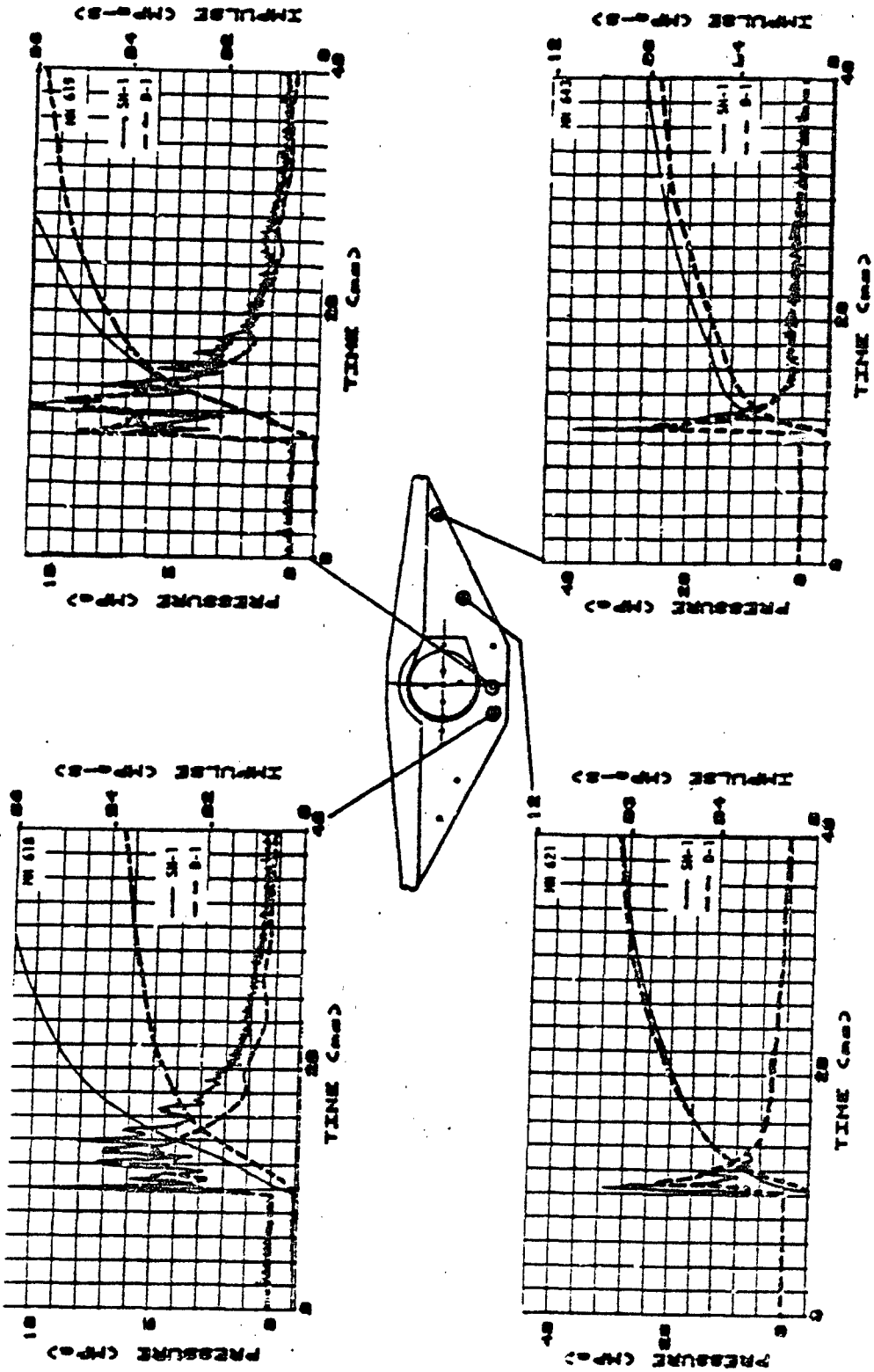

Figure 11. SH-1 to D-1 pressure and impulse comparison.

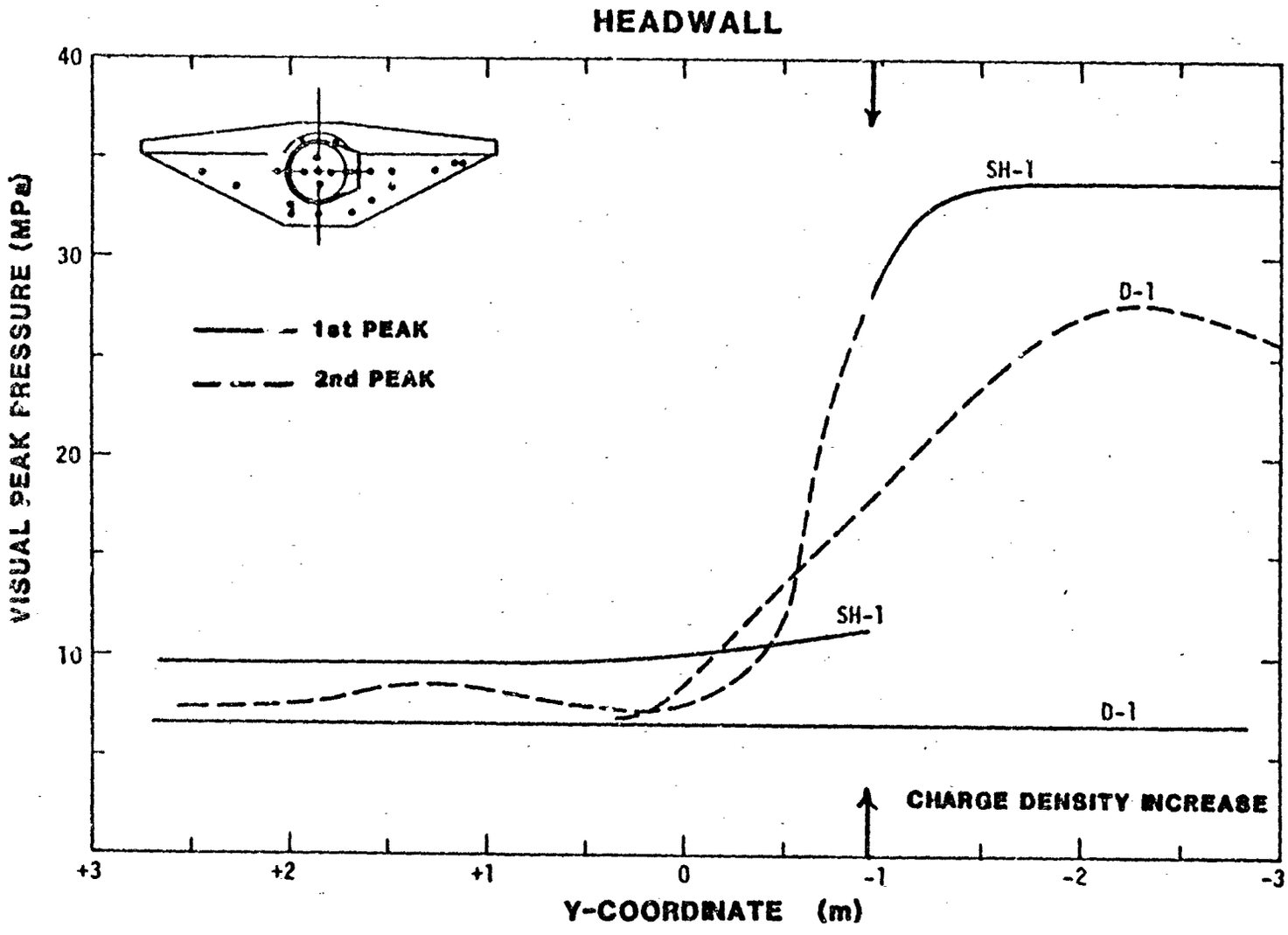

Figure 12. D-1 to SH-1 1st to 2nd Peak Pressure Comparisons

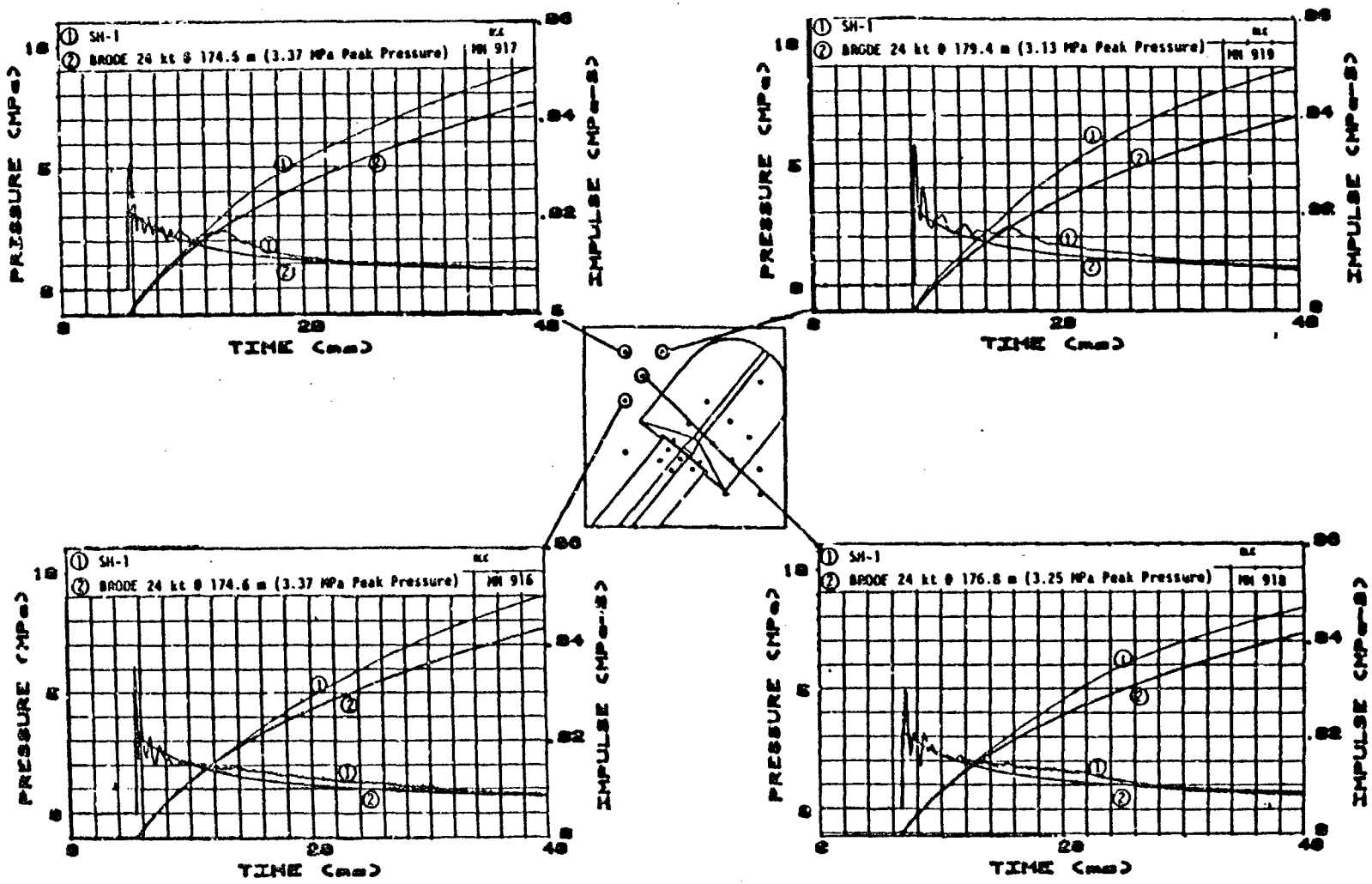

Figure 13. SH-1 to 24 kt Brode pressure and impulse comparison.

SUMMARY

The Shaped-HEST simulator performed very well as a nuclear Blast and Shock loader for exposed surface structures. Evaluation of the SH-1 simulator adequacy was a primary concern as to modeling the complex nuclear airblast loading waveforms. This HEST technique reflects the best state-of-the-art as a low cost simulator alternative to the DABS. Comparable load characteristics were produced. Overpressure waveforms very similar to the 24 KT nuclear waveform at the 3 MPa range were produced in the free-field regions (zones 8-1 and 8-2). The airblast waveforms produced over the top of the structure were quite comparable to those produced in the D-1 test. Along the headwall and closure double peaked waveforms were produced which were very similar to those produced in D-1. The zone 4 high pressure region along the downstream headwall produced secondary peaks very similar to the D-1 test. Propagation of the HEST blast wave over the testbed was uniform and planar, providing proper times of arrival in each of the test zones. Peak overpressures were slightly high in the free field as compared with the 3 MPa nuclear and 25 to 50 percent higher than the D-1 test across the headwall and the face of the structure. Impulse loading appears to be correspondingly high in most regions and approximately 20 percent higher over the closure. The HEST-generated high amplitude spikes and high frequency oscillations are present in the blast pressure waveforms during the first few milliseconds, but effectively produced minimal energy transfer.

Further HEST development to adjust and improve the quality of the nuclear airblast simulation provided in SH-1 is recommended prior to full-size test applications. However, the simulator has proven its utility for producing both multiple shock effects and multi-pressure loadings on reflection and drag sensitive structures.

Appendix I - References

1. Furbee, E., et al, "A Status and Capability Report on Nuclear Airblast and Ground Shock Simulators for Large Scale Structural Testing," AFWL-TR-79-195, Air Force Weapons Laboratory, Kirtland AFB NM, Jul 1980, pp. 7-21, 44-53.

2. Noble, M., et al, "D-1 Pretest Prediction," AFWL-TR-81-106, Air Force Weapons Laboratory, Kirtland AFB NM, Oct 1981, pp. 7-32.

3. Noble, M., et al, "D-1 Quick Look," AFWL-TR-81-107, Air Force Weapons Laboratory, Kirtland AFB NM, Nov 1981, pp. 31-67

4. Noble, M., Edwards, J. and Bell, K., "SH-1 Simulation Environment Pretest Prediction," AFWL-TR-81-220, Air Force Weapons Laboratory, Kirtland AFB NM, Feb 1982, pp. 1-13.

5. Noble, M., et al, "SH-1 Quick Look," AFWL-TR-81-221, Air Force Weapons Laboratory, Kirtland AFB NM, Mar 1982, pp. 14-68.

Appendix II - Notation

The following symbols are used in this paper:

cm = centimeter

ft = feet

gms = grams

gr = grains per foot

KT = Kiloton

kg = Kilogram

lbs = pounds

MPa = Megapascals

MT = Megaton

m = meter

ms = millisecond

s = second

t_s = simulator disassembly time

y = structure coordinate horizontal axis

1/5 Size VHS Series Blast and Shock Simulation by Michael L. Noble. The capability of a High Explosive Simulation Technique (HEST) simulator to adequately duplicate complex airblast waveforms was demonstrated. Dynamic test comparisons showed the HEST simulator's utility for providing both multiple shock effects and multi-pressure loadings on reflection and drag sensitive structures.

1/5 SIZE VHS SERIES BLAST AND SHOCK SIMULATIONS

KEY WORDS: Civil Defense; Explosives; Field Tests; Military Engineering; Technology Assessment; Dynamic Air Blast Simulator (DABS); High Explosive Simulation Technique (HEST); Airblast; Simulator.

ABSTRACT: The simulation objective of the 1/5 Verifiable Horizontal Shelter (VHS) test series was to demonstrate the capability of a High Explosive Simulation Technique (HEST) simulator to adequately duplicate complex airblast waveform loadings. A principal feature of the HEST design was the requirement to produce double-peaked resultant overpressures. The modeling baseline was established by a test (D-1) producing dynamic flow. The HEST test (SH-1) comparably matched the loading waveforms both in relative magnitude and phase characteristics. The HEST simulator has proven its utility for both multiple shock effects and multi-pressure loadings on reflection and drag sensitive structures.

SMALL-SCALE TESTS OF MX VERTICAL SHELTER STRUCTURES

James. K. Gran,* John R. Bruce,* and James D. Colton†

Abstract

The purpose of this research was to assess the applicability of geometric scaling at very small scale to study the response of buried reinforced concrete vertical shelter structures subjected to airblast loading. The approach was to build and test two 1/30-scale models and compare the responses with those from corresponding 1/6-scale tests. One of the structures tested was designed to respond elastically, and the other was designed to respond inelastically. The 1/30-scale and 1/6-scale models were built with as much geometric and material similitude as practical. Special fabrication techniques were developed for the 1/30-scale models. Concrete sand (ASTM C33) was used for the backfilled soil at both scales. The airblast from a nuclear burst was simulated with a high explosive simulation technique (HEST).

A comparison of the 1/30-scale and 1/6-scale tests shows that the surface loads and soil responses matched and that the structural responses agreed very well. For the elastic structures, concrete surface strains measured in the 1/30-scale test and reinforcing steel strains measured in the 1/6-scale test showed that the direct loading wave, the reflections from the base and the closure, the base and closure flexure, interface friction, and soil resistance to punchdown were all accurately reproduced at 1/30-scale.

For the inelastic structures, the responses agreed up to the time of failure in the 1/6-scale structure. Failure in the 1/6-scale structure occurred at an apparently locally weak section of concrete. Concrete surface strains measured in the 1/30-scale test and reinforcing steel strains measured in the 1/6-scale test showed excellent agreement above the failure location. The 1/30-scale strains throughout the structure were also in excellent agreement with the predictions of numerical analysis.

*Research Engineer, SRI International.

†Director of Engineering Mechanics Department, SRI International.

Introduction

The major objective of this research was to assess the applicability of very small-scale modeling to the study of blast-loaded buried reinforced concrete structures. This included an assessment of the geometric and material similitude attainable for 1/30-scale models, the accuracy with which the surface loads and soil/structure interface loads could be modeled at 1/30-scale, and, of course, the fidelity of the overall structural response. The approach was to build and test two 1/30-scale models of MX vertical shelter designs and compare the responses with those from 1/6-scale tests conducted by the Civil Engineering Research Facility (CERF) at the University of New Mexico.[1] The 1/30-scale and 1/6-scale models were built with as much geometric and material similitude as practical. They were not identical to the 1/3-scale structures tested in the VST Program.[7]

The response of a vertical shelter under airblast loading is illustrated in Fig. 1. The direct load from the air blast on the structure produces flexure of the closure plate and an axial compression stress wave that propagates down the length of the structure. The airblast also produces a compressive stress wave in the soil that propagates at a lower velocity than the structure wave. This soil wave produces radial compression and vertical shear along the soil/structure interface. The magnitude of the interface shear load depends on the interface roughness and soil properties. The wave in the structure may be elastic or inelastic and may produce failure during its first passage down the tube. When the wave reaches the base of the structure, it reflects and a relief wave propagates back up the tube. The base responds in bending the shear modes and the soil beneath the base arches. This may also result in structural failure. Two or three more transits of the stress wave may occur in an elastic structure before the wave disperses and significantly attenuates. Eventually, the soil wave completely engulfs the structure, but by then surface load is nearly gone and the structure is nearly at rest.

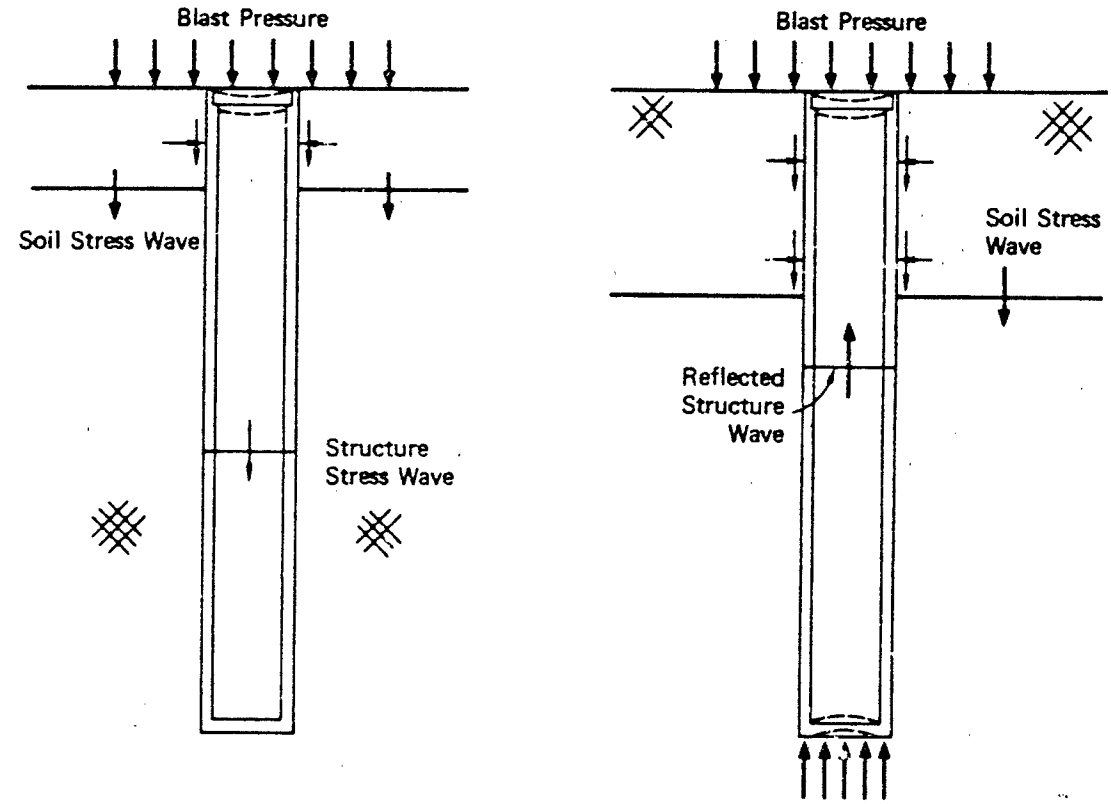

FIGURE 1 VERTICAL SHELTER RESPONSE TO AIRBLAST LOADING

Small-Scale Structural Models

The two designs that were built and tested at 1/30-scale were the 'B' structure, designed to respond elastically, and the 'A' structure, designed to respond inelastically. Geometric similitude was maintained in both the external structural dimensions and the details of the reinforcement. The overall length of the models was 1280 mm and the inside diameter was 142 mm. The wall thickness of the 'B' structure was 20 mm; for the 'A' structure it was 10 mm. Measurements showed that in both structures the walls were held to within 10% of the design thickness, except at the base where 15% variations were measured. The main reinforcement for both structures was 1% steel in the longitudinal and circumferential directions, placed in two layers. Radial stirrups at each of the approximately 4000 bar intersections provided shear reinforcement. To match the reinforcement layout of the 1/6-scale structures, wires approximately 1 mm in diameter were used in the 1/30-scale models.

The degree of material similitude achieved in the 1/30-scale models is illustrated in Fig. 2. The microconcrete used in both the 'B' and 'A' structures consisted of graded sand, water, and Portland cement, with no admixes. The strength of sample cylinders form the 'B' structure averaged 39.1 MPa with a standard deviation of 3.1 MPa. The strength of the sample cylinders form the 'A' structure averaged 23.0 MPa with a standard deviation of 2.7 MPa. In neither case was any trend apparent in the strength variation along the length of the structures. Typical stress-strain records from the 1/30-scale microconcrete are shown in Fig. 2(a), where they are compared with records from the 1/6-scale concrete.

The main reinforcement was made of steel welding wire that was deformed and heat-treated to produce the desired bond and strength properties. Tensile tests showed that uniform strength was achieved along the length of the 1.5-m-long heat-treated wires, and strength varied less than 5% from wire to wire. A typical stress-strain record is shown in Fig. 2(b), where it is compared with 1/6-scale data. A close-up photograph of the deformed wires is shown in Fig. 2(c). The results of direct pullout bond tests are shown in Fig. 2(d), where they are compared with 1/6-scale test results and prototypical bond data.

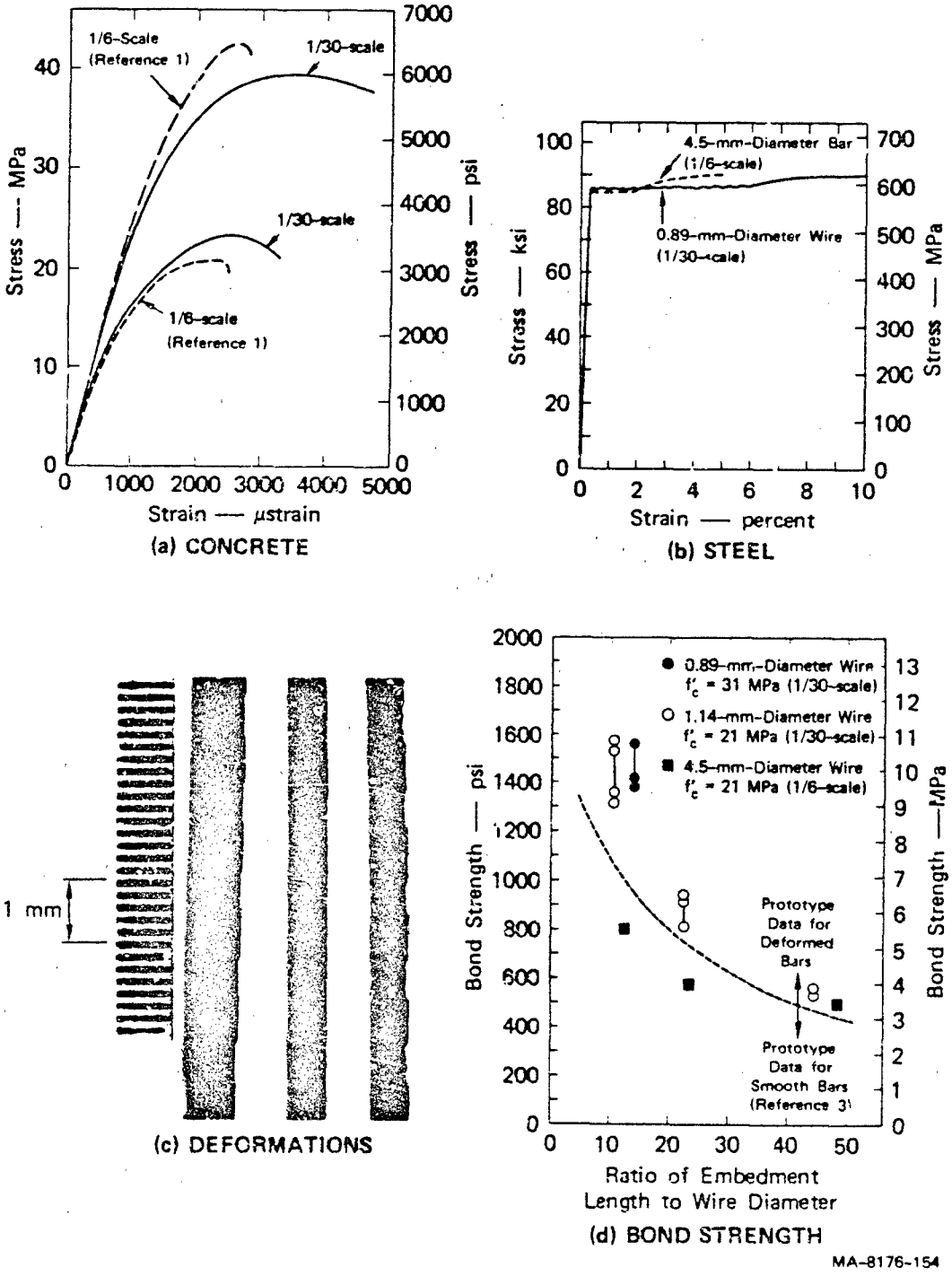

FIGURE 2 MATERIAL SIMILITUDE IN 1/30-SCALE MODELS

Test Configuration and Load Simulation

The 1/30-scale experiments were conducted in the Compact Reusable Airblast Simulator (CRABS) constructed at SRI's Corral Hollow Experimental Site. The CRABS facility, shown in Fig. 3, is geometrically similar to the Giant Reusable Airblast Simulator (GRABS) used for the 1/6-scale tests. Concrete sand (ASTM C33) was used for the backfilled soil at both scales. It was rained into place from a height exceeding 0.75 m to achieve a uniform density of about 1750 kg/m^3. The surface pressure was generated with a HEST charge.

Several types of instrumentation were used to record the loads and the structural response. A typical instrumentation layout is shown in Fig. 3. The measurements included blast pressure, vertical soil acceleration, radial and vertical soil stress, concrete strain, structural acceleration, and interface pressure. All the gage signals were conditioned and recorded in analog form, then digitized electronically at a sampling rate of 6 μs/point. In the gage records discussed below, the gage locations are given in terms of the ratio of the gage depth to the overall length of the structure (d/L). For the purpose of comparison, all the data from the 1/6-scale tests were digitized manually and scaled[2] to correspond to the 1/30-scale records.

The design load for the vertical shelter is the airblast from a 5 MT nuclear burst at the 8.3 MPa range. The Brode approximation[3] to this load was simulated at both scales using a HEST charge. The explosive charge design for the 1/30-scale tests was scaled from the 1/6-scale charge: the 1/30-scale charge consisted of four layers of Primacord explosive and polystyrene foam, covered by a 0.44-m-deep layer of sand. Direct comparisons of typical blast pressure and soil stress measurements in the structural tests are shown in Fig. 4. As indicated, the surface pressure and impulse compare very well with the design load. The soil stress measurements also compare well at both scales, although the wave speed in the 1/6-scale tests was consistently slightly higher than in the 1/30-scale tests. The cause of this difference has not been determined, but the effect on the structural response was insignificant.

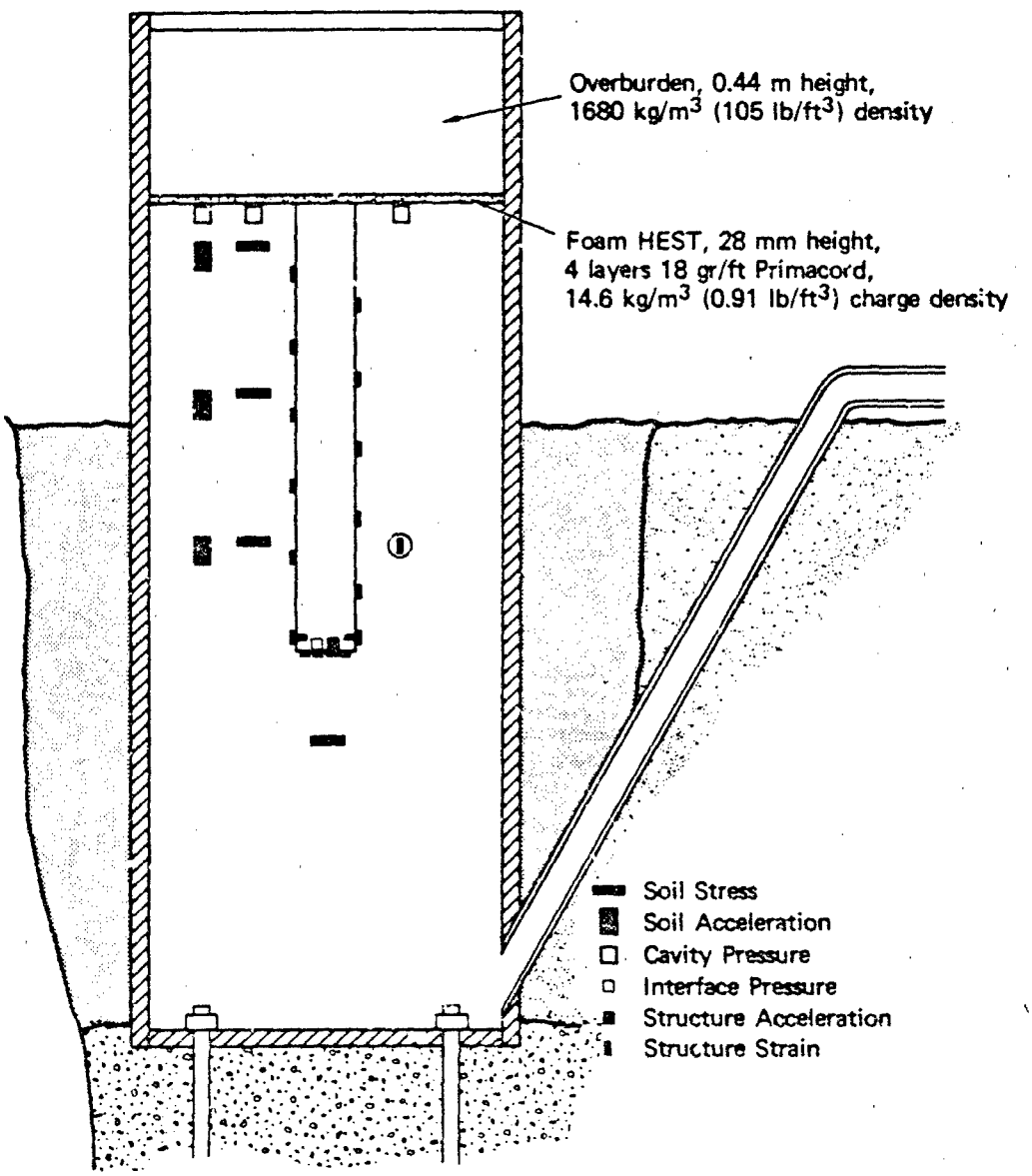

FIGURE 3 CRABS FACILITY AND TYPICAL TEST SETUP FOR 1/30-SCALE TESTS

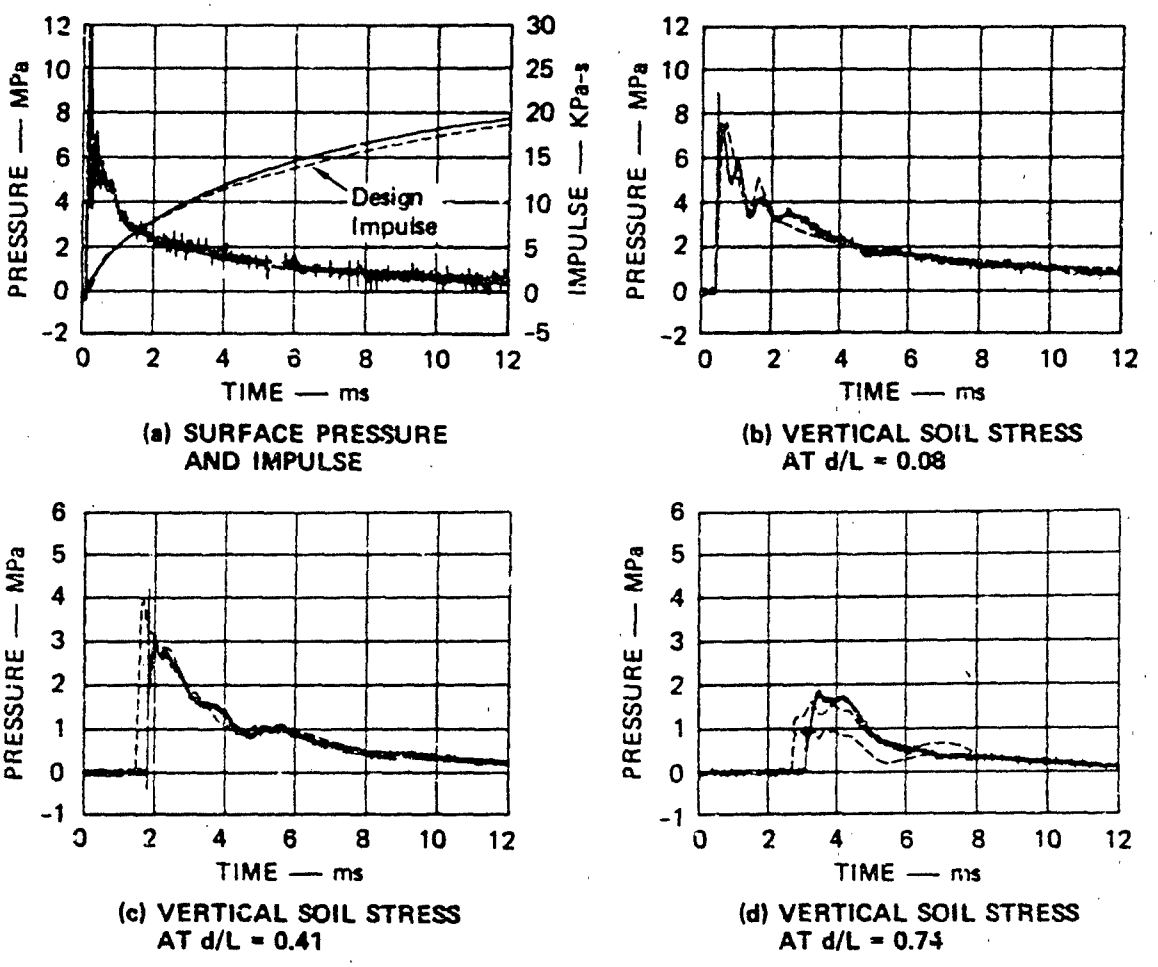

FIGURE 4 BLAST PRESSURE AND SOIL STRESSES

—— 1/30-scale; – – – 1/6-scale

Interface Shear Load Measurements

Before the structural tests, an independent set of experiments was conducted to characterize the soil/structure interface properties of the 1/30-scale models. The configuration for these tests is shown in Fig. 5. The test device was a segmented concrete column extending from the base of the CRABS facility up through the explosive cavity. The cylindrical segments were connected by load-measuring "dogbones." The surface of the concrete was representative of the 1/30-scale and 1/6-scale structures. By measuring the forces between the column segments, the acceleration of the segments, and the normal interface stress, a relation between average normal stress and average shear stress at the interface was obtained for each segment. A reasonable fit to the data from these experiments is the bilinear curve consisting of the assumed soil strength envelope (zero cohesion, 30° friction angle) and an estimated interface strength envelope (0.14 MPa cohesion, 10° fricton angle). This fit is nearly identical to the model suggested by Huck[4] for smooth concrete and sand.

'B' Structure Comparison

A comparison of the results from the 1/30-scale and 1/6-scale tests of the 'B' structure shows that the surface loads and soil responses matched and that the structural responses agreed very well. The direct loading wave, the reflection from the base, the base response, and the soil shear loading were all reproduced accurately at 1/30-scale.

Concrete surface strains measured in the 1/30-scale test and reinforcing steel strains measured in the 1/6-scale test are compared in Fig. 6. The initial small oscillations in the records are the result of electrical noise generated from the detonation of the explosive. When the direct blast load wave in the structure arrived at a particular location, the axial strain rose sharply in compression. The tensile reflection of this wave from the base then reduced the axial strain sharply. Between 0.5 ms and 1.0 ms after the initial shock arrival, depending on the location, the strain again rose because of both a second stress wave reflection (from the top) and the continually increasing soil/structure interface shear load. Not shown are the circumferential

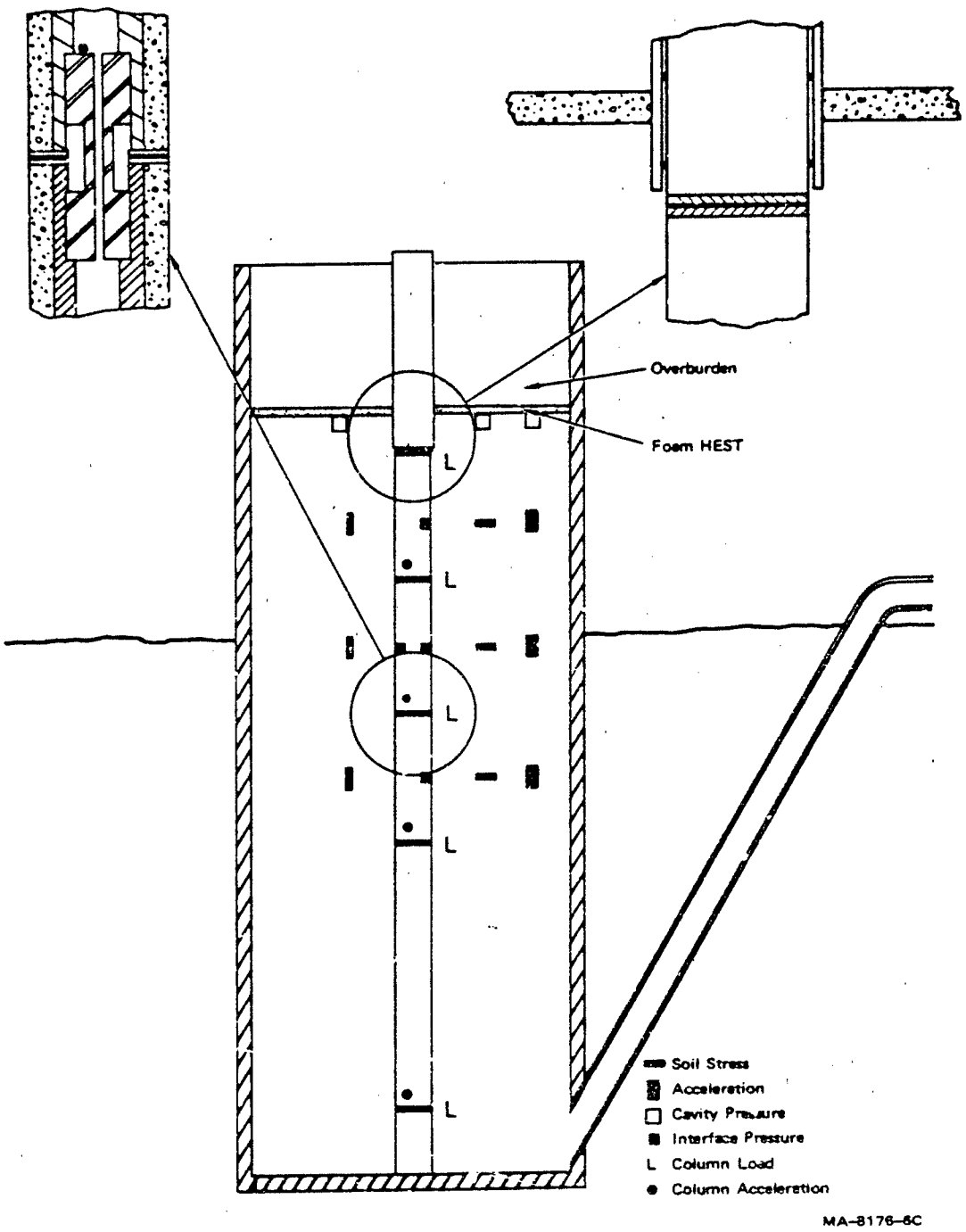

FIGURE 5 MEASUREMENT OF INTERFACE SHEAR LOADS

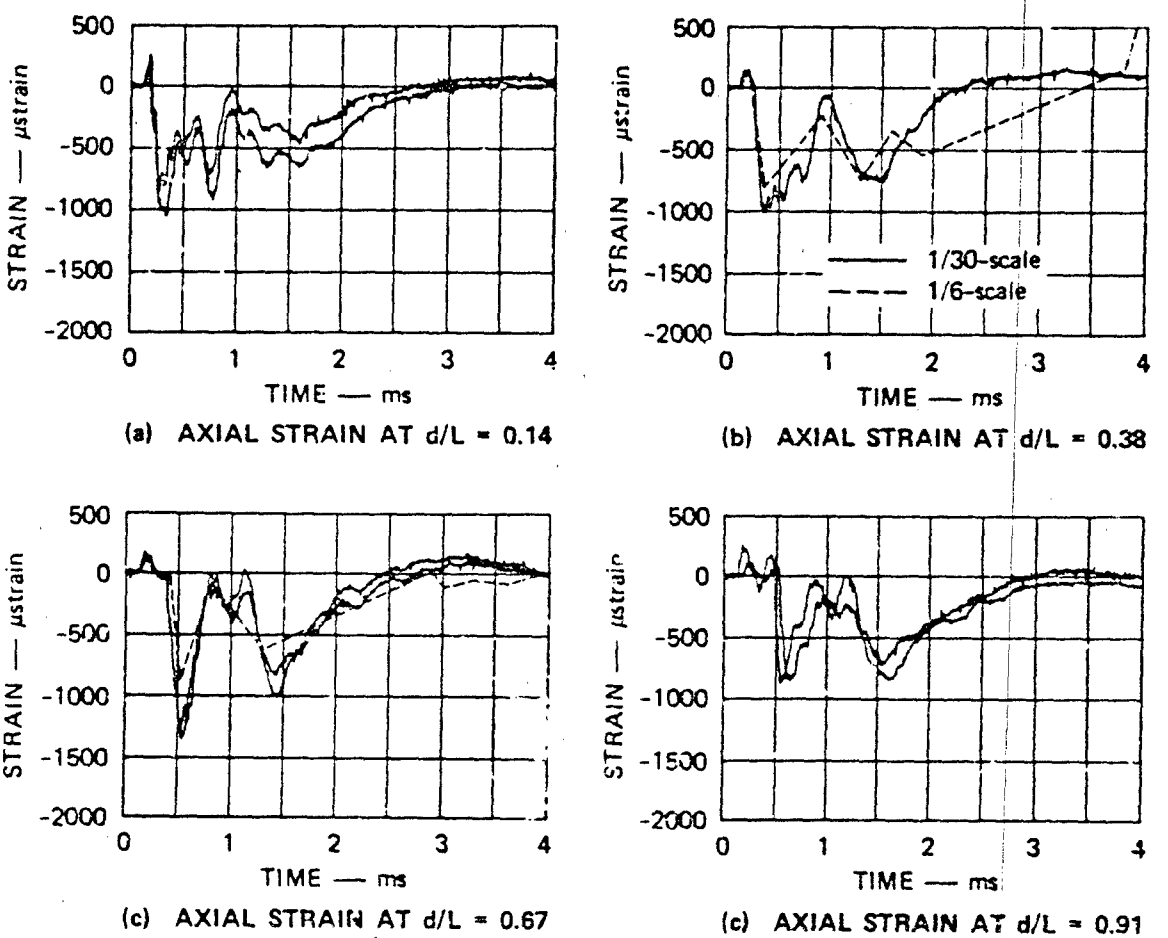

FIGURE 6 'B' STRUCTURE STRAINS

—— 1/30-scale concrete strains; ----1/6-scale steel strains

strains, which were first tensile because of the axial compression, but then fell abruptly into compression when the soil wave arrived. The comparison of the 1/30-scale records with the 1/6-scale records indicates that all the features of the response were captured in the 1/30-scale test, although the magnitude of the strains was slightly higher in the smaller model. Also, in the 1/30-scale test the peak axial compressive strain measured during the first wave transit increased with depth to about d/L = 0.67 and then decreased. Because strain was measured at only two axial locations in the 1/6-scale test, a complete comparison of the variation of peak strain along the length of the structure cannot be made.

The records showing the base response are compared in Fig. 7. Oscillations in the base acceleration and velocity indicate that flexural vibrations of the base plate occurred for about 1 ms. The difference in the magnitudes of the interface pressures from the two tests is a result of the difference in the gage locations: the 1/30-scale pressure was measured very near the center of the base, whereas the 1/6-scale pressure was measured nearer the perimeter of the base. The difference in magnitude indicates that soil arching occurred beneath the base. The soil stress measured directly below the structures, at d/L = 1.20, shows that nearly the same total load was put into the soil at both scales.

'A' Structure Comparison

A comparison of results from the 1/30-scale and 1/6-scale tests of the 'A' structure shows that the surface loads and soil response were matched and that the structural responses agreed up to the time of failure in the 1/6-scale structure. The damage in the 1/30-scale 'A' structure model is shown in Fig. 8(a). The apparent chronology is that the wave in the structure from the direct blast loading propagated all the way to the base without causing failure, and peak strains of 2200, 2000, and 2300 microstrain were recorded at d/L = 0.12, 0.38, and 0.67 locations, respectively. When the wave reached the base, or shortly thereafter, failure occurred at the tube/base junction because of a combination of axial compression, toroidal bending, and shear. In comparison, the 1/6-scale 'A' structure model, shown in Fig. 8(b), failed at d/L = 0.40 when the

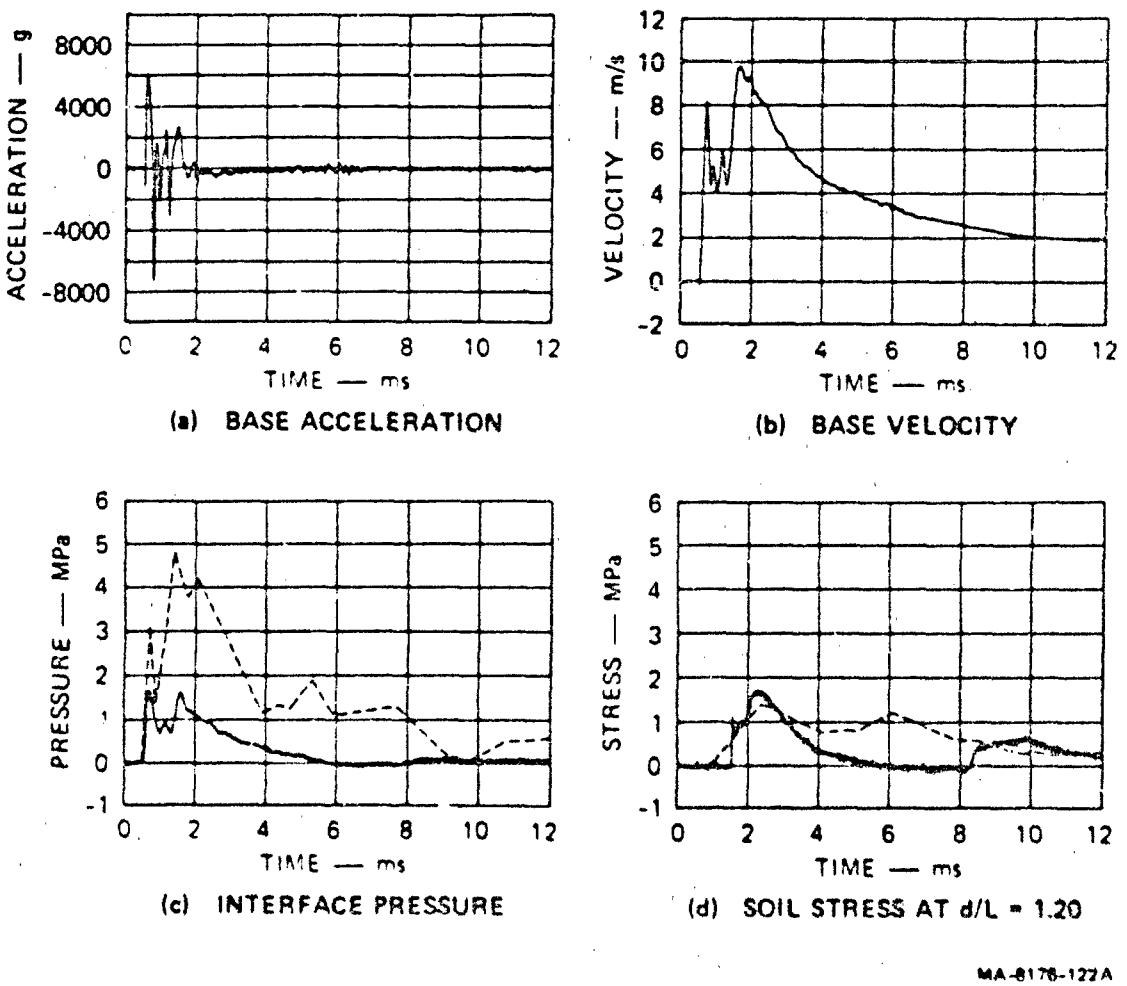

FIGURE 7 'B' STRUCTURE BASE RESPONSE

—— 1/30-scale, – – – 1/6-scale

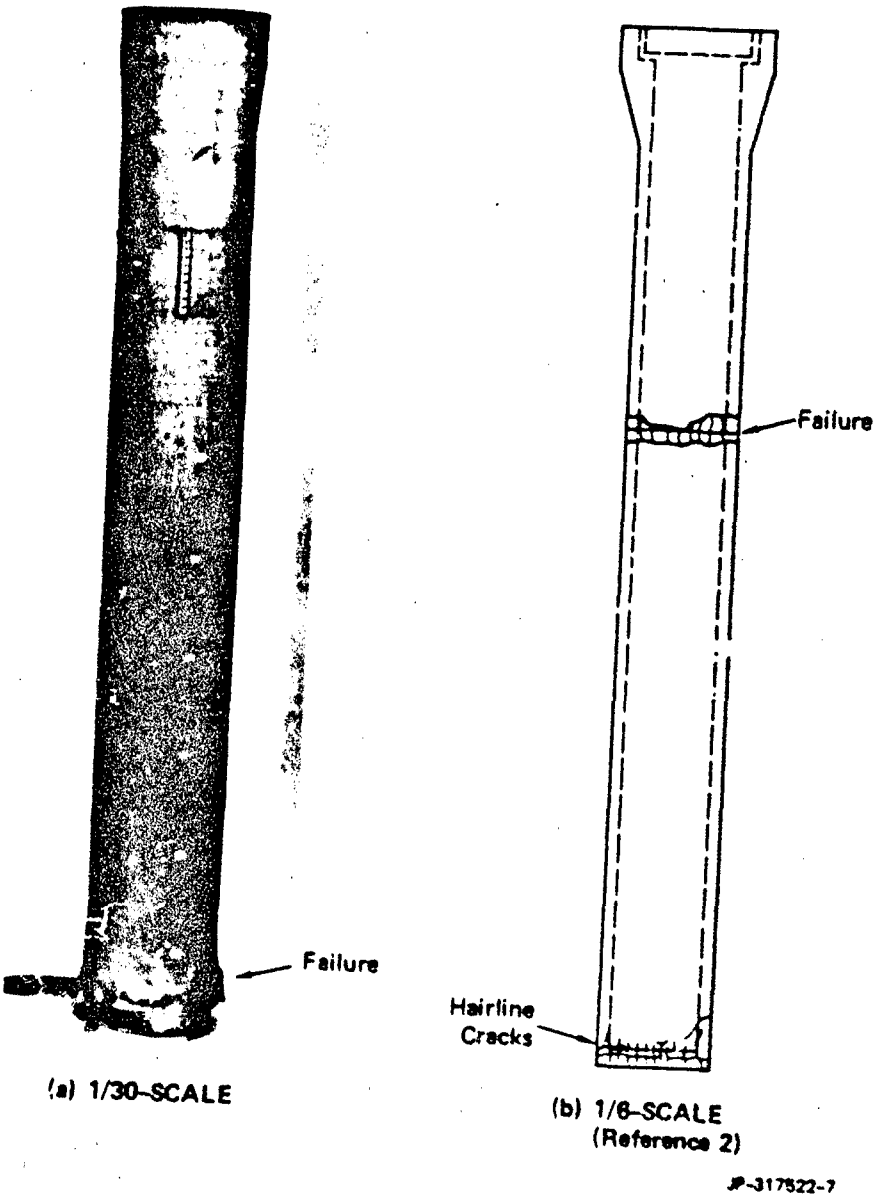

FIGURE 8 'A' STRUCTURE DAMAGE

stress wave in the structure reached that depth. The failure occurred in the vicinity of a construction joint that may have been a locally weak or brittle section. The decreased load that propagated past the failure location also damaged the base slightly.

Concrete surface strains measured in the 1/30-scale test and reinforcing steel strains measured in the 1/6-scale test are shown in Fig. 9. The comparison at d/L = 0.12 is excellent and suggests that both structures behaved the same at very high (although different) strain rates, even though the unconfined static strength of both structures was exceeded by a factor of about 2. Because failure occurred at the d/L = 0.40 depth in the 1/6-scale test but not in the 1/30-scale test, the strain comparison at d/L = 0.38 is not good and at d/L = 0.72 it is meaningless.

In Fig. 10 the 1/30-scale strains from the d/L = 0.12, 0.38, and 0.72 locations are compared with the results of elastic-plastic finite element calculations performed by other researchers.[5,6] The agreement is good at all three locations, and neither the analyses nor the 1/30-scale experiment predict the d/L = 0.38-0.40 depth to be a critical location. However, during the first millisecond of response (1/30-scale) the analyses predict strains of 4000 to 5000 microstrain at about the d/L = 0.22 location. This is the depth at which the soil stress wave meets the reflection of the structure wave. Apparently, above that point the peak strain is limited by the radial pressure in the soil, and below that point the peak strain is limited by the relief wave from the base of the structure. Unfortunately, strain was not measured at this predicted critical location in either of the experiments because the phenomenology was not well enough understood at the time the experiments were conducted.

The records showing the base response are compared in Fig. 11. In contrast with the 'B' structure, significant acceleration in the 1/30-scale 'A' structure was sustained for only about 800 μs, and flexural vibration of the base plate is not evident in the velocity record. This suggests that failure took place very soon after the arrival of the direct loading wave. The 1/30-scale base damage is shown in Fig. 11(c). The soil stress measured at d/L = 1.20 [Fig. 11(d)] indicates that in the

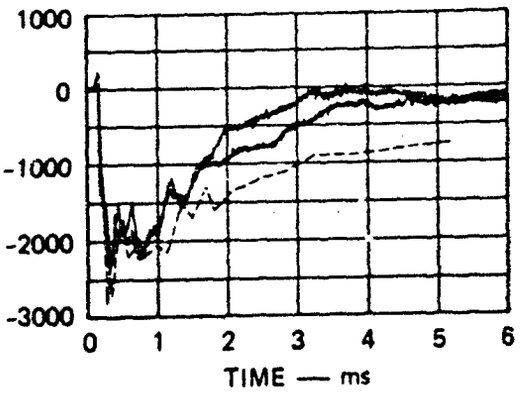

(a) AXIAL STRAIN AT d/L = 0.12

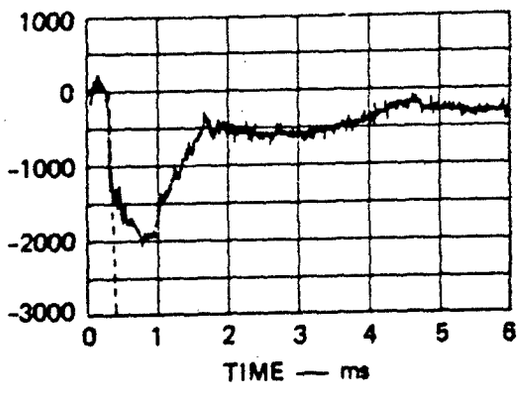

(b) AXIAL STRAIN AT d/L = 0.38

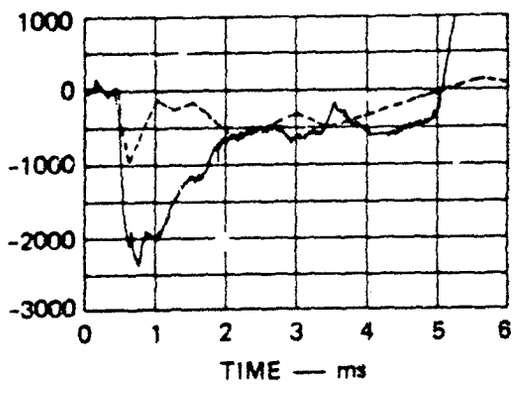

(c) AXIAL STRAIN AT d/L = 0.72

MA-8176-160

FIGURE 9 'A' STRUCTURE TUBE STRAINS

—— 1/30-scale concrete strains; ---- 1/6-scale steel strains.

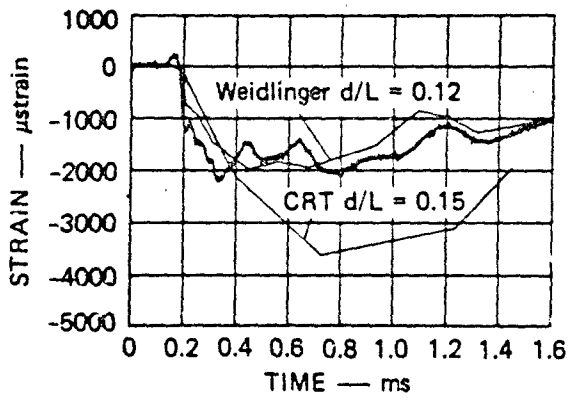

(a) AXIAL STRAIN AT d/L = 0.12

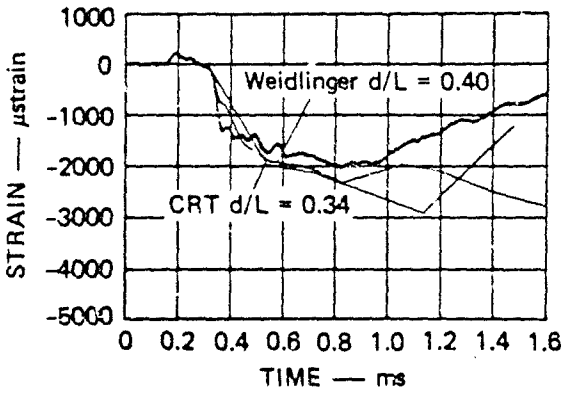

(b) AXIAL STRAIN AT d/L = 0.38

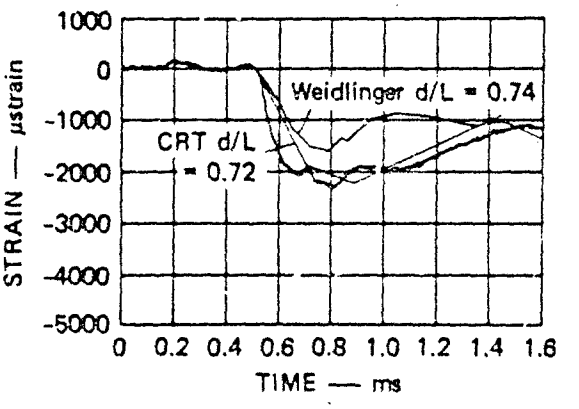

(c) AXIAL STRAIN AT d/L = 0.72

MA-81'6-161

FIGURE 10 'A' STRUCTURE TUBE STRAINS COMPARED WITH ANALYTICAL PREDICTIONS

Analytical predictions are from References 6 and 7.

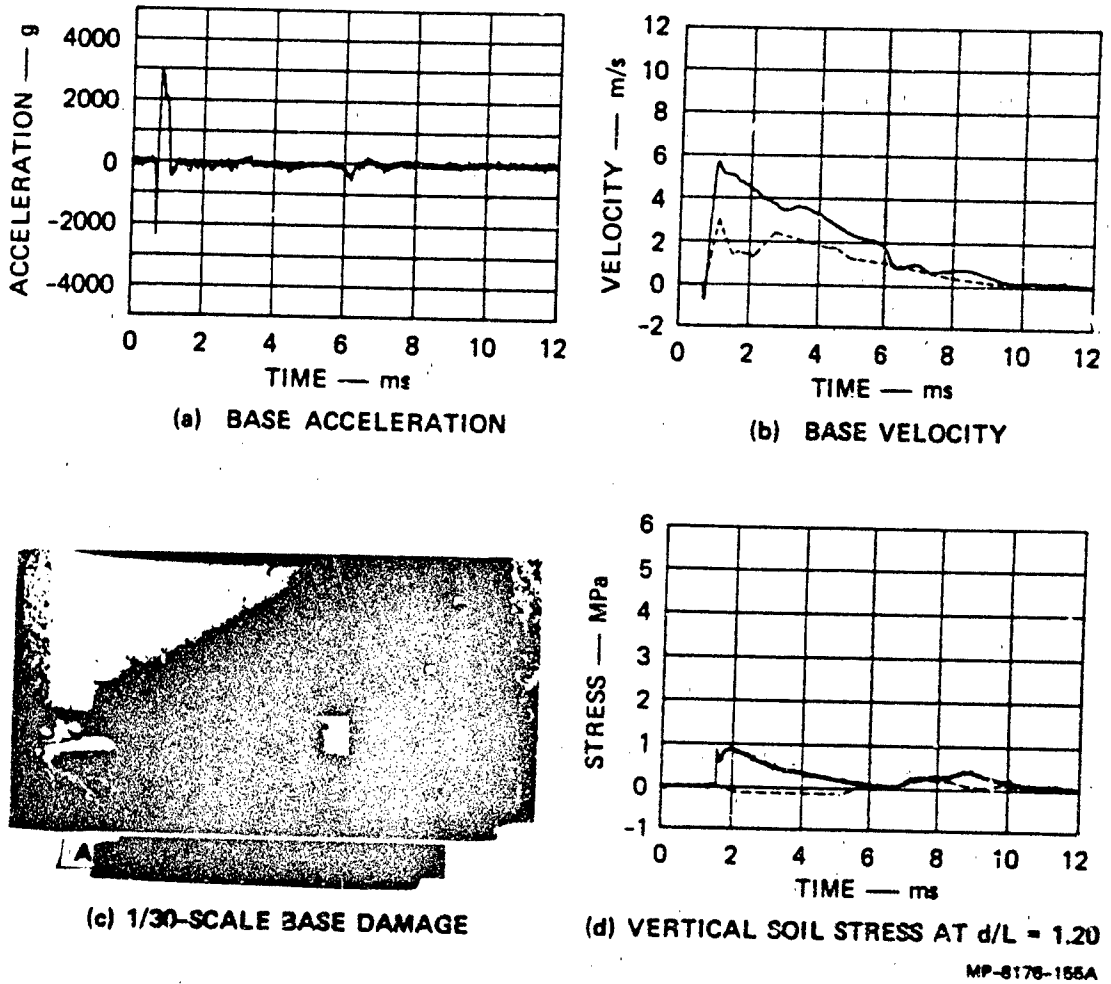

FIGURE 11 'A' STRUCTURE BASE RESPONSE

—— 1/30-scale; - - - - 1/6-scale

1/30-scale test a significant force was exerted by the base on the soil long after the assumed time of structural failure. In contrast, the 1/6-scale soil stress is much lower because comparatively little load propagated past the early failure at d/L = 0.40.

Analyses

Three computer calculations were conducted to aid in the understanding of the experimental results. In the first calculation, an elastic analysis of the 'A' structure was conducted to help determine the nature of the wave reflected from the base and to estimate the potential for failure at the tube/base junction. The results showed that the reflection from the base is predominantly tensile and that the principal strains at the tube/base junction are large enough to cause either compressive failure or tensile failure within 25 μs of the arrival of the wave at the base. However, because plasticity effects were not included, the actual time of the failure observed in the 1/30-scale 'A' structure test cannot be determined from this first-approximation analysis.

In the second analysis, the effect of nonscaling gravity on the early time response of a vertical shelter in cohesionless soil was studied. It was concluded that, over the range of scale factors from 1/30 to 1/3, the effect of gravity's not scaling does not cause significant differences during the transit of the first structural wave. This is the time period during which failure occurred in the 'A' structure in all three scales of the experiments.

In the third calculation, the individual effects of the direct end load and the interface shear load were investigated in a wave analysis of the 'B' structure. The comparison between this analysis and the experiments indicates that most of the experimentally observed response is caused by the direct end load, including the second rise in compression between 1.0 ms and 1.5 ms. The interface shear load has a significant effect on the magnitude of the strains at any particular time, but it has almost no effect on the shape of the strain records.

Effects of Scale

The excellent agreement between the 1/30-scale and 1/6-scale 'B' structure responses indicates that all the significant response effects that occurred in the 'B' structure tests scaled very well. These effects include elastic wave propagation and reflection in the structure, closure and base flexure, interface friction, and soil resistance to punchdown. The slight differences in the magnitude of the tube strains may be due to slight differences in concrete material properties. Gravity effects are negligible. The difference in strain rate does not produce any significant difference in response, although the variation of peak strain along the length of the structure may be a function of strain rate.

The 1/30-scale and 1/6-scale 'A' structure responses also showed excellent agreement up to the time that failure occurred in the 1/6-scale model. In particular, strains measured at the end of the transition section match very well. The only explanation for the failure in the 1/6-scale structure at the $d/L = 0.40$ location is the existence of a weak section. The failure location coincides with the top of a lift in the concrete formwork, where the concrete could have been weakened by the settlement of the aggregate. The excellent agreement between the 1/30-scale measurements and the computer analyses is further evidence that the smaller-scale model responded properly. Neither the 1/30-scale test nor the finite element analyses predict the $d/L = 0.40$ location to be critical during the first passage of the stress wave down the tube, i.e., when failure occurred in the 1/6-scale model.

After failure occurred in the 1/6-scale structure, the responses at the two scales, of course, differed. Lower strains in the tube and a lower base velocity in the 1/6-scale model resulted from the lower stress below the failed section. The higher stress wave in the 1/30-scale model produced higher strains in the lower tube and caused failure at the tube/base junction when the wave reached the base. Thus, the 1/30-scale test revealed that one weak point of the 'A' structure design is the tube/base junction. Failure at the tube/base junction isolated the base from subsequent loading through the tube, including downdrag effects. Thus, both

the magnitude and the character of the base velocities differed at the two scales because of the difference in failure locations.

Unfortunately, in comparison with the 1/30-scale models and the 1/6-scale models, the 1/3-scale VST[7] models had different geometry (wall thickness variations), different material properties (higher concrete strength and lower steel strength), different loads (higher pressure), different soil (in-situ HAVE HOST), and different interface characteristics (cast-in-place roughness). Thus, it is very difficult to isolate the effects of nonscaling parameters by comparing 1/30-scale and 1/6-scale results with the 1/3-scale VST results.

For example, the strains measured in the 1/3-scale 'B' structure are about twice as high as those in the 1/6-scale and 1/30-scale structures. It appears that the combination of higher surface pressure, the cast-in-place interface condition, and the cohesion of the in-situ soil produced overall higher loads on the structure and thus higher strains. It does not appear that the differences between the 1/3-scale VST 'B' structure data and the data taken at the two smaller scales are results of scale per se.

The 1/3-scale VST 'A' structure response was similar to the 1/6-scale response in that failure occurred during the first passage of the stress wave in the structure. However, because the failure location was in the transition section, the strains before failure cannot be compared. The quicker failure in VST may have resulted from the higher load, a weak section, or the stronger interface condition.

Conclusions and Recommendations

The conclusions of this study are as follows:

(1) The geometric and material similitude in the 1/30-scale models was excellent, and the quality control was at least as good as that of the larger scale models.

(2) The blast pressure and soil structure interaction loads were accurately modeled for the conditions tested, but in-situ soil and cast-in-place interface roughness may pose modeling problems at any scale.

(3) The structural response of the 1/30-scale models was generally in excellent agreement with the 1/6-scale response. The only major discrepancy was the location of failure in the 'A' structure, and this is attributed to a locally weak section in the 1/6-scale model.

(4) The effects of nonscaling gravity were negligible for the cases studied. The effects of nonscaling strain rate were not obvious.

The tests at all three scales clearly made important contributions to the understanding of vertical shelter response. Furthermore, the response of a vertical shelter under airblast loading is dominated by those parameters that scale properly, e.g., geometry, material properties, and loads. This makes small-scale testing an excellent tool for concept screening and for verification of analytical models. However, small-scale testing should not be substituted for large-scale proof testing. Construction techniques can cause differences in response, especially as they affect strength, geometry, and interface conditions. Also, in-situ soil properties may not be accurately modeled with backfilled soil.

Acknowledgement

This work[8] was sponsored by the Defense Nuclear Agency. The technical monitor was USAF Maj. M. E. Furbee.

References

1. G. Landon, J. Stephens, and I. Narain, "Giant Reusable Airblast Simulation (CRABS) on Vertical Shelter (GOVS)," Final Report AFWL-TR-80-157, University of New Mexico, Albuquerque, New Mexico (May 1980).

2. J. N. Goodier, "Dimensional Analysis," Appendix II in Handbook of Experimental Stress Analysis, M. Hetenyi, ed. (John Wiley & Sons, New York, 1950).

3. H. L. Brode, "Height of Burst Effects at High Overpressures," Final Report RM-6301-DASA, Rand Corporation, Santa Monica, California (July 1970).

4. P. J. Huck, "Dynamic Response of Soil/Concrete Interfaces at High Pressure," Final Report AFWL-TR-73-264, IIT Research Institute, Chicago, Illinois (April 1974).

5. R. H. England and Y. M. Ito, "Analysis of Small-Scale Vertical Shelter Model Experiments in Simulated Air Blast Environments," Final Report, Contract DNA001-79-C-0255, California Research and Technology, Inc., Woodland Hills, California (to be published).

6. J. Isenberg and F. Wang, "Analysis of Three Structural Design Concepts for Vertical Shelters," Final Report No. R7924, Contract No. F04704-78-C-0019, Weidlinger Associates, Menlo Park, California (June 1979).

7. L. M. Swartz, "VST Critical Measurements," Civil Engineering Research Division, Air Force Weapons Laboratory, Kirtland AFB, New Mexico (October 1979).

8. J. K. Gran and J. R. Bruce, "Small-Scale Tests of MX Vertical Shelter Structures," SRI International, Menlo Park, California, Final Report DNA 5375F (April 1980).

LABORATORY INVESTIGATION OF EXPANSION, VENTING, AND SHOCK ATTENUATION IN THE MX TRENCH[1,2]

James K. Gran,* John R. Bruce,* and James D. Colton†

Abstract

An experimental program using 1/26-scale models of a buried concrete trench was conducted to study the dynamics of expansion and venting caused by an airblast propagating down the trench, and to study the effects of the expansion and venting on the attenuation of the airblast. The trench models were made of steel fiber-reinforced concrete and were buried in sand. The airblast was produced with an explosively driven shock tube. Expansion and venting dynamics of short trench sections were studied for flat-topped pressure pulses ranging from 700 psi to 2600 psi. Radial expansion histories and vent-times were recorded. Shock attenuation was studied with 60-ft-long trenches in which the peak pressure of an exponential waveform decreased from 4000 psi to 300 psi as the shock propagated the length of the trench. The effects of expansion were isolated by comparing the attenuation in a concrete trench to that in a steel trench. Expansion reduced the peak pressure slightly at distances greater than 40 ft. The data were used to validate computer models for shock attenuation in the MX trench.

Introduction

An important aspect of the MX trench is its response to air shock waves created inside the trench. The objectives of the work presented here were twofold: (1) to determine the expansion and venting response of the trench under internal pressure loading and (2) to determine the effects of attenuation mechanisms (viscous wall drag, trench expansion, and trench-to-surface venting) on the air shock wave inside the trench.

---

*Research Engineer, SRI International

†Director of Engineering Mechanics Department, SRI International

Expansion and Venting Tests

Experimental Setup

The expansion and venting tests were conducted with the assembly shown in Fig. 1. The trench is subjected to the largest internal pressure when the shock wave produced by the explosive has traversed the run-up section and the model, and reflects from the reflecting wall at the end of the model. The assembly rested in a soil bin that provided two feet of soil to each side and below the model trench. Pressure was measured in the shock tube run-up section and at the reflecting wall. Response was photographed with two high-speed cameras, one viewing the end of the trench through the Lucite window, the other viewing the soil surface from the side.

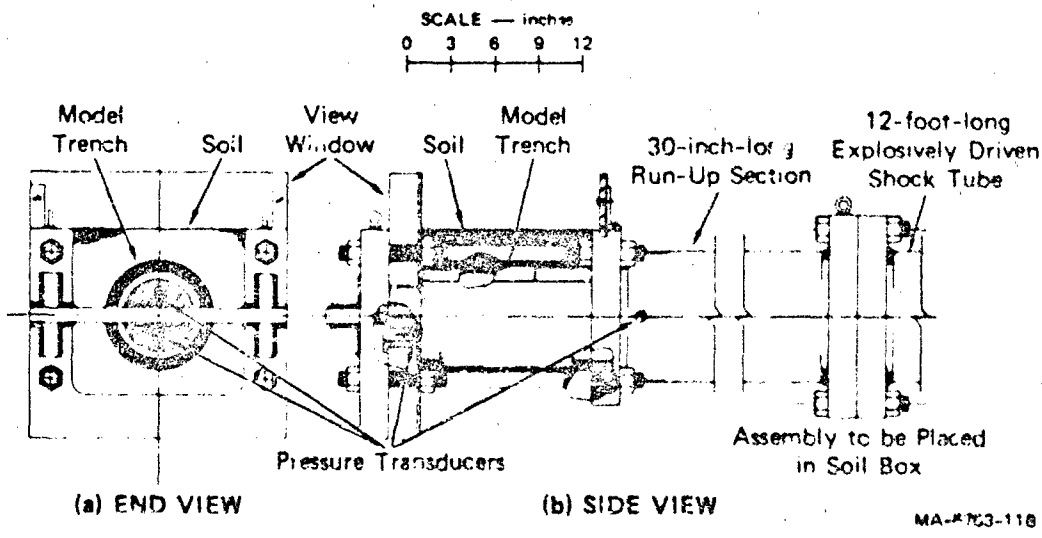

FIGURE 1 EXPANSION AND VENTING EXPERIMENT ASSEMBLY

Eight strands of explosive cord in the shock tube were used to generate nominally flat-topped shock waves with reflected pressures ranging from about 700 psi to about 2600 psi. These loads were calibrated with a steel tube in place of the model trench. The calibration pressure records are shown in Fig. 2.

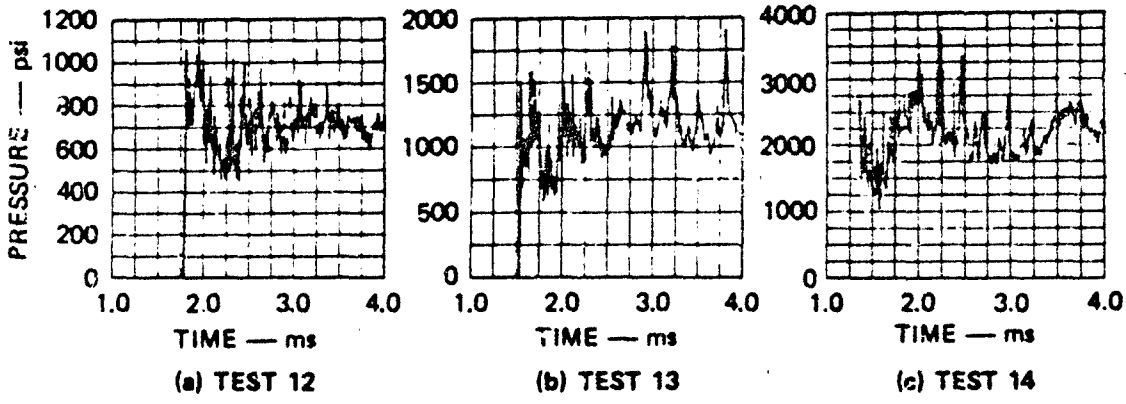

FIGURE 2 PRESSURE MEASURED AT THE REFLECTING WALL IN THE SHOCK TUBE CALIBRATION TESTS

The expansion and venting tests were performed using 6-in.-ID, 12-in.-long trench models having a wall thickness of 0.75 in. Two longitudinal 0.56-in.-deep saw cuts offset 110 degrees from each other and two transverse 0.56-in.-deep saw cuts at the third points separated the roof blocks. A typical trench model is shown in Fig. 3.

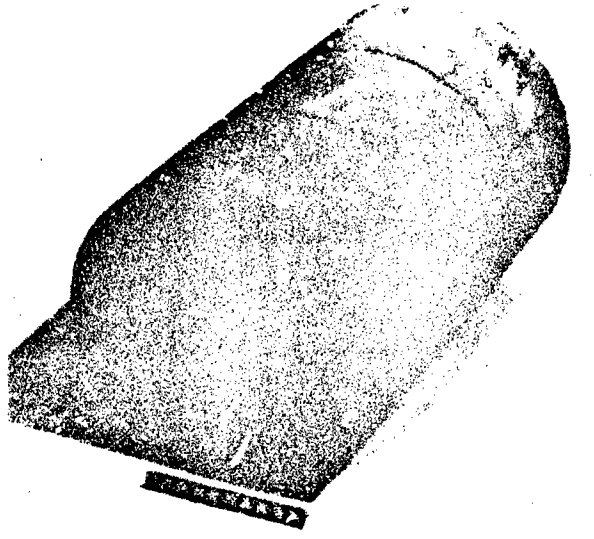

FIGURE 3 FIBER-REINFORCED CONCRETE TRENCH MODEL WITH SAW-CUT ROOF BLOCKS

The formula used for the fiber-reinforced concrete was similar to that used by the Air Force Weapons Laboratory (AFWL) in the fabrication of 1/2-scale trench models. The steel fibers are U.S. Steel Fibercon, 0.010 in. in diameter and 0.5 in. long. They represent about 1.7% of the concrete mix by weight (0.5% by volume). Eight unconfined compression tests (ASTM C39-64) and 5 split-cylinder tension tests (ASTM C496-71) were performed on 3-in.-diameter, 6-in.-long samples.[3] The compression strength varied from 6590 psi to 8420 psi and averaged 7430 psi. The split-cylinder tension strength varied from 820 psi to 1010 psi and averaged 900 psi.

The soil used in the expansion and venting experiments was obtained from a designated location at the HAVE HOST test site on the Luke Air Force Range in Arizona where AFWL's 1/2-scale tests were performed. The soil was packed around the model trench manually, and samples were taken to measure the soil density and moisture content. Densities (except Test 20, the dry soil test) ranged from 117 to 122 lb/ft^3 with moisture contents from 2.6 to 3.9%. The soil cover depth was 2.3 in.

Experimental Results

Many expansion and venting experiments were conducted. Only five are described in this paper. The parameters of these experiments are given in Table 1.

Table 1

TEST PARAMETER FOR EXPANSION AND VENTING TESTS

	Test Number				
Parameter	17	18	19	20	22
Soil density	122	122	122	120-122	118
Moisture content	3.3	2.6	2.8	0.3-1.9	3.6
Peak pressure	700	1100	1100	1100	2600

The following general features were observed in this set of experiments:

(1) Several longitudinal cracks form in a circumferentially symmetric distribution in the trench wall almost immediately (within 0.3 ms) after the arrival of the shock wave. Fig. 4 shows the cracking patterns observed in Test 17 and Fig. 5(a) shows the recovered trench fragments. Fig. 5(b) shows the crack pattern observed in an AFWL 1/2-scale test. The patterns are the same for both scales.

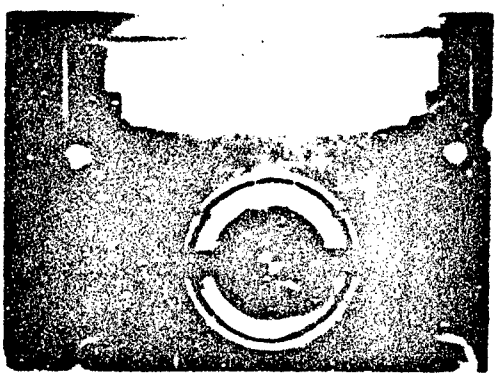

(t = 2.20 ms, Test 17)

MP-6307-1

FIGURE 4 TRENCH CRACKING PATTERN

(2) The expansion of the trench into the soil is cylindrically symmetric until the rarefaction wave returns from the free soil surface to the trench roof. Fig. 6 illustrates this phenomenon as observed in Test 17. In this illustration, the shock wave arrives at the reflecting wall at 1.7 ms, and the trench begins to expand symmetrically. Based on a soil wave speed of 465 ft/s (observed in a previous test), the pressure wave in the soil reaches the surface about 0.45 ms later, after which the soil surface begins to move. After another 0.45 ms, the relief wave from the soil surface reaches the crown, ending the symmetric phase of the expansion.

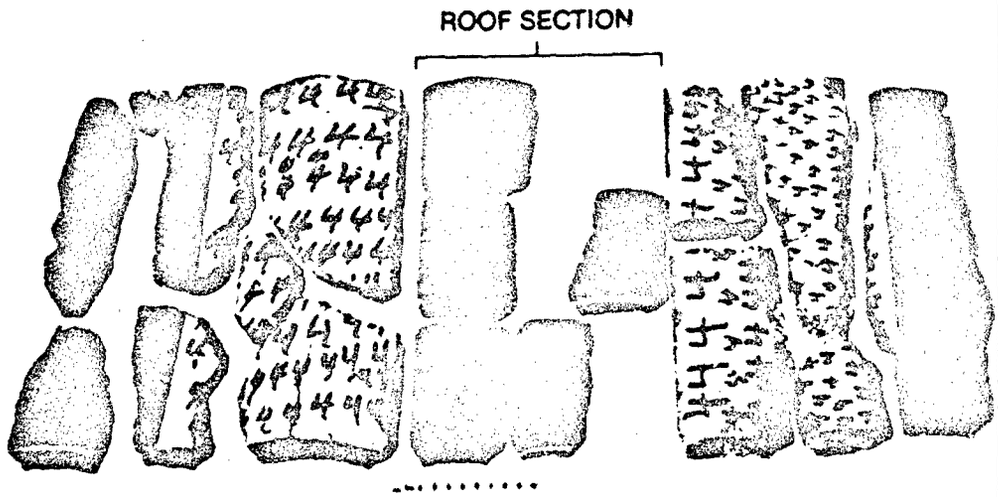

(a) RECOVERED TRENCH FRAGMENTS FROM SRI TEST 17 (1/26-Scale)

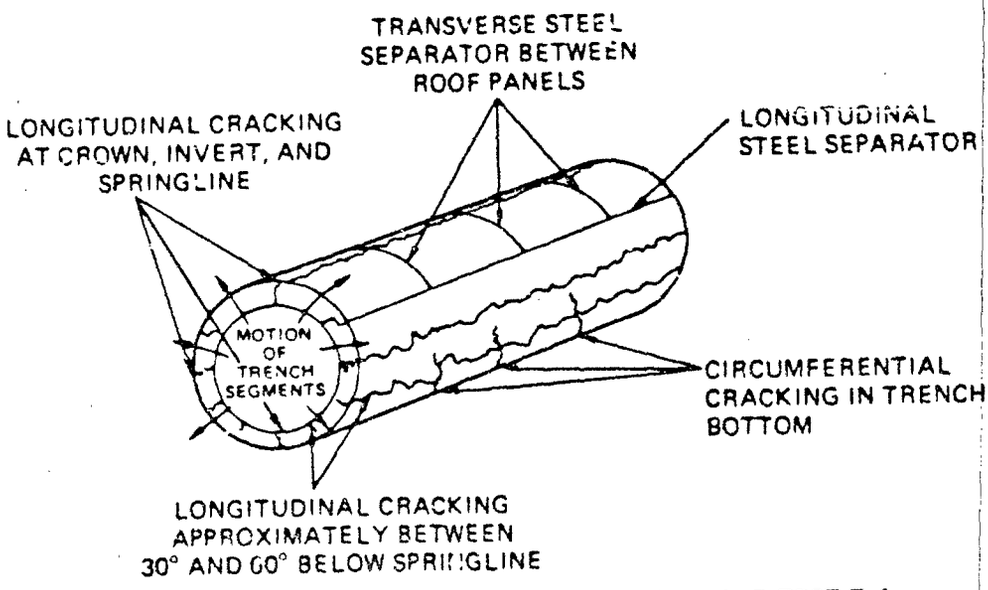

(b) CRACK PATTERN OBSERVED IN AFWL 1/2-SCALE TEST T-1

MP-6307-17R

FIGURE 5 COMPARISON OF TRENCH CRACK PATTERNS BETWEEN SRI 1/26-SCALE TESTS AND AFWL 1/2-SCALE TEST T-1

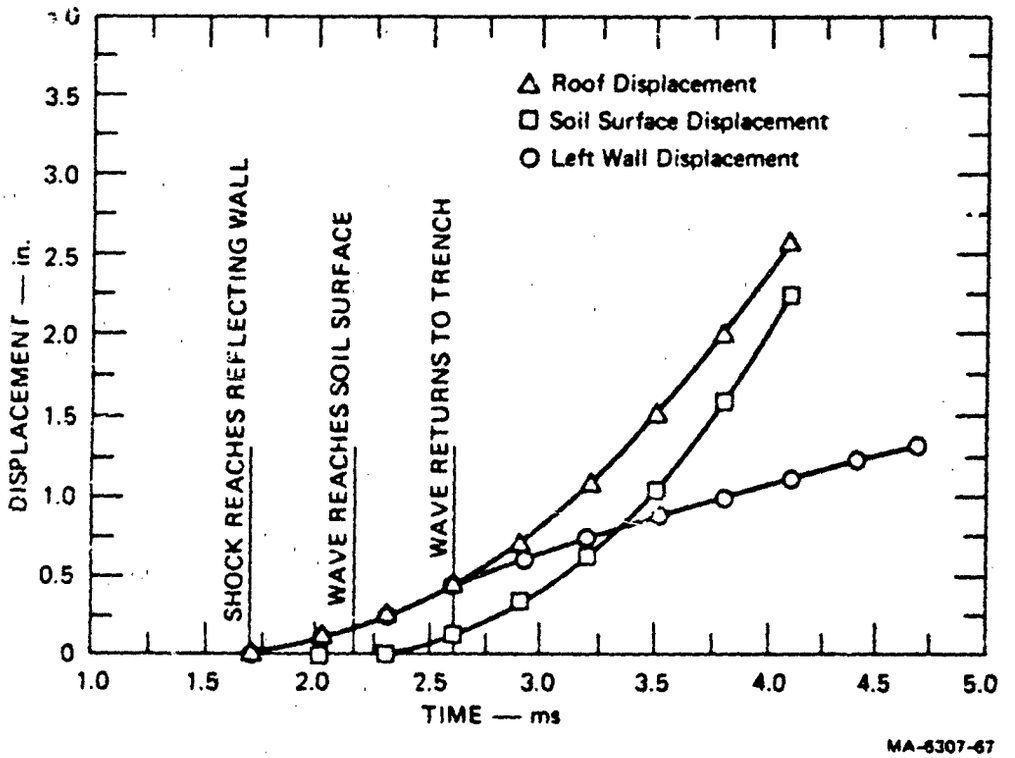

FIGURE 6 SYMMETRIC TRENCH EXPANSION PHASE (Test 17)

(3) After the symmetric expansion phase, the slug of roof fragments moves vertically with little or no change of shape until venting occurs. The soil above the crown mounds up without much lateral flow. The expansion of the trench at the springlines and floor continues to be approximately symmetric. Fig. 7 illustrates this phase of expansion in Test 17.

(4) Venting begins at the roof crack nearest the crown, when the trench roof has moved to about the level of the original soil surface. Initiation of venting in Test 17 is shown in Fig. 8.

(t = 3.70 ms, Test 17)

MP-6307-15C

FIGURE 7 ASYMMETRIC EXPANSION PHASE

(t = 4.20 ms, Test 17)

MP-6307-15D

FIGURE 8 INITIATION OF VENTING AT CRACK NEAREST CROWN

(5) Once venting begins (near the reflecting wall), the soil surface unzips along the length of the trench at about the same rate as the propagation of the reflected shock wave. This phenomenon as observed in Test 17, is illustrated in Fig. 9. (The unzipping phenomenon was difficult to observe with short test sections, especially at the higher pressures, but the shock attenuation tests with long trenchs verified this response feature.)

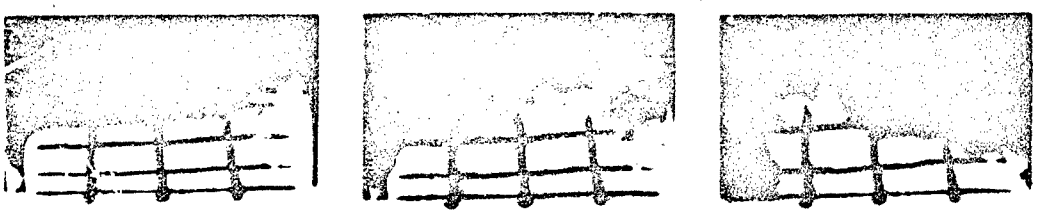

(a) t = 4.10 ms (b) t = 4.50 ms (c) t = 4.95 ms

MP-6307-16C

FIGURE 9 SIDE VIEW OF GROUND SURFACE ABOVE THE TRENCH MODEL
(Photo pins used to measure absolute roof displacement)

The effect of pressure on venting is illustrated in Fig. 10, where the time of venting and the roof displacement at the time of venting are plotted against pressure. For this series of tests, a higher pressure caused venting to occur sooner and with less roof displacement. The lines drawn through the data are not fitted curves; they indicate only the trend. The data from Tests 18 and 19 do not lie near the lines. Even though in Tests 18 and 19 several measurements were repeatable, the venting data from these tests are considered anomalous because premature venting initiated through a path provided by a photo pin positioned to provide data on the motion of the trench roof.

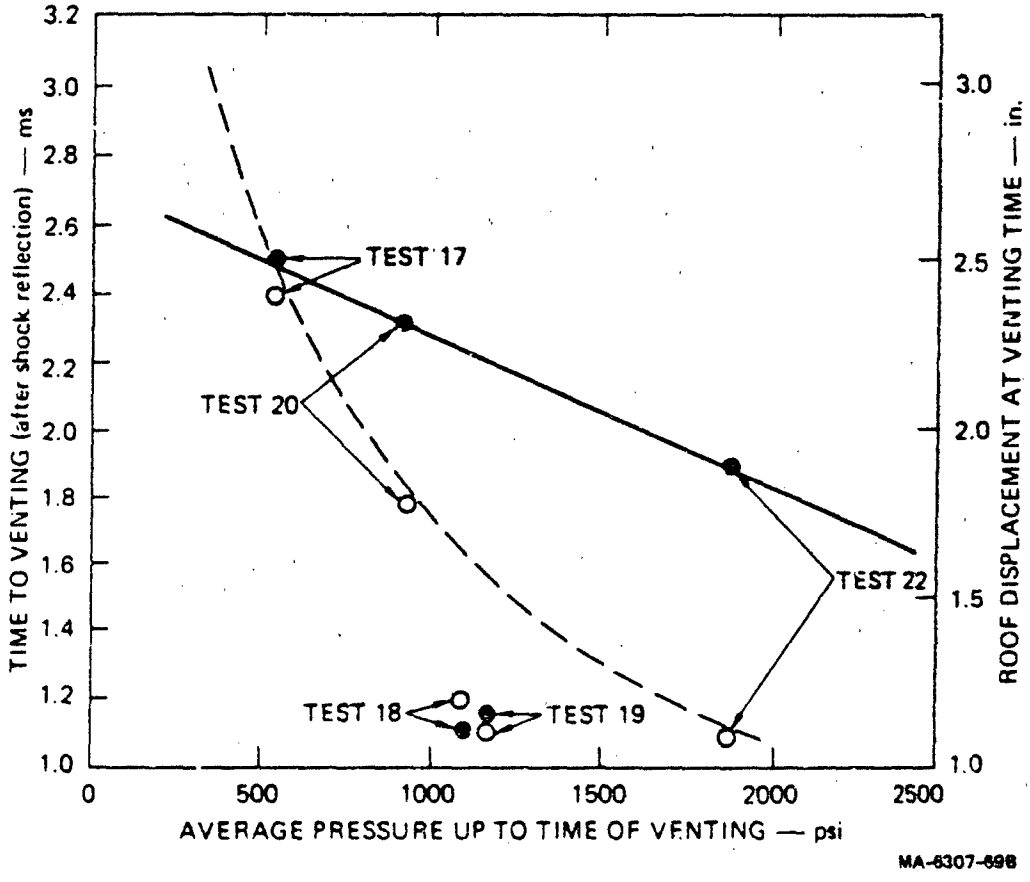

FIGURE 10 EFFECT OF PRESSURE ON VENTING TIME AND ROOF DISPLACEMENT AT VENTING TIME FOR REINFORCED CONCRETE TRENCHES

(○ – venting time, ● – roof displacement)

The effect of pressure on trench fragmentation is illustrated in Table 2, which lists the number of longitudinal cracks seen in the reinforced concrete trench models at various pressures. These data suggest that slightly more cracking occurs at higher pressures; however more data is needed to substantiate this possibility.

Table 2

EFFECT OF PRESSURE ON LONGITUDINAL CRACKING

Test Number	Nominal Peak Pressure	Number of Cracks
17	700	8
18	1100	10
19	1100	9
20	1100	7
22	2600	12

Analysis of Experimental Data

To assure the consistency of the data, we performed some basic analyses, in which we treated response features separately and did not attempt to calculate the entire response in a single analysis. The response features analyzed were:

(1) Roof motion calculated from the pressure measured at the reflecting wall.

(2) Trench expansion at the springlines and invert calculated from the pressure measured at the reflecting wall.

The motion of the roof was calculated to verify the consistency of the pressure measurements and the roof displacement measurements. A one-dimensional model was adequate to calculate the displacement of the roof up to the original soil surface level.

The mathematical model used to predict the roof displacement consists of an infinitesimal ring element of roof material and cover soil

loaded by internal pressure. Inertial effects are dominant over the effects of material strength, therefore, material strength was neglected. The roof/soil ring element was assumed to have a constant mass. A kinematic constraint (consistent with observation) required the thickness of the ring element to remain constant. Thus, as the inside radius grows, the loaded area increases and the mass density of the ring element decreases. The equation of motion for this model is

$$Pa\ (d\theta) = \rho \frac{(b^2 - a^2)}{2} \frac{d^2}{dt^2} (a+b)/2$$

where P is the pressure, a is the inside radius, b is the outside radius, and ρ is the mass density of the ring. The assumptions of constant mass and constant thickness reduce this equation to

$$2\pi\ Pa = m \frac{d^2 a}{dt^2}$$

where m is the mass per unit length of a full ring.

This model was used to calculate the roof displacement for each of the expansion and venting tests. Figure 11 compares the results of the calculations with roof displacement measurements taken from the films for tests with peak reflected pressures of 700 psi (Test 17), 1100 psi (Test 18), and 2600 psi (Test 22). The soil displacement for Test 17 is also given, indicating that about 0.4 in. of compression occurred in the soil cover. The correlation of the calculations with the data enhances the reliability of the pressure and displacement measurements and indicates that the simple model for predicting roof motion is adequate.

The trench expansion into the surrounding soil was calculated to verify the consistency of the pressure and displacement data, and also to confirm the soil wave speed observed in the high-speed movies. The problem was formulated for an axisymmetric, plane strain analysis. Calculations were made with SRI PUFF, a finite difference computer code capable of analyzing two-dimensional continua undergoing large deformation.[5]

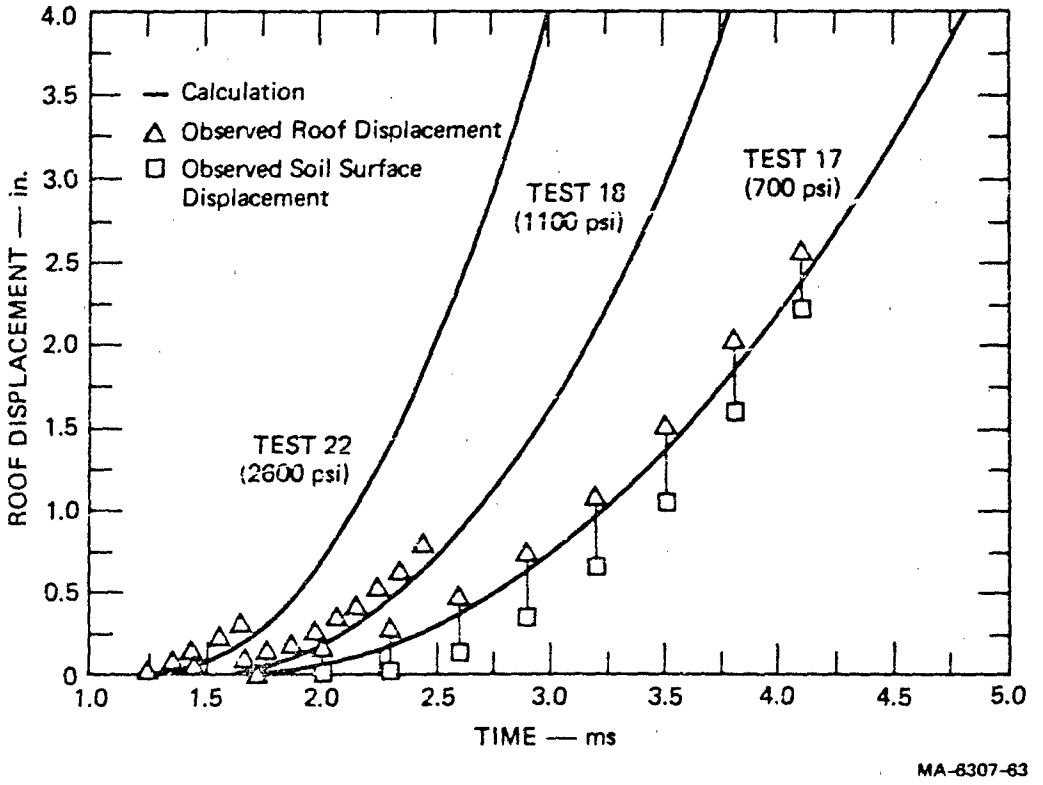

FIGURE 11 COMPARISON OF CALCULATED AND MEASURED ROOF DISPLACEMENT

The trench wall was modeled with typical concrete properties, allowing fracture at a low tensile stress. The radial compressive deformation of the concrete is negligible compared with the radial displacement. The soil was modeled as a Mohr-Coulomb material without dilatancy due to shear. In this model, the dilatational response is governed only by a variable bulk modulus (K). The distortional response is governed by two parameters, the cohesion c and the friction angle ϕ.

The soil properties were determined from the U.S. Army Waterways Experiment Station's (WES) uniaxial strain test data on HAVE HOST backfill.[4] In the calculations, the loading pressure-volume path was made to follow the $\sigma_z - \varepsilon_z$ curves given in Ref. 4. For unloading, a bulk modulus equal to the maximum loading modulus was used. A good

correlation with the expansion test data was obtained using soil parameters computed from WES's lower bound curve for low density soil even though our measured wet soil density was 5% to 10% higher than WES's low density soil.

One reason for using the lower bound low density stress-strain curve is that the bulk modulus computed from that curve, up to about 4% vertical strain, agrees with the bulk modulus estimated from our observed wave speed. Also, we calculated the trench expansion due to the pressure measured in Test 17 (700 psi nominal) using both the lower bound low density soil data and the upper bound high density soil data. The values of c and ϕ were taken directly from the WES data. The results of these two calculations are shown in Fig. 12, along with the Test 17 results. Clearly, the low density soil data produce a more accurate expansion calculation.

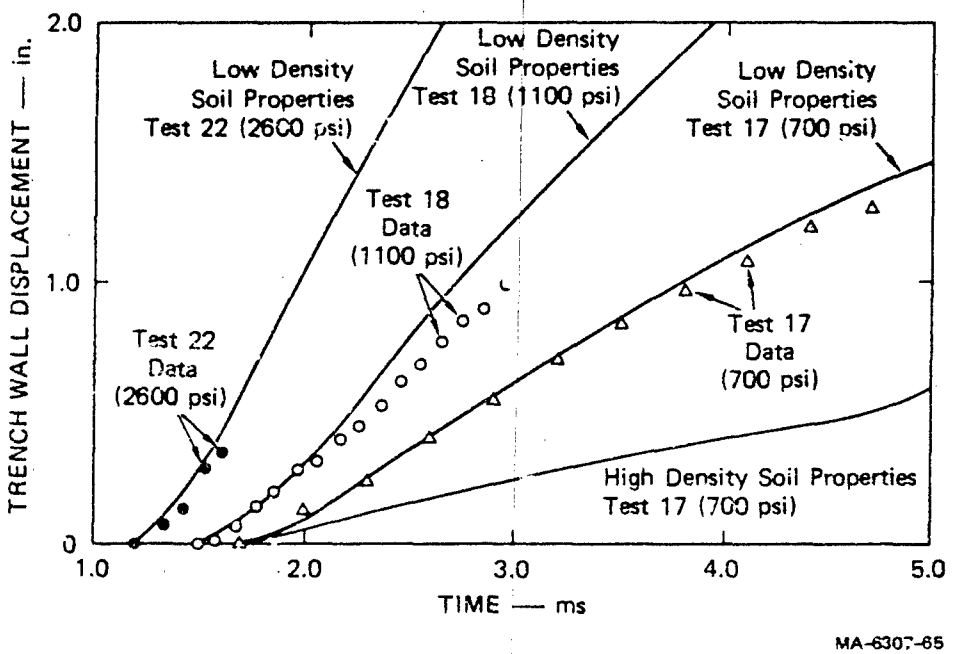

FIGURE 12 COMPARISON OF CALCULATED AND MEASURED SPRINGLINE AND INVERT DISPLACEMENTS

We then calculated the wall motion using the pressures measured in Test 18 (1100 psi nominal) and Test 22 (2600 psi nominal) with the low density soil data. These calculations are also compared with the experimental results in Fig. 12. Again, the calculations and the experiments correlate well enough to confirm the reliability of the pressure and expansion data and indicate that the computational model is adequate.

Shock Attenuation Tests

Experimental Setup

The shock attenuation tests were conducted using the assembly shown in Fig. 13. A 1-in.-thick pad of COMP B was used as the explosive because of its well-characterized equation of state. To achieve a nearly plane wave, we detonated the COMP B pad simultaneously at nineteen points spaced as uniformly as possible over the back surface of the pad.

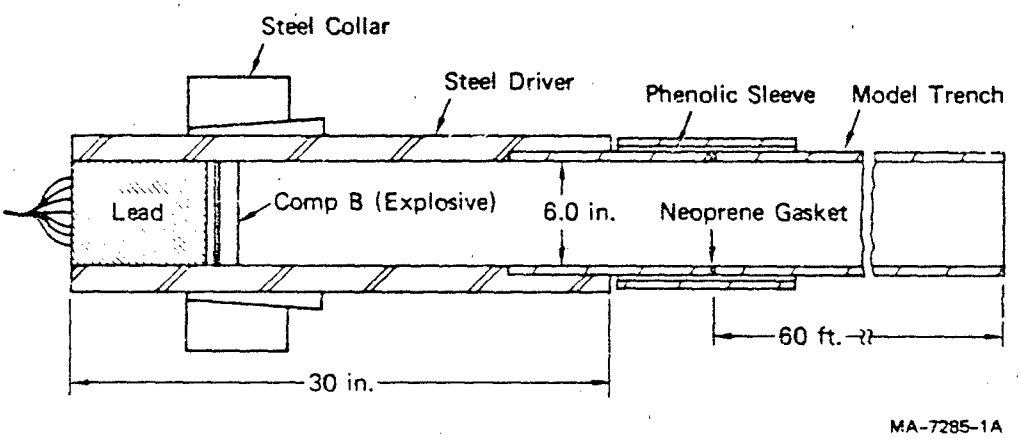

FIGURE 13 SHOCK TUBE DRIVER CONFIGURATION

The relative effects of the various attenuation mechanisms were determined by measuring shock attenuation in a steel pipe, a deep-buried fiber-reinforced concrete trench, and a shallow-buried fiber-reinforced concrete trench, each having a length of 60 ft (120 diameters).

Shock pressure in the trench was measured with pressure gages in the wall of the trench (grout was used to place the gages in the concrete trenches). The gage configuration had an average density approximating that of the trench so that the gages would move with the trench wall. The time of arrival (TOA) of transition zone between shocked air and the detonation products was also measured with custom-made ionization probes which were sensitive to the electrical conductivity of the gas in the tube.

Steel Pipe Experiment

In the first shock attenuation test, the concrete trench was replaced by a steel pipe. This test defined the shock attenuation due to frictional drag on the walls of the pipe and due to rarefactions originating upstream because of the finite thickness of the explosive charge. The pressure records are shown in Fig. 14. The peak pressure decreased from about 4000 psi near the source to about 700 psi near the open end of the pipe.

To check the pressure data, we calculated peak pressures from TOA data and compared them with the measured peak pressure. Shock velocity at each station was obtained by fitting a polynomial to the TOA data and differentiating this polynomial with respect to time. A fourth-degree polynomial gave the best fit. Based on the equations for conservation of mass and momentum, the relationship between shock velocity and pressure is

$$P_1 - P_o = \frac{2}{\gamma + 1} \frac{U^2}{v_o}$$

where v is specific volume, U is shock velocity, γ is the ratio of specific heats, and P is the pressure. The subscript o refers to conditions ahead of the shock front; the subscript 1 refers to conditions behind the shock front.

This equation was then used to calculate the peak gage pressure P_1-P_o at each station. For the shocked air, we used values of γ ranging from $\gamma = 1.22$ at a pressure of 4500 psi to $\gamma = 1.38$ at 300 psi. The

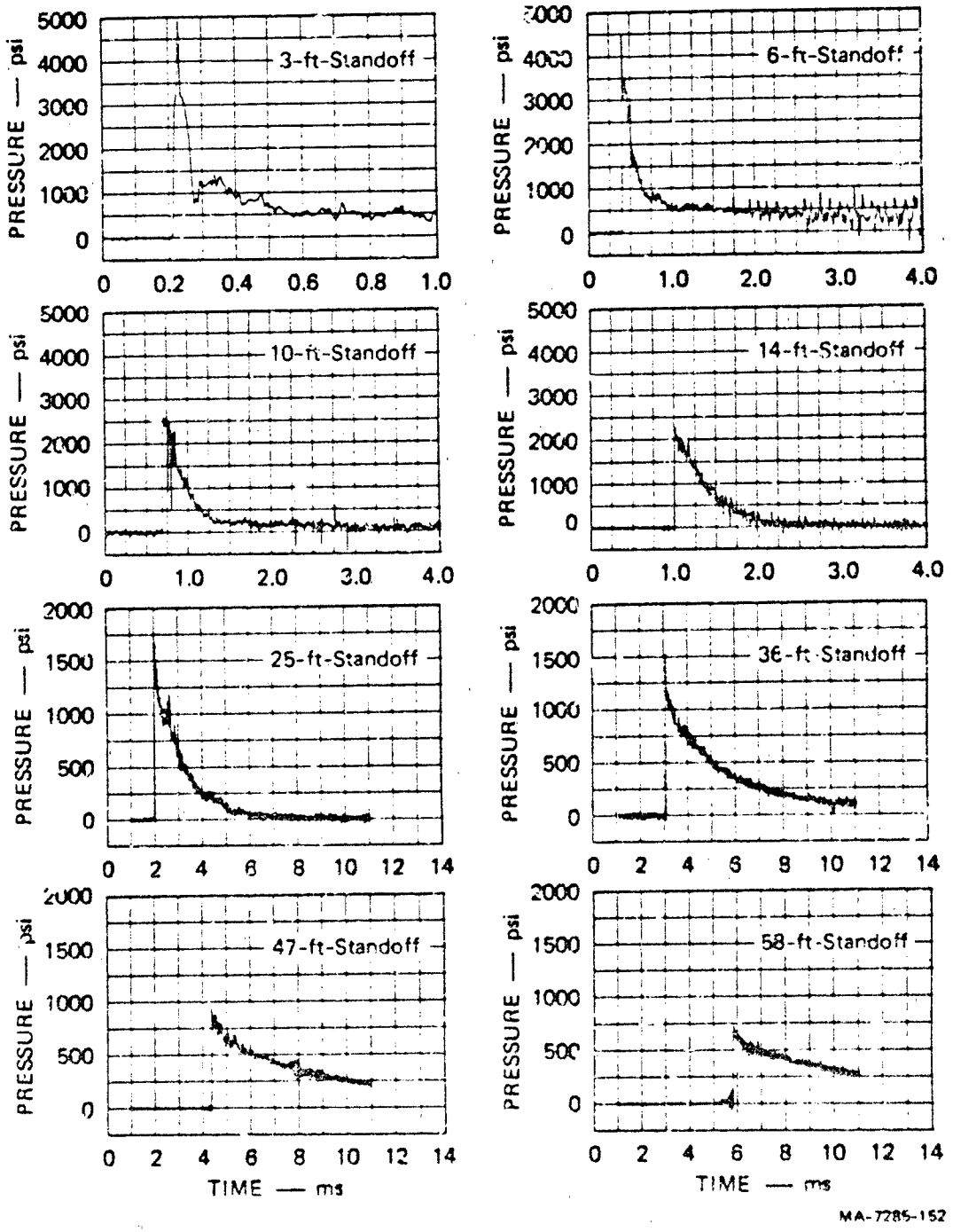

FIGURE 14 PRESSURE RECORDS FROM A SHOCK ATTENUATION TEST WITH STEEL PIPE

comparison between the calculated and measured peak pressures for the three tests with steel pipe is shown in Fig. 15.

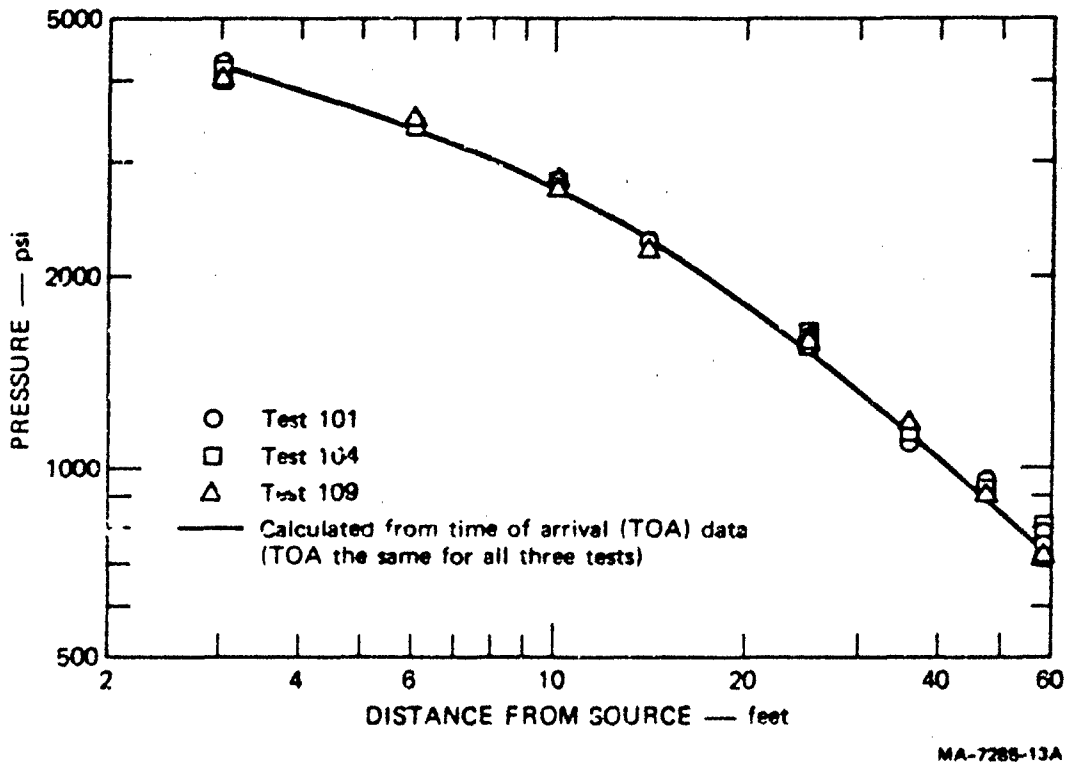

FIGURE 15 PEAK PRESSURE VERSUS DISTANCE FOR THE THREE SHOCK ATTENUATION TESTS USING STEEL PIPE

A typical ionization probe record is shown in Fig. 16. The probe records showed that the start of the transition zone ranges from 0.2 ms behind the shock front and 14 ft from the source to 3.5 ms behind the shock front and 58 ft from the source. The probe records and the pressure records were used to construct a plot of TOA of the shock front and of the transition zone versus distance from the source. This plot is shown in Fig. 17.

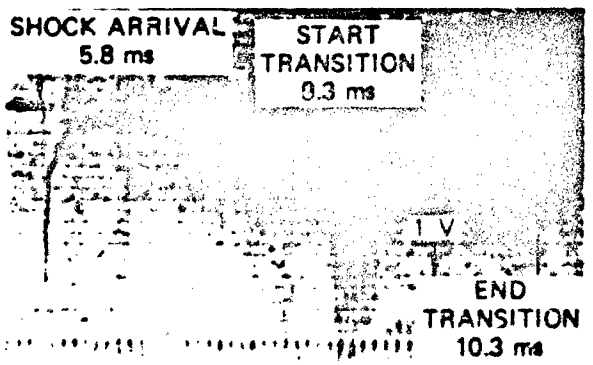

FIGURE 16 TYPICAL IONIZATION PROBE RECORD
(Test with steel pipe, 58-ft-standoff)

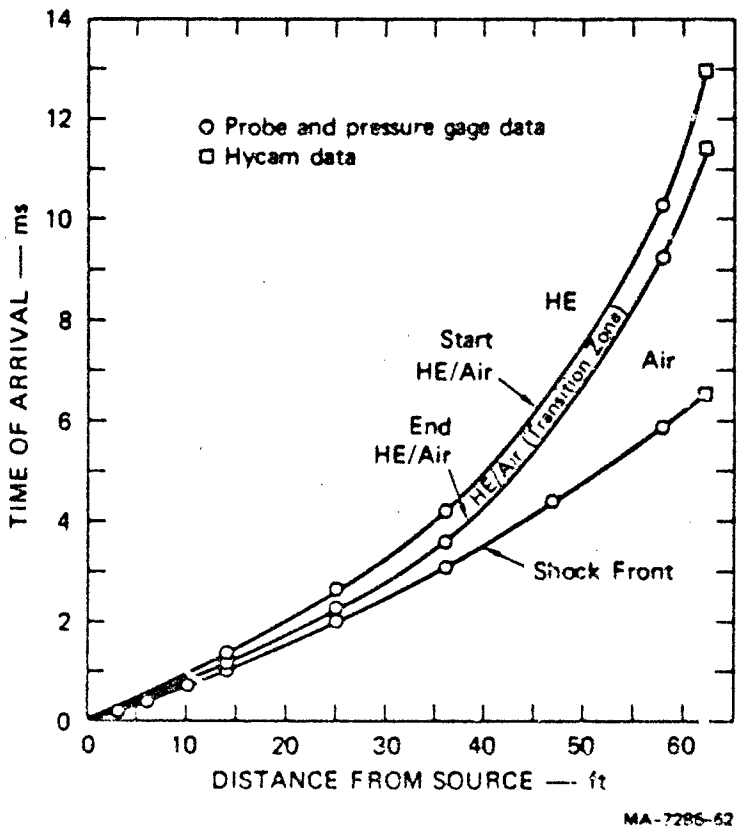

FIGURE 17 TOA (SHOCK AND POINT CONTACT) VERSUS DISTANCE FROM SOURCE FROM TEST 109
1-inch-thick Comp B Charge

Concrete Trench Experiments

Two tests were conducted with concrete trenches. In Test 116, the concrete trench was buried 12 to 15 in. deep, so the only added attenuation effect relative to the steel tube was trench expansion. In Test 117, the trench was buried 2.3 in. deep, a depth scaled from the baseline design. This test had the added effects of asymmetrical expansion and trench- to-surface venting.

The 60-ft-long concrete trenches were made up of 21 fiber-reinforced concrete trench sections, each with a 6-in.-ID, a 1-in.-thick wall, and a length between 30 and 36 in. The same concrete and fiber mix was used as in the short sections tested to study expansion and venting. The compressive strength ranged from 4100 psi to 8600 psi and averaged 6800 psi. The tensile splitting strength ranged from 800 psi to 1800 psi and averaged 1400 psi. In the field, the individual trench sections were joined together with epoxy. A laser was used for alignment.

The soil was obtained from the same location at the HAVE BOOST site as used in the expansion and venting tests. It was backfilled into a 3-ft-wide, 3-ft-deep excavation. For Test 117, the laser was used to aid in leveling the soil surface to within $\pm$0.1 in. For both tests, the soil was backfilled in layers of 4 to 6 in. Each layer was compacted to a nominal 110 lb/ft^3 dry density at a water content of 3 to 5 percent using a mechanical, gasoline-engine-driven tamper. Actual dry densities measured ranged from 108 lb/ft^3 to 116 lb/ft^3, with an average of 111 lb/ft^3. Measured water contents ranged from 2.9 to 5.3 percent.

Radial displacement of the trench wall was measured with linear variable displacement transducers (LVDTs). The LVDT core was connected to the outer trench wall at the springline by a 2.5-in.-long push rod. Each LVDT body was backed up by a 1.5-in.-diameter, 6-in.-long steel slug located 6 in. from the trench wall. Thus, the slug remained stationary until the shock wave in the soil reached it (about 0.5 ms). Because of its mass, the slug moved only a short distance thereafter. These tests were also photographed with three high-speed cameras.

In both tests, the concrete trench fractured over the entire 60-ft length. For the deep-buried trench in Test 116, there was only minor breakout, with most pieces still under the soil cover. In Test 117, with the shallow depth of burial, the roof of the concrete trench was thrown into the air and pieces were lying to either side of the trench axis. The trench below the springlines expanded radially 0.5 to 1.5 in., yet was roughly in its original orientation. The fracture patterns for Tests 116 and 117 were similar. The predominant fracture was longitudinal. Longitudinal cracks were from a few inches long to 4 or 5 ft. The majority of longitudinal cracks ran uninterrupted past the trench joints. However, some trench joints failed, causing the longitudinal crack to end at the joint. The trench fragments were smaller closer to the driver, indicating that the number of cracks increases with the pressure. The relation between pressure and number of cracks was similar to that found in the expansion and venting tests on short concrete trench sections. The high-speed movies showed that in Test 117, venting took place after the trench crown had displaced between 2.2 in. and 3.9 in. These displacements are higher than observed in the short section expansion and venting tests, possibly because of the thicker trench wall and the lower pressure at the time of venting.

Interpretation of Results

We then compared the shock attenuation for the three types of tests: steel pipe, deeply buried concrete trench, and concrete trench with scaled soil cover. Figure 18 shows a log-log plot for the peak pressure versus distance for each type of test. The curves are the peak pressures calculated from the TOA data. (As discussed earlier, these curves agree with the discrete peak pressures measured in the tests.) The pressure attenuation for the steel pipe, shown by the solid line, is caused primarily by the finite thickness of the source and by frictional drag on the pipe walls. The pressure attenuation for the deep-buried concrete trench, shown by the upper dashed line, should be the same as that of the steel pipe except for the effect of trench expansion. Comparison of the solid and upper dashed lines show that the effect of

trench expansion was to decrease the peak pressure by 55 percent at 58 ft from the source.

The pressure attenuation for the concrete trench with the scaled soil cover, shown by the lower dashed line, should be the same as that of the deep-buried concrete trench except for the effects of asymmetrical expansion and trench-to-surface venting. Comparison of the dashed lines shows no difference in peak pressure for the first 40 ft of propagation and only a 15 percent decrease in peak pressure after a distance of 58 ft. In these data, the effect of asymmetrical expansion of the trench crown and the effect of venting cannot be separated; however, it is clear that the combined attenuation effects of asymmetric expansion and venting are minimal compared with the effect of simple expansion.

Average springline velocities over the first millisecond after shock arrival were determined from the LVDT records and are plotted in Fig. 19. The closeness of the data from the two tests suggests that for the range of pressures and trench lengths in the these tests, the attenuating effect of upstream asymmetric expansion and venting also has little or no effect on the impulse for up to 1 millisecond after shock arrival downstream.

Conclusions

The major conclusions from the expansion and venting tests are that

(1) Approximately symmetric longitudinal cracks form in the trench soon after shock arrival.

(2) After reflections from the free surface of the soil, the roof fragments and soil move vertically as a slug.

(3) Venting occurs directly above the roof when the bottom of the slug reaches the original soil surface.

The data from the shock attenuation tests showed consistently lower peak pressures as more attenuation mechanisms were introduced. For example, the effect of trench expansion (concrete trench versus steel pipe) was to decrease the peak pressure by 55 percent at an L/D of 116. For the test of a concrete trench with a scaled soil cover, the peak

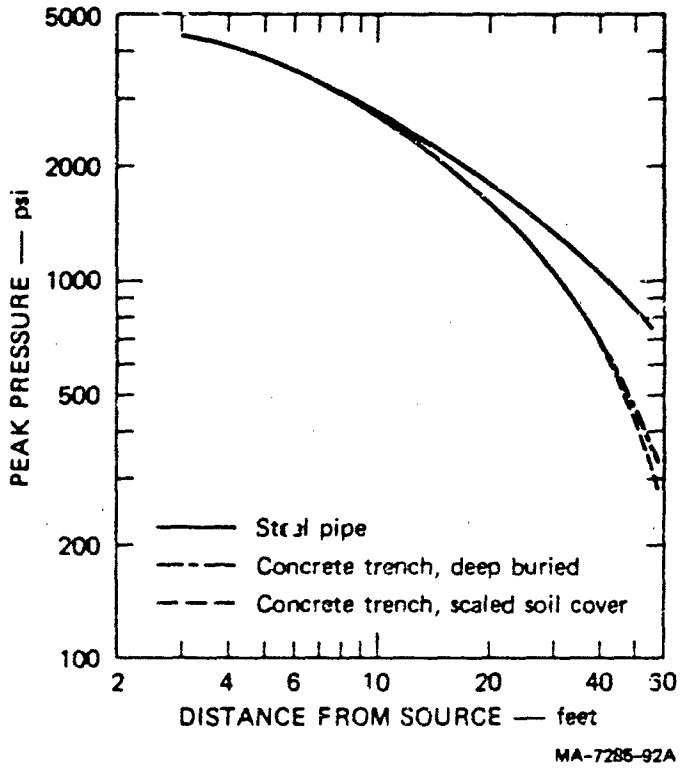

FIGURE 18 COMPARISON OF PEAK PRESSURE VERSUS DISTANCE FOR TEST 109 (STEEL PIPE), TEST 116 (CONCRETE TRENCH, DEEP BURIED) AND TEST 117 (CONCRETE TRENCH, SCALED SOIL COVER)

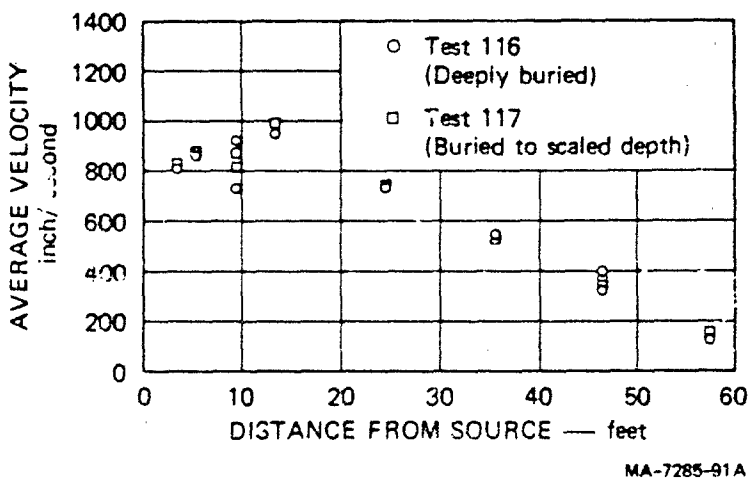

FIGURE 19 AVERAGE SPRINGLINE VELOCITY VERSUS DISTANCE FROM SOURCE

pressure was the same as that of the deep-buried concrete trench for the first 40 ft (L/D = 80). Thus asymmetrical expansion of the trench and venting has no effect on peak pressure up to L/D = 80 and has only a small effect (15 percent decrease) on peak pressure at L/D = 116.

Acknowledgment

This work was sponsored by the Defense Nuclear Agency under Contracts DNA001-77-C-0232 and DNA001-78-C-0198, and was monitored by Dr. George Ullrich.

References

1. J. R. Bruce and J. K. Gran, "Laboratory Investigation of Expansion and Venting and Plug Response in the MX Trench," SRI International, Menlo Park, CA, Final Report DNA5235F (1 February 1979).

2. J. R. Bruce and J. K. Gran, "Laboratory Investigation of Shock Attenuation and Spur Response in the MX Trench," SRI International, Menlo Park, CA, Final Report DNA 5086F (28 February 1979).

3. Testing Engineers, Inc., Santa Clara, CA.

4. J. G. Jackson, Jr., Waterways Experiment Station, Vicksburg, Mississippi, "Recommended Calculational Properties for HAVE HOST High-Density Backfill," letter to AFWL, Kirtland AFB, New Mexico (7 July 1977); "Recommended Calculational Properties for HAVE HOST Low-Density Backfill," letter to AFWL, Kirtland AFB, New Mexico (5 April 1977).

5. L. Seaman, "SRI PUFF 3 Computer Code for Stress Wave Propagation," prepared for Air Force Weapons Laboratory, Air Force Systems Command, Kirtland AFB, New Mexico, Technical Report No. AFWL-TR-70-51, Stanford Research Institute, Menlo Park, California (September 1970).

6. S. J. Ayala, "HAVE HOST T-1 Quick Look," Preliminary Report prepared by AFWL/DEP for the Space and Missile Systems Organization (SAMSO), Project 627A, Program Element 6330F under DNA Contract. Subtask H35HAXSX355, Program Element 62710H (25 August 1977).

DYNAMIC CYLINDER TEST PROGRAM

by

Jerry E. Stephens, A.M. ASCE[1]

INTRODUCTION

The Dynamic Cylinder Test (DCT) program consists of three tests on models of the tube section of the generic, horizontal Missile-X (MX) shelter (see Table 1). The objective of the program is to analytically and experimentally determine the loads on and response of the shelter and adjacent soil media subjected to nuclear airblast and airblast-induced ground shock loadings. The first two tests in the program, the DCT-1 and DCT-2 tests, have been completed. The particular areas of concern in these tests were,

1. the effects of structural detail (SALT ports, breakout joints, mass simulator support (MSS) beams, floor, and thickness-to-radius (t/r) ratio of the tube) on shelter response,

2. the character of the loadings across the structure/soil interfaces, and

3. the development/refinement of nuclear blast simulation techniques.

The DCT-1 and DCT-2 tests were performed by the New Mexico Engineering Research Institute (NMERI) at the Civil Engineering Research Facility (CERF) on Kirtland Air Force Base (KAFB), Albuquerque, New Mexico. In the DCT-1 test, three shelter models were subjected to a side-on airblast

---

[1] Research Engineer, Structural Mechanics Division, University of New Mexico, New Mexico Engineering Research Institute, Albuquerque, New Mexico.

TABLE 1. DCT TEST MATRIX

Test Event	Scale	Model	Structural Features		Airblast Environment
			Details	t/r*	
1	1/5	A	Floor		3 MPa, 24 kt
		B	SALT Ports, Breakout Joints, Floor	0.22	Sideon; Simulate
		C	SALT Ports, Floor	0.22	1/10 Slope Berm
2	1/4.22	D	SALT Ports, Egress Beams	0.28	4 MPa, 40 kt
		E	SALT Ports, Egress Beams	0.19	Transverse; 18 MPa Axial; 50 deg Attack Angle
3	1/4	F	SALT Ports, Egress Beams (Precast)	0.24	4 MPa, Transverse;
		G	SALT Ports, Egress Beams (Cast-in-Place)	0.24	18 MPa, Axial; 50 deg Attack Angle

* Cylinder wall thickness to inside radius ratio

loading. In the DCT-2 test, two shelter models were subjected to a combined axial and transverse airblast load. The simulated nuclear airblast loadings were generated using a High Explosive Simulation Technique (HEST). The instrumentation in the tests consisted of steel strain, relative displacement, acceleration, structure/media interaction (SMI), and normal stress gages in the models; and blast pressure and soil stress and acceleration gages in the adjacent soil (freefield).

The behavior of the test structures was modeled analytically prior to the tests. The effectiveness of the modeling techniques was evaluated by comparing the calculated results with the test data.

TEST ARTICLE

Description

The DCT-1 and DCT-2 test structures were 1/5-size and 1/4.22 size models, respectively, of the cylinder (tube) section of the generic MX horizontal shelter, as shown in Figure 1. The DCT-1 structures, designated the A, B, and C models, were open reinforced concrete cylinders with a common outside diameter of 1.341 m and a cylinder t/r ratio of 0.22 (Figure 2). Model A was a monolithic cylinder without SALT ports or breakout joints. Model B had both SALT ports and breakout joints. Model C had only SALT ports. The DCT-2 structures were reinforced concrete canisters capped with removeable closures. These structures, designated the D and E models, had a common outside diameter of 1.341 m and cylinder t/r ratios of 0.28 and 0.19, respectively (Figure 3). The inside surface of the DCT-2 models was lined with sheet steel. These models also had SALT ports and mass simulator support beams.

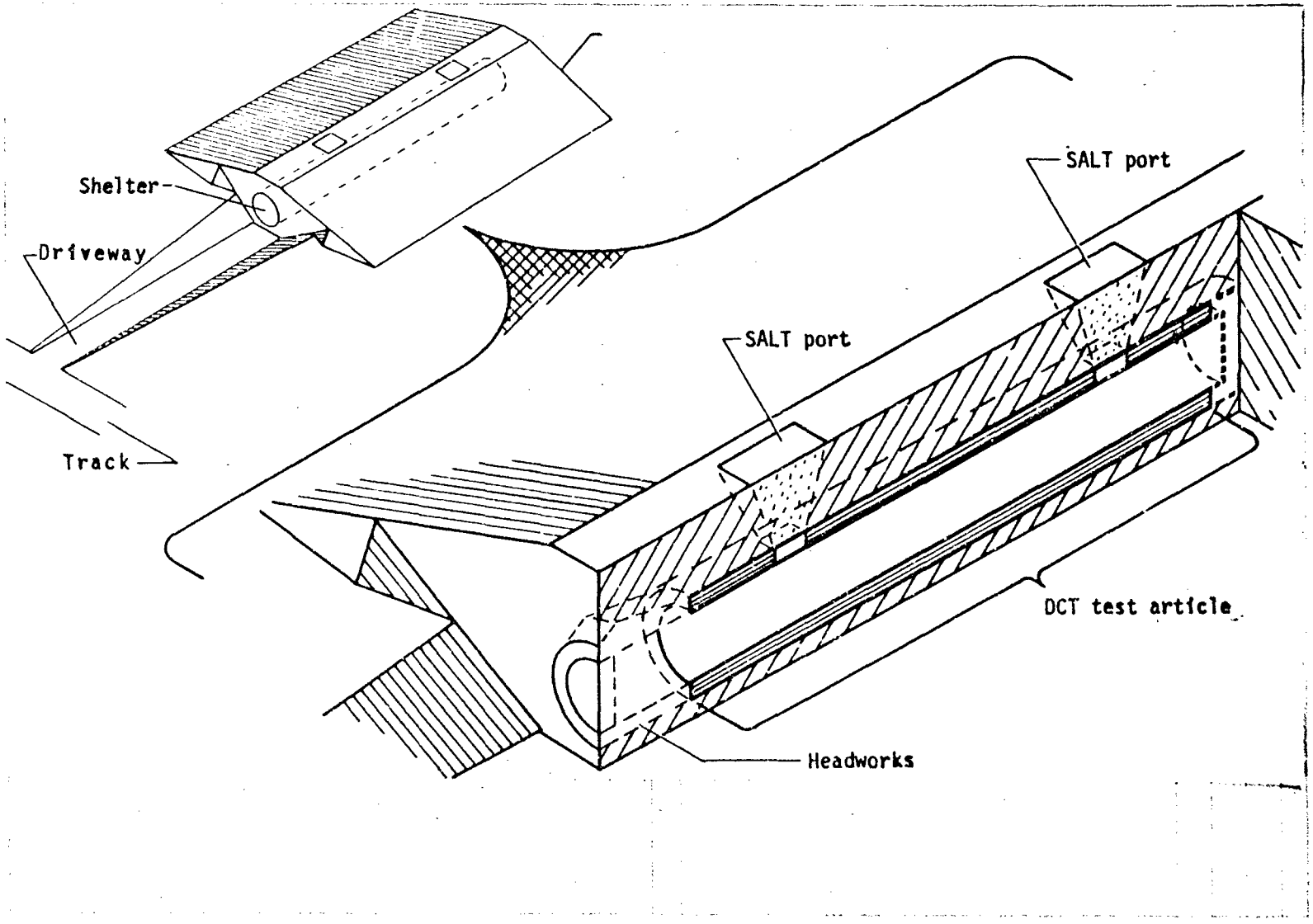
Shelter
Driveway
Track
SALT port
SALT port
DCT test article
Headworks

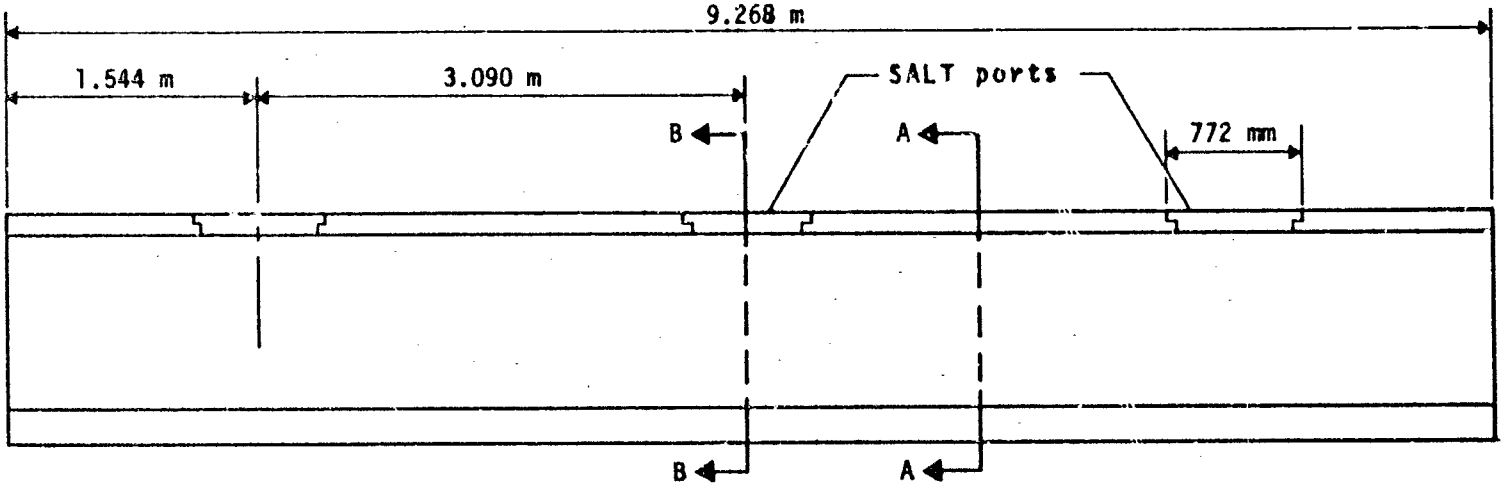

Longitudinal Section

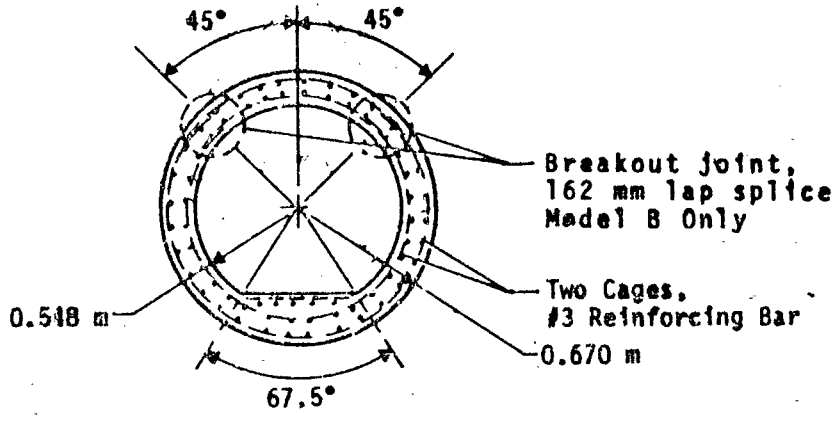

Section A-A

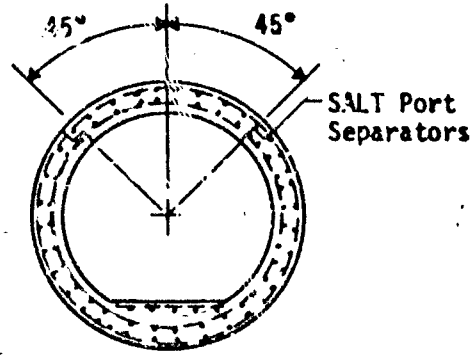

Section B-B
Models B&C Only

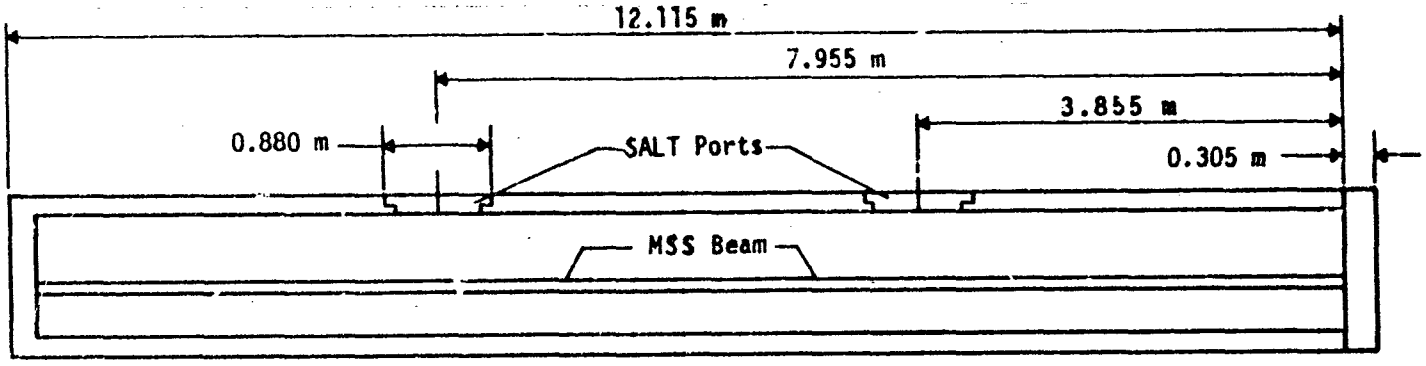

Longitudinal Section

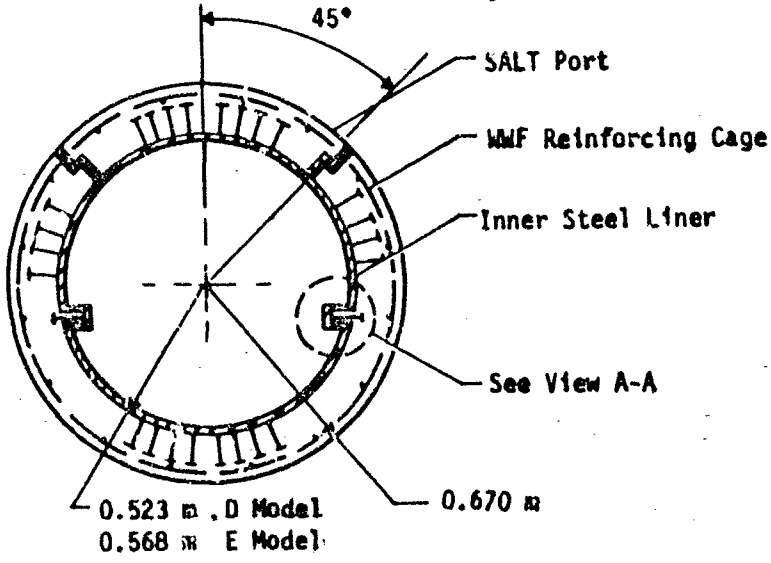

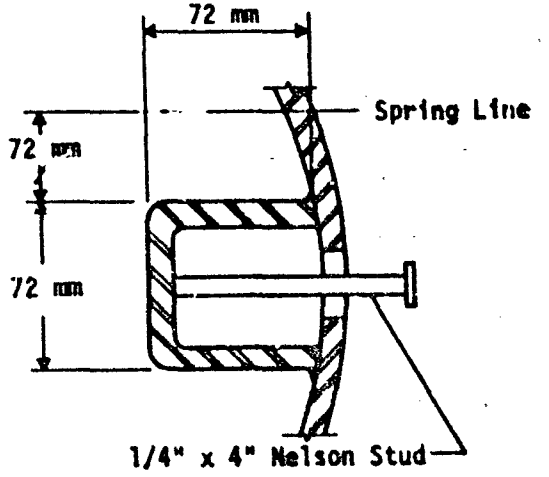

Egress Beam
View A-A

The concrete in the DCT-1 and DCT-2 models had a design 28-day unconfined compression strength of 59 MPa. The mix proportions for the concrete are shown in Table 2. The location, percentage, and strength of the reinforcing steels used in the models are indicated in Table 3.

The SALT ports in the DCT-1 and DCT-2 models were removeable panels spaced along the crown of the structure. The DCT-1 models each had three ports; the DCT-2 models, two ports. These ports modeled the missile-presence verification inspection panels planned for the actual shelter (such ports will possibly be required by future Strategic Arms Limitation Talks (SALT) agreement). Each port consisted of a steel lined opening and mating lid, as shown in Figure 4a. The ports were reinforced consistent with the reinforcing in the main structure, with the addition of shear ties encircling both the lids and the openings.

The breakout joints in the DCT-1 B model consisted of lap splices in the circumferential reinforcing bars located 45 deg on either side of the crown of the cylinder, as shown in Figure 4b. These splices were purposely underdesigned to facilitate breakout of the missile through the crown of the cylinder pursuant to launch.

Each DCT-2 model contained two MSS beams cast integrally on the model walls immediately below the springlines, as shown in Figure 4c. These beams, running the full length of the cylinders, act as support rails for a missile mass simulator deception device planned for the MX system.

The closures and end walls on the DCT-2 models, constructed of reinforced concrete, were purposely overdesigned to insure their survival during the test.

TABLE 2. CONCRETE MIX PROPORTIONS FOR THE DCT-1 AND DCT-2 MODELS

Material	Quantity	
	DCT-1	DCT-2
Cement (Type I)	474 kg	595 kg
Fly ash	84 kg	----
Fine aggregate (washed sand)	605 kg	648 kg
Coarse aggregate (9.5 mm crushed stone)	949 kg	943 kg
Water	193 kg	191 kg
Pozzolith (Master Builders 300R)	1820 ml	3312 ml
High range water reducer (Master Builders LA-8)	7278 ml	11325 ml
Yield	1 m^3	1 m^3
Slump	222 mm	222 mm
Water/Cement ratio	0.35	0.32

TABLE 3. SUMMARY OF THE REINFORCING IN THE DCT-1 AND DCT-2 MODELS

Model	Reinforcement			
	Description	Type	Percent by Volume	
			Long.	Circum.
DCT-1				
A,B,C	Inner Cage	#3 Grade 60 Bars	0.5	0.5
	Outer Cage	#3 Grade 60 Bars	0.5	0.5
DCT-2				
D	Inner Liner	2.7 mm A36 Plate	1.6	1.8
	Outer Cage	#3 Grade 60 Bars	0.2	0.5
E	Inner Liner	2.7 mm A36 Plate	2.4	2.6
	Outer Cage	#3 Grade 60 Bars	0.2	0.5

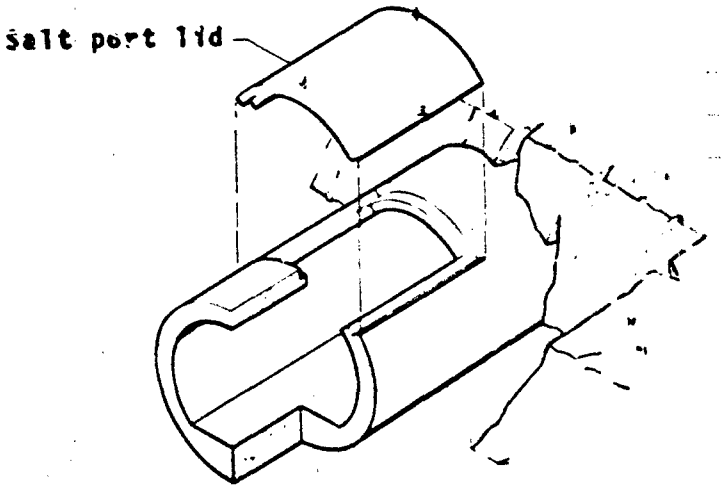

a. SALT port detail

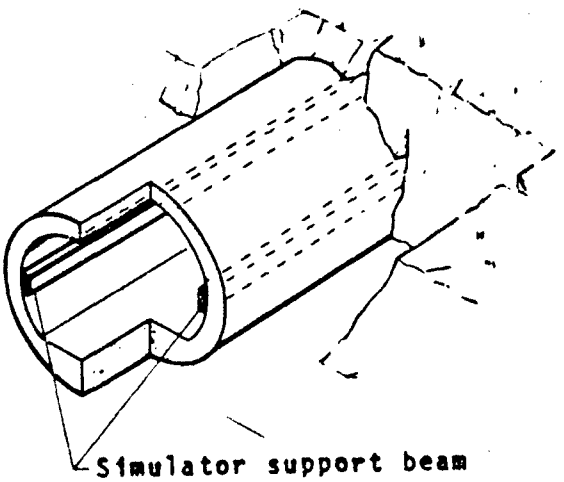

b. MSS beam detail

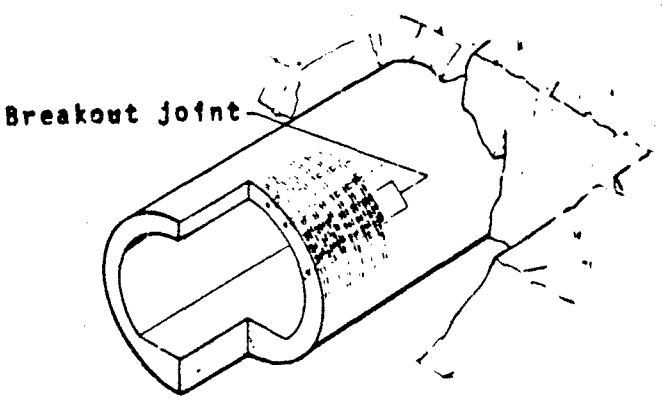

c. Breakout joint detail.

Fabrication

The DCT-1 and DCT-2 models were cast in a vertical orientation. The inside of the DCT-1 models was formed using reuseable segmented steel cylinders; the inside of the DCT-2 models, using the models permanent inner steel lining. The requisite reinforcing cages were fabricated around the inner forms. The outside forms, consisting of reuseable segmented steel cylinders, slipped over the completed inner form/reinforcing cage assembly. A uniform wall thickness was maintained in the models by placing steel spacer rods between the inner and outer forms.

The models were cast using two vertical steel pipes placed between the inner and outer form walls. The pipes were placed in the models during form assembly. The pipes were gradually withdrawn as the level of concrete rose in the forms. Inspection holes were drilled in the lower wall of each SALT port frame and an inspection panel cut in the outside form to permit observation of the consolidation of the concrete under the frame. During casting, the concrete was consolidated using both external and internal vibration. The SALT port lids were cast separately from the models using the same basic concrete used in the models but with a lower slump (less water reducing agent was added to the mix).

The models were allowed to cure in the forms undisturbed for a minimum of seven days. The forms were subsequently stripped, the exposed concrete surfaces sprayed with curing compound, and the models turned to their normal horizontal orientation. Turning of the models was accomplished using a special lifting fixture fabricated for this purpose.

During model fabrication, specimens were cast from each batch of concrete for material strength and response testing. All sampling and

testing was performed in accordance with the applicable American Society for Testing and Materials (ASTM) standards.

TEST FACILITY

The DCT-1 and DCT-2 tests were conducted at the CERF McCormick Ranch test site. The layout of the DCT-1 and DCT-2 testbeds is shown in Figures 5 and 6, respectively. The soil profiles at the two testbed locations are shown in Figure 7. In the DCT-1 test, the models were situated parallel in the testbed, perpendicular to the direction of propagation of the airblast load. In the DCT-2 test, the models were placed parallel in the testbed, parallel to the direction of propagation of the airblast load. The DCT-1 models were buried 305 mm below the ground surface; the DCT-2 models, 361 mm. In both tests the models were placed in 120 deg cradles cut in situ McCormick Ranch soil. The DCT-1 models rested on a thin layer of soil matching grout poured in the cradles. The DCT-2 models were seated in the cradles on a 25 mm layer of moist sand. On either side of the cradles was a 356 mm wide horizontal bench. The sides of the trenches around the models sloped at 45 deg from the edge of the bench to the ground surface. The trenches were backfilled with native McCormick Ranch soil compacted to a target unit weight of 1760 kg/m^3. The density of the recompacted material was checked at 200 mm intervals using a Troxler nuclear density meter. At the SALT ports, a sheet of plastic was placed in the backfill isolating the fill material over the ports from the rest of the backfill. The backfill over the SALT ports in the DCT-1 B model was compacted to a target unit weight of 1602 kg/m^3. The backfill over the rest of the SALT ports was compacted to a target unit weight of 1760 kg/m^3.

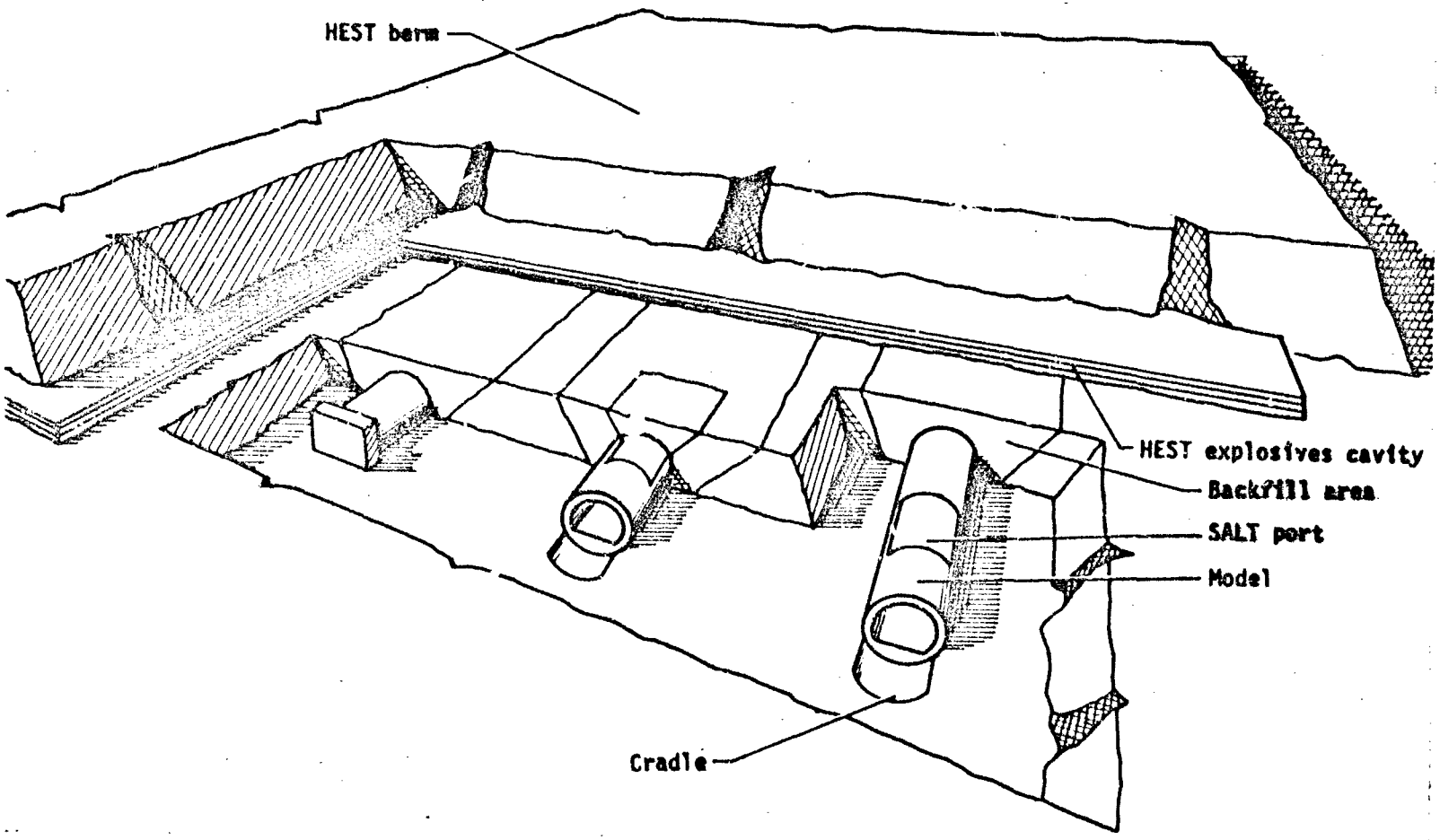
HEST berm
HEST explosives cavity
Backfill area
SALT port
Model
Cradle

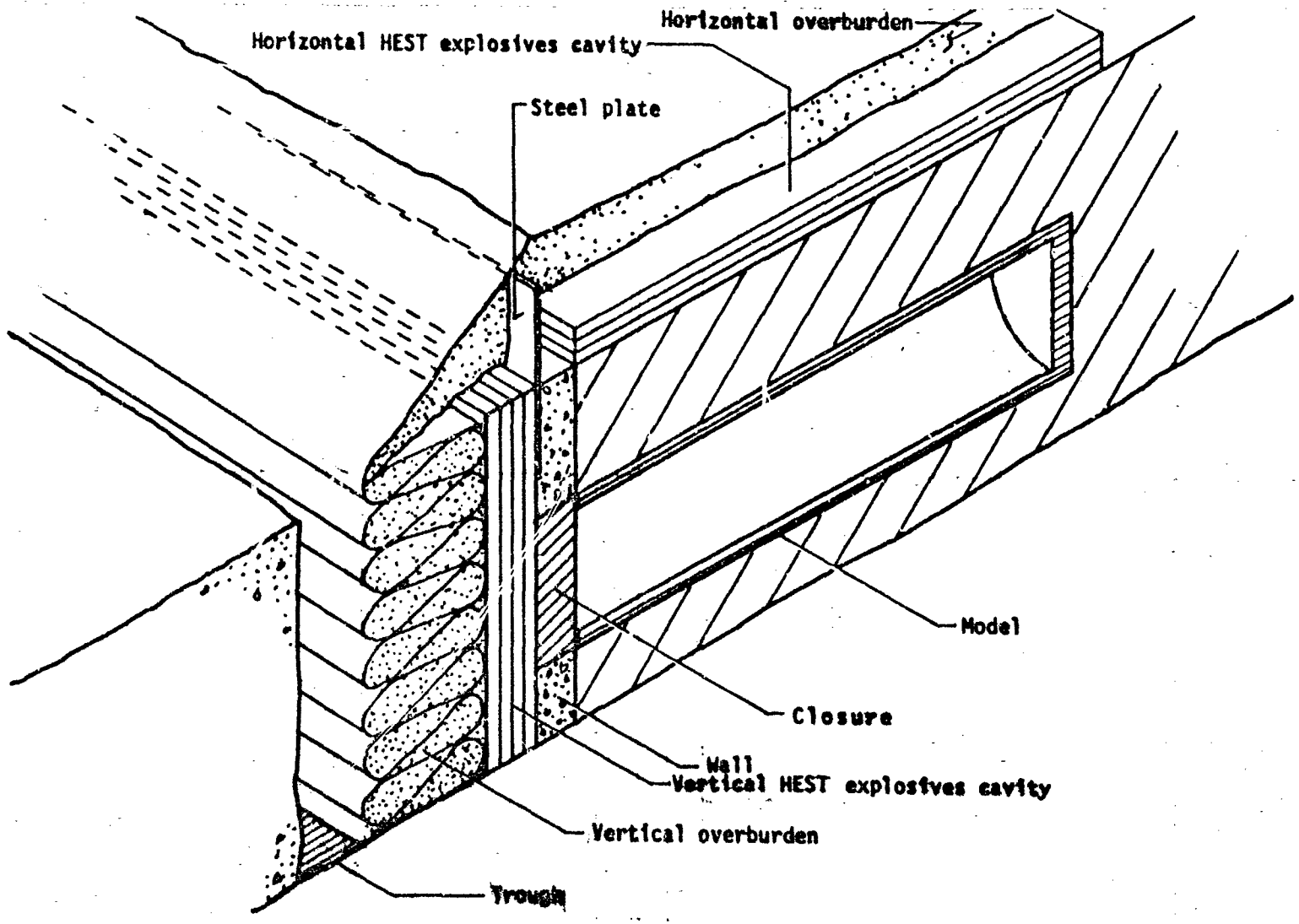
Horizontal overburden
Horizontal HEST explosives cavity
Steel plate
Model
Closure
Wall
Vertical HEST explosives cavity
Vertical overburden
Trough

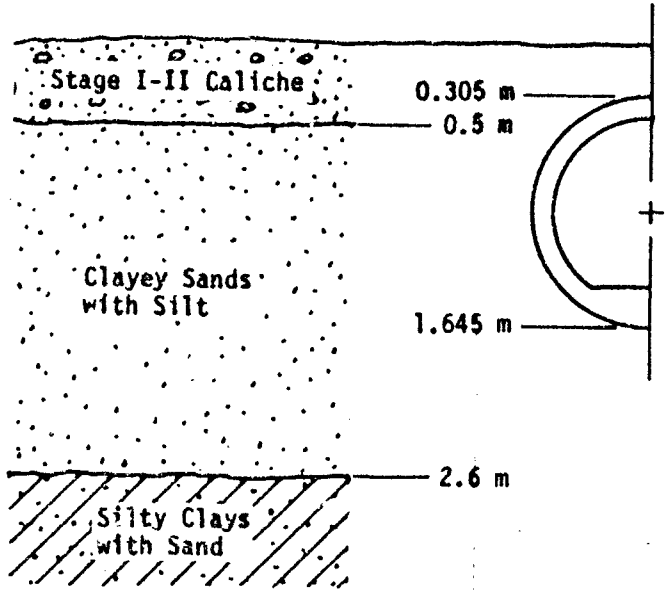

a) DCT-1 in situ soil profile

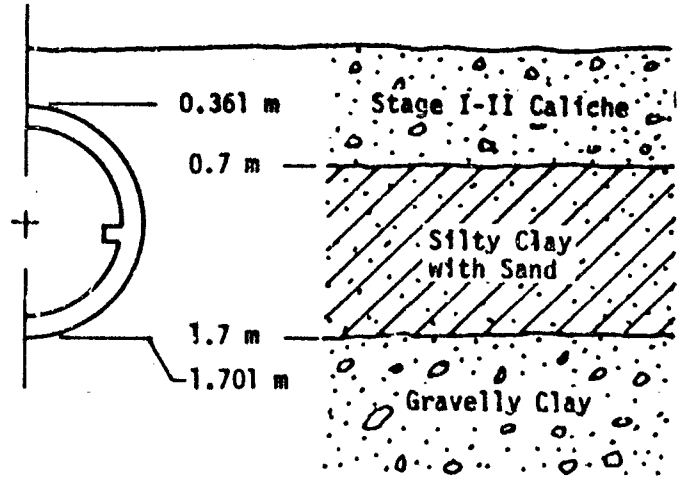

b) DCT-2 in situ soil profile

In the DCT-2 test, at the closure end of the models, a concrete headwall was constructed transverse to the models. The models extended through this wall, with the surface of their closures flush with the surface of the wall. The wall, 229 mm thick, was constructed of concrete with a design 28-day unconfined compression strength of 34 MPa. The wall was reinforced 0.5 percent by volume. This headwall functioned as part of the environment simulator and was not intended to accurately model any portion of the actual shelter system.

TEST ENVIRONMENT

The DCT-1 and DCT-2 test environments were generated using HEST's. A HEST is a method for simulating the incident airblast overpressure and airblast-induced ground shock motions resulting from a nuclear explosion; it consists of an explosion cavity confined by an earthen overburden placed over a testbed. The desired peak overpressure and impulse time history are produced by varying the charge and overburden densities and the cavity and overburden dimensions. The proposed HESTs for the DCT-1 and DCT-2 tests were designed using the Air Force Weapons Laboratory (AFWL) Lock-up Impulse Code (Reference 1).

The required environment for the DCT-1 test consisted of a traveling airblast at the 3.0 MPa peak overpressure range from the near surface detonation of a 24 kt (scaled) yield nuclear weapon (Figure 8). The airblast had to sweep the testbed side-on to the structures at a rate simulating a nuclear airblast traversing a berm with slope of 1/10. The airblast pressure and impulse time histories for this environment are shown in Figure 9. The HEST designed to generate this environment

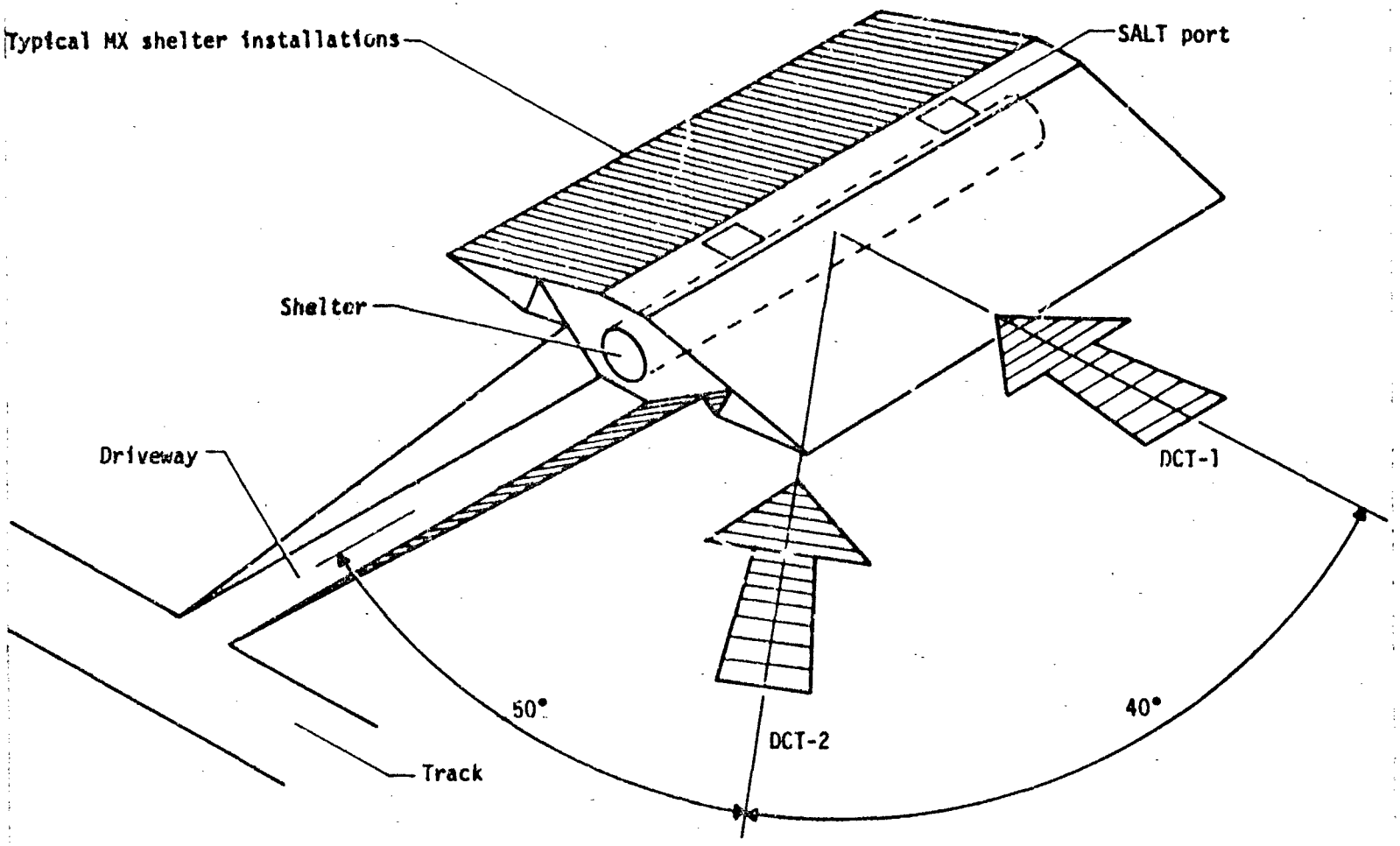
Typical MX shelter installations
SALT port
Shelter
Driveway
DCT-1
DCT-2
50°
40°
Track

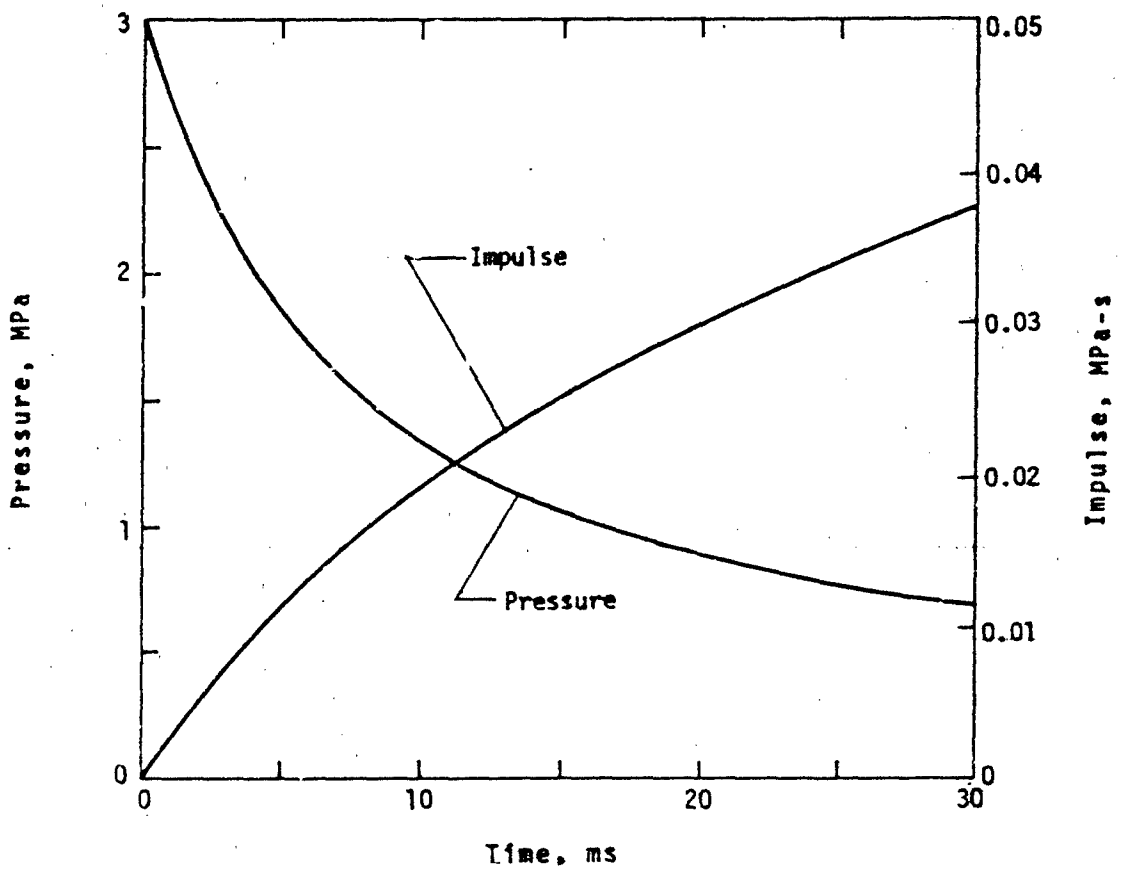
Pressure, MPa
Impulse, MPa-s
Time, ms
Impulse
Pressure
0
1
2
3
0
0.01
0.02
0.03
0.04
0.05
0
10
20
30

consisted of a 100 percent foam filled explosion cavity, 333 mm high, covered with 1.22 m of overburden, as shown in Figure 5. The charge density of the cavity was 6.25 kg/m^3. The cavity contained four layers of 0.085 kg/m detonation cord. The cord was placed in skewed parallel arrays to produce the desired airblast propagation rate. The sweep rate of the airblast was adjusted to a value of 1653 m/s so that the angle of incidence of the shock wave induced in the soil matched that which would be induced for an airblast sweeping a 1/10 slope. The overburden on the explosion cavity consisted of uncemented, uncompacted McCormick Ranch soil placed at a unit weight of 1442 kg/m^3.

The required environment for the DCT-2 test consisted of a traveling nuclear airblast with a 4.0 MPa peak overpressure and scaled 40 kt yield. The airblast had to sweep across the models at an attack angle of 50 deg (Figure 8). This environment was modeled by applying a combined axial and transverse load to the structures using a vertical and a horizontal HEST, respectively. The airblast pressure and impulse curves associated with these environments are shown in Figure 10. The vertical HEST, generating a design 18.0 MPa peak overpressure, consisted of a 100 percent foam filled explosion cavity, 457 mm wide, bermed with 1.83 m of soil placed at 1441 kg/m^3 (Figure 6). The HEST was constructed directly against the headwall and model closures. The charge density in the HEST cavity was 16.66 kg/m^3. The cavity contained six layers of 0.085 kg/m detonation cord. The HEST was fired vertically from top to bottom at a shock propagation rate of 6400 m/s (maximum burn rate for the detonation cord used). The horizontal HEST, generating the transverse load, consisted of a 100 percent foam filled cavity 318 mm high, covered with

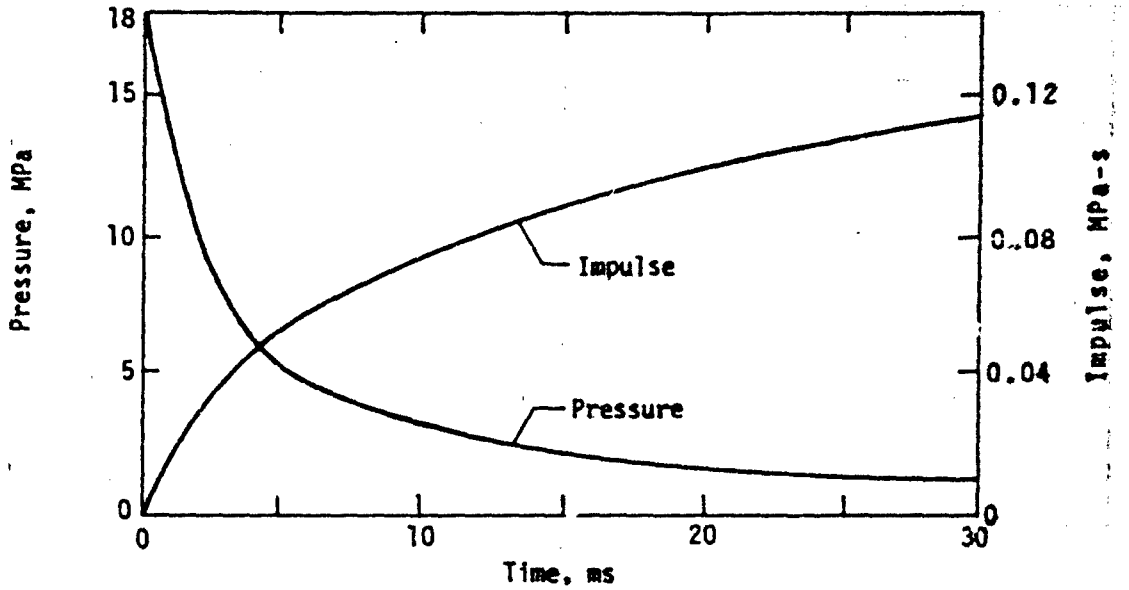

a. Design axial airblast environment.

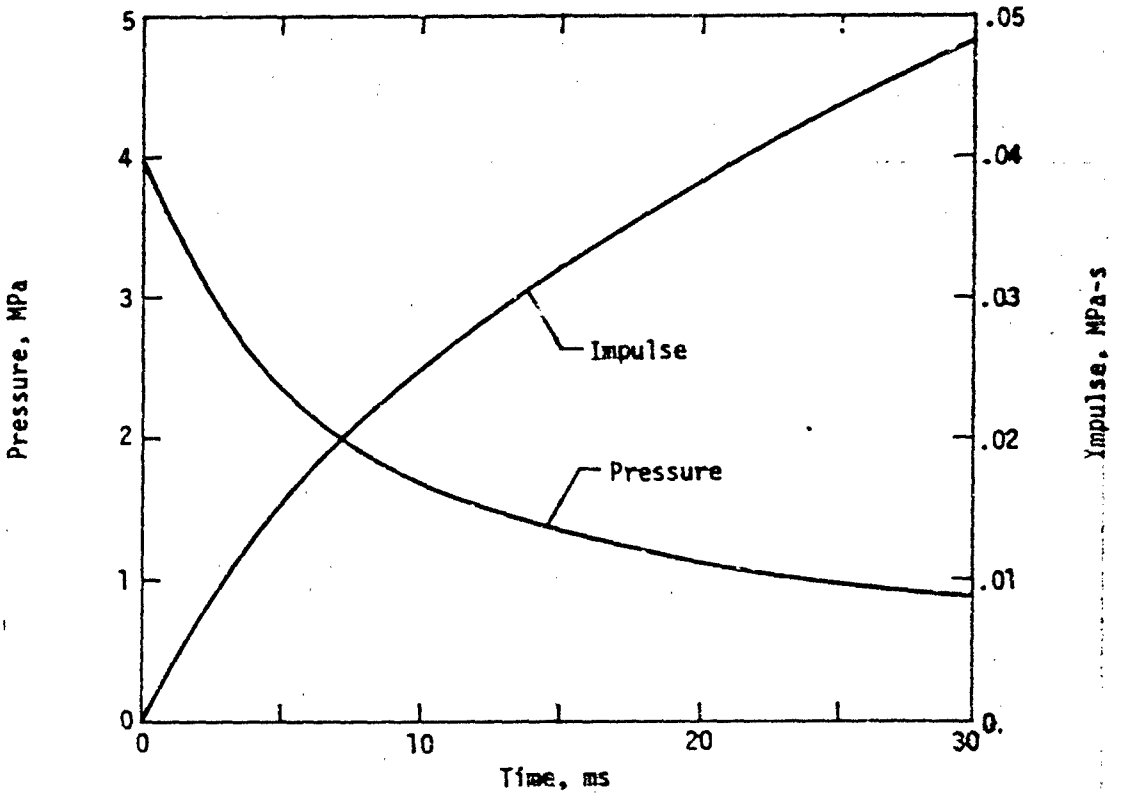

b. Design transverse airblast environment.

1.83 m of overburden placed at a unit weight of 1441 kg/m (Figure 6). The charge density in the cavity was 8.01 kg/m . The cavity contained four layers of 0.085 kg/m detonation cord. The cord was placed in skewed parallel arrays to produce an airblast propagation rate parallel to the models of 3005 m/s. Detonation of the vertical and horizontal HESTs was staggered so as to simulate the smooth sweep of an airblast across the testbed.

Prior to each of the main test events, two calibration tests were conducted using the proposed HEST designs to check the adequacy of the generated simulations.

INSTRUMENTATION

The instrumentation layouts for the DCT-1 and DCT-2 tests are shown in Figures 11 and 12, respectively. The structural instrumentation in the models consisted of strain, relative displacement, acceleration, and SMI gages. Stress and acceleration gages were also placed in the recompacted soil immediately adjacent to the models and in situ soil. The airblast loading generated by the HESTs was measured using blast pressure gages. The number and type of transducer employed for each kind of measurement are indicated in Table 4. The instrumentation in the DCT-1 test was positioned primarily to monitor ovaling response of the cylinders. In the DCT-2 test, the instrumentation was positioned to monitor both the ovaling and axial response of the models.

Hoop strain was measured at several locations on the circumferential reinforcing bars in the DCT-1 models and on the circumferential reinforcing bars and liner steel in the DCT-2 models. Axial strain measurements were

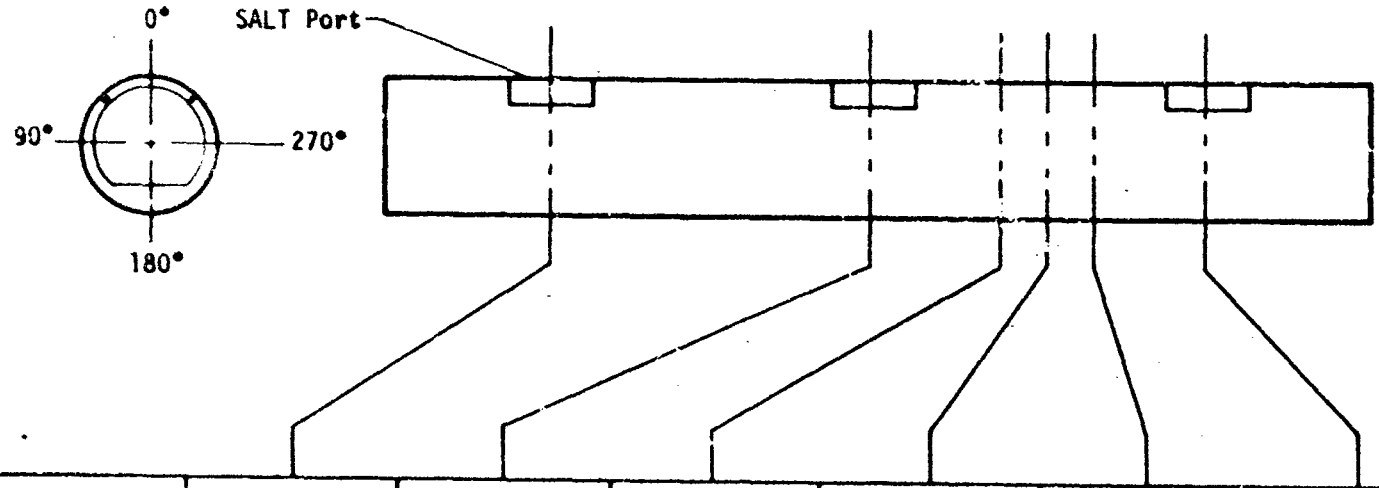

Hoop Strain	0, 90, 147, 214, 270	0, 90, 180, 270	—	0, 45, 90, 180, 270	—	—
Relative Displacement	—	—	—	—	0-180 90-270	0-180 90-270
Radial Acceleration	0, 90, 180	—	0, 90, 180	—	—	—
SHI	0, 90, 180, 270	0, 56, 90, 135, 180, 225, 270, 304	—	—	—	0, 90, 180, 270
	Azimuth					

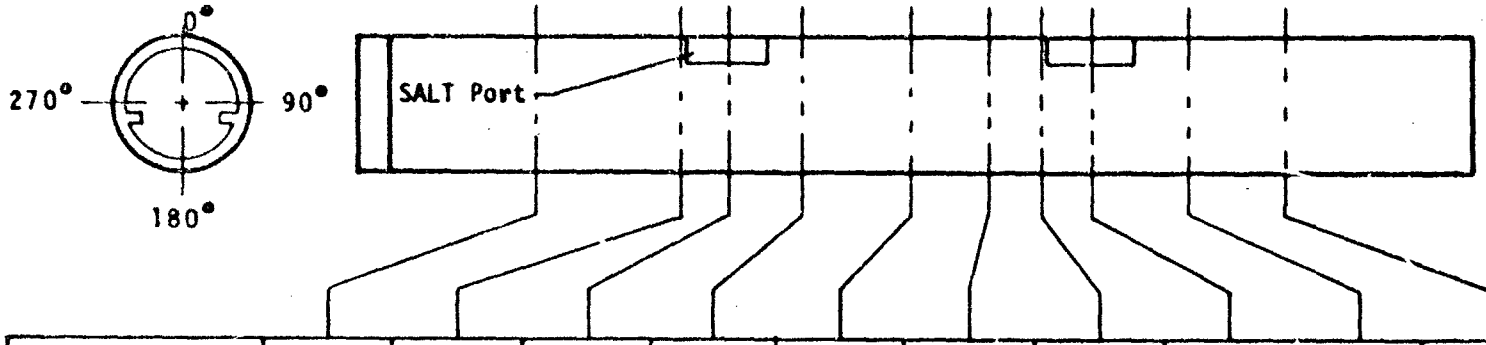

Hoop Strain	—	0, 180, 270, 304	0, 180 225,270 304	0, 180 225,270 304	—	—	—	0, 180 270,304	—	—
Longitudinal Strain	0, 180, 270	0, 180 270,304	0, 180 225,270 304	0, 180, 270	0, 180 225,270 304	—	—	0, 180 270,304	—	0, 180, 270
Relative Displacement	—	—	0-180, 90-270	—	—	0-180, 90-270	—	—	0-180, 90-270	—
Radial Acceleration	—	—	—	—	0, 180, 270	—	0	0, 180, 270	—	—
Longitudinal Acceleration	270	—	270	—	270	—	270	270	270	—
SMI	—	—	0, 56, 90, 135 180	—	0, 56, 90, 135 180	—	—	0, 56, 90, 135 180	—	—
	Azimuth									

TABLE 4. SUMMARY OF DCT-1 AND DCT-2 INSTRUMENTATION

Location	Type	Make/Model	Number of Channels	
			DCT-1	DCT-2
Freefield	Blast Pressure	Kulite HKS-11-375-5K	12	19
	Acceleration	Endevco 2264A-2KR	32	33
	Soil Stress	Kulite LQK-080-8U hard diaphragm	34	19
Structure	Steel Strain	Micro-Measurements MM-EA-06-500GC-350 (Rebar)	87	92
		Bean BAE-06-250BB-350TE (Liner)	--	39
	Relative Displacement	Maurey	12	12
	Acceleration	Endevco 2264A-2KR	18	28
	SMI	NMERI-built	96	78
TOTAL			291	320

also taken on the longitudinal reinforcing bars in the DCT-2 models. Epoxy bonded gages were used at all strain gage locations. At each reinforcing bar installation, two gages were mounted on the bar. These gages were wired so that local bending effects cancelled.

Crown-to-invert and springline-to-springline relative displacements were measured at several locations in each model using linear potentiometers. The potentiometers were mounted across passive relative displacement gages.

Radial structural accelerations were measured at the crown, invert, and springlines of all models. At the springlines of the DCT-2 models, longitudinal accelerations were also measured. The accelerometers were mounted on the interior wall of the models.

Force interactions at the soil/structure interface were measured in both tests using NMERI built SMI gages. The SMI transducer provides a measurement of three mutually orthogonal dynamic stress vector histories, normal stress, circumferential shear stress, and longitudinal shear stress, at the structure/media interface (Reference 2). The SMI gages were mounted in canisters cast in the models during construction. In both the DCT-1 and DCT-2 tests, normal and circumferential shear stress were measured at several locations around the models' circumference. In the DCT-2 test, longitudinal structure/soil shear stresses were also monitored.

High speed motion picture documentation of the response of the interior of the DCT-2 models was performed. Emphasis was placed on observing the behavior of the SALT ports.

All power and signal wires to the model instrumentation were routed on the inside of the models. The wires were collectively exited through

cable access pipes at the ends of the models.

Soil stress and motion were measured in the DCT-1 and DCT-2 tests with soil-stress gages (WES type) and accelerometers, respectively. The soil stress gages, mounted in aluminum paddles, were positioned to measure radial soil stress at the crown, invert, and springlines of the models. Soil accelerations were measured with accelerometers mounted in epoxy canisters. Measurements were taken at the soil stress gage locations and at locations between the models in situ material.

The airblast loading generated by the HESTs were measured with blast pressure gages mounted on the surface of the explosion cavities. The gages in the horizontal HESTs were mounted in concrete cylinders placed in the soil flush with the surface of the testbed. The gages in the vertical HEST (DCT-2 only) were mounted in steel canisters cast in the headwall and model closures.

The instrumentation signals were recorded in vans located 600 m from the testbeds. Conditioning and amplification of the electrical signals from the strain, acceleration, and blast pressure measurements were provided by downhole mini-conditioners located in a splice bunker 30 m from the testbeds. The signals from the relative displacement, SMI, and soil stress gages were amplified and conditioned in the vans. The signals were recorded using 28 tract Ampex recorders.

PRETEST ANALYSIS

DCT-1 Test

The DCT-1 pretest calculations were performed using the finite element computer code SAMSON and the finite difference code DEPROSS.

SAMSON is a two-dimensional (2-D) dynamic finite element computer code originally developed by the Illinois Institute of Technology Research Institute; it has been modified and expanded by AFWL (Reference 3). The code is particularly suited for handling problems involving nonlinear material properties and a large number of degrees of freedom. The SAMSON code was used in the DCT-1 test to predict ovaling related velocity, displacement, and strain in the structures and stress at the soil/structure interfaces. DEPROSS is a dynamic finite difference code developed at the Massachusetts Institute of Technology (Reference 4). The DEPROSS code can accomodate both geometric and material nonlinearities in a structure. The DEPROSS code was used to investigate the response of the breakout joints in the B model.

The 2-D model used for the DCT-1 SAMSON prediction consisted of the test structure, the McCormick Ranch backfill, and a section of the in situ McCormick Ranch soil. Roller boundary conditions were applied at both the vertical boundaries and the bottom nodes of the structure/soil-island grid. Sliding separating boundaries were assumed at the contact surface between the structure and soils, and between the SALT ports and the main portion of the structure. The sliding phenomenon is characterized in the SAMSON code by the Coulomb friction law and is limited to small displacement behavior. The reinforced concrete, in situ soil, and backfill soils in the model were treated as piecewise linear elastic-plastic materials. The surface of the structure/soil-island was loaded with a piecewise linear approximation of the design airblast pressure time history.

In the DCT-1 DEPROSS calculations only half of the cylinder was modeled since the structure and loading were assumed symmetric. The model

of the structure was divided into circumferential segments, with the segments divided into discrete concrete and steel layers. The concrete and steel were modeled as piecewise linear elastic-plastic materials. The model was loaded by forces applied through the displacement of springs representing the soil adjacent to the structure. The outside ends of the springs were driven by soil motions derived from the motions of the boundary of a void in a soil medium under a surface airblast load.

Based on the SAMSON and DEPROSS calculations, the following predictions were made for the DCT-1 test.

1. The principal structural response would be ovaling, with the long axis of the elliptical deflected shape horizontal. Tensile strains would develop sufficient to cause cracking in the models on the inner surfaces at the crown and invert and outer surfaces at the springlines.

2. The strains at the breakout joints in model B would be significantly below yield values.

3. The peak reflected interface normal stresses at the crown of the models would be approximately twice the level of the incident peak overpressure. The largest reflected peak overpressures would occur over the SALT ports with loose backfill (model B).

4. The peak interface normal stresses at the springlines and invert of the models would be, respectively, 80 and 50 percent lower than the peak normal stress at the crown.

DCT-2 Test

The DCT-2 pretest predictions were performed using three simplified computational techniques. A computer or minicomputer is required for these techniques. They are, however, fairly inexpensive and offer a

detailed treatment of the dynamics of the response of the test structures. The three techniques employed were,

1. A Two-Degree-of-Freedom (TDOF) Program to investigate the ovaling response and to determine an average normal load around the circumference of the structure.

2. A Multi-Degree-of-Freedom Elastic-Plastic Spring Mass Program (MDFSMI) to model the axial response.

3. A Multi-Degree-of-Freedom Beam-Column (BEAMCO) Model to investigate the beam-column action.

These simplified procedures assume that the effects of ovaling and axial/beam bending can be decoupled and solved separately.

The ovaling of the cylinders was predicted by a program that models the cylinder as two masses lumped at the crown and invert. The masses are connected by a spring which represents the stiffness of the cylinder in flexure and includes the stiffness resulting from the soil adjacent to the springlines. This system is driven by forces applied through the displacement of springs representing the soil adjacent to the crown and invert. The forced displacements on the outside ends of the soil springs are derived from the displacements of the boundaries of a void in an elastic medium under a pressure load. The calculated displacements of the crown and invert of the cylinder are used to determine a change in curvature and thus bending strains and stresses in the cylinder (Reference 5).

The dynamic axial response of the structures was calculated using a computer code called SPRING (Reference 6). It is a one-dimensional (axial only) multi-degree-of-freedom spring-mass code that models the

structure as a series of lumped masses joined by springs and dashpots. The computer code SPRING has a subroutine, MATCON, that is used to calculate the forces generated by the springs that represent the concrete. The material model used by MATCON is a strain softening model that unloads along the slope of the initial elastic modulus. The material model also contains a tension cut off. In addition to the concrete, the structures also contained steel liners and reinforcing bars, each of different strength. The steel springs were modeled by an elastic plastic material that allows cyclic loading and tensile or compressive failure. One set of SPRING calculations was performed including shear force interactions at the structure/soil interface.

The beam column response of the structures was modeled using BEAMCO. BEAMCO, a modified version of the code DEPROSS, is a multi-degree-of-freedom spring-lumped-mass program that treats the cylindrical shelter as an equivalent (equal area and moment of inertia) rectangular beam resting on an elastic foundation (Reference 5). The applied loading used in the BEAMCO calculations consisted of a time dependent axial load and an end moment applied at the front of the model. An end moment was applied to the model purely for investigative purposes and did not represent any expected load condition. Axial shear forces were also applied to the BEAMCO model to simulate the shear at the soil/structure interface resulting from axial displacements of the shelter relative to the soil. In the BEAMCO analysis, the structure was represented by 80 mass nodes, the first three simulating the headworks and door region; the remaining ones, the tube. Each node was divided into eight equal flanges. The foundations soils were treated as elastic material represented by springs applied

perpendicular to the axis of the cylinder (beam).

Based on the simplified calculations performed, the following predictions were made for the DCT-2 test,

1. The cylinders would not fail in the ovaling mode.

2. The cylinders would not fail under the axial load, unless the axial load acted eccentrically.

TEST RESULTS

The DCT-1 models sustained minimal damage during the test. All the models ovaled under the applied load, with the long axis of the elliptical deflected shape horizontal. The ovaling deformation caused longitudinal tension cracks in the model walls on the inside surface at the crown and invert and outside surface at the springlines. A sketch of the typical damage observed in a DCT-1 model is presented in Figure 13. Similar patterns and degrees of distress were observed in all the models. The structural response data obtained from the test was similar for all models and supported the distress patterns observed. The level of damage of the SALT ports was consistent with the damage observed in the main structure, with the exception of a longitudinal compression crack seen on the outside surface of the SALT ports in the B model. The effect on shelter response of varying structural details (breakout joint, floor, and SALT port) and SALT port backfill densities was minimal. The SMI data from the test indicated the structures moved vertically downward relative to the soil and translated horizontally in the direction of propagation of the air-blast.

In the DCT-2 test, the models exhibited both ovaling and axial/beam

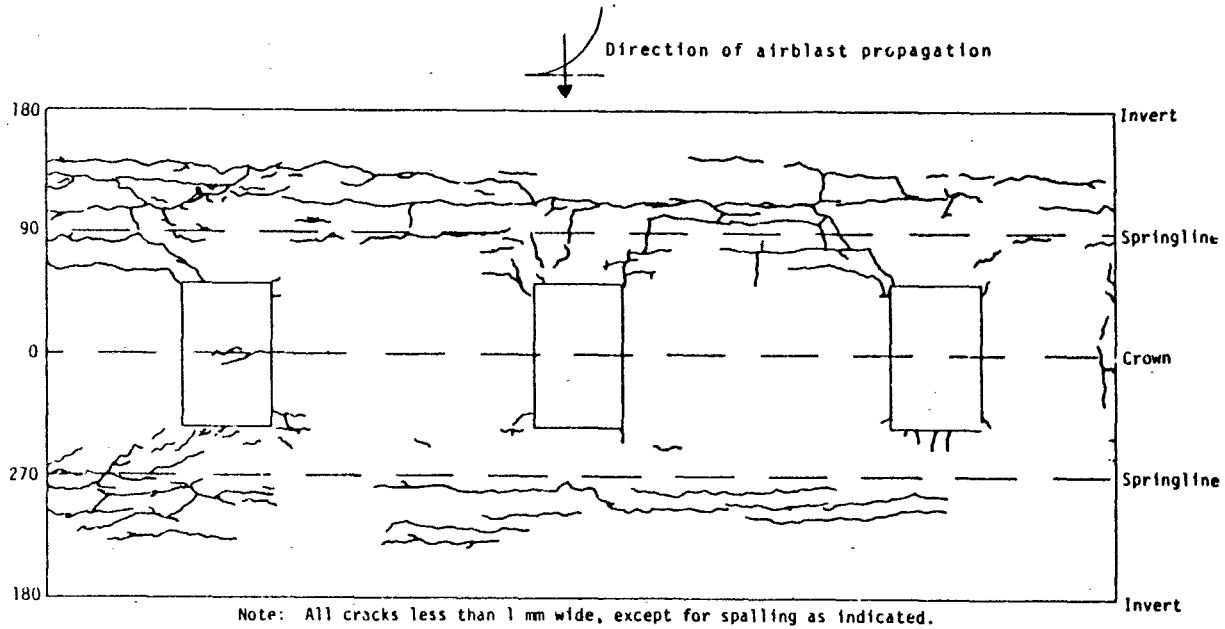

Note: All cracks less than 1 mm wide, except for spalling as indicated.

bending distress. A sketch of the damage observed on the exterior surface of the DCT-2 D model is presented in Figure 14. The damage sustained by the thinner walled E model was similar in nature to, but more severe in degree than, the damage sustained by the D model. Longitudinal tension cracks were observed in the exterior surfaces of the models at the springlines, indicating ovaling of the models occurred under the transverse load. Circumferential tension cracks were observed at the invert of the models opposite the SALT ports. At the first SALT port, these tension cracks were accompanied by compression buckling of the interior steel liner in the upper (crown) portion of the models. In the E model, major compression cracks were observed in the exterior wall paralleling the compression buckles in the interior steel liner. This distress pattern (tension at the invert, compression at the crown) is consistent with that produced by longitudinally bending the structure in a "smile" mode. The test data, presently under examination, supports these observed distress patterns.

SUMMARY AND CONCLUSIONS

The objective of the Dynamic Cylinder Test (DCT) program was to analytically and experimentally determine the response of a buried MX horizontal shelter subjected to a nuclear airblast. The first two tests in the program, the DCT-1 and DCT-2 tests, have been completed. These tests were concerned with the effect of structural detail on shelter response and the character of the structure/soil interaction loadings on the shelter. Pretest predictions were performed for each test. The prediction techniques were evaluated using the test data.

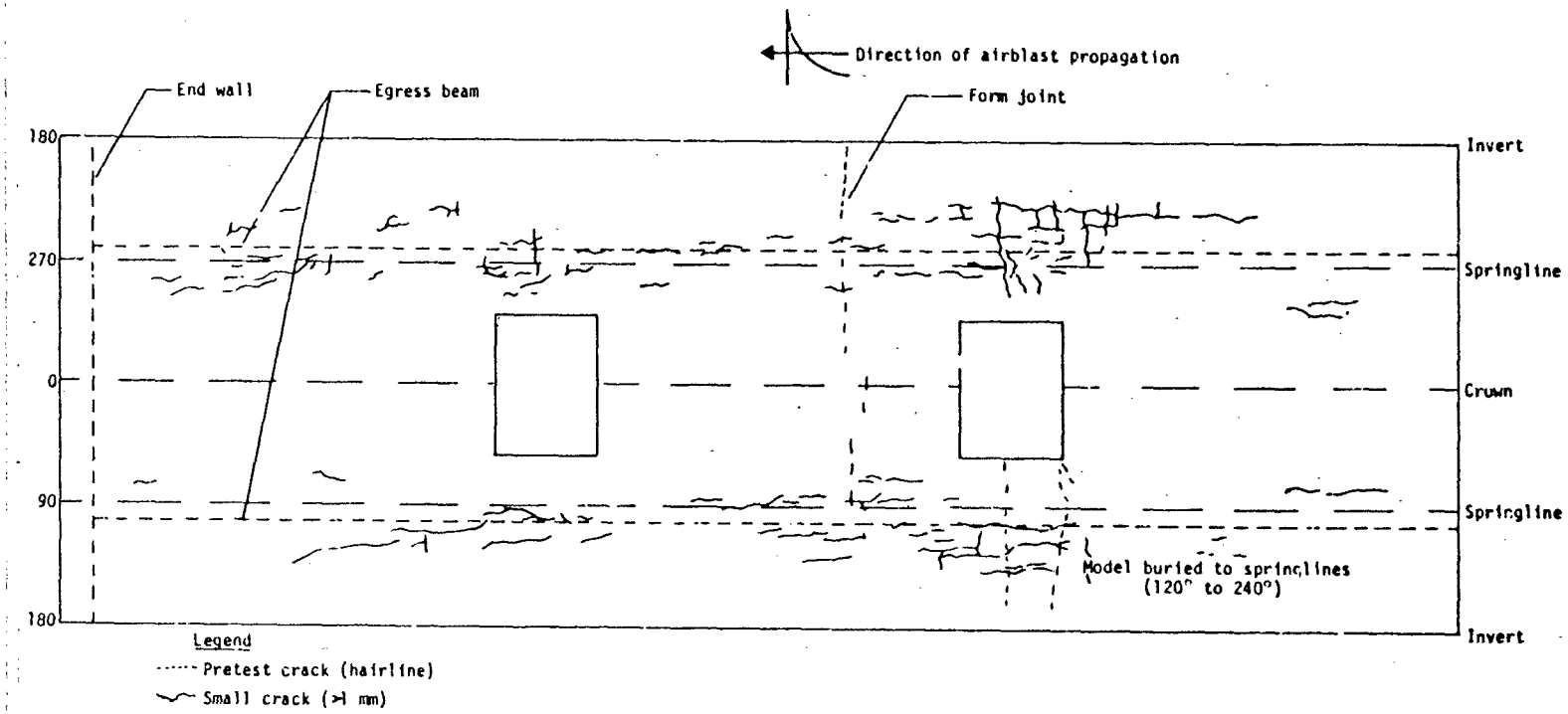
Direction of airblast propagation
End wall
Egress beam
Form joint
180
270
0
90
180
Invert
Springline
Crown
Springline
Invert
Model buried to springlines
(120° to 240°)
Legend
Pretest crack (hairline)
Small crack (>1 mm)

In the DCT-1 test, three 1/5-size models of the cylinder (tube) section of the shelter were loaded sideon with a simulated nuclear airblast. The test articles, constructed of reinforced concrete, consisted of a monolithic tube, a tube with inspection panels, and a tube with inspection panels and missile breakout joints. In the DCT-2 test, two 1/4.22-size models of the shelter tube were subjected to a combined axial and transverse load. The two models had different wall thicknesses. The structural instrumentation in both tests consisted of strain, acceleration, relative displacement, and structure/media interaction gages. The free-field instrumentation in the tests consisted of blast pressure gages and soil stress and acceleration gages. The DCT-2 test also included high speed photographic documentation of the interior of the models during the test.

The DCT-1 structures ovaled under the sideon load. The observed distress patterns, similar in all the models, consisted of longitudinal tension cracks on the inside wall at the crown and invert, and on the outside wall at the springlines. The presence of inspection panels and breakout joints in the models had minimal effect on response. The DCT-2 structures ovaled in a similar fashion to the DCT-1 models under the transverse load applied in the DCT-2 test. In the DCT-2 test, axial/beam bending distress was also observed in the models. A significant axial/beam bending failure occurred in the thin walled model at the first SALT port.

The behavior of the DCT-1 structures was modeled analytically prior to the test using a finite element and a finite difference computer code. A comparison of the test and predicted response indicated both codes

correctly predicted the overall behavior of the models. Problems were encountered in both calculations with the parameters input in the soil material models and the techniques selected to model behavior at the soil/structure interface. The pretest predictions for the DCT-2 test were performed using a spring-mass, a two-degree-of-freedom, and a beam on elastic foundation code to determine axial, ovaling, and longitudinal bending response of the structures, respectively. These codes, general by nature, adequately predicted the gross response of the structures.

REFERENCES

1. Wampler, H., Leigh, G., Furbee, M., and Seusy, F., "A Status and Capability Report on Nuclear Airblast Simulation Using HEST," presented at the 6th International Symposium on Military Applications on Blast Simulation, Cahors, France, 25-29 June 1979.

2. Pickett, Stephen F., "Development and Evaluation of a Triaxial Interface Stress Transducer," *AFWL-TR-77-90*, Air Force Weapons Laboratory, Kirtland Air Force Base, New Mexico, August 1977.

3. Bartel, H. Dean, and Cole, Donald M., "User Manual for SAMSON and Family," Technical Note No. *DE-TN-74-009*, Air Force Weapons Laboratory, Kirtland Air Force Base, New Mexico, December 1974.

4. Balmer, H. A., "Improved Computer Programs--DEPROSS 1, 2, and 3--To Calculate the Dynamic Elastic-Plastic Two-Dimensional Response of Impulsively Loaded Beams, Rings, Plates and Shells of Revolution," *ASRL-TR-128-3*, Massachusetts Institute of Technology, Cambridge, Massachusetts, August 1965.

5. Stephens, Jerry E., Landon, Gary E., and Wampler, H. W., "Dynamic Cylinder Test (DCT) 2 Test Report," *TA8-3*, Letter Report to the Air Force Weapons Laboratory, New Mexico Engineering Research Institute, University of New Mexico, Albuquerque, New Mexico, January 1982.

6. "SPRING: A One-Dimensional Spring Mass Computer Code," *AFWL-DE-TN-78-009*, Air Force Weapons Laboratory, Kirtland Air Force Base, New Mexico, November 1978.

ACKNOWLEDGEMENT

This work was performed under contract to the Air Force Weapons Laboratory and all findings of the test program will be available in an AFWL technical report to be completed in April 1982.

KEY WORDS: dynamics; missile; Missile-X (MX); nuclear explosions; reinforced concrete; structural analysis; structure/media interaction

ABSTRACT: The response of buried horizontal MX missile shelters to simulated nuclear airblast and airblast induced ground shock loadings is investigated. Two tests were conducted on scaled reinforced concrete models to examine the effect of structural variations on shelter response and to characterize the loadings across the shelter/soil interface. Pretest calculations were performed for each test. The effectiveness of the calculation techniques was evaluated through comparison of the test and predicted results.

SUMMARY: Dynamic Cylinder Test Program, by Jerry E. Stephens. In the Dynamic Cylinder Test Program the response of horizontal Missile-X (MX) shelters to nuclear airblast loadings was investigated both experimentally and analytically. The program emphasized the effect of structural variations on response and load characterization across structure/soil interfaces.

PROTECTIVE VERTICAL SHELTERS

by

Ian Narain, A.M. ASCE[1]
Jerry Stephens, A.M. ASCE[2]
Gary Landon, A.M. ASCE[3]

INTRODUCTION

This paper describes the test program entitled GOVS (Giant Reusable Airblast Simulator (GRABS) on Vertical Shelters) which was an investigation of the response of vertical shelters for Missile-X (MX) to vertical airblast and to airblast-induced ground-shock loadings. Specifically under investigation in these tests were the effects of site geology (depth to bedrock) and structural detail (presence of a shelter transition section, thickness-to-radius ratio (t/r) of the shelter tube section, and concrete strength) on shelter response. In addition, the results of these tests were used to evaluate analytical computer procedures, to correlate static and dynamic test data, and to provide information for research relating to shock isolation systems (SIS).

The GOVS program consisted of three tests conducted on models one-sixth the size of a generic vertical shelter. The models were constructed, instrumented, and dynamically tested by the New Mexico Engineering Research Institute (NMERI) at the Eric H. Wang Civil Engineering Research Facility (CERF) on Kirtland Air Force Base (KAFB), Albuquerque, New Mexico. One

---

[1] Research Engineer, Structural Mechanics Division, University of New Mexico, New Mexico Engineering Research Institute, Albuquerque, New Mexico.
[2] Research Engineer, Structural Mechanics Division, University of New Mexico, New Mexico Engineering Research Institute, Albuquerque, New Mexico.
[3] Research Engineer, Structural Mechanics Division, University of New Mexico, New Mexico Engineering Research Institute, Albuquerque, New Mexico.

model of shelter configuration A and two models of shelter configuration B were tested individually in the GRABS facility at CERF (see Figure 1).

The test-bed for each test was composed of dry sand rained into place at a uniform density around the test structure. Model instrumentation included blast-pressure gages, accelerometers, velocity gages, strain gages, structure-media interaction (SMI) gages, interface-pressure gages, and relative-displacement gages. Test-bed instrumentation consisted of blast-pressure, soil-stress, and acceleration gages.

The design environment for GOVS-1 consisted of a vertical airblast (1700 psi) with a peak overpressure of 8.3 MPa and a scaled yield of 23 kt (scaled 5 Mt). The design environments for GOVS-2 and GOVS-3 were the same as the actual GOVS-1 test environment. This environment was generated by the High-Explosives Simulation Technique (HEST). Three calibration tests were conducted in the GRABS facility to define the HEST structure for the GOVS tests.

A SAMSON dynamic finite-element computer code provided pretest predictions of stresses and motions within both the structure and the free-field. The code generated acceleration, velocity, displacement, and stress and strain histories for the structure and the soil. An axisymmetric model of the test layout was assumed. The structure and test-bed materials were modeled in the calculation as piecewise linear, elastic-plastic materials.

TEST DESCRIPTION

Shelter Models

The generic MX vertical shelter is basically a large, reinforced-concrete canister capped with a removable closure. The specific

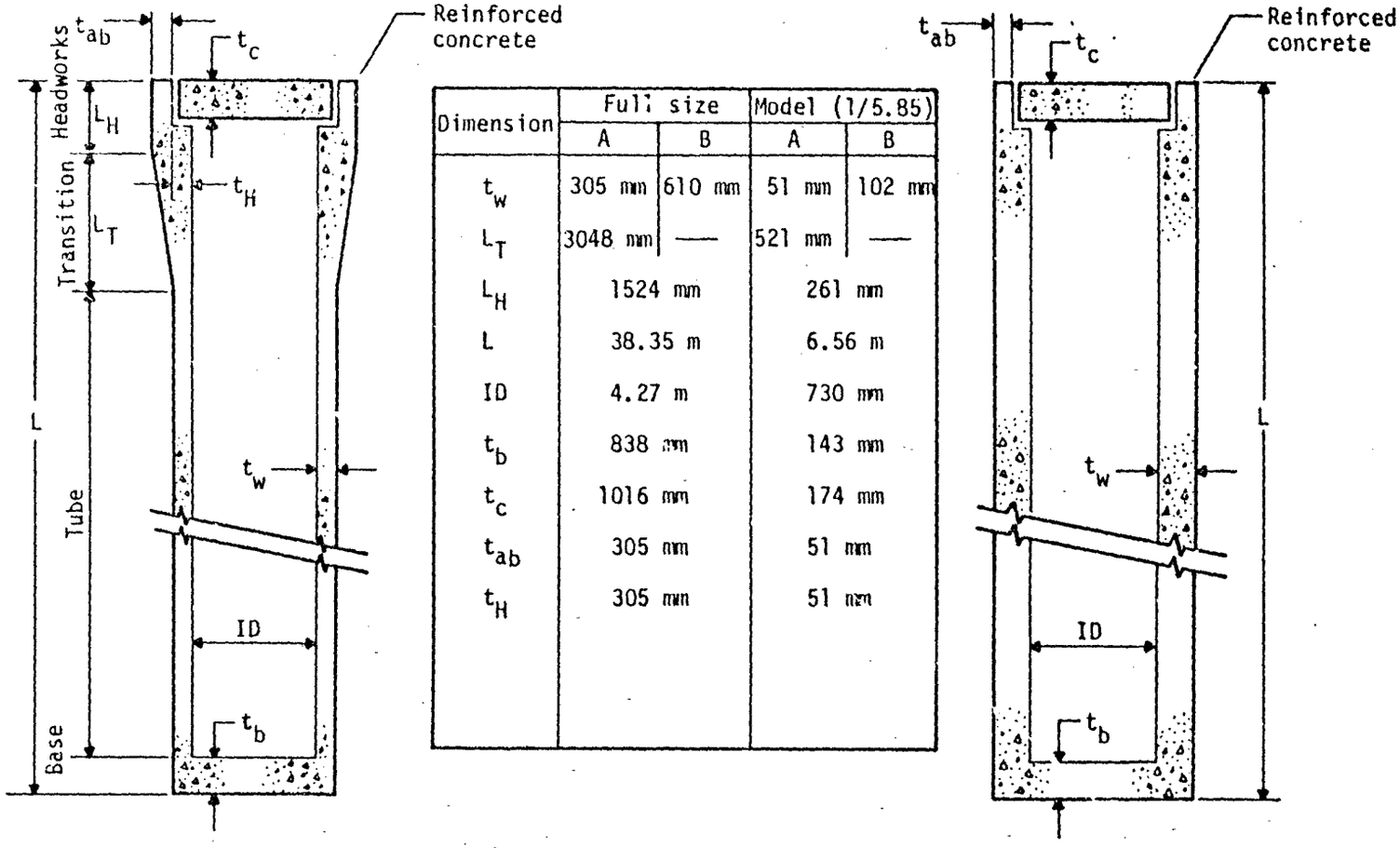

Dimension	Full size		Model (1/5.85)	
	A	B	A	B
t_w	305 mm	610 mm	51 mm	102 mm
L_T	3048 mm	—	521 mm	—
L_H	1524 mm		261 mm	
L	38.35 m		6.56 m	
ID	4.27 m		730 mm	
t_b	838 mm		143 mm	
t_c	1016 mm		174 mm	
t_{ab}	305 mm		51 mm	
t_H	305 mm		51 mm	

Configuration B

configurations of vertical shelter types A and B are shown in Figure 1. Both the full-size shelter dimensions and the corresponding model dimensions are indicated on this figure. The model dimensions were scaled from the full-size dimensions by a factor of 1/5.85, rather than 1/6, so that commercially available form material could be used in the construction of the model. The geometry of the closure, headworks, and base was identical for both shelter configurations. The tube in shelter A, however, had a full-size wall thickness of 305 mm in comparison to the 610-mm tube wall thickness for full-size shelter B. The reduction of the wall thickness in shelter A was accomplished by means of a transition section placed between the headworks and the tube.

The shelter models were constructed of conventionally reinforced concrete. The concrete in the A and B models had design 28-day unconfined compression strengths of 27.6 MPa and 41.1 MPa, respectively. The mix proportions are reported in Table 1. Type II high-early portland cement was used in the mixes. The maximum size of the aggregate in the concrete was 6.4 mm.

The percentages of steel reinforcement used in the GOVS models are listed in Table 2. The primary reinforcement in the headworks, transition, and tube of model A was D-2.5 deformed wire. The primary reinforcement in the headworks and tube of the B models was No. 2 deformed bars. All model bases were reinforced with No. 4 deformed bars. The stirrups in the models consisted of 2.4-mm-diameter wire for the A model and 3.2-mm-diameter wire for the B models. The tensile yield strengths of the D-2.5 deformed wire, the No. 2 deformed bars, and the No. 4 deformed bars were 483, 480, and 414 MPa, respectively.

TABLE 1. GOVS CONCRETE MIX PROPORTIONS (PER YARDS)

Content	Model A	Models B1 and B2 and all Closures
Cement, in kilograms	299	342
Fine aggregate, in kilograms	927	795
Coarse (6.4-millimeters) aggregate, in kilograms	245	532
Water, in kilograms	189	155
Pozzoligh, in milliliters	1183	1124
Entrained air, as a percentage	3	3
Slump, in millimeters	127	127
Water/cement ratio	0.63	0.45

TABLE 2. MODEL REINFORCEMENT PERCENTAGES

Model	Longitudinal Steel, as a Percentage of Volume	Hoop Steel, as a Percentage of Volume	Radial Steel, as a Percentage of Volume
	GOVS	GOVS	GOVS
A			
Headworks	0.94	0.50	0.12
Transition	0.98	0.99	0.13
Tube	1.03	1.00	0.11
B			
Headworks	0.97	0.50	----
Tube	0.97	1.00	0.19

The structure closures, identical for all three models, were reinforced with No. 4 bars. The concrete used in the closures had a 28-day unconfined compression strength of 41.4 MPa. The shells and liners were studded with 6.44-mm-diameter Nelson studs. In each model, the closure was anchored with eight 12.7-mm-diameter A325 bolts (tensile ultimate strength of 828 MPa) to a steel ring welded to the headworks liner. A pressure penetration seal, which consisted of a 51-mm-wide by 3.3-mm-thick circular plate, was welded to the closure liners.

MODEL FABRICATION

Fabrication of the models was accomplished in three phases, form assembly, constructing the reinforcing cage, and casting and curing the concrete. The vertical shelter models were constructed in an inverted position. The forms for the inside walls were fiber-void tubes. The bottom end of the void tube was anchored against the steel lining of the headworks. Approximately 2 m of sand were placed in the tube for additional support. The upper end of the tube was capped with a plywood disk. The reinforcing cage for each model was fabricated around the completed inside form. All instrumentation leads were routed to the inside of the model.

The outside form was slipped over the assembled reinforcing cage. This form consisted of a steel liner divided longitudinally into five approximately equal segments. The segment-to-segment connections were covered with steel bands. A uniform wall thickness was maintained in the tube section by steel rod spacers placed between the inner and outer forms. Each model was cast in five approximately equal sections from two batches

of concrete. A steel funnel clamped around the tops of the form segments was used to facilitate concrete placement. The concrete was consolidated by four air-driven form vibrators, three attached to the funnel and one attached to the base plate of the model.

When the model had been cast, the exposed concrete surfaces were sprayed with curing compound. The model was allowed to cure for about one week. The outside forms were then stripped, and the model was placed in a horizontal position and was transported to the GRABS facility, where the inside forms were stripped. The models were instrumented at the test site while they were still lying in the horizontal position.

Test specimens were cast from each batch of concrete for material strength and response testing. The sampling and testing program for this concrete is summarized in Table 3. Most of the concrete specimens were molded and cured in the laboratory according to the standards of the American Society for Testing and Materials (ASTM); exceptions are indicated in Table 3. In addition to the tests on the concrete specimens, tensile stress-strain tests and pull-out tests were conducted on each size of reinforcing bar (wire) used in the models.

INSTRUMENTATION

Both electrical (active) and mechanical (passive) measurements were taken during the GOVS events. The electrical gages measured strain, SMI, blast pressure, model motions, free-field motion and stress, interface pressure, and relative model displacement. The mechanical devices measured only relative model displacement. Model and free-field instrumentation locations are given in Figure 2. An average of 163 channels

TABLE 3. GOVS MATERIAL TESTING PROGRAM

Test	ASTM Specification	Specimen Size	Number of Specimens per Batch	Test Schedule	Comments
Concrete slump	C143-74	---	1	---	---
Concrete compressive strength	C 39-72	152- by 305-mm cylinders	32[a]	4 at 07 days 4 at 14 days 4 at 21 days 4 at 28 days 4 at 35 days 4 at test day	Stress-strain curves for 28-day tests
Concrete flexural strength	C 78-75	152- by 152- by 508-mm beams	6[b]	2 at 28 days 4 at test day	Load-deflection curves for 28-day tests
Concrete splitting tensile strength	C496-71	152- by 305-mm cylinders	6[b]	2 at 28 days 4 at test day	---
Reinforcing bar tensile test	---	---	---	---	Four tensile-stress/strain tests for each size of bar

[a] Sixteen specimens molded and cured according to ASTM C31-69; sixteen specimens covered and cured with the model. Two cylinders from each curing process tested on the days indicated.

[b] All concrete specimens molded and laboratory-cured according to ASTM C31-69 except that two specimens for each test (tested on test day) were covered and cured with the models.

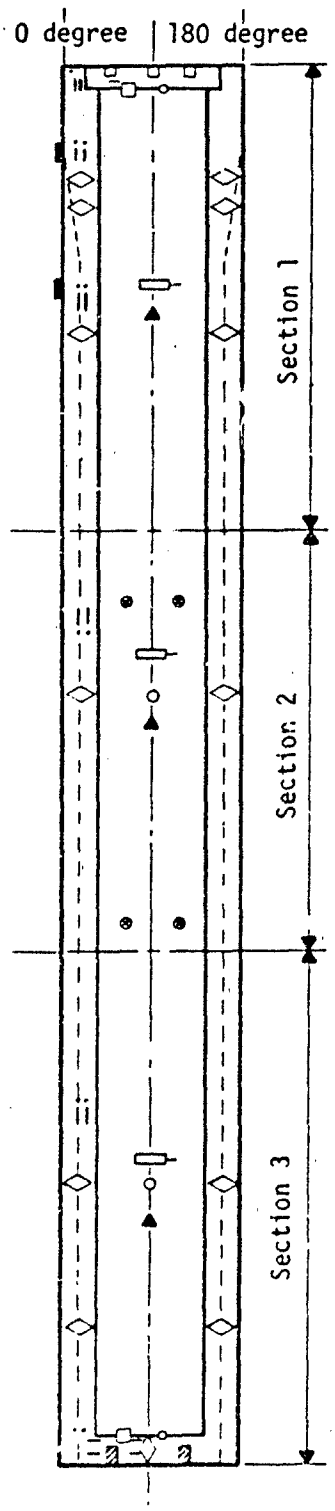

Measurement	Symbol	Number
Blast Pressure (BP)	▯	4
Velocity (V)	▭	1
Acceleration (A)	○	3
Structure-Media Interaction (SMI)	◇	18
Steel Strain (SE)	▮ or ●	28
Concrete Strain (CE)	▮	4
Relative Displacement (RD)		
0-180 degree	▭-	1
90-270 degree	▲	1

Acceleration (A)	○	2
Structure-Media Interaction (SMI)	◇	6
Steel Strain (SE)	▮ or ●	6
Relative Displacement (RD)	▭ or ▲	2
Cable Exits	⊛	4
Concrete Strain (CE)	▮	0

Velocity (V)	▭	1
Acceleration (A)	○	5
Structure-Media Interaction (SMI)	◇	13
Steel Strain (SE)	▮ or	14
Relative Displacement (RD)	▭- or ▲	2
Interface Pressure (IP)	▮	4
Concrete Strain (CE)	▮	0

Note: Dotted lines indicate model A structure.

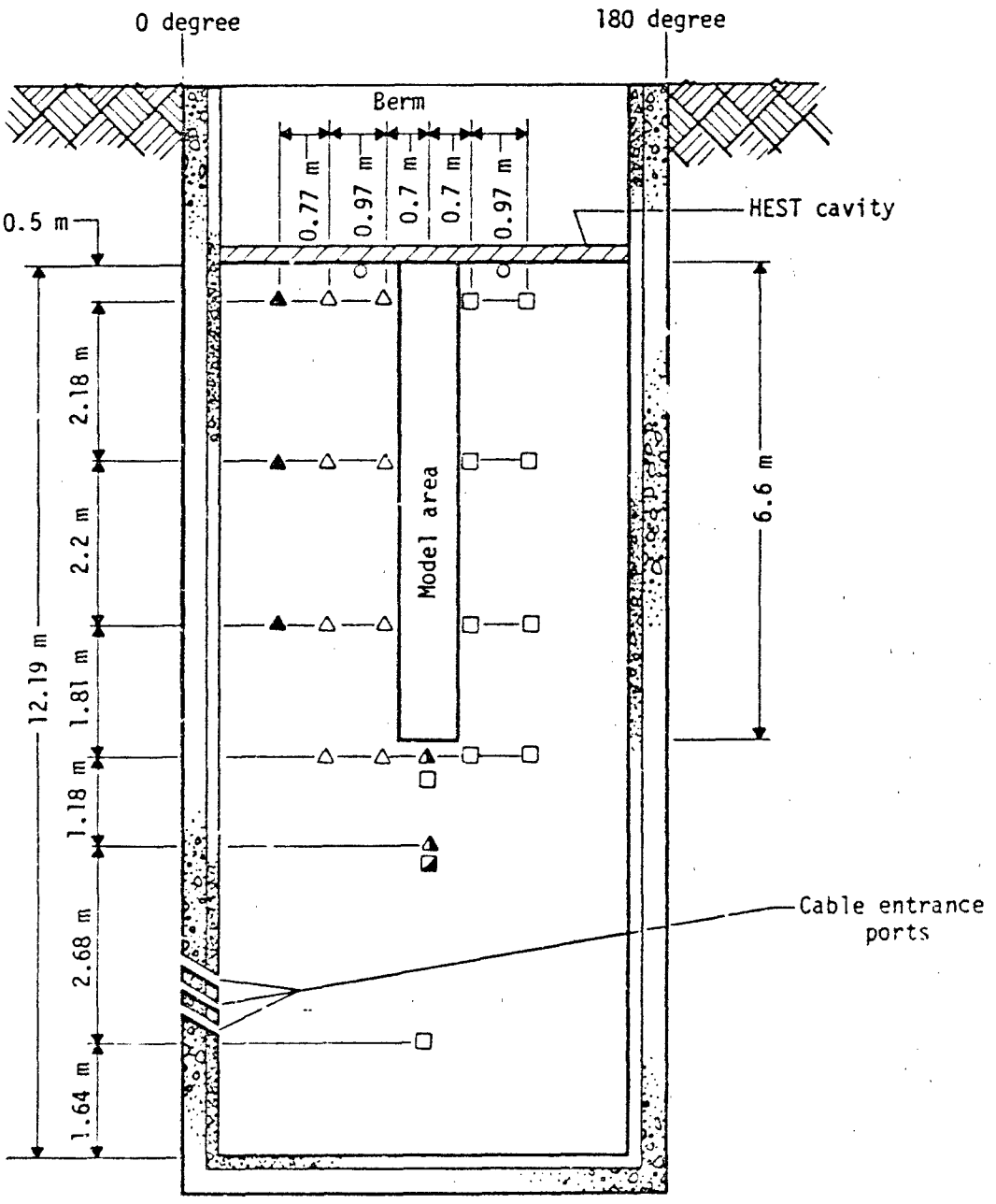
0 degree
180 degree
Berm
0.77 m
0.97 m
0.7 m
0.7 m
0.97 m
HEST cavity
0.5 m
2.18 m
2.2 m
1.81 m
1.18 m
2.68 m
1.64 m
12.19 m
Model area
6.6 m
Cable entrance ports
o Blast pressure gage
□ Soil stress gage vertical and radial
■ Soil stress gage radial
◪ Soil stress gage vertical
△ Soil accelerometer vertical and radial
▲ Soil accelerometer radial
▲ Soil accelerometer vertical

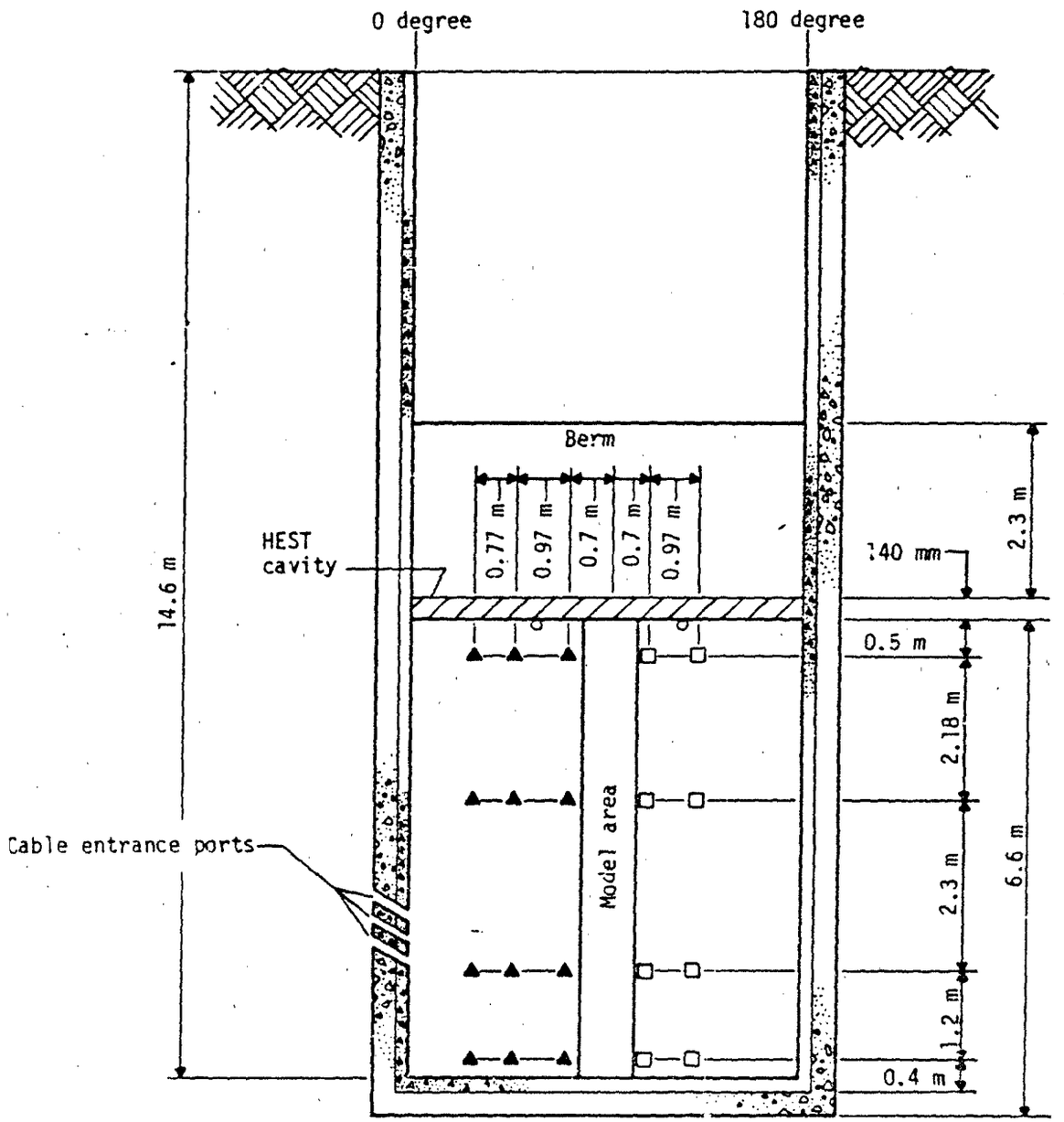

- ○ Blast pressure gage
- □ Soil stress gage vertical and radial
- ■ Soil stress gage radial
- ◪ Soil stress gage vertical
- △ Soil accelerometer vertical and radial
- ▲ Soil accelerometer radial
- ▲ Soil accelerometer vertical

was recorded in each test.

Strain measurements were taken on the reinforcing bar (rebar), on the steel liners of the closure and the headworks, and on the faces of each model wall. The closure gages were located where they would indicate flexural behavior, as were the rebar gages in the model base. Vertical gages installed on the longitudinal rebar in the model measured axial and flexural behavior. Gages were placed on the hoop reinforcement to indicate tangential compression and extension modes of behavior.

Blast-pressure measurements were taken in both the model closure and the free-field. Four gages were located in the closure and six in the free-field to ensure adequate pressure-history data and also to check the symmetry and uniformity of the loading. The blast-pressure gages, enclosed in steel canisters, were cast in the concrete during the construction of the closures and were enclosed in 305-mm-diameter by 610-mm-deep concrete canisters for the free-field measurements. All blast-pressure gages were protected with a debris shield.

Velocity gages and accelerometers were used for measuring model motions. Velocity measurements were taken on the bottom of the closure and on the base of the model in the vertical direction with Sandia-type DX velocity gages. Acceleration measurements were also taken on the model closure and base and at two other locations along the length of the tube.

Structure-media interaction measurements were taken electronically with NMERI-built SMI gages and Waterways Experiment Station (WES) Air Force-Modified (WAM) interface pressure gages. The SMI transducer provides a measurement of three mutually orthogonal dynamic stress vector histories, normal stress, horizontal shear stress and tangential shear stress, at the

structure-media interface (Reference 5). The gages were mounted in canisters cast in the model during construction and were located in such a way that normal, vertical, and tangential input loading to the structure could be determined at critical points.

Radial compression and extension of the tube section were measured with active linear potentiometers mounted in parallel on passive scratch gages.

Free-field stress and motion were measured with soil-stress gages (WES type) and accelerometers, respectively. Radial sensing gages were paired with vertical sensing gages at various locations to determine vertical-to-horizontal stress and motion ratios. The soil-stress gages, with vertical sensing axes, were firmly pressed into the test-bed and covered with rained sand. The soil-stress gages, with horizontal or radial sensing axes, were positioned on vertical support wires which were implanted into the test-bed. Soil accelerations were measured with accelerometers mounted in epoxy canisters.

The transducer data were recorded in vans, which were located approximately 150 m from the test facility. The recording equipment used in the GOVS test events is listed in Table 4. The recorded test data were reduced to computer-produced plots by the Air Force Weapons Laboratory (AFWL) Data Processing Division.

TEST FACILITY

The GRABS facility, located on KAFB, consists of a 5.49-m-diameter, 14.63-m-deep reinforced concrete cylinder emplaced in a massive limestone formation. The facility has a 533-mm-thick wall and a 533-mm-thick base;

TABLE 4. GOVS RECORDING EQUIPMENT

Recording Van	Signal Conditioners	Amplifiers	Recording Equipment	
			Free-field	Model
Van E7	B&F 1-700	B&F 702-10D	BH VR 3700 B, 3300	---
Van 4	B&F 1-234-1	B&F 702-10D	---	BH VR 3700 B Ampex CP 100

both are lined with 6.4-mm-thick steel plate. Construction of the test facility is described in Reference 2. The geometry of the test facility, and the rock properties, is shown in Figure 3. One model of shelter configuration A and two models of shelter configuration B were tested individually in the GRABS facility, also shown in Figure 3.

Before the test-bed material was placed in the facility, the necessary instrumentation cables were pulled through cable entrance holes located near the base of the facility. At the mouth of the access holes the cables were packed in foam to seal the access and isolate the cables from shock. The cables were connected to a junction box at the surface.

The test-bed material was a locally provided, washed and dried concrete sand conforming to ASTM Specification C-33. The sand was placed in the facility by a raining technique. Stockpiled sand was transported by a front-end loader to a hopper that carried sand into the raining device. The device, shown in Figure 4, was rotated around the circumference of the test facility. The flow pattern was controlled by varying the number of holes in the bottom of the device. This system was capable of delivering sand at a rate of approximately 38 m^3/h.

It has been shown that when sand is rained from the height required for the particles to achieve terminal velocity, a near-maximum uniform density is obtained. Experiments conducted by NMERI have shown that the sand must be rained from a height of at least 610 mm if it is to reach terminal velocity. The height of free-fall for the sand in the GRABS facility ranged from 2.3 m to 14.6 m. Density measurements were taken at 1-m intervals during the test-bed buildup. A Troxler nuclear moisture densitometer with probe depths of 152 mm, 203 mm, and 305 mm was used for

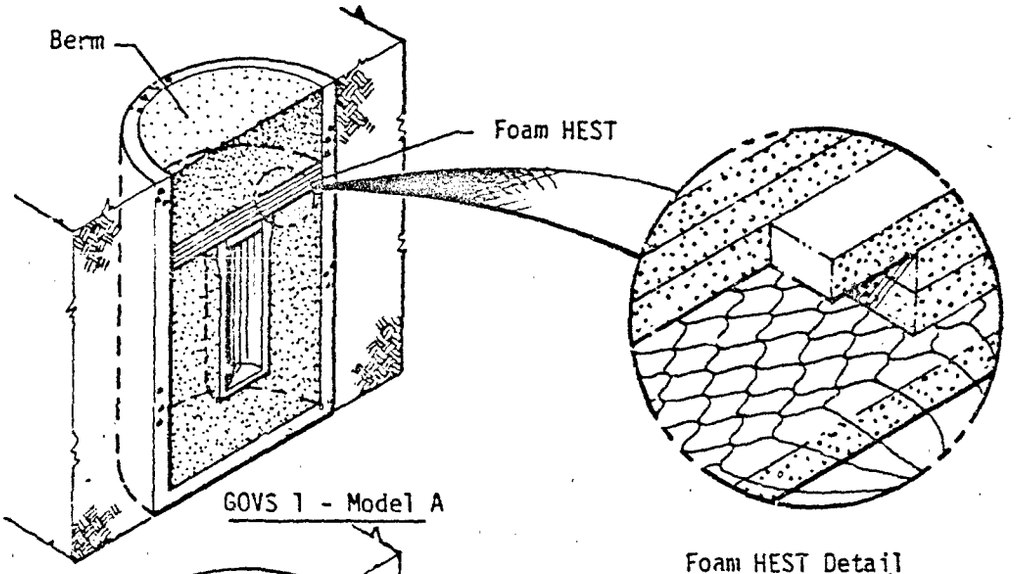

GOVS 1 - Model A

Foam HEST Detail

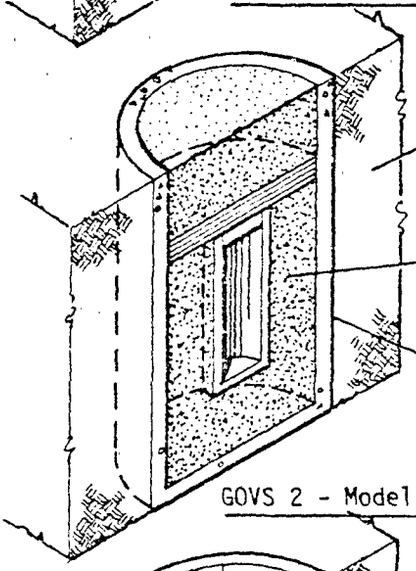

GOVS 2 - Model B1

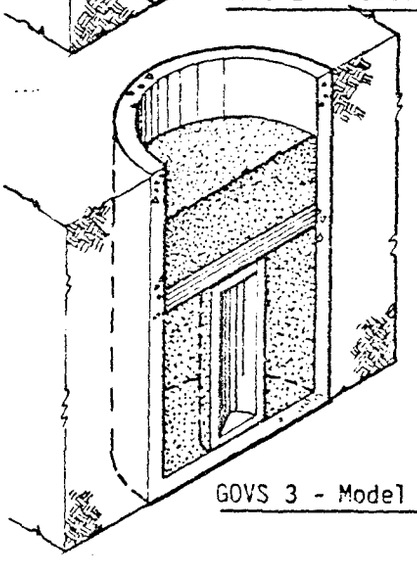

GOVS 3 - Model B2

Typical liner properties

Reinforcement:	Top 6.10 m	Bottom 8.53 m
Vertical:	1.00%	0.25%
Hoop:	4.50%	2.00%

Steel plate liner: 6.4 mm thick

Assumed rock properties

E = 5170 MPa
No tensile capability

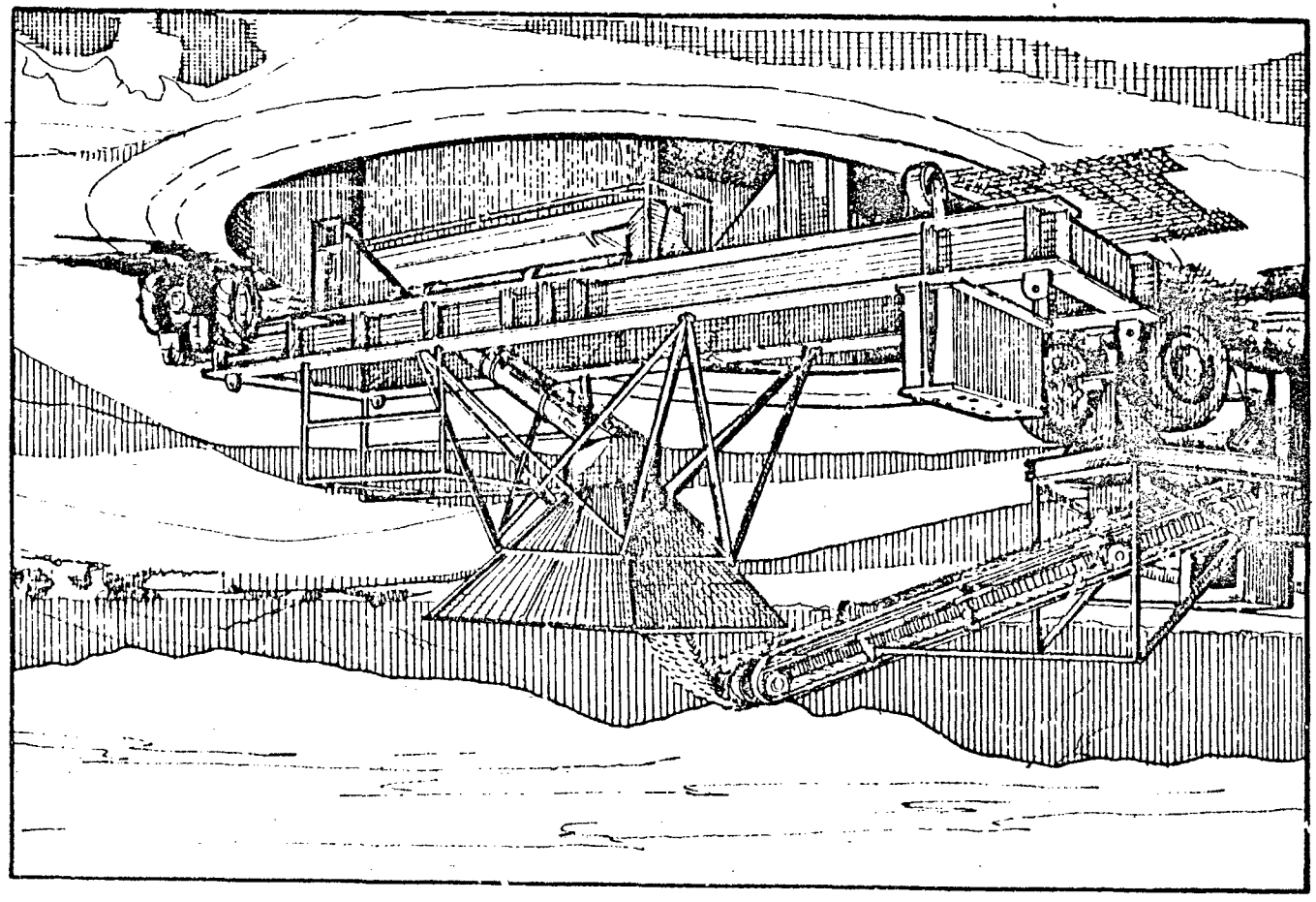

this purpose. The average test-bed unit density was 1746 kg/m^3.

The models were seated in the test-bed at the proper depths. In the GOVS-3 test, the model was carefully seated in a grout solution directly on the bottom of the facility. Instrumentation cables entered the model through 50-mm-diameter holes spaced along the length of the model, and were protected by an encasement of polyvinylchloride (PVC) pipe near the entrance holes. At each instrumentation level the cables were routed horizontally to the wall of the facility, down the side, and then out through the cable exit ports.

When the sand-raining, the free-field instrumentation placement, and the structural gage placement had been completed, the closure was bolted to the model with eight 13-mm-diameter bolts torqued to approximately 200 N-m. Preparations for the placement of the explosive charge were now complete.

TEST ENVIRONMENT

The required environment for the GOVS test events was a vertical airblast having a peak overpressure of 8.3 MPa and a scaled yield of 23 kt (scaled 5 Mt) with a simulation time of 12.5 ms. The scaled Brode pressure-history and impulse curves for the desired environment are plotted in Figure 5. A HEST structure (Reference 7) was used to generate the environment. A modified form of the Lock-up Impulse Code (Reference 7) developed for the HP 9820 programmable calculator was used in the initial design of the HEST.

Because experimental data on the performance of the foam-cavity HEST in a confined environment were unavailable, three calibration tests were

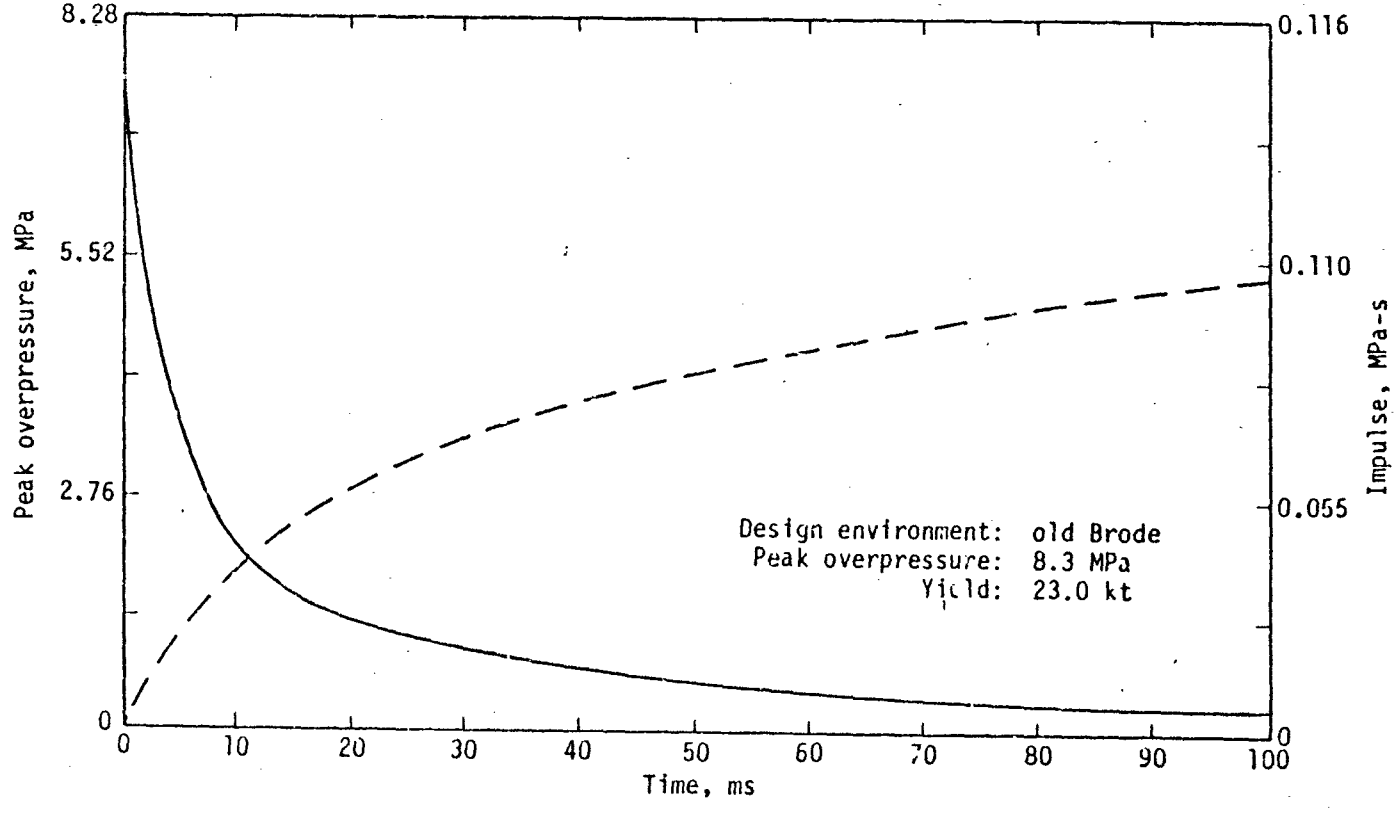
8.28
5.52
2.76
0
Peak overpressure, MPa
0.116
0.110
0.055
0
Impulse, MPa-s
0
10
20
30
40
50
60
70
80
90
100
Time, ms
Design environment: old Brode
Peak overpressure: 8.3 MPa
Yield: 23.0 kt

conducted to define the HEST. The final design of the HEST used in the GOVS test events consisted of a 100-percent foam-filled cavity, 140 mm high. Four layers of 13.7-gr/mm detonating cord were evenly distributed throughout the cavity. The charge density of the explosives was 14.7 kg/m^3; the total weight of the explosives was 48.8 kg. A single-point detonation scheme at the center of the HEST was used to ignite the system.

Approximately 300 mm of sand was rained in above the HEST as a base for the soil surcharge. The surcharge, which consisted of McCormick Ranch soil, was dropped into the facility. The total height of the overburden, sand and surcharge, was 2.29 m. Its density was 1326 kg/m^3 and its total weight was 71,823 kg.

PRETEST PREDICTIONS

A SAMSON dynamic finite-element computer code (Reference 1) was used for the GOVS pretest predictions (References 3, 4, and 6). The SAMSON code was developed by the Illinois Institute of Technology Research Institute, and it was later modified and expanded by AFWL. The code is particularly suited for handling problems involving nonlinear material properties and a large number of degrees of freedom. It was designed specifically to investigate SMI problems.

The two-dimensional (2-D) model used for the GOVS SAMSON predictions consisted of the test structure, the sand test-bed, the wall of the GRABS facility, and the limestone along the side of and beneath the GRABS facility. Only a unit arc section of the test configuration was modeled because of the axial symmetry of the applied load and the symmetry of the test-bed. The centerline of the model was fixed radially, but was left

free to translate vertically. The exterior boundaries of the model were totally fixed.

Sliding-separating boundaries were used in the meshes to model the interfaces between the sand and the test structure and between the sand and the liner of the GRABS facility. The sliding phenomenon is characterized in the SAMSON code by the Coulomb friction law and is limited to small displacement behavior.

The surface of the test-bed in the finite-element model was loaded with a double exponential fit to an average pressure history generated from the third calibration shot for the GOVS-1 calculation. The pressure history used for the GOVS-2 and GOVS-3 calculations was a double exponential fit to an average of the GOVS-1 data. The environments used in the calculations are shown in Figure 6. For input into SAMSON, this pressure history was approximated as a series of linear segments. The pressure was applied as a sweeping wave traveling from the centerline of the test-bed to the wall of the GRABS facility. A traveling wave was used in the calculation to simulate the conditions of a single centerpoint HEST detonation.

On the basis of the calculations, the following predictions were made:

GOVS-1

1. The entire shelter would translate as a rigid body, with an average peak vertical velocity of 6 m/s to 8 m/s and a permanent downward displacement of approximately 100 mm.
2. The closure would permanently deform downward at its center, with tensile cracking of the concrete occurring in the bottom at the center.

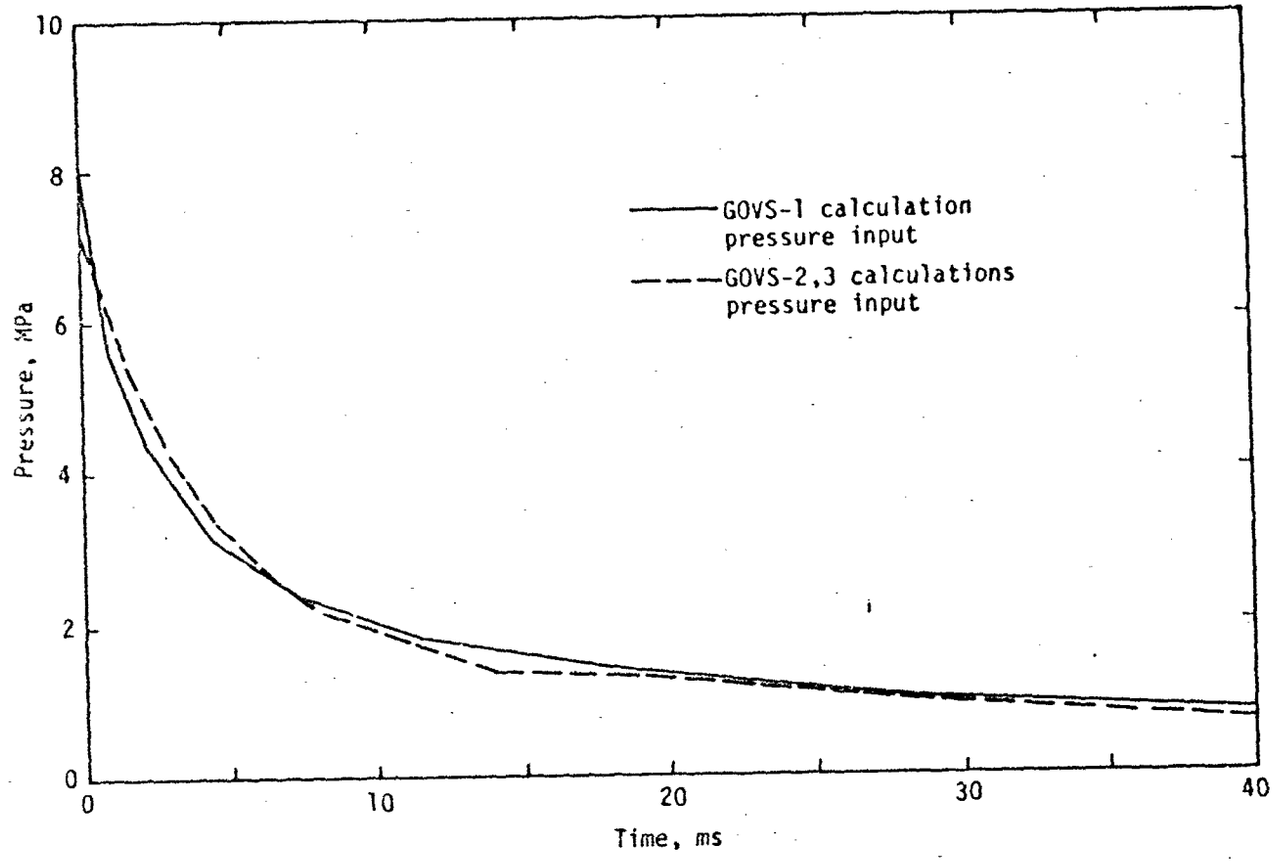
10
8
6
4
2
0
Pressure, MPa
0
10
20
30
40
Time, ms
GOVS-1 calculation pressure input
GOVS-2,3 calculations pressure input

3. The concrete below the closure bearing would undergo limited plastic deformation.
4. The concrete wall of the tube would be severely distressed immediately below the transition, with extensive concrete cracking and buckling of the reinforcing steel occurring over at least a 0.3-m-length of the tube.

GOVS-2 (Results of the GOVS-1 test were considered in the GOVS-2 predictions.)

1. The entire shelter would translate as a rigid body, with an average peak velocity of 5 m/s to 6 m/s and a permanent downward displacement of approximately 70 mm.
2. The closure would displace downward but remain elastic.
3. The concrete below the closure would also remain elastic.
4. The concrete wall of the tube would remain elastic, and the primary response would be axial compression.
5. The base would undergo bending, which would be minimally transmitted to the wall.

GOVS-3 (Results of the GOVS-1 and GOVS-2 tests were considered in the GOVS-3 predictions.)

1. The closure would displace downward but would remain elastic.
2. The primary response of the structure would be axial compression, and the structure would remain in the elastic region.
3. The base would undergo slight bending but would remain elastic.
4. Possible areas of distress would include:
   a. The bearing area of the structure, where crushing of the concrete might occur.
   b. The intersection of the base and the wall of the structure, where high compressive stresses might develop.

TEST RESULTS

The GOVS-1 test structure experienced significant distress in the tube and base. Several circumferential compression cracks were observed in the top portion of the tube, and a major compression failure occurred in the tube wall at the 2.5-m elevation, as shown in Figure 7. The strain-gage data from this region indicated that the distress had been caused by the direct airblast loading of the structure. The base of the structure experienced toroidal bending, and tension cracks developed in the bottom of the tube and in the top surface of the base.

Unlike the GOVS-1 model, the GOVS-2 model did not fail under the airblast loading. However, the structure did experience minimal distress in the tube section at a depth of approximately 6.35 m. At this location, circumferential compression cracks and longitudinal tension cracks were observed on the outside wall of the structure around 75 percent of the circumference, as depicted in Figure 7. Circumferential-strain gage data from this region indicated that the distress was a result of toroidal bending of the tube wall at the base.

The GOVS-3 test structure experienced significant distress in the tube section at a depth of 6 m, where circumferential compression cracks were observed on both the inside and outside faces of the model wall and around its entire circumference, as shown in Figure 7. Larger cracks exposing buckled reinforcing bars on the inside face of the wall indicated that toroidal bending of the tube section had occurred at this location. It is apparent from the test data that the failure was not caused by direct airblast loading but by a combination of shear loading at the soil-structure interface and a shock wave reflected from the base of the model.

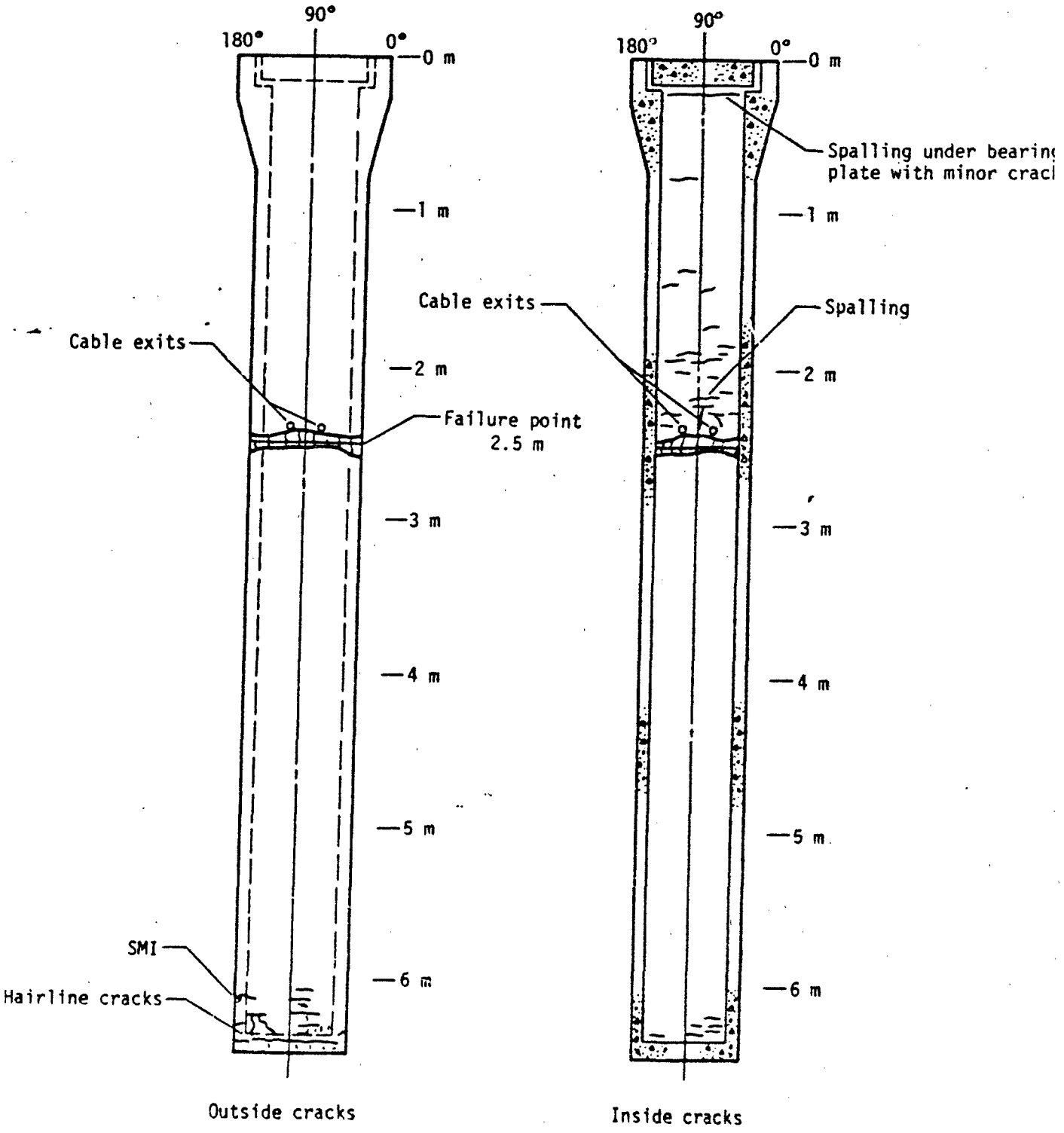
90°
180°
0°
0 m
1 m
2 m
3 m
4 m
5 m
6 m
Cable exits
Failure point
2.5 m
SMI
Hairline cracks
Outside cracks
90°
180°
0°
0 m
Spalling under bearing
plate with minor cracl
1 m
Cable exits
Spalling
2 m
3 m
4 m
5 m
6 m
Inside cracks

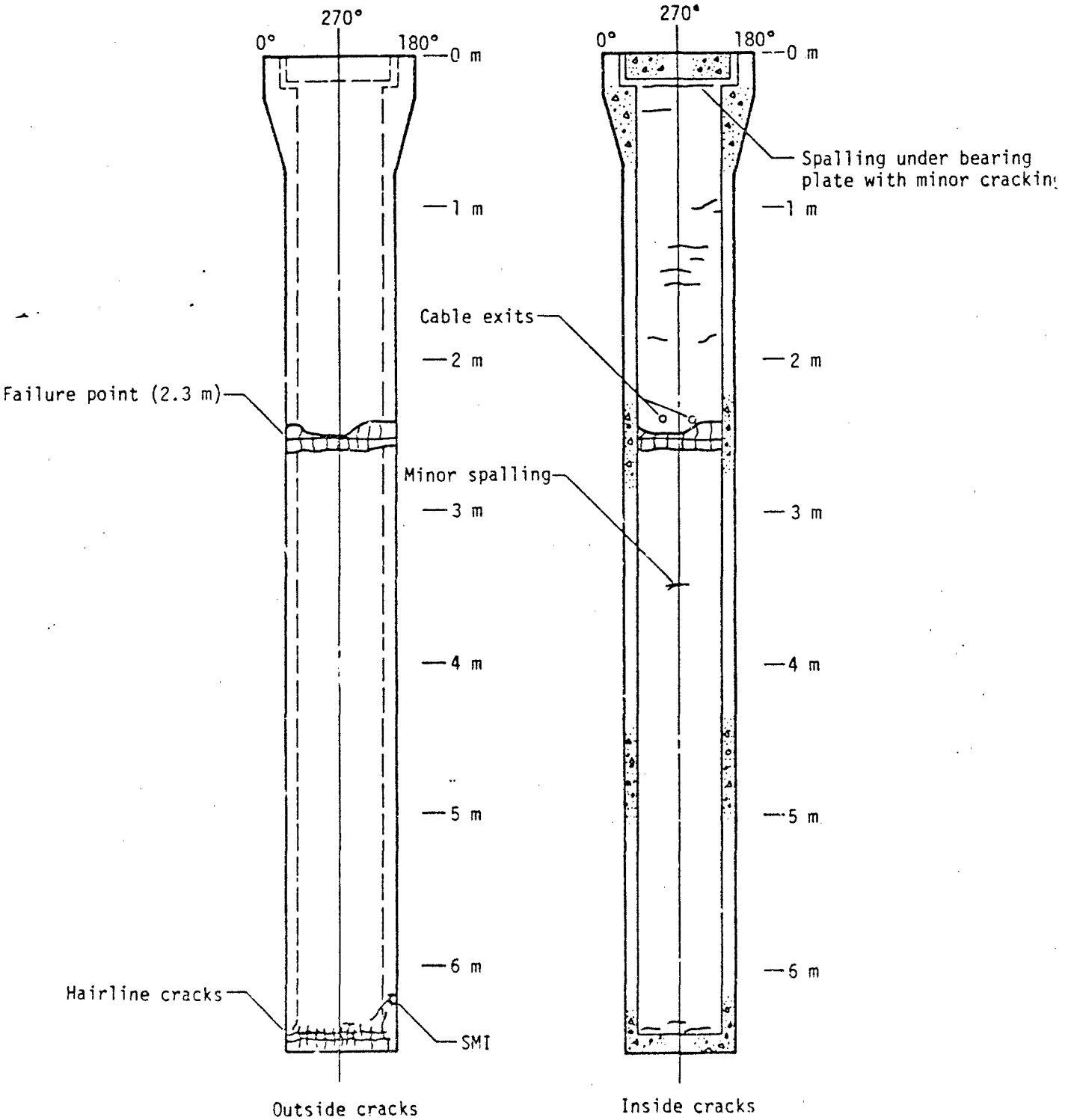
270°
0°
180°
0 m
1 m
2 m
3 m
4 m
5 m
6 m
Failure point (2.3 m)
Hairline cracks
SMI
Outside cracks
270°
0°
180°
0 m
Spalling under bearing plate with minor crackin
1 m
Cable exits
2 m
Minor spalling
3 m
4 m
5 m
6 m
Inside cracks

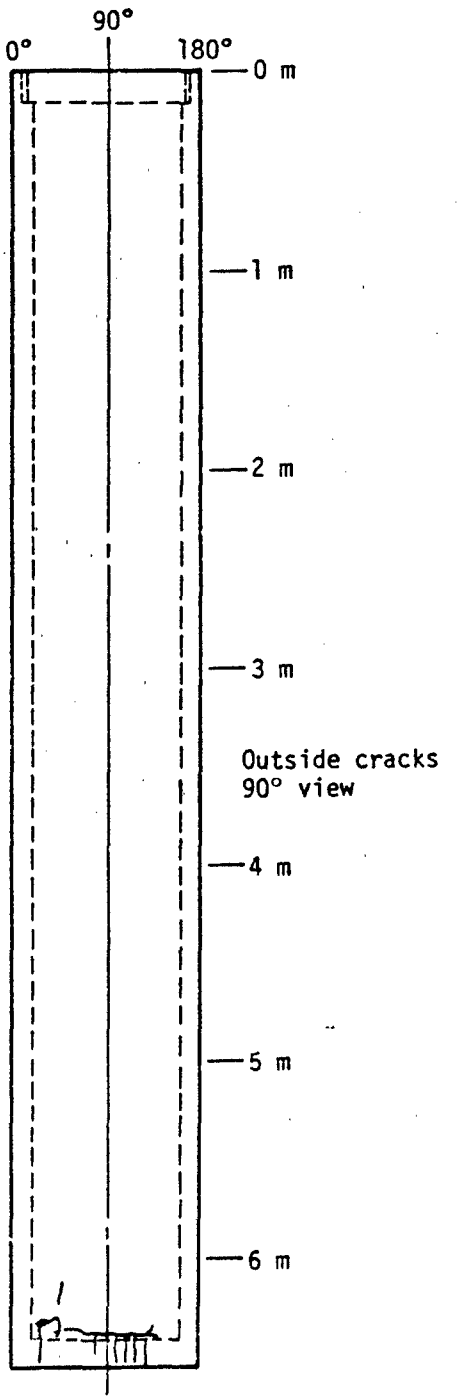
90°
0°
180°
0 m
1 m
2 m
3 m
Outside cracks
90° view
4 m
5 m
6 m

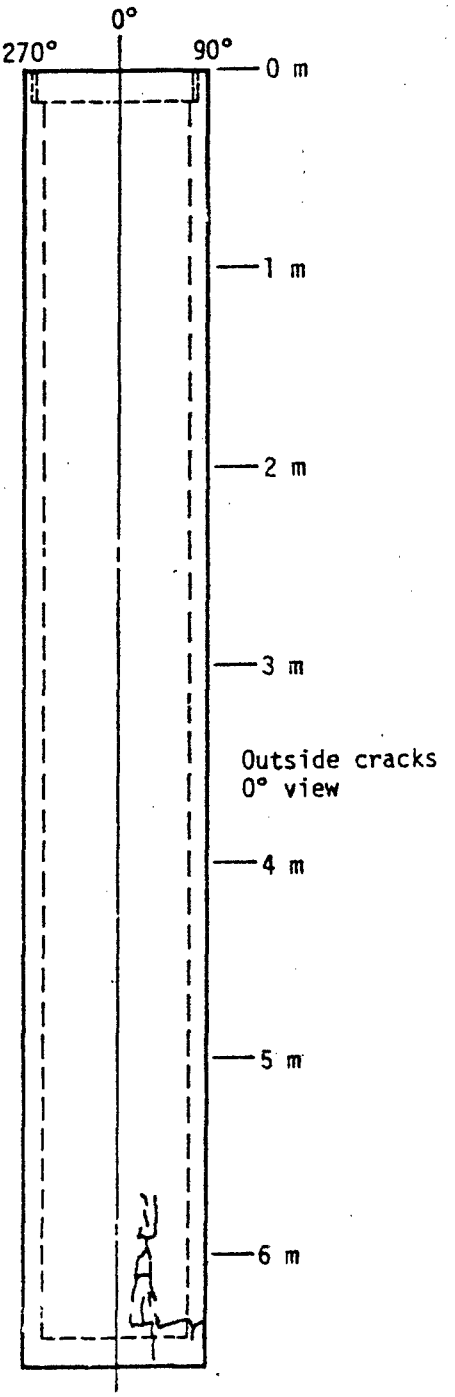
0°
270°
90°
0 m
1 m
2 m
3 m
Outside cracks
0° view
4 m
5 m
6 m

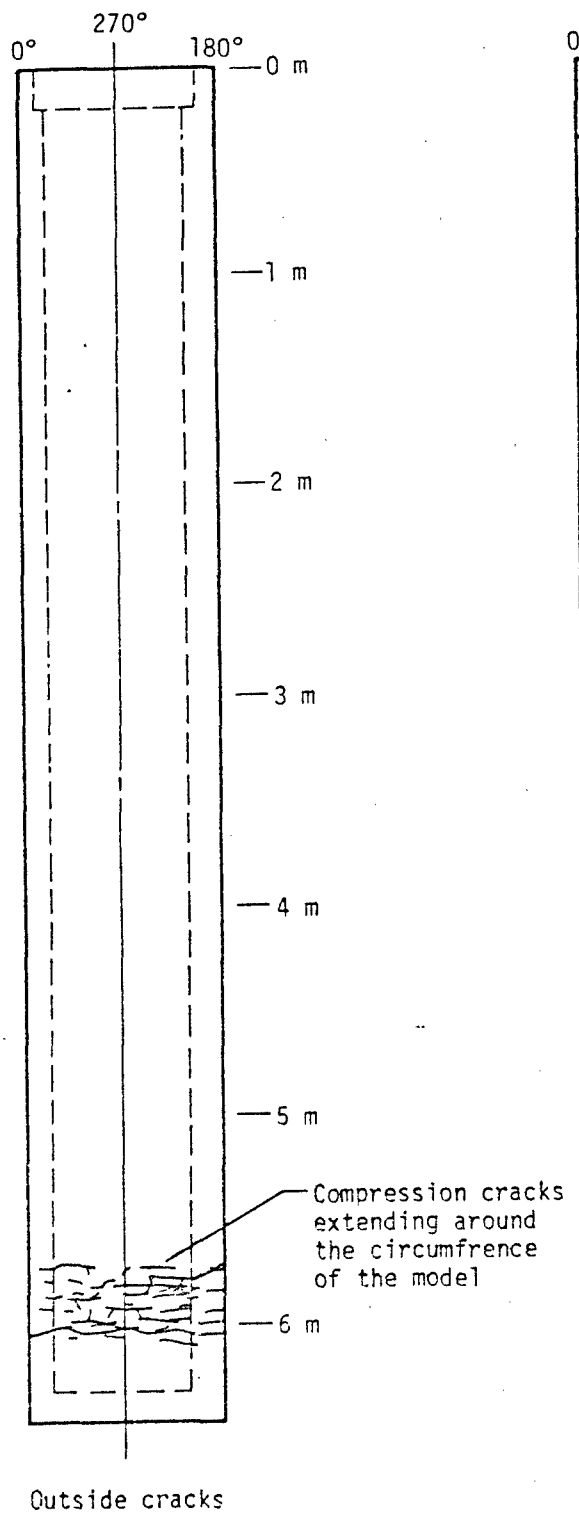

Outside cracks

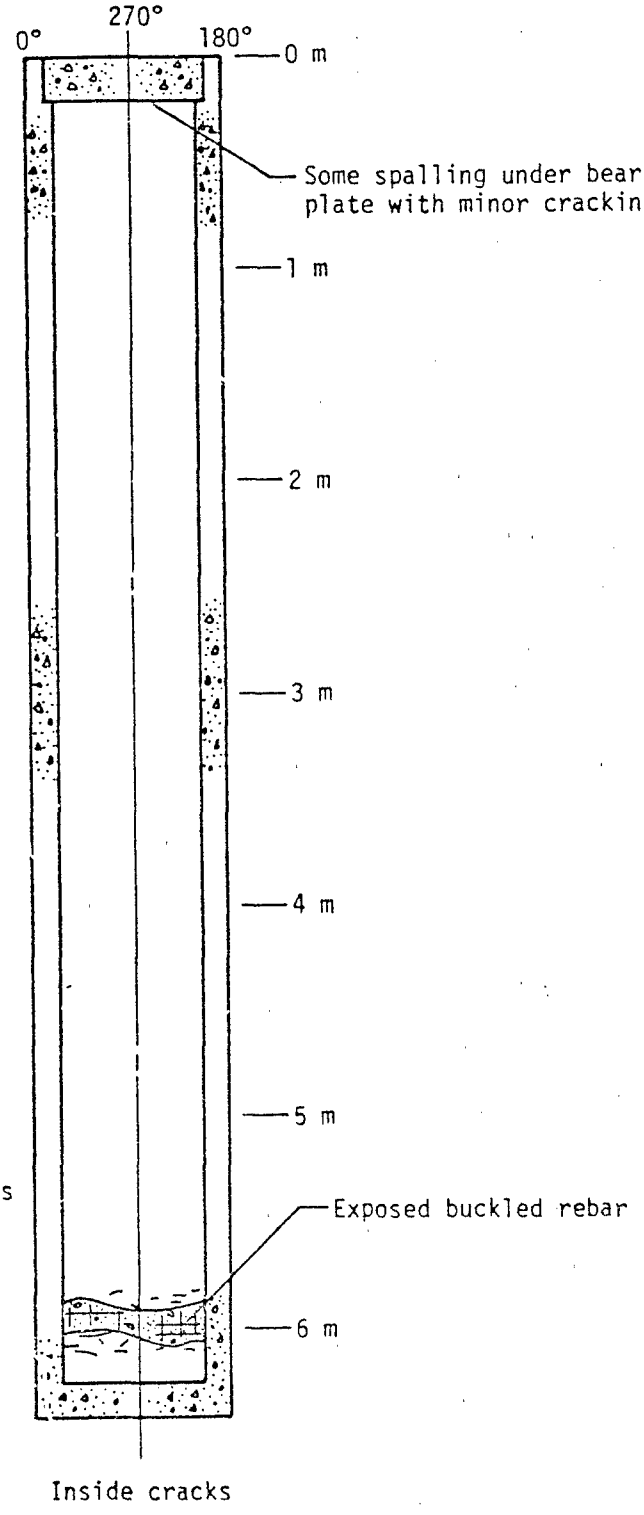

Inside cracks

CONCLUSIONS

The GOVS test series provided data that were used to investigate the effects of variations in the structural details of the shelter models and in site geology on the response of a vertical shelter to airblast loading. The effects of varying structural details were evaluated by a comparison of the GOVS-1 and GOVS-2 test results. The effects of varying structure-to-bedrock depth were evaluated by a comparison of the GOVS-2 and GOVS-3 test data. The test data were also compared to pretest predictions made by a 2-D SAMSON dynamic finite-element computer code for the purpose of evaluating the predictions.

When the GOVS-1 and GOVS-2 test results are compared, it is apparent that the lower strength of the concrete in the GOVS-1 model and the presence of the shelter transition section (with the correspondingly lower t/r ratio of the tube section) had adverse effects on the response of the GOVS-1 model. The GOVS-1 model experienced significant distress in the tube and base, whereas the GOVS-2 model experienced only minimal distress in the tube section near the base. It can be concluded that the variations in structural detail affected the response of the models as follows:

1. The headworks and transition region of the GOVS-1 model flexed considerably more toward the interior of the structure than did that of the stiffer GOVS-2 model.
2. The initial peak strain at the top of the tube in the GOVS-1 model exceeded that of the GOVS-2 model because of the reduced cross-sectional area and lower strength of the concrete in the former.
3. The GOVS-1 tube section, with its lower t/r ratio, deflected more

radially inward than did the GOVS-2 tube section.

4. The behavior of the bases of the models was similar. Toroidal bending of the structure wall in this region was evident in both models. This bending, however, was much more pronounced in the GOVS-1 model with its thinner wall and less stiff concrete.

The effect of placing the vertical shelter directly on bedrock was evaluated by a comparison of the GOVS-2 and GOVS-3 tests. In both tests, the predominant model response was axial compression. In the GOVS-3 test, however, a shock reflection from the bedrock magnified the tube stresses and strains in the region of the base of the structure. The stresses and strains caused by this reflection produced severe distress in the base of the GOVS-3 model. Because the two tests were similar in every detail except depth to bedrock, it can be concluded that it is not desirable to place a shelter directly on bedrock.

The pretest calculations and predictions performed by the SAMSON dynamic finite-element computer code were in good agreement with the test data. The calculations for the first two tests accurately predicted the overall response of the structures. However, discrepancies between the predicted and the measured timing of the free-field soil stresses and magnitude of the interface normal and shear stress indicated that the material model for the soil and the friction coefficients at the soil-structure interface should be modified. Consequently, these parameters were modified for the GOVS-3 calculation, and when the predicted and the test data for the GOVS-3 were compared, it was concluded that the modifications had adequately corrected the irregularities found in the previous calculations. However, uncertainties associated with the accurate

modeling of the behavior of the soil-structure interface invite further study.

REFERENCES

1. Bartel, H. Dean, and Cole, Donald M., "User Manual for SAMSON and Family", Technical Note No. *DE-TN-74-009,* Air Force Weapons Laboratory, Kirtland Air Force Base, New Mexico, December 1974.

2. Eddings, J. A., Jackson, T. M., and Lane, G. E., Jr., "Development of a Giant Reusable Airblast Simulator (GRABS)", *AFWL-TR-77-220,* Civil Engineering Research Division, Air Force Weapons Laboratory, Kirtland Air Force Base, New Mexico, June 1973.

3. Landon, Gary E., "GRABS Over Vertical Shelter (GOVS) Test 3, Pretest Predictions", *SSR-56A,* Letter Report to Air Force Weapons Laboratory, New Mexico Engineering Research Institute, University of New Mexico, Albuquerque, New Mexico, February 1980.

4. Narain, Ian G., "GRABS Over Vertical Shelter (GOVS) Test 2, Pretest Predictions", *SSR-52A,* Letter Report to Air Force Weapons Laboratory, New Mexico Engineering Research Institute, University of New Mexico, Albuquerque, New Mexico, July 1979.

5. Pickett, Stephen F., "Development and Evaluation of a Triaxial Interface Stress Transducer", *AFWL-TR-77-90,* Air Force Weapons Laboratory, Kirtland Air Force Base, New Mexico, August 1977.

6. Stephens, Jerry E., "GRABS Over Vertical Shelter (GOVS) Test 1, Pretest Predictions", *SSR-51A,* Letter Report to Air Force Weapons Laboratory, New Mexico Engineering Research Institute, University of New Mexico, Albuquerque, New Mexico, May 1979.

7. Wampler, H., Leigh, G., Furbee, M., and Seusy, F., "A Status and Capability Report on Nuclear Airblast Simulation Using HEST", presented at 6th International Symposium on Military Applications on Blast Simulation, Cahors, France, 25-29 June 1979.

ACKNOWLEDGEMENT

This work was performed under contract to the Air Force Weapons Laboratory and all findings of the test program are available in the following report:

Landon, Gary E., Narain, Ian G., and Stephens, Jerry E., "Giant Reusable Airblast Simulator (GRABS) on Vertical Shelters (GOVS)", *AFWL-TR-80-157,* Final Report to Air Force Weapons Laboratory, Kirtland Air Force Base, New Mexico, November 1980.

SUMMARY: Protective Vertical Shelters, by Ian G. Narain, Jerry E. Stephens and Gary E. Landon. The GOVS test program, consisting of three tests on Missile-X (MX) vertical shelters, was concerned with the effects of site geology and structural detail on shelter response. Pretest calculations were performed for each test.

KEY WORDS: Axisymmetric model; Dynamic response; Giant reusable airblast simulator (GRABS); GRABS on vertical shelters (GOVS); Structure-media interaction; Missile-X (MX); Reinforced concrete; Shelter configuration; Vertical airblast; Vertical shelters

ABSTRACT: The response of buried vertical MX shelters to vertical airblast and to airblast-induced ground-shock loadings is examined. Three tests were conducted on 1/6 scale reinforced concrete models to investigate the effects of site geology and structural detail on shelter response. The experimental data provided an insight into shelter response, and was also used to evaluate the accuracy of pretest calculations and predictions.

DETERMINATION OF SOIL PROPERTIES THROUGH GROUND MOTION ANALYSIS

John Frye
&
Norman Lipner

5 June, 1981

ABSTRACT

A method of calculating in situ one dimensional stress-strain soil properties from vertical ground motion is presented. The method relies on the fact that superseismic air blast ground surface loadings produce ground motions that are very nearly vertical and one dimensional in character. Therefore the equations of motion that govern the response are simple and may be integrated to obtain one dimensional stress-strain relations. Thus, results from tests that incorporate superseismic air blast surface loading and sensors to measure vertical motion at various depths in the soil can be used to calculate soil stress-strain properties directly. The method accounts for multiple records at a given depth and features techniques for characterizing response histories and interpolating velocities at depths between those where measurements have been made. As an example, for the DISC HEST Test I event, conducted in Ralston Valley, Nevada as part of the MX development program, the site properties are computed based on the free field data.

DETERMINATION OF SOIL PROPERTIES THROUGH GROUND MOTION ANALYSIS

J. W. Frye[1] and N. Lipner[2], M. ASCE

INTRODUCTION

The ground response to overhead highly superseismic airblast loading (airblast shock speed faster than ground shock speeds) is nearly one-dimensional uniaxial strain and the motions are nearly vertical. Soil properties for prediction of these motions have typically been determined from dynamic uniaxial strain laboratory tests. However, the process of extracting soil samples from the field can disturb the material and, as a result, the laboratory properties could be different from the in situ material behavior.

An approach to determine the in situ properties is to perform a field test where the ground surface is loaded by superseismic airblast. Data from sensors that measure vertical motion at various depths in the ground could then be used to calculate the uniaxial strain properties of the soil by use of the one-dimensional equation of motion.

One type of surface loading that has been used to obtain a one-dimensional response is the DISC (Dynamic In Situ Compressibility) HEST (High Explosive Simulation Technique) test shown in Figure 1. This test employs a circular region of explosives that is center detonated. The detonation propagates outward fast enough that the early-time response to peak velocity is essentially one-dimensional within some region under the loaded area that is governed by the disc radius and the soil properties. Because of the finite propagation velocity, time at any range from the centerline is measured with respect to the arrival of the overhead airblast at that range.

---

1. Member of the Technical Staff, Hardness and Survivability Laboratory, TRW, Redondo Beach, CA 90278

2. Department Head, Hardness and Survivability Laboratory, TRW, Redondo Beach, CA 90278

ANALYSIS FORMULATION

The one-dimensional equation of motion relates the vertical normal stress gradient to the acceleration of the soil.

$$\frac{\partial \sigma_z}{\partial z} = \rho \ddot{u}_z \tag{1}$$

Here z is the vertical coordinate (Fig. 1), σ_z is the normal stress in the z direction (tensile stress is positive), and ρ is the soil density. Equation (1) can be integrated with respect to depth from the ground surface to a depth z to obtain the following equation for stress:

$$\sigma_z = -p(t) + \int_o^z \rho \dot{v}_z dz \tag{2}$$

where the constant of integration, $p(t)$, is the surface pressure-time history, a boundary condition of the problem, and the first time derivative of velocity, $\dot{v}_z$, replaces the second time derivative of displacement.

The one-dimensional strain, ε_z, is the derivative of the vertical displacement with respect to depth.

$$\varepsilon_z = \frac{\partial u_z}{\partial z} \tag{3}$$

Taking the time derivative of Equation (3) provides the following relation for the strain rate $\dot{\varepsilon}_z$:

$$\dot{\varepsilon}_z = \frac{\partial \dot{u}_z}{\partial z} = \frac{\partial v_z}{\partial z} \tag{4}$$

and integrating Equation (4) gives the following relation for strain in terms of velocity:

$$\varepsilon_z = \int_o^t \frac{\partial v_z}{\partial z} dt \tag{5}$$

The constant of integration is zero because the strain in the soil is

measured with respect to the geostatic strain and, therefore, is zero at time zero.

From Equations (2) and (5) it is seen that if the vertical component of velocity is defined with respect to time and depth, then stress and strain may be directly calculated from derivatives of the velocity by performing integrations with respect to depth and time. The pressure time history at the surface and estimates of the soil density are also required by Equation (2).

Evaluation of the integrals of Equations (2) and (5) requires knowledge of the velocity field for the complete space-time region of interest. In a test, motion sensors at only a limited number of depths can be implanted because of cost, as well as physical constraints. Therefore, a method must be developed to interpolate from the data available for a limited number of depths to the velocity history at any depth.

In many test events, more than one record is available at some depths, so that if one sensor is faulty, all of the velocity-time information concerning that particular depth is not lost. Data records available for a particular depth will vary from one another due to a number of reasons, such as variation from one location to another of soil properties and surface pressure-time histories. In examining the velocity-time records taken at a particular depth, it is not always obvious that one particular record is the most accurate and representative of all. Thus, some method of including all acceptable records taken at a particular depth must be employed in defining the velocity-time history to be used in the interpolation process. Clearly some records that show anomalous results, not representative of motions that are physically plausable, should be excluded from consideration Such records might be taken from sensors that either were poorly installed,

were destroyed by the shock loading, or produced records that were extremely noisy.

The method chosen for interpolating the measured velocity records uses a transformed coordinate system with a time-like coordinate s that remains constant with depth along specific characteristics of the velocity time history. At the beginning of motion, s is always taken as zero; at peak velocity, s equals 1.0; and at the end of the velocity record, s assumes some large value such as 10. Other values of s are chosen to follow percentages of the peak velocity, as shown in Figure 2. Mathematically, the transformation is as follows:

$$z' = z$$
$$s = f(z,t) \tag{6}$$

where z' is the depth coordinate of the new coordinate system.

This transformation is piecewise linear between depths where velocity records are available. Averaged characteristic information available from the records at each depth is used. At constant depth, the time-like coordinate s is related to t through a series of straight line segments between s and t values established for particular velocity record characteristics. Details of the formulation of the transformation and other matters concerning the interpolation between records at different depths are given in the appendix.

The interpolation of the velocity between depths where data are available is done in the z', s coordinate system along lines of constant s values; i.e., the interpolation is performed with respect to specific velocity record characteristics. Peak velocities at adjacent depths where data are available are used to interpolate the peak velocity at in-between depths. Thus, half-peak velocity data are used to interpolate half-peak velocities,

and so on.

In order to establish a unique definition of the velocity history at a given depth, the velocity record is broken up into a series of segments that begin and end at specific s coordinates. The segments are taken to be the same at all depths forming a grid work in the x', s space as shown in Figure 3. The velocity history at each depth and over each segment is represented as a cubic function with the beginning and end of each segment having the same velocity value as adjacent segments so that step changes in velocity (infinite acceleration) are ruled out. The parameters of the cubic interpolation functions are evaluated based on a least square fit to the velocity records at the depth in question.

Interpolation between depths is done using an exponential function that begins at the adjacent upper depth and ends on the adjacent lower depth. Extrapolation of velocities to depths above the shallowest depth for which data are available is performed by extrapolating the exponential interpolation function derived for the region between the two shallowest depths. Velocity at depths below the deepest depth for which data are available is obtained, in a similar manner, from the interpolation function of the two deepest depths.

Having established a method of deriving unique velocity records for all depths and times from the measured data, stresses and strains are calculated from Equations (2) and (5) using central differencing and standard numerical integration techniques. The results of the analysis have been found to be rather insensitive to the discretization used in the numerical analysis. The major factors in the analysis appear to be the choice of velocity histories and of interpolation segments.

ANALYSIS RESULTS

Soil stress strain relations have been calculated from one-dimensional finite difference calculation results, as a check on the analysis, and from DISC HEST test data. The finite difference calculation considered two dry soil layers over a wet soil half-space (Reference 1). The dry soil layers had linear loading and linear unloading moduli. The loading modulus for the lower dry soil material was 1.5 times as stiff as for the surface layer; the unloading moduli in both layers were about an order of magnitude stiffer than the loading (Fig. 4). The velocity histories from the calculation were input into the analysis developed herein, with the stress-strain curve results shown in Figure 4. For this analysis, velocity histories were used at every 1.83 m (6 ft) of depth from the surface down to 18.29 m (60 ft) and every 3.05 m (10 ft) of depth from 18.29 m (60 ft) down to 45.72 m (150 ft).

The technique is able to track properties that change with depth and is able to follow unloading along entirely different slopes than the loading curve. The unloading results are less satisfactory than those for the loading portion of the response. However, because the unloading is so steep, a small change in strain can make a large difference in the slope of the curve. The results also show that the method predicts a gradual, rather than a sharp, change in properties with depth. This is attributed to smoothing and other approximations inherent in the use of exponential and cubic functions to perform the required interpolations.

When using theoretical results, velocity records are available at the surface as well as at large depths. With experimental data, surface velocity histories are not known and histories at deep depths are likely to be influenced by free surface reflections from outside the loaded area that produce multi-dimensional response characteristics.

After gaining experience with the technique using analytical results, it was then applied to data from the DISC HEST Test I event (Reference 2) conducted in Ralston Valley, Nevada. The HEST cavity radius on this test was 13.7 m (45 ft), and data was obtained at eight depths down to 15.2 m (50 ft) (Fig. 5). The data appeared to be relatively free of noise, allowing most of the records to be incorporated in the evaluation of the velocity field history. A total of fourteen records over the eight depths (Fig. 6) were included in the analysis. Figure 7 shows a family of interpolated velocity histories obtained from the analysis.

The airblast pressure history was measured at several points on the ground surface within the HEST cavity. A best fit through the pressure records (Reference 2) is shown in Figure 8. This pressure history was initially used in Equation (2) to calculate stress histories at depths of interest, but unsatisfactory results were obtained. The main problem was that, at the onset of incipient motion ($s = 0$) at some depths, the stress was nonzero because the two terms on the right hand side of Equation (2) did not exactly cancel. This occurred because the averaged surface overpressure and the velocity field interpolated from the data were not completely consistent.

An alternate approach is to compute a surface pressure loading from the velocity field. Setting the stress equal to zero in Equation (2)

at the arrival of motion at any depth, d_0 yields

$$0 = -p(t) + \int_0^{d_0(t)} \rho \dot{v}_z \, dz$$

$$p(t) = \int_0^{d_0(t)} \rho \dot{v}_z \, dz \qquad (7)$$

A pressure history derived from the ground motion response is shown in Figure 8 compared with the best fit pressure history. The pressure histories agree reasonably well in the early time of the motion. The initial slope of the calculated pressure loading is not as steep as that obtained from measurements. This is probably due to smoothing of the velocity histories by the interpolation process and the difficulty of exactly predicting ground motion at and near the surface from measurements made below the surface. The impulse histories of the measured and calculated surface loadings are also shown in Figure 8. They compare very well in the early time of the motion indicating that the interpolation process averages out variations in the velocity histories in a manner that preserves the overall character and energy content of the response. After about 25 ms of response, the calculated and measured pressure and impulse histories begin a significant divergence. This can be attributed to the reduction of the vertical ground accelerations by edge effects. The divergence of the pressure histories may serve as a time marker for the demarcation of when two-dimensional response becomes important.

Examination of the data in Figure 7 shows that peak velocity is achieved within 25 ms down to a depth of about 8 m. For larger depths, the time to peak velocity increases with depth at a faster rate than might be expected for one-dimensional response. Information on properties at deeper depths can be obtained from two-dimensional finite difference calculations, however, assumptions are required to obtain the uniaxial strain properties at the depths because the response is two-dimensional and essentially only vertical motion records are available.

Figure 9 shows the interpolated uniaxial strain stress-strain plots obtained from the velocity field and the derived surface overpressure. The initial slope of the stress-strain curves and the 4 MPa secant modulus are plotted as a function of depth in Figure 10 and compared with the seismic velocity profile of the site. The loading properties show relatively small variation with depth down to 9 m. The unloading properties are not well behaved, but most of the unloading occurs after the 25 ms of one-dimensional simulation time.

The initial slope of the interpolated stress-strain curves produces a modulus that compares better with the seismic results (except very near the surface) than does the 4 MPa modulus. This is to be expected since the moduli obtained from seismic measurements are representative of the soil response at very low stress values. The 4 MPa modulus is consistently lower than the seismic or initial slope values. This reflects the softening of the soil with increasing stress, characteristic of cemented granular soil.

The seismic profile shows a soft soil layer in the top 1.5 m (5 ft) that is not present in the results of the interpolated stress-strain curves. It is possible that the material is behaving stiffer than would be expected from the seismic profile, because of strain rate effects. However, the

fact that the interpolated peak surface pressure is lower than (about 15 percent) the averaged pressure gage data indicates that the near surface motions were actually larger than those used in the analysis, which would result in softer near surface properties.

Better results might be obtained by making use of seismic velocity information in extrapolating velocity field data to obtain surface values. The second depth that velocity data was recorded in DISC HEST Test I was at 1.5 m, the same depth that a sudden hardening of soil modulus was indicated by seismic data. Thus the second velocity history occured at a transition region in soil properties. The velocity response at this depth then contained information that was more characteristic of the soil below the transition boundary. Therefore, the extrapolation of motion field to the surface was influenced by the second seismic layer. An alternate approach to performing the extrapolation would be to increase the peak surface velocity until the interpolated peak surface pressure was in agreement with the data. In cases where it is important to more accurately define the material properties in this very near surface layer, then gages at two depths within the layer (such as 0.5 and 1.0 m) should be used in the experiment.

CLOSURE

The purpose of this paper is to demonstrate a methodology for determining uniaxial strain mechanical properties of soil solely from velocity time histories obtained from a high explosive field test event. It is similar to the LASS (Lagrangian Analysis of Stress and Strain) methodology developed by SRII (Reference 3) for analysis of spherical motions. However, for the spherical case both stress and velocity data are needed.

Analysis of in situ field test data is generally the most accurate technique for determining in situ mechanical properties. The material property inversion technique described herein represents a first step in the analysis of the data; the complete development of properties at a site would consider all available relevant information, such as seismic and laboratory test results. The properties derived from in situ data might then be smoothed or adjusted based on auxiliary data, as long as these changes were within the uncertainties of the in situ analysis. These revised properties would then be used in one- and two-dimensional finite difference calculations to verify their adequacy.

CONCLUSIONS

(1) Dynamic stress-strain properties of in situ soil may be derived directly from velocity histories taken from surface pressure loading tests, using the method described herein, down to depths where the ground motion is sufficiently one-dimensional. Results have been obtained from experimental data for the DISC HEST Test I event.

(2) Surface pressure histories may be derived from the velocity data for the duration of one-dimensional response. This can provide a check on the consistency between pressure and velocity data. The time when the measured and derived surface pressure loading diverges is an indication of the duration of one-dimensional response. In the DISC HEST Test I event, the measured and derived impulse histories were in reasonable agreement out to about 25 ms.

(3) The interpolation functions used in the technique are effective in deriving soil velocity as a continuous function of depth and time. Since the functions are based on measured rather than hypothesized soil response characteristics they should be able to be applied to tests with different soil types with equal success. This approach can also be generalized to apply to motion fields that are dependent on two spacial coordinates.

ACKNOWLEDGEMENT

This work was performed for the USAF Ballistic Missile Office under the direction of Lt. Col. Donald H. Gage. We acknowledge the support of Dr. J. S. Zelasko of the US Army Engineer Waterways Experiment Station who provided us the DISC HEST Test I field test data and the finite difference calculational results.

Appendix I - Derivation of Coordinate Transformation and Interpolation Functions

There are a number of characteristic times that are clearly important in describing a velocity record (Fig. 2). The two times of dominant importance are the time when the motion begins and the time when the velocity reaches its greatest absolute amplitude. Other points such as the end of the record and time where the velocity attains given fractions of the peak velocity serve to complete a listing of the important characteristic time points of the record. The points that serve to best describe the records may be assigned labels that we will denote by the symbol s. For convenience, the labels can be made numeric and assigned values that increase with time for a given record. By convention the start of motion is at s=0; the peak velocity is at s=1.0; and the end of the record is assigned a large number such as s=10. Points between the peak velocity and the end of the record have s values between 1 and 10 and points between the start of motion and the peak velocity have s values between 0 and 1.

Once a set of s labels have been chosen they can be applied to all of the records at all of the depths. The value of s remains constant with depth along a characteristic line connecting similar time points of different records. At a given depth, points with particular values of s form clusters. The best estimate of where particular s points ought to fall can be obtained by calculating mean values.

$$\bar{t}(x_i, s) = \frac{1}{n_i} \sum_{j=i}^{n_i} t_j(x_i, s) \qquad \text{(A-1)}$$

where $t(x_i, s)$ is the time of characteristic point s at depth x_i and record j; $\bar{t}(x_i, s)$ is the average time of characteristic point s for depth x_i; and n_i is the number of records at depth x_i.

To estimate values of s between depths where records exist, a straight line can be drawn between the average time of the various s labels for existing records. In this way, a family of segmented constant s curves may be obtained, which can be considered as a new time-depth coordinate system. Specific features of the velocity response history, for each depth, occur at constant values of tne time like s coordinate. The symbols of the new coordinates x', s are related to the x, t coordinates by the following transformation relations.

$$x' = x \qquad \text{(A-2)}$$
$$s = f(x, t)$$

In order to further define the function $f(x,t)$ the variation of s as a function of t at a given depth must be specified. The simplest choice, and the one that will be shown here, is to let s vary as a linear function of t between each of the labeled values of s. The linear function has the advantage that it guarantees that a unique mapping of s onto t coordinates exists and vice versa. This linear relation between s and t is illustrated

in Figure A-1 and shown in equation form below

$$s = s^{(i)} + (s^{(i+1)} - s^{(i)}) \frac{[t-\bar{t}(z,s^{(i)})]}{[\bar{t}(z,s^{(i+1)}) - \bar{t}(z,s^{(i)})]} \qquad \text{(A-3)}$$

$$\text{for } \bar{t}(z,s^{(i)}) \le t \le \bar{t}(z,s^{(i+1)})$$

where $s^{(i)}$ is the value of s at the i'th characteristic point on the velocity history. Equation (A-3) can be rearranged to give the solution of t as a function of s.

$$t = \bar{t}(z,s^{(i)}) + \frac{[\bar{t}(z,s^{(i+1)}) - \bar{t}(z,s^{(i)})](s-s^{(i)})}{(s^{(i+1)} - s^{(i)})} \qquad \text{(A-4)}$$

$$\text{for } s^{(i)} \le s \le s^{(i+1)}$$

The terms $\bar{t}(z^{(i)},s)$ are linear functions of depth. In equation form the relation for $\bar{t}(z,s^{(i)})$ is

$$\bar{t}(z,s^{(i)}) = \bar{t}(z_j,s^{(i)}) + \frac{[\bar{t}(z_{j+1},s^{(i)}) - \bar{t}(z_j,s^{(i)})](z-z_j)}{(z_{j+1}-z_j)} \qquad \text{(A-5)}$$

$$\text{for } z_j \le z \le z_{j+1}$$

Equations (A-3) and (A-5) define the function $f(z,t)$ of equation (A-2). The inverse transformation equation is

$$z = z' \qquad \text{(A-6)}$$
$$t = g(z',s)$$

The advantage of the coordinate system is that it provides a convenient framework for interpolating velocities between depths. Points at $s=1$ will be related to peak velocity values only; points with $s=1/2$ will be related to velocity values that are at 1/2 of the peak value, and so forth.

At each depth a variety of records are typically available. For those records at a given depth that are valid, we have the problem of forming a function that is representative of the velocity response history. Since the records are complex it is impractical to consider

using one equation to represent the entire time history at a given depth. An equation of this kind would likely be complicated and might vary in form dependi g on the depth. A more realistic approach is to segment the velocity record and treat each segment independently of the other but at the end points of a segment have velocity values that match up with those of adjacent segments. For convenience we will require that common s values be used to define segment boundaries. It is usually better to have a larger number of segments to define the history at the beginning of the motion than at the end of the velocity record. The time history at the beginning of the motion changes more rapidly than at the end and thus should be more carefully described.

Lagrangian interpolation functions are particularly well suited for establishing the velocity histories for the various segments of the response at a particular depth. These kinds of functions can be readily defined to any desired order, but the higher order functions have unfavorable properties. Since the function must describe the velocity history over only a segment of the total time of the record, a cubic function should be adequate to give a good description of the required motion. The general form of a cubic Lagrangian interpolation function is as follows:

$$w_{ij}(s) = \frac{(a_{i2}-s)(a_{i3}-s)(a_{i4}-s)\ v_{ij1}}{(a_{i2}-a_{i1})(a_{i3}-a_{i1})(a_{i4}-a_{i1})} + \frac{(a_{i1}-s)(a_{i3}-s)(a_{i4}-s)\ v_{ij2}}{(a_{i1}-a_{i2})(a_{i3}-a_{i2})(a_{i4}-a_{i2})} + \frac{(a_{i1}-s)(a_{i2}-s)(a_{i4}-s)\ v_{ij3}}{(a_{i1}-a_{i3})(a_{i2}-a_{i3})(a_{i4}-a_{i3})} + \frac{(a_{i1}-s)(a_{i2}-s)(a_{i3}-s)\ v_{ij4}}{(a_{i1}-a_{i4})(a_{i2}-a_{i4})(a_{i3}-a_{i4})} \tag{A-7}$$

Here v_{ij1}, v_{ij2}, v_{ij3} and v_{ij4} are the velocities at each of four s coordinate locations a_{i1}, a_{i2}, a_{i3} and a_{i4} within segment i and at depth j, and w_{ij} is the function defining the velocity history for the i'th segment and j'th depth. The locations a_{i1} and a_{i4} will be considered to occur at the

beginning and end of segment i.

At the point where s is zero, the value of velocity is zero also. This is always true by definition since the $s=0$ point is taken to be the point in time where the motion response begins. Thus, for the first interpolation segment between $s=0$ and $s=s_1$, where s_1 is the value at the end of the first segment, the value v_{ij1} is zero. The values v_{ij2}, v_{ij3} and v_{ij4} are still unknown.

For any given time history at a particular depth, errors will occur between the velocity given by Equation (A-7) and the time history value. For a given value s the error can be written as

$$E_{jk}(s) = V_{jk}(s) - w_{ij}(s) \tag{A-8}$$

or

$$E_{jk}(s) = V_{jk}(s) - h_{i1}v_{ij1} - h_{i2}v_{ij2} - h_{i3}v_{ij3} - h_{i4}v_{ij4} \tag{A-9}$$

where $V_{jk}(s)$ and $E_{jk}(s)$ are the velocity and velocity error, respectively, for time history k at coordinate s and depth j and

$$\begin{aligned}
h_{i1} &= \frac{(a_{i2}-s)(a_{i3}-s)(a_{i4}-s)}{(a_{i2}-a_{i1})(a_{i3}-a_{i1})(a_{i4}-a_{i1})} \\
h_{i2} &= \frac{(a_{i1}-s)(a_{i3}-s)(a_{i4}-s)}{(a_{i1}-a_{i2})(a_{i3}-a_{i2})(a_{i4}-a_{i2})} \\
h_{i3} &= \frac{(a_{i1}-s)(a_{i2}-s)(a_{i4}-s)}{(a_{i1}-a_{i3})(a_{i2}-a_{i3})(a_{i4}-a_{i3})} \\
h_{i4} &= \frac{(a_{i1}-s)(a_{i2}-s)(a_{i3}-s)}{(a_{i1}-a_{i4})(a_{i2}-a_{i4})(a_{i3}-a_{i4})}
\end{aligned} \tag{A-10}$$

The error value $E_{jk}(s)$ may be either positive or negative; however, only the absolute amplitude of the error value is of importance. The square of the error value $E_{jk}(s)$ is always positive and is then a better

error measure for the purposes of judging the ability of the function $w_{jk}(s)$ to fit the velocity-time response $V_{jk}(s)$.

The total error is not just that measured at one coordinate value for one record but is the integral for all points s over the segment summed for all of the records available at a given depth.

$$E_{Tji} = \sum_{k=1}^{n_j} \int_{s_{i-1}}^{s_i} E_{jk}(s)ds \tag{A-11}$$

$$E_{Tji} = \sum_{k=1}^{n_j} \int_{s_{i-1}}^{s_i} [V_{jk}(s)-h_{i1}v_{ij1}-h_{i2}v_{ij2}-h_{i3}v_{ij3}-h_{i4}v_{ij4}]^2 ds \tag{A-12}$$

We must select velocities v_{ij2}, v_{ij3}, and v_{ij4} that minimize the total error E_{Tji}. We will assume that the value v_{ij1} is always constrained by continuity requirements with segment $i-1$. If we evaluate the segments in order starting with $i=1$, we need only match the constant v_{1j4} for segment 1 with the constant v_{2j1} for segment 2 to preserve continuity of velocity between segment 1 and 2. The constant v_{1j1} is always zero since it corresponds to the beginning of motion. In evaluating the constants for segment 1, we need only find values for v_{1j2}, v_{1j3} and v_{1j4}. If v_{1j4} is set equal to v_{2j1} then for the second segment only the values v_{2j2}, v_{2j3} and v_{2j4} need be evaluated. The process can be continued for all of the segments.

The positions a_{i1} and a_{i4} then must fall at the beginning and end of the segment. Thus $a_{i1} = s_{i-1}$ and $a_{i4} = s_i$. The points a_{i2} and a_{i3} can be chosen as equally spaced along the segment. Thus

$$\begin{aligned} a_{i1} &= s_{i-1} \\ a_{i2} &= s_{i-1} + \tfrac{1}{3}(s_i - s_{i-1}) \\ a_{i3} &= s_{i-1} + \tfrac{2}{3}(s_i - s_{i-1}) \\ a_{i4} &= s_i \end{aligned} \tag{A-13}$$

The error function E_{Tji} is always positive and is a quadratic function of the terms v_{ij2}, v_{ij3} and v_{ij4}. It follows that its minimum occurs where the derivatives of E_{Tji} with respect to v_{ij2}, v_{ij3} and v_{ij4} are all zero. These conditions produce the equations for the determination of the unknown velocity constants.

$$\frac{\partial E_{Tji}}{\partial v_{ij2}} = 0 = \sum_{k=1}^{n_j} \int_{s_{i-1}}^{s_i} [-V_{jk}h_{i2} + h_{i1}h_{i2}v_{ij1} + h_{i2}^2 v_{ij2} + h_{i2}h_{i3}v_{ij3} + h_{i2}h_{i4}v_{ij4}]ds \tag{A-14}$$

$$\frac{\partial E_{Tji}}{\partial v_{ij3}} = 0 = \sum_{k=1}^{n_j} \int_{s_{i-1}}^{s_i} [-V_{jk}h_{i3} + h_{i1}h_{i3}v_{ij1} + h_{i2}h_{i3}v_{ij2} + h_{i3}^2 v_{ij3} + h_{i3}h_{i4}v_{ij4}]ds \tag{A-15}$$

$$\frac{\partial E_{Tji}}{\partial v_{ij4}} = 0 = \sum_{k=1}^{n_j} \int_{s_{i-1}}^{s_i} [-V_{jk}h_{i4} + h_{i1}h_{i4}v_{ij1} + h_{i2}h_{i4}v_{ij2} + h_{i3}h_{i4}v_{ij3} + h_{i4}^2 v_{ij4}]ds \tag{A-16}$$

Evaluating each term of the summation and integration processes of Equations (A-14), (A-15) and (A-16) separately and placing terms of known value on the right hand side of the equation with terms of unknown value on the left hand side of the equation produces the following results:

$$\begin{aligned} c_{22}v_{ij2} + c_{23}v_{ij3} + c_{24}v_{ij4} &= F_2 \\ c_{23}v_{ij2} + c_{33}v_{ij3} + c_{34}v_{ij4} &= F_3 \\ c_{24}v_{ij2} + c_{34}v_{ij3} + c_{44}v_{ij4} &= F_4 \end{aligned} \tag{A-17}$$

where

$$c_{22} = \sum_{k=1}^{n_j} \int_{s_{i-1}}^{s_i} h_{i2}^2 ds \qquad \text{(A-18)}$$

$$c_{23} = \sum_{k=1}^{n_j} \int_{s_{i-1}}^{s_i} h_{i2} h_{i3} ds \qquad \text{(A-19)}$$

$$c_{24} = \sum_{k=1}^{n_j} \int_{s_{i-1}}^{s_i} h_{i2} h_{i4} ds \qquad \text{(A-20)}$$

$$c_{33} = \sum_{k=1}^{n_j} \int_{s_{i-1}}^{s_i} h_{i3}^2 ds \qquad \text{(A-21)}$$

$$c_{34} = \sum_{k=1}^{n_j} \int_{s_{i-1}}^{s_i} h_{i3} h_{i4} ds \qquad \text{(A-22)}$$

$$c_{44} = \sum_{k=1}^{n_j} \int_{s_{i-1}}^{s_i} h_{i4}^2 ds \qquad \text{(A-23)}$$

$$F_2 = \sum_{k=1}^{n_j} \int_{s_{i-1}}^{s_i} (V_{jk} h_{i2} - h_{i1} h_{i2} v_{ij1}) ds \qquad \text{(A-24)}$$

$$F_3 = \sum_{k=1}^{n_j} \int_{s_{i-1}}^{s_i} (V_{jk} h_{i3} - h_{i1} h_{i3} v_{ij1}) ds \qquad \text{(A-25)}$$

$$F_4 = \sum_{k=1}^{n_j} \int_{s_{i-1}}^{s_i} (V_{jk} h_{i4} - h_{i1} h_{i4} v_{ij1}) ds \qquad \text{(A-26)}$$

Equations (A-17) are a set of three linear relations with constant coefficients and three unknowns that can be readily solved. The solution is not a major problem once the constant coefficients c_{22}, c_{23}, etc., and the right hand side constants F_2, F_3 and F_4 are known. However, these constants require an integration that is not trivial. The functions h_{i1}, h_{i2}, h_{i3} and h_{i4} are not simple, and the velocity functions V_{jk} are typically defined at a finite number of points rather than in a continuous manner due to the digital definition of the record. The integrations for the coefficients of the equation can be carried out numerically with no difficulty since the functions are defined for all values s within the segment. A standard procedure for performing the numerical integration is to divide up the segment into a large number of intervals, and then evaluate the integral based on the function values at the beginning and end of each of the intervals.

For the integration of the constants F_2, F_3 and F_4, it will be necessary to define values of V_{jk} at points s where digitized velocity data are undefined. This problem is resolved by assuming that the velocity in each record varies linearly between the defined values. Figure A-1 illustrates the assumed

variation of the velocity record with respect to s and time. By making the assumption of linearity between the defined velocity record points, the velocity record becomes in effect defined at all points and the integrations of Equations (A-24), (A-25) and (A-26) can be carried out to obtain the constants F_2, F_3 and F_4.

With the determination of the constants v_{ijk} for all segments at all depths, a set of velocity records are available at each depth that are representative of an optimal average of all valid velocity records. The problems now remaining are how to interpolate between depths where velocity records are recorded and also how to interpolate from the velocity record at the shallowest depth up to the surface and to depths below the deepest where data is available.

There are any number of schemes that could be applied to the interpolation of the velocity records between depths. One could use linear, quadratic, cubic or higher order polynomials, or one could use functions that are appealing on a physical basis. Since some characteristics of velocity histories are known to decay in an approximately exponential manner with depth within a given material, exponential functions should provide useful vehicles for interpolating the velocity records. After some experimentation, it was found that the exponential functions in fact produced more favorable results than the polynomial functions. The major drawback to the polynomial functions is their tendency to oscillate. This oscillation produces velocity responses that can increase with respect to depth instead of decrease even though all of the points used in the interpolation show a decrease in velocity with respect to depth.

The simplest type of exponential fit involves placing an exponential function between two points. Suppose it is required to determine the

variation of velocity between depths j and $j+1$ along a time-like coordinate line s. Using Equation (A-7), the velocities $w_{i(j+1)}$ and w_{ij} are obtained. The equation must then satisfy the following constraints.

$$\begin{aligned} w_{ij} &= e^{(a+bz'_j)} \\ w_{i(j+1)} &= e^{(a+bz'_{j+1})} \end{aligned} \tag{A-27}$$

The constants a and b are unknown and z'_j and z'_{j+1} are the depth values at depths j and $j+1$. The equation can be solved for a and b by taking the log of both sides of the equation.

$$\begin{aligned} \log w_{ij} &= a + bz'_j \\ \log w_{i(j+1)} &= a + bz'_{j+1} \end{aligned} \tag{A-28}$$

Solving for a and b produces the following

$$a = \frac{z'_{j+1} \log (w_{ij}) - z'_j \log (w_{i(j+1)})}{(z'_{i+1} - z'_i)} \tag{A-29}$$

$$b = \frac{\log (w_{i(j+1)}) - \log (w_{ij})}{(z'_{i+1} - z'_i)} \tag{A-30}$$

Knowing the constants a and b, the velocity $w(z')$ is solved from the relation

$$w(z') = e^{(a+bz')} \qquad (z'_{j+1} \leq z' \leq z'_j) \tag{A-31}$$

A special problem arises when the velocities are negative or change sign between depths. In the case of negative velocities w_{ij} and $w_{i(j+1)}$ in Equation (A-29) and (A-30) are replaced by absolute values and the sign of the right hand side of Equation (A-31) is made negative instead of positive. In the case where the velocity changes sign a new velocity term $w'(z')$ is defined by adding or subtracting from $w(z')$ a constant equal to twice the absolute value of the velocity at the lower depth point.

$$w'(z') = w(z') \pm 2|w_{i(j+1)}| \qquad \text{(A-32)}$$

For instance if $w(z'_j)$ is negative and $w(z'_{j+1})$ is positive then $2|w_{i(j+1)}|$ is subtracted from $w(z')$ to compute $w'(z')$. $w(z'_{j+1})$ would then be equal to $-w_{i(j+1)}$. The experimental interpolation is computed in terms of $w'(t')$ which always has the same sign. $w(z')$ is calculated from $w'(t')$ by appropriately adding or subtracting the constant $2|w_{i(j+1)}|$ from $w'(z')$.

$$w(z') = w'(z') \mp 2\, w_{i(j+1)} \qquad \text{(A-33)}$$

The selection of the constant $2|w_{i(j+1)}|$ is arbitrary but is not a critical one since sign changes in velocity occur at late times in the velocity histories where soil motions are not critical in determining loading slopes of the soil stress-strain behavior.

To extrapolate velocities to the surface, the velocity records of the two shallowest depths must be used. The only piece of information available at the surface is the time of the start of the pressure loading. The first s label line at s=0 can then be drawn from the first depth to this point at the surface. The s label at s=1 should fall no more than a millisecond behind the label for s=0 since the rise time of the blast loading is very short. The s labels falling after s=1 can be extended up to the surface based on their slope between the two shallowest depths. These considerations are illustrated in Figure (A-2).

Having established the s coordinates for extrapolating the velocity, it remains to establish how the velocity varies in the upper layer of soil. The recommended approach is to simply extend the exponential velocity fit between the two shallowest depths. If the exponential form of the function has a physical basis then this form ought to be the best possible to use given no other information about the velocity in this

region. In a similar manner the two lowest depths with data are used to extrapolate down below the region where information is available.

The velocity time history for all times and depths is thus obtained by three fundamental steps. First, a coordinate transformation between z,t and z',s coordinates is established where certain s values relate to particular features of the velocity-time record. Second, a set of cubic Lagrangian velocity functions are established at each depth to fit a set of velocity records using a least square error criteria. Third, an exponential function is used to extrapolate velocity values from the Lagrangian function along lines of constant s between depths where the velocity functions are defined.

Apoendix II - Notation

The following symbols are used in this paper:

$a_{i1}, a_{i2}, a_{i3}, a_{i4}$ = time-like s coordirate locations within interpolation segment i.

a, b = Unknown constants in the evaluation of the exponential function used to interpolate between depths.

c_{ij} = coefficients of set of linear equations used in least square solution for v_{ijk}.

$d_o(t)$ = shallowest depth at time t where soil motion and stress due to soil motion are zero.

$E_{jk}(s)$ = error between velocity record j at depth k and Lagrangian interpolation function for time-like coordinate s.

$f(z,t)$ = function defining time like coordinate s in terms of z and t.

$g(z',s)$ = function defining time t in terms of z' and s.

$h_{i1}, h_{i2}, h_{i3}, h_{i4}$ = components of Lagrangian interpolation functions $w_{ij}(s)$.

n_i = the number of records at depth i.

p = pressure at surface

s = time-like coordinate that remains constant with depth for particular features of the velocity response history.

s_i, s_{i-1} = time-like coordinates at the beginning and end of interpolation segment i.

t = time

$\bar{t}(z_i, s)$ = the average time of characteristic point s for depth z_i.

$t_j(z_i, s)$ = the time of characteristic point s for depth z_i and record j.

u_z = displacement in vertical direction (positive direction is up).

$V_{jk}(s)$ = velocity of record j and depth k for time-like coordinate s.

Appendix II - Notation (continued)

v_t = velocity in vertical direction (positive direction is down).

$v_{ij1}, v_{ij2}, v_{ij3}, v_{ij4}$ = velocity values used with Lagrangian interpolation function for interpolation segment i at depth j.

$w_{ij}(s)$ = Langrangian interpolation function written in terms of time-like coordinate s for interpolation segment i at depth j.

x = vertical coordinate (positive direction is down) [(x,t) coordinate system].

x' = vertical coordinate (x',s) coordinate system

ρ = soil density

σ_z = normal stress in z direction (tensile stress is positive).

Appendix III - References

1. Zelasko, J. S., "Sensitivity of MX-Relevant Vertical Ground Shock Environments to Depth to Groundwater and Soil Compressibility Variations", U.S. Army Engineer Waterways Experiment Station, April, 1980.

2. Jackson, A. E., et al, "Ralston Valley Soil Compressibility Study: Quick-Look Report for DISC Test I", U.S. Army Engineer Waterways Experiment Station Structures Laboratory, Vicksburg, Mississippi, May, 1981.

3. Grady, D. E., et al, "In Situ Constitutive Relations of Soils and Rocks", DNA 3671Z, SRI International, Menlo Park, California, March, 1974.

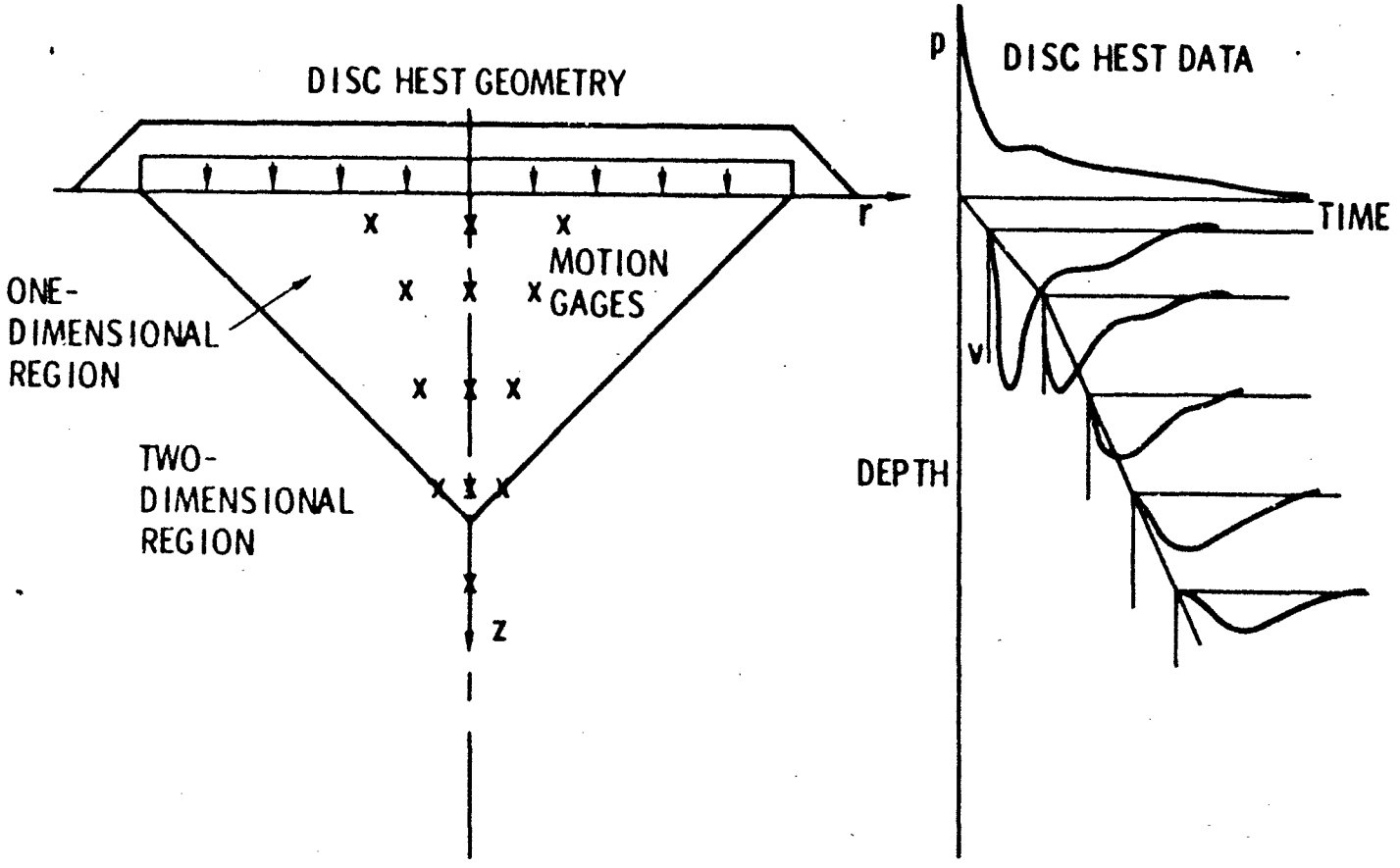

Fig. 1.-DISC HEST Test

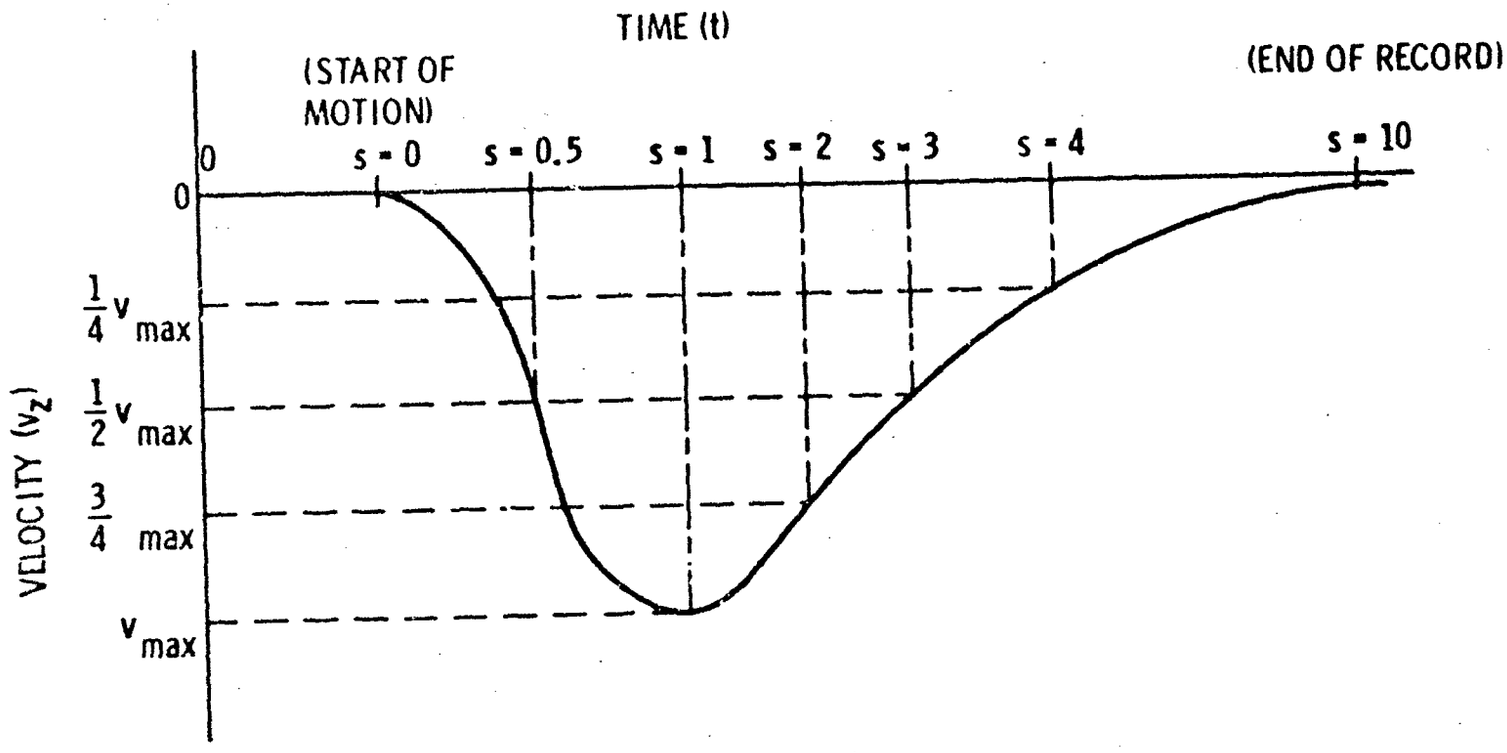

Fig. 2.-Typical Velocity versus Time Response

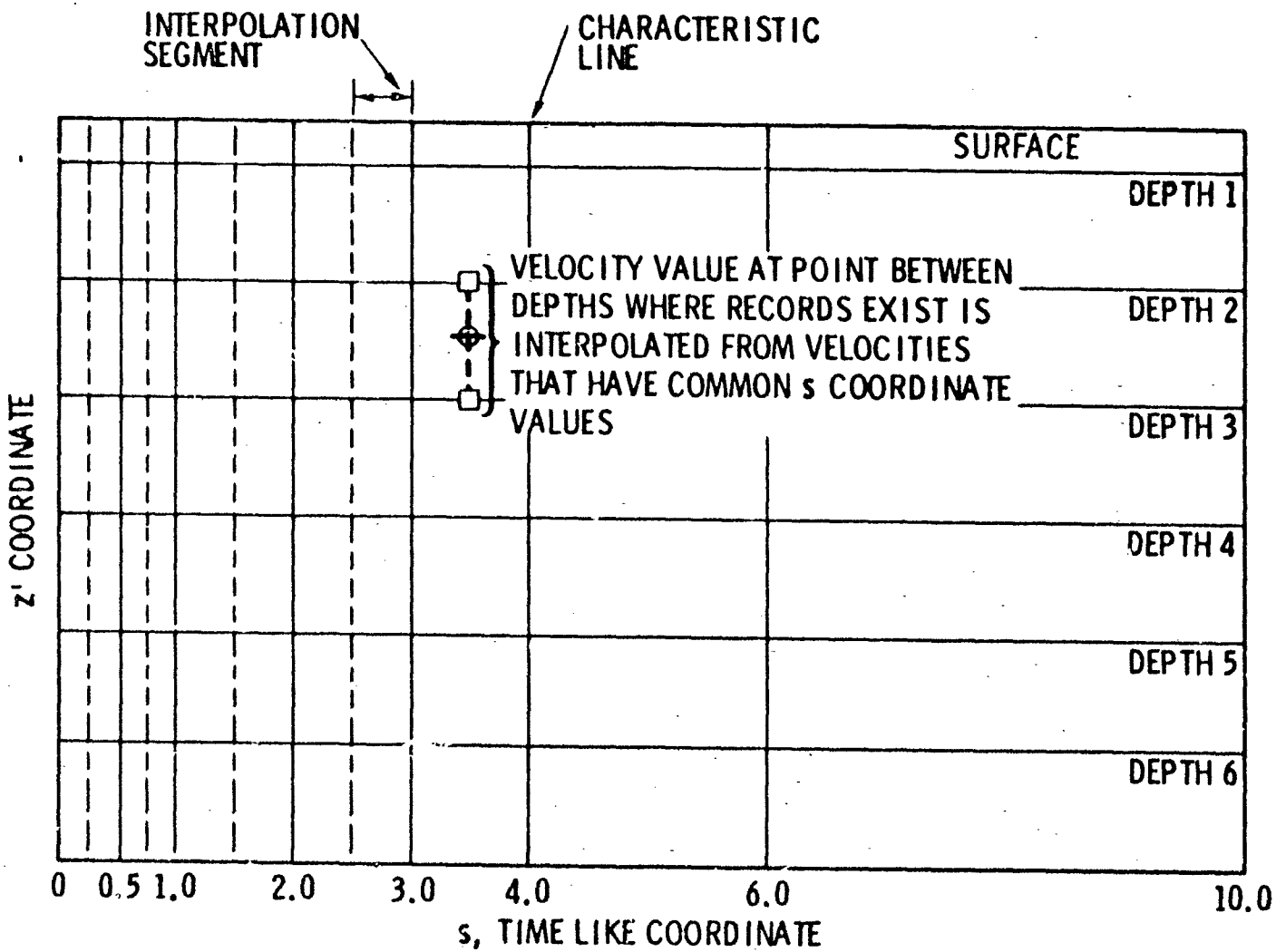

Fig. 3.-z', s Coordinate Space with Interpolation Segment Boundaries

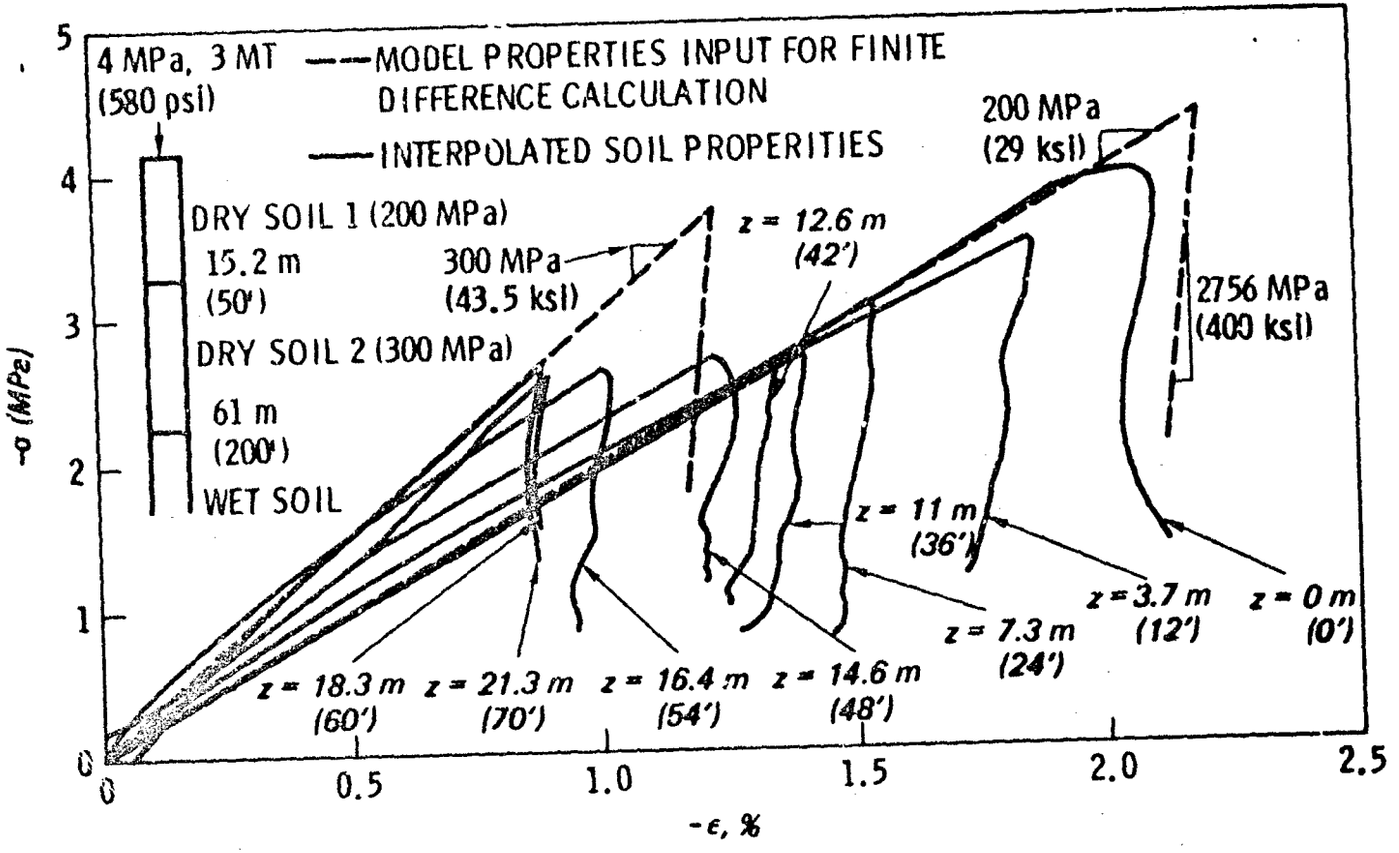

Fig. 4.-Comparison of Results for Layered Bilinear Material

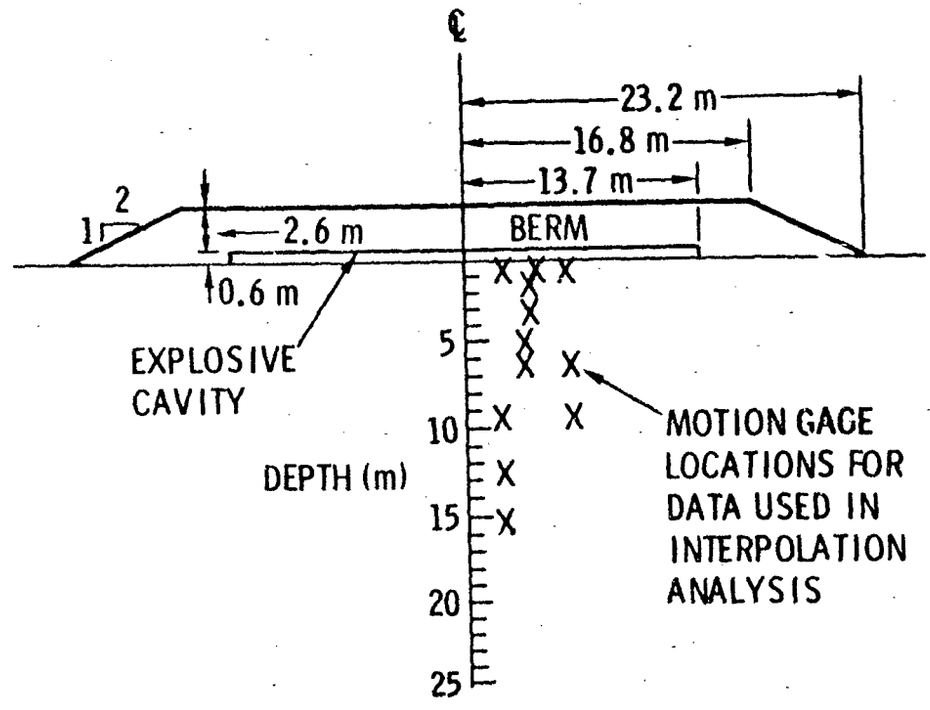

Fig. 5.-DISC HEST Test I

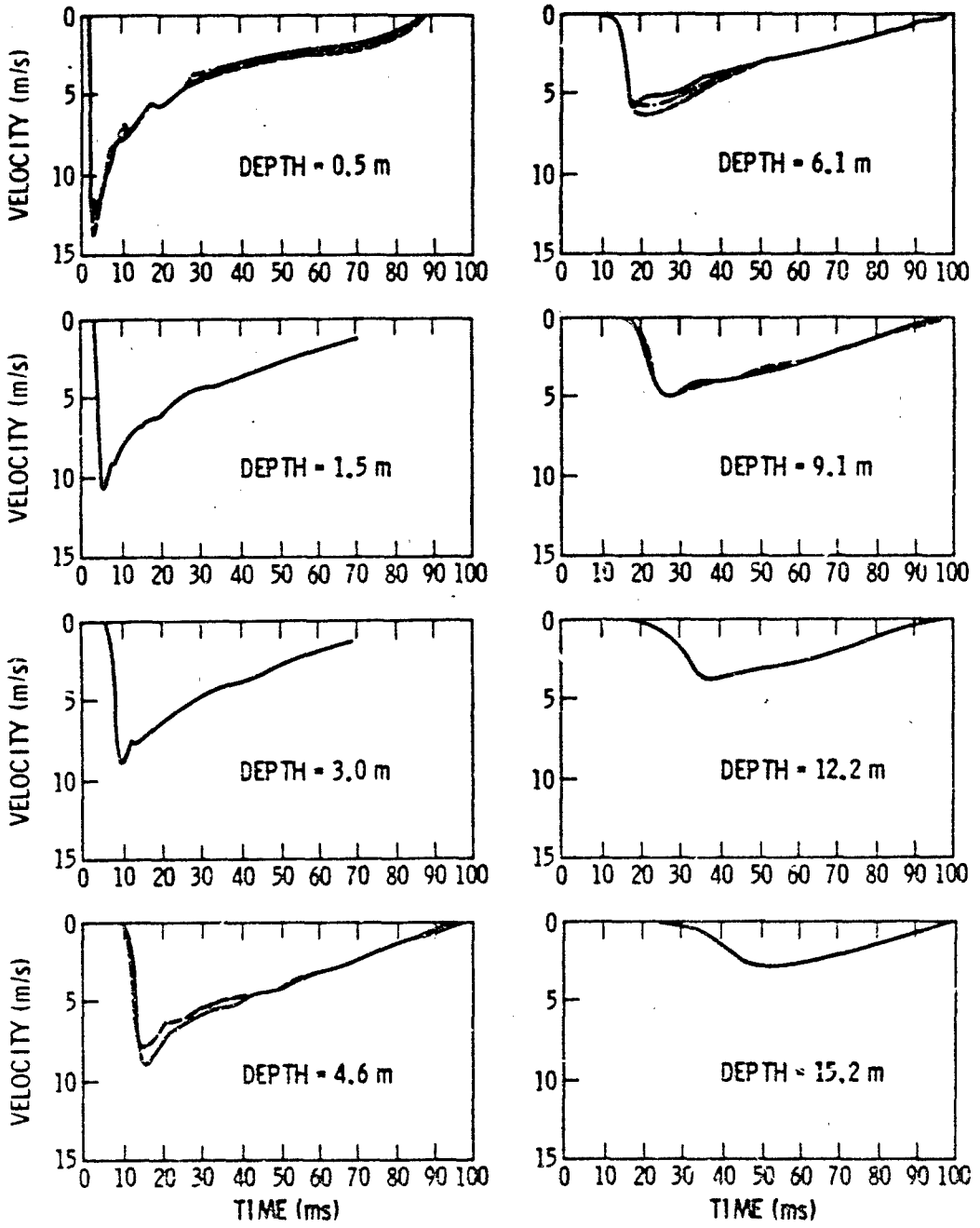

Fig. 6.-Velocity Records for DISC HEST Test I Analysis

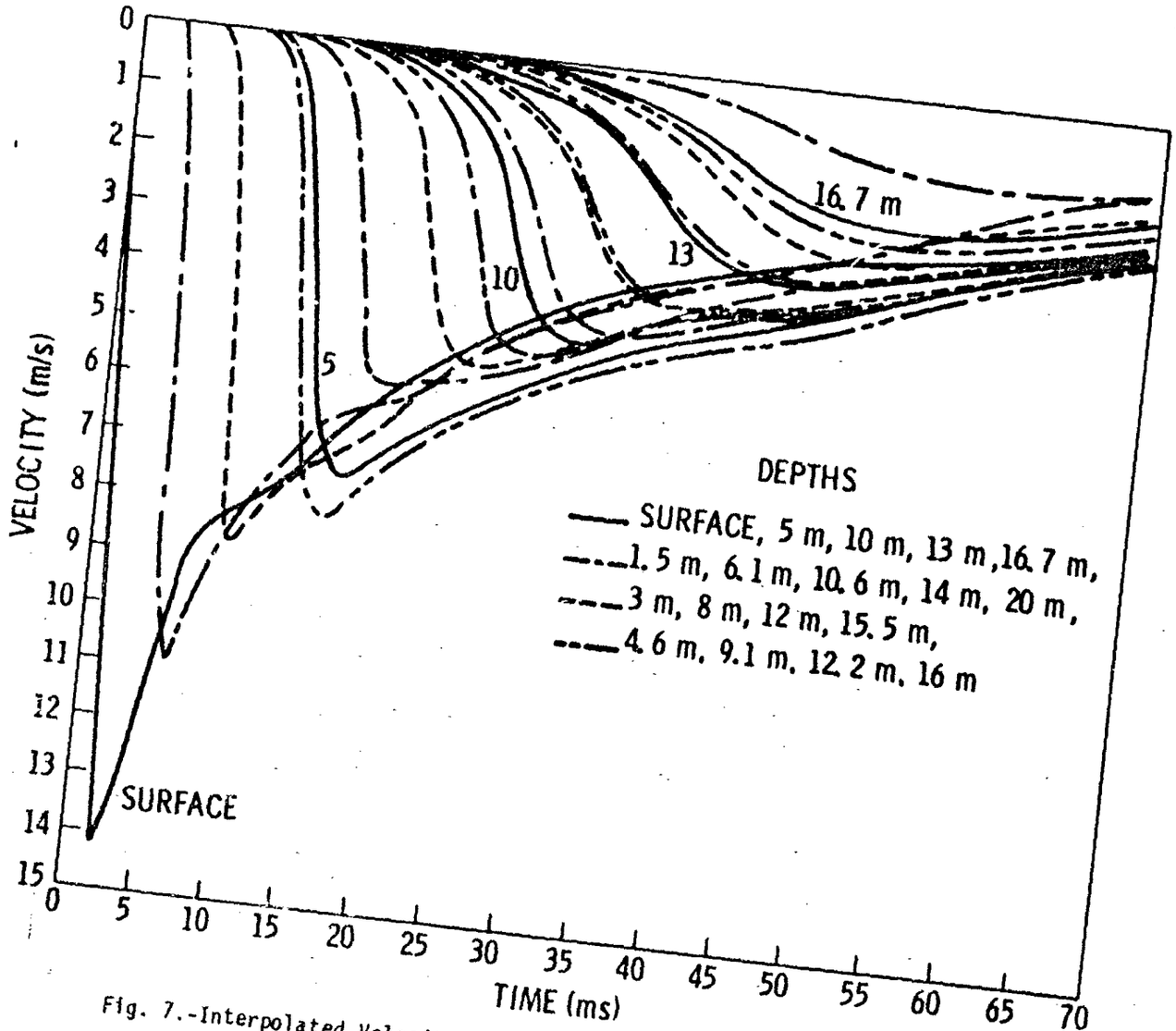

Fig. 7.-Interpolated Velocity History for DISC HEST Test I Analysis

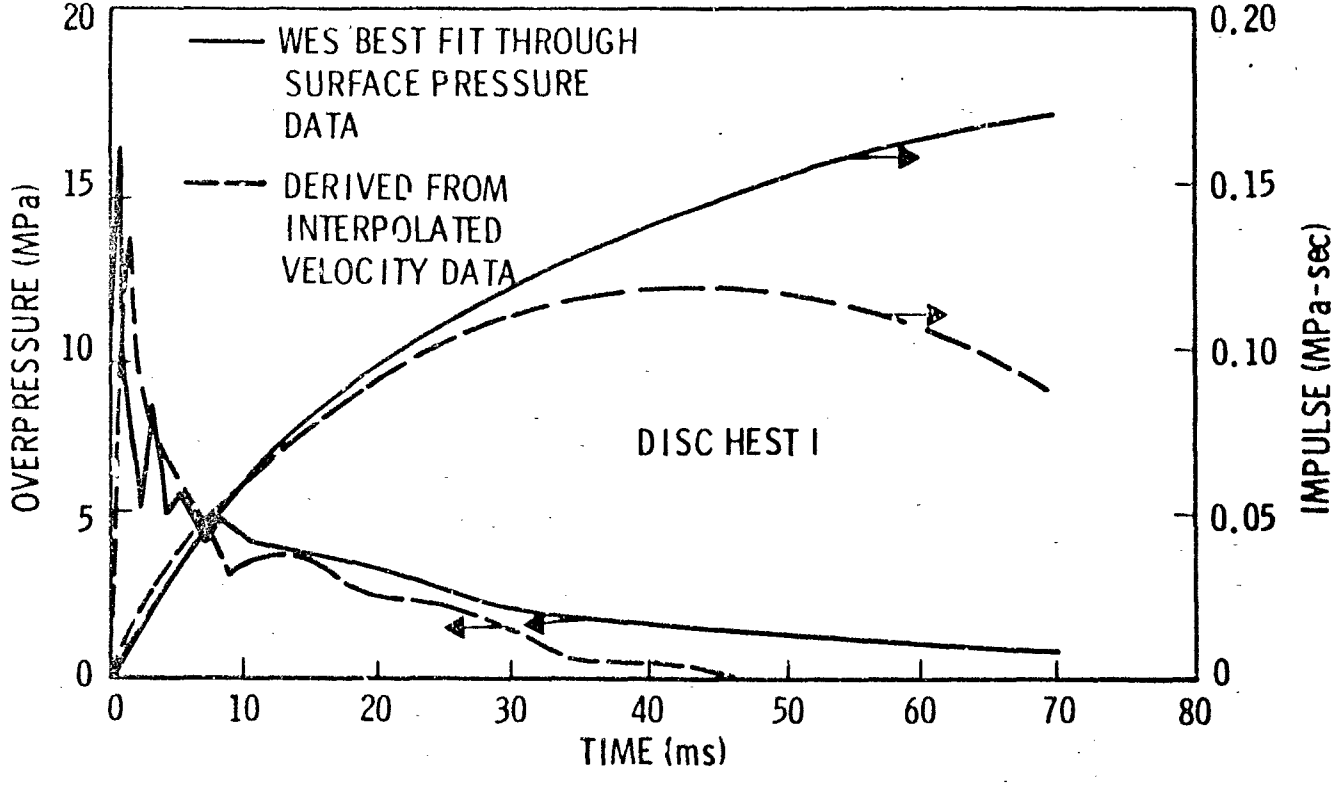

Fig. 8.-Surface Pressure and Impulse Comparison

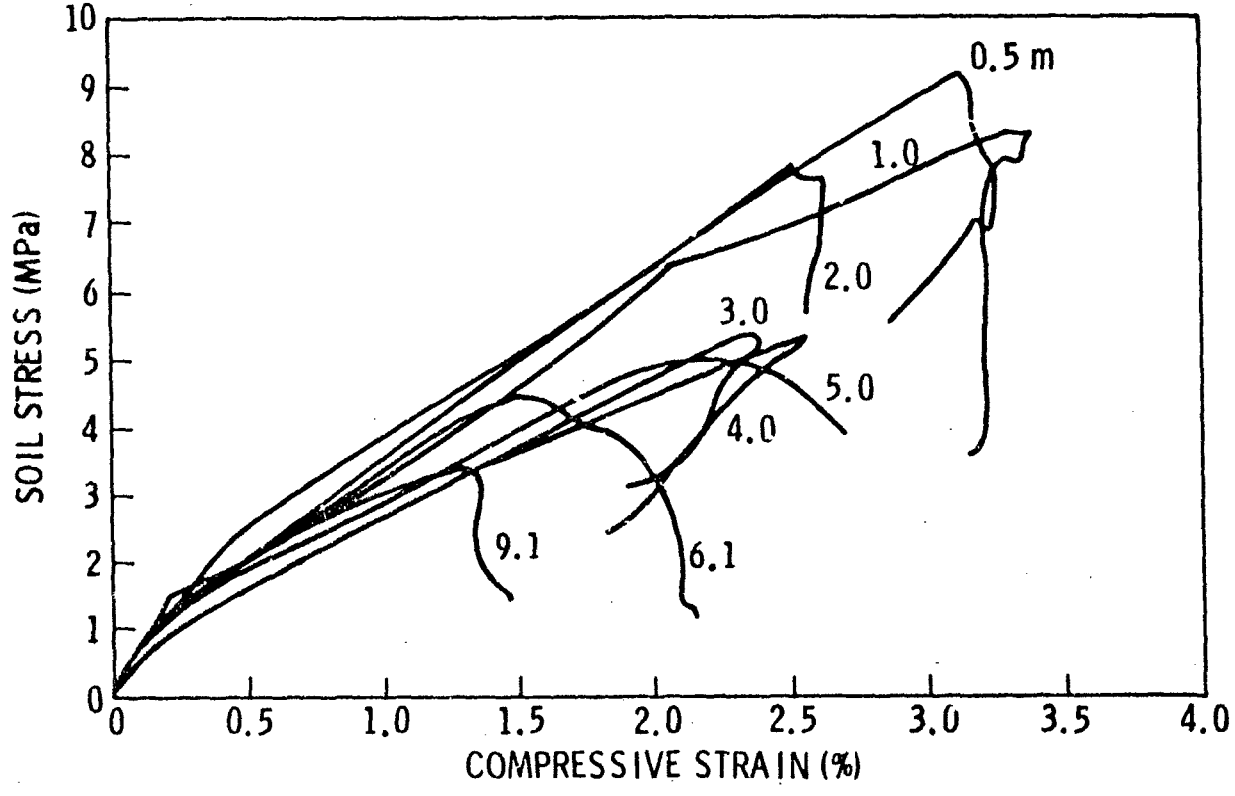

Fig. 9.-Soil Stress-Strain Histories for DISC HEST Test I

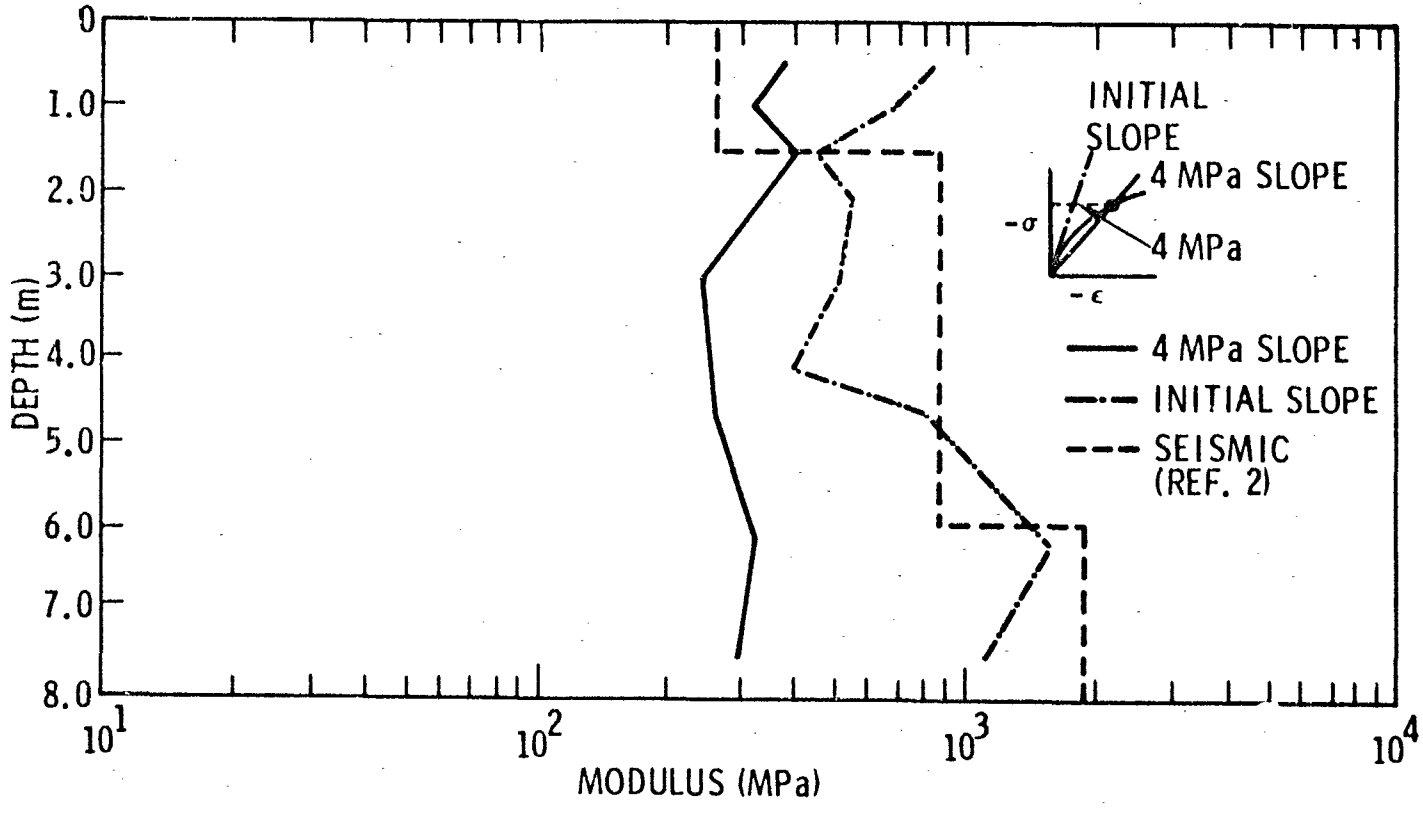

Fig. 10.-Soil Modulus versus Depth

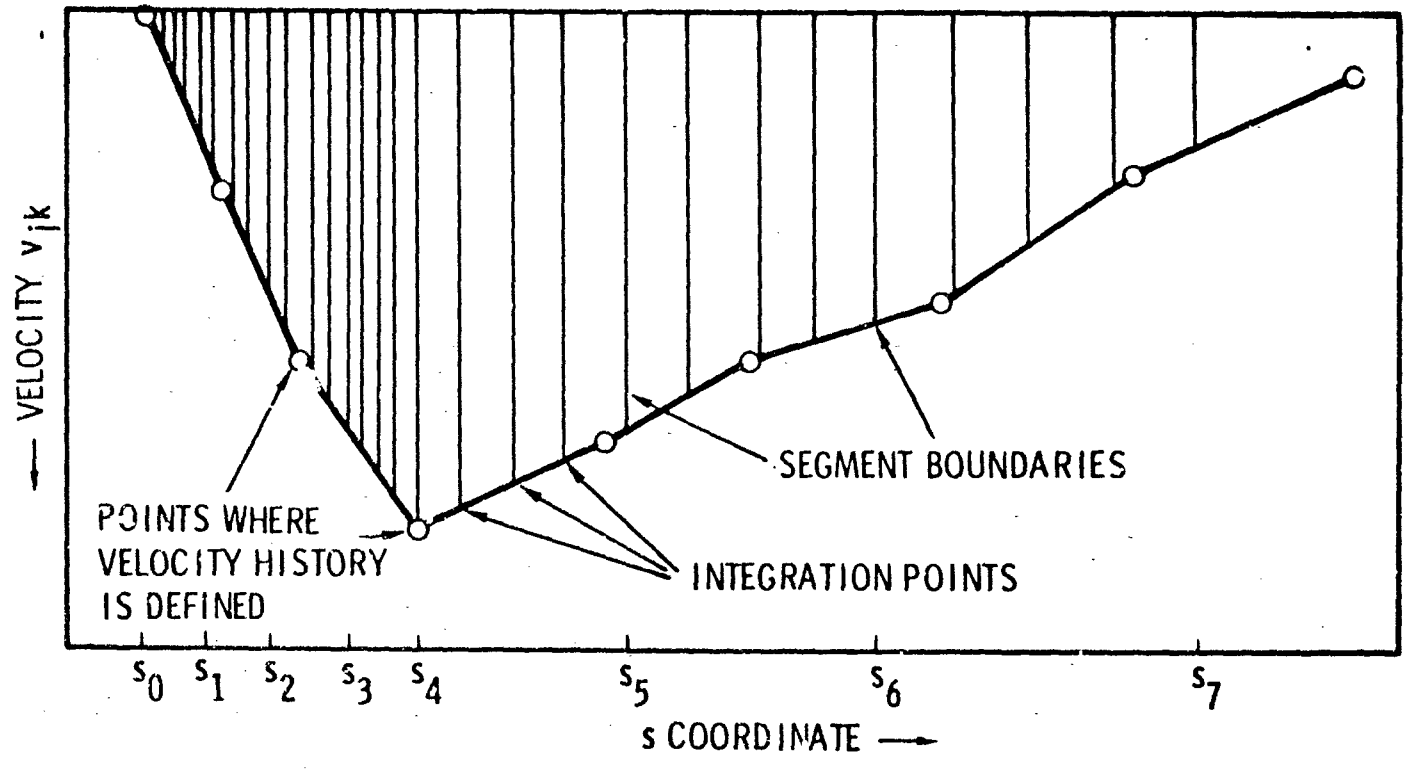

Fig. A-1.-Piecewise Definition of Velocity History

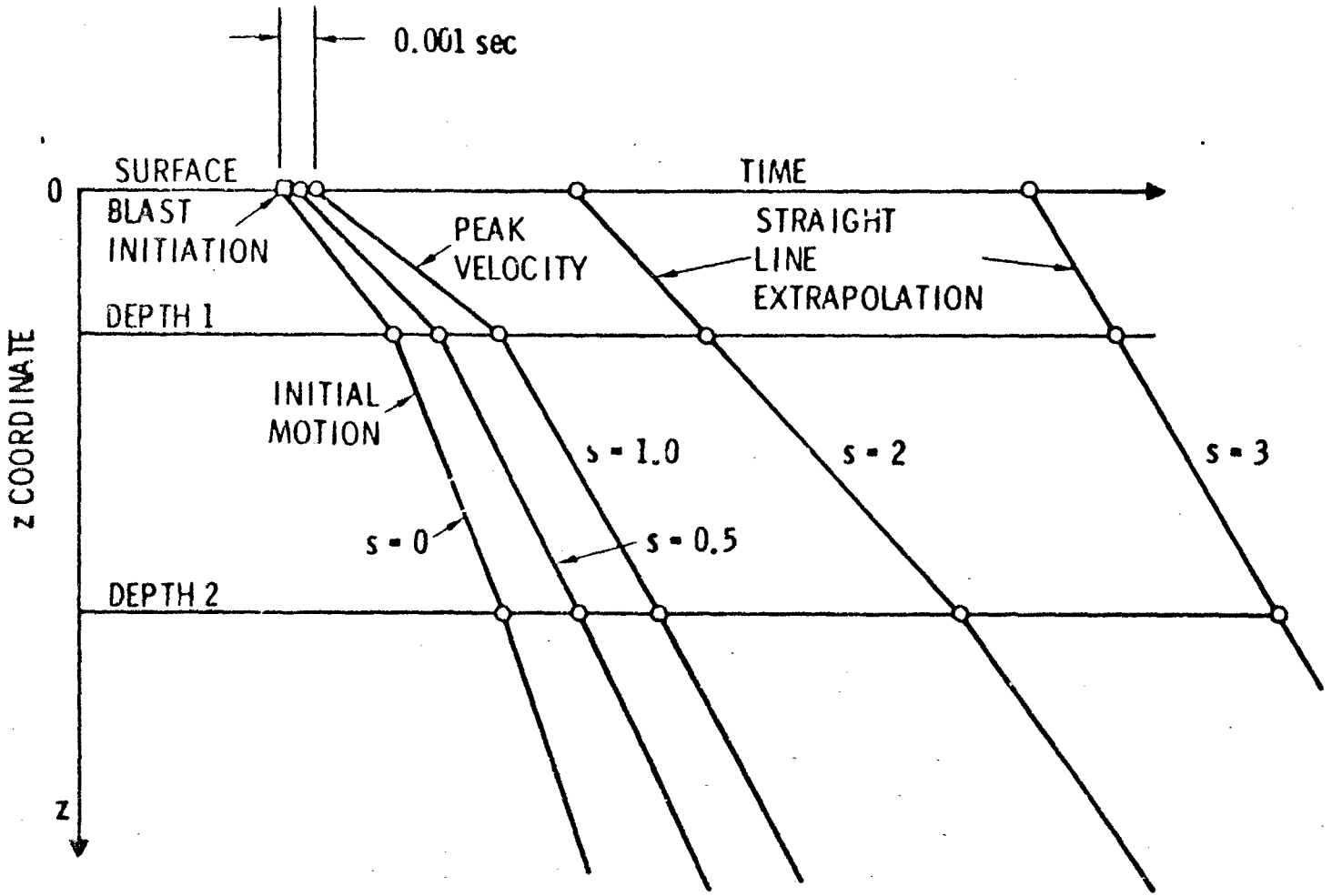

Fig. A-2.-s Label Configuration Between Surface and Shallowest Depths